NASA Contractor Report 187198

Probabilistic Structural Analysis Methods (PSAM) for Select Space Propulsion System Components (4th Annual Report)

Southwest Research Institute
San Antonio, Texas

October 1991

Prepared for
Lewis Research Center
Under Contract NAS3-24389

National Aeronautics and
Space Administration

TABLE OF CONTENTS

TABLE OF CONTENTS
(Continued)

TABLE OF CONTENTS
(Continued)

TABLE OF CONTENTS
(Continued)

TABLE OF CONTENTS
(Continued)

LIST OF TABLES

LIST OF TABLES
(Continued)

LIST OF FIGURES

LIST OF FIGURES
(Continued)

LIST OF FIGURES
(Continued)

LIST OF FIGURES
(Continued)

LIST OF FIGURES
(Continued)

1.0 PROJECT OVERVIEW

1.1 Introduction

The current report summarizes the fourth year of technical developments on the NESSUS system for Probabilistic Structural Analysis Methods. The described FY'88 effort focused on the continued expansion of the Probabilistic FEM code, the implementation of the Probabilistic Boundary Element Method (PBEM), and the implementation of the Probabilistic Approximate Methods (PAppM) code.

The team for this past year's effort included the following individuals and organizations:

SwRI:	Dr. T.A. Cruse Dr. O.H. Burnside Dr. Y.-T. Wu Dr. S.T. Raveendra Dr. S.V. Harren Dr. R.C. McClung Mr. H.R Millwater Ms. J.P. Buckingham
Consultant:	Mr. J.B. Dias
University of Arizona:	Prof. P. Wirsching Mr. Y. Torng
Rocketdyne:	Dr. K.R. Rajagopal

The report focuses on changes and additions to the NESSUS system, and does not cover the work performed prior to FY'88; that work are covered in the previous versions of this annual report.

1.2 Summary of Major FY'88 Accomplishments

The principal focus for the PFEM code in FY'88 was the addition of a multilevel structural dynamics capability. The strategy employed for the structural dynamics code was developed by Dr. James Unruh at SwRI, including consultations with the staff at Rocketdyne. The strategy includes a Level 0 model (probabilistic loads), Level 1 (parametric treatment of material, geometry uncertainty), and Level 2 (full probabilistic variables). The details of these levels is covered in Chapter 3. The implementation details within the FEM package are covered in Chapter 2.

The probabilistic methods research is reported in Chapter 4. The focus of this work was to further validate the Fast Probability Integration algorithm, developed by Dr. Wu of SwRI, and to introduce the integrated FPI/Monte Carlo capability. The addition of Monte Carlo meets the contract requirement for two independent probability methods in NESSUS.

Chapter 5 is concerned with the NESSUS/EXPERT module. The EXPERT module is to address critical issues of the user interface for NESSUS. Continued effort was devoted to the menu structure, error checking, and HELP file portions of NESSUS/EXPERT. Extension of EXPERT to include the probabilistic variables was made in FY'88. The users continue to acquire applications knowledge for additions to the rule base of NESSUS/EXPERT.

Chapter 6 addresses the significant amount of work performed on the Probabilistic Boundary Element Code (PBEM) to add it to the NESSUS framework. Particular focus was given to the use of domain integration methods that reduce the domain integral to "equivalent" boundary integrals. These were implemented for thermal and steady-state dynamic loading, inhomogeneous material properties and plasticity.

Four additional validation problems were completed in FY'88, and are reviewed in Chapter 7 and Appendix F. The validation results continue to demonstrate the robust character of the NESSUS code over a wide range of analysis types.

Rocketdyne reports in Chapter 8 on the extensive verification work accomplished on Problem 1 (Turbine Blade) and Problem 2 (Oxidizer Duct). Both application focused on structural dynamics issues; the first for normal mode vibration, and the second for forced, random vibration. Experimental data existed for the first problem and showed good confirmation of the NESSUS predictions.

One of the potentially-powerful tools developed within the NESSUS framework are the approximate methods. These methods show promise for giving a quick understanding of what design variables are driving the uncertainty in system response variables. The applications problems and the technical approach are outlined in Chapter 9.

The Level 3 stochastic thermoviscoplastic material model development is summarized in Chapter 10. The elements of the algorithm are developed in a generalized manner, and implemented for elasticity + creep, with void growth failure. Application of probabilistic methods to history dependent problems such as this require special attention to account properly for the history dependence of the subject problem.

Significant contributions on the Reliability Methods used in PSAM have been prepared by the University of Arizona (under the direction of Prof. Paul Wirsching) are included in the Appendices. Validation studies for approximate methods are also included. A special study of the efficiency and functioning of the NASA-sponsored BEST3D code is summarized in Appendix H.

1.3 Future Effort

FY'89 is the final year of the current technical effort. The code development effort will be completed and documented. The full nonlinear material and geometric features will be implemented. Application of the NESSUS code will be made to the oxidizer post (creep) and the transfer duct (large deflection) problems.

The next major FEM code delivery is expected to be in February of 1989. Final FEM coding will be done in May. The verification studies for the PBEM and PAppM codes will be completed.

Continued effort into FY'90-'92 has been proposed. The principal focus of that effort is on the development of a comprehensive package for full reliability evaluation. Damage state, failure criteria, and probabilistic structural analysis models will have to be combined.

1.4 Publications

The following papers and presentations were accomplished during the past year:

1. "Designing for an Uncertain World," T.A. Cruse, accepted by Aerospace America.

2. "Validation of the NESSUS Probabilistic Finite Element Analysis Computer Program," Y.-T. Wu and O.H. Burnside, 29th AIAA/ASME/ASCE/AHS/ASC Structures, Structural Dynamics, and Materials Conference, Williamsburg, Virginia, April 18-20, 1988.

3. "NESSUS/EXPERT - An Expert System for Probabilistic Structural Analysis Methods Methods," H.R. Millwater, K. Palmer, and P. Fink, 29th AIAA/ASME/ASCE/AHS/ASC Structures, Structural Dynamics, and Materials Conference, Williamsburg, Virginia, April 18-20, 1988.

4. "Efficient Probabilistic Structural Analysis Using an Advanced Mean Value Method," Y.-T. Wu and O.H. Burnside, 1988 ASCE Specialty Conference, Virginia Polytechnic Institute and State University, Blacksburg, Virginia, May 25-27, 1988.

5. "Probabilistic Methods for Structural Response Analysis," Y.-T. Wu, O.H. Burnside, and T.A. Cruse, ASME Symposium on Computational Probabilistic Methods, UC-Berkeley, California, June 20-22, 1988. (Also pending publication in COMPUTATIONAL METHODS OF RELIABILITY ANALYSIS, edited by Wing Kam Liu and Ted Belytschko, Elmepress International).

6. "Probabilistic Structural Analysis Methods and Applications," T.A. Cruse, J.B. Dias, and K.R. Rajagopal, Symposium on Advances and Trends in Computational Structural Mechanics and Fluid Dynamics, Washington, DC, October 17-19, 1988.

7. "Probabilistic Structural Analysis for Advanced Space Propulsion Systems," T.A. Cruse, J.F. Unruh, Y.-T. Wu and S.V. Harren. Submitted to the 24th International Gas Turbine Conference, ASME.

A bound volume of this and other PSAM related material has been forwarded to the NASA Program Manager.

2.0 NESSUS FINITE ELEMENT CODE DEVELOPMENT

2.1 Introduction

The NESSUS finite element code is being developed within the framework of the probabilistic structural analysis (PSAM) development effort, coordinated by Southwest Research Institute for the NASA Lewis Research Center. The main objective of this effort is the development of advanced probabilistic structural analysis methods, which combine the versatility of modern finite element methods with the latest developments in the areas of probabilistic modeling and structural reliability.

2.1.1 Status at the End of FY'87

Much of the development effort during FY'87 was geared towards providing more sophisticated analysis capabilities for dealing with complex engineering problems. The major development tasks included:

- Extension of the iterative perturbation algorithms for linear elastostatics to a three field mixed-iterative finite element formulation.
- Development of a consistent strategy for tracking several perturbations across multiple increments of static loading.
- Extension of the stochastic eigenvalue capability to account for random initial stress fields and the associated stress-stiffening effects.
- Development of a new family of continuum-type finite elements based on independent strain interpolation.
- Development of finite deformation algorithms for handling deterministic problems involving geometric nonlinearities.
- Extended facilities for database manipulation and management.

By the end of FY'87 the NESSUS finite element code offered sophisticated modeling capabilities for handling a wide range of probabilistic elastostatic and eigenvalue problems. NESSUS 2.5 was released to the members of the PSAM team in September '87 and was being exercised on several validation and verification problems by the end of FY'87. This version supported the ability to carry perturbation results across multiple static load increments, and to perform dynamic eigenvalue problems using the initial stress field computed at any one of these increments. This version also included a full library of continuum elements based on independent strain interpolation. The ability to perform elastostatic analysis for the perturbed problem using either the displacement method or the mixed-iterative formulation was fully supported in this version of the code.

2.1.2 Code Deliveries in FY'88

Linear dynamics problems were the focus of much of the development effort in the NESSUS finite element code during FY'88. Other significant developments included buckling problems, Level 1 analysis and transient dynamics.

NESSUS 2.6 was released to the members of the PSAM development team in December '87. This version included an alternate algorithm for the solution of the perturbed dynamic eigenvalue problem, allowing the computation of accurate results in problems where the available number of unperturbed modes is inadequate for the use of a perturbation expansion series.

NESSUS 2.7 was released to the members of the PSAM team in January '88. This version introduced the ability of solving stochastic linearized buckling eigenvalue problems for structures with uncertain geometric imperfections, material properties and load patterns.

NESSUS 3.0 was released to the members of the PSAM team in May '88. This version included an extensive redesign of the harmonic and random vibration capabilities, support for the extended database format, and the ability to perform probabilistic harmonic and random vibration analyses for uncertain structural systems subjected to uncertain loading environments.

NESSUS 3.1 was released to the members of the PSAM team in August '88. This version included the Level 1 perturbation post-processor, together with a more closely integrated implementation of the FPI analysis module. A new automated frequency band discretization scheme to facilitate input definition for random vibration analysis was also introduced in this version.

The development of a perturbation strategy for transient elastodynamics was nearing completion by the end of FY'88. However, this capability is not yet available in the released version of the NESSUS finite element code.

2.1.3 Operating Systems

Special versions of the NESSUS finite element code have been developed to support a number of different operating systems. NESSUS 3.1 is currently available under the following widely used operating systems:

- The VAX/VMS™ Operating System.
- A standard UNIX™ version using Berkeley 4.2 extensions.
- The CRAY/COS™ Operating System.
- The CRAY/UNICOS™ version of UNIX™.

The NESSUS finite element code is written in standard FORTRAN-77. In order to enhance portability, all system-dependent functions are intentionally encapsulated in a small set of system routines which must be customized for the individual operating system. These system-dependent routines perform tasks such as obtaining the calendar date and time, keeping track of central processor usage ("computer time"), and controlling file opening and closure.

A set of command procedures and editor scripts used to generate customized versions of the NESSUS finite element code for different operating systems has also been developed. These utilities are written in the DCL™ command language and run under the VAX/VMS™ Operating System [1].

2.2 Buckling Analysis of Uncertain Systems

Structural stability (buckling) problems are well-known to exhibit a great degree of sensitivity to initial imperfections in the geometry, the boundary conditions and the imposed load pattern. As these imperfections may result from fabrication tolerances, initial straining during assembly, and even from damage incurred during storage and transport of the components, the nature and distribution of these imperfections is rarely the same for all samples, and very often can only be described in statistical terms.

Although the effects of initial imperfections are more clearly observed in a formal finite deformation nonlinear buckling analysis, the study of a simpler linearized buckling eigenvalue problem often provides a good first-order approximation to the behavior of the real structure. Therefore, the solution of the stochastic version of the linearized buckling eigenvalue problem for random initial imperfections remains a more cost-effective way to provide useful engineering information on the buckling behavior of real structures.

Typical perturbation methods for linearized eigenvalue problems [2,3] are based on regular perturbation expansions of the perturbed eigenvalues and eigenvectors in terms of the solution to the unperturbed eigenproblem. The objective is to obtain a *linear combination* of the unperturbed modes which is, in some sense, close to the solution of the perturbed problem. A key assumption for this class of methods is that the set of unperturbed modes must be sufficiently "rich" to adequately represent a "good" approximation to the solution of the perturbed eigenproblem.

VAX/VMS and CDL are trademarks of Digital Equipment Corporation.
UNIX is a trademark of AT&T Bell Laboratories.
CRAY/COS and UNICOS are trademarks of Cray Research, Inc.

This assumption is not overly restrictive when dealing with typical dynamic eigenvalue problems, in which a sufficiently large number of unperturbed modes are usually available. By contrast, in a standard buckling eigenvalue problem, only the lowest mode (or at most a few of the lowest modes) are of practical interest to the analyst. As a result, the available set of unperturbed modes is hardly adequate for the use of a perturbation expansion approach.

The strategy adopted in the NESSUS finite element code for the solution of the perturbed linearized buckling eigenvalue problem amounts to a "smart" subspace iteration re-solution of the perturbed problem. With this approach, the converged vectors for the unperturbed problem are used as the initial trial vectors for subspace iteration with the perturbed system. Because the unperturbed vectors typically represent a "good guess" to the actual mode shapes of the perturbed system, the subspace iteration algorithm will tend to converge on the exact solution to the perturbed problem with a reduced number of subspace iterations. Although this strategy cannot avoid the re-factorization of a large stiffness matrix at every perturbation, it allows very accurate computation of the solution the perturbed problem even when only one unperturbed buckling mode is available.

This strategy was first implemented in NESSUS 2.6 as an optional algorithm for solving dynamic eigenvalue problems when the number of unperturbed modes is insufficient for the use of a perturbation expansion approach. The ability to solve stochastic linearized buckling eigenvalue problems using this approach was first introduced in NESSUS 2.7. The present implementation allows some flexibility regarding the choice of the initial stress field used to construct the geometric stiffness matrix for the perturbed buckling problem, which can be obtained using either a displacement-based or mixed-iterative stress recovery procedure.

2.3 Revised Linear Dynamics Capability

Methods of linear dynamics based on mode superposition techniques are widely used in aerospace applications for predicting the response of elastic structures subjected to harmonic and random excitations. These results are particularly useful for the estimation of low and high-cycle fatigue life of components exposed to severe vibration environments.

The ability to perform basic harmonic and random vibration analyses for deterministic structures has been available in the NESSUS finite element code since version 1.0. However, a review of the existing code capabilities by Rocketdyne in the Winter of '87 indicated the desirability of developing a more sophisticated analysis capability. The desired enhancements included:

- A more flexible and general input format for linear dynamics.
- The ability to include multiple cases of harmonic and random excitation within a single computer run.

- Presentation of harmonic excitation results in terms of real and imaginary components and/or phase and amplitude information.
- Harmonic base excitation input in terms of acceleration, not displacement.
- Random base excitation input also in terms of acceleration.
- An extended perturbation database format allowing for combination of different dynamic response cases as a post-processing operation.

The Rocketdyne recommendations were reviewed by SwRI and incorporated in a specification for an extended linear dynamics capability in the NESSUS finite element code. This revised linear dynamics capability was first offered in NESSUS 3.0. One further enhancement, the automated frequency band discretization scheme, was added in NESSUS 3.1.

2.3.1 Harmonic Excitation Problems

The revised linear dynamics capability allows for the analysis of an arbitrary number of harmonic excitation cases at multiple driving frequencies. Each harmonic excitation case consists of a single or multiple point excitation at a prescribed driving frequency, with the amplitude and phase of the excitation specified individually at the nodes. These excitations can be of three types:

- Harmonic point load excitations.
- Harmonic base accelerations.
- Harmonic nodal pressure excitation.

Harmonic point load excitations are sinusoidal forces of the form

$$f_j(\omega) = \bar{f}_j \; e^{i(\omega t - \phi_j)} \tag{2.1}$$

where $\bar{f}_j$ is the amplitude and ϕ_j the phase of the excitation at a frequency ω. These loads are applied at the nodes of the finite element model, and can have active components in one or more spatial directions. Both the amplitude and phase of the excitation may be different for each component. Harmonic base excitations are prescribed sinusoidal base accelerations of the form

$$\ddot{u}_j(\omega) = \bar{\ddot{u}}_j \; e^{i(\omega t - \phi_j)} \tag{2.2}$$

where $\bar{u}_j$ is the amplitude and ϕ_j the phase of the excitation at a frequency ω. These accelerations are also applied at the nodes of the finite element model, and can have active components with different phase and amplitude in each spatial direction. A penalty-type approach is used to impose prescribed base accelerations, which are then

converted to a set of equivalent nodal forces using D'Allembert's Principle. Harmonic nodal pressure excitation involves sinusoidal time-varying surface pressures of the form

$$G_{ij}(\omega) = \bar{f}_i \, \bar{f}_j \, \rho_{ij}(\omega) \, \mathrm{psd}(\omega) \qquad (2.3)$$

where $\bar{p}$, is the amplitude and ϕ, the phase of the excitation at a frequency ω. This option is only available for meshes of continuum-type elements, having well defined outward normals at each surface node. The harmonic pressures are specified over a list of surface nodes and act in the direction *opposite* to the outward normal at each node. The amplitude and phase of the pressure can be specified individually at each node, resulting in an arbitrary spatial pressure pattern which varies sinusoidally in time.

The output for each harmonic excitation case includes:

- The harmonic excitation frequency.
- The real and imaginary parts of the displacements.
- The real and imaginary parts of the strains.
- The real and imaginary parts of the stresses.

These quantities are sufficient to completely describe the harmonic response of the system at a given driving frequency. Additional response information, such as the amplitude and phase of a given response variable at a point, can easily be derived from these results with a simple post-processing operation. Many of the programs used to access data stored in the perturbation database are also capable of performing similar types of data reduction.

The results for each harmonic excitation case are computed separately and stored individually in the perturbation database. A number of different case combination rules can then be used for post-processing this information in order to obtain the desired low and high cycle fatigue life predictions.

2.3.2 Random Vibration Problems

The revised linear dynamics capability also included several enhancements to the random vibration drivers in the NESSUS finite element code. The newer versions of the code allow for the analysis of an arbitrary number of power spectrum excitation cases within a single run. Each power spectrum excitation case consists of a user-defined PSD profile, specifying the power of the excitation as a function of the frequency, a spatial distribution, indicating the location and intensity of the excitation, and an optional correlation model, which may or may not be frequency-dependent. This model is sufficiently general to describe *any* zero-mean Gaussian excitation which is *separable* in frequency and space, that is to say, which can

be modeled as the product of two functions: one defined over frequency, the other over space. There are three types of power spectrum excitations:

- o Random point load excitations.
- o Random base accelerations.
- o Random nodal pressure excitations.

Random point load excitations correspond to a forcing function which can be described by a one-sided spectral density function of the form

$$G_{ij}(\omega) = \bar{\ddot{u}}_i \; \bar{\ddot{u}}_j \; \rho_{ij}(\omega) \; \mathrm{psd}(\omega) \tag{2.4}$$

where $\bar{f}_i$ and $\bar{f}_j$ denote the local intensities of the random loading at nodes i and j, $\rho_{ij}(\omega)$ is the correlation between nodes i and j, and PSD (ω) represents the normalized power of excitation at frequency ω. These excitations may have active components in one or more spatial directions. Random base accelerations are described by spectral density functions of the form

$$G_{ij}(\omega) = \bar{p}_i \; \bar{p}_j \; \rho_{ij}(\omega) \; \mathrm{psd}(\omega) \tag{2.5}$$

where u_i and u_j denote the local amplitudes of the imposed base acceleration at nodes i and j, respectively. These excitations may have active components in one or more spatial directions. A penalty-type approach is used to impose the prescribed random base accelerations. Finally, random nodal pressure excitations are characterized by spectral density functions of the form

$$p_j(\omega) = \bar{p}_j \; e^{\,i\,(\omega t - \phi_j)} \tag{2.6}$$

where $\bar{p}_i$ and $\bar{p}_j$ denote the local magnitudes of the random pressure at nodes i and j, acting in the direction *opposite* to the outward boundary normal at the corresponding node. This option is only available for meshes of continuum-type elements, having well defined outward normals at each surface node.

Time-average mean square values of the response variables are obtained by integrating the one-sided spectral density of each response variable over a prescribed range of excitation frequencies. The current code implementation provides very fine control over the way these results are reported. By default, only the overall mean square results integrated over the entire range of excitation frequencies are reported. Alternatively, the user may chose to compute and store a set of partial mean square results, each

corresponding to a different range of excitation frequencies. This allows a greater flexibility in the way results from different power spectrum excitations are combined for the final post-processing phase.

The output for each excitation frequency range includes:

- The excitation frequency range.
- The mean square displacement values.
- The mean square strain values.
- The mean square stress values.
- The stress velocity values.

These values are computed separately for each frequency range of every power spectrum excitation case, and stored individually in the perturbation database as distinct spectral response cases. Different case combination rules can then be used for combining the results from different power spectrum excitations to obtain the desired low and high cycle fatigue life predictions.

2.3.3 Automated Frequency Band Discretization

The quality of the solution to a random vibration problem is very dependent on the accuracy of the integration of the spectral density of the response over the full range of excitation frequencies. This is particularly important in the analysis of lightly damped systems, which tend to exhibit very sharp response amplification "peaks" at the resonant frequencies. Very often these "peaks" account for much of the area under the spectral density function, and must therefore be integrated with extreme accuracy.

Closed-form solutions have been developed for a single degree of freedom oscillator subjected to idealized random excitations [1]. These results have been generalized to obtain *approximate* closed-form integrals for more realistic types of random excitation. However, for more complex structures subjected to very general random excitation, one must resort to methods of numerical integration.

All methods of numerical integration are based on sampling the integrand at a discrete number of integration points. The density of the integration points is related to the accuracy of the integration. It is intuitively obvious that a smooth, slowly varying function can be accurately integrated with relatively few integration points, whereas a less smooth, rapidly varying integrand will require more frequent sampling in order to achieve comparable accuracy.

In principle, it would be possible to determine an appropriate integration step size based on the sharpest "peak" of the frequency response function, and to use that minimum step size uniformly throughout the full range of excitation frequencies. Such a strategy

would be certain to yield a very accurate result, but it would also fail to take advantage of the smoothness of the frequency response function away from the resonant frequencies.

A more efficient algorithm should be able to divide the entire frequency band into a set of uneven intervals, using a smaller integration step only in the neighbourhood of the resonant frequencies. The appropriate step size at each resonant frequency can be defined as a fraction of the half-power width of the resonant "peak" at that frequency, which is a function of both the natural frequency and the damping ratio. Such a strategy would permit tailoring the frequency band discretization to achieve a very accurate integration with a much reduced number of function evaluations.

It is important to note that the choice of the "optimal" frequency band discretization requires advance knowledge of the resonant frequencies of the system. Therefore, the "optimal" discretization can only be determined after solving the dynamic eigenvalue problem for the system. Furthermore, in the random vibration analysis of uncertain structures, these natural frequencies will vary in response to random fluctuations of the stiffness and mass of the structure, resulting in a different "optimal" frequency band discretization for each realization of the problem.

The strategy adopted for the NESSUS finite element code uses an adaptive algorithm for *automated* frequency band discretization. The user is asked to provide a set of coarse macro-frequency bands, which are in turn subdivided into a number of smaller equally spaced intervals. In addition, the user can also specify the minimum number of intervals to be used for integrating the half-power band around each resonant "peak." The code will then select an appropriate frequency band discretization that meets all of the above criteria.

A typical frequency band discretization is shown in Figure 2.1. The exact location and width of the two resonance half-power bands, denoted by **A** and **B** in the figure, are determined internally by the code. In this example, both are subdivided into four equal intervals. The least damped "peak" will have a narrower half-power band, resulting in a tighter integration step size. The half power bands from adjacent resonances will sometimes overlap as shown in the figure. Below these there are two additional bars, denoted by **C** and **D**, representing two coarse macro-frequency bands defined by the user. The code will then automatically generate the final frequency band discretization **E** such that, at every frequency ω_k, the integration step size is no greater than the minimum of the three step size criteria **A**, **B** and **C** directly above.

Because the exact location and width of the half-power bands at the resonant frequencies are determined internally by the code, the algorithm can respond to changes in natural frequency and damping by adjusting the final frequency band discretization accordingly. Several variable-order Gauss rules can be used to integrate the frequency

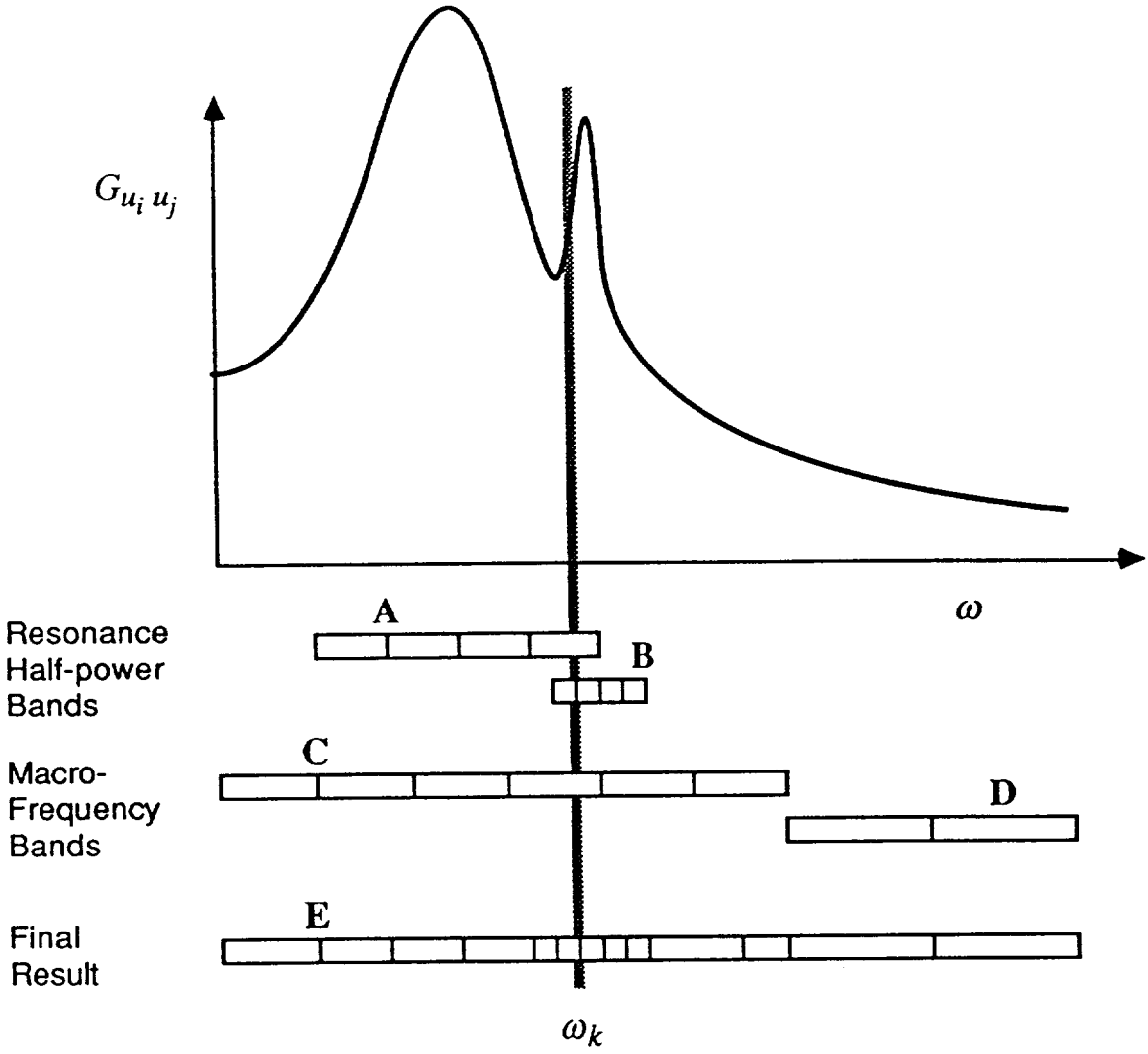

Figure 2.1 Automated Frequency Band Discretization

response function within each integration step. These rules are known for providing optimal accuracy for integrating polynomials with the smallest number of function evaluations.

2.4 Linear Dynamics of Uncertain Systems

The linear dynamics capabilities discussed in the preceding section have been extended to account for structures having random stiffness, mass and damping characteristics. Uncertainties in the parameters defining harmonic and random excitations can also be considered in the analysis. The ability to perform harmonic and random vibration analysis for uncertain structures was first introduced in version 3.1 of the NESSUS finite element code.

The effects of randomness in the structure are accounted for by computing the changes in the natural frequencies and mode shapes induced by small perturbations to the random parameters characterizing the structure. These changes in natural frequency in mode shape will, in turn, affect the dynamic characteristics of the system, and result in a different response to harmonic and random excitations. In this manner one can determine how uncertainties in the structure propagate to the response, and use of standard probability analysis methods (such as fast probability integration) to estimate the statistical characteristics of the response.

The analysis of uncertainties in the excitation parameters and damping is somewhat simpler. These parameters have no effect on the natural frequencies and mode shapes of the system and, therefore, need only be accounted for in the frequency domain phase of the analysis. Many conditional tests are built into the code to take full advantage of these special cases by skipping most unnecessary computations without direct user intervention.

2.5 Transient Dynamics of Uncertain Systems

The ability to perform transient elastodynamic analysis of uncertain systems by direct time integration has been implemented in the development version of the NESSUS finite element code. These capabilities will also be available in the next release version of the NESSUS finite element code.

Probabilistic transient elastodynamics problems can be approached with the use of perturbation algorithms for generating a set of parallel time histories corresponding to small fluctuations of the random variables present. These perturbed time histories provide information on how the uncertainties in the problem parameters propagate through time and affect the transient response at different points in time. It is interesting to note that these uncertainties need not increase monotonically with time, and will sometimes exhibit a nearly periodical *reduction* in uncertainty at certain points in time. These points correspond to closely spaced crossings of the unperturbed path by one or more perturbed time-histories (Figure 2.2).

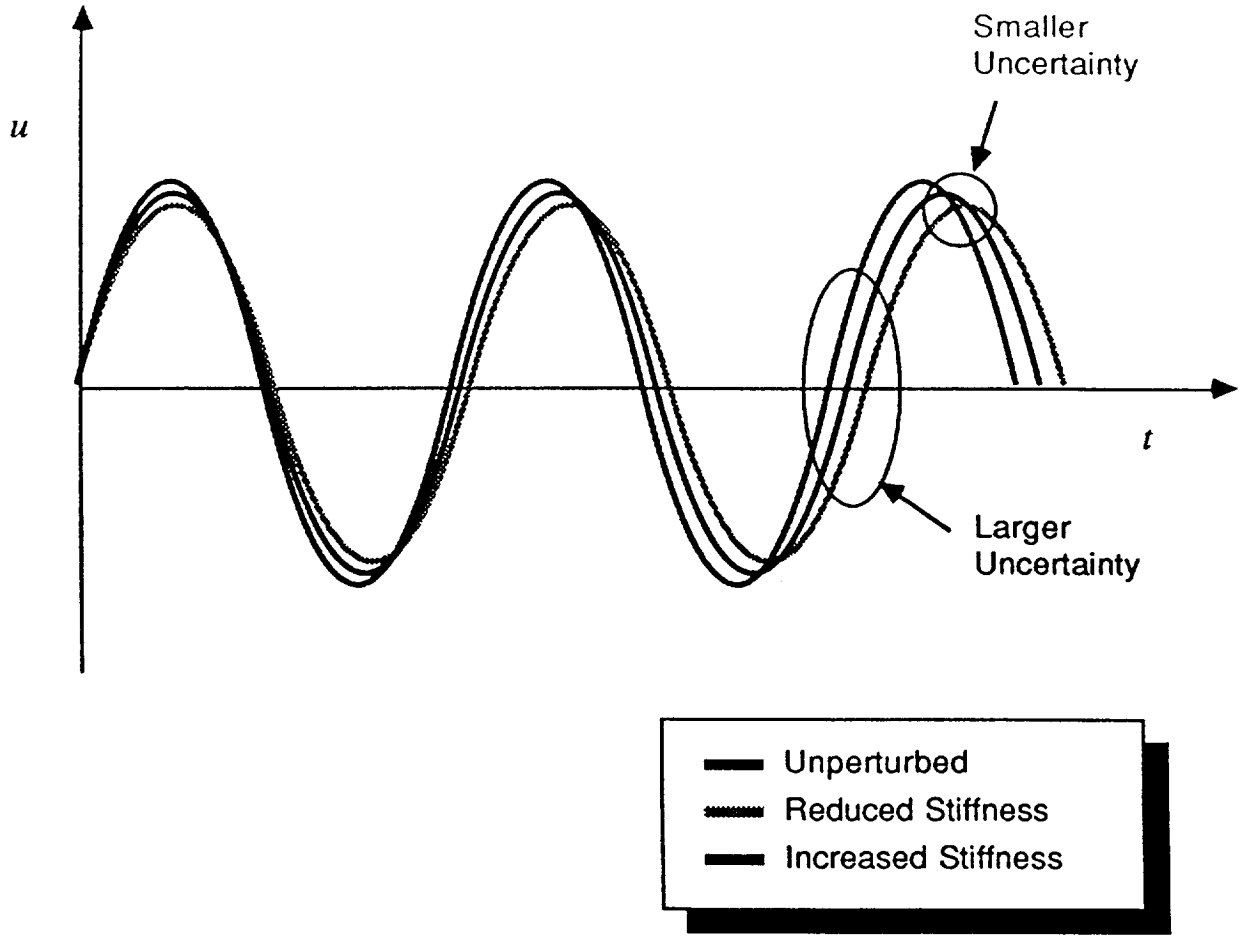

Figure 2.2 A Simple Set of Perturbed Time Histories

The strategy used to generate perturbed time-histories is a generalization of the elastostatic perturbation algorithm implemented in the NESSUS finite element code. This algorithm is based on the use of the unperturbed dynamic operator for the generalized Newmark-β family of integration algorithms to construct an iterated series of approximations converging on the solution to the exact perturbed problem. In order to preserve consistency (i.e., in order to converge on the correct solution), the position, velocity and acceleration at each increment must be tracked separately for each perturbation. All of the perturbations are carried forward in time within each time step.

Transient elastodynamics problems can be solved with the NESSUS finite element using either a displacement-based finite element formulation or a more elaborate mixed-iterative procedure. Preliminary experience with the dynamic perturbation algorithm exhibited very good performance if used in conjunction with the displacement method. As observed in the static case, the mixed-iterative strategy usually requires a much smaller perturbation size in order to achieve comparable performance. Although the mixed method will perform reasonably well for much of the analysis, its performance degrades significantly in increments where the direction of motion must be reversed. The problem can be mitigated by reducing the step size for those time steps. This negates one of the major advantages of the mixed-iterative formulation for transient elastodynamics, which appears to exhibit remarkably small algorithmic damping and phase error even at relatively large time steps. By comparison, the displacement formulation exhibits poorer accuracy in terms of algorithmic damping and phase error at large time steps, but remains far more robust with respect to perturbation size.

The current implementation can account for uncertainties in the stiffness, mass, damping and initial conditions for the transient problem. The effects of uncertainties in initial conditions will tend to become less significant for long time scales, but may contribute significantly to the response uncertainty during the initial start-up transient phase.

2.6 The Extended Database Format

The implementation of the revised linear dynamics capability in the NESSUS finite element code originated a need to systematically organize and store multiple cases of frequency response data corresponding to an arbitrary number of harmonic and random vibration excitations.

Earlier versions of the perturbation database (Figure 2.3) consisted of one pair of two-way linked lists. One of these contains the solutions to eigenvalue problems for dynamic modes or buckling analysis. The other is used to store the system's response at every increment or time step. This format offered no provision for storing *multiple* cases of frequency response data within a single increment. In addition, the format envisioned for reporting some of these frequency response quantities (e.g., real and imaginary components) did not neatly fall into any of the standard data types available in the database.

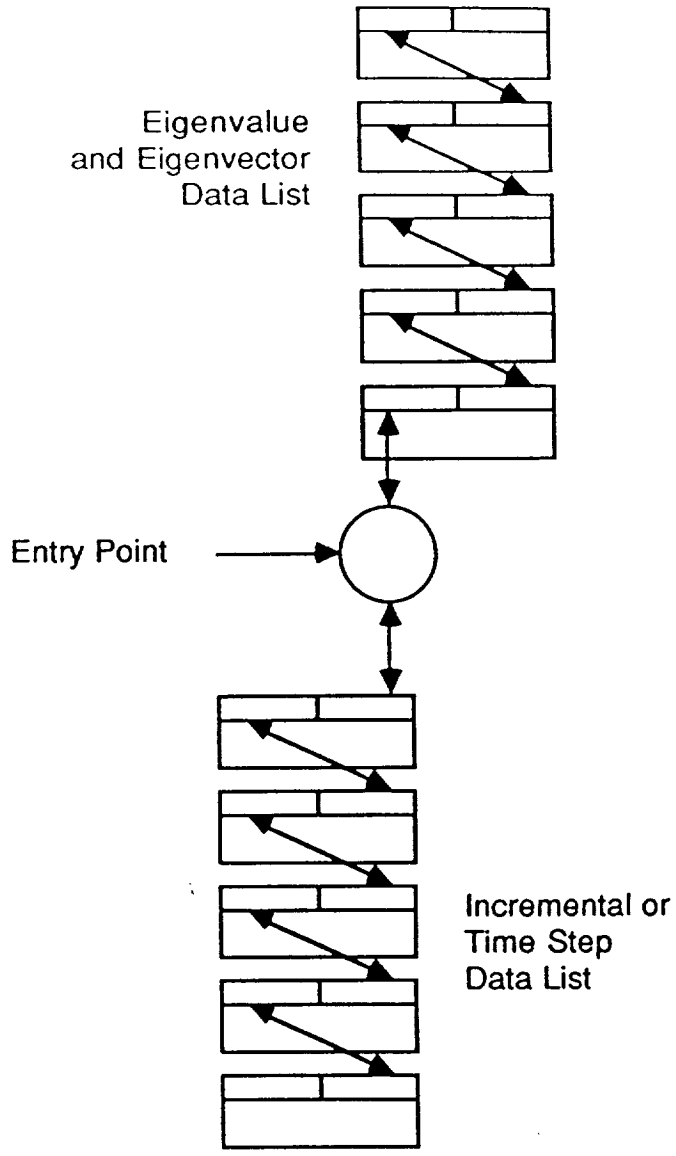

Figure 2.3 The Earlier Perturbation Database Layout

Different approaches for incorporating multiple cases of spectral response data into the existing framework of the perturbation database were evaluated. The most promising solutions included the following three options:

o To nest the frequency response data within each increment.

This option would provide a simple interface to the perturbation database and allow for the storage of frequency response data for different initial stress states, however, the resulting database format would be incompatible with earlier database versions, and all database interfaces would have to be rewritten. In addition, the efficiency of searching for a given block of data could degrade significantly for very large databases.

o To branch a one-way frequency response data list from each increment.

This option would offer the best overall efficiency when searching for a given block of data. The ability to store frequency response data at one or more initial stress states would be retained. The new format would have some degree of compatibility with earlier database versions, however, this strategy would involve a far more complicated database interface, which would be very cumbersome to modify later on.

o To introduce a third two-way linked list for frequency response data.

This option would retain a very simple database interface. It would also offer the greatest degree of compatibility with earlier database versions. The efficiency of searching for a given block of data remains very good, however, a small loss of generality is incurred by restricting the storage of frequency response data to a single prescribed initial stress state.

The third option appears to offer the most elegant and well-balanced solution to the requirements for an extended database format, and was selected for implementation in NESSUS 3.0. The extended database format (Figure 2.4) consists of three two-way ordered linked lists terminated by null pointers at the ends. Both the eigenvalue and eigenvector data list and the incremental or time step data list are *identical* to those used in earlier database versions, and remain fully compatible with the earlier interfaces. A new spectral response case list was added, containing results for both harmonic and power spectrum excitations. All lists are used to store both unperturbed and perturbed values.

The database interface subroutines used in the FPI and PFEM modules were rewritten to provide full support for the extended database format. Several simple post-processing operations are built into this interface, allowing the user to query for data not explicitly stored in the database, but easily derived from the information present in the database. A new set of database decoding and encoding utilities, fully supporting the extended database format, were also included in the release of NESSUS 3.0.

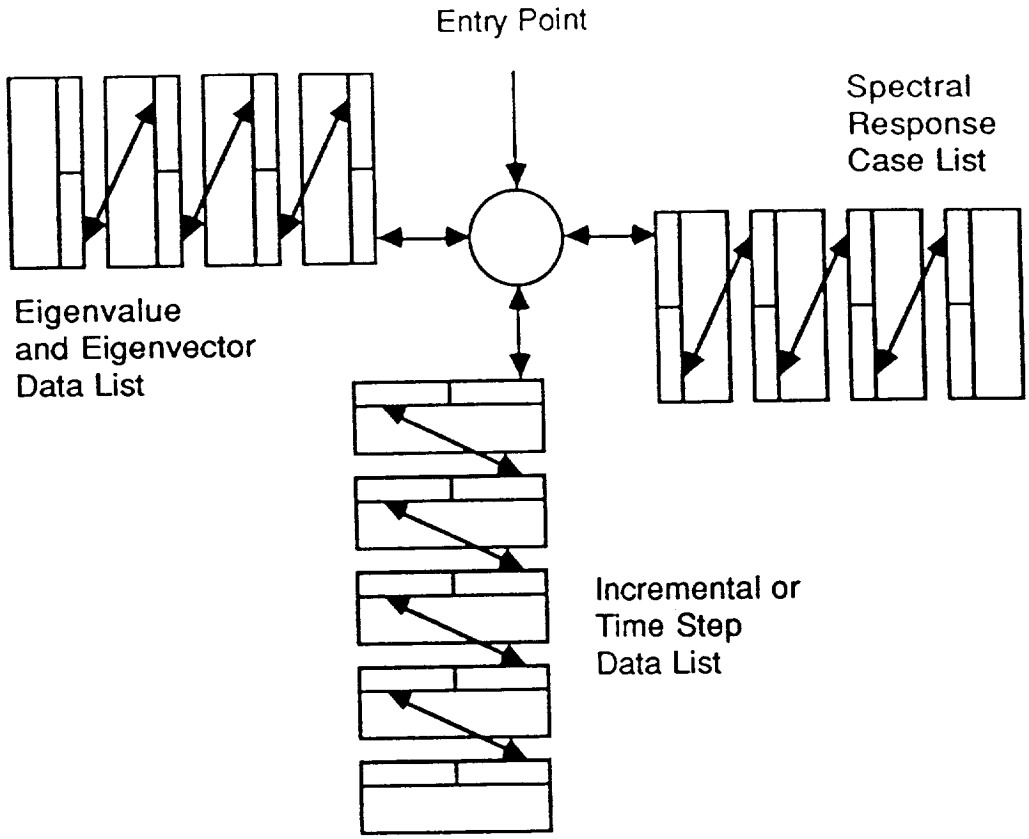

Figure 2.4 Extended Perturbation Database Layout

2.7 The Level 1 Post-Processor

The LEVEL1 module, introduced in NESSUS 3.1, is a software implementation of the Level 1 perturbation analysis strategy formulated by Southwest Research Institute. Level 1 analysis is based on the simplifying assumption that the uncertainties in the problem can be adequately modeled in terms of a set of *global scalings* of the applied force, stiffness and damping matrices. Under these assumptions, the perturbed system response may be obtained by applying appropriate scaling factors to an available unperturbed solution. Therefore, this type of analysis can be performed as a purely post-processing operation on the deterministic results stored in the perturbation database.

A typical Level 1 analysis (Figure 2.5) involves the following steps:

Step 1: Run the deterministic problem using the FEM module and compute the unperturbed solution. The total number of Level 1 random variables should be specified in order to reserve the appropriate database slots, but no perturbations are run at this stage.

Step 2: The FEM module writes the unperturbed solution to the perturbation database, including a specified number of empty slots for the Level 1 random variables.

Step 3: The LEVEL1 post-processor is started. This program recovers the unperturbed solution from the perturbation database and modifies it with the appropriate scaling factors to generate the Level 1 perturbations.

Step 4: The resulting Level 1 perturbations are written back into the perturbation database. The final result will be the original perturbation database expanded to include a new set of perturbations generated by the LEVEL1 post-processor.

If necessary, steps 3 through 4 may be repeated several times.

It should be emphasized that Level 1 is a *simplified* type of analysis and, as such, it is limited to a somewhat restrictive class of problems. The analysis of more complex engineering problems will require the use of more general perturbation methods. Still, Level 1 analysis offers a quick and efficient way to perform simple "what if..." experiments in order to get a basic understanding of how such uncertainties would affect the behavior of the response.

2.8 Additional Types of Random Variables

Several new types of random variables were introduced in the NESSUS finite element code within the past year. Many of the new random variable types are used to parametrize uncertainties pertaining only to dynamic problems, which were the focus of attention of much of the recent development effort.

Earlier versions of the NESSUS finite element code allowed the specification of very general random variables defined in terms of:

- Geometry parameters

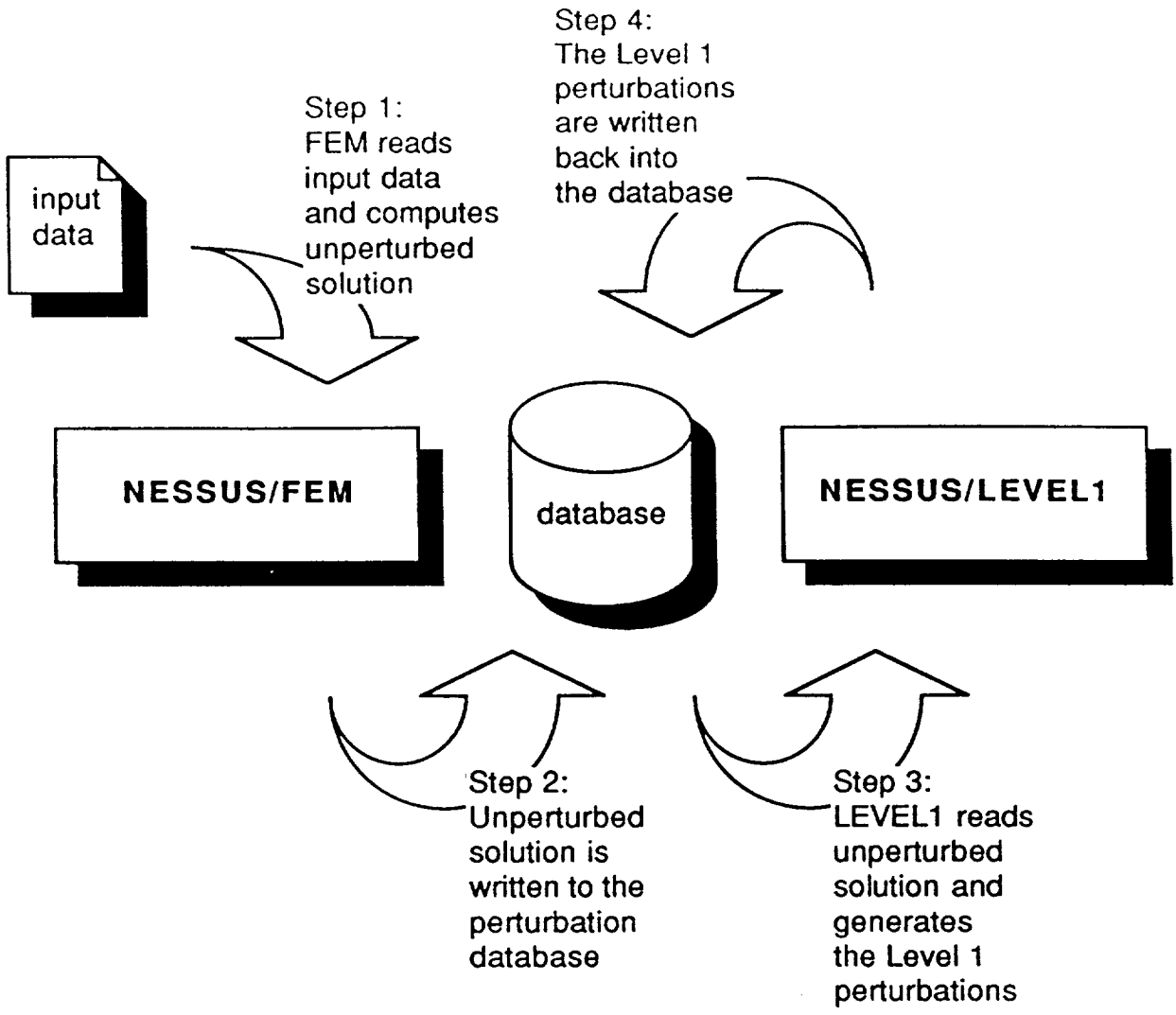

Figure 2.5 Data Flow During a Level Analysis

- Material properties
- Beam section properties
- Ground spring stiffness
- Concentrated point loads
- Element edge and surface tractions
- Nodal pressure loading
- Temperature distribution
- Centrifugal and gravity loading
- Anisotropy orientation

NESSUS 3.0 added the following twelve new random variable types:

- Concentrated masses
- Rayleigh damping coefficients
- Viscous damping ratio
- Friction damping ratio
- Harmonic excitation frequencies
- Amplitude and phase of harmonic nodal loads
- Amplitude and phase of harmonic base accelerations
- Amplitude and phase of harmonic nodal pressure
- Profile of the power spectrum density
- Intensity of random nodal load excitation
- Intensity of random base acceleration excitations
- Intensity of random nodal pressure excitation

Three other random variable types have been added for the transient code:

- Initial displacements
- Initial velocities
- Initial accelerations

The format for defining random variables in terms of these quantities was designed to follow the format for deterministic input as closely as possible.

It should be noted that many of these random variable types affect only minor aspects of the overall analysis. Several conditional tests were built into the code to detect perturbations having no effect on the outcome of certain phases of the analysis, allowing the code to skip many unnecessary computations. If appropriate, a "dummy" perturbation may be added into the database. Such "dummy" perturbations are simulated by

creating new logical links within the perturbation database, thereby avoiding the storage of unnecessary data without disturbing the overall structure of the existing database.

2.9 Miscellaneous Changes and Improvements

Several minor changes and improvements were made to the NESSUS finite element code in order to enhance the versatility and usefulness of the code. Among these, the most significant enhancements include:

- A concentrated point mass option was added.
- The input for closed-form beam section properties was cleaned-up and documented. Provisions for non-structural beam section mass properties were also introduced into the relevant code subroutines.
- A new user routine for specifying arbitrary power spectrum correlation functions was added. This subroutine allows the specification of both real and imaginary correlation terms, accounting for phase information.
- A similar user routine was coded into the NESSUS/PRE module, allowing the specification of more complex correlation models directly by the user.
- The NESSUS/PRE module was extended to accommodate spatially correlated fields of harmonic and power spectrum excitation.
- A power shift option was added into the NESSUS/PRE module, allowing for spectral decomposition of random fields in which some components are fully correlated or have zero uncertainty.

2.10 Future Effort

The planned effort for FY'89 will focus on the development of probabilistic nonlinear mechanics capabilities, and will include a major code cleanup and documentation effort. The extension of probabilistic finite element methods to nonlinear problems will address both material and geometric nonlinearities. In order to maintain a purely nodal record of the deformation history, allowing for stress recovery directly at the nodes, the mixed-iterative finite element formulation will be used for both types of nonlinear analysis.

2.10.1 Material Nonlinearities

The nonlinear behavior of a material at a point is usually derived from the total strain history for that point in terms of an *evolution equation* involving several *material parameters* and *state variables*. Uncertainties in nonlinear material response arise from two sources:

- Uncertainties in the strain history at a point resulting from the random nature of the geometry, boundary conditions and loading history.

- Uncertainties in the material parameters resulting from material inhomogeneity and variations in the processing of different material batches.

For a given realization of the strain history and the material parameters at a point, the evolution equation can be used to solve for the evolution history of the remaining state variables.

In probabilistic finite element analysis, the uncertainties in strain history are expressed in terms of the evolution of a random discrete strain field which is determined by the particular finite element formulation. Therefore, random strain histories can be handled in a way that is not substantially different from the way random strain histories are obtained for incremental elastostatics or transient elastodynamics problems.

The major new ingredients involve uncertainties in the material parameters present in the evolution equations. The development of stochastic material models for use in probabilistic finite element analysis will require the introduction of uncertainty into the evolution equations, expressed in terms of the random material parameters. Therefore, stochastic material models will be characterized in terms of distributions for yield stress, hardening moduli, creep constants, and other relevant material parameters.

The extension of the iterative perturbation strategy to situations involving at least mild material nonlinearities appears to be straightforward. The basic solution strategy involves tracking a set of multiple perturbed time-histories, using the unperturbed tangent stiffness at the beginning of the increment to precondition the iteration. In addition, the values of the appropriate state variables at several sampling points need to be carried forward between increments in a consistent manner. Because the mixed-iterative formulation involves only the nodal values of these state variables, this operation can be performed using the existing database format.

Difficulties will arise if the perturbed solutions stray too far from the unperturbed path in the course of the analysis. This problem may be aggravated by the presence of the incompressibility constraints associated with the evolution equations for deviatoric rate-independent plasticity.

2.10.2 Geometric Nonlinearities

Geometric nonlinearities account for many of the most challenging problems in computational mechanics. The solutions to these problems are known to be extremely sensitive to initial imperfections in the geometry of the original structure, which very often may only be described in statistical terms. This behavior is often indicative of the presence of complex multi-furcation points at which the solution can take any one of several distinct equilibrium paths.

The deterministic finite deformation algorithms currently implemented in the NESSUS finite element code are based on a Lagrangian mesh description using the "updated Lagrangian" formulation. The strategy involves repeated updates of the mesh geometry to the current configuration, allowing the evaluation of the appropriate finite element integrals over the volume of the deformed body. As a result, the finite element equations remain very similar to the ones developed for the small deformation case, and the only additional terms are used to account for deformation gradients and rotation tensors.

The "updated Lagrangean" formulation is particularly well suited for use in conjunction with the iterative perturbation algorithms coded in the NESSUS finite element code. At each perturbation, the current configuration may be obtained by *composition* of the initial geometry perturbation (if any) with the total motion computed for that perturbation. In this manner, the residual vector is computed by integrating the stresses over the *deformed* volume of the *perturbed* body, accounting for both nonlinear and perturbation effects. In order to perform this operation correctly, the total deformation gradients for all perturbed problems must be carried forward between increments in a consistent manner. Again, the mixed-iterative formulation requires only the nodal values of the deformation gradients, allowing the use of the existing database to store the full deformation history for each perturbation.

It should be noted that, even with the best available finite element technology, the solution of seemingly simple *deterministic* finite deformation problems can become extremely complex. However, it is anticipated that existing finite element methods will prove sufficiently robust to allow probabilistic analysis of somewhat mild forms of geometric nonlinearity. The analysis of complex post-buckling behavior may remain one of the most intractable problems of probabilistic mechanics for yet some time, but at least the task of *detecting* the presence of a bifurcation represents a much simpler problem, involving the solution of a stochastic eigenvalue problem.

2.10.3 Code Documentation

A major code documentation effort is planned at the end of FY'89. This will include the preparation of final versions of the User's Manual, the System's Manual and a Theoretical Manual. Some time will also need to be devoted to cleaning-up the final version of the code and reconciling any discrepancies remaining after the freezing of major new development work. Release of the final version of the NESSUS finite element code with the full documentation is expected towards the end of FY'89.

2.11 References

[1] S.H. Crandall and W.D. Mark, 1963, *Random Vibration in Mechanical Systems*, Academic Press, New York.

[2] F. Kikuchi and T. Aizawa, 1985, "A Numerical Method for Free Vibration Analysis of Structures with Small Design Changes," *Bull. JSME*, 28, 1733-1740.

[3] J. Simo, 1985, "Regular Perturbation Schemes for the Iterative Solution of Symmetric Eigenvalue Problems," *MARC Analysis Research Corporation Report*.

3.0 STRUCTURAL DYNAMICS FOR STOCHASTIC STRUCTURES AND LOADS

3.1 Introduction

The structural dynamics solution capability for probabilistic analysis in the NESSUS code is organized by various levels of stochastic variation. The NESSUS code allows progressively increasing levels of complexity in random variable content to provide the analyst a stair-step approach to understanding the significance of the analysis results by comparison to results generated using less detailed random variation. The random variation can be described as existing in the structure itself; in its imposed loading in a global sense; or in an integral way by specifying certain structural elements, properties, etc., or particular loading points that exhibit unique random variation which cannot be handled in a global sense.

In the NESSUS code, the dynamic response of a structure with stochastic variation in physical properties of the structure or loading can be synthesized in the frequency domain *via* modal analyses or in the time domain *via* direct time integration of the system equations of motion. A brief description of the analysis approaches will now be given along with basic equations to illustrate the level of stochastic variation.

3.2 Frequency Domain Modeling

Three levels of frequency domain modeling exist in the NESSUS code as indicated by the level content given in the table below. A brief description of each of the modeling levels will now be given with an outline of the corresponding dynamic equations of motion to explicitly demonstrate the differences in the various modeling levels.

Table 3.1

Dynamic Analysis Modeling-Frequency Domain

LEVEL 0	LEVEL 1	LEVEL 2
Deterministic Structure	Global Uncertainty	Full Uncertainty
Modal Analysis	Scaled Eigenvectors	Perturbed Eigenvectors
Periodic	Uncertain Periodic	Random Periodic
Deterministic Random	Uncertain Random	Uncertain Random

3.2.1 Level 0 - Deterministic

In Level 0 analysis, the structure is considered to be deterministic as well as the loading, except for the case of a specified power spectral density loading function. This is the type of analysis most often considered for random loading of structures. In the usual manner the frequency domain solution begins with an expansion of the nodal equations of motions in terms of the homogeneous system eigenvalues and

eigenvectors, normally referred to as the system undamped normal modes. For viscous like damping proportional to the system mass or stiffness the expanded equations of motion become a set of NR uncoupled single degree of freedom (DOF) oscillators,

$$\ddot{q}_r(t) + 2\beta_r\omega_r\dot{q}_r(t) + \omega_r^2 q_r(t) = l_r(t), \tag{3.1}$$

$$r = 1, 2, 3 \ldots NR$$

where $q_r(t)$ is the modal DOF, β_r the equivalent viscous damping coefficient, ω_r the undamped normal mode frequency, and $l_r(t)$ the generalized modal loading for the r^{th} modal DOF. The structural nodal motions, u, are related to the modal DOF *via* the system eigenvectors as

$$\{u\} = [\phi_r]\{q_r\} \tag{3.2}$$

where ϕ_r is the r^{th} mode eigenvector.

The generalized modal loading is determined from the applied nodal loading, $f(S,t)$, *via*,

$$l_r(t) = \int_s \phi_r(s) f(s,t) ds \tag{3.3}$$

where the integration is over the structural surface, S. For case of periodic loading, where the excitation occurs at distinct frequencies ω, the generalized loading takes the form

$$L_r(\omega) = \int_s \phi_r(s) F(s) e^{-i\theta(s)} ds \tag{3.4}$$

where $F(S)$ is the spatial variation in the applied periodic loading and $\theta(S)$ is the relative phase variation across the structure. The explicit periodic variation of the form $e^{i\omega t}$ is implied in the above equation *via* the use of upper case variables. The modal response, $Q_r(\omega)$ to the periodic loading takes the form

$$Q_r(\omega) = H(\omega) L_r(\omega) \tag{3.5}$$

where $H(\omega)$ is the single DOF transfer function. The resulting motion at the i^{th} structural node is computed from the equation above as

$$U_i(\omega) = \sum_{r=1}^{NR} [\phi_{ir}] Q_r(\omega) \tag{3.6}$$

For a deterministic random loading in the form of a stationary Gaussian power spectral density (PSD) the one sided modal cross-spectral density between the m^{th} and n^{th} modal responses, $G(\omega)q_m q_n$ is computed from

$$G(\omega)q_m q_n = H(\omega)_m H(\omega)_n^* \int_s \int_{s'} \phi(s)_m PSD(s, s', \omega) \phi(s)_n ds ds' \tag{3.7}$$

where the asterisk denotes the complex conjugate operator. The double surface integral is generally referred to as the cross-joint acceptance function for the structure, $J(\omega)_{mn}$. The cross-joint acceptance function describes how the input couples to the structure over its length or span. The corresponding displacement cross-spectral density function, $G(\omega)u_iu_j$ takes the form

$$G(\omega)u_iu_j = \sum_{m=1}^{NR}\sum_{n=1}^{NR}\phi_{im}\phi_{jn}H(\omega)_m H(\omega)^*_n J(\omega)_{mn} \tag{3.8}$$

where the summation is over all the retained modal responses.

Stress modal functions are defined from the element stress displacement relationships and similar mathematical expressions result to describe the stress auto-power spectral density for an element. Often, the cross modal terms are neglected; if they are computed, only the real part of the spectra has physical significance.

3.2.2 Level 1 - Global Probabilistic

A global probabilistic variation in the structure or loading is considered in Level 1 analysis. The global variation can occur in the following forms.

A. Stiffness Variation

$$[\tilde{K}] = [K_0]\{1 + Y(\tilde{x})\} = [K_0]\tilde{Y} \tag{3.9}$$

B. Mass Variation

$$[\tilde{M}] = [M_0]\{1 + Z(\tilde{x})\} = [M_0]\tilde{Z}. \tag{3.10}$$

C. Damping Variation

Viscous:

$$[\tilde{C}] = [C_0]\{1 + W(\tilde{x}) = [C_0]\tilde{W}. \tag{3.11}$$

Structural:

$$\tilde{g} = g_0\{1 + W(x)\} = g_0\tilde{W}. \tag{3.12}$$

These global variations or uncertainties scale the dynamic response variable mean values. The system eigenvectors, or mode shapes, scale as

$$\{\tilde{\phi}_r\} = \tilde{Z}^{-1/2}\{\phi_{0r}\} \tag{3.13}$$

The system eigenvalues, or frequencies squared, scale as

$$\tilde{\lambda}_r = (\tilde{Y}/\tilde{Z})\lambda_{0r} \tag{3.14}$$

and the viscous proportional damping ratios scale as

$$\tilde{\beta}_r = [\tilde{W}/(\tilde{Z}\tilde{Y})^{1/2}]\beta_{0r} \tag{3.15}$$

where $\{\phi_{0r}\}$, λ_{0r}, and β_{0r} and are, respectively, the r^{th} mean eigenvector, eigenvalue, and viscous damping ratio.

D. Periodic Load Variation

$$\tilde{f}(s)e^{i(\tilde{\omega}t-\tilde{\theta}(s))} = \tilde{R} f_0(s) e^{i\theta_0(s)\tilde{P}_0 i\omega\tilde{C}t} \tag{3.16}$$

where $\tilde{R}, \tilde{P}$, and $\tilde{C}$ are respectively, the global stochastic variation in the periodic load magnitude, phase, and driving frequency and $f_0(S), \theta(S)$, and ω are respectively, the mean applied load, phase, and driving frequency.

E. PSD Variation

$$\tilde{PSD}(s,\omega) = \{1 + R(\bar{x})\}^2 PSD_0(s,\omega) = \tilde{R}^2 PSD_0(s,\omega) \tag{3.17}$$

where $\tilde{R}$ is the global stochastic variation in the random loading, and $PSD_0(S,\omega)$ is the measured or most probable mean loading spectra. Here we do not distinguish between variation in PSD level, phase, or frequency on a global basis since such detail would not be unique.

The r^{th} generalized modal response to random periodic loading of a structure with global stochastic variation of its mass, stiffness, and damping properties takes the form

$$\tilde{Q}_r(\omega) = \tilde{H}(\omega,\beta)_r \tilde{L}_r(\omega) \tag{3.18}$$

where $L_r(\omega)$ is the Fourier transform of the r^{th} generalized force of the mean loading and $H_r(\omega,\beta)$ is the random oscillator transfer function for proportional viscous damping. An identical expression results for structural damping by replacing the transfer function with $H(\omega,g)$. The general form of the transfer function for viscous damping is

$$\tilde{H}(\omega,g) = \tilde{Z}/[\tilde{Y}\omega_{0r}^2 - \tilde{C}^2\tilde{Z}\omega^2 + i2\beta_{0r}\omega_{0r}\omega\tilde{V}\tilde{C}] \tag{3.19}$$

and for structural damping it is

$$\tilde{H}(\omega,g) = \tilde{Z}/[\tilde{Y}\omega_{0r}^2 - \tilde{C}^2\tilde{Z}\omega^2 + ig\omega_{0r}^2\tilde{V}\tilde{Y}] \tag{3.20}$$

The generalized load for the r^{th} modal degree of freedom would take the first order form

$$\tilde{L}_r(\omega) = \tilde{Z}^{1/2}\tilde{R}\int_s \phi_{0r}(s) f_0(s) \exp[-i\phi_0(s)]ds \tag{3.21}$$

$$-i\tilde{Z}^{1/2}\tilde{R}P(\bar{x})\int_s \phi_{0r}(s) f_0(s)\theta_0(s)\exp[-i\theta_0(s)]ds$$

$$+[\text{Higher Order Terms of } P(\bar{x})]$$

where $P(\bar{x})$ is the zero mean random variation of the phase $\tilde{\theta}$. Nodal responses such as displacements, velocities, and accelerations would then be expressed, respectively, as

$$\tilde{U}_i(\omega) = Re\left[\tilde{Z}^{-1/2}\sum_{r=1}^{NR}\phi_{0ir}\{\tilde{Q}_r(\omega)\}\right]. \tag{3.22a}$$

$$\dot{\tilde{U}}_i(\omega) = Re\left[-i\omega\tilde{C}\tilde{Z}^{-1/2}\sum_{r=1}^{NR}\phi_{0ir}\{\tilde{Q}_r(\omega)\}\right]. \tag{3.22b}$$

and

$$\ddot{U}_i(\omega) = Re\left[-\omega^2 C^2 Z^{-1/2} \sum_{r=1}^{NR} \phi_{0ir} \{\bar{Q}_r(\omega)\} \right]. \tag{3.22c}$$

where the Re operator denotes the real part of the resultant. The element stresses would then be computed from the stress displacement relationships for the given element.

The major concern when introducing random excitation in the form of a power spectral density function (PSD) is how to introduce uncertainty in the structure and loading. In NESSUS the approach has been to assume that the uncertainty in the structure is independent of the uncertainty in the loading and vice versa. With this assumption, the modal cross-spectral density function becomes

$$\bar{G}(\omega)_{q_m q_n} = \bar{R}^2 Z^{-1} \bar{H}(\omega)_m \bar{H}(\omega)_n^* J(\omega)_{mn} \tag{3.23}$$

where the cross-joint acceptance function, $J_{mn}(\omega)$, does not exhibit global random variation due to the assumed independence in the structure and loading and as such takes the form as specified in eqn. (3.7).

The displacement cross spectral density between the i^{th} and j^{th} nodes becomes

$$\bar{G}(\omega)_{u_i u_j} = \bar{R}^2 Z^{-2} \sum_{m=1}^{NR} \sum_{n=1}^{NR} \phi_{0im} \phi_{0jn} \bar{H}(\omega)_m \bar{H}(\omega)_n^* J(\omega)_{mn} \tag{3.24}$$

and likewise the velocities and accelerations are, respectively

$$\bar{G}(\omega)_{\dot{u}_i \dot{u}_j} = -\omega^2 \bar{C} Z \bar{G}(\omega)_{u_i u_j}, \tag{3.25}$$

and

$$\bar{G}(\omega)_{\ddot{u}_i \ddot{u}_j} = \omega^4 \bar{C}^4 \bar{G}(\omega)_{u_i u_j} \tag{3.26}$$

Stress modal functions are again defined from the element stress-displacement relationships; similar mathematical expressions result to describe the stress auto-power spectral density for an element. As with the deterministic case, the cross modal terms are often neglected; if they are computed, only the real part of the spectra has physical significance.

3.2.3 Level 2 - Full Uncertainty

When considering full uncertainty throughout the structure, or parts thereof, and uncertainty in the loading with partially correlated random variables, explicit solutions to the dynamic response of the structure are no longer possible except in a few special cases. For the general case NESSUS synthesizes the partially correlated variables into uncorrelated modes [1]. The system eigenvalues/eigenvectors are then computed, along with structural responses for a given loading, for each independent uncorrelated mode. The results are stored in a data bank and efficient probabilistic methods [2] are then used to construct dynamic response distribution functions for the response variables of interest.

3.3 Time Domain Modeling

For transient loading analyses the deterministic and full uncertainty cases are treated similarly. A Newmark & Beta direct time integration scheme [3] is employed to obtain the time history response of the structure. For the case of full uncertainty the partially correlated variables are synthesized into uncorrelated modes and each independent structural variation and loading case is solved independently. The analysis results are stored in a data bank and probabilistic methods are then used to construct response distribution functions.

3.4 Dynamic Loading Functions

The dynamic loading functions available in NESSUS are in the form of point harmonic loads, nodal harmonic pressures, surface distributed random loading, base excited point harmonic accelerations or acceleration power spectral density excitation, and explicit time history nodal loadings. Generic load models with multiple levels of progressive sophistication to simulate the composite load spectra that are induced in space propulsion system components representative of Space Shuttle Main Engines are being generated by Rockwell International Corporation, Rocketdyne Division engineers. Every effort has been made in the NESSUS code to accommodate a wide variety of possible loading scenarios. A major task underway is the integration of specific loading descriptions into the NESSUS loads data base.

3.5 References

[1] Y.-T. Wu, O.H. Burnside, and T.A. Cruse, 1988, ASME Symposium on Computational Probabilistic Methods, UC-Berkeley, California, June 20, 1988, (pending publication in *Computational Mechanics of Reliability Analysis*, edited by Wing Kam Liu and Ted Belytschko, Elempress International).

[2] Y.-T. Wu, 1987, "Demonstration of a New Fast Probability Integration Method for Reliability Analysis, *Journal of Engineering for Industry, ASME*, 109, 24-28.

[3] K. J., Bathe, 1982, *Finite Element Procedure in Engineering Analysis*, Prentice-Hall, Inc.

4.0 NESSUS PROBABILITY ALGORITHM DEVELOPMENT

4.1 Introduction

This chapter summarizes the NESSUS probability algorithms development during the past year.

Section 4.2 reports on the performance of the advanced mean-value-first-order (AMVFO) method. The AMVFO method, developed originally for the NESSUS analysis, has been shown to be very effective in solving the NESSUS validation problems [4] as well as the turbine blade verification problem.

Section 4.3 describes the development of a methodology for estimating the probabilistic solution for the entire structural component using limited perturbation solutions at selected nodes.

The turbine blade verification problem has led to the extension of the AMVFO method to a more general class of problems involving strongly non-monotonic performance functions. Section 4.4 presents a simple solution to modify the AMVFO solution for this new class of problems.

Section 4.5 reports on the efforts of integrating the FPI and a fast Monte Carlo code. The integration has been completed and tested successfully. This new simulation capability allows an independent checking of the FPI results.

The NESSUS/FPI code has also been modified for PAAM analyses. The details of the modification is provided in Section 4.6.

One major NESSUS analysis capability is dynamics analysis which is being validated (see Chapter 7). Section 4.7 discusses the strategies for the uncertainty characterizations of the dynamics loads.

Section 4.8 reports on the progress of code development for solving problems involving non-normal dependent random variables.

4.2 Advanced Mean Value First Order Method (University of Arizona Report)

The probability distribution of a response function (e.g., stresses, displacements) can be calculated efficiently employing the advanced mean value first order method (AMVFO), an abbreviated form of the most probable point locus method (MPPL). The scheme, first developed for the PSAM program by Wu has wide application in probabilistic mechanics and design. Following is a description of AMVFO and MPPL.

Consider a response function

$$Z = Z(\underline{X}) \tag{4.1}$$

where $\underline{X}$ is a vector of n random design factors. Z can be either explicit or implicit. Determine the CDF of Z, denoted as F_Z. If Z is an explicit function of $\underline{X}$, then the construction of the F_Z, is straightforward using Monte Carlo or fast probability integration. All numerical reliability methods require many (100 to 10,000) function evaluations, a very fast operation with a digital computer if Z is an <u>explicit</u> function of $\underline{X}$.

However, when Z is an implicit function (e.g., $Z(\underline{X})$ defined only through a finite element code) a single function evaluation may be costly. So the fundamental question is how do we construct a high quality CDF of Z with a very minimum of function evaluations?

The most probable point locus method (MPPL) as proposed by Y.-T. Wu may be close to the optimum in requiring a minimum number of function evaluations relative to the accuracy of F_Z. There is no formal proof of this, but intuition suggests that it would be difficult to produce a reasonable estimate of F_Z with fewer function evaluations.

A detailed description of MPPL, an iterative process, is given in Appendix A. In summary, the system follows the steps:

1. Approximate Z as a linear function of $\underline{X}$. This requires solutions at the mean value and at small perturbations about the mean to evaluate the parameters of the linear function.

2. Now that an explicit function (albeit approximate) is available, reliability methods, (e.g., [3]) can be used to approximate probabilities in selected points in the sample space of Z. This first approximation to F_Z, CDF of Z, called the mean value first order (MVFO) method is, in general, not likely to be accurate.

3. To improve the estimate of F_Z, the function Z is evaluated at each design point. These are "improved Z's at each probability level. This "first move" in MPPL is called AMVFO. As shown in Appendices A and B, AMVFO provides remarkably accurate estimates of F_Z in most cases.

4. A linear approximation to Z can be obtained at each of the design points. This requires again perturbed solutions to Z. And again, a fast probability integration method can be employed for point probability estimates in the "second move" to construct F_Z. An improved F_Z is obtained at each Z.

5. For the "third move," the function is evaluated at the design points computed in step 4.

While steps 4 and 5 can be repeated to improve the estimate of Z, it has been found that AMVFO consistently proves an accurate estimate of F_Z as demonstrated in Appendix B.

The critical issue is that the number of costly function evaluations must be limited for an efficient solution to F_Z. Figure 4.1 dramatically illustrates the power of AMVFO in this regard. In summary, AMVFO generally is expected to provide a high quality F_Z with a minimum of function evaluations.

The detailed summary of MPPL of Appendix A provides examples which illustrate the MPPL process. And presented in Appendix B is a summary of the experiences with AMVFO by the team at the University of Arizona. Attempts were made to find problems for which AMVFO would perform poorly.

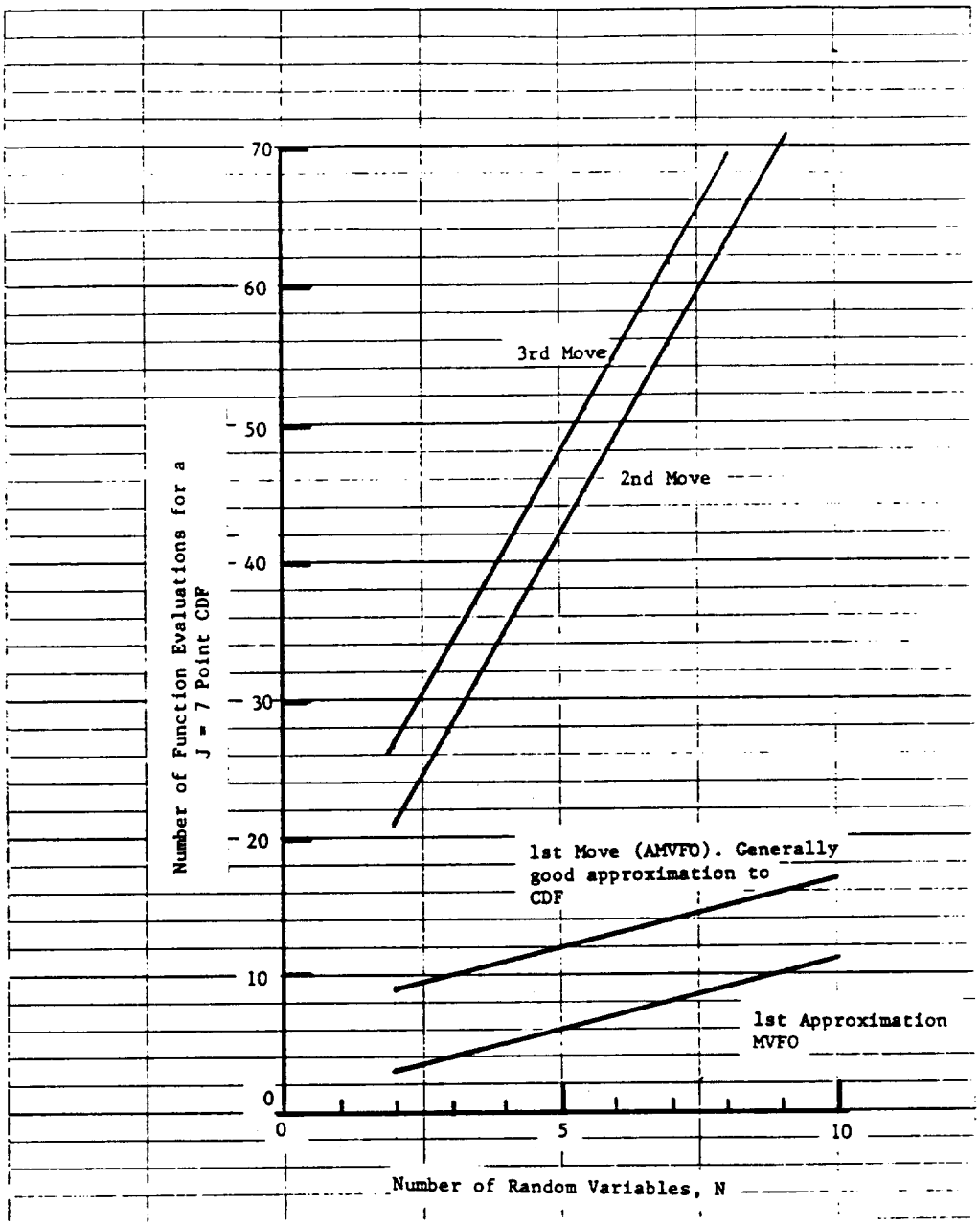

Figure 4.1 Number of Function Evaluations vs. Number of Variables for a J = 7 Point CDF

The general conclusion from the study was that AMVFO seems to be robust. The largest errors in $\beta = \Phi^{-1}(F_z)$ were about 10% (Φ is the standard normal CDF).

4.3 The Field Problem

The most probable point locus (MPPL) method has been shown to be a very efficient and effective way of establishing the CDF of an explicit (or implicit) function. Wu has proposed an extension of MPPL to construct the marginal CDF's of a vector of correlated response variables, $Z = Z(\underline{X})$ where Z is a vector of response functions.

Consider two response functions Z_1 - Z_2 which are correlated.

$$Z_1 = Z_1(\underline{X}) \tag{4.2}$$

$$Z_2 = Z_2(\underline{X}) \tag{4.3}$$

where $\underline{X}$ is a vector of random design factors.

Here, Z_1 is known to be the "most important" variable and is called the master. Coordinate Z_2 is the slave. Note that Z_1 and Z_2 are correlated. The CDF's of both Z_1 and Z_2 can be established by direct application of MPPL. But there is promise that the CDF of Z_2 could be constructed more efficiently by (a) employing MPPL to obtain the CDF of Z_1, and (b) estimating the CDF of Z_2 at each point knowing the correlation coefficient between Z_1 and Z_2 based on linear approximations to Z_1 and Z_2. In the special case, where the response functions are linear and the random variables are normal, this process produces the exact CDF of Z_2. For the general case where the response functions are nonlinear and/or the random variables are non-normal, it is hoped that the approximation to the CDF of the slave variable is "accurate." This scheme will be referred to herein as "Wu's approximation." A detailed description of the operation of the field problem is provided in Appendix C.

An example presented here is a case where the quality of the slave variable, Z_2, is poor for a low correlation coefficient between Z_1 and Z_2. However, it will be demonstrated that as the correlation coefficient gets closer to 1 (by adjusting the parameters of Z_1 and Z_2) the quality of the approximation to the CDF of Z_2 improves.

Consider a specific example:

$$Z_1 = a_{11}X + a_{12}Y + a_{13}Z \tag{4.4}$$

$$Z_2 = a_{21}X + a_{22}Y + a_{23}Z \tag{4.5}$$

The random variables have the following distributions:

X - WEIBULL (10, 1.0)*
Y - FRECHET (10, 1.0)
U - EXTREME VALUE (10, 1.0)

*mean and standard deviation

Consider the case where,

$$(a_{11}, a_{12}, a_{13}) = (2., 1., 2.) \tag{4.6}$$

$$(a_{21}, a_{22}, a_{23}) = (1., -1., 1.) \tag{4.7}$$

Employing the most probable point locus method, and the scheme as proposed by Wu, the CDF's of Z_1 (master) and Z_2 (slave) were constructed. They are plotted in Figure 4.2. The poor agreement between the exact CDF and the Wu approximation for the slave comes as no surprise because of the relatively low correlation coefficient, $\rho = 0.58$. However, the quality of the slave improves as ρ approaches 1. This example provides an illustration of how the Wu approximation approaches the exact for increased values of the correlation coefficient.

Five cases are considered that are summarized in Table 4.1. The corresponding CDF's are plotted in Figures 4.2 through 4.6. Clearly, the quality of the Wu approximation to the CDF of the slave improves as ρ approaches 1. However, there is still significant error for "high" correlation coefficients. As a subjective comment, it is noted by this author that the errors in the Wu approximation for other cases studied were smaller. In fact, this example was chosen because of the relatively poor quality of the slave CDF.

In general, the algorithm presented will provide a reasonable first approximation of the CDF of the slave variables. However, in some cases the errors may be significant. Additional research on this topic seems appropriate.

Table 4.1

Summary of Examples

	Parameters		Corr. Coeff.
Case	$(a_{11}, a_{12}, 2_{13})$	(a_{21}, a_{22}, a_{23})	(ρ)
1	2., 1., 2.	1., -1., 1.	0.58
2	2., 1., 2.	1., -0.58, 1.	0.75
3	2., 0.6, 2.	1., -0.5, 1.	0.853
4	2., -1., 2.	1., -1., 1.	0.962
5	2., -1.3, 1.	1., -1., 1.	0.983

4.4 The AMVFO Method for Non-Monotonic Response Functions

The turbine blade verification study has led to the extension of the advanced mean-value-first-order (AMVFO) method for non-monotonic response functions. Previously, it was assumed that only one most probable point (MPP) exists in the probability region of interest.

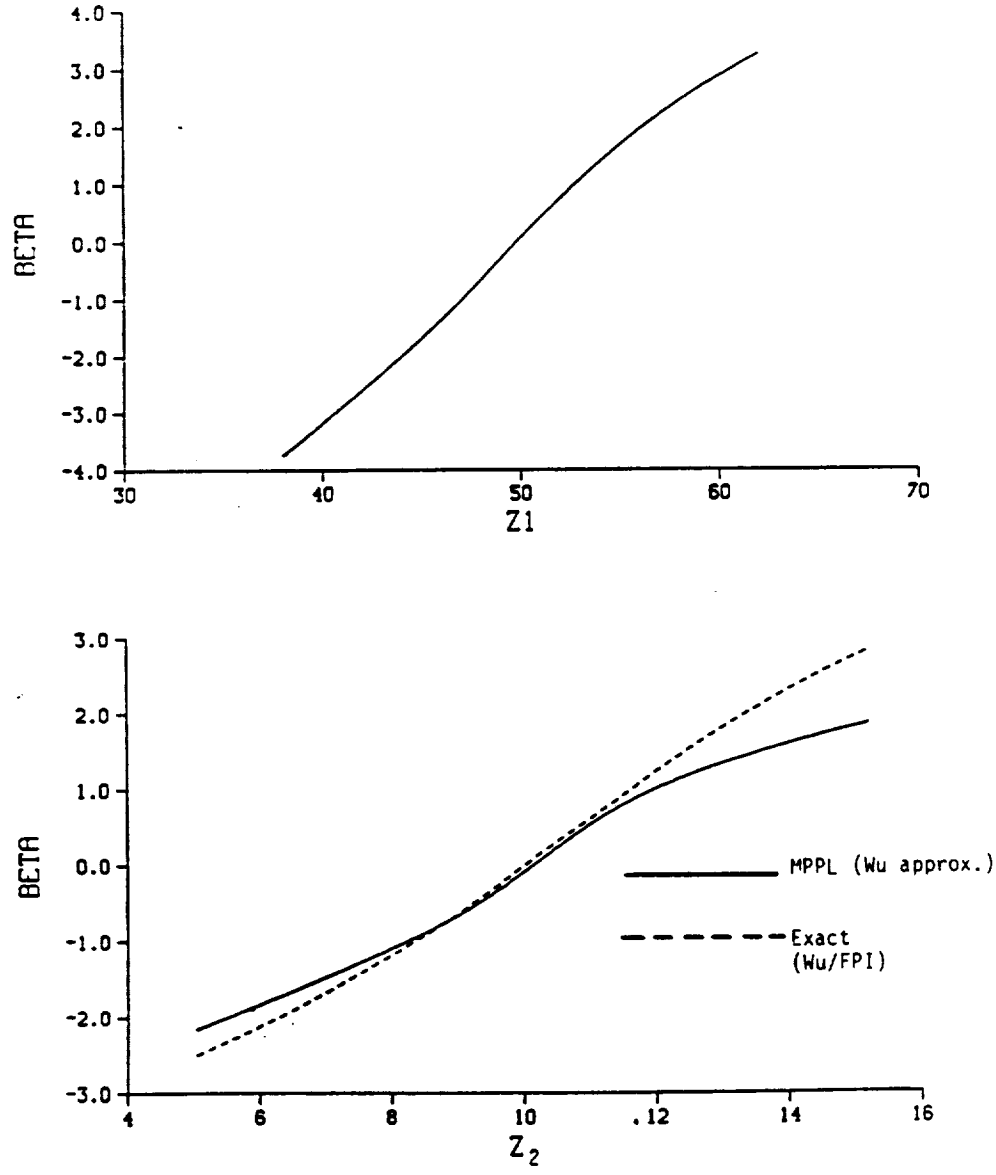

Figure 4.2 Case 1: $\rho = 0.58$

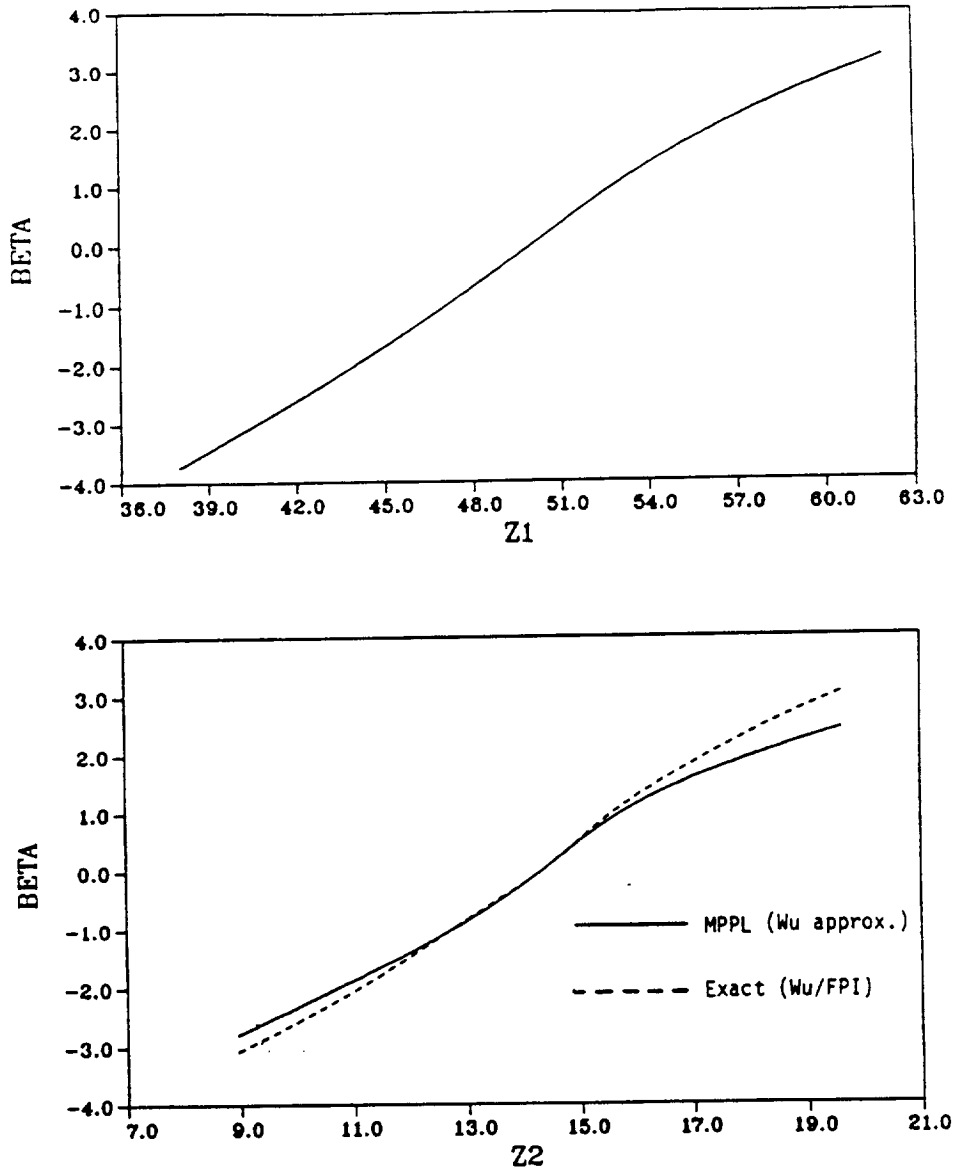

Figure 4.3 Case 2: $\rho = 0.75$

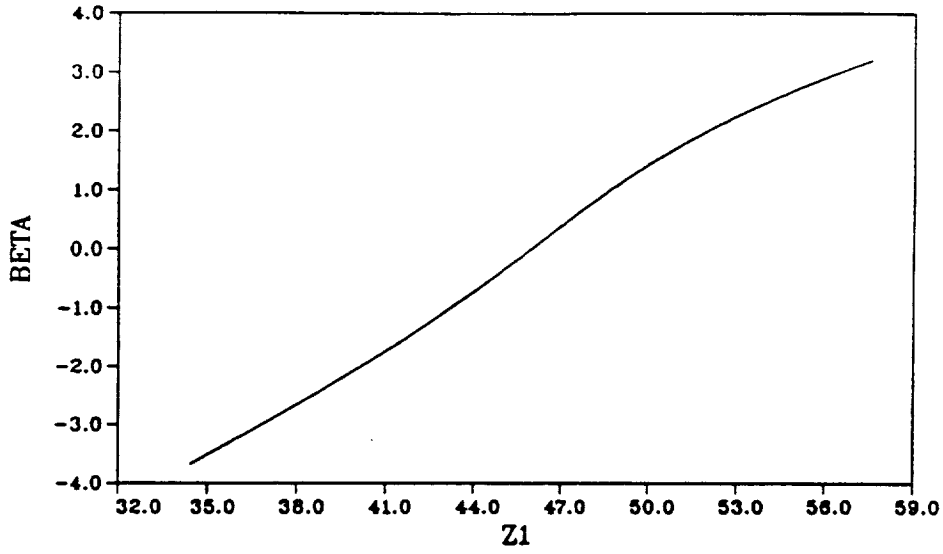

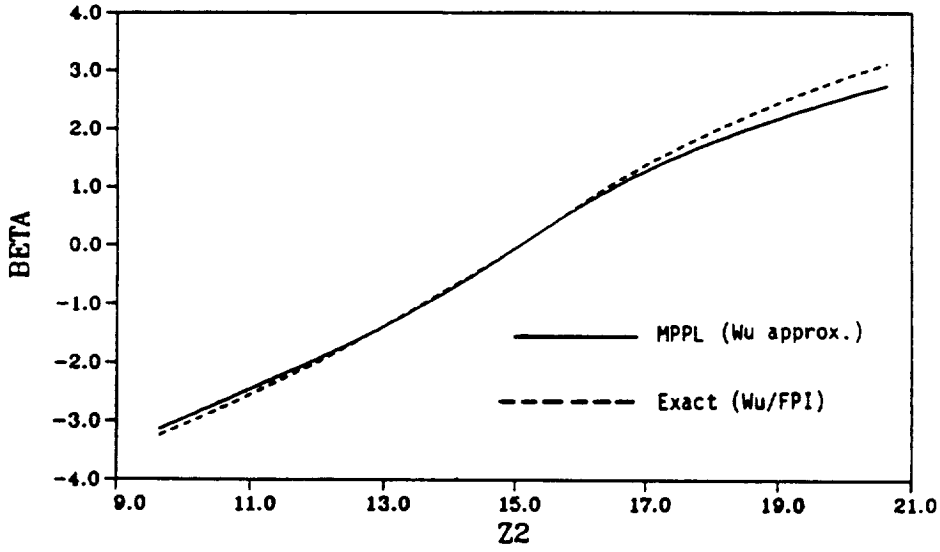

Figure 4.4 **Case 3:** $\rho = 0.853$

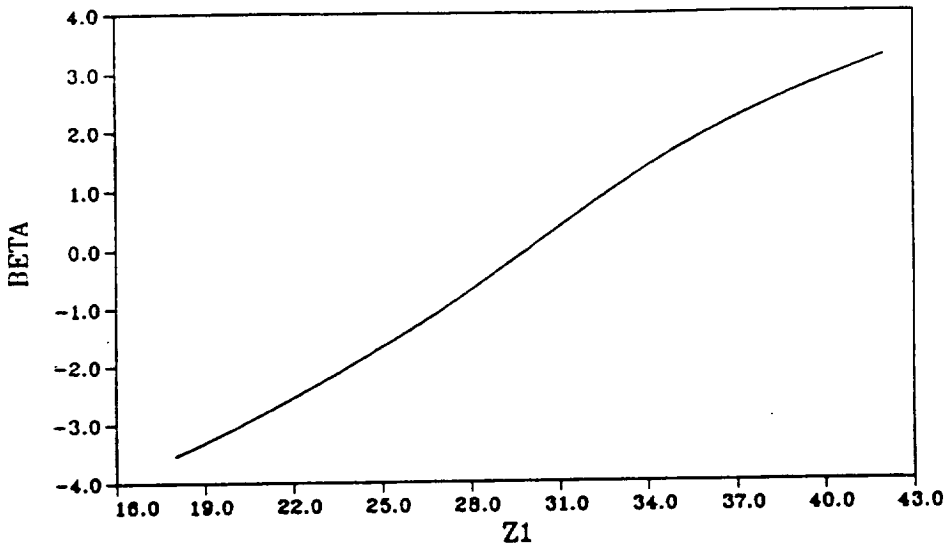

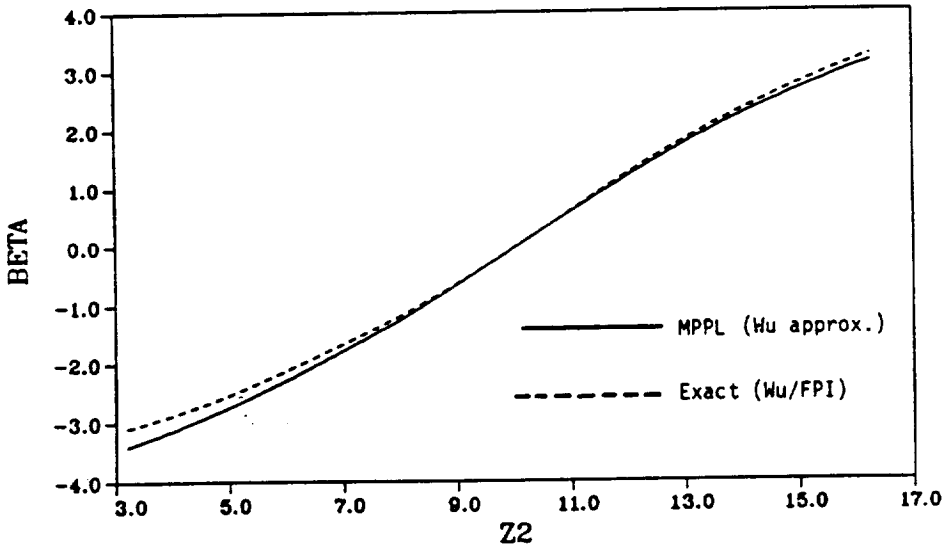

Figure 4.5 Case 4: ρ = 0.962

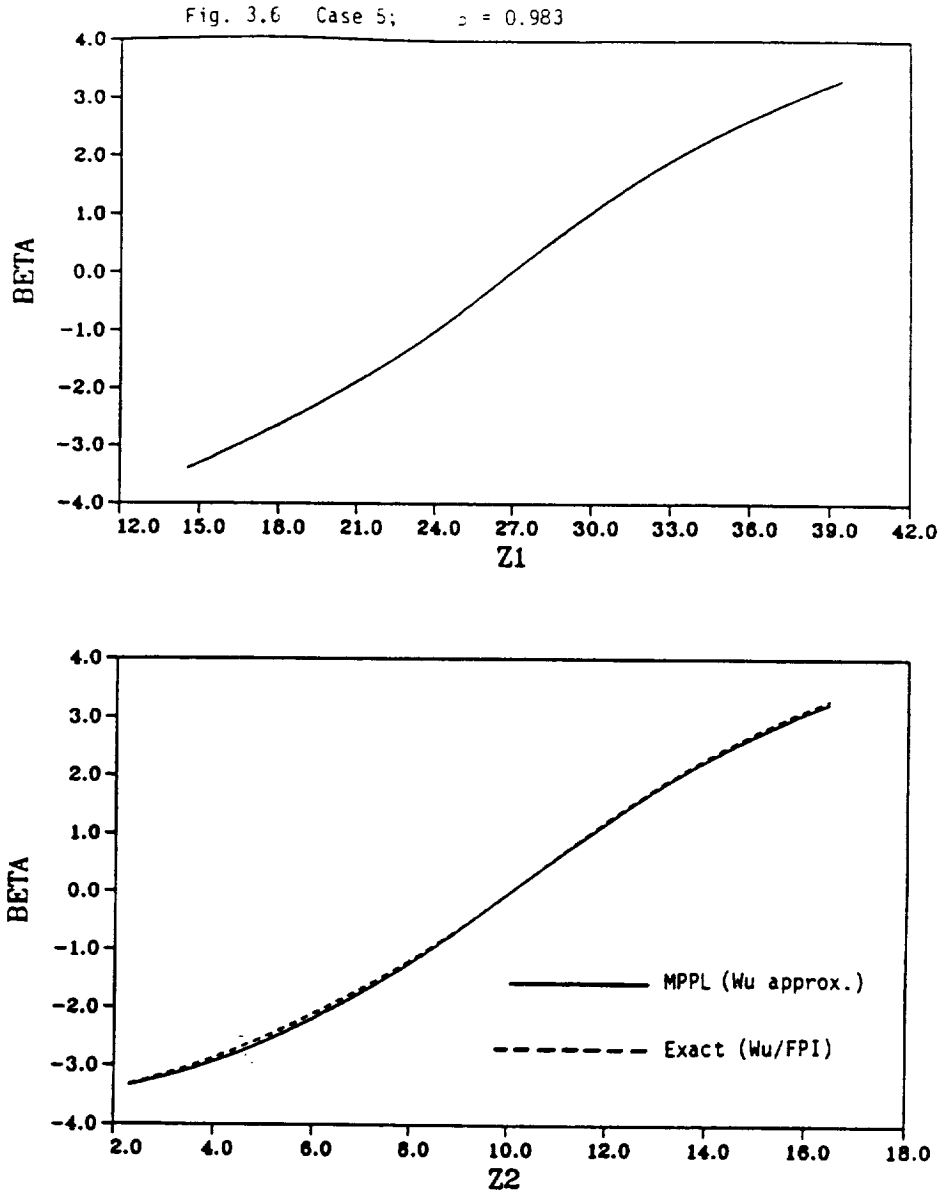

Figure 4.6 Case 5: $\rho = 0.983$

In the turbine blade analysis, the modulus of elasticity is a function of material orientation. The first bending frequency is, in theory, a non-monotonic function. Based on the previous AMVFO solution procedure, the resulting CDF would be non-monotonic which violates the definition of CDF.

In general, the AMVFO solution requires modification if more than one MPP exist. To solve the problem, all the significant MPPs should be identified first and then the probability solution should be modified by assuming multiple performance functions. The system reliability analysis methods [6], particularly the reliability bounds theory, can be applied to estimate the probability.

An efficient, approximate solution has been proposed [7] by assuming that Z is a non-monotonic function on the MPPL of Z_1, the mean-based linear approximation. Under this assumption, the CDF produced by the earlier AMVFO procedure would be a non-monotonic function. The corrected CDF can be obtained by assuming multiple, fully-correlated Z-functions. For example, for the two-MPP cases, the modified CDF can be derived by subtracting or superimposing two probabilities associated with the two CDF's. The solution procedures for concave and convex Z functions are illustrated, respectively, in Figures 4.7 and 4.8. Note that the modified CDF's are truncated at the left or right tails. This reflects the facts that the Z functions are non-monotonic, having lower or upper bounds.

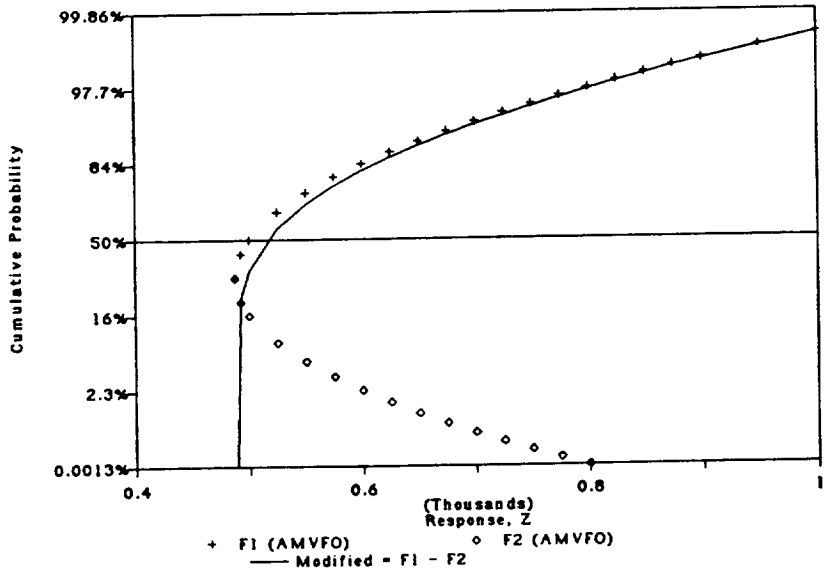

Figure 4.7 Modified AMVFO for Two-MPP (Case 1: Concave Z Function)

Figure 4.8 Modified AMVFO for Two-MPP
(Case 2: Convex Z Function)

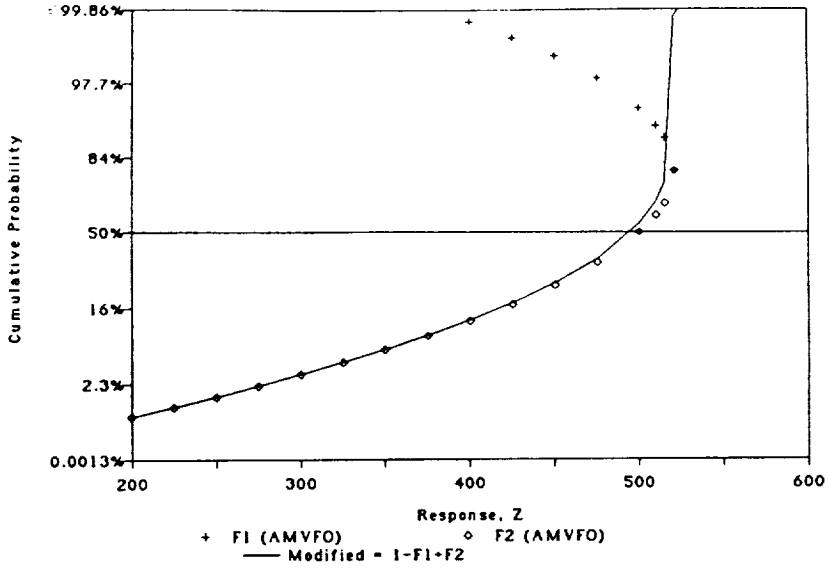

Based on the new procedure, it appears that the previous turbine blade analysis result remains valid. However, the modified AMVFO procedure suggests that the first-mode turbine blade frequency is virtually truncated, i.e., the frequency distribution has a lower bound. In addition, the new procedure suggests that a modification to the AMVFO solution will be needed if the uncertainties of the material orientation angles get higher such that the non-monotonic effect becomes more significant.

The new procedure also indicates that, in performing iterations following the AMVFO solution, it is important to keep track of both most probable points to avoid oscillation between two solution points.

4.5 The Integrated NESSUS/FPI/Monte Carlo Program

The Monte Carlo program HARBITZ (using Harbitz's method, [8]) developed at the University of Arizona [2] has been modified and included in the NESSUS/FPI program.

Two Monte Carlo options are now available in the NESSUS/FPI code (Version 3.1):

Option 1: The Monte Carlo routine utilizes the minimum distance (produced from FPI) to define a reduced sample space. The user can also input a reduction factor to decrease the minimum distance.

Option 2: The Monte Carlo routine bypasses the FPI routine and assumes that the minimum distance is zero. This option provides an independent solution. The procedure is, however, different from the standard Monte Carlo procedure in that the Harbitz's sampling procedure starts from a standardized Gaussian sampling space.

In the NESSUS analysis, the FPI algorithm is being applied at two levels. At the first level, the NESSUS/FPI code generates probabilistic output using the response function established based on the NESSUS database. At this level, NESSUS/FPI is accurate relative to the accuracy of the response function. At the second level, which is more critical to the NESSUS accuracy, the FPI algorithm directs the FEM module to "move" to another perturbation center (the most probable point generated from NESSUS/FPI). The first level is generally efficient because the response function is explicitly defined. At the second level, however, finite element solutions are required to define the response function (i.e., the response function is implicitly defined), and the computation time becomes dominant.

The NESSUS fast Monte Carlo procedure is designed to be an alternative to the NESSUS/FPI only at the first level. The major reason is that, even with the "fast" Monte Carlo method, it appears generally impractical to generate a "sufficient" number of NESSUS simulation solutions.

4.6 Modification to FPI

In additional to the new Monte Carlo routine, the NESSUS/FPI module was modified for the PAAM analysis. The modified FPI module includes a user-defined function routine (RESPON) in which the response/performance function is defined as:

$$Z(\underline{X}) = function(X_1, X_2, \ldots\ldots, X_n) \tag{4.8}$$

A routine was added to compute the response sensitivities (i.e., first- and second-order derivatives) numerically. Finally the Rackwitz-Fiessler iteration algorithm [6,9] is used to search for the most probable point. This new capability allows a more convenient definition of the response/performance function. Previously, the function must be defined in the following form:

$$X_1 = function(X_2, X_3, \ldots\ldots, X_n) \tag{4.9}$$

to allow for the use of an unconstrained optimization routine to search for the most probable point.

The new capability has been tested successfully using several examples including a PAAM example involving a Lox Post response function.

4.7 Strategies for Uncertainty Characterization of Dynamic Loads

Three basic types of dynamic loads have been considered in the context of NESSUS analysis. These are: periodic, random and transient (shock). For each type of loads, random variables need to be defined to characterize the uncertainty in the load.

For static loading, it is straightforward to treat the amplitudes of the loads as random variables. When the loading is dynamic, the uncertainty of the loading becomes more difficult to model. In general, a dynamic loading can be treated as a stochastic process $X(t)$. A stochastic process is a history containing an uncountable infinity of random variables, one for each t. The statistical properties of $X(t)$ are completely determined in terms of its n^{th}-order distribution

$$F(x_1,\ldots,x_n;t_1,\ldots,t_n) = P\{X(t_1)\le x_1,\ldots,X(t_n)\le x_n\} \qquad (4.10)$$

From the practical viewpoint, only certain averages are used. As an example, the statistics of a normal process are completely determined in terms of its mean and standard deviation.

For periodic loading, NESSUS treats the amplitude and phase as random variables. For stationary random loading, NESSUS treats the mean and the PSD as random variables. The PSD function is defined at several frequency points. At each point, the PSD can be described as a random variable. A special case is one in which the random variables are fully correlated so that only one random variable, i.e., a random scale factor of the PSD function, is needed. For multiple points random excitation, the correlations between each PSD function must be known.

For transient loading, it is possible to define a random variable for each time step if the loading can be described by using a reasonably small number of time steps. This model is more applicable when the loading function is relatively smooth and predictable over a period of time (i.e., the opposite of a white noise process in which the correlation is zero between loads at any two instances). In general, this model becomes impractical if the required number of time steps (thus the required number of random variables) is large. Therefore, simple stochastic process models which require only a few statistics would be more practical. If such models can be used to approximate the actual processes, then the uncertainty can be more easily characterized by treating the model statistics as random variables.

A sample of the NESSUS dynamics validation problems is given in Chapter 7. In this example, a cantilever beam is subjected to random base excitation. The random variables include the material properties, the geometries and the acceleration spectral density (ASD). The ASD is modeled as a truncated white noise with uncertain intensity and the cutoff frequency is also modelled as a random variable.

4.8 Non-normal Random Variables

The strategies for problems involving dependent non-normal random variables have been documented in [2,7]. Two computer subroutines have been written to facilitate the required random variables transformations. A strategy was defined to integrate these subroutines with the NESSUS modules to automate the solution process.

4.9 References

[1] "Probabilistic Structural Analysis Methods (PSAM)," 2nd Annual Report, NASA Contract NAS3-24389.

[2] "Probabilistic Structural Analysis Methods (PSAM)," 3rd Annual Report, NASA Contract NAS3-24389.

[3] Y.-T. Wu, and P.H. Wirsching, 1987, "A New Algorithm for Structural Reliability Estimation," *Journal of Engineering Mechanics, ASCE*, 113, No. 9, Sept., pp. 1319-1336.

[4] Y.-T. Wu, and O.H. Burnside, 1988, "Validation of the NESSUS Probabilistic Finite Element Analysis Computer Program," *Proceedings of the 29th AIAA/ASME/ASCE/AHS Structures, Structural Dynamics and Materials Conference*, Part 3, pp. 1267-1274.

[5] Y.-T. Wu, O.H. Burnside, and J. Dominguez, 1987, "Efficient Probabilistic Fracture Mechanics Analysis," *Proceedings of the Fourth International Conference on Numerical Methods in Fracture Mechanics*, Pineridge Press, Swansea, U. K., pp. 85-100.

[6] A. H.-S. Ang, and W.H. Tang, 1984, *Probability Concepts in Engineering Planning and Design*, Vol. II, John Wiley & Sons, New York.

[7] "Probabilistic Methods for Structural Response Analysis," by Y.-T. Wu, O.H. Burnside and T.A. Cruse, presented at the ASME/SES Summer Meeting, California, June 1988, published in *Computational Probabilistic Methods*, W.K. Liu et al. (Eds.), AMD-Vol. 93, ASME, pp. 1-14. (Also pending publication in *Computational Mechanics of Reliability Analysis*, edited by W.K. Liu and T. Belytschko, Elmepress International)

[8] A. Harbitz, 1986, "An Efficient Sampling Method for Probability of Failure Calculation," *Structural Safety*, Vol. 3, pp. 109-115.

[9] R. Rackwitz, and B. Fiessler, 1978, "Structural Reliability Under Combined Load Sequences," *Journal of Computers and Structures*, 9, pp. 489-494.

5.0 NESSUS/EXPERT

5.1 Summary

NESSUS/EXPERT has been designed as an expert system to assist in the use of the probabilistic finite element code NESSUS/FEM and the fast probability integrator (FPI). These codes contain a significant amount of new technology and features and require data unique to probabilistic analysis of structures. As a result, NESSUS/EXPERT performs a broad variety of operations to insure a successful PSAM analysis.

NESSUS/EXPERT has been designed to be an interactive user friendly expert system. The backbone of the system is an intelligent menu selection procedure to guide the user in appropriate input choices. Help screens explain input formats and provide detailed explanations of NESSUS keywords and act as an on-line user's manual. Error checking is provided at various levels to insure functional input data to the NESSUS and FPI programs. NESSUS/EXPERT also provides advice and default values of probabilistic input to assist the user in selecting data for which the user is unfamiliar or a knowledge base is not established.

5.1.1 Menu Structure

NESSUS/EXPERT is intended as an aid to probabilistic design. Therefore, all input is driven by a user-friendly interactive menu system. The menus are divided into functional modules for easy input. An overview of the NESSUS/EXPERT menu system is shown in Figure 5.1.

An intelligent menu selection procedure guides the user through data input. NESSUS/EXPERT will disable certain menu selections based on existing model data in order to prevent an input error. For example, if the model is composed of plate elements, the beam section input module will not be active thus preventing the user from inputting incorrect information.

5.1.2 Help Screens

Help screens are provided for NESSUS keywords. Help screens provide detailed information on a keyword. These help screens cover the usual finite element keywords and NESSUS specific keywords. Thus, the user can obtain information on usual finite element inputs such as plasticity theories as well as NESSUS specific keywords such as convergence criteria.

Help screens serve in one sense as an on-line users manual. The proper format of input and the definition of the input variables can be obtained on-line. For example, the help screen describing the element connectivity, shown in Figure 5.2, describes the input variables and proper input format.

In a more detailed sense, the user can get detailed explanations of a keyword and its consequences. As an example, the user may have a finite element model of a rotating structure and wants to know if the

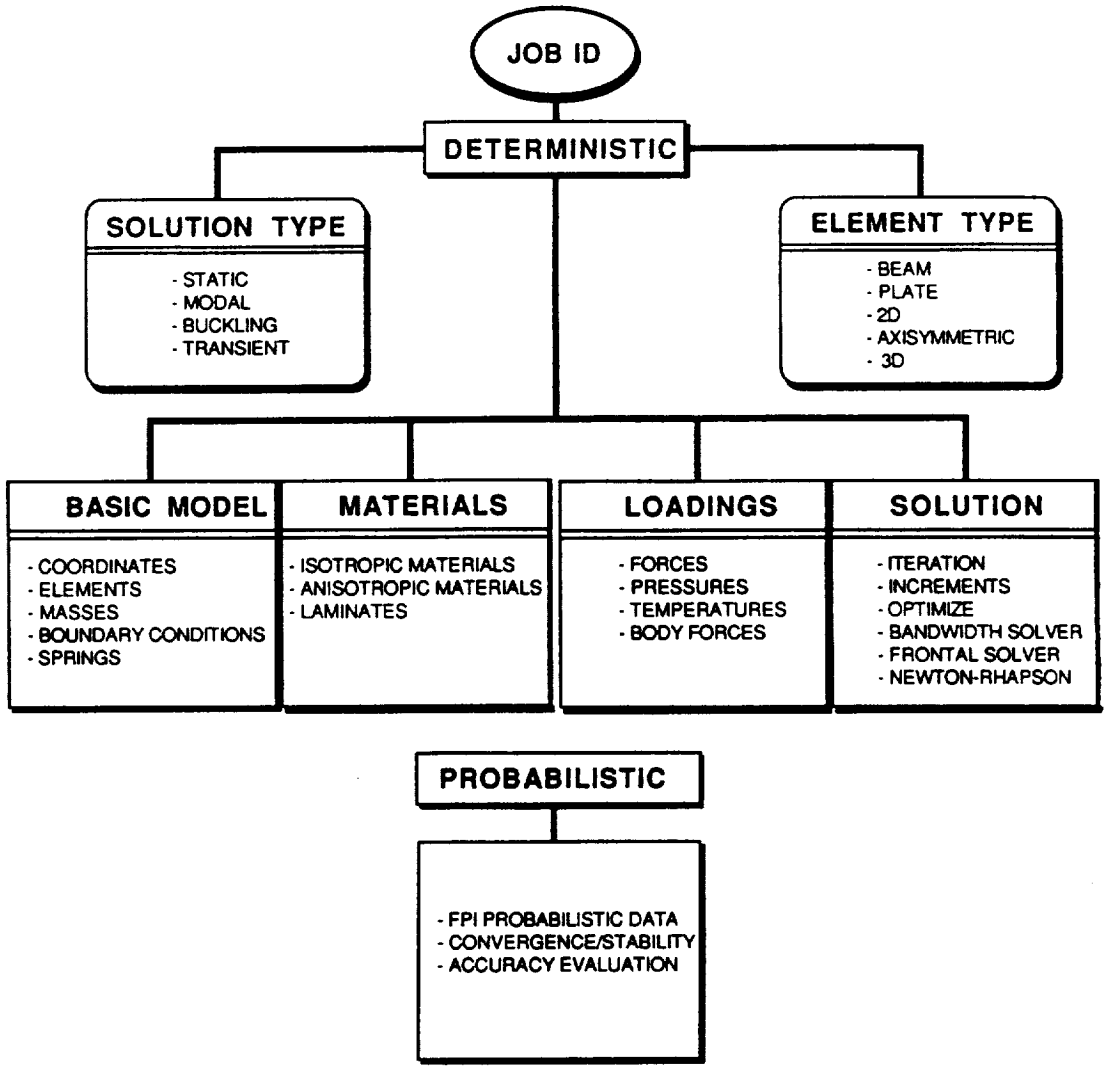

Figure 5.1 NESSUS/EXPERT Menu System

*** CENTRIFUGAL MASS HELP SCREEN ***

Centrifugal mass effects account for the changes in centrifugal inertia that result from deforming the structure(i.e. follower effects for centrifugal loading). Centrifugal mass effects are important in the analysis of high-speed rotation machinery.

When this option is selected, centrifugal mass stiffness effects due to angular velocity are included at the increment number specified. Centrifugal mass has one parameter. Increment number at which centrifugal mass stiffness effects are to be included.

The angular velocity is defined with the DISTRIBUTED LOAD data input.

The axis about which the angular velocity occurs is defined with the BODY FORCE data input.

Figure 5.2 Help Screen for Element Connectivity

centrifugal mass option is appropriate and the expected consequences. The help screen, Figure 5.2, describes the centrifugal mass option and confirms the input format.

5.1.3 Error Checking

Finite element methodology by itself is a complicated task and often requires a large amount of data for realistic engineering problems. A large amount of engineering time is often spent debugging input data of a finite element model. In addition, the NESSUS/FEM probabilistic finite element program contains new technology developed explicitly for probabilistic finite element analysis. Thus, not only are the data requirements expanded, but even knowledgeable deterministic finite element users will not be well versed in many of the options in NESSUS/FEM. Therefore, one of the requirements of NESSUS/EXPERT is to analyze the input data for errors and allow corrections in the interactive mode. Wasted engineering time and computer time while iteratively debugging the input data is eliminated.

NESSUS/EXPERT performs error checking on several levels to insure a correct input deck. For example, if material properties are being input for an elastic isotropic material, the user must enter: beginning node, ending node, elastic modulus, and Poisson's ratio.

As an initial check, NESSUS/EXPERT makes sure the correct number of entries have been made; in this case four entries. On the next level, the value of the material properties is checked for physical sense. For example, the elastic modulus must be positive and Poisson's ratio is bounded by the limits -1 and +1/2.

If an error is detected at this level a descriptive error message is printed and the user is reprompted. Error checking at this point is within a single keyword - namely material properties. NESSUS/EXPERT also provides error checking between keywords. For example, if forces are input for nodes that do not exist, NESSUS/EXPERT will compare the nodal data in the loading module with the nodal data in the coordinates module. Error checking across keywords is performed only when leaving a keyword because sometimes a large amount of data must be checked. If an error is detected the undefined node numbers are identified and the user has the option of ignoring the error message, reentering the data, or defining the new nodes. A NESSUS/EXPERT error screen is shown in Figure 5.3.

A final level of error checking and warning messages is performed when the user attempts to build the NESSUS/FEM input deck from the NESSUS/EXPERT input. All high level checking between keywords is performed and appropriate messages issued.

5.1.4 Language Implementation

Previous reports have discussed the evolution of the NESSUS/EXPERT implementation language into a combination of FORTRAN and CLIPS, a C language expert system tool. This combination is utilized to exploit

*** CONSISTENCY CHECK FOR TURBINE BLADE ***

Forces are defined for the following undefined nodes.

107 108

TYPE C to enter coordinate data for the node(s) OR
F to change the force definition(s)
I to ignore the inconsistency for now.

Figure 5.3 Error Screen for Forces on Undefined Nodes

the strengths of each language. The present work has continued with the Clips - Fortran hybrid implementation. This language implementation has allowed high-level decision making on one hand and low level data checking and interfacing with engineering codes on the other.

5.1.5 Probabilistic Input

In many real life engineering problems, probabilistic knowledge of the random input variables is not known. The mean, standard deviation and the probability density function PDF is required input for the FPI program. The probabilistic response of a structure may be sensitive to the PDF chosen. The probability data for a random variable may not always be known; however, a distinction can be made between appropriate and inappropriate choices.

A large amount of statistical data has been accumulated for various random variables. NESSUS/EXPERT can offer the best known default distributions and coefficient of variations for a random variable. Table 5.1 shows a list of the default distributions and COV's that have been gathered from engineering data and experience. Thus, if statistical information is not known about a particular random variable, NESSUS/EXPERT will provide a realistic choice.

Help screens and warning messages provide the user with additional information. For example, if the user selects a Weibull distribution for a loading random variable, a warning message "the Weibull distribution is not generally recommended for loading random variables" will appear. This list of recommended statistical data can be modified for any random variable. For example, if good data on pressure distributions on a turbine blade become available, the data can be incorporated into the list of recommended values. Thus, expert can serve as a user-defined repository of statistical data. This can aid new users who are unsure of appropriate input data.

In addition, the menu structure for selecting probabilistic input has been defined and a preliminary version input in EXPERT.

The majority of the work has concentrating on implementing the NESSUS/FEM model data into the menu system. As a result, a fairly robust menu system is currently available for building the FEM models. The majority of the keywords through NESSUS release 2.5 are implemented. The NESSUS/EXPERT capabilities have been tested by running several example problems with EXPERT. A diagnostics list has been developed for the expert system. The diagnostics have been split into high and low priority items. The high priority items must be completed before releasing the code. Although, many minor bugs were found the system is a fairly complete implementation of the NESSUS keywords.

5.1.6 Limitations

One inconvenience of EXPERT is the length of time to load rules at the beginning of an expert session. EXPERT consists of approximately 600 rules which must be loaded in at startup. This takes roughly 7 minutes

Table 5.1

Default Distributions and COV's for
NESSUS Random Variables

VARIABLE	DISTRIBUTION	COV
Young's Modulus	Normal	.02
Poisson's Ratio	Normal	.02
Shear Modulus	Normal	.02
Density	Normal	.02
Thermal coefficient	Normal	.05
Yield stress	Wiebull	.07
Geometry	Normal	.005
Thickness	Normal	.005
Temperature	Lognormal	.05
Pressures	Lognormal	.04
Forces	Lognormal	.02
S-sect area	Normal	.007
Inertia	Lognormal	.02
Torsional constant	Lognormal	.01
Springs	Lognormal	.02
Material Orientation	Normal	
Other	Lognormal	

on a VAX. This is an irritating length of time if EXPERT must be entered more than once. A Clips version containing compiles rules was found to be limited to only 180 rules. Apparently, NESSUS/EXPERT is one of the largest implementations in Clips.

5.1.7 Future Effort

NESSUS/EXPERT needs to be exercised on a variety of realistic engineering problems to thoroughly test and debug the code. While the menu structure is fairly complete it must be updated to reflect recent changes in the NESSUS/FEM code such as harmonic excitation and random vibration capabilities. The menu structure for probabilistic input has been defined but has not been implemented. Also, other heuristics such as selecting perturbation sizes and convergence criteria must be determined and implemented.

5.2 PFEM

PFEM is a utility which automatically links the NESSUS finite element program and the FPI fast probability integrator. The advantages are :

- o user intervention is reduced.
- o batch analyses are now possible.

PFEM will coordinate the analysis and data exchange between FEM and FPI depending on the options chosen.

5.2.1 Capabilities

1) perform MVFO analysis on a range of nodes.
2) perform AMVFO on a single node. The AMVFO option will compute moves based on MVFO results insert moves into NESSUS/FEM input file and run NESSUS/FEM for each probability level.

5.2.2 Status

Previously, PFEM coordinated execution between the separate executables NESSUS/FEM and FPI with a certain amount of system dependent code. Because of the recent integration of the FPI code into the NESSUS/FEM framework much of the PFEM code must be rewritten. The data exchange and file handling mechanisms must be changed. Although the final integrated package will be a much nicer program and be system dependent, the integration has slowed development of the PFEM module.

6.0 NESSUS BOUNDARY ELEMENT CODE DEVELOPMENT

6.1 Introduction

Analytical methods have been developed for reducing certain types of body forces to equivalent boundary integrals. The first publication concerned three dimensional body forces due to steady state thermal loading and due to centrifugal acceleration [1]. This approach was then extended to the axisymmetric problem [2]. Subsequently, [3] summarized this approach.

The limitation in the analytical approach is that many body force-like problems can not be treated in the exact manner employed for the above studies. Examples of these important problems include non-steady thermal loading, vibration, temperature dependent properties, plasticity, etc. For such problems, the body forces have been modeled using domain elements, thereby voiding much of the BIE advantage of reducing problem dimensionality.

Relatively recently, a new and very powerful approach was identified by [4] which offers an alternative to the direct use of domain elements for these classes of problems. The method, which they have called the dual reciprocity method, uses global interpolation functions to replace standard domain interpolations, *a la* finite elements. The dual reciprocity formalism results in boundary integral equations that are approximately equivalent to the domain integrals of the standard BIE formulation. They have extended the method to transient dynamic problems [5].

Following this work of Nardini and Brebbia, Banerjee and co-workers [6,7] have used the same approach, but in a different formalism. The formalism draws very directly on the notion of particular integrals to the governing equations. The formalism of particular integrals results in a clearer understanding of the common features for a full range of body force problems. The particular integral approach will therefore be adopted herein.

6.2 Probabilistic Boundary Element Analysis

The Probabilistic Boundary Element Program (PBEM) is an adaptation of the boundary element code BEST3D to perform probabilistic analysis of structures. The purpose of PBEM is analogous to NESSUS/FEM, that is to obtain structural sensitivity data. The actual probabilistic analysis is done with FPI using the sensitivity data. The database connecting PBEM and FPI is identical to that of NESSUS/FEM. Thus, the existing codes PREFPI and FPI can be used without modification.

Initial programming efforts have focused on implementing the necessary input formats, storage algorithms and perturbation algorithms for a variety of random variables. In addition, an effort has been made to give the code the same look and feel as the NESSUS/FEM code wherever possible. Currently, the method of obtaining the structural response to a perturbed problem is through resolution although more efficient methods will be examined for future implementation.

A summary of the salient code features are:

- o resolution technique used for perturbation random variables
- o perturbation input format similar to NESSUS/FEM
- o probabilistic BEM input format similar to deterministic BEM input
- o identical database format as NESSUS/FEM
- o coding for storing and retrieving the probabilistic data similar to deterministic coding

Much attention has been paid to the look and feel of the PBEM code. Wherever possible, input formats similar to NESSUS/FEM formats have been used, such as the method of defining random variables and perturbations. In addition, the method of defining the boundary element probabilistic data is similar to the deterministic input format. The coding for storing and retrieving the probabilistic data is very similar to the coding for deterministic data. Typically deterministic routines were copied, renamed and used for probabilistic data. The PBEM code dumps all data to a database identical to the NESSUS/FEM database. Thus, the PREFPI program can be used to retrieve data and format input files for FPI analysis. An example problem of the probabilistic analysis to a beam under axial load using PBEM is contained in Appendix G.

The current status of the PBEM code is:

RANDOM VARIABLE	COMMENTS
MATERIALS	No temperature dependency
Elastic Modulus	Multiple GMR's OK
Poisson's ratio	
Thermal Coefficient	
Density	
GEOMETRY	Multiple GMR's OK
Coordinates	
	Only 1 BC set
BOUNDARY CONDITIONS	
Displacement	
Traction	
	OK
BODY FORCES	
Centrifugal	

RESULTS DUMPED TO IDENTICAL DATABASE AS FEM

- o Resolution technique used for all perturbations.
- o Any combination of presently allowed random variables OK.
- o No time dependency.

- o Convenient random variable input.
- o Perturbation definition similar to FEM definitions.

6.3 Domain Integral Formulation

6.3.1 Betti's Theorem

The reciprocal work theorem is written first in terms of the stress $(\underline{\sigma}, \underline{\Sigma})$ and strain tensors $\underline{\epsilon}, \underline{E}$ for two solution states. The first state, denoted by lower case Greek symbols, refers to the physical state for which we desire the solution; the second state, denoted by upper case Greek symbols refers to the fundamental solution [8] for the linear elastic problem. Letting superscripts (T, E, P, Θ) refer to total, elastic, plastic, and thermal strains, we obtain the reciprocal strain energy theorem in the form

$$\int_{<R>} \underline{\sigma} \cdot \underline{E} dV = \int_{<R>} \underline{\epsilon}^{E} \cdot \underline{\Sigma} dV \tag{6.1}$$

In (6.1), $<R>$ denotes the volumetric principal value integral. That is, the volume integral extends over the entire region of interest, but excludes the small sphere surrounding the point load singularity from the fundamental solution.

The Reciprocal Work Theorem of (6.1) is easily proved for linear elastic materials in terms of Hooke's law

$$\begin{aligned} \underline{\sigma} &= \underline{C} \cdot \underline{\epsilon}^{E} \\ \underline{\Sigma} &= \underline{C} \cdot \underline{E} \end{aligned} \tag{6.2}$$

The elastic strain can now be written in terms of the total, and other, strains as

$$\int_{<R>} \underline{\sigma} \cdot \underline{E} dV = \int_{<R>} (\underline{\epsilon}^{T} - \underline{\epsilon}^{P} - \underline{\epsilon}^{\Theta}) \cdot \underline{\Sigma} dV \tag{6.3}$$

The total strain in (6.3) may be written in terms of the displacement gradient operator $\underline{B}$ as

$$\begin{aligned} \underline{\epsilon}^{T} &= \underline{B} \cdot \underline{u} \\ \underline{E}^{T} &= \underline{B} \cdot \underline{U} \end{aligned} \tag{6.4}$$

where $\underline{u}, \underline{U}$ refer to the displacements for the physical solution and the fundamental solution, respectively. Then the reciprocal work theorem can be written as

$$\int_{<R>} \underline{\sigma} \cdot (\underline{B} \cdot \underline{U}) dV = \int_{<R>} (\underline{B} \cdot \underline{u}) \underline{\Sigma} dV - \int_{<R>} (\underline{\epsilon}^{P} + \underline{\epsilon}^{\Theta}) \cdot \underline{\Sigma} dV \tag{6.5}$$

6.3.2 Somigliana Identity

The reciprocal work theorem in (6.5) contains two integrals which can be converted through the application of the divergence theorem to boundary integrals. The divergence theorem poses the requirement that the strain be continuous, and can be show to result in the following form of (6.5)

$$\int_{S+S_\epsilon} \underline{t}\cdot\underline{U}\,dS + \int_{<R>} \rho\underline{b}\cdot\underline{U}\,dV = \int_{S+S_\epsilon} \underline{u}\cdot\underline{T}\,dS - \int_{<R>} (\underline{\epsilon}^I + \underline{\epsilon}^0)\cdot\underline{\Sigma}\,dV \tag{6.6}$$

The body force per unit mass, $\underline{b}$, appears in (6.6) because of equilibrium requirements, and the application of the divergence theorem

$$\nabla\cdot\underline{\sigma} + \rho\underline{b} = 0 \tag{6.7}$$

The terms in (6.6) which are written at the boundary of the region, denoted $S+S_\epsilon$, include the surface to the physical problem as well as the surface to the small excluded sphere of radius ϵ. The domain integrals in (6.6) are required for equilibrium to be exactly satisfied in the presence of non-elastic strains and body forces.

It can be shown that the left-hand-side integral over S_ϵ in (6.6) is zero in the limit as $\epsilon \to 0$. The corresponding RHS integral in (6.6) can be shown to be $\underline{u}(p)\cdot\underline{\delta}$ where $\underline{\delta}$ is the Kroenecker delta. The free term that results is associated with the point load of the fundamental solution, which is taken to be located at an internal solution point $p(\underline{x})$. Re-writing eqn. (6.6) results in the well-known Somigliana identity for the displacement at $p(\underline{x})$

$$\underline{u}\cdot\underline{\delta} = \int_S \underline{t}\cdot\underline{U}\,dS - \int_S \underline{u}\cdot\underline{T}\,dS + \int_{<R>} (\underline{\epsilon}^I + \underline{\epsilon}^0)\cdot\underline{\Sigma}\,dV + \int_{<R>} \rho\underline{b}\cdot\underline{U}\,dV \tag{6.8}$$

Equation (6.7) is a re-statement of equilibrium in that differentiation of the Somigliana identity results in exactly satisfying the equilibrium requirements, now in the presence of a body force, and inelastic strains.

6.3.3 Boundary Integral Equation (BIE)

The BIE is obtained from Somigliana's identity by allowing the interior solution point to approach the boundary, *viz.* $p(\underline{x}) \to P(\underline{x})$. Again from [9], it is possible to determine that the point load term in (6.7) is replaced by its boundary equivalent, denoted $\underline{C}$, such that

$$\underline{u}\cdot\underline{C} + \int_S \underline{u}\cdot\underline{T}\,dS = \int_S \underline{t}\cdot\underline{U}\,dS + \int_{<R>} (\underline{\epsilon}^I + \underline{\epsilon}^0)\cdot\underline{\Sigma}\,dV + \int_{<R>} \rho\underline{b}\cdot\underline{U}\,dV \tag{6.9}$$

Equation (6.9) is the BIE for the formulation with body force and inelastic strains. Clearly, the BIE is not strictly a *boundary-integral equation* due to the presence of the domain integrals. The remainder of this note deals with the issue of modifying the domain integrals into *equivalent* boundary integrals.

6.4 Reduction of Domain Integrals to Boundary Integrals

6.4.1 Outline of Procedure

The procedure for the domain integrals involving thermal and body force loads is essentially the same. First, the domain variable is written in terms of the Navier operator relationship for that domain variable. The domain variable is then approximated by a global interpolation, which allows the domain variable to be approximated by the superposition of relatively simple domain variables. Finally, knowing the particular solution of the problem, we can write a boundary integral equation for the particular solution of the problem. The difference between the original integral and the particular integral equation give us an *equivalent* boundary integral without the domain terms.

The replacement of the domain variable by simple global interpolation operators allows us to integrate the Navier operator for that problem. The quality of the *equivalent* boundary integral is then based on the quality of the assumed interpolation formulae for the thermal strain and the body force loading term. In particular cases it is possible to obtain exactly equivalent boundary integrals, as cited in Section 6.1. The exact cases correspond to steady state thermal loading and centrifugal acceleration body force loading.

The problem with the procedure is the ability of the global interpolation functions to accurately match the physical variable. This issue will be discussed in detail with examples in a later section. However, the accuracy of the *equivalent* boundary integral is *solely* dependent on the accuracy of the global interpolation. Unfortunately, insufficient attention has been paid to this vital issue in the literature; also, there seems to be little research into the development of improved global interpolation schemes. This is in spite of the great value of being able to replace the domain integrals by *equivalent* boundary integrals.

6.4.2 Thermal Strain

We now seek to find a particular solution, $\underline{u}^{\bullet}$ to the Navier equations of elastic equilibrium in the presence of thermal loading. Stress equilibrium is given by eqn. (6.7), the stress-strain relation by (6.2), and the strain-displacement relation by (6.4), such that

$$\frac{\nu}{1-2\nu}\nabla(\nabla\cdot\underline{u}^{\bullet})+\nabla^2\underline{u}^{\bullet}-\alpha\left(\frac{1+\nu}{1-2\nu}\right)\nabla\theta=0 \tag{6.10}$$

Let eqn. (6.10) be written symbolically as

$$\underline{N}\cdot\underline{u}^{\bullet}-\beta\nabla\theta=0 \tag{6.11}$$

where $\beta = \alpha \cdot (1+\nu)/(1-2\nu)$. The particular solution to (6.11) implies additional boundary displacements, $\underline{u}^*(Q)$, and boundary tractions, $\underline{t}^*(Q)$ which must be considered along with the physical boundary conditions. In general, we must consider an approximate solution to eqn. (6.11). The usual manner is to model the domain integral using "finite elements" and an assumed nodal interpolation of the temperatures.

For the current approach, the temperatures will be represented by interpolation functions that are tied to the surface, and not to internal nodes. In either case, the temperature field is approximate; the nature of this approximation and its effect on the solution accuracy will be discussed in Section 6.5.

We can now express a boundary integral equation similar to eqn. (6.9) for the particular solution as

$$\underline{u}^* \cdot \underline{C} + \int_S \underline{u}^* \cdot \underline{T} dS = \int_S \underline{t}^* \cdot \underline{U} dS + \int_{<R>} \tilde{\underline{\epsilon}}^* \cdot \underline{\Sigma} dV \tag{6.12}$$

where $\tilde{\underline{\epsilon}}^* = \alpha \underline{\delta} \tilde{\theta}$. The tildes denote that the actual quantity has been replaced by an approximation.

By subtracting eqn. (6.12) from eqn. (6.9), we obtain an equivalent boundary integral equation of the form

$$\hat{\underline{u}} \cdot \underline{C} + \int_S \hat{\underline{u}} \cdot \underline{T} dS = \int_S \hat{\underline{t}} \cdot \underline{U} dS + \underline{E}^* \tag{6.13a}$$

Where $\hat{\underline{u}} = \underline{u} - \underline{u}^*$, $\hat{\underline{t}} = \underline{t} - \underline{t}^*$, and $\underline{E}^*$ is the error term given by

$$\underline{E}^* = \int_{<R>} (\underline{\epsilon}^* - \tilde{\underline{\epsilon}}^*) \cdot \underline{\Sigma} dV \tag{6.13b}$$

To complete the procedure, we now require a particular solution to the governing differential eqn. (6.11).

The Helmholtz decomposition theorem for an arbitrary vector says that the vector may be written as the sum of scalar and vector potentials as

$$\underline{u}^* = \nabla \psi + \nabla \times \underline{\phi} \tag{6.14}$$

For the case of the particular solution to (6.11) we may take $\underline{\phi} = 0$ without loss of generality. In this case the Navier equations of equilibrium become

$$\left(\frac{1-\nu}{1+\nu}\right) \nabla^2 \psi = \alpha \theta \tag{6.15}$$

within an arbitrary constant of integration.

The critical question raised in the use of such particular solutions is not their effect on the BIE formulation, but rather how one is to represent such particular solutions. The standard methodology that is

employed in such particular solution formulations is to replace the known field (in this case, temperatures) by a simple, global interpolation field, for example

$$\tilde{\theta}(q) = \sum_{j=1}^{N} K(q,Q_j)\Phi(Q_j) \tag{6.16}$$

where $\tilde{\theta}(q)$ is the temperature interpolation $q(\underline{x})$, $\Phi(Q)$ is a set of unknown coefficients, and $K(q,Q)$ is a global interpolation function. The usual method is to take the global interpolation function to be a simple function

$$K(q,Q) = R_o[1 - r(q,Q)/R_o] \tag{6.17}$$

where r(q,Q) is the distance between the interpolated point q and the boundary point Q, and R_o is a scale constant such as the maximum size of the region. The quality of this interpolation function for generalized thermal loads is discussed in Section 6.5.

When the simple form of the interpolation field (6.16) is used to approximate the temperatures in the Navier eqn. (6.15), the form for the potential function $\psi(q)$ can be found

$$\psi(q) = \left(\frac{1+\nu}{1-\nu}\right)\alpha \sum_{j=1}^{N} X(q,Q)\Phi(Q) \tag{6.18}$$

where the integrated global interpolation function is given by

$$X(q,Q) = R_o\left(2 - \frac{r(q,Q)}{R_o}\right)\frac{r(q,Q)^2}{12} \tag{6.19}$$

The corresponding displacement field for (6.19) is given from (6.12) as

$$\underline{u}^* = \left(\frac{1+\nu}{1-\nu}\right)\alpha \sum_{j=1}^{N} R_o\left(4 - 3\frac{r(q,Q)}{R_o}\right)\frac{\underline{x}-\underline{\xi}}{12} \tag{6.20}$$

where $\underline{x}-\underline{\xi}$ is the Cartesian distance from $Q(\underline{\xi})$ *to* $q(\underline{x})$. Equation (6.20) is then the solution to eqn. (6.11), for the assumed global interpolation of temperatures. Stresses and surface tractions may then be derived from the displacement terms in eqn. (6.20).

The derived particular traction and displacement solutions to the approximation for eqn. (6.11) are to be substituted into eqn. (6.13a). Assuming that the error is zero, eqn. (6.13a) results in two coupled sets of boundary integral equations, one known and one unknown. Following discretization, the set of BIE matrix equations is solved in the normal fashion.

Other terms may need to be included in the global interpolation field including a linear field. Modeling very early transients will likely require the use of a one dimensional temperature field of the form $e^{-\lambda\xi}$, where ξ is the inward normal distance from the free surface and λ is the appropriate inverse-distance variable in terms of the heat conduction properties of the medium. Such additional terms are expected to improve

the nature of the global interpolation process, thereby improving the accuracy of the equivalent boundary integral for the transient thermal loads.

6.4.3 Body Force Load

The body force that will be considered in the current formulation is for modal vibration of the body. Gravitational and rotational inertia body forces can be treated exactly by boundary integrals, as shown by [1].

The Navier equation of equilibrium for the body force load can be expressed as

$$\underline{N}\cdot\underline{u}^d+\rho\underline{b}=0 \tag{6.21}$$

As before, we can express the equivalent boundary integral equation for this case as

$$\bar{\underline{u}}\cdot\underline{C}+\int_S\bar{\underline{u}}\cdot\underline{T}dS=\int_S\bar{\underline{t}}\cdot\underline{U}dS+\underline{E}^d \tag{6.22}$$

Where $\bar{\underline{u}}=\underline{u}-\underline{u}^d$, $\bar{\underline{t}}=\underline{t}-\underline{t}^d$, and the error terms is given as

$$\underline{E}^d=\int_{<R>}\rho(\underline{b}-\bar{\underline{b}})\cdot\underline{U}dV \tag{6.23}$$

The challenge, of course, is to find a suitable particular solution to the operating differential eqn. (6.21) for a given body force problem. In general, we can say that no generalized solution exists except for simple problems such as rotational inertia loading.

The problem of interest in the current note is that for normal mode vibration, where

$$\rho\underline{b}=\rho\Omega^2\underline{u} \tag{6.24}$$

for which the particular solution from (6.21) is sought

$$\underline{N}\cdot\underline{u}^d+\rho\Omega^2\underline{u}=0 \tag{6.25}$$

If we now replace the actual displacement field, $\underline{u}$, by an approximate interpolation over the domain, as given by

$$\bar{\underline{u}}=\sum_{j=1}^{N}K(q,Q_j)\underline{\Phi}^d(Q_j) \tag{6.26}$$

then a particular solution for $\underline{u}^d$ can be found from (6.25) as

$$\underline{u}^d=\rho\Omega^2\sum_{j=1}^{N}\underline{G}(q,Q_j)\cdot\underline{\Phi}^d(Q_j) \tag{6.27}$$

The form of the particular solution $\underline{G}$ can be found by inspection to be given by the polynomial

$$\underline{G}=C_1(\underline{\delta}r(q,Q)^2+\underline{y}\otimes\underline{y})+C_2\underline{\delta}r(q,Q)^3+C_3r(q,Q)\underline{y}\otimes\underline{y} \tag{6.28a}$$

For the interpolation function given by eqn. (6.17),

$$C_1 = -\rho\Omega^2 \frac{(1-2\nu)R_o}{(14-16\nu)\mu}$$

$$C_2 = \rho\Omega^2 \frac{(11-12\nu)}{144(1-\nu)\mu)} \qquad (6.28b)$$

$$C_3 = -\rho\Omega^2 \frac{1}{48(1-\nu)\mu}$$

The ability of this interpolation to represent modal vibration displacement fields is discussed in Section 6.5.

Again, now that the particular displacement solution is known, the particular tractions can be obtained, and both terms substituted into eqn. (6.22). Treating the error as having zero contribution, the boundary integral equation is factored into the standard terms and those with the particular solution.

6.4.4 Temperature Dependent Material Properties

For most applications in the design of thermally loaded structures, such as for gas turbine engine structures, the material properties are temperature dependent. Temperature dependence introduces inhomogeneities in terms of the boundary integral equation formulation that also appear as domain integrals.

Consider Hooke's law for the elastic material with temperature dependent shear modulus and Poission's ratio $\mu(\Theta)$ and $\nu(\Theta)$

$$\underline{\sigma} = \frac{2\mu\nu}{1-2\nu}\delta e + 2\mu\underline{\epsilon} \qquad (6.29)$$

where $e = tr\ \underline{\epsilon}$. If we assume that the two material properties $\mu(\Theta)$ and $\nu(\Theta)$ can be written in terms of an average or nominal constant plus the thermal deviation from this constant then

$$\underline{\sigma} = \frac{2\mu_o\nu_o}{1-2\nu_o}\delta e + 2\mu_o\underline{\epsilon} + \frac{2\mu(\Theta)\nu(\Theta)}{1-2\nu(\Theta)}\delta e + 2\mu(\Theta)\underline{\epsilon} \qquad (6.30)$$

The resulting form for Hooke's law can then be simplified as

$$\underline{\sigma} = \underline{C}_o \cdot \underline{\epsilon} + \underline{C}'(\Theta) \cdot \underline{\epsilon} \qquad (6.31)$$

The reason for separating the constant terms from the temperature dependency is to allow the direct use of Betti's reciprocal work theorem in formulating the boundary-integral equation. Beginning with the domain formulation, we obtain

$$\int_{<R>} (\underline{\sigma} - \underline{\sigma}') \cdot \underline{E} dV = \int_{<R>} \underline{\epsilon}^f \cdot \underline{\Sigma} dV \qquad (6.32)$$

where the initial stress due to the material inhomogeneity $\underline{\sigma}'$ is given from (6.31) as

$$\underline{\sigma}' = \underline{C}'(\Theta) \cdot \underline{\epsilon} \qquad (6.33)$$

Application of the equilibrium requirement on the stress field in (6.31) results in the following Navier equation of equilibrium for the displacement field in terms of the inhomogeneity field

$$\underline{N}\cdot\underline{u}' + \nabla\cdot\underline{\sigma}' = 0 \tag{6.34}$$

The inhomogeneous Navier equation appears in the same form as that for the dynamic body force result (6.25). Consistent with the previous approach, the term for the gradient of the inhomogeneous stress term, $\nabla\cdot\underline{\sigma}'$, would be replaced by a global interpolation function for which a particular solution to (6.34) could be found. The resulting substitution would approximate the inhomogeneous stress state, as follows

$$\nabla\cdot\tilde{\underline{\sigma}}' = \nabla\cdot(\underline{C}'(\theta)\cdot\underline{\epsilon}) \tag{6.35}$$

The global interpolation function in (6.35) must be evaluated by fitting the terms to values of the gradient operator

$$\nabla\cdot(\underline{C}'(\theta)\cdot\underline{\epsilon}) = (\nabla\cdot\underline{C}')\cdot\underline{\epsilon} + \underline{C}'(\theta)\cdot(\nabla\cdot\underline{\epsilon}) \tag{6.36}$$

In order for (6.36) to be evaluated it will be necessary to specify the gradients of both the local temperature and local strain at each interpolation or collocation point. Neither of these two gradient operators is generally computed in heat conduction or in stress analysis modeling. Thus, it will be necessary as part of implementing (6.36) to fit each field to its own global interpolation, from which the gradient can be computed

$$\begin{aligned}\nabla\cdot\underline{C}'(\theta) &= \nabla\cdot\left(\sum_{j=1}^{N} K(q,Q_j)\cdot\underline{\Phi}^{c}(Q_j)\right)\\ \nabla\cdot\underline{\epsilon} &= \nabla\cdot\left(\sum_{j=1}^{N} K(q,Q_j)\cdot\underline{\Phi}^{\epsilon}(Q_j)\right)\end{aligned} \tag{6.37}$$

The second approach, and the one reported herein, is to replace the product term by the global interpolation

$$\tilde{\underline{\sigma}}' = \underline{C}'(\theta)\cdot\underline{\epsilon} \approx \sum_{j=1}^{N} K(q,Q_j)\cdot\underline{\Phi}'(Q_j) \tag{6.38}$$

The global interpolation in (6.38) is then operated on to approximate the second term in (6.34). The particular solution for $\underline{u}'$ can then be found as

$$\underline{u}' = \sum_{j=1}^{N} \underline{G}(q,Q_j)\cdot\underline{\Phi}'(Q_j) \tag{6.39}$$

where

$$\underline{G}(q,Q_j) = \{C_1 + r(q,Q_j)C_3\}\underline{\delta}\otimes\underline{y} + \{C_2 + r(q,Q_j)C_4\}\underline{\delta}\otimes\underline{y} + C_3\frac{\underline{y}\otimes\underline{y}\otimes\underline{y}}{r(q,Q_j)} \tag{6.40}$$

and

$$C_1 = -\frac{R_o}{30(1-\nu_o)\mu_o}$$

$$C_2 = -\frac{R_o(9-10\nu_o)}{30(1-\nu_o)\mu_o} \qquad (6.41)$$

$$C_3 = \frac{1}{48(1-\nu_o)\mu_o}$$

$$C_4 = -\frac{11-12\nu_o}{48(1-\nu_o)\mu_o}$$

The resulting interpolation for $\underline{\tilde{u}}'$ is of lower order than the previous interpolations, in that the global function $K(q,Q_j)$ is differentiated prior to finding the particular solution to Navier's equation for this problem (6.34). The accuracy of the domain integral approximation is degraded some, as discussed more fully in Chapter 4.

Using the particular integral solution, we obtain an *equivalent* boundary integral equation of the form

$$\hat{\underline{u}}\cdot\underline{C} + \int_S \hat{\underline{u}}\cdot\underline{T}\,dS = \int_S \hat{\underline{t}}\cdot\underline{U}\,dS + \underline{E}' \qquad (6.42)$$

Where $\hat{\underline{u}} = \underline{u} - \underline{u}'$, $\hat{\underline{t}} = \underline{t} - \underline{t}'$, and the error term is

$$\underline{E}' = \int_{<R>} (\underline{\sigma}' - \bar{\underline{\sigma}}')\cdot\underline{\epsilon}\,dV \qquad (6.43)$$

Solution of the above equation requires iteration in that the boundary interpolation variables $\underline{\Phi}'(Q_j)$ in (6.38) depend on the solution variable $\underline{\epsilon}$.

6.5 Numerical Results

6.5.1 The Form of the Global Interpolation Function

The boundary integral equations given by (6.13a), (6.22) and (6.42) are exact statements of the body force boundary value problems. The numerical implementation of these equations, however, requires both the surface and volume discretization unless the error terms are assumed to be zero; in that case, the solution requires the discretization of the surface only. The error terms are given by the volume integrals involving the difference between the actual and assumed body force variable times appropriate kernels as indicated by eqns. (6.13b), (6.23) and (6.43). Therefore, the accuracy of the solution depends on how well the assumed field approximates the actual body force field. In the earlier works of other authors [4-7] and in the present work, the body force fields are approximated by a global interpolation function given by eqns. (6.16) and (6.17). The choice of the global interpolation function is restricted by two conditions. The first requirement is that the function must be able to approximate the given field adequately,

the second condition is that the function must be such that we can find a particular solution to the governing differential eqns. (6.11), (6.24) and (6.34).

Figure 6.1 shows a map of the interpolated temperature field at the base of a cube subjected to constant temperature. The figure indicates that the approximate field deviates from the actual field by up to 15.6 %. However, the fields match exactly at the nodes, thus, the error in global sense is minimized by a suitable selection of interpolation nodes.

6.5.2 Application to Thermal Loading

For validation purposes, we analyzed a fully restrained cube subjected to a uniform temperature field. The cube was modeled using 6 quadratic boundary elements and the temperature field was interpolated in terms of the 20 boundary nodes of the elements. The stresses computed were within 0.0005 percent of the theoretical results indicating good accuracy.

To further assess the validity of the procedure, we selected a hollow sphere with external radius to internal radius ratio of 2. A 22.5° segment of the body was modeled using 22 quadratic boundary elements as shown in Figure 6.2. For the description of the temperature field by the interpolation function, we considered all 68 boundary nodes that coincide with the surface discretization.

We considered a linear temperature variation in the radial direction given by $\Theta = 10r$, where r is the distance from the center. Analytical solution corresponding to radial temperature variation can be found in Boley and Weiner [10]. Figure 6.3 shows a comparison of the theoretical and computed values of the radial displacements along the radius of the sphere. These results show excellent agreement between the theoretical and computed values. The normalized hoop stress along the radius in Figure 6.4 also indicates excellent agreement between the theoretical and computed values. These results confirm the validity of the procedure as well as indicate the ability of the global interpolation function to approximate the linear temperature field adequately in a global sense.

To examine the appropriateness of the interpolation function for higher order variation of temperature fields, we imposed quadratic variation, given by $\Theta = 100 + 10r + r^2$, and cubic radial variation, given by $\Theta = 100 + 10r + r^2 + 0.2r^3$, of temperatures to the spherical model. The results for hoop stresses shown in Figure 6.5, for the quadratic variation of temperature, and in Figure 6.6, for the cubic variation of temperature, again indicate excellent agreement between the theoretical and computed values. The accuracy of these results provide a good indication of the ability of the global interpolation function to match higher variation of body force field in a global sense.

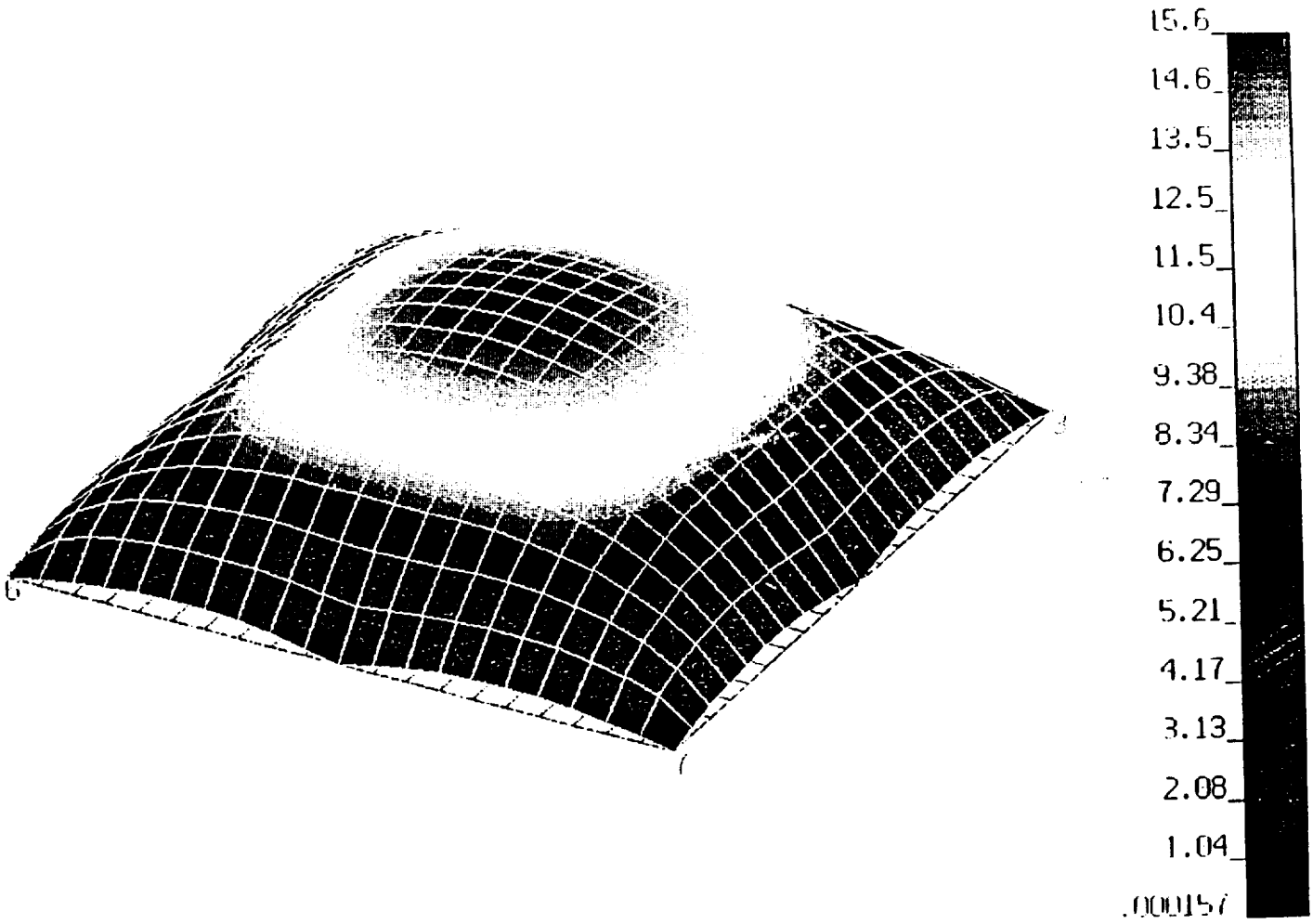

Figure 6.1 Error of Interpolated Temperature Field at the Base of a Cube Subjected to Uniform Temperature of 100

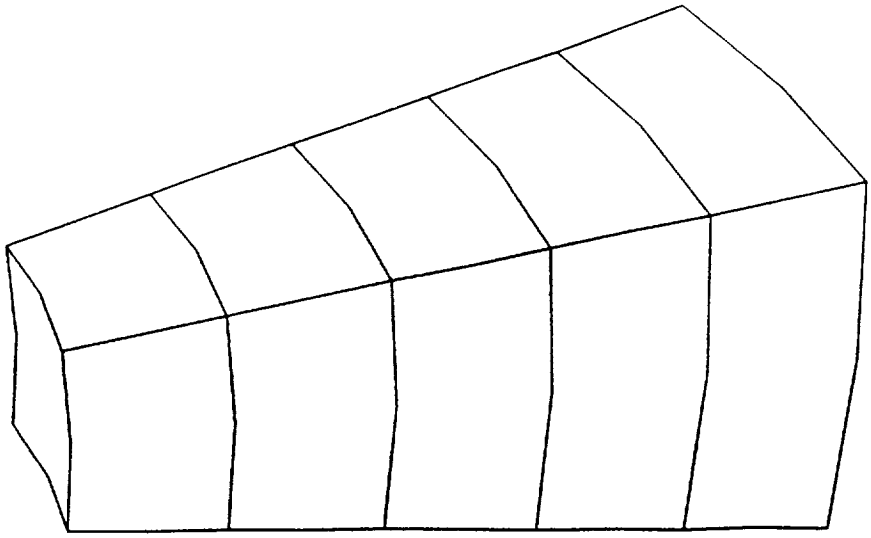

$E = 2600$

$\nu = 0.3$

$\alpha = 10^{-4}$

Figure 6.2 BEM Map for Hollow Sphere

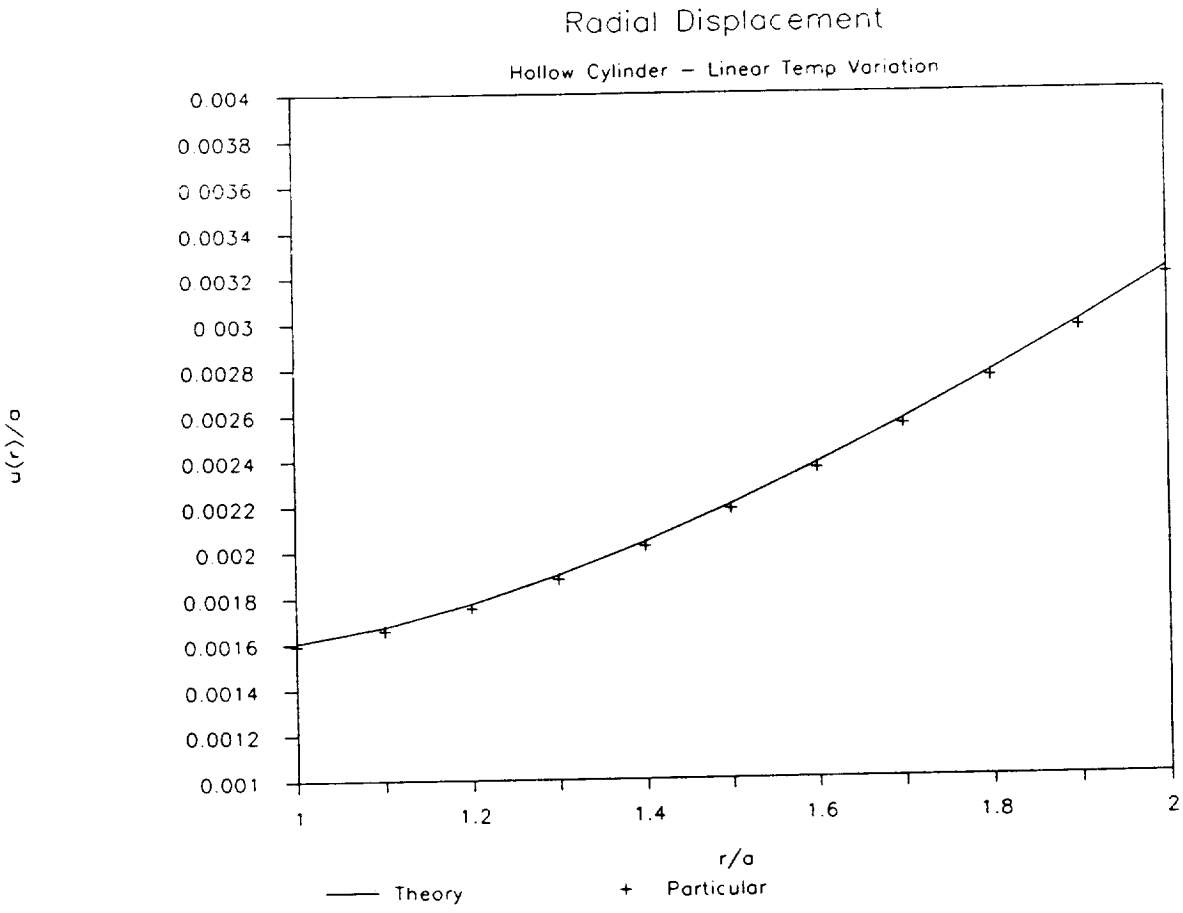

Figure 6.3 Radial Displacement Along the Radius of a Hollow Sphere Subjected to Linear Temperature Field

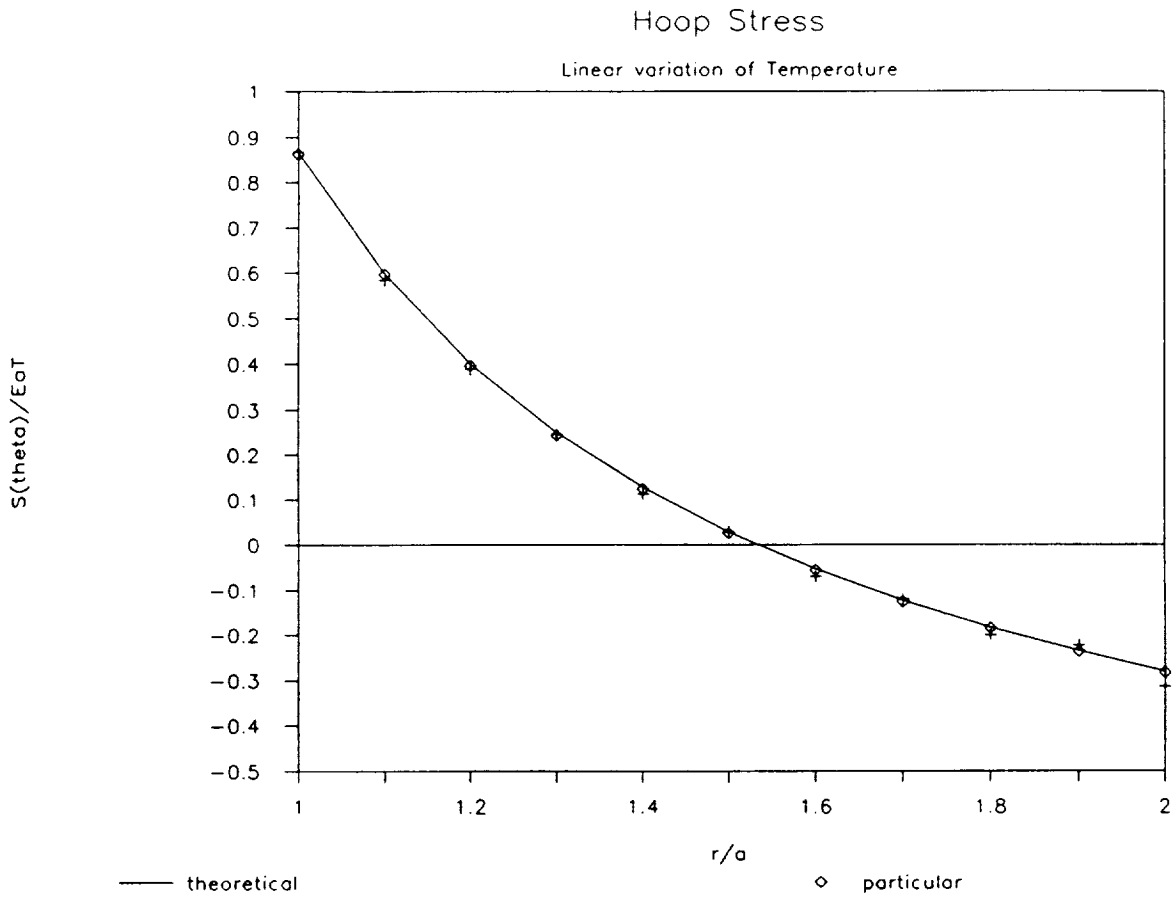

Figure 6.4 Hoop Stress Along the Radius of Hollow Sphere Subjected to Linear Temperature Variation

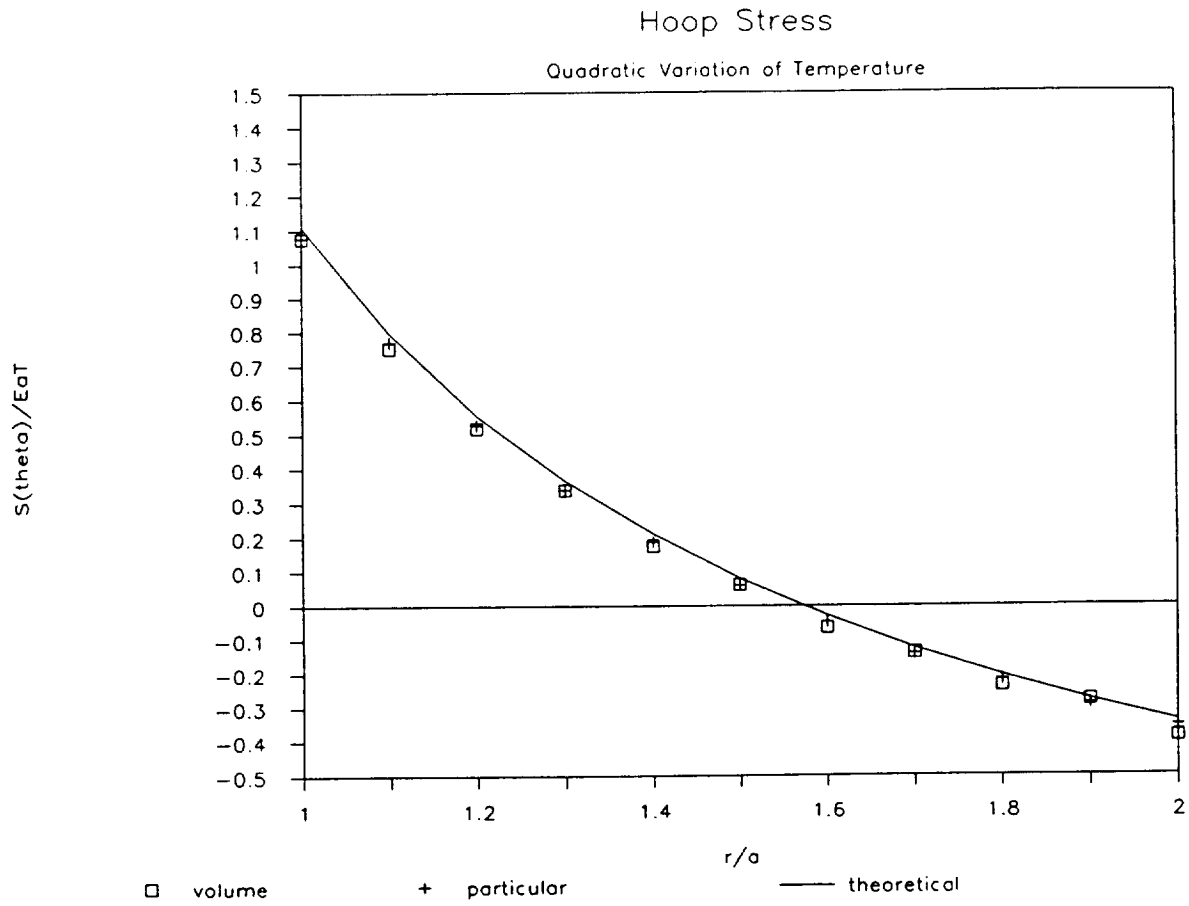

Figure 6.5 Hoop Stress Along the Radius of Hollow Sphere Subjected to Quadratic Temperature Variation

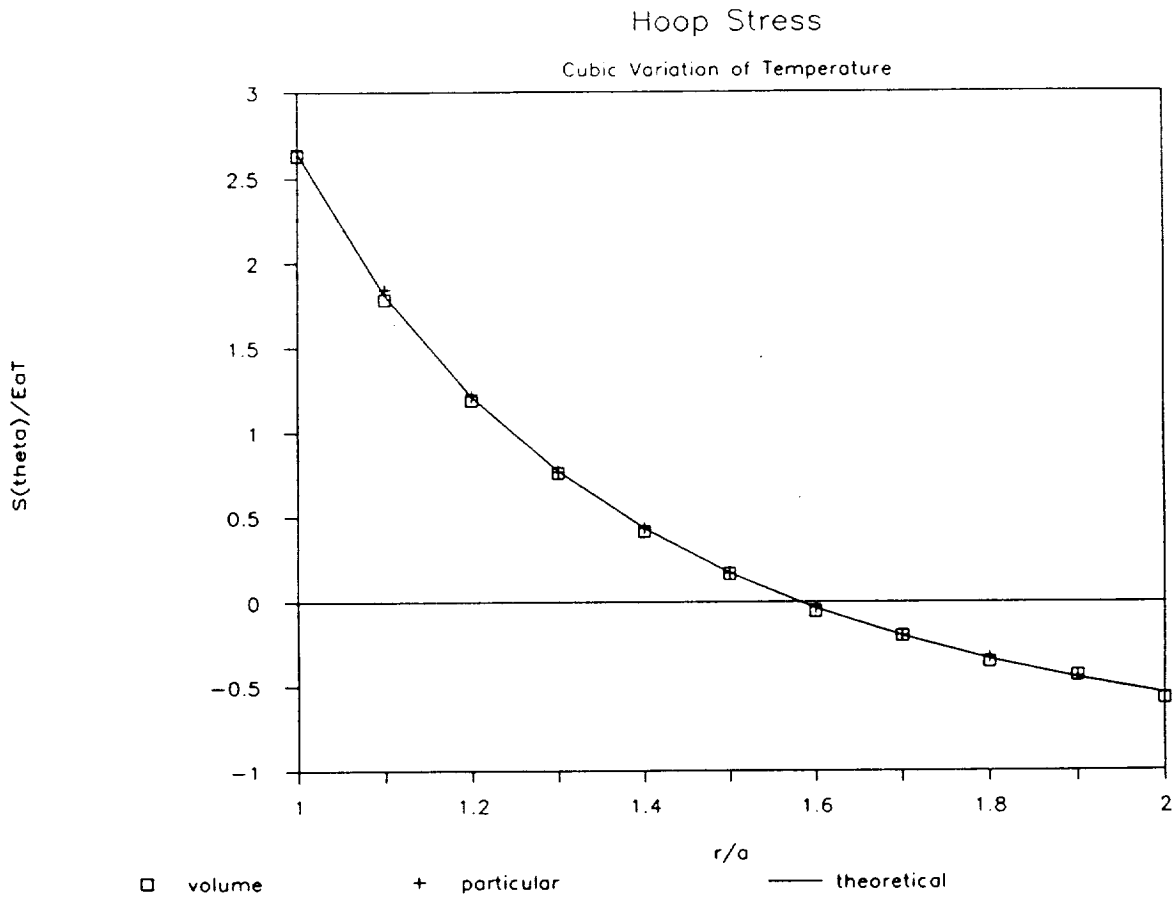

Figure 6.6 Hoop Stress Along the Radius of Hollow Sphere Subjected to Cubic Temperature Variation

6.5.3 Application to Vibration Response

The free vibration analysis part of the code was verified by comparing the mode frequencies of a cantilever beam obtained by using finite element and boundary element procedures. The free-vibration analysis procedure is essentially identical to the work reported previously [4,6], however, the displacement particular solution given by eqn. (6.28) includes one additional term compared to the corresponding solutions reported previously [4,6].

Table 6.1 shows the vibration modes for the cantilever model shown in Figure 6.7. These results indicate that the inclusion of additional term does not alter the computed values, however, the cost is increased due to the need to compute this additional term.

Table 6.1

Vibration Modes for the Cantilever Model

	Mode 1	Mode 2	Mode 3	Nodes/ Elements	CPU (sec) VAX 8700
Beam Theory	472	708	4507		
BEST3D [6]	523	945	4028	44/14	282
PBEM (current)	523	946	4024	44/14	323

To further investigate the accuracy and convergence characteristics of the procedure, we selected two boundary element models, Figure 6.8, and two finite element models, Figure 6.9. Table 6.2 compares the first five modes of vibration for the cantilever models. The computed values show that the results were improved by the use of finer meshes; the results using the finer boundary element map seems to give the *best* results at somewhat higher computational cost.

Table 6.2

First Five Modes of Vibration for the Cantilever Models

	Mode 1	Mode 2	Mode 3	Mode 4	Mode 5	Nodes/ Elements	CPU (sec) VAX 8700
BEM-1	2686	5441	13485	16810	25382	44/14	352
BEM-2	2810	5333	12736	16255	24523	86/28	1676
FEM-1	3033	5449	13191	17227	25141	195/96	158
FEM-2	2885	5354	12778	16224	24522	1125/768	801

6.5.4 Application to Temperature Dependent Properties

To validate inhomogeneous material procedure, initially we considered a cube with linear variation of Young's modulus in one direction subjected to a uniform tensile force applied in the same direction. The cube was modeled using 6 quadratic boundary elements and for the interpolation of the initial stress field due to material inhomogeneity we used all boundary nodes of the elements as shown in Figure 6.10. The results for tensile stresses were in error of up to 16 percent. To see the effect of additional interior points on interpolation, we used 20 interior points in addition to the 20 boundary points used before. The use of interior points for the interpolation reduced the maximum error for stresses to about 6 percent. The reason for higher error for the material inhomogeneity case than the results obtained from a similar model for the thermal problem can be seen from the fact that in the thermal and free vibration analyses, only one field was approximated by the interpolation function. In the inhomogeneous material analysis, initial stresses are defined as the product of the strains and the difference in material properties, eqn. (6.33). While the stresses within the cube were constant, the strains were not since the Young's modulus varied. The interpolation function, therefore, was used for the approximation of the product of varying material properties and varying strain field.

To further investigate the procedure for temperature dependent material properties, we modeled a hollow cylinder with an external radius to internal radius ratio of 2. Figure 6.11 shows the BEM map used for this problem. The cylinder was subjected to a linear variation of temperature field along the radius, given by $\Theta = 10r$. It was assumed that the Young's modulus varied linearly with the temperature given by $E = E_o(1-10^4\Theta)$. The normalized hoop stress along the radius using the current procedure is compared to the corresponding results using the finite element method in Figure 6.12. These results indicate good agreement between the boundary element and finite element procedures.

6.6 Current Status and Future Efforts

The major part of the past year was mainly spent on developing a boundary element procedure for body force problems using a surface transformation technique that eliminates domain modeling. The computer code for thermal, free-vibration, and temperature dependent material problems has been completed. A preliminary verification of the code and the procedure has been established as indicated by the numerical examples given in the previous section. An additional particular solution for known thermal gradients may be incorporated in this code which would effectively eliminate large number of interior collocation points. As part of the next year effort, the particular solution corresponding to high thermal gradients will be included in the computer code.

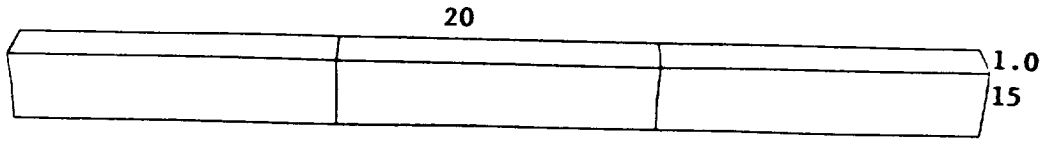

$E = 30 \times 10^6$

$\nu = 0.3$

Figure 6.7 BEM Map for Slender Cantilever Beam

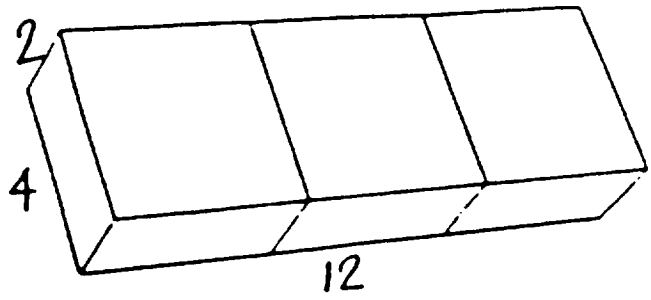

a) BEM Map 1

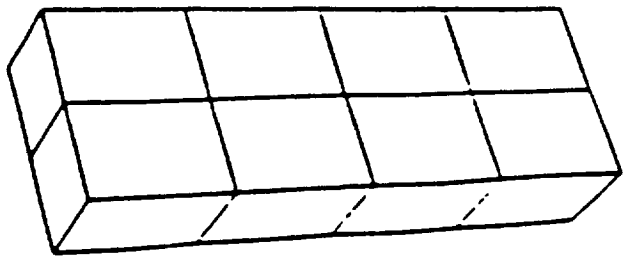

b) BEM Map 2

$E = 30 \times 10^6$

$\nu = 0.3$

Figure 6.8 BEM Maps for Cantilever Beam

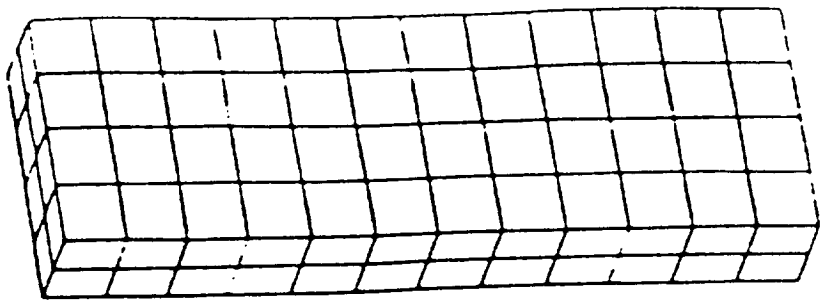

a) FEM Map 1

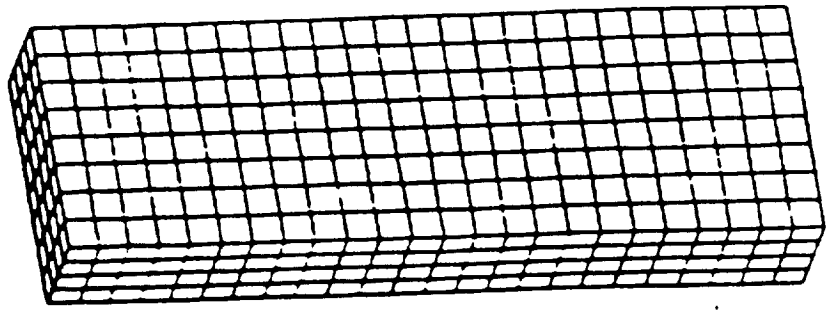

b) FEM Map 2

$E = 30 \times 10^6$

$\nu = 0.3$

Figure 6.9 FEM Maps for Cantilever Beam

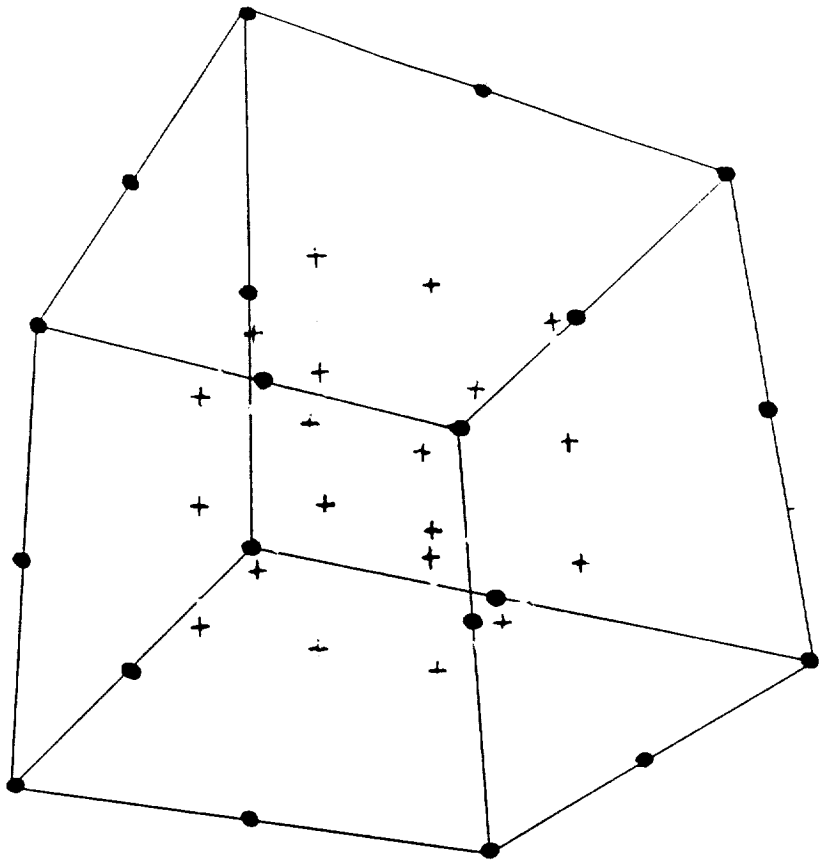

Figure 6.10 BEM Map of Cube with Interior Nodes for Interpolation

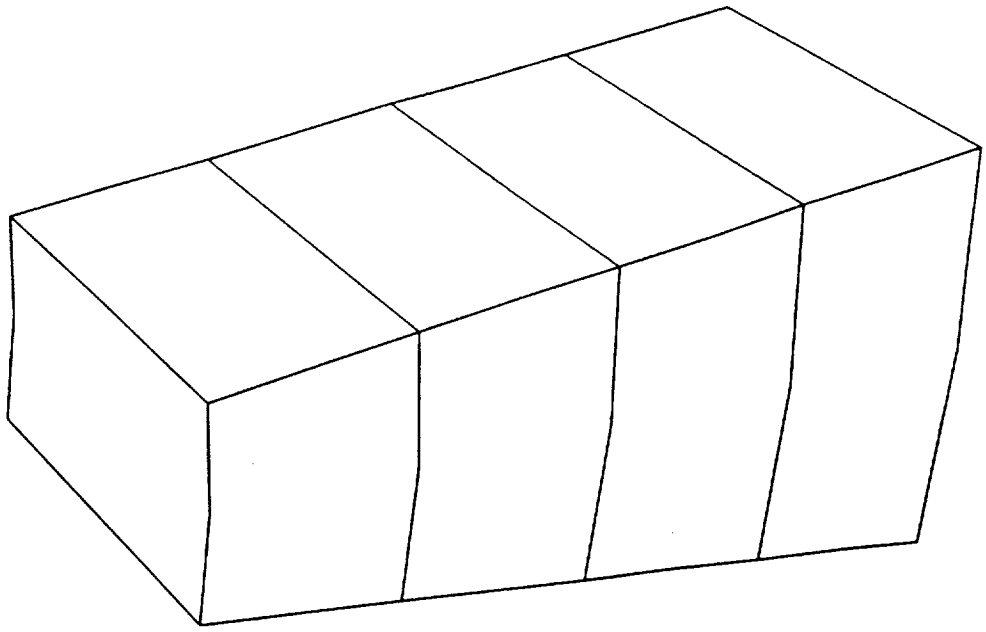

Figure 6.11 BEM Map for Hollow Cylinder

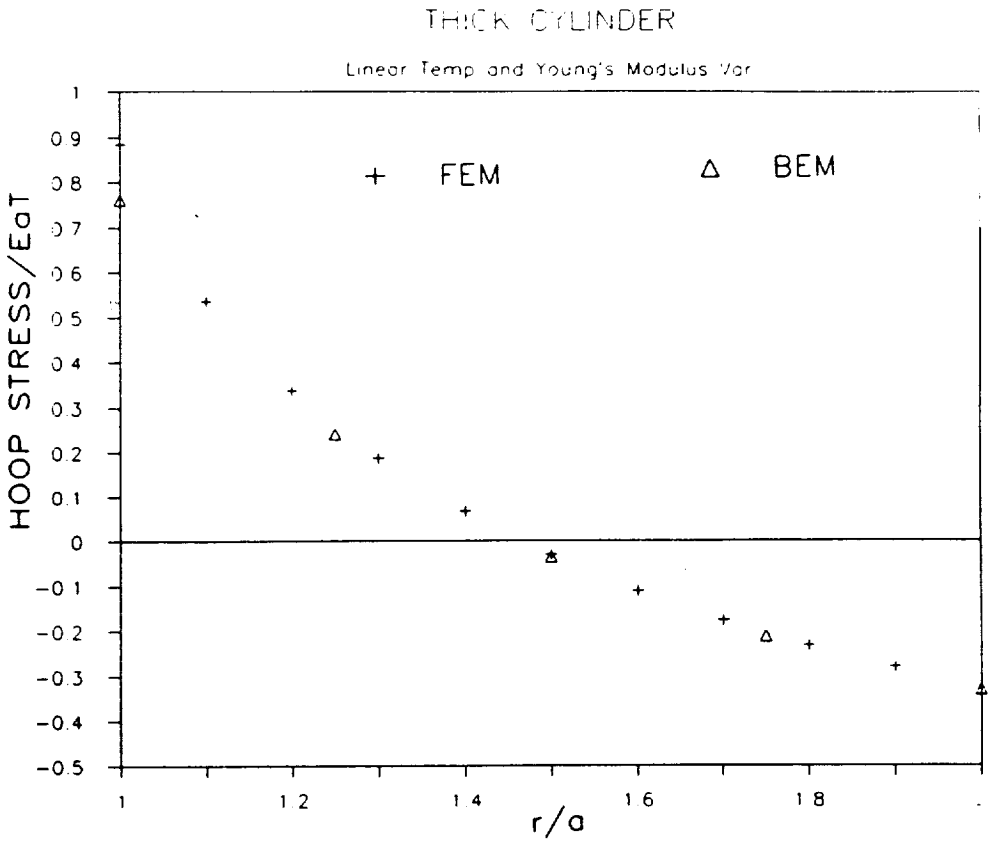

$E_o = 30 \times 10^6$

$\nu = 0.3$

Figure 6.12 Hoop Stress Along the Radius of Hollow Cylinder Subjected to Linear Variation of Temperature with Linear Temperature Dependent Young's Modulus

While the results reported are encouraging, the role of interpolation function in the accuracy of the solution needs further investigation. The investigation on the selection of interpolation function which was partly established in the past year will be concluded in the next year.

The examples presented in the previous section established the validity of the procedure for body force problems. The next year effort will focus on solving specific problems identified by the project, such as the turbine blade model. Before the application of the procedure to large-scale problems, the efficiency of the computer code needs to improved. As indicated in the report corresponding to the validation of the BEST3D code, the BEM procedure for some class of problems is not as efficient as the FEM procedure. In most instances, a large part of the computational effort was spent on the evaluation of discretized surface integrals. The numerical implementation procedure used in the current code is essentially identical to the technique used in the BEST3D [11] computer program except the inclusion of a variable transformation procedure. The variable transformation procedure implemented in the current code slightly improves the efficiency of the numerical integration effort, however, the results do not seem to be as reliable as the sub-segmentation scheme results. An improved numerical implementation is necessary to make the BEM solution tool attractive to a wide-class of problems. Investigation into the development of improved numerical integration procedures will be pursued as part of next years effort.

6.7 References

[1] T.A. Cruse, 1975, Boundary-Integral Equation Method for Three Dimensional Elastic Fracture Mechanics Analysis, AFOSR-TR-75 -0813.

[2] T.A. Cruse, D.W. Snow, and R.B. Wilson, 1977, Numerical Solutions in Axisymmetric Elasticity, *Computers & Structures*, 7, 445-451.

[3] D.J. Danson, 1982, A Boundary Element Formulation of Problems in Linear Isotropic Elasticity with Body Forces, *Recent Advances in Boundary Element Methods*, 3, 105-122.

[4] D. Nardini and C.A. Brebbia, 1982, A New Approach to Free Vibration Analysis Using Boundary Elements, *Boundary Element Methods in Engineering*, C. A. Brebbia (Ed.).

[5] D. Nardini and C.A. Brebbia, 1985, Boundary Integral Formulation of Mass Matrices for Dynamic Analysis, *Topics in Boundary Element Research*, 2, Springer-Verlag.

[6] S. Ahmad and P.K. Banerjee, 1987, Treatment of Body Forces in 2D Elastostatic BEM Using Particular Integrals, *Journal of Applied Mechs., ASME*, 54, 866-870.

[7] D.A. Pape and P.K. Banerjee, 1987, Treatment of Body Forces in 2D Elastostatic BEM Using Particular Integrals, *Journal of Applied Mechs. ASME*, 54, 866-870.

[8] T.A. Cruse, 1988, *Boundary Element Analysis in Computational Fracture Mechanics*, Kluwer Academic Publishers.

[9] T.A. Cruse, 1969, Numerical Solutions in Three-Dimensional Elastostatics, *Intl. J. Solids Struct.*, 5, 1259-1274.

[10] B.A. Boley and J.H. Weiner, 1960, *Theory of Thermal Stresses*, John Wiley & Sons, Inc.

[11] R.B. Wilson and P.K. Banerjee, 1987, BEST3D User's Manual, NASA Contract NAS3-23697.

7.0 NESSUS CODE VALIDATION STUDIES

7.1 Overview of Code Validation Effort

To validate the NESSUS code, a set of problems were chosen to exercise various features of the finite element and probabilistic modules. The validation problems were selected on the basis that (1) a closed-form analytical solution could be generated for the structural response and that (2) an "exact" probabilistic solution could be generated from this closed-form solution, either analytically or through Monte Carlo simulation.

A plan for validating the NESSUS probabilistic finite element code was included in the PSAM First Year Annual Report (Vol. III, Section 7.4). The original plan consisted of nine validation problems. The number of the problems has increased to fourteen (see Table 7.1) to test other capabilities of the NESSUS code.

During FY'87, eight validation problems were successfully solved. These include case numbers 1 to 3, 5 to 7, 9 and 10. The results were summarized in the PSAM Third Year Annual Report (Vol. I, Appendix A).

During FY'88, four validation problems have been solved. The descriptions for these four problems and the problems to be completed in FY'89 are listed in Table 7.1. Other validation problems may be added as needed. More detailed summaries of the validation cases completed during FY'88 are documented in Appendix F using a standard format designed to include all the required input data and information. In addition to validating the code, a new user can use these problems to gain confidence that he is using the code correctly.

For each problem, several levels of accuracy were obtained by using the NESSUS code and the probabilistic algorithm. As a first step, a mean-based perturbation database was generated to generate a linear response surface. The result is the MVFO solution.

In the second step, one or several probability levels were selected. For each probability level, the MVFO solution was then improved by replacing the center of perturbation (the "deterministic state" in the NESSUS/FEM module) by the most probable points generated using the previously established linear response surface. The "new" deterministic solution was then paired with the "old" MVFO probability estimate to form the AMVFO solution.

The probability estimates were further improved by using the perturbation solutions around the updated point. This procedure is called the "first iteration." The solution can be further improved by using additional iterations until the solution converges. The NESSUS probabilistic analysis algorithms are documented in [3].

In all the validation problems studied, it was found that the first-iteration solutions were sufficiently accurate and that even the AMVFO solutions provided good accuracy for most cases. Therefore, additional iterations were not conducted.

In the presentation of the results, an 'adjusted exact' CDF was defined for each problem. The adjusted solution was defined to match the analytical deterministic (using mean or median values) solution with the FEM solution. The adjusted CDF provides a more reasonable reference to judge the accuracy of the NESSUS probabilistic solution.

In generating the CDFs, the analysis concentrated on only one of the tails of the distribution, depending on which tail was considered more important in a reliability design.

When closed form probability solutions are not available, exact solutions were obtained by using Monte Carlo simulation. The "exact" solutions were compared with NESSUS results to validate the code as well as the solution algorithm.

7.2 Validation Results Completed in FY'88

7.2.1 Analysis of Rotating Beam

This problem is similar to validation case 5 [2] which uses plate finite element. The present problem uses Timoshenko beam elements. The rotating beam, as illustrated in Figure V-1 of Appendix F, was modeled using 20 beam elements. There are five random variables: Modulus of elasticity, length, thickness, width, density, rotational frequency and inside radius.

The response functions consider the tip axial displacement and the first bending frequency. The analytical solutions were derived using Galerkin's method.

The NESSUS/PFEM module has been used successfully to obtain the AMVFO solution at several selected probability levels. The agreement between the NESSUS solution and the 'adjusted' exact solution is excellent.

7.2.2 Static Analysis of Spherical Shell

This validation problem (case 8) considers a spherical shell as illustrated in Figure V8-1 of Appendix F. This problem validates the NESSUS's shell modeling capability. The FEM model uses 200 shell elements (NESSUS element type 75) including 180 four-node elements and 20 collapsed, 3-node elements. The analytical deterministic solution for the maximum stress (at fixed base) is available. The difference between the theoretical solution and the NESSUS solution is 3%.

There are two random variables: internal pressure and thickness. By assuming that both random variables are lognormally distributed, the response is also a lognormal random variable. In solving the probabilistic analysis problem, the convergence limit must be small enough to force at least one iteration in the NESSUS perturbation to generate a correct perturbation solution. Figure V8-2 in Appendix F shows very good agreement between the 'adjusted exact' solutions and the NESSUS AMVFO solutions.

7.2.3 Buckling Analysis

This problem considers the critical buckling pressure of a thin shell under uniform external pressure as illustrated in Figure V11-1. The goal was to establish the CDF of the critical pressure.

The FEM model uses 40 four-node shell elements. There are two random variables. Based on the analytical solution and the distribution assumption, an exact CDF can be obtained.

The MVFO and the AMVFO solutions were obtained. Figure V11-2 clearly shows that the NESSUS AMVFO solution agrees very well with the adjusted solution even though there is a 11% difference between the analytical solution and the FEM solution, computed at the median values of the random variables. This suggests that the response variable sensitivities are approximately the same for both the analytical and the FEM models.

The fact that the adjusted exact solutions match well with the NESSUS solutions suggests that the characteristic of a tail distribution (i.e., the 'shape' of a tail distribution) may be preserved if the physical characteristics (e.g., the response sensitivities) are essentially correct. This validation result suggests a strategy for efficient CDF approximation for complicated structural components. For example, it may be possible to use a coarse (but reasonable) FEM model to establish the shape of the tail distribution, then use a refined FEM model to calibrate (i.e., shift) the CDF using a deterministic solution.

7.2.4 Random Vibration Analysis of Beam

In this validation problem, a cantilever beam is subjected to random base excitation. The random variables include the modulus of elasticity, material density, damping factor, length, thickness, width, acceleration spectral density and cutoff frequency. The acceleration spectral density is modeled as a truncated white noise with cutoff frequency properly selected to excite, approximately, only the first mode. The response function considers RMS (root-mean-square) of the tip displacement. The finite element model, the random variables definition and the probabilistic results are included in Appendix F. The agreement is excellent between the NESSUS probabilistic result and the adjusted 'exact' solution based on the Monte Carlo simulation.

7.3 Validation Plans for FY'89

According to the previous validation plan (see Table 7.1), there are two random vibration problems left. In addition, three new validation problems are proposed to validate transient and nonlinear capabilities. Descriptions of these planned problems are given in the following. Other problems may be added as necessary.

7.3.1 Random Vibration Analysis of Cylindrical Shell (Case 13)

This problem considers a cylindrical shell subjected to a random uniform ring loading at a section of the shell [4].

7.3.2 Random Pressure Loads on Plate (Case 14)

The goal of this validation case is to validate the NESSUS's capability to solve random pressure field problems. In this validation case, a plate is subjected to a random pressure field [5].

7.3.3 Elastic Response of a Pulse-Loaded Beam (Case 15)

This problem considers a simply supported beam subjected to a uniformly distributed pulse-load. The transient response (maximum displacement) will be considered in the response variable [6].

7.3.4 Elastic-Plastic Static Response of a Beam (Case 16)

This problem is similar to the previous problem except the load will be gradually applied up to beyond yielding of the beam. Perfect plasticity will be assumed [7].

7.3.5 Elastic-Plastic Response of a Pulse-Loaded Beam (Case 17)

The previous pulse-loaded beam problem (Case 15) will be extended to consider elastic-plastic transient response [8].

7.4 References

[1] "Probabilistic Structural Analysis Methods (PSAM)," 1st Annual Report, NASA Contract NAS3-24389, Vol. III, Section 5.

[2] "Probabilistic Structural Analysis Methods (PSAM)," 3rd Annual Report, NASA Contract NAS3-24389 Appendix A.

[3] Y.-T. Wu, O.H. Burnside, and T.A. Cruse, 1988, "Probabilistic Methods for Structural Response Analysis," Presented at the ASME/SES Summer Meeting, California, Published in *Computational Probabilistic Methods*, W. K., Liu et al. eds., AMD-Vol. 93, ASME, pp. 1-14.

[4] I. Elishakoff, A.Th. van Zanten, and S.H. Crandall, 1979, "Wide-Band Random Axisymmetric Vibration of Cylindrical Shells," *Journal of Applied Mechanics*, 46.

[5] I, Dyer, 1959, "Response of Plates to a Decaying and Convecting Random Pressure Field," *The Journal of the Acoustical Society of America*, 31.

[6] W. Nowacki, 1963, *Dynamics of Elastic Systems*, John Wiley & Sons, Inc., New York.

[7] W. Prager, and P.G. Hodge, Jr., 1968, *Theory of Perfectly Plastic Solids*, Dover Publications, Inc., New York.

[8] P.S. Symonds, "Plastic Deformations of Pulse-Loaded Structures - An Elementary of Estimation Techniques," Private Communication.

8.0 NESSUS CODE VERIFICATION STUDY

8.1 Introduction to Probabilistic Frequency Analysis of a Turbine Blade

The NESSUS verification studies in FY'88 were directed towards the linear dynamic analysis capabilities. The first verification application of NESSUS' dynamic analysis capabilities was the probabilistic frequency analysis of a typical space propulsion system turbine blade. The variations in the frequencies of the first few modes of the turbine blade must be monitored and controlled to avoid resonance conditions. This can occur due to the periodic excitation forces generated by disturbances to the gas path generated by upstream nozzles and struts. The methodology for determining the probabilistic frequency response is very similar to that of obtaining probabilistic response of static response variables. Since the frequency response function can by highly nonlinear, it requires special precautions by the user to validate the results obtained.

8.2 Initial Verification Studies For the Frequency Computation

The purpose of the initial verification studies was to verify the NESSUS frequency results with results obtained from other programs and also to check the performance of perturbation based frequency extraction alogrithm as implemented in NESSUS. It was also the purpose of the initial verification studies to check the correctness of material orientation effects as implemented in NESSUS for single crystal materials.

A 4x4x10 (Figure 8.1) cantilever beam element model was used to verify the frequency analysis results for two material orientations. The anisotropic material properties used are also shown in Figure 8.1. The NESSUS results using Type 7 and Type 154 elements are compared with ANSYS results in Table 8.1 for two material angle orientations. For the identical formulation of Type 7 isoparametric element, both programs give identical results. However, it is known that Type 7 elements are excessively stiff and selective reduced integration schemes are inappropriate for anisotropic materials. The enhanced continuum element Type 154 is much more flexible and is capable of representing pure bending modes accurately. Thus, the NESSUS results are in closer agreement with ANSYS results when compared with an element formulation containing bubble functions.

The next phase of initial verification studies were directed towards obtaining the frequencies for the perturbed system. There are two options available in NESSUS to extract eigenvalues and eigenvectors for the perturbed system. In one method, the subspace iteration technique is simply applied to the perturbed system with initial trial eigenvectors as that obtained from the deterministic structure. In the second method, an iterative procedure is used to obtain the eigenvalues and eigenvectors from the subset of modes of the deterministic system. Both the procedures were applied to a perturbed system, using the simple cantilever beam model as well as using a large turbine blade model (Figure 8.2). The material overtation angle was used as the perturbation variable. The results of the perturbation of 10 degrees and 2 degrees material orientation angles are shown in Table 8.2 and Table 8.3 respectively for the simple beam model.

$$
D = \begin{bmatrix}
35,750993E6 & 22,475380E6 & 22,475380E6 & 0. & 0. & 0. \\
 & 35,750993E6 & 22,475380E6 & 0. & 0. & 0. \\
 & & 35,750993E6 & 0. & 0. & 0. \\
\text{SYMMETRIC} & & & 18.6E6 & 0. & 0. \\
 & & & & 18.6E6 & \\
 & & & & & 18.6E6
\end{bmatrix}
$$

ANISOTROPIC D-MATRIX USED IN THE SOLID BEAM TEST EXAMPLES

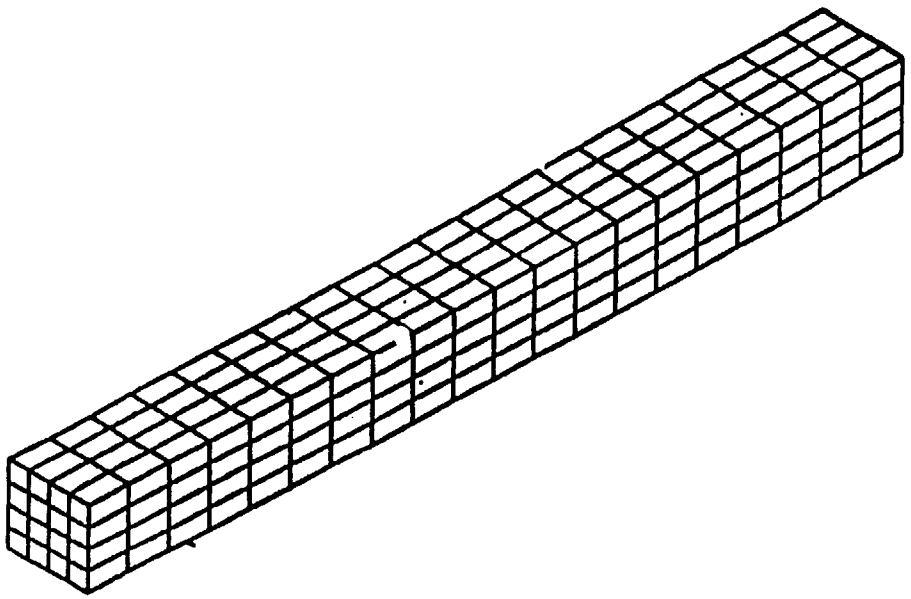

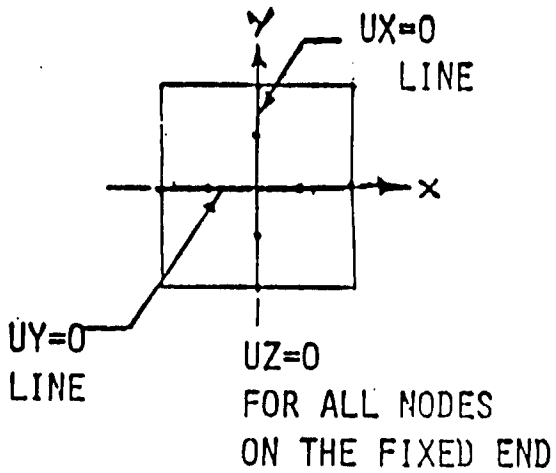

Figure 8.1 4x4x20 Cantilever Beam Model

Table 8.1

Frequency Comparison Between ANSYS and NESSUS

Mode Number	Frequency in Hz							
	000 Orientation				111 Orientation (0.35.26°.45°)			
	ANSYS		NESSUS		ANSYS		NESSUS	
	w/extra DISP	w/o extra DISP	Type 7	Type 154	w/extra DISP	w/o extra DISP	Type 7	Type 154
1	241.92	273.59	273.59	244.08	375.86	387.20	387.20	376.45
2	241.92	273.59	273.59	244.08	375.89	387.27	387.27	376.45
3	1488.52	1679.44	1679.43	1503.56	2196.95	2259.12	2259.12	2200.56
4	1488.52	1679.44	1679.43	1503.56	2197.32	2259.92	2259.92	2200.95
5	3465.85	3486.99	3486.99	3474.01	2394.08	2411.69	2411.66	2415.45
6	3756.19	3756.68	3756.64	3756.57	5630.77	5780.51	5780.50	5641.07
7	4069.13	4576.12	4576.08	4117.47	5630.88	5784.38	5784.37	5641.07
8	4069.13	4576.12	4576.08	4117.47	5897.45	5897.48	5897.49	5897.48
9	7739.56	8669.63	8669.56	7849.53	7199.82	7255.17	7255.09	7264.43
10	7739.56	8669.63	8669.56	7849.53	9979.06	10236.77	10235.70	10000.3
11	10415.6	10481.3	10481.3	10440.1	9983.75	10246.32	10246.30	10000.52
12	11274.8	11288.3	11288.2	11286.1	12058.9	12160.32	12160.20	12168.6
13	12380.9	13812.6	13812.5	12589.7	14946.7	15330.19	15330.10	14984.3
14	12381.8	13813.6	13812.5	12589.7	14963.2	15350.84	15350.80	15001.1
15	17480.7	17554.0	17536.7	17460.3	17009.7	17170.71	17170.10	17166.7
16	17875.7	18945.7	18874.3	18225.4	17721.2	17721.48	17719.80	17719.6
17	18033.7	19867.5	19863.9	18225.4	20387.3	20916.21	20884.4	20412.5
18	19439.0	20119.8	19863.9	18863.8	20495.1	21044.40	20916.1	20449.1
19	24280.8	24928.2	24694.6	24570.5	22487.6	22683.70	22331.30	22300.4
20	24710.8	26742.0	26551.6	24666.3	26525.4	27164.30	26813.80	26198.6

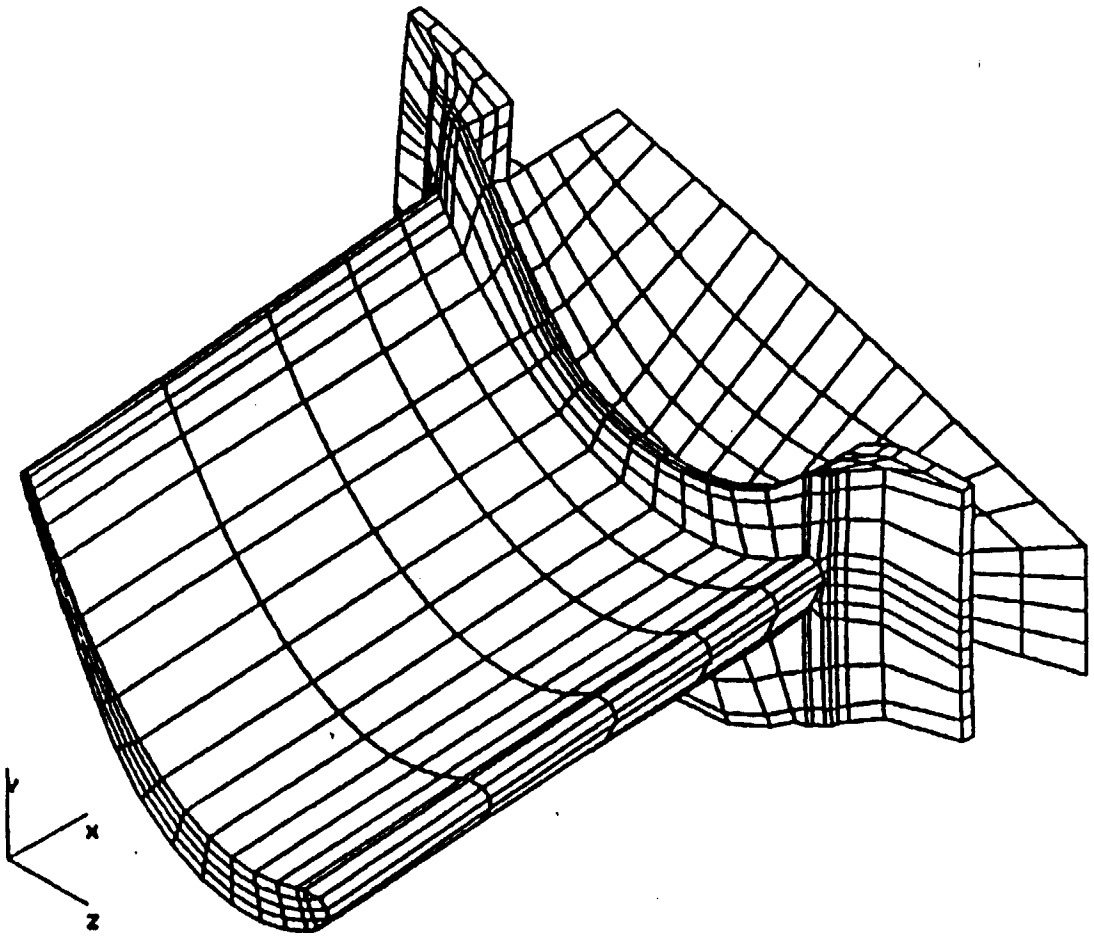

Figure 8.2 Turbine Blade Model Used in Earlier Static Analysis Verification Studies

Table 8.2

Comparison of Perturbation and Resolution Procedures
(10 degree perturbation)

		Perturbation Analysis				Perturbation
						4 Recomputed
	Deterministic	1	2	3	4	With Move
Mode	Hz	Hz	Hz	Hz	Hz	Option
1	387.20	387.62		380.96	375.10	366.22
2	387.27	387.48		385.54	381.93	372.14
3	2259.12	2271.07		2224.33	2203.57	2135.88
4	2259.92	2268.15		2270.72	2242.3	2204.12
5	2411.66	2484.53		2508.50	2507.5	2517.29
6	5780.50	5874.64		5757.82	5814.46	5447.45
7	5784.37	5861.54		5920.51	5908.00	5575.18
8	5897.49	5821.04		5758.80	5640.34	5764.66
9	7255.10	7473.48		7544.10	7789.21	7567.71
10	10235.7	10355.7		10151.2	10240.8	9595.08
Covergence in Terms	12 Iterations	.6	No Covergence		11	11 Iterations

1 10 degree Perturbation about Z

2 10 degree Perturbation about Y

3 10 degree Perturbation about X

4 10 degree Perturbation about Z, Y, X simultaneously

Table 8.3

Comparison of Perturbation and Resolution Procedures (2 degree perturbation) Cantilever Beam Model

Mode	Deterministic Hz	Perturbation Analysis 1 Hz	2 Hz	3 Hz	4 Hz	Perturbation 4 Recomputed With Move Option
1	387.20	387.265	386.50	386.732	386.281	386.37
2	387.27	387.235	387.473	387.395	387.38	386.37
3	2259.12	2260.25	2252.77	2257.78	2251.93	2255.2
4	2259.92	2259.62	2264.55	2259.99	2264.29	2255.2
5	2411.66	2414.69	2417.31	2415.98	2420.89	2417.5
6	5780.50	5824.36	5789.24	5818.26	5789.96	5810.4
7	5784.37	5821.58	5845.72	5825.21	5855.52	5810.4
8	5897.49	5821.04	5825.37	5818.26	5813.57	5810.4
9	7255.10	7264.15	7272.29	7267.56	7282.78	7272.2
10	10235.7	10240.7	10183.00	10232.2	10186.6	10149.7
Covergence in Terms	12 Iterations	1	4	4	5	12 Iterations

Model Data
320 Elements
525 Nodes

Max Profile = 164
Height

Ave. Profile = 96
Height

N.D.O.F. = 1575
Blank Common
Needed = 3,185,631

CPU Time for
Deterministic = 89.57 sec.
Frequency Extraction
(IBM 3090)

Materials Axis:
Perturbations

1	2 degree	Perturbation about Z
2	2 degree	Perturbation about Y
3	2 degree	Perturbation about X
4	2 degree	Perturbation about Z, Y, X Simultaneously

Avg. CPU time for
Pert. Frequency
Extraction per
Perturbation 85.88 secs.

Relative Residual = 1E-6.

The larger angle perturbation was initially tried as the amount of change in frequency was only about 5% for 10 degree material orientation perturbation.

The results indicated that the perturbed procedure took about as much as 95% of the resolution method with no convergence for certain vectors. There was also significant percentage differences in the sensitivity information for larger angle perturbation. In order to verify whether the above conclusions are also applicable to larger models, a turbine blade model which was used in earlier probabilistic finite element static analysis was used in the frequency extraction exercise. The model is shown in Figure 8.2 and the details of the model and the results are shown in Table 8.4. The results supported the conclusion that the marginal increase in cost using resolution procedures are preferable as they obtain more accurate sensitivities and convergence characteristics are much more predictable. Thus, further probabilistic frequency analysis verification exercises used the resolution procedure.

8.3 Probabilistic Frequency Analysis of Turbine Blade

Experience in verification exercises using the turbine blade model shown in Figure 8.2 and the results reported in Table 8.4 demonstrated the high core demand due to incore solution capabilities implemented in NESSUS. This is particularly so in dynamic analysis as stiffness, mass and damping matrices are stored entirely in core. This may not be a hindrance for dynamic analysis of large models using NESSUS as machines with 16, 64 and 256 million words of high speed memory may soon be widely available. However, it can be serious a problem in running NESSUS in small core machines, especially dynamic analysis. Further, experience with virtual machines indicate excessive paging for large sized models. In general, a single refined model as shown in Figure 8.3 is desirable for use in static analysis, frequency and response analysis and fatigue life determination. However, due to the core demand a coarser model shown in Figure 8.4 was used for probabilistic frequency analysis. Further, when probabilistic methods are used in the initial design phase to improve or estimate reliability, coarser models are adequate.

The random variables and the assumed statistical parameters are shown in Table 8.5. The analysis considered the variations in material axis orientations, material elastic constants and geometric variations. The material axis variations are typical for cast blades observed from inspection data for directionally solidified blades. The variations in elastic constants were mainly obtained from expert opinion. Geometric variations were introduced in the analysis through variations of the spatial location of the blade with respect to stacking axis. It has been observed that for cast blades with a machined firtree, the majority of the variations occur during machining operations in the form of variations in geometric lean, tilt and twist angles. Thus, the geometric random variables are used in the analysis procedure as rigid body shift of the

Table 8.4

Turbine Blade Solid Model Frequency Analysis Runs

Mode	Deterministic Hz	Perturbed Frequency Based on Recalculation	Perturbed Frequency Based on Pert. Algor. Hz
1	4566.71	4586.16	4608.76
2	9150.45	9185.40	9207.24
3	11225.10	11158.30	11172.9
4	15117.90	15025.8	15077.9
5	21013.30	20978.5	21071.8

Number of DOF = 5946

Max. Profile Column Height = 578

Average Profile Column Height = 361

Blank Common Words Needed = 19,881,747

Deterministic Analysis CP Time = 5151.84 Secs. (IBM 3090)

Solution Time for Perturbation = 4,349.86 Secs. (IBM 3090)

Convergence in Order (2) Terms

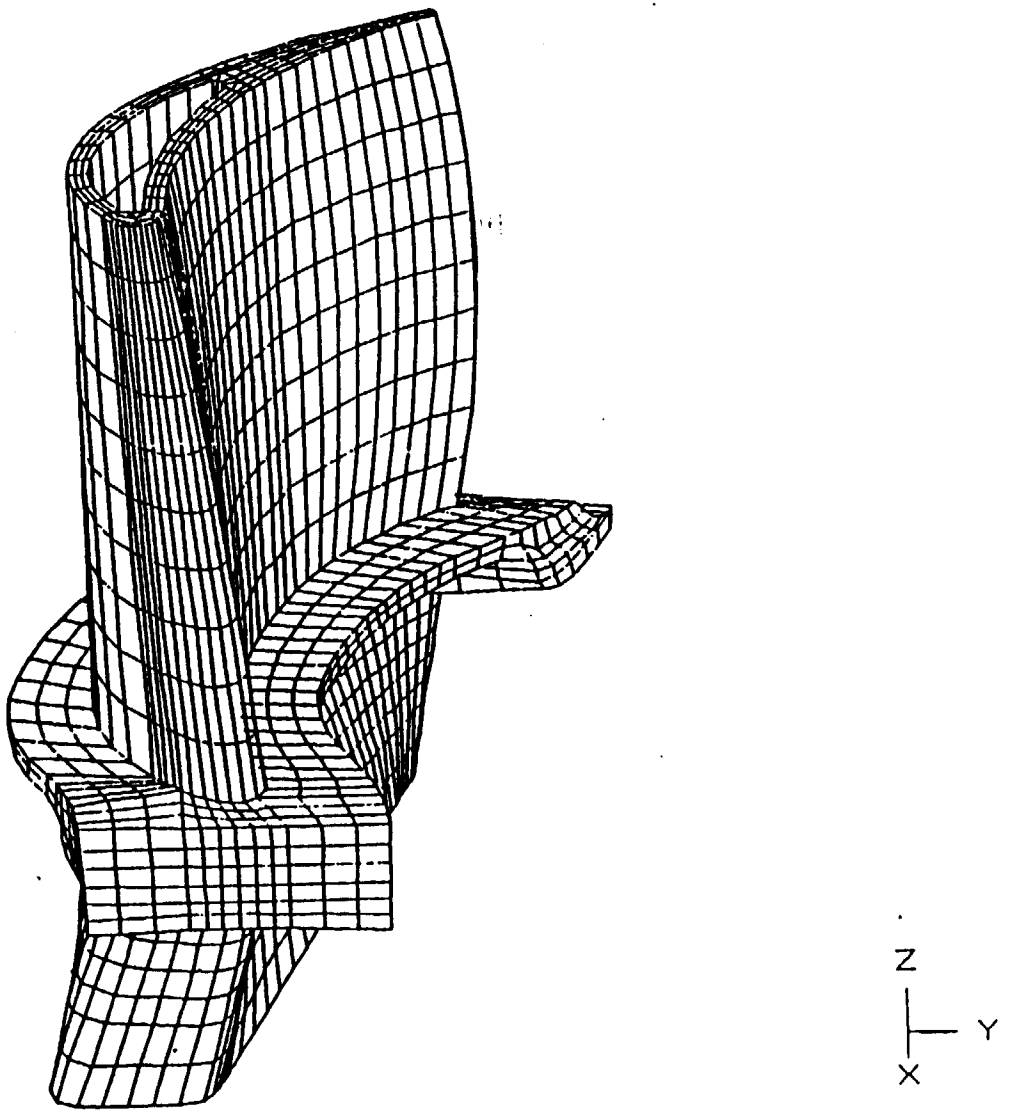

Figure 8.3 Normal Production Base Line Blade Model

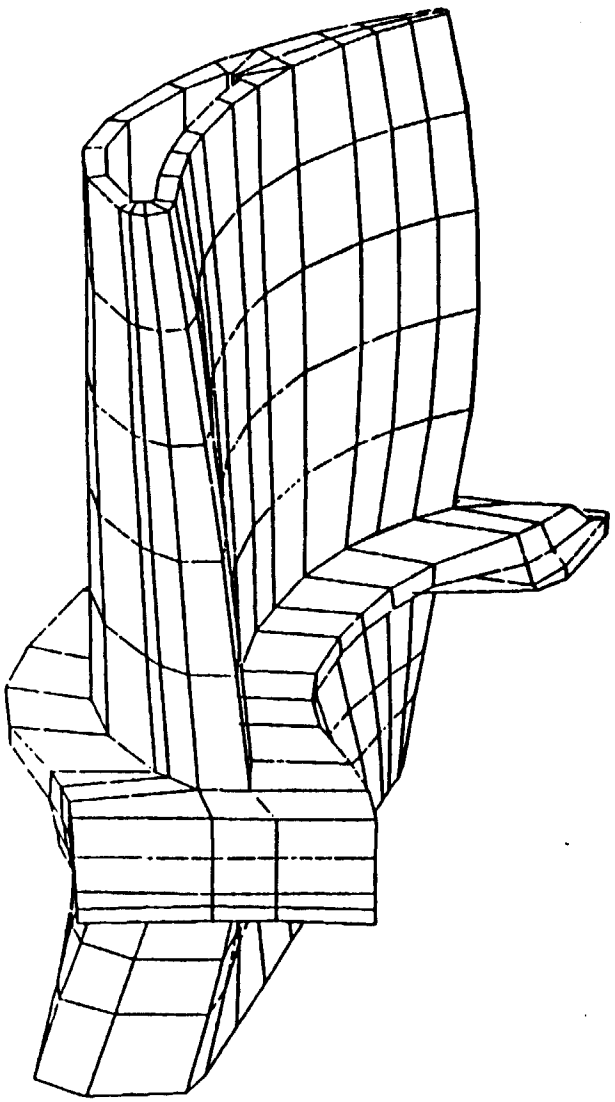

NO.	DESCRIPTION	QUANTITY
1	NUMBER OF NODES:	811
2	NUMBER OF ELEMENTS: (TYPE 154, ENHANCED CONTINUUM ELEMENT)	359
3	NUMBER OF D.O.F.	2,118
4	MAXIMUM PROF HEIGHT	275
5	AVERAGE PROF HEIGHT	191
6	STORAGE NEEDED FOR STATIC SOLUTION	819,143 WORDS
7	STORAGE NEEDED FOR MODAL SOLUTION (10 PERTURBATION, 10 RANDOM VARIABLES)	1,758,715 WORDS

Figure 8.4 NESSUS Coarse Blade Model for Dynamic Analysis

Table 8.5

Random Variables Considered for
Probabilistic Frequency Analysis

NO	RANDOM VARIABLE DESCRIPTION	NOTATION	MEAN	STANDARD DEVIATION	DISTRIBUTION
1	MATERIAL AXIS ABOUT Z	THETA Z	-0.087266 RADIANS	0.067544 RADIANS	NORMAL
2	MATERIAL AXIS ABOUT Y	THETA Y	-0.034907 RADIANS	0.067544 RADIANS	NORMAL
3	MATERIAL AXIS ABOUT X	THETA X	+0.052360 RADIANS	0.067544 RADIANS	NORMAL
4	ELASTIC MODULUS	E	18.38E6 KSI	0.4595E6 KSI	NORMAL
5	POISSON'S RATIO	NU	0.386	0.00965	NORMAL
6	SHEAR MODULUS	G	18.63E6 KSI	0.46575E6 KSI	NORMAL
7	MASS DENSITY	RHO	0.805E-3	0.493E-5	NORMAL
8	GEOMETRIC LEAN ANGLE ABOUT X	LEAN	0.0	0.14 DEGREES	NORMAL
9	GEOMETRIC TILT ANGLE ABOUT Y	TILT	0.0	0.14 DEGREES	NORMAL
10	GEOMETRIC TWIST ANGLE ABOUT Z	TWIST	0.0	0.30 DEGREES	NORMAL

blade with reference to the turbine radial line. The variations in the mass of the blade observed in practice were introduced as variations in mass density.

In the probabilistic frequency analysis of turbine blade reported in this study, the stress stiffening effects have been included. The stress stiffening effect is small for short and stiff blades such as the ones used in this study. However, the stress stiffening effects were included to capture the effect of rigid body geometry shifts on centrifugal stresses and thereby frequency due stress stiffening.

The analysis procedure used in this study used the mean value first order method and the advanced mean value first order method implemented in NESSUS/FPI. For the mean value first order method one deterministic and ten perturbation runs were made for the ten random variables considered. Each perturbation case for modal analysis was preceded by a corresponding perturbation case for static analysis to obtain the correct initial stresses. In summary, one deterministic static analysis plus one deterministic modal analysis followed by ten perturbed static analysis and ten perturbed modal analysis were conducted to obtain mean value first order solutions. All the above cases were made in a single computer run. The results of the deterministic modal analysis are shown in Figure 8.5 through Figure 8.7 in the form of contour plots.

Perturbation about the mean value were obtained using NESSUS/FEM and NESSUS/FPI was used to obtain the first estimate of the distribution of frequencies using MVFO method. This is displayed in Figures 8.8 through 8.10 under the legend MVFO.

The probabilistic sensitivities obtained using MVFO method is tabulated in Table 8.6 for the first modes of interest. The results point out the elastic material property variations, either due the material angle orientation or the variations in the properties themselves contribute most to the variations in the frequencies of the blade. It further points out that the variations in primary material axis orientation plays a dominant role in Mode 1 and Mode 2 while the variations in shear modulus and secondary axis orientation play a dominant role for variations in Mode 3. The effect of these dominant random variables on mode shapes is also of interest. Figures 8.11 through 8.13 show the respective mode shapes for the dominant random variable perturbed by one standard deviation. It is seen that there is no significant change in mode shapes. The results of the estimate obtained using MVFO method are also compared with operational experience for similar but different set of blades in Table 8.7. The wider variation for Mode 3 observed in the experimental data can be attributed to the directionally solidified sample blades for which the secondary axis orientation was not controlled. The analytical results will be compared in the future with single crystal blade test samples where all the material axis orientations are better controlled and test data becomes available.

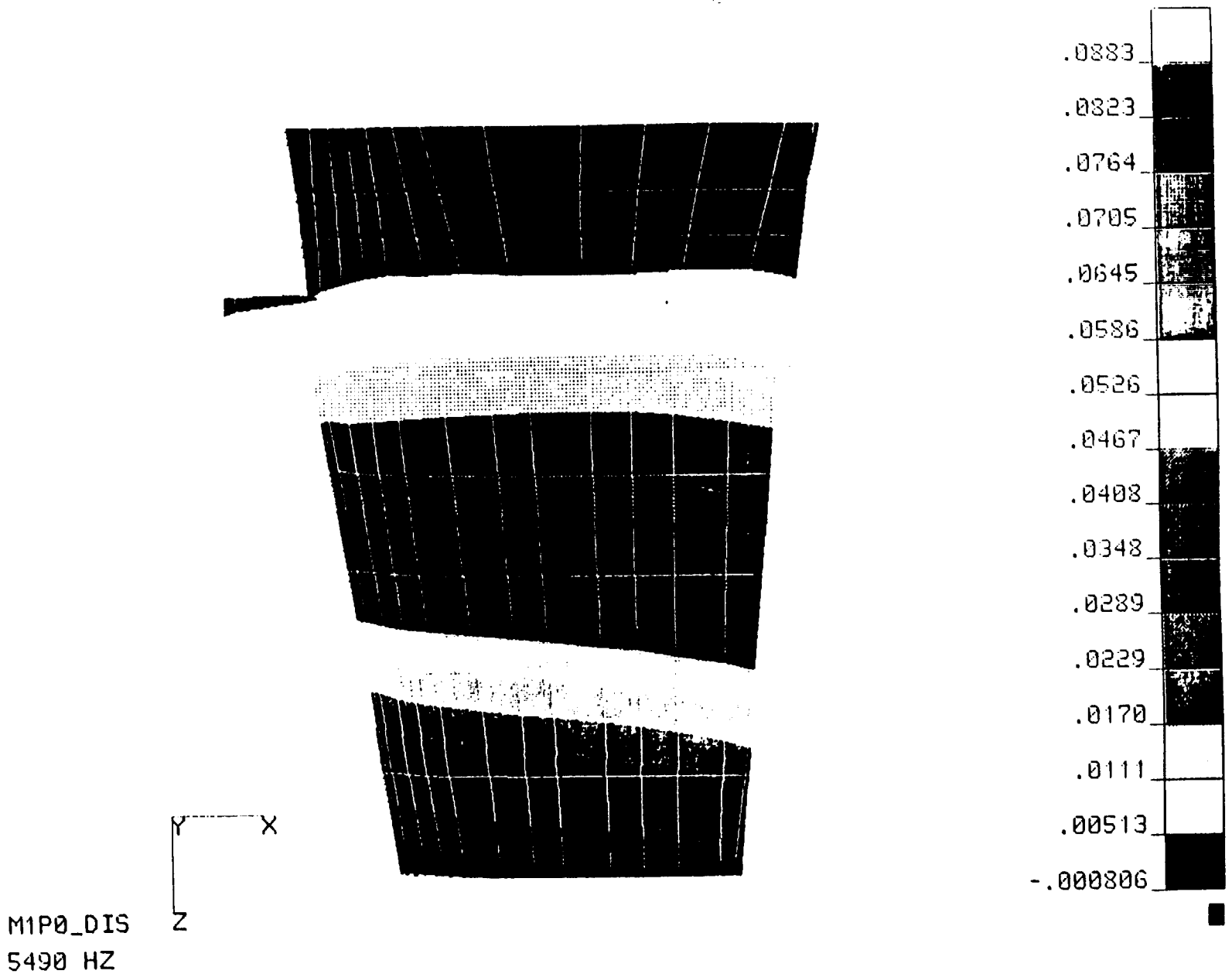

Figure 8.5 Y - Modal Displacement Contour Plot for Mode 1

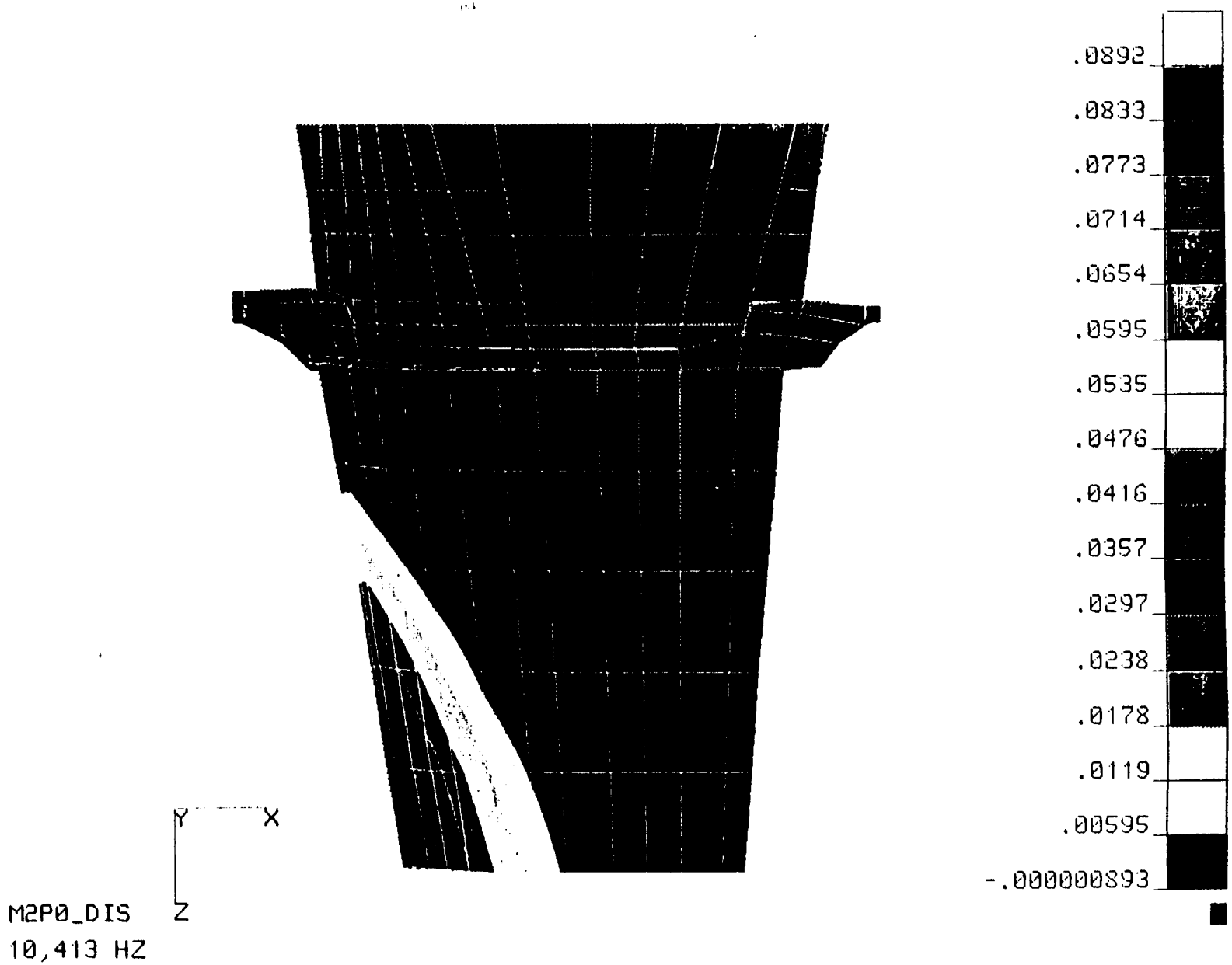

Figure 8.6 X - Modal Displacement Contour Plot for Mode 2

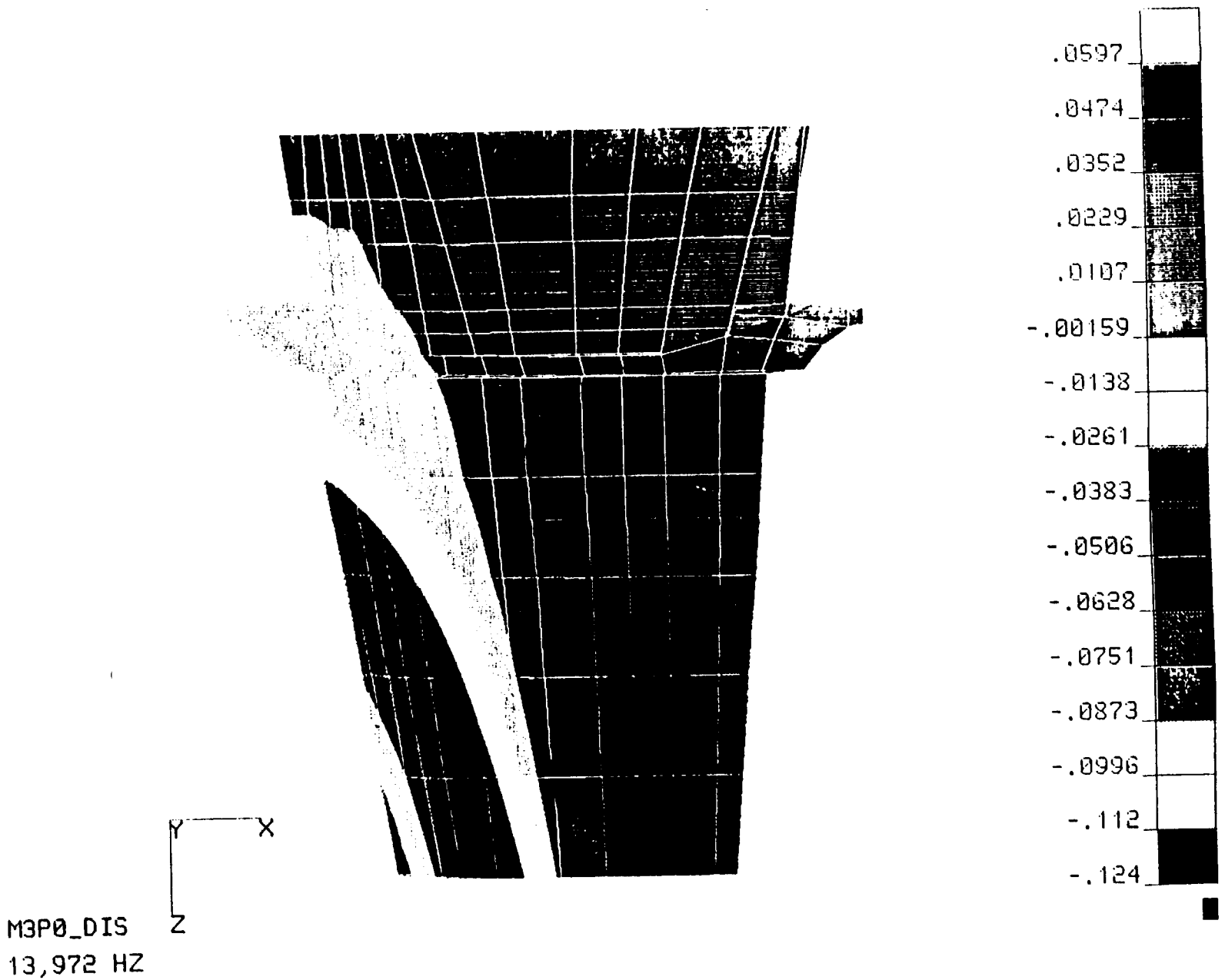

Figure 8.7 Y - Modal Displacement Contour Plot for Mode 3

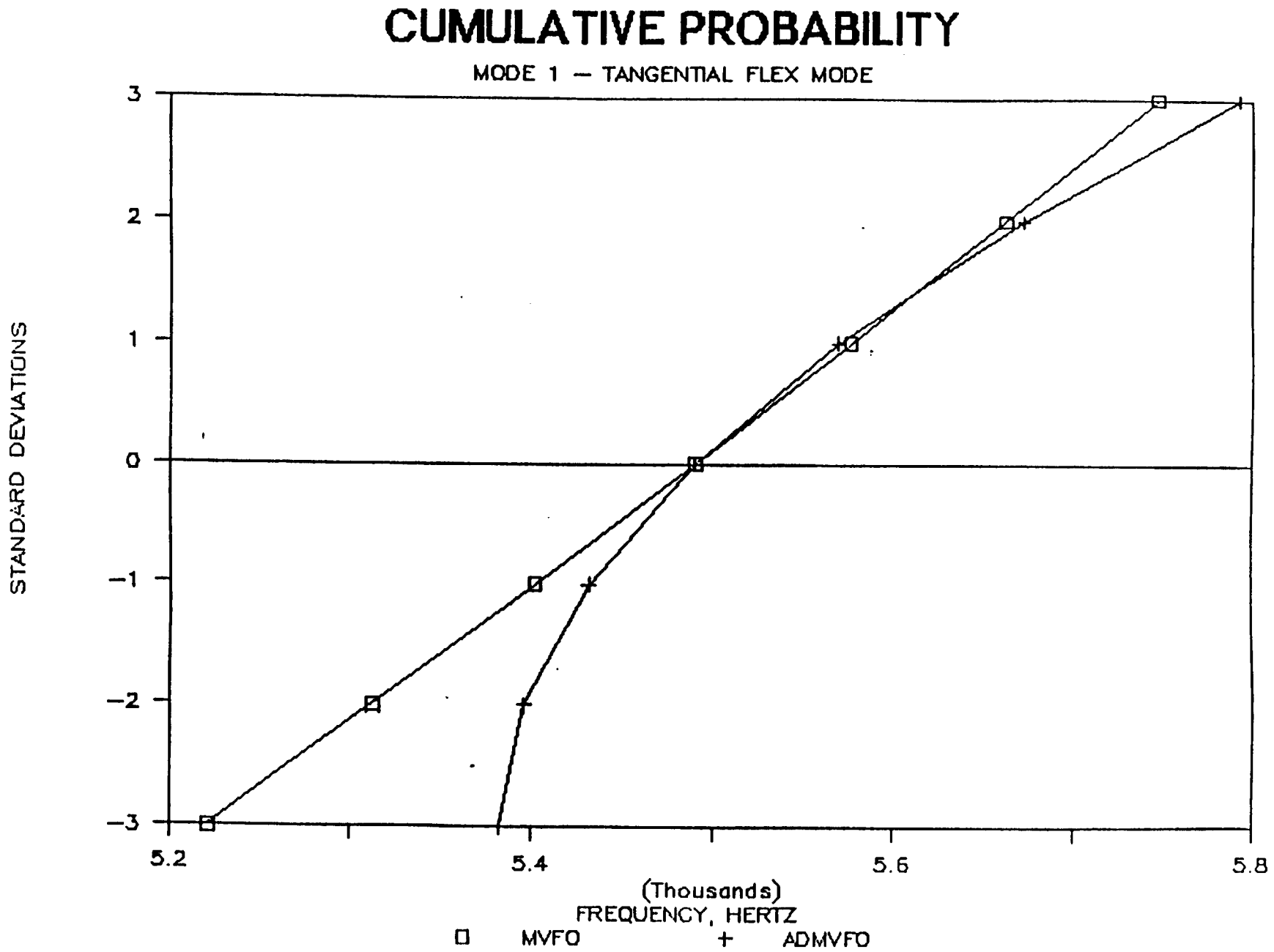

Figure 8.8 MVFO and ADMVFO Method Distributions for Mode 1

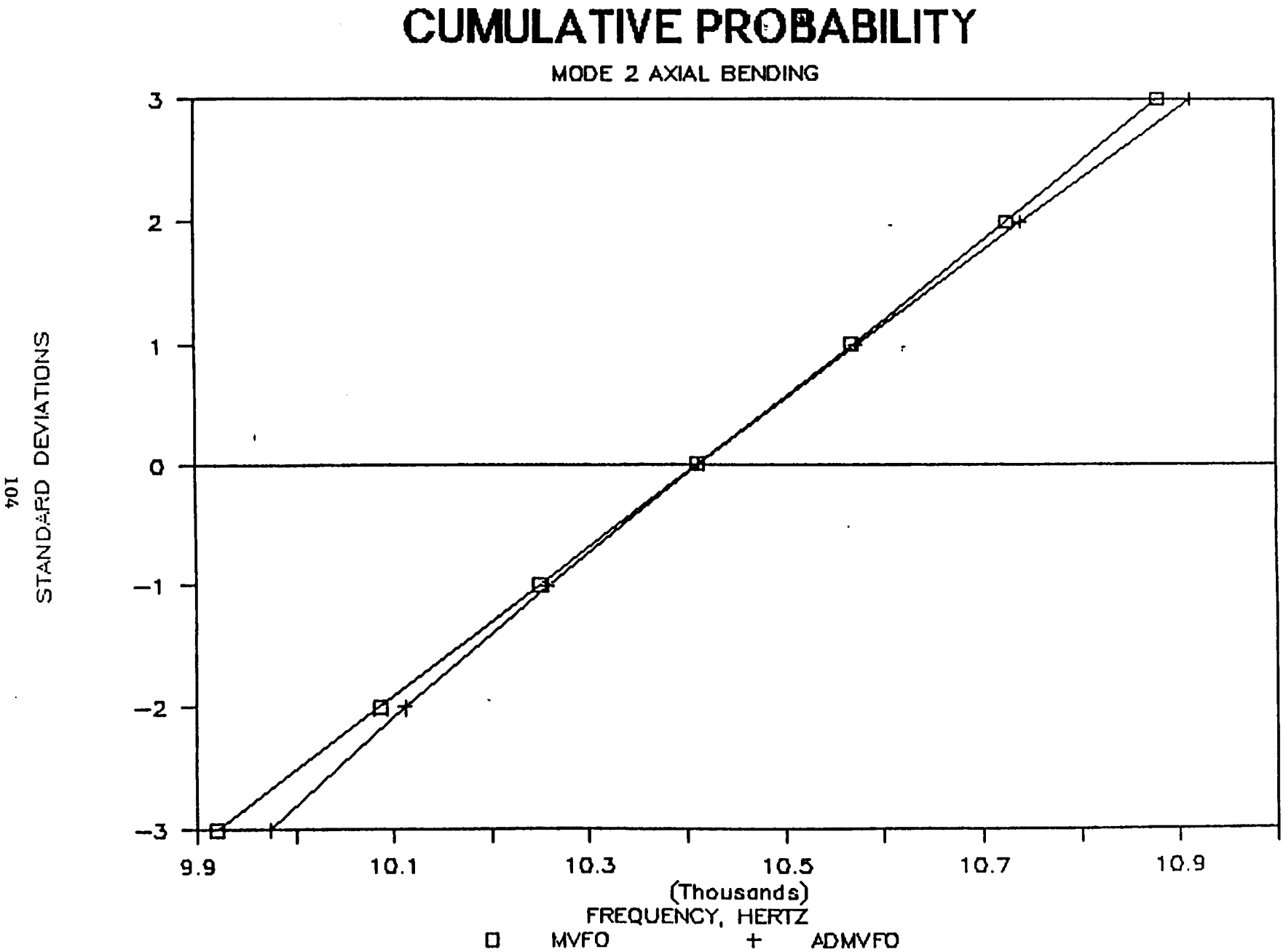

Figure 8.9 MVFO and ADMVFO Method Distributions for Mode 2

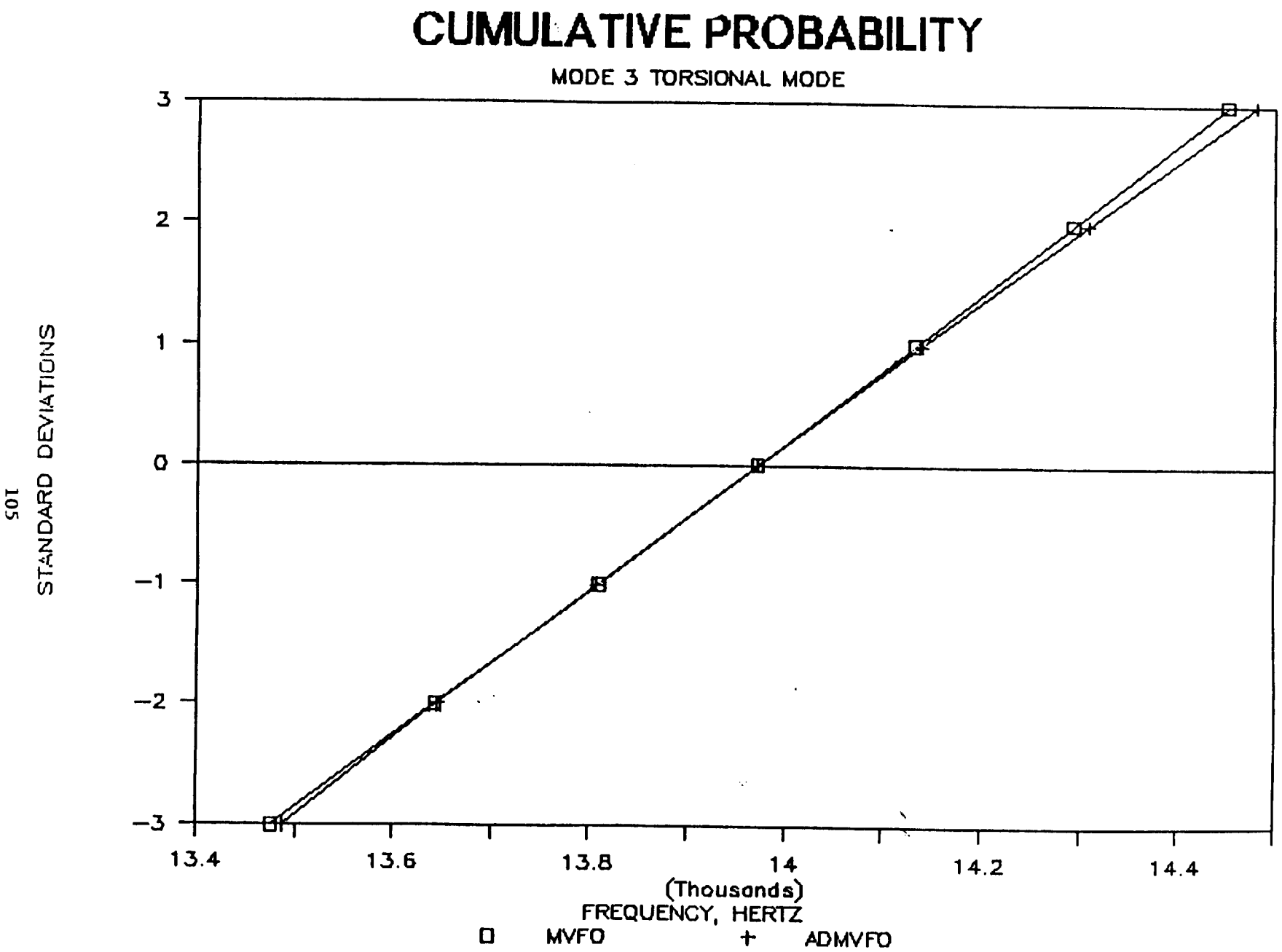
CUMULATIVE PROBABILITY
MODE 3 TORSIONAL MODE
STANDARD DEVIATIONS
3
2
1
0
−1
−2
−3
13.4
13.6
13.8
14
14.2
14.4
(Thousands)
FREQUENCY, HERTZ
MVFO
ADMVFO

Table 8.6

Probabilistic Sensitivities for the Turbine Blade Frequency Problem

RANDOM VARIABLE	MODE 1 TAMGENTIAL BENDING	MODE 2 AXIAL BENDING	MODE 3 TORSION
THETA Z	0.071	0.288	0.466[2]
THETA Y	0.214[3]	0.585[1]	0.091
THETA X	0.716[1]	0.320[3]	0.138
E	0.613[2]	0.489[2]	0.363[3]
NU	0.0142	0.310	0.301
G	0.099	0.312	0.684[1]
RHO	0.174	0.196	0.256
LEAN	0.015	0.004	0.005
TILT	0.002	0.039	0.028
TWIST	0.014	0.009	0.012

* Superscript Denotes Ranking of the Random Variables

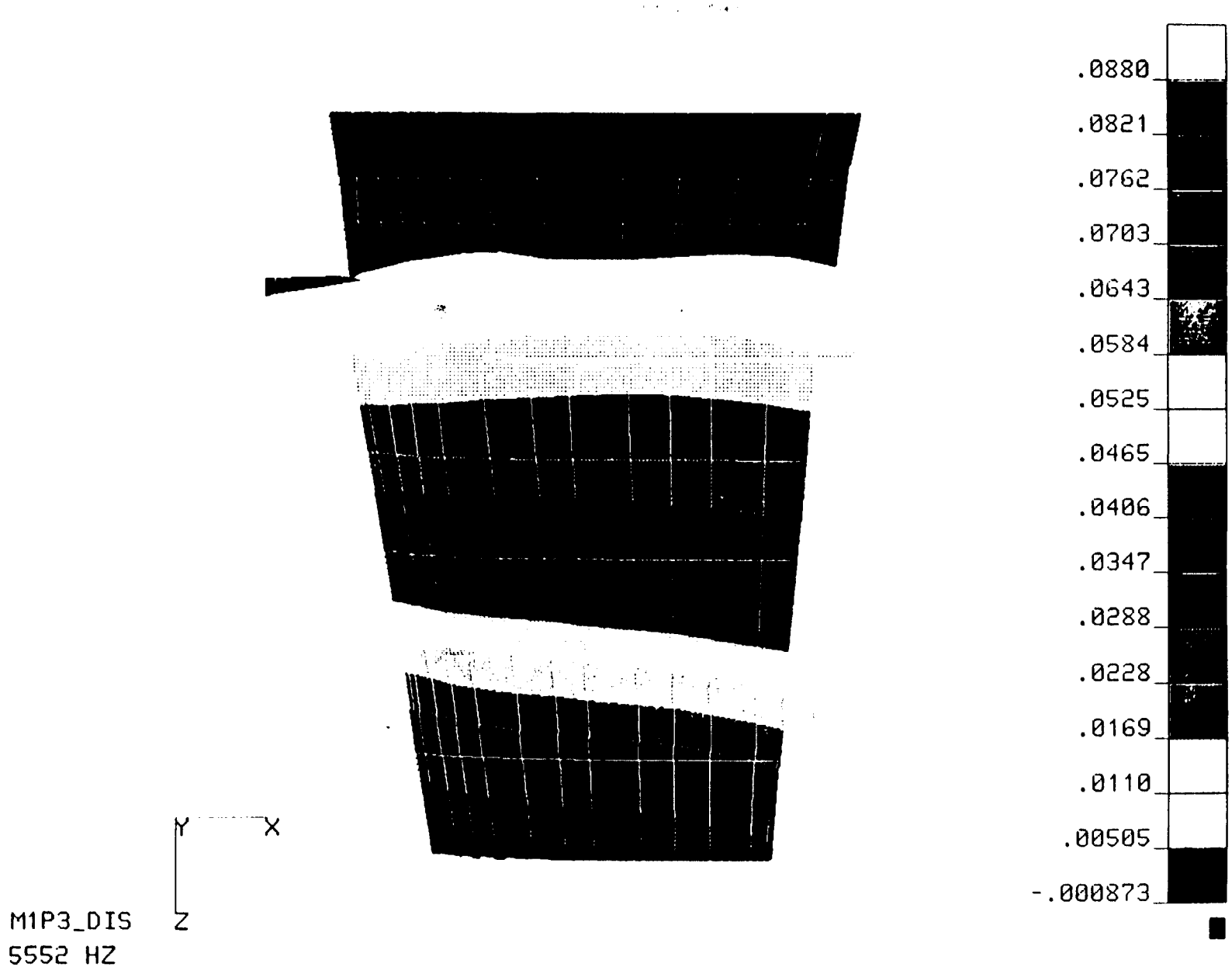

Figure 8.11 Mode 1, Displacement Y Direction Contour Plots of the Perturbed Structure Due to Theta-X Perturbed by One Standard Deviation

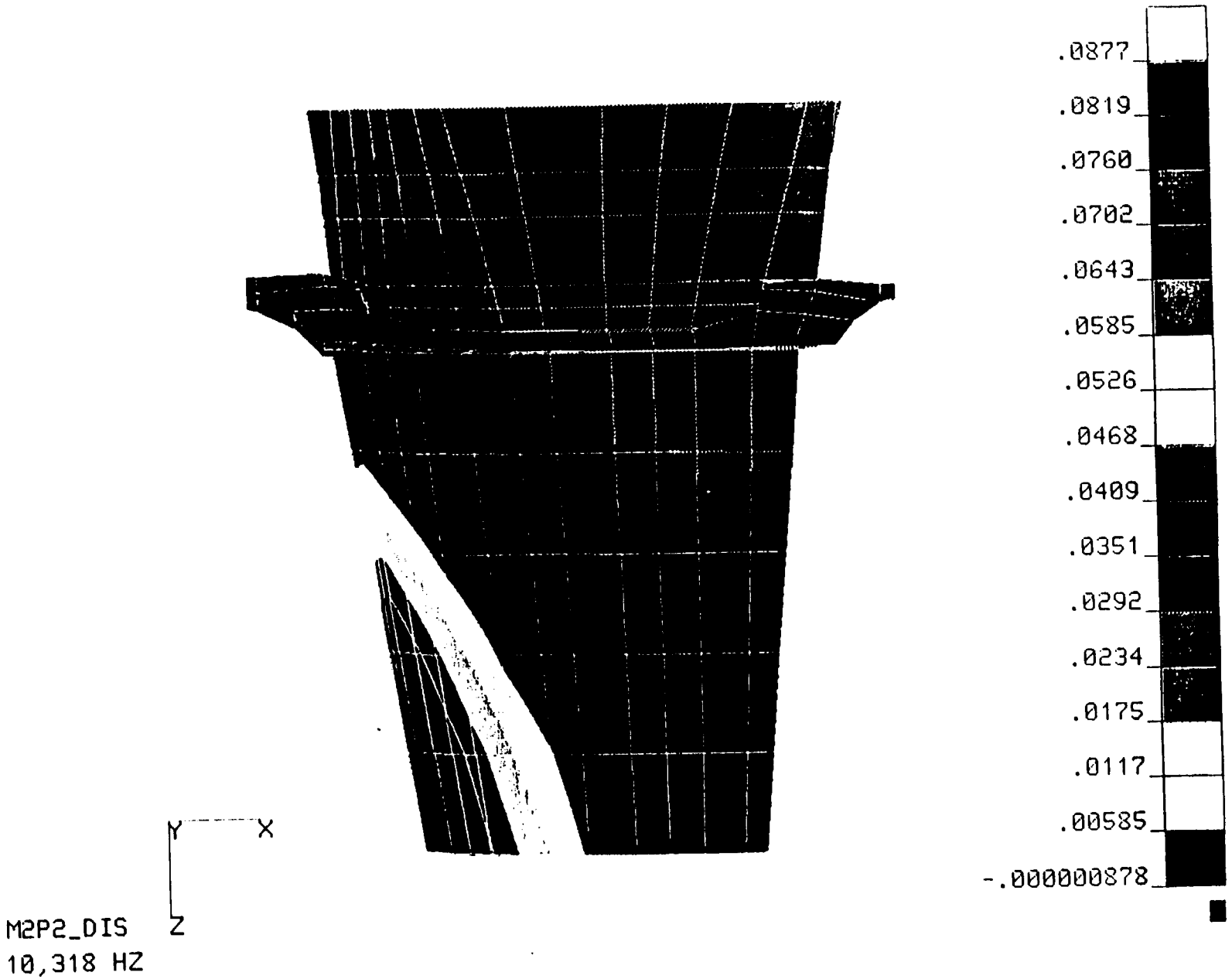

Figure 8.12 **Mode 2, Displacement X Direction Contour Plots of the Perturbed Structure Due to Theta-Y Perturbed by One Standard Deviation**

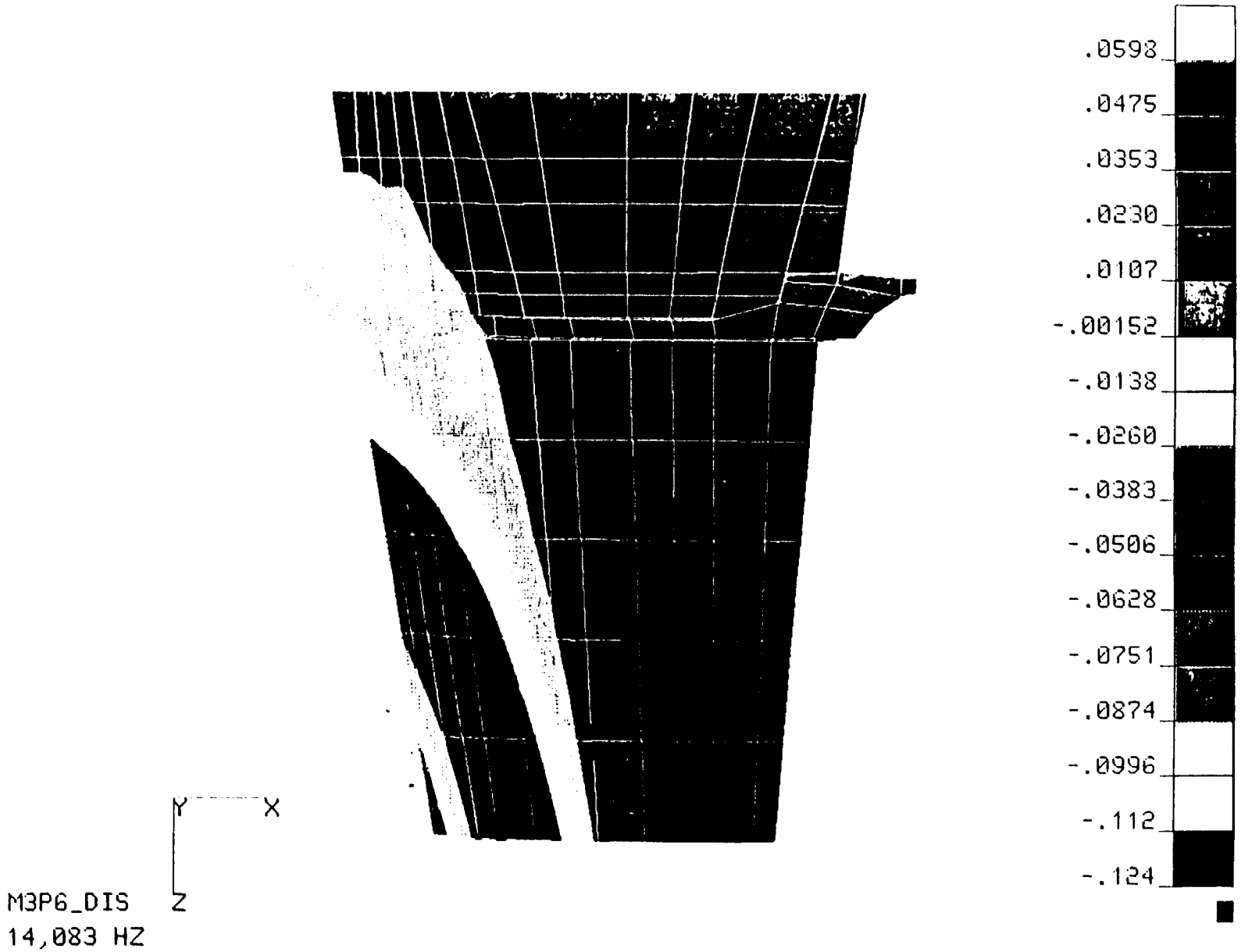

Figure 8.13 Mode 3, Y Displacement Contour Plot of the Perturbed Structure Due to Sheer Modulus Perturbed by One Standard Deviation

Table 8.7

Comparison of Calculated Frequency Variations
with Variations Observed in Practice

MODE	MEAN VALUE	STANDARD DEVIATION	COV	REPRESENTATIVE TEST SAMPLES *
1.	5,490 Hz	89	0.016	0.020
2.	10,412 Hz	162	0.016	0.013
3.	13,972 Hz	163	0.011	0.031

* D.S. LOX BLADES, SAMPLE SIZE 78

Improved estimates to the distributions were obtained by using ADMVFO method where the design points were successively moved for the seven point cumulative distribution function. The ADMVFO method results are displayed in the same Figures 8.8 through 8.10. While variations from the linear response surface assumption is small for mode 2 and mode 3, the deviation is significant for mode 1. It is also observed that the first mode of the turbine blade frequency exhibits a truncated distribution in the lower tail region. Further it pointed out the possibility of having more than one Most Probable Point (MPP) in the probability region of interest with the response surface being nonlinear concave or convex function. This is due to the cyclical nature of the material orientation effects on the elastic properties of the material in the primary directions of bending of the blade. Additional exercises using the suggested ADMVFO method with iterations resulted in obtaining different most probable points during successive iteration. This resulted in constructing a simple model and exercising it for a nonmonotonic response surface. The details of this study is reported below. Since the material orientation angles are the random variables that can cause nonmonotonic response surface, a simple cantilever model Figure 8.14 was constructed and exercised with the three material orientation angles as random variables. For mode 1, the primary material axis orientation is the dominant variable and its effect on response surface is schematically shown in Figure 8.15. The results from the MVFO method and the uncorrected results from the ADMVFO method are shown in Figure 8.16. The results from ADMVFO method as shown are invalid as the cumulative distribution function is not increasing monotonically. The modified monotonically increasing CDF is obtained by adjusting the CDF curve for probabilities calculated in the lower tail region as shown in Figure 8.16. This exercise pointed out the additional constraints that must be coded when FEM and FPI packages are tightly coupled to automatically produce an accurate cummulative distribution function using ADMVFO method.

8.4 Dynamic Analysis Solution Strategies for Systems Subjected to Multisupport Excitation

Most of the space propulsion duct components are attached to the engine and/or vehicle structure at multiple support points and are subjected to shock and vibration from more than one source at these attachment points. These components are in general, modelled as systems subjected to multisupport random or harmonic excitation. The governing equation of motion of such a system can be written in the form:

$$M_G \ddot{X}_G + C_G \dot{X}_G + K_G X_G = F_G \qquad (8.1)$$

Figure 8.14 Solid Element Cantilever Beam Model with Single Crystal Material Properties

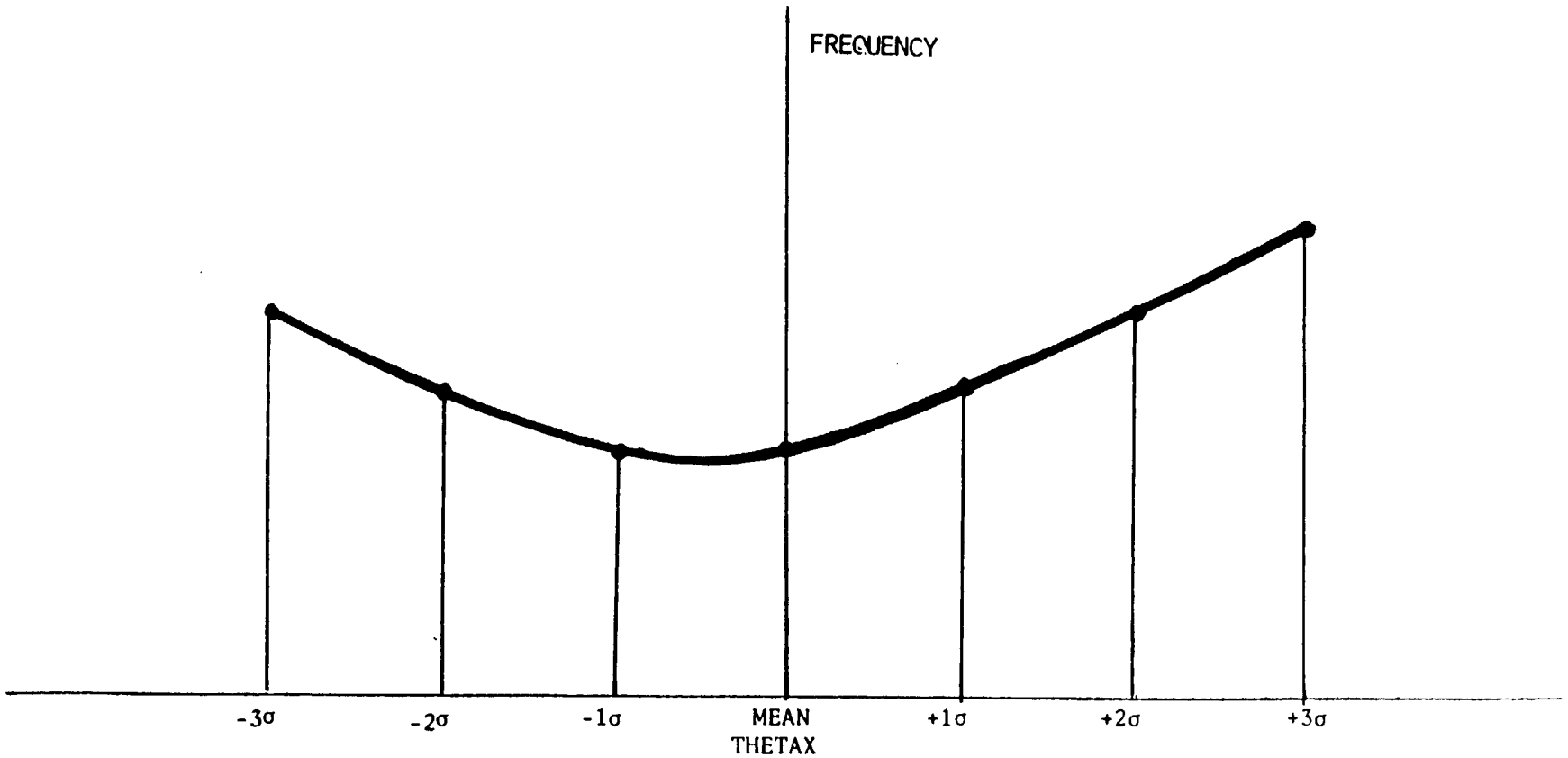

Figure 8.15 Approximate Shape of the Response Function as Function of Dominant Random Variable Sensitivity Factor 0.9

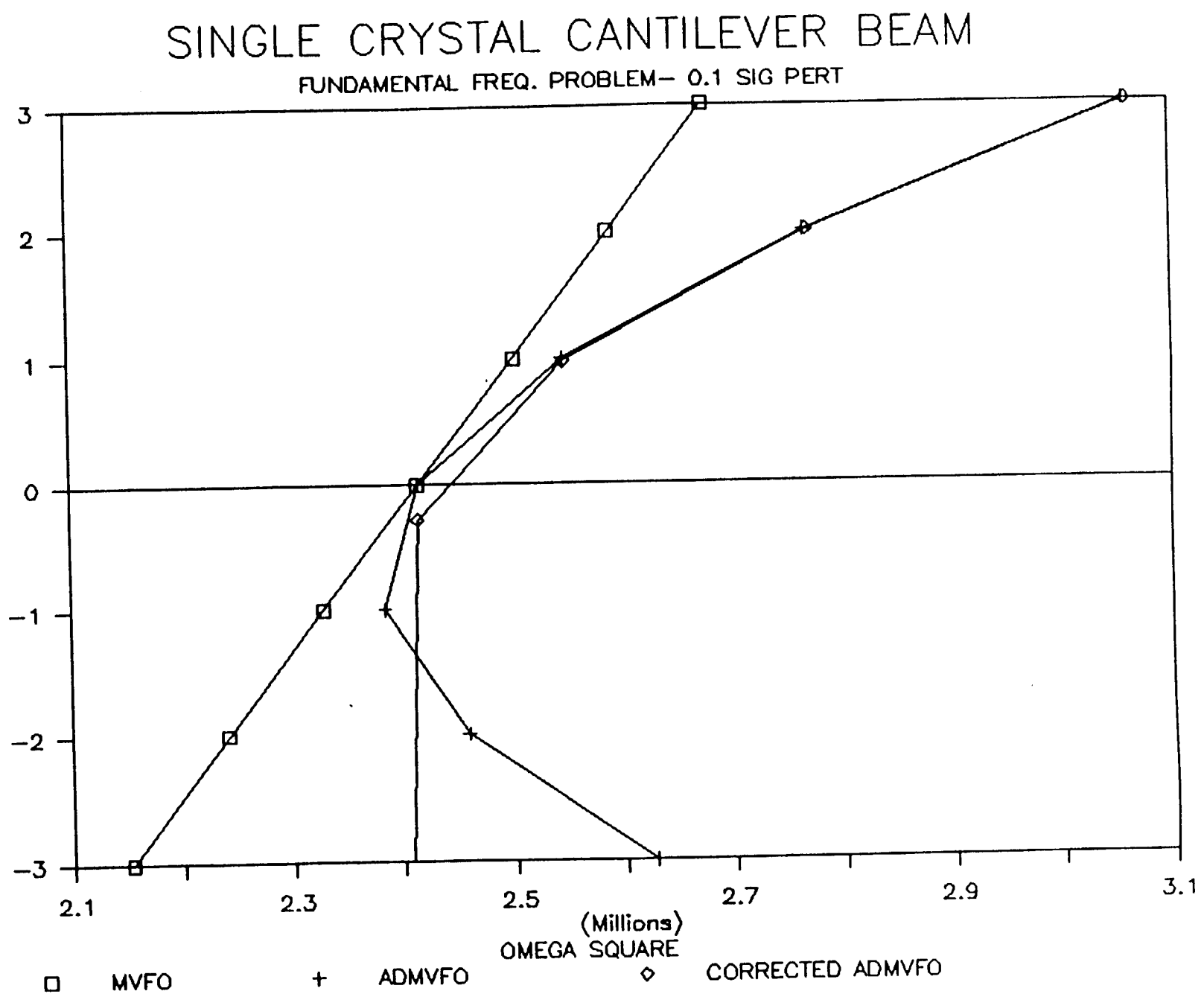

Figure 8.16 Adjusted CDF for Cantilever Beam Model Exhibiting Multiple Most Probable Points

Where M_G, C_G and K_G are the mass, damping and stiffness matrices respectively. F_G is the global force vectors. Equation (8.1) can also be re-written in the partitioned form:

$$\begin{bmatrix} M_{aa} & M_{ab} \\ M_{ab}^T & M_{bb} \end{bmatrix} \begin{Bmatrix} \ddot{X}_a \\ \ddot{X}_b \end{Bmatrix} + \begin{bmatrix} C_{aa} & C_{ab} \\ C_{ab}^T & C_{bb} \end{bmatrix} \begin{Bmatrix} \dot{X}_a \\ \dot{X}_b \end{Bmatrix} \tag{8.2}$$

$$+ \begin{bmatrix} K_{aa} & K_{ab} \\ K_{ab}^T & K_{bb} \end{bmatrix} \begin{Bmatrix} X_a \\ X_b \end{Bmatrix} = \begin{Bmatrix} F_a \\ F_b \end{Bmatrix}$$

Where X_a is the absolute nodal displacement vector of size n and X_b is the base displacement vector of size m. F_a is the nodal force vector, (from pressure load, etc.) which is a null vector in absence of nodal loads. F_b is the unknown base reaction. The subscript a and b in the matrices K, C, and M correspond to nodal (free) and base (prescribed) degrees-of-freedom (DOF) respectively.

Different methods are available that can handle such multisupport excitation problems. The first one is the direct approach of writing governing equation of motion in terms of absolute displacement along nodal DOF. The main disadvantage of this approach is that, the right hand side of the equation has all three items, the base displacement, velocity and acceleration as excitation to the system.

The second approach, known as "unit base displacement" or more commonly "influence coefficient" or "pseudo-static" displacement approach. Here the natural frequencies and mode shapes of the system are obtained by restraining all the base DOF. Next, a sequence of static analyses are performed to obtain the influence coefficients (i.e., static response of the system) by prescribing unit displacements along base DOF, applied one at a time, while keeping the remaining base DOF fixed. These influence coefficients are then utilized to obtain the response of systems subjected to multibase motions.

The third approach is analogous to penalty mass used in static analysis to handle prescribed displacement problem. This is commonly referred as "Big Mass", "Seismic Mass" or "Penalty Mass" approach. A large mass several order of magnitude larger than the system mass is lumped along each base DOF. The natural frequencies and mode shapes of this free-free system, that include the rigid body modes and near zero frequency modes in addition to the regular modes (fixed base) are then obtained using a negative power shift. Prescribed support motions are (approximately) achieved in an indirect way by exciting the support masses along the base DOF with forces equal to the penalty mass times the corresponding prescribed acceleration. This approach can be carried out in both "NESSUS" and "STARDYNE". STARDYNE

is a commercial code that is used in the industry particularly to solve random vibration problems. The NESSUS results are compared with STARDYNE results as part of this code verification effort. The subsequent sections will be restricted to the "penalty mass" approach, with a discussion of its relative advantages or limitations in handling the multisupport excitation problem.

8.4.1 Big Mass (Penalty Mass) Approach

In this approach the prescribed support degrees of freedom are also treated as unknowns. Huge masses, several orders of magnitude higher than the sum of all the diagonal terms in the mass matrix, are lumped at each base DOF. The unknown base force vector F_b is treated as a known vector with magnitude equal to the big mass multiplied by corresponding prescribed accelerations. The governing equation of motion of this entire free-free model will be the similar to eqn. (8.2) and is given by:

$$\begin{bmatrix} M_{aa} & M_{ab} \\ M_{ab}^T & M_{bb} \end{bmatrix} \begin{Bmatrix} \ddot{X}_a \\ \ddot{X}_u \end{Bmatrix} + \begin{bmatrix} C_{aa} & C_{ab} \\ C_{ab}^T & C_{bb} \end{bmatrix} \begin{Bmatrix} \dot{X}_a \\ \dot{X}_u \end{Bmatrix} + \begin{bmatrix} K_{aa} & K_{ab} \\ K_{ab}^T & K_{bb} \end{bmatrix} \begin{Bmatrix} X_a \\ X_u \end{Bmatrix} = \begin{bmatrix} 0 & 0 \\ 0 & M_{bb} \end{bmatrix} \begin{Bmatrix} 0 \\ \ddot{X}_b \end{Bmatrix} \tag{8.3}$$

Rearranging the 2nd of the above equation we get:

$$M_{bb}\,\ddot{X}_u = \left[-M_{ab}^T\,\ddot{X}_a - C_{ab}^T\,\dot{X}_a - C_{bb}\,X_u - K_{ab}^T\,X_a - K_{bb}\,X_u \right] + M_{bb}\,\ddot{X}_b \tag{8.4}$$

Observing the above equation, one can see that the terms within the square bracket are the products of two smaller numbers and can be ignored as compared to the other term in the right hand side. This is the penalty mass approach of indirectly pushing the unknown base acceleration $\ddot{X}_u$ towards the prescribed acceleration $\ddot{X}_b$, i.e.

$$\ddot{X}_u \rightarrow \ddot{X}_b \text{ as penalty mass} \rightarrow \infty \tag{8.5}$$

or

$$\ddot{X}_u \simeq \ddot{X}_b \text{ for very large Mass}$$

It should be noted at this point that even if the rigid body mode of the system is eliminated by attaching the base points to the ground by some springs with finite stiffness (same or lower order of magnitude as the other elements), the governing equation of motion will look exactly the same as eqn. (8.3), except that elements of K_{bb} will increase slightly. Therefore, relation (8.4) will still hold good. This approach will referred in the future as 'modified or constrained Big Mass' approach. The governing equations of motion (8.3) can be expressed in the compact form:

$$M\ddot{X} + C\dot{X} + KX = G_m\ddot{X}_b \tag{8.6}$$

Where the number of unknown DOF N, is (n+m). The vector X represents absolute nodal displacement.

This approach can be carried out in both "NESSUS" and "STARDYNE" for the verification models. At present, "NESSUS" uses an inbuilt penalty mass approach to handle multisupport excitation problems. The "Big Mass" approach is, however, quite prone to numerical problem (instability) and one must be careful in selecting the optimum penalty mass that is neither too big to cause ill conditioning of the mass matrix, nor too small to yield the desired base motion. The order of magnitude of the penalty mass is the most important parameter that determines the accuracy of this approach. Theoretically speaking, when the ratio of the penalty mass to the system mass approach infinity, the response at the base points approach the corresponding desired base motions specified indirectly as forces. However, in a digital computing machine with only finite significant digits, this creates a numerical problem. The penalty mass should not be too large as compared to the average diagonal elements of the mass matrix of the system to cause ill conditioning of the matrices, at the same time, it should be sufficiently large compared to the total mass of the system, so that the base responses are quite close to the prescribed base motion. The optimum order of magnitude is actually a machine dependent parameter and one would like to select a value as large as possible without getting into numerical trouble.

On a 64 bit machine, a penalty mass of five or six order of magnitude higher than the average diagonal (non-zero) mass of the system may be considered as an optimum value (compromise between two extremes), since there will still be six to eight more significant digits left depending on the precision of the machine. It should be noted at this point that as one starts refining a model, the average value of the diagonal elements of mass matrix get smaller, thus allowing a smaller penalty mass to avoid ill conditioning. This will cause a larger difference between base response and prescribed base motion. For this reason, the inbuilt feature in NESSUS that uses a penalty mass million times larger

than the SRSS value of positive diagonal elements of mass matrix was avoided in order to have a direct and better control over the selection of penalty mass.

For systems with large number of dynamic DOF, free free models often encounter a numerical problem during the modal extraction. It has been observed that there is a tendency of missing rigid body and near zero frequency modes and/or converging to the same mode twice. This ill conditioning problem is aggravated even further when the number of free supports (and consequently lumped big masses) increases. This problem can be handled in several ways. One such approach that is adopted in the verification problems is the "constrained penalty mass approach". In this approach, the system is properly (and preferably symmetrically) supported to remove all the rigid body modes (RBM) by flexible springs that are grounded at one end and attached to the penalty mass at the other end. There is no need to specify a negative power shift for this stable system. The three RBM are then replaced by three additional near zero frequency modes. Those mode shapes, however, must be very close to the rigid body modes for the free free system.

The added springs to support the lumped masses should have stiffness, preferably one or more order of magnitude lower than the overall system stiffness (not the stiffness of individual element). The system stiffness along each support DOF can be easily obtained from a static run with unit displacement along that DOF, while keeping all other support DOF fixed. The reactive force at that support point along that DOF in an equilibrium check is the corresponding system stiffness. It should be noted at this point that one needs to know only the order of magnitude of the system stiffness. Furthermore, there is no need to use different spring stiffness at different support points along a particular direction, but the stiffness in different directions, must be different for a better convergence of approximate rigid body modes.

8.4.2 Modal Analysis

Expanding the displacements in terms of modal coordinates a_i, and mode shapes Φ_i, i.e.,

$$X = \sum_{i=1}^{N} a_i \Phi_i \tag{8.7}$$

and assuming damping matrix satisfies the orthogonality condition, eqn. (8.6) decouples into modal equations of the form:

$$\ddot{a}_i + 2\zeta_i\omega_i\dot{a}_i + \omega_i^2 a_i = \sum_{j=1}^{m} \Upsilon_{m_{ij}} \ddot{x}_{b_j} \tag{8.8}$$

$$(i = 1, 2, \ldots, N)$$

Where ω_i and ζ_i are the i^{-th} natural frequency and modal damping ratio respectively, and the participation matrix is:

$$\Gamma_m = \Phi^T G_m \tag{8.9}$$

where Φ is the modal matrix

$$\Phi = [\Phi_1 \mid \Phi_2 \mid \ldots \Phi_N] \tag{8.10}$$

8.4.3 Random Vibration Analysis (Frequency Domain Approach)

Here only a brief outline of the modal, frequency domain, random vibration solution procedure is presented for a simple case that corresponds to the "penalty mass approach", where excitation is represented by base acceleration only. Assuming base acceleration to be uncorrelated, the power spectral density function (PSDF) of modal coordinates and its derivatives can be written in the form:

$$S_{a_k a_j}(\Omega) = \frac{\sum_{\ell=1}^{m} S_{\ddot{x}_{b_\ell} \ddot{x}_{b_\ell}}(\Omega)\ \Gamma_{m_{k\ell}}\ \Gamma_{m_{j\ell}}}{\{\omega_k^2 - \Omega^2 + i2\zeta_k\omega_k\Omega\}\quad\{\omega_j^2 - \Omega^2 - i2\zeta_j\omega_j\Omega\}}$$

$$S_{\dot{a}_k \dot{a}_j}(\Omega) = \Omega^2 S_{a_k a_j}(\Omega) \tag{8.11}$$

$$S_{\ddot{a}_k \ddot{a}_j}(\Omega) = \Omega^4\ S_{a_k a_j}(\Omega)$$

$$i = \sqrt{-1}$$

Where $S_{\ddot{x}_{b_\ell} \ddot{x}_{b_\ell}}(\Omega)$ is the prescribed PSDF of ℓ-th base acceleration.

The covariance matrix of modal coordinates (or its derivatives) can be obtained by integrating the area under the PSDF curve over the entire frequency range, i.e.,

$$E\left[a_k^{(n)} a_j^{(n)}\right] = \int_{-\infty}^{\infty} \frac{\Omega^{2n}}{2} S_{a_k a_j}(\Omega).d\Omega = \sigma_{a_k a_j} \tag{8.12}$$

where $E[\cdot]$ denotes expected value.

The integration in eqn. (8.12) is carried out (usually) numerically over a finite prescribed frequency range. Once the covariance matrix of modal coordinates is obtained any arbitrary response quantity that can be expressed as a linear combination of the modes can be evaluated by using the simple superposition principle.

8.4.4 Modal Superposition

Let R be vector with known covariance matrix Σ_{RR}, given by:

$$\Sigma_{RR} = E[RR^T] \tag{8.13a}$$

Let $\cup$ be a vector that can be written as linear combination of R, i.e.,

$$\{U\} = [D_{UR}] \cdot \{R\} \tag{8.13b}$$

Where D_{UR} is the linear transformation matrix. The covariance matrix of $\cup$ can be easily obtained from:

$$\Sigma_{UU} = E[UU^T] = D_{UR} \cdot \Sigma_{RR} D_{UR}^T \tag{8.14}$$

In the "Big mass" approach, e.g., the absolute displacement can be expressed as:

$$\{X\} = [\Phi]\{A\}$$

Where Φ is the modal matrix and A is the modal coordinate. The covariance matrix of displacement response can be obtained by using eqn. (8.14), i.e.,

$$\Sigma_{XX} = E[X X^T] = \Phi \Sigma_{AA} \Phi^T$$

Where Σ_{AA} is the covariance matrix of modal coordinates that is already known. Covariance matrix of velocity and acceleration of nodal points can be obtained in exactly the same way. Covariance matrix of any other response quantity can be similarly evaluated e.g., to obtain stresses the DUR matrix will represent the stress-displacement matrix, for stress resultants it is nothing but the element stiffness matrix.

8.5 Simple Verification Problems

Test Problem 1

Consider a very simple spring mass model supported at two points A and B as shown in Figure 8.17. The governing equation of motion of this undamped DOF system is given by:

$$\ddot{x}_2 + \omega^2 x_2 = \frac{\omega^2}{2}(x_1 + x_3) \tag{8.15}$$

where $\omega = 2K/m$ = natural frequency

Consider the case when the symmetry of response is destroyed by applying two different amplitudes of excitation at the two support points, i.e.

$$\ddot{X}_1 = A_0 \sin\Omega t$$

and

$$\ddot{X}_3 = 2A_0 \cos\Omega t$$

The steady state response governed by eqn. 8.15 is:

$$X_2 = -\frac{A_0/\omega^2}{2r^2(1 - r^2)} \{\sin\Omega t + 2\cos\Omega t\} \tag{8.16}$$

The spring forces in the two members are not the same due to loss of symmetry. They are given by:

$$F_1 = k(X_2 - X_1) = \frac{-kA_0/\omega^2}{2r^2(1 - r^2)} \{(2r^2 - 1)\sin\Omega t + 2\cos\Omega t\}$$

$$F_2 = k(X_3 - X_2) = \frac{-kA_0/\omega^2}{2r^2(1 - r^2)} \{-\sin\Omega t + (2 - 4r^2)\cos\Omega t\} \tag{8.17}$$

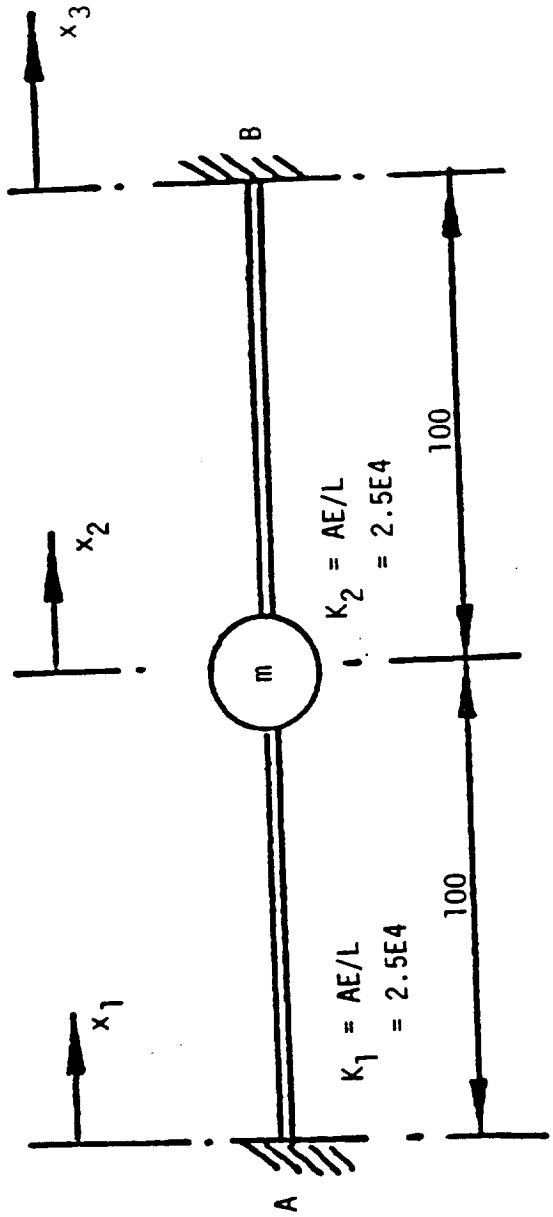

Figure 8.17 Simple Verification Problem 1

The normalized amplitude of spring forces are given by:

$$\beta_1 = |F_1| / (kA_0/\omega^2) = (2r^2 - 1)^2 + 4 \; / \{2r^2(1-r^2)\}$$
$$\beta_2 = |F_2| / (kA_0/\omega^2) = (2-4r^2)^2 + 1 \; / \{2r^2(1-r^2)\} \qquad (8.18)$$

8.5.1 Penalty (Big) Mass Approach

In this approach, two large masses are lumped at the two support point as shown in Figure 8.18. The governing equation of motion of the free-free system is given by:

$$\begin{bmatrix} M & & \\ & m & \\ & & M \end{bmatrix} \begin{Bmatrix} \ddot{x}_1 \\ \ddot{x}_2 \\ \ddot{x}_3 \end{Bmatrix} + \begin{bmatrix} K & -K & 0 \\ -K & 2K & -K \\ 0 & -K & K \end{bmatrix} \begin{Bmatrix} x_1 \\ x_2 \\ x_3 \end{Bmatrix}$$
$$= \begin{Bmatrix} f_1 \\ 0 \\ f_3 \end{Bmatrix} = \begin{Bmatrix} M\ddot{x}_1' \\ 0 \\ M\ddot{x}_3' \end{Bmatrix} \qquad (8.19)$$

where $\ddot{X}_1'$ and $\ddot{X}_3'$ are the desired (prescribed) acceleration at the two support points. $\ddot{X}_1$ and $\ddot{X}_3$ are the corresponding response (achieved base acceleration) of the two big lumped masses. Solving the eigenvalue problem, the three natural frequencies and ode shapes are given by:

$$\omega_{1,2,3} = \begin{Bmatrix} 0 \\ \omega_0 \quad \alpha/2 \\ \omega_0 \quad 1 + \alpha/2 \end{Bmatrix} \qquad (8.20)$$

$$\Phi_1 = \begin{Bmatrix} 1 \\ 1 \\ 1 \end{Bmatrix} \; ; \; \Phi_2 = \begin{Bmatrix} 1 \\ 0 \\ -1 \end{Bmatrix} \; ; \; \Phi_3 = \begin{Bmatrix} -\alpha/2 \\ 1 \\ -\alpha/2 \end{Bmatrix}$$

where

$$\alpha = \frac{m}{M} \text{ and } \omega_0 = \sqrt{\frac{2K}{m}}$$

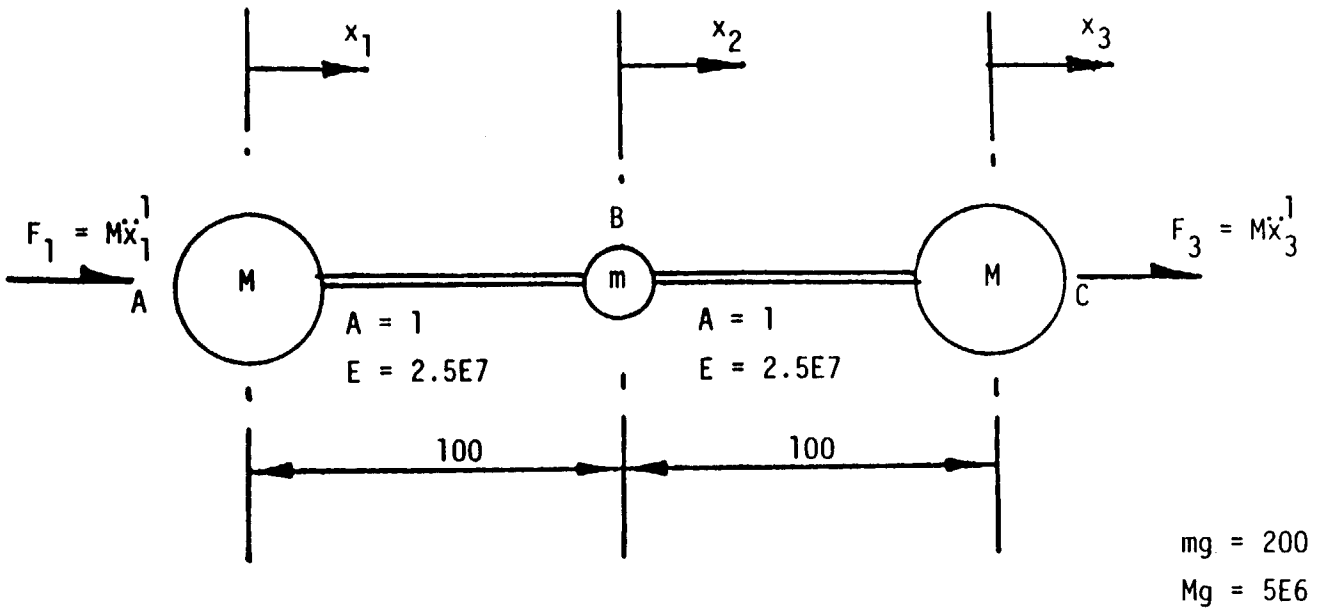

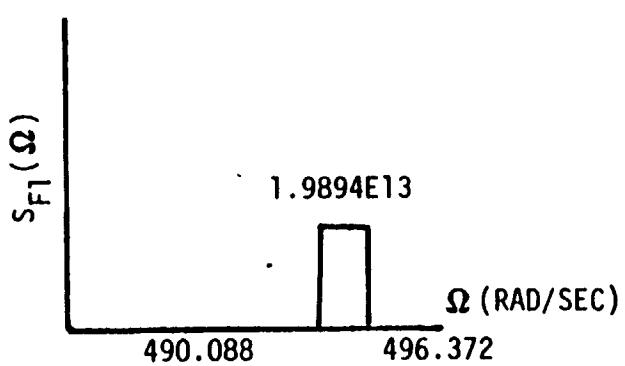

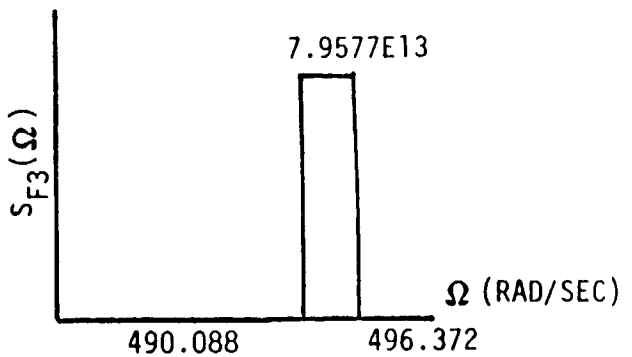

Figure 8.18 Simple Verification Problem 1 Penalty Mass Model

The first mode is the rigid body mode which does not contribute to the stress response. However, this must be included if correct displacement, velocity and acceleration responses are needed. The second one is a near zero frequency mode that handles the differential support motion. The third one is a normal mode that is approximately the same as the mode with fixed base support.

Expanding the displacements in terms of modal coordinates a_i and the mode Φ_i shapes, eqn. (8.19) decouples into modal equations of the form:

$$\begin{aligned}
\ddot{a}_1 + \omega_1^2 a_1 &= \frac{1}{2+\alpha}(\ddot{x}_1' + \ddot{x}_3') \\
\ddot{a}_2 + \omega_2^2 a_2 &= \frac{1}{2}(\ddot{x}_1' - \ddot{x}_3') \\
\ddot{a}_3 + \omega_3^2 a_3 &= \frac{-1}{2+\alpha}(\ddot{x}_1' + \ddot{x}_3')
\end{aligned} \tag{8.21}$$

Once the modal coordinates are solved, the displacement responses can be easily obtained by using modal superposition. The steady state response of the modal coordinates due to excitation type II, i.e., $\ddot{x}_1' = A_o \mathrm{Sin}\Omega t$ and $\ddot{x}_3' = 2A_o \mathrm{Cos}\Omega t$

$$\begin{aligned}
a_1 &= \frac{A_0}{(2+\alpha)(\omega_1^2 - \Omega^2)}\{\mathrm{Sin}\Omega t + 2\mathrm{Cos}\Omega t\} \\
a_2 &= \frac{A_0}{2(\omega_2^2 - \Omega^2)}\{\mathrm{Sin}\Omega t - 2\mathrm{Cos}\Omega t\} \\
a_3 &= \frac{-A_0}{(2+\alpha)(\omega_3^2 - \Omega^2)}\{\mathrm{Sin}\Omega t + 2\mathrm{Cos}\Omega t\}
\end{aligned} \tag{8.22}$$

It should be noted at this point that ω_1 is not exactly equal to zero when computed on a digital computer because of round off errors. However, it is very small (several orders of magnitude smaller than the near zero frequency ω_2). The displacement responses can be obtained by modal superposition. They are given by:

$$x_1 = a_1 + a_2 - \frac{\alpha}{2} a_3$$

$$x_2 = a_1 + a_3 \qquad (8.23)$$

$$x_3 = a_1 - a_2 - \frac{\alpha}{2} a_3$$

Substituting back eqn. (8.22) into eqn. (8.23), we get:

$$x_1 = A_0 \left[\left\{ \frac{1}{(2+\alpha)(\omega_1^2 - \Omega^2)} + \frac{1}{2(\omega_2^2 - \Omega^2)} + \frac{\alpha}{2(2+\alpha)(\omega_3^2 - \Omega^2)} \right\} \mathrm{Sin}\Omega t \right.$$

$$\left. + \left\{ \frac{1}{(2+\alpha)(\omega_1^2 - \Omega^2)} - \frac{1}{2(\omega_2^2 - \Omega^2)} + \frac{\alpha}{2(2+\alpha)(\omega_3^2 - \Omega^2)} \right\} 2\mathrm{Cos}\Omega t \right] \qquad (8.24)$$

Now assuming Ω is much larger as compared to ω_1 and ω_2, we obtain:

$$X_1 \simeq A_0 \left[\frac{4+\alpha}{-2(2+\alpha)\Omega^2} \cdot \mathrm{Sin}\Omega t + \frac{3\alpha^2\omega}{(2+\alpha)\Omega^2(\omega_3^2 - \Omega^2)} \cdot \mathrm{Cos}\Omega t \right] \qquad (8.25)$$

Finally, considering the fact that the mass ratio a << 1 the above expression yields:

$$x_1 \simeq \frac{-A_0}{\Omega^2} \mathrm{Sin}\Omega t = x_1' = \text{prescribed base motion at support 1.}$$

Similarly, one can show that

$$x_3 \simeq \frac{-2A_0}{\Omega^2} \cdot \mathrm{Cos}\Omega t = x_3' = \text{prescribed base motion at support 2}$$

and the absolute displacement at node 2

$$X_2 = \frac{-A_0/\omega_3^2}{r_3^2 (1 - r_3^2)(2+\alpha)} \cdot \{\mathrm{Sin}\Omega t + 2\mathrm{Cos}\Omega t\} \qquad (8.26)$$

comparing the above expression with the one in eqn. (9.16), we see that they are identically the same as $\alpha \to 0$.

For the NESSUS verification run K = 250000, mg = 200 and Mg = 5.0E6 (i.e., α = .4E -4) were selected. The system parameters are shown in Figure 8.18. The mode shapes and the natural frequencies are obtained in NESSUS using a negative power shift. The NESSUS results can be compared to that from analytical expressions in eqn. (8.20). They are presented in Table 8.8. NESSUS modal results agree quite well with the analytical solution.

The analytical results obtained earlier in eqns. 8.16-8.18 are valid for harmonic excitation. Similar relationships also hold good between RMS excitation and RMS responses for a narrow banded random excitation when the two base motions are completely uncorrelated. An acceleration PSD level of 5 g^2/Hz over a band of 1 Hz for DOF x, and 20 g^2/Hz at the other end (DOF x3) were selected. This is achieved indirectly by specifying a force PSD equal to big mass squared times the corresponding acceleration PSD. They are also shown in Figure 8.18.

The responses computed using the "Big Mass" approach and the analytical expressions described earlier are observed to be reasonable close. The RMS displacements along nodal DOF are presented in Table 8.9. The RMS stress resultants are presented in Table 8.10.

It is worthwhile to mention that the free free model used in the penalty mass approach can often lead to inaccurate modal solution, specially for large models. This can be avoided by using a constrained penalty mass approach.

8.5.2 Constrained Penalty Mass Approach

As discussed earlier, this is just an extension of the "Big Mass" approach where the rigid body mode is eliminated from the system by constraining the big masses by flexible springs as shown in Figure 8.19. Here both of the big masses are constrained for the sake of symmetry even though only one of them needs to be constrained to make the system stable. The governing equation of motion then takes the form:

$$\begin{bmatrix} M & & \\ & m & \\ & & M \end{bmatrix} \begin{Bmatrix} \ddot{x}_1 \\ \ddot{x}_2 \\ \ddot{x}_3 \end{Bmatrix} + \begin{bmatrix} (K+\beta K) & -K & 0 \\ -K & 2K & -K \\ 0 & -K & (K+\beta K) \end{bmatrix} \begin{Bmatrix} x_1 \\ x_2 \\ x_3 \end{Bmatrix} = \begin{Bmatrix} M\ddot{x}_1' \\ 0 \\ M\ddot{x}_3' \end{Bmatrix} \quad (8.27)$$

which is exactly the same as eqn. (8.19) except that the diagonal terms in the stiffness matrix associated with the big mass d.o.f. increased, making the stiffness matrix nonsingular. Here also for large M, $\ddot{X}_1$ and $\ddot{X}_3$ will approach $\ddot{X}_1'$ and $\ddot{X}_3'$, the prescribed base motions as long as β is small (preferably less than 1). The natural frequencies are given by:

Table 8.8

Comparison of NESSUS and Analytical Eigen Values and Eigen Vectors for Simple Verification Problem 1

		DOF			Nat. Freq. (Rad/sec)
		1	2	3	
NESSUS Free-Free Big Mass	MODE - 1	.6216E-2	.6216E-2	.6216E-2	7.0711E-2
	MODE - 2	.6216E-2	.389E-12	-.6216E-2	4.3949
	MODE - 3	-.2778E-4	1.3899	-.2778E-4	982.861
Analytical (α = 0.4E-4)	MODE - 1	1.0	1.0	-1.0	0.0
	MODE - 2	1.0	0.0	-1.0	4.3954
	MODE - 3	-.2E-4	1.0	-.2E-4	982.873

Table 8.9

RMS Displacement Comparison for Simple Verification Problem 1

	NODE 1	NODE 2	NODE 3
ANALYTICAL	.00358	.00533	.00716
NESSUS	.00355	.005307	.007104

Table 8.10

RMS Axial Stress Comparison

	BEAM 1	BEAM 2
ANALYTICAL	1229.2	843.2
NESSUS	1222.98	836.2

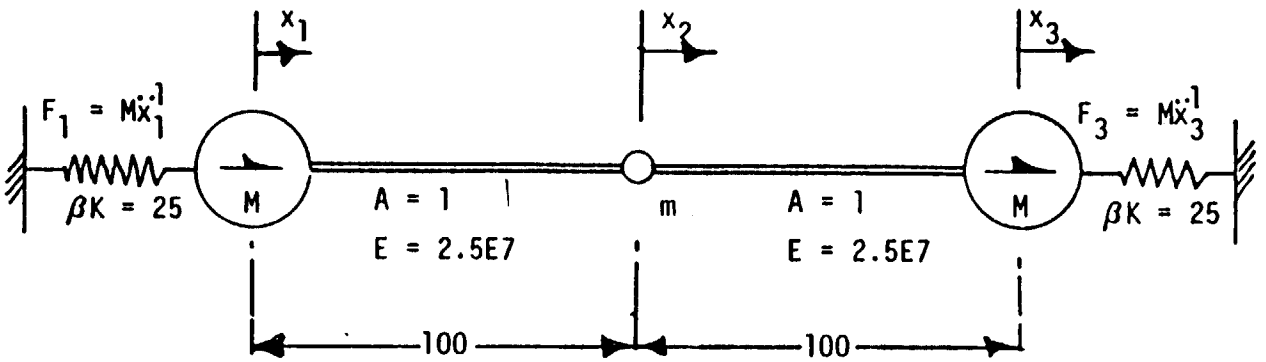

Figure 8.19 Simple Verification Problem 1 Using Constrained Big Mass

$$\omega_1 = \omega_0 \quad \alpha(1+\beta)/2 \tag{8.28}$$

$$\omega_{2,3} = \frac{\omega_0}{2} \left[\left(1 + \frac{\alpha(1+\beta)}{2}\right) \mp \left(1 + \frac{\alpha(1+\beta)}{2}\right)^2 - \alpha(2\beta+1) \right]^{1/2}$$

Looking into the expressions for natural frequencies it can be observed that it is more sensitive to α values than the β values. A recommended value of β will be .001 to .0001, i.e., the stiffness of the additional springs to be three or four orders of magnitude lower than the system stiffness. The recommended α value will be around 10^{-6} for 64 bit machines, that alone in this example can reduce the first two frequencies close to zero and the third one much closer to the actual natural frequency. However, even with this relatively large α and β values, the responses were observed to be reasonably close to this correct solution.

The system parameters are shown in Figure 8.19. The natural frequencies and the mode shapes can be obtained for this stable system with a negative power shift. They are presented in Table 8.11. The natural frequencies computed from the analytical expression in eqn. (8.28) is also presented in the table for comparison.

The RMS responses, both displacement and stress resultants for this example problem are not presented here since they are almost the same as that of the unconstrained penalty mass approach as presented in Tables 8.9 and 8.10.

For this simple verification problem the RMS displacement responses along nodal degrees-of-freedom and RMS stress resultants at the nodes are observed to be fairly close to that obtained by analytical solution.

Test Problem 2

In this test problem a 2 DOF lumped mass system as shown in Figure 8.20 is considered. Constrained penalty mass approach is used to obtain the response of the system subjected to multibase random excitation. The natural frequencies and the mode shapes of this stable system is obtained in NESSUS and STARDYNE without a negative power shift. They are presented in Table 8.12. The modal characteristics obtained using the two different programs agree reasonably well.

The system is subjected to band limited white noise excitation at the two support points as shown in Figure 8.21. Two different types of excitation are considered. One fully correlated and the other one fully uncorrelated base motion. The RMS displacement responses for these two load cases are presented in Table 8.13. Exact values of the prescribed base motions are presented in Table 8.14. This is a check for the accuracy of the Big Mass approach where prescribed base motion is achieved indirectly.

Table 8.11

Modal Analysis Results for Simple Verification Problem 2

MODE NO	MODE 1	NODE 2	NODE 3	FREQUENCY RAD/SEC	ANALYTICAL α=.4E-4, n=.1E-4
MODE 1	6216E-2	6216E-2	.62160E-2	4.3954E-2	4.3954E-2
MODE 2	-.62161E-2	.97392E-15	.62161E-2	4.39566E0	4.3956
MODE 3	+.27799E-4	-1.3899	+.27799E-4	982.861	982.858

Table 8.12

Natural Frequencies & Mode Shapes for
Simple Verification Problem 2

MODE #	PROGRAM	FREQUENCY Hz	MODE SHAPES			
			BASE 1	X_1	X_2	BASE 2
1	STARDYNE	.872 E-7	1.0	1.0	1.0	1.0
	NESSUS	.69954E-3	.006216	.006216	.006216	.006216
2	STARDYNE	.5712	1.0	.33333	-.33333	-1.000
	NESSUS	.5712	.0062161	.0020721	-.0020720	-.0062161
3	STARDYNE	113.690	-.000025	.67944	1.000	-.00038
	NESSUS	113.690	-.00002938	.77606	1.1422	-.0000432
4	STARDYNE	235.772	-.0000088	1.000	-.27177	.0000024
	NESSUS	235.772	+.0000159	-1.8060	+.49084	-.000004321

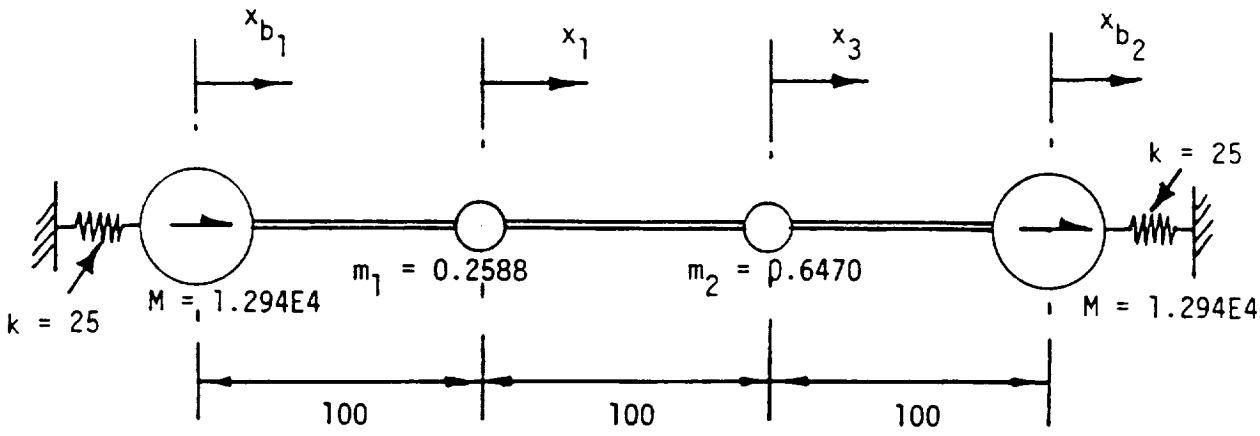

Figure 8.20 Simple Verification Problem 2 Using Constrained Mass

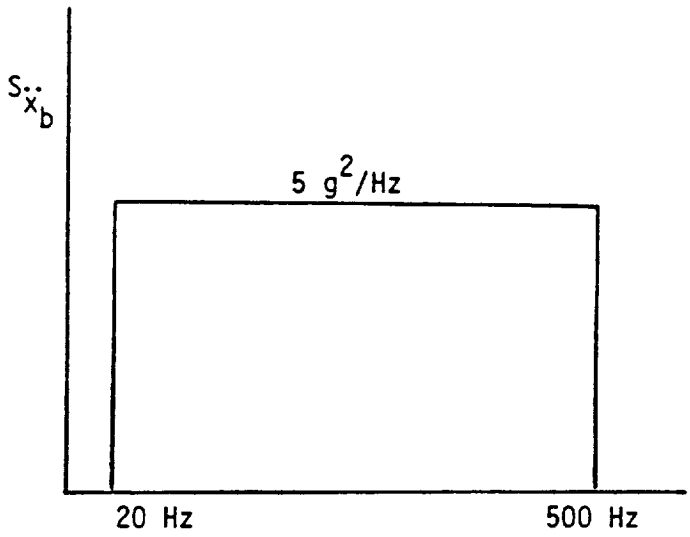

Figure 8.21 Base Accelerations Applied to Simple Verification Problem 2

Table 8.13

RMS Displacement Responses for
Simple Verification Problem 2

PROGRAM	BASE	X_1	X_2	
STARDYNE	.14131	.12730	.14395	uncorrelated
NESSUS	.14130	.12730	.14396	
STARDYNE	.14127	.17221	.19592	Fully correlated
NESSUS	.14126	.17221	.19595	

Table 8.14

Exact Value of Prescribed RMS Base Motions for Simple Verification Problem 2

RMS $\ddot{X}_b$ inch/Sec2	RMS $\dot{X}_b$ inch/sec	RMS X_b inch	NESSUS X_b
48.9898	30.1277	.14126	.14130

The RMS stress resultants in the members are presented in Table 8.15. It is worth mentioning at this point that NESSUS stress resultants are computed and stored on a node base rather than element based computation performed in STARDYNE. Therefore, duplicate nodes were defined in NESSUS so that appropriate comparisons can be made. Once again, for this example, NESSUS results were observed to be reasonably close to that of STARDYNE results.

8.6 Introduction to High Pressure Oxidizer Duct Verification Problem

This study concentrates on conventional random vibration analysis as well as uncertain random vibration analysis of high pressure ducts, typical of the ducts used in Space Propulsion Systems. The dynamic loads in a high pressure ducting system typically include:

1) Random base excitation loads with uncertain power
2) Harmonic pump generated base excitation loads with uncertain amplitude and frequency
3) Internal random pressure loading of uncertain correlation characteristics and power.

The major variations in system parameters can include:

1) Damping variations
2) Thickness variations
3) Variation in stress concentration factors due to variable weld offsets.

The initial verification efforts concentrated on verification of NESSUS results and capabilities exercised on typical line element duct model. The results represented here are restricted to conventional random vibration analysis. Continuing efforts in FY'89 addresses the uncertain random vibration and probabilistic harmonic excitation features available in NESSUS.

8.7 Random Vibration Analysis of High Pressure Oxidizer Duct Using NESSUS

A NESSUS model of a high pressure oxidizer turbopump discharge duct was generated. The model shown in Figure 8.22 was generated using two noded linear isoparametric beam element (Type 98) available in NESSUS. Figure 8.23 is another visual representation of the same duct model showing the duct radius, flange radius, and the valve attachment sizes. The statistics of the finite element model is shown in Table 8.16. Finite element models of high pressure ducts typically contain the following features:

1) Pipe elements with provisions for internal fluid mass.
2) Elbow curved pipe elements with provisions for approximating increased flexibility either through ASME flexibility factors or other ways to account for ovalization. Effects of high internal pressure are also included in the above calculations.

Table 8.15

RMS Stress Responses for Simple Verification Problem 2

	STATIONARY RMS STRESSES (P/A)			
	Member 1	Member 2	Member 3	
STARDYNE	22627	19061	27133	Uncorrelated
NESSUS	22630	19061	27133	
STARDYNE	20131	10240	30290	Fully Correlated
NESSUS	20738	10244	30302	

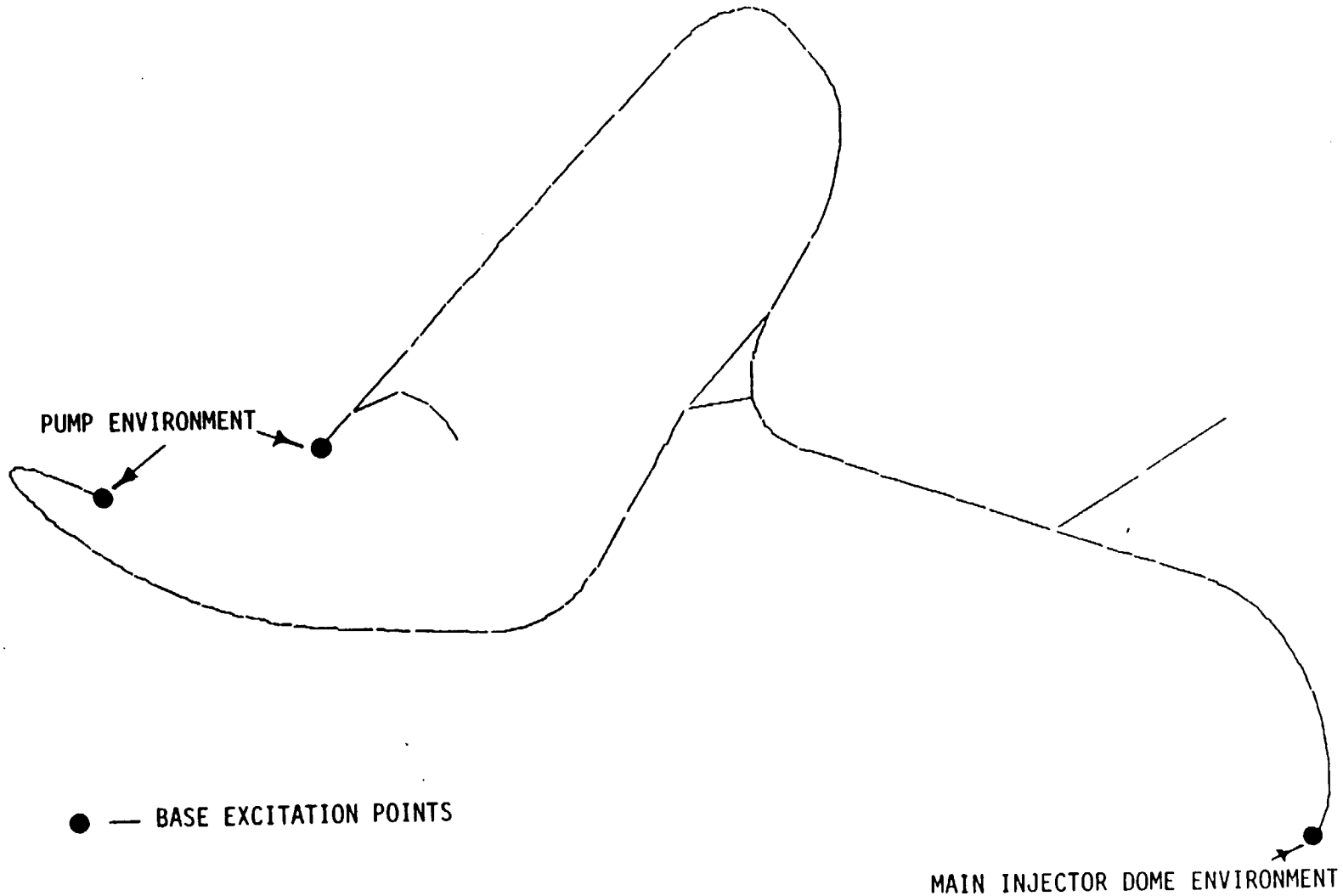

Figure 8.22 Finite Element Model of the High Pressure Duct Using Line Elements (Type 98)

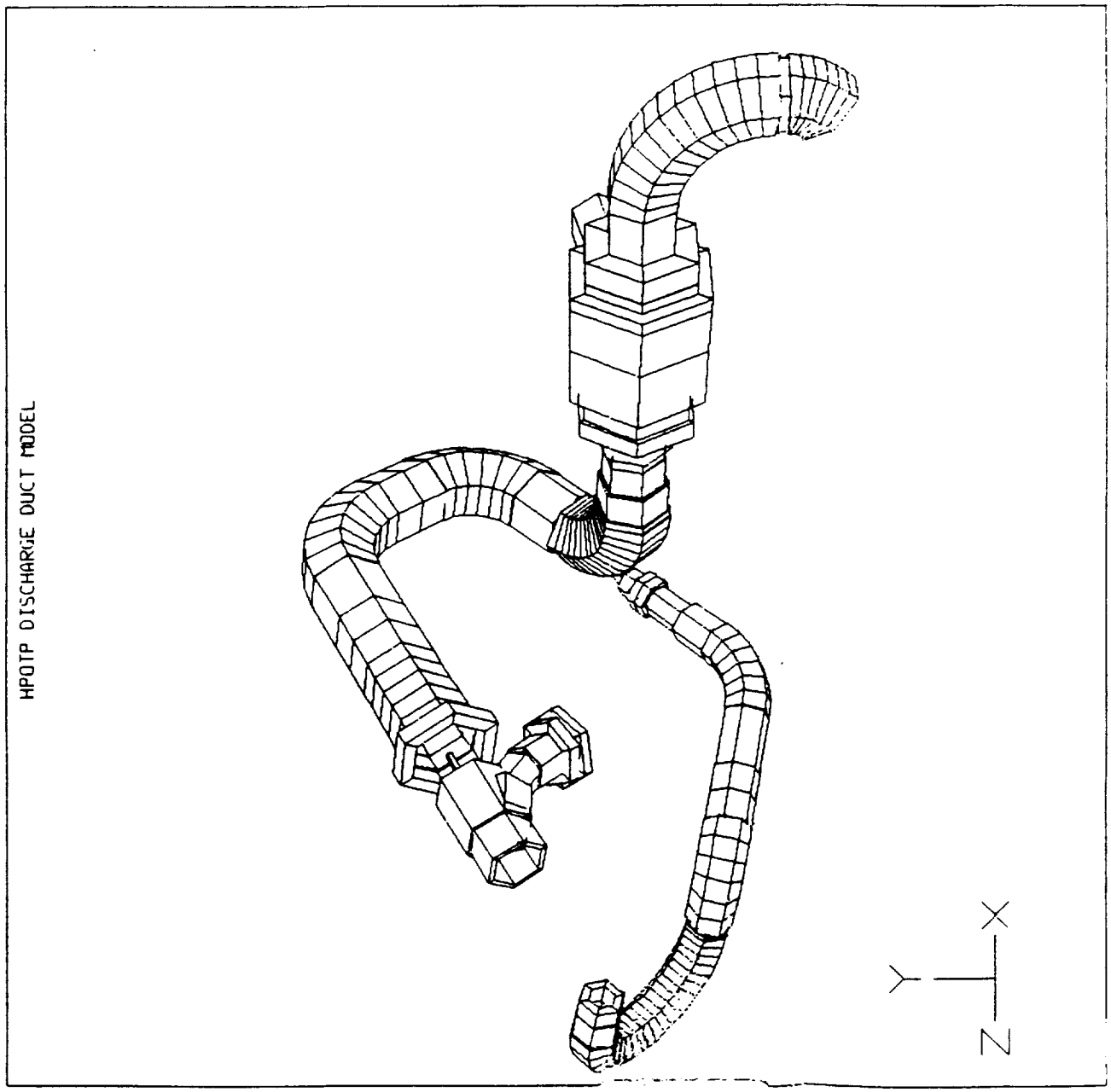

Table 8.16

Model Statistics for the Full Duct Verification Model

Item	Description	Value
1	Number of nodes	280
2	Number of elements	188
3	Number of duplicate modes	40
4	Number of point masses	60
5	Number of boundary D.O.F.	9
6	Number of D.O.F.	1128
7	Maximum profile height	29
8	Average profile height	13
9	Number of Spectral cases	6
10	Number of words needed in blank common	1214583

Table 8.17

Comparison of Natural Frequencies Obtained Using STARDYNE and NESSUS for the High Pressure DUCT

MODE	NESSUS HZ		STARDYNE HZ
	Constrained Big Mass Approach	Free-Free Model With Shift Option **	
1.	.050*	.01639*	.050*
2.	.060	.0524*	.061
3.	.071*	.0612*	.071*
4.	.074	.1888	.074
5.	.081	.1907	.082
6.	.087*	.3269	.087*
7.	.097	.40211	.097
8.	.107	.6052	.107
9.	.119	.8525	.119
10.	61.66	61.66	61.53
11.	97.96	97.96	95.94
12.	134.06	134.07	132.1
13.	140.21	140.22	140.1
14.	175.35	175.35	175.6
15.	197.32	197.32	199.9
16.	251.71	251.72	246.6
17.	275.36	275.37	273.2
18.	299.50	299.50	288.7
19.	380.15	380.15	375.3
20.	422.99	422.99	419.2
21.	516.41	516.42	496.1
22.	555.71	555.72	538.5
23.	575.21	575.21	592.6
24.	635.26	635.27	636.1
25.	694.71	694.72	674.6
26.	768.29	768.29	795.6

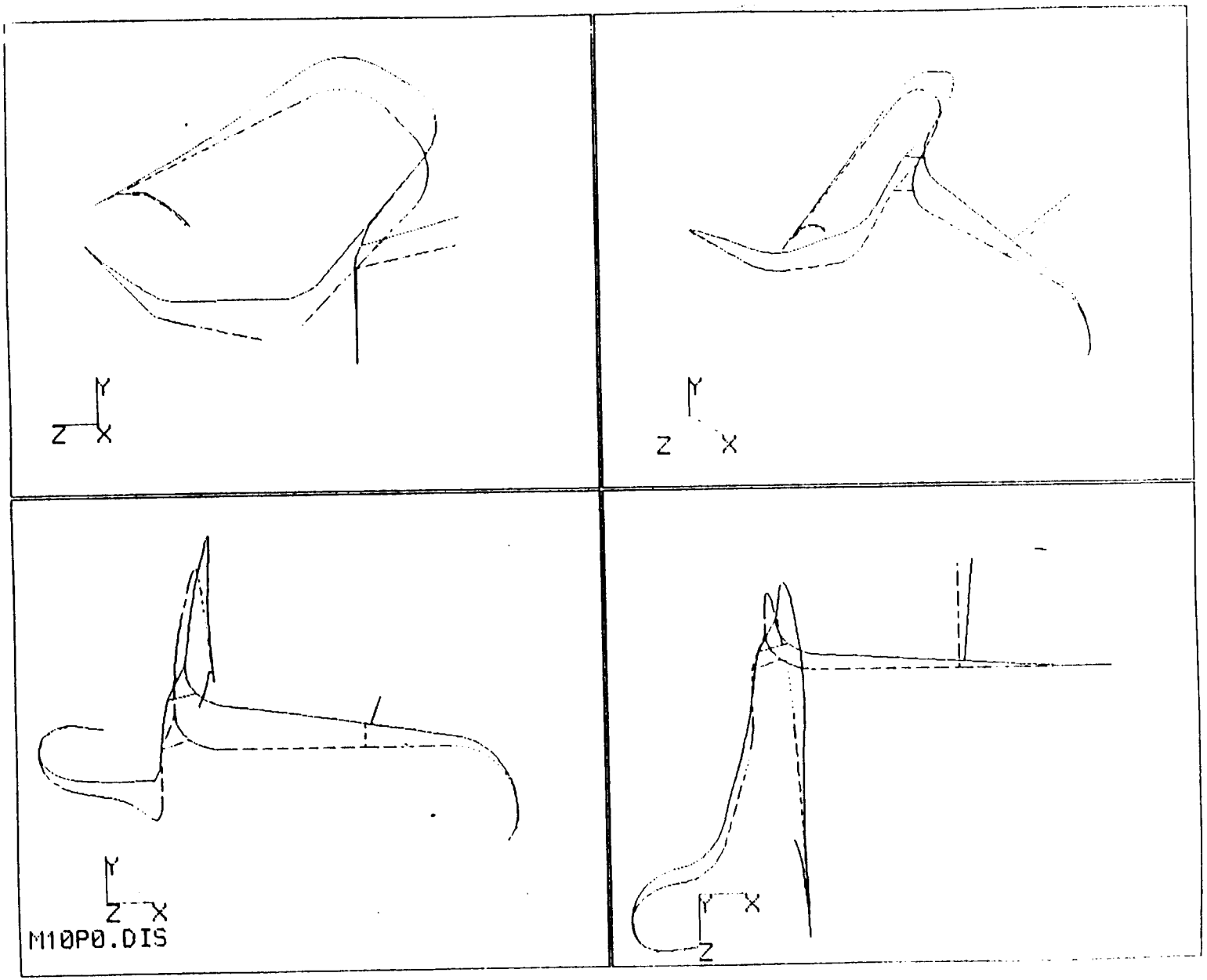

Figure 8.24 First Mode, Frequency 61 Hz

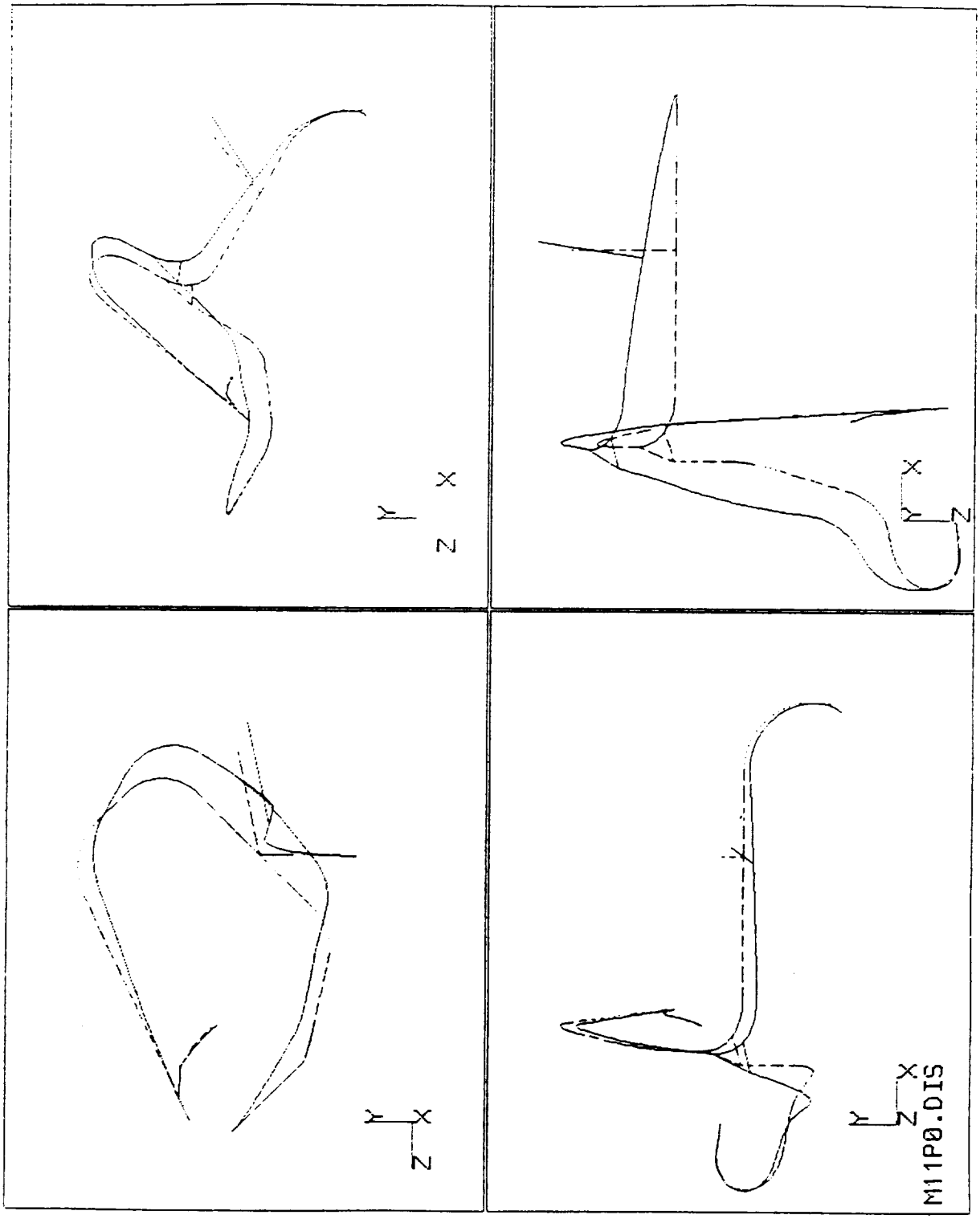

Figure 8.25 Second Mode, Frequency 98 Hz

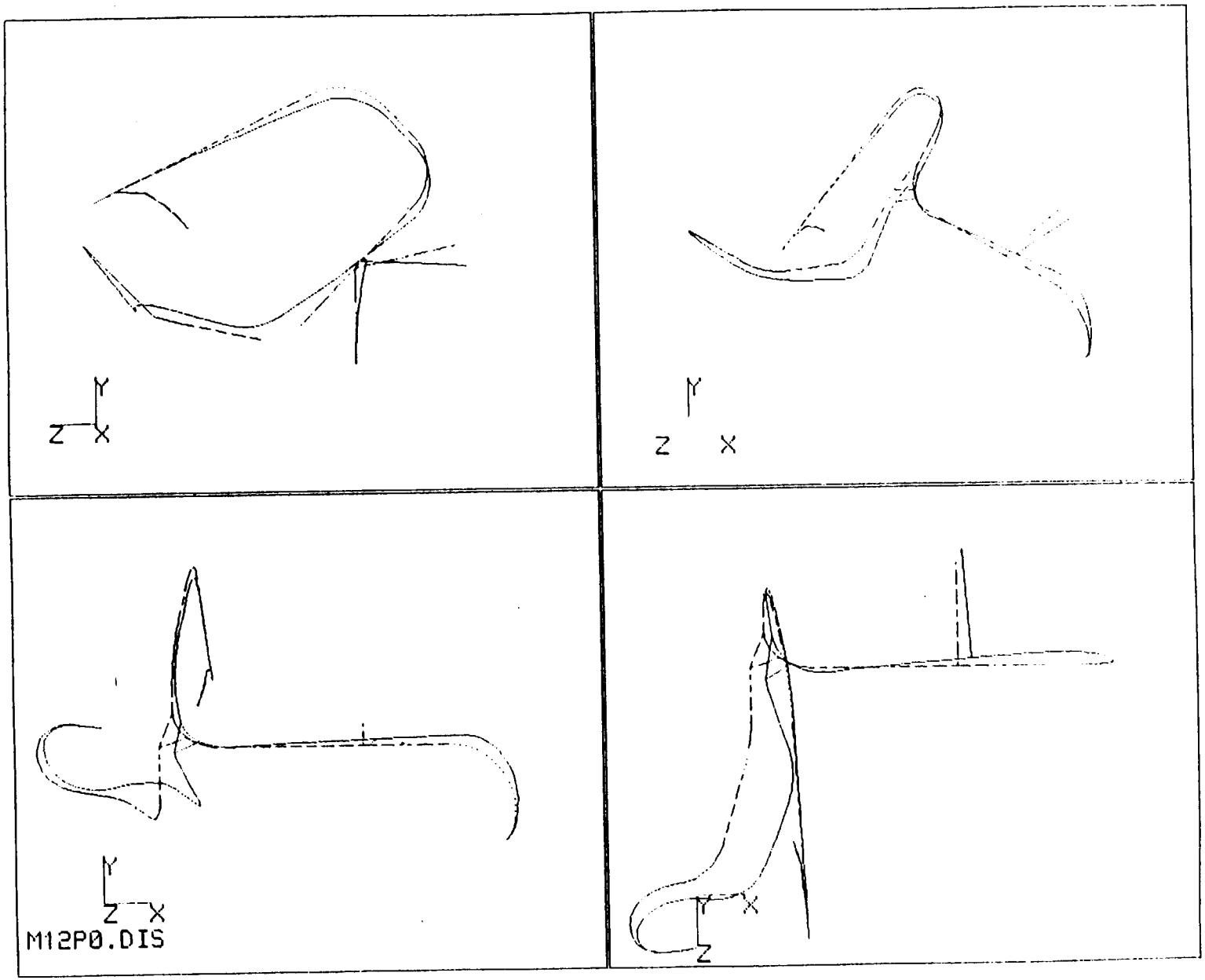

Figure 8.26 Third Mode, Frequency 134 Hz

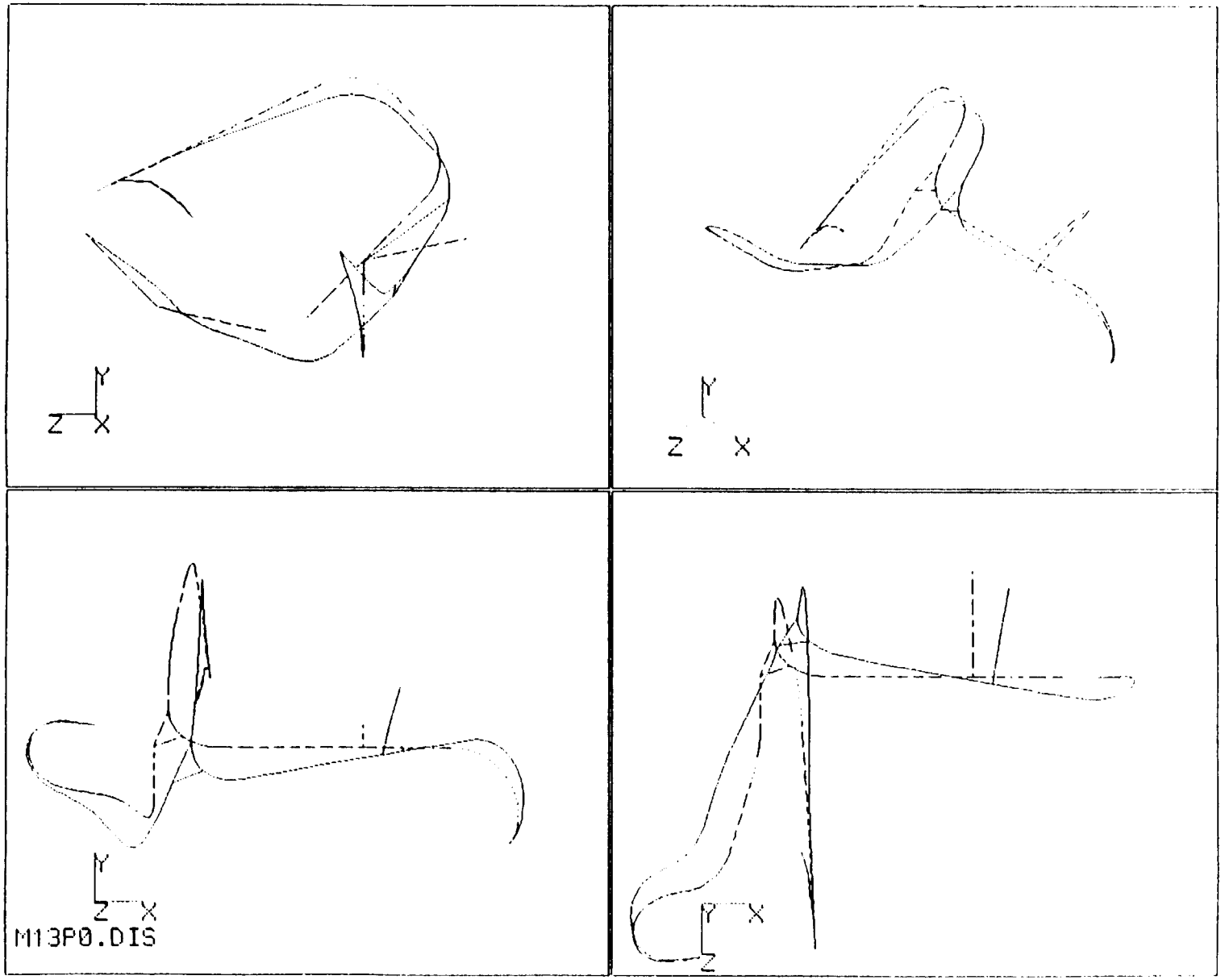

Figure 8.27 Fourth Mode, Frequency 140 Hz

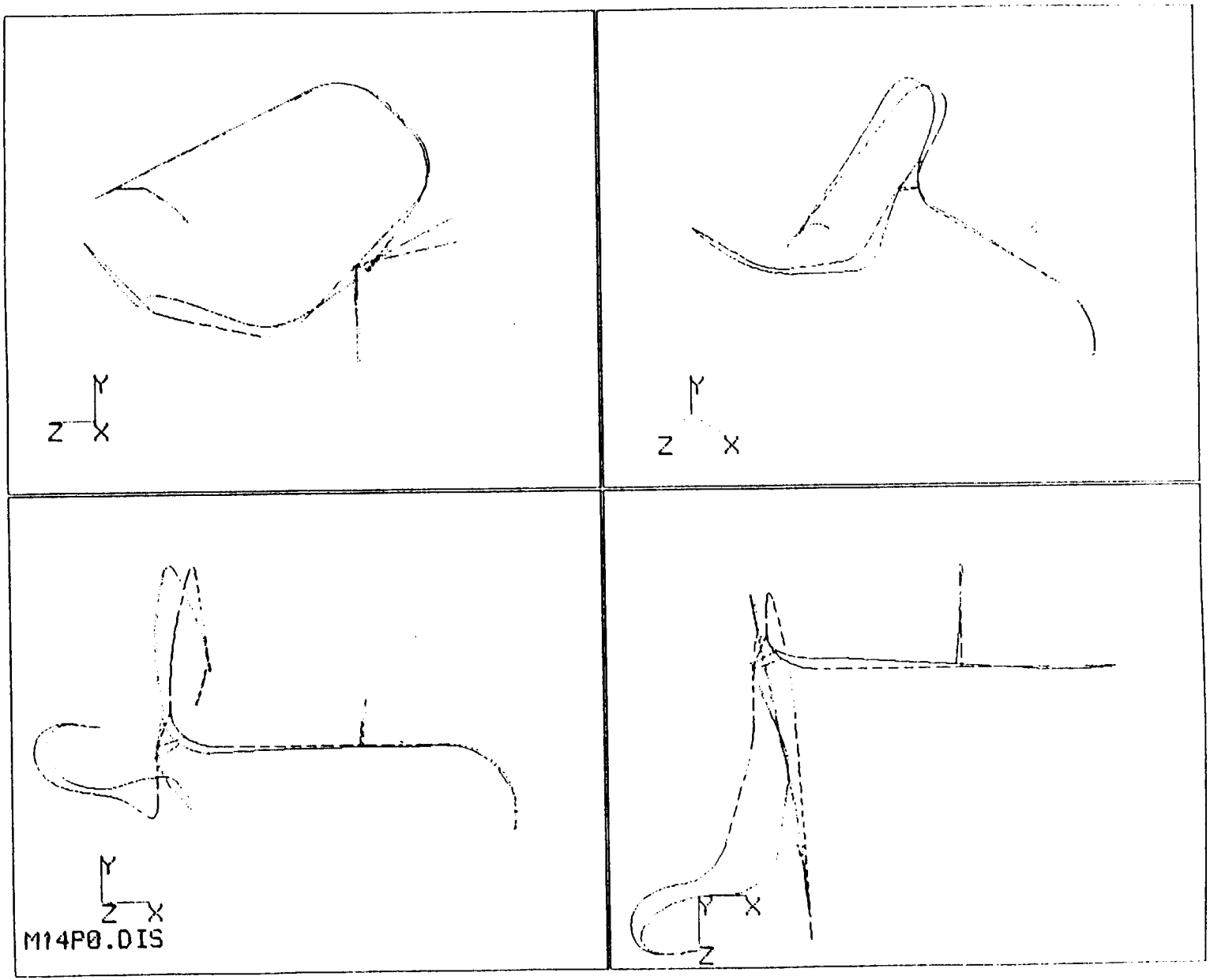

Figure 8.28 Fifth Mode, Frequency 175 Hz

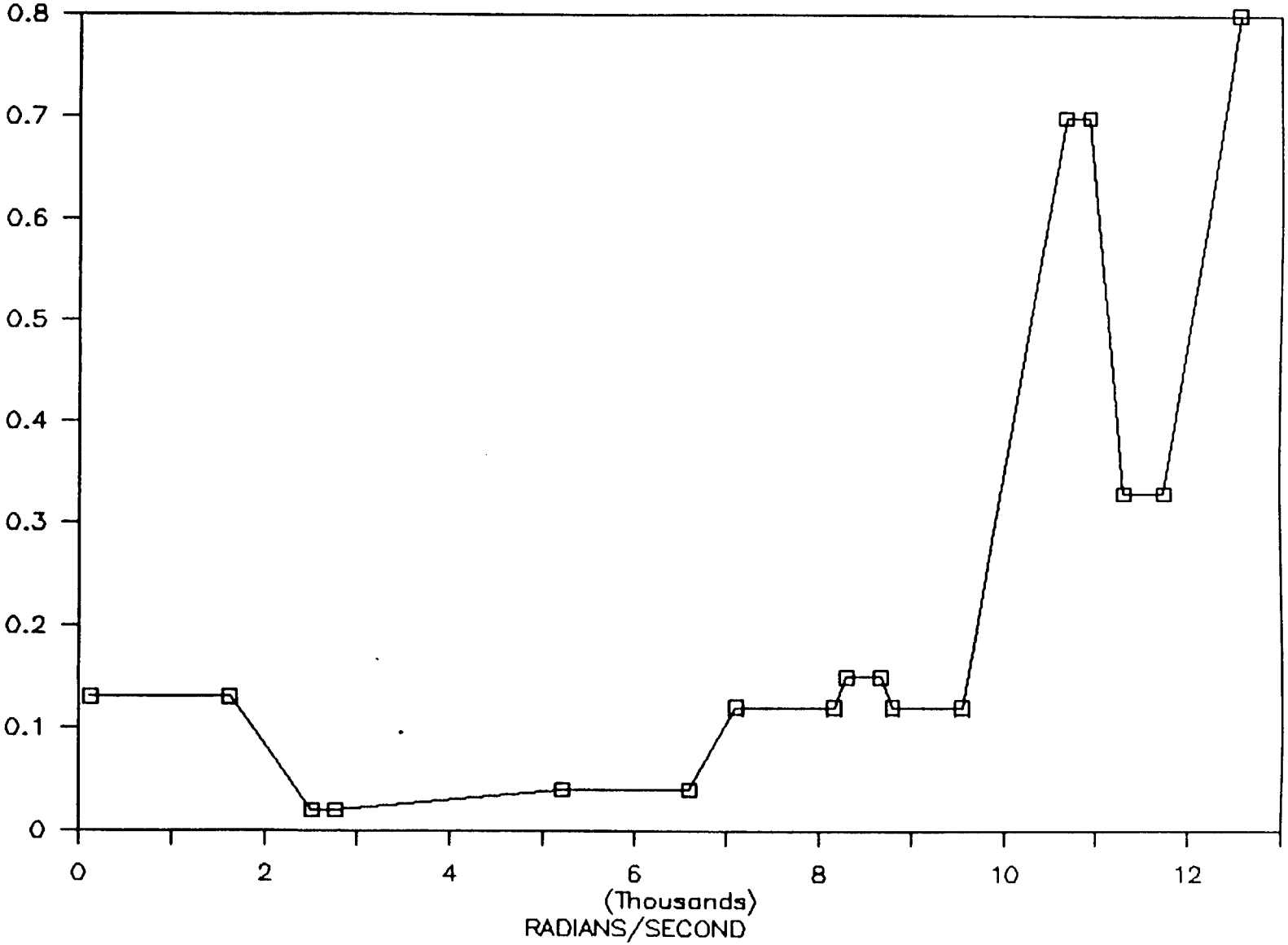

Figure 8.29 Pump X-Axis Vibration Environment

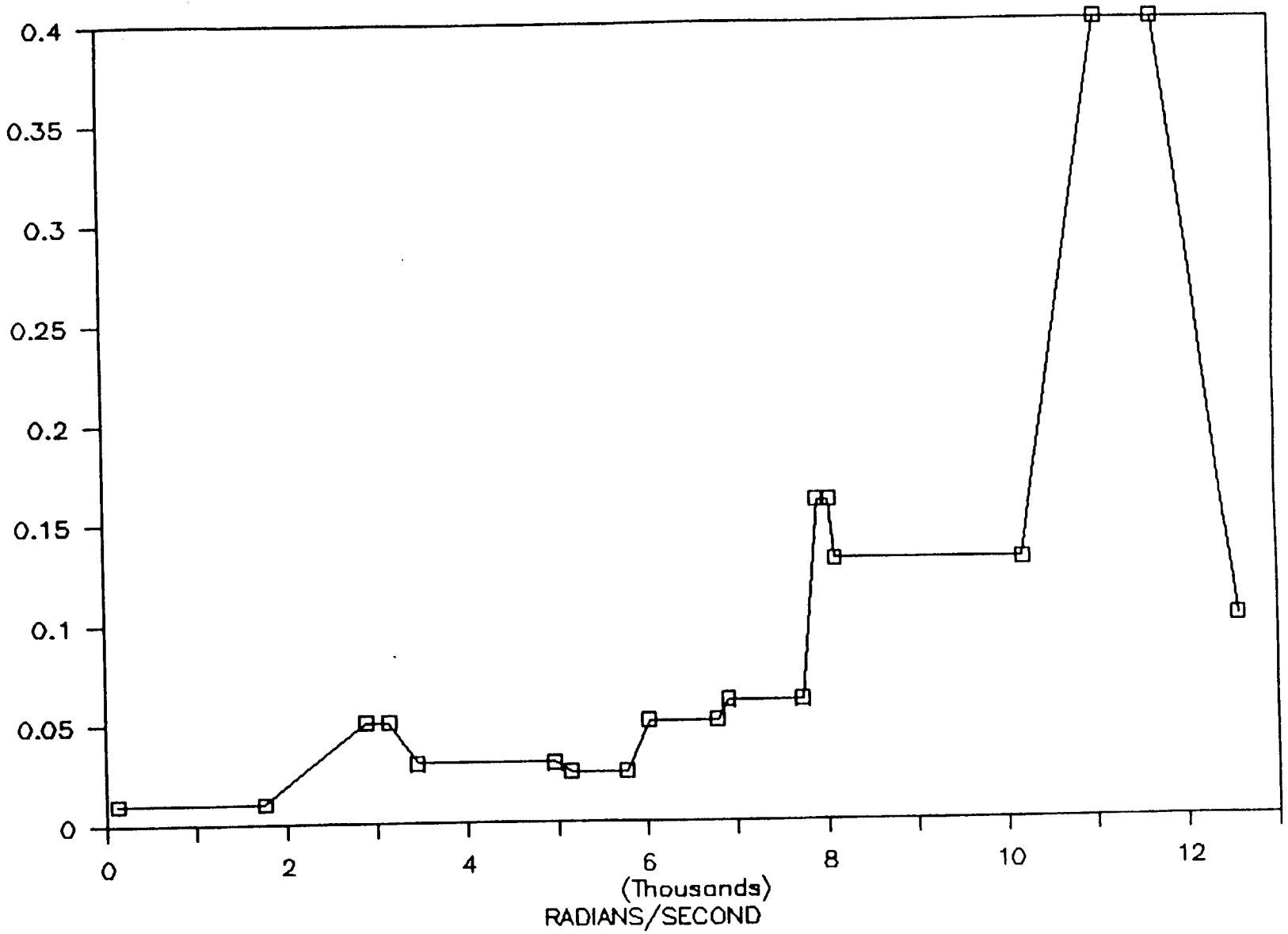

Figure 8.30 Pump Y and Z Axis Vibration Environment

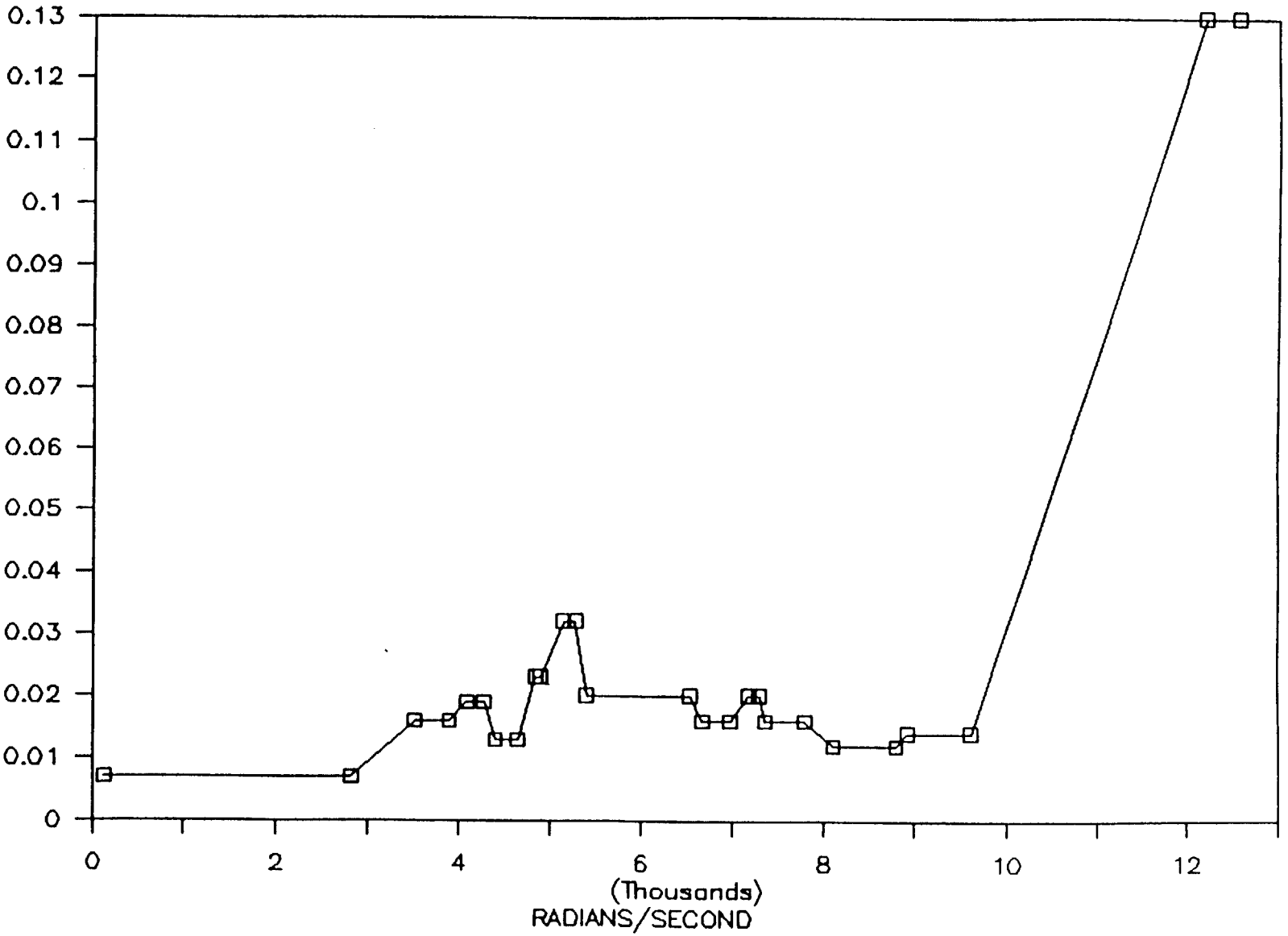

Figure 8.31 Main Injector X-Axis Environment

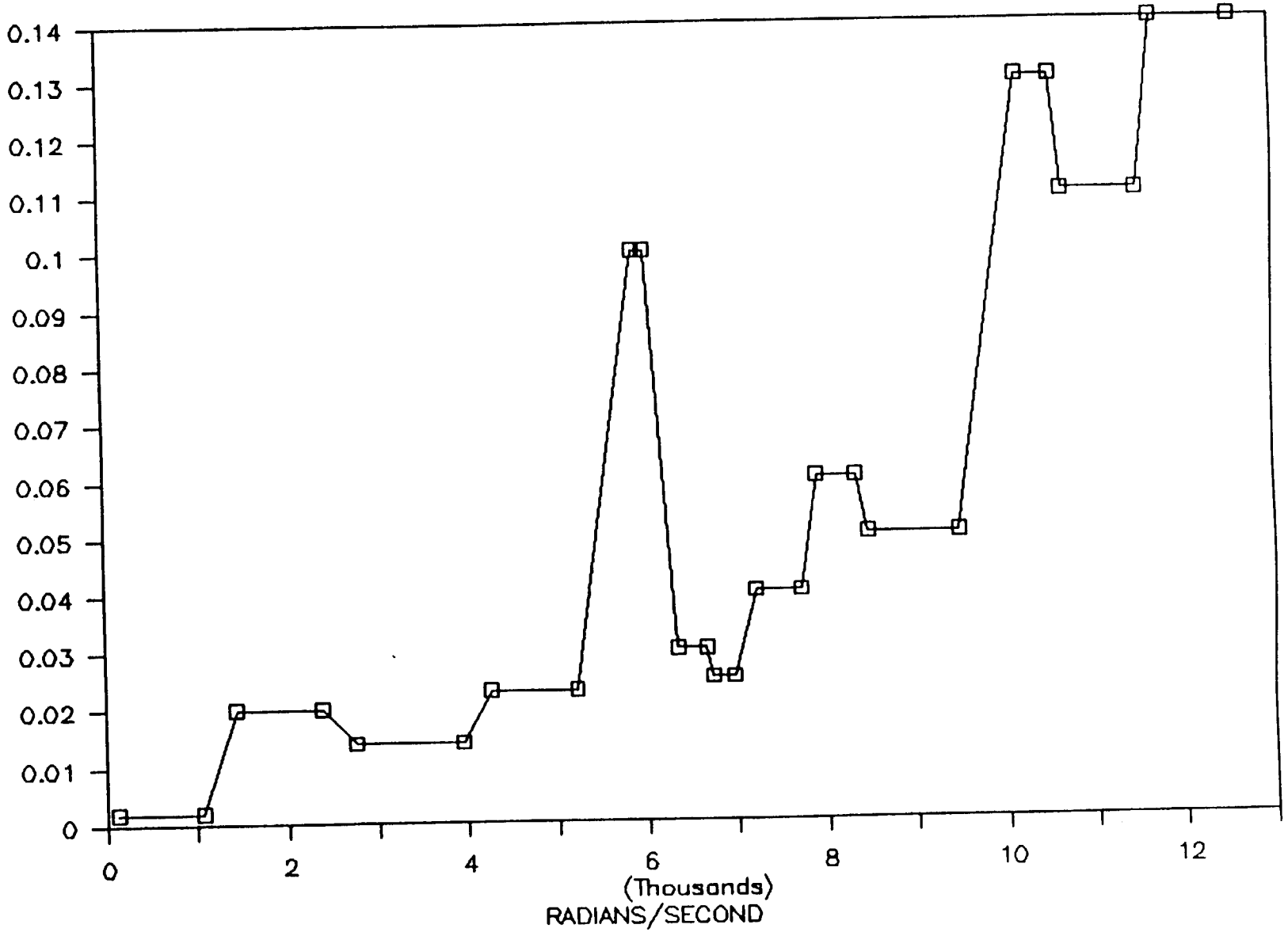

Figure 8.32 Main Injector Y-Axis Environment

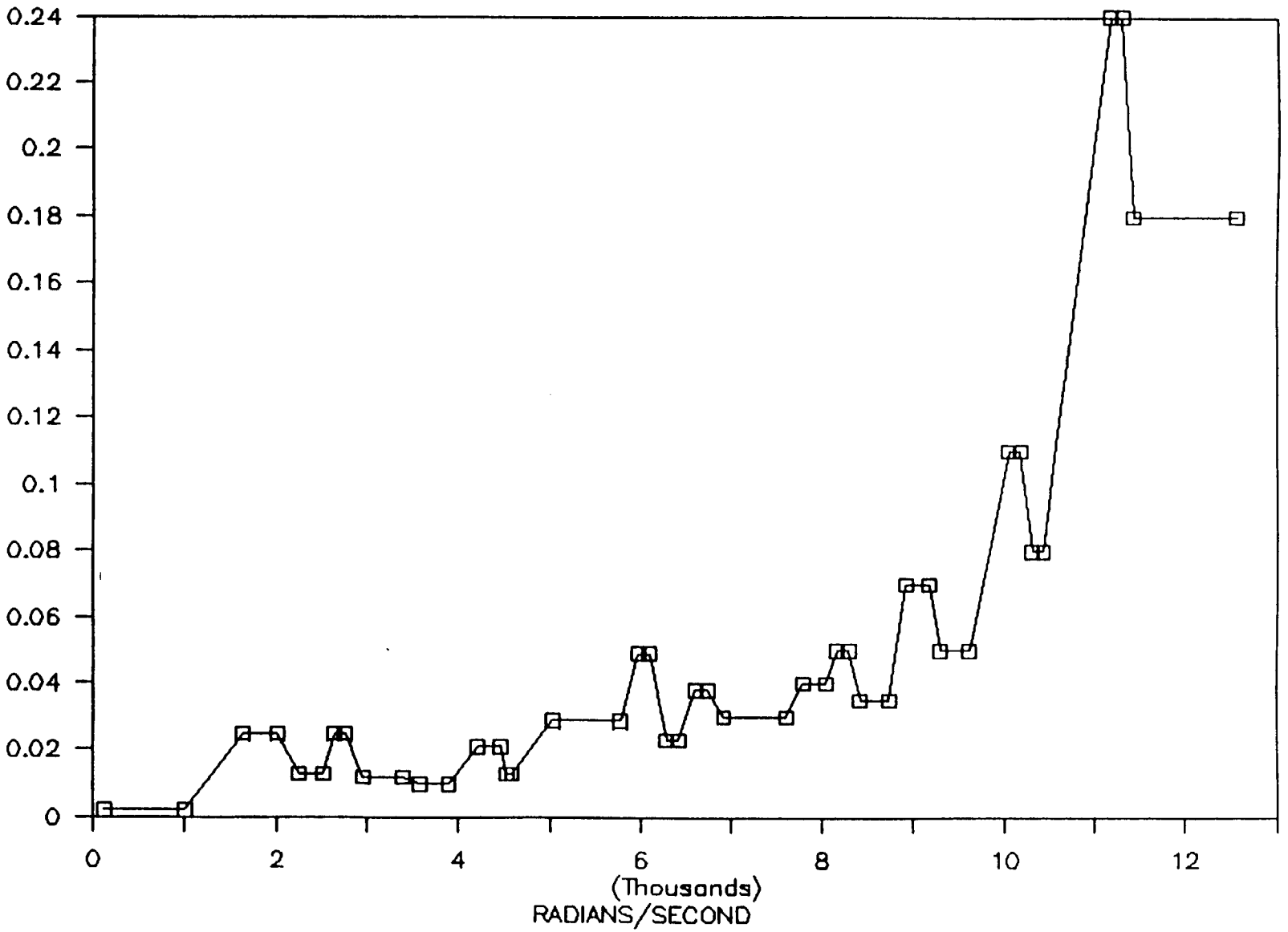

Figure 8.33 Main Injector Z-Axis Environment

Six spectral cases were run using five different PSD's shown in Figures 8.29 through Figure 8.33. These six base acceleration spectral cases are identified in Figure 8.34. The RMS displacements at a typical node 27 due to power spectrum case 6 is compared in Table 8.18 between NESSUS and STARDYNE. The results are in good agreement. The result of the various frequency band discretization and gauss quadrature used is also reported in the same Table 8.17 using NESSUS. This was done to find the optimum numerical integration scheme. The results indicate there is further room to coarsen up the frequency band discretization and still obtain acceptable results. While the random response calculation part of the code itself performed satisfactorily when compared to STARDYNE, the automatic frequency band discretization part of NESSUS code appears inefficient. It took more than an order of magnitude more CPU time (>50) to calculate the frequency band discretization values for numerical integration than it took to calculate the actual response. Thus, improvement to the automatic frequency band discretization scheme is necessary and will be accomplished in FY'89. As an alternate, the user can completely specify the frequency discretization scheme and override the automatic algorithm. The advantage of the automatic algorithm is that the user does not have to know the location of deterministic as well as perturbed structure resonance frequencies to obtain an accurate response calculation.

Next, the stress resultant values between NESSUS and STARDYNE are compared. It must be noted that NESSUS does not calculate stresses for beam elements. In its current state of development, it only outputs and stores only stress resultants (beam end moments, shear forces, and axial forces) in the perturbation database. It must also be mentioned that for shell elements, both stress resultants and stresses in layers are stored in the perturbation database. Further experience with NESSUS TYPE 98 two noded isoparametric beam has shown that appropriate choice of Loubniac parameter used to calculate nodal stresses is highly important. Use of trapezoidal rule for nodal stress recovery is imperative to obtain accurate nodal stress resultants. Use of other options can result in very inaccurate stress resultants for general stress gradients.

R.M.S. stress resultants for a typical node are compared in Table 8.19. The axial and torsional stress resultants are directly comparable between the two programs. However, the shear and end moments are affected by the orientation of the transverse local beam axis. While the orientation of local axes are close between the two models, they are nevertheless, slightly different and cannot directly be compared. In general, STARDYNE stress resultant results for the same node are lower. This can be explained as the cubic displacement function finite element used in STARDYNE is more flexible than the linear isoparametric beam element used in NESSUS. Further comparisons between NESSUS and STARDYNE stress resultant results are made in Table 8.20. In this case, the magnitude of the maximum R.M.S. stress resultant and its location are compared between the two codes for all the six spectral cases. The results are in very good agreement. In some instance in Table 8.19, the maximum stress resultants for NESSUS model occur at a node within the elbow approximated using linear

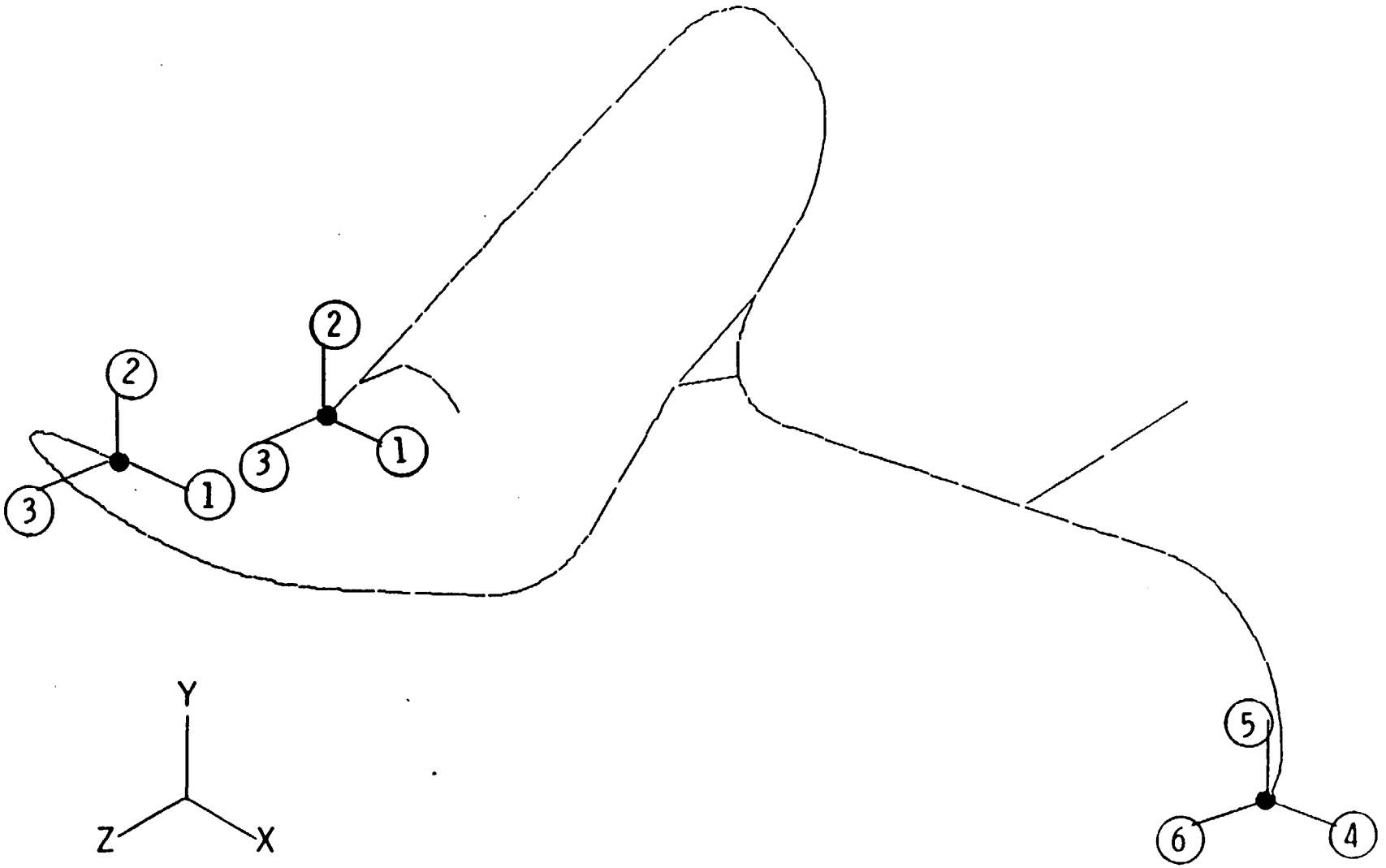

Figure 8.34 High Pressure Duct Six Spectral Random Base Excitation Cases Identified

Table 8.18

Comparison of RMS Displacement Responses
for Power Spectrum 6 for Main Duct Mode 27

	CASE NO.	MEAN SQUARE DISPLACEMENTS AT MODE 27						CP TIME SECS
		X	Y	Z	ROT X	ROT Y	ROT Z	
NESSUS	1	5.662E-4	7.371E-4	1.3176E-3	8.4740E-5	9.071E-5	5.167E-5	520*
	2	5.662E-4	7.371E-4	1.3176E-3	8.4740E-5	9.071E-5	5.167E-5	342*
	3	5.662E-4	7.371E-4	1.3176E-3	8.4740E-5	9.071E-5	5.167E-5	236*
	4	5.662E-4	7.371E-4	1.3176E-3	8.4740E-5	9.071E-5	5.167E-5	207*
STARDYNE		5.3765E-4	7.2249E-4	1.2942E-3	8.9958E-5	8.3006E-5	4.3293E-5	30**

Case 1: 40HZ Macro interval, 10 half band segments, 5 gauss point integration scheme.

Case 2: 80HZ Macro interval, 5 half band segments, 5 gauss point integration scheme.

Case 3: 80HZ Macro interval, 4 half band segments, 3 gauss point integration scheme.

Case 4: 80HZ Macro interval, 3 half band segments, 3 gauss point integration scheme.

* VAX 11/750
** CDC 990

Table 8.19

Comparison of RMS Stress Resultant Responses for Power Spectrum 6 for Main Duct Node 20

PROGRAM	CASE NO.	R.M.S. STRESS RESULTANT (LBS OR INCH LBS)					
		SHEAR X	SHEAR Y	AXIAL Z	MOMENT X	MOMENT Y	TORSION
NESSUS	1	56	54	76	215	182	203
	2	56	54	76	215	182	203
STARDYNE		40*	54*	71	178*	183*	161

Case 1: 40 Hz Macro interval, 10 half band segments, 5 point gauss integration scheme 2325 function evaluations.

Case 2: 80 Hz Macro interval, 3 half band segments, 3 point gauss integration scheme 465 function evaluations.

* Local beam coordinates differ between NESSUS and STARDYNE.

Table 8.20

Comparison of Maximum RMS Stress Resultant for Axial and Torsion Between NESSUS and STARDYNE

Spectral Case No.	Program	Axial		Torsion	
		Value	Node No.	Value	Node No.
1	NESSUS	219	276*	1156	84*
	STARDYNE	198 (204)	30	1048 (1062)	28
2	NESSUS	249	120*	712	93*
	STARDYNE	242 (235)	49	697 (697)	27
3	NESSUS	179	276*	1398	136
	STARDYNE	168 (172)	46	1409	136
4	NESSUS	583	109*	887	83*
	STARDYNE	605 (573)	44	781 (794)	28
5	NESSUS	246	46	570	30
	STARDYNE	224	46	496	30
6	NESSUS	81	63	927	136
	STARDYNE	71	15	795	136

* Occurs Within an Elbow, no Comparable Node in STARDYNE.
Values in paranthesis are NESSUS values corresponding to that node.

elements. For such cases, there was no corresponding node in STARDYNE model. The physical location of the maximum stressed nodes between the two codes can be seen in Figure 8.35.

To obtain an overall general comparison of the results between the two codes, fringe plots for torsional and axial stress resultants are shown in Figures 8.36 through 8.43 for power spectral case 1 and power spectral case 6. There is overall agreement between NESSUS and STARDYNE results. The NESSUS result for axial and torsional stress resultants for spectral case 2 through 5 are also shown in Figures 8.44 through Figure 8.51.

In summary, NESSUS random vibration analysis capabilities have been tested and verified using high pressure duct verification model. The results are in agreement with STARDYNE results for both R.M.S. displacements and R.M.S. stress resultants. Where analytical results exist for a simple case, such as documented in Section 8.5, the NESSUS results agree with analytical results. The nodal velocities and accelerations were not compared and verified as they are neither output nor stored in the perturbation data base.

The probabilistic structural analysis of duct verification efforts will continue in FY'89. The verification efforts will focus on a few critical system parameters as random variables such as damping and more emphasis will be placed on the treatment of load variations. The load random variables considered will include harmonic load amplitude and frequency variation and variations in the power level of PSD (area under PSD). The random variables that affect the shape of the acceleration P.S.D. diagrams are less well characterized. The output from probabilistic harmonic analysis and uncertain random vibration analysis would consist of characterization of R.M.S. stress resultants (cumulative distribution function) and characterization of stress velocity (cumulative distribution function). With the above two quantities expected value of fatigue life and its coefficient of variation can be calculated.

8.8 Enhancements to Post-Processing Interface to NESSUS

Additional enhancements to post processing interface between NESSUS and PATRAN was completed and is now being tested. The enhancements include translation of new items such as modal stresses and modal strains to PATRAN neutral results file. Additional capabilities were further added to translate spectral data to PATRAN neutral results file. The data includes displacements, stresses and strains. Additional options for obtaining combinations of spectral cases were added to the code. Code has built in logic to vector sum the real and imaginary parts of harmonic cases and then add to the mean square values for random excitation cases with user defined factors for each case to obtain R.S.S. values. The graphical presentation of the results reported in the verification studies were post-processed in PATRAN using this interface.

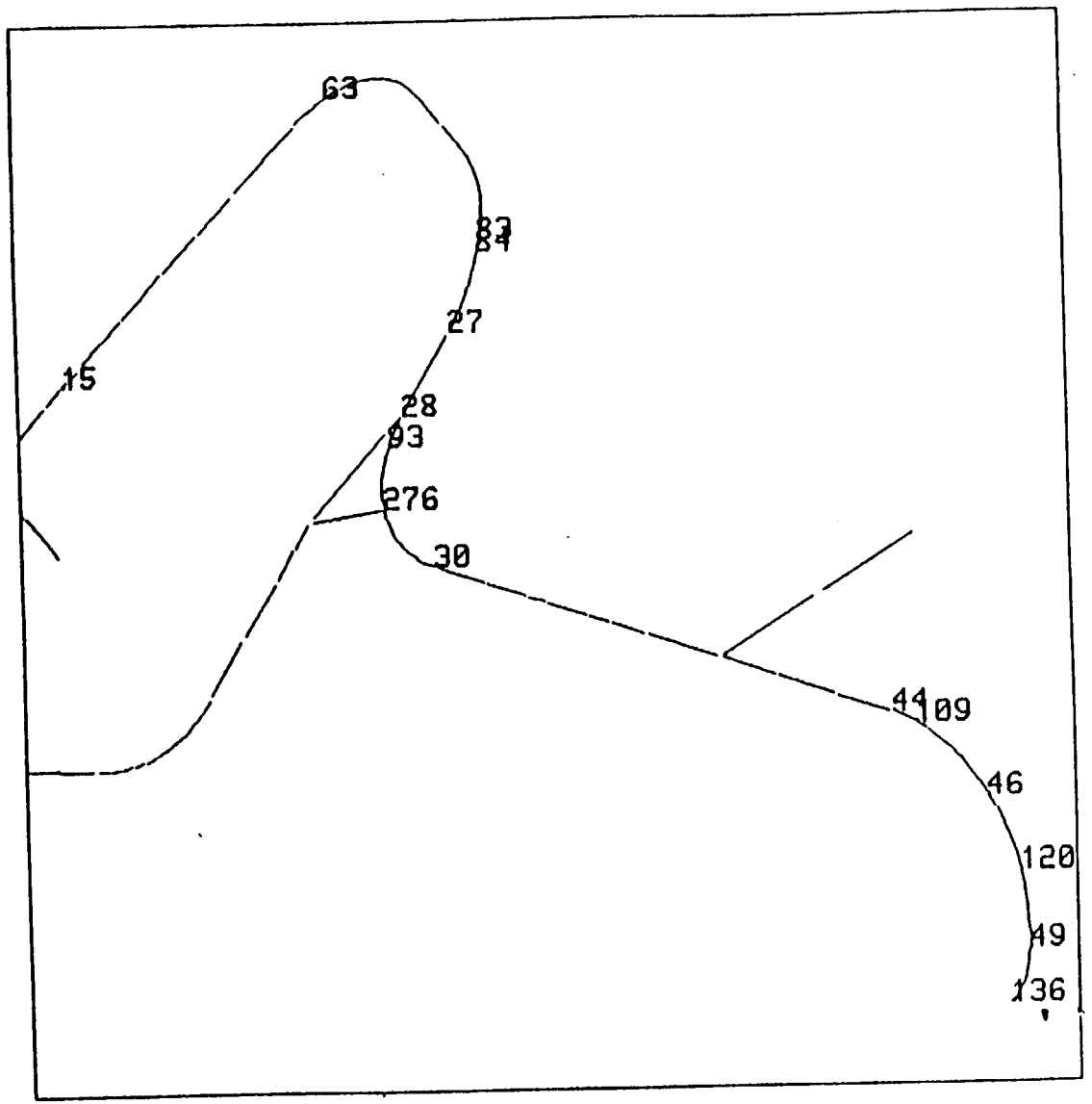

Figure 8.35 Identification & Critical Nodes in the High Pressure Duct for the Six Spectral Cases (Axial and Torsion)

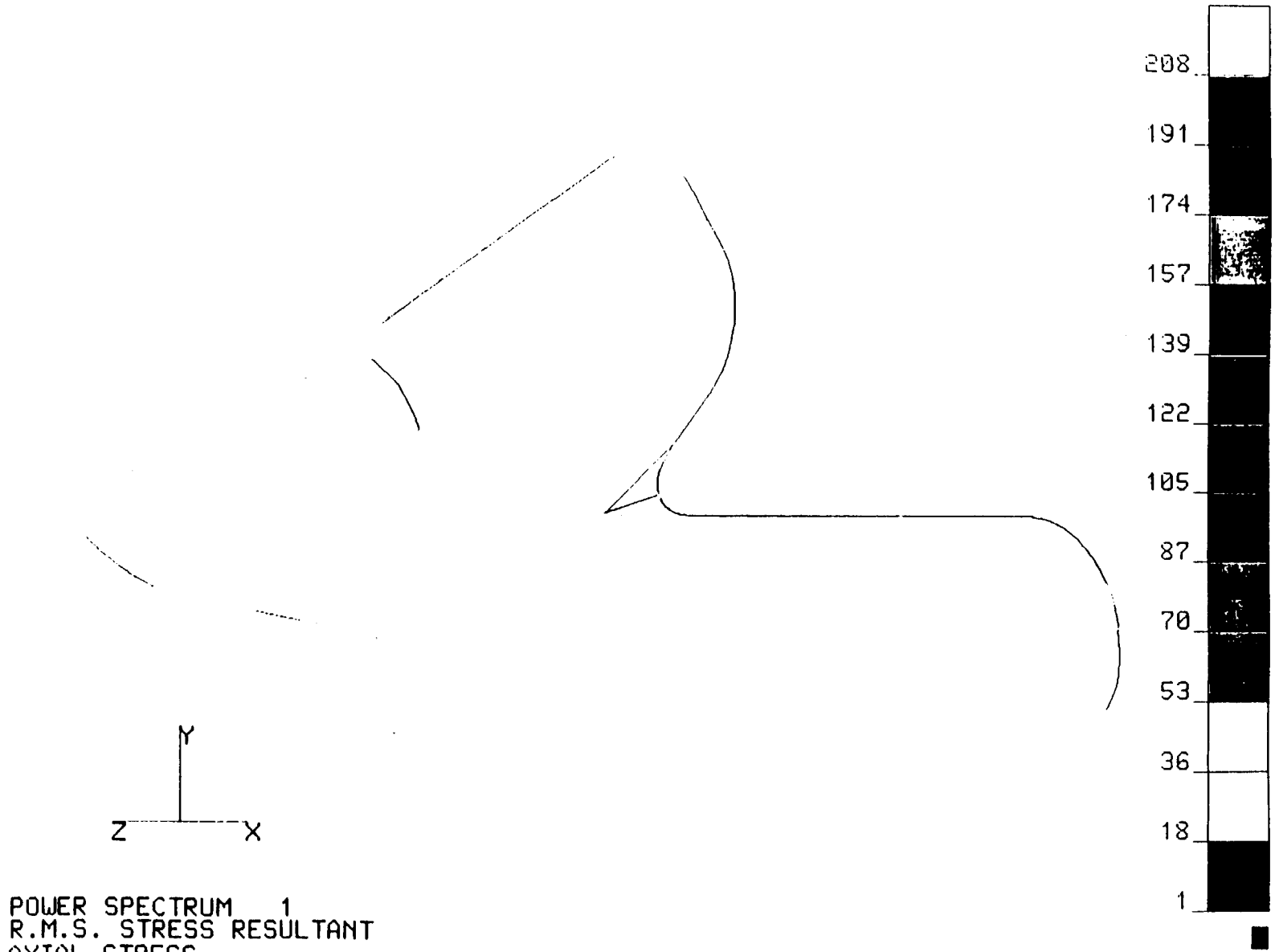

Figure 8.36 NESSUS Axial Stress Results Due to Power Spectrum 1

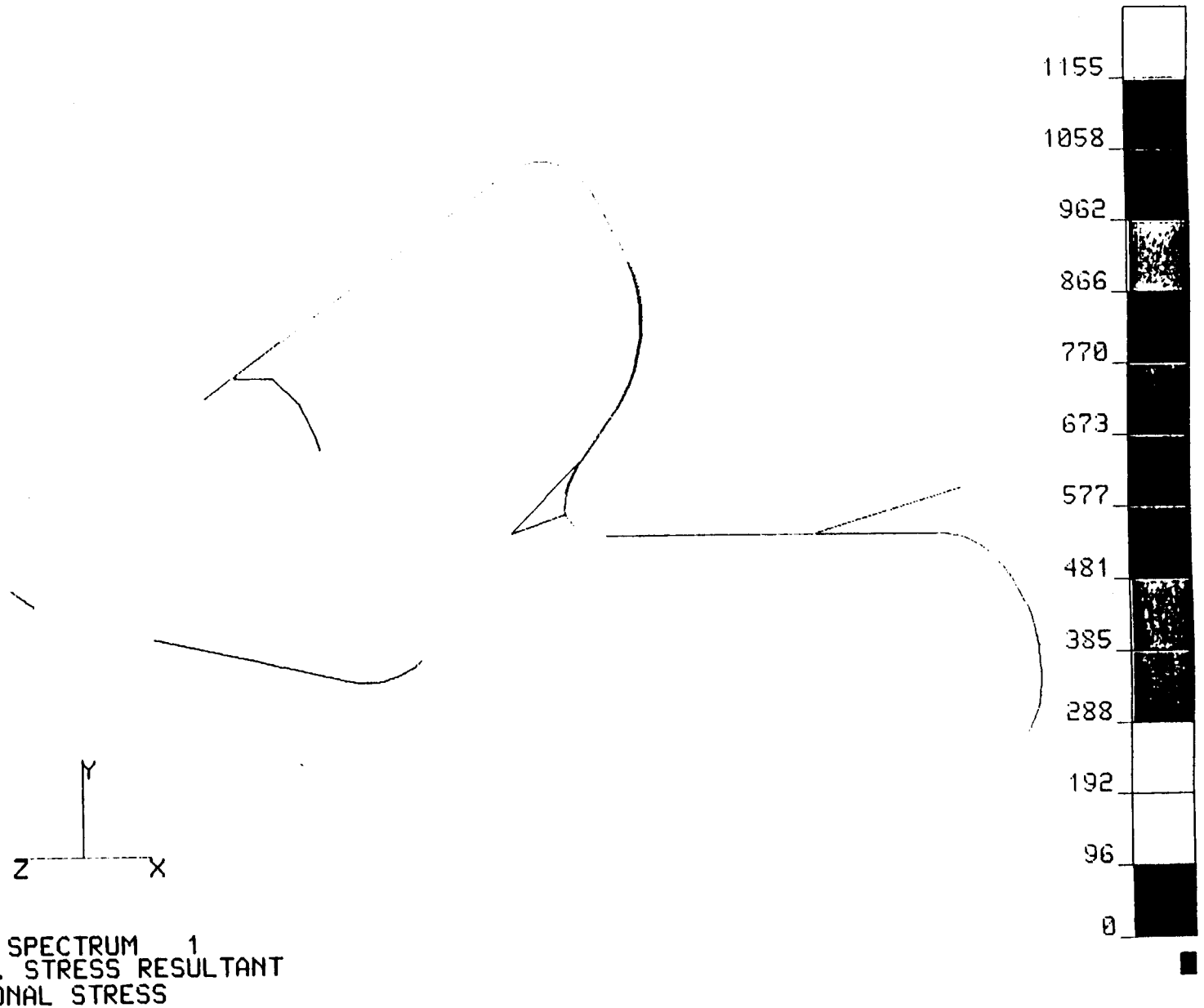

Figure 8.37 NESSUS Torsional Stress Results Due to Power Spectrum 1

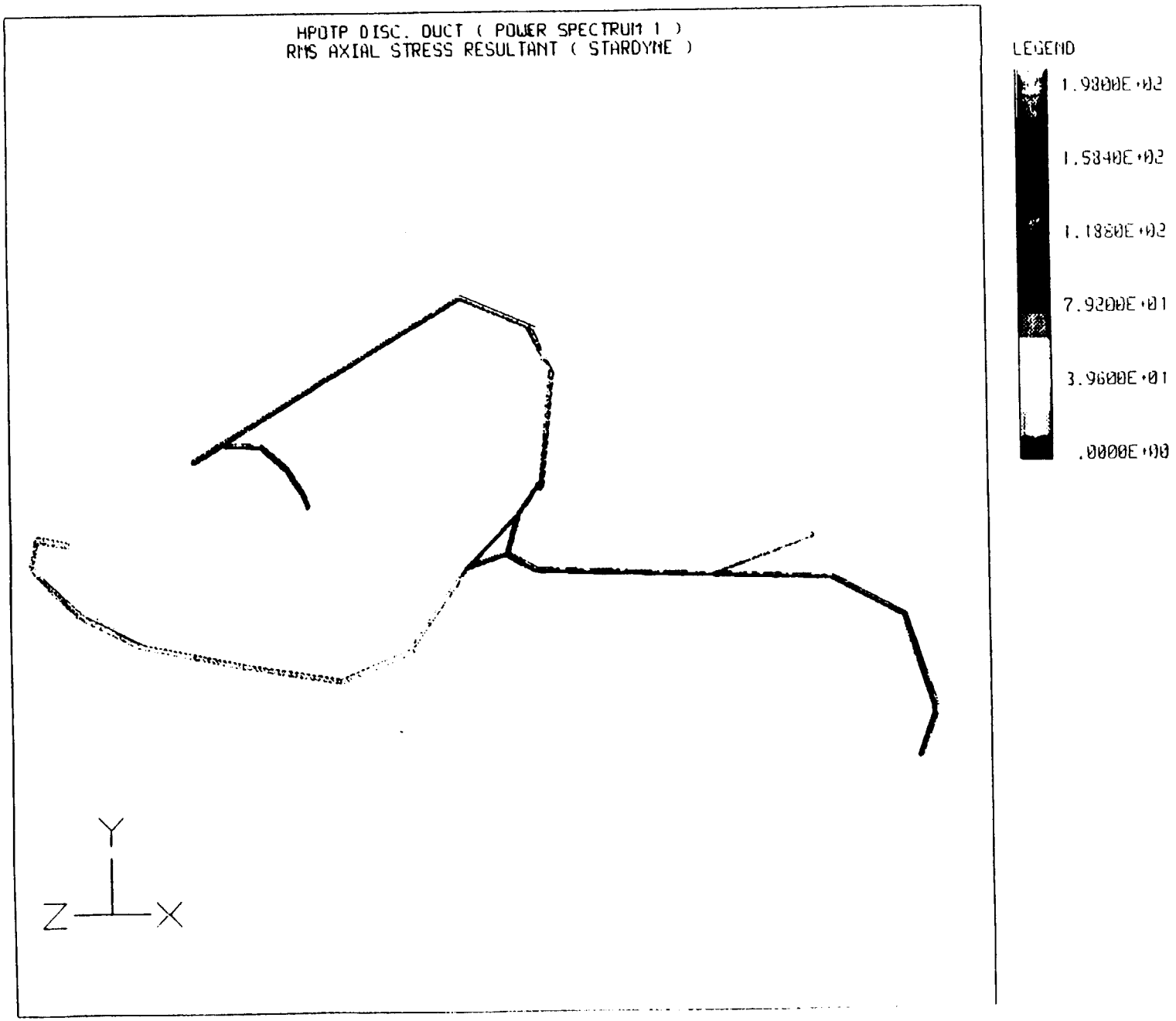

Figure 8.38 STARDYNE Axial Stress Results Due to Power Spectrum 1

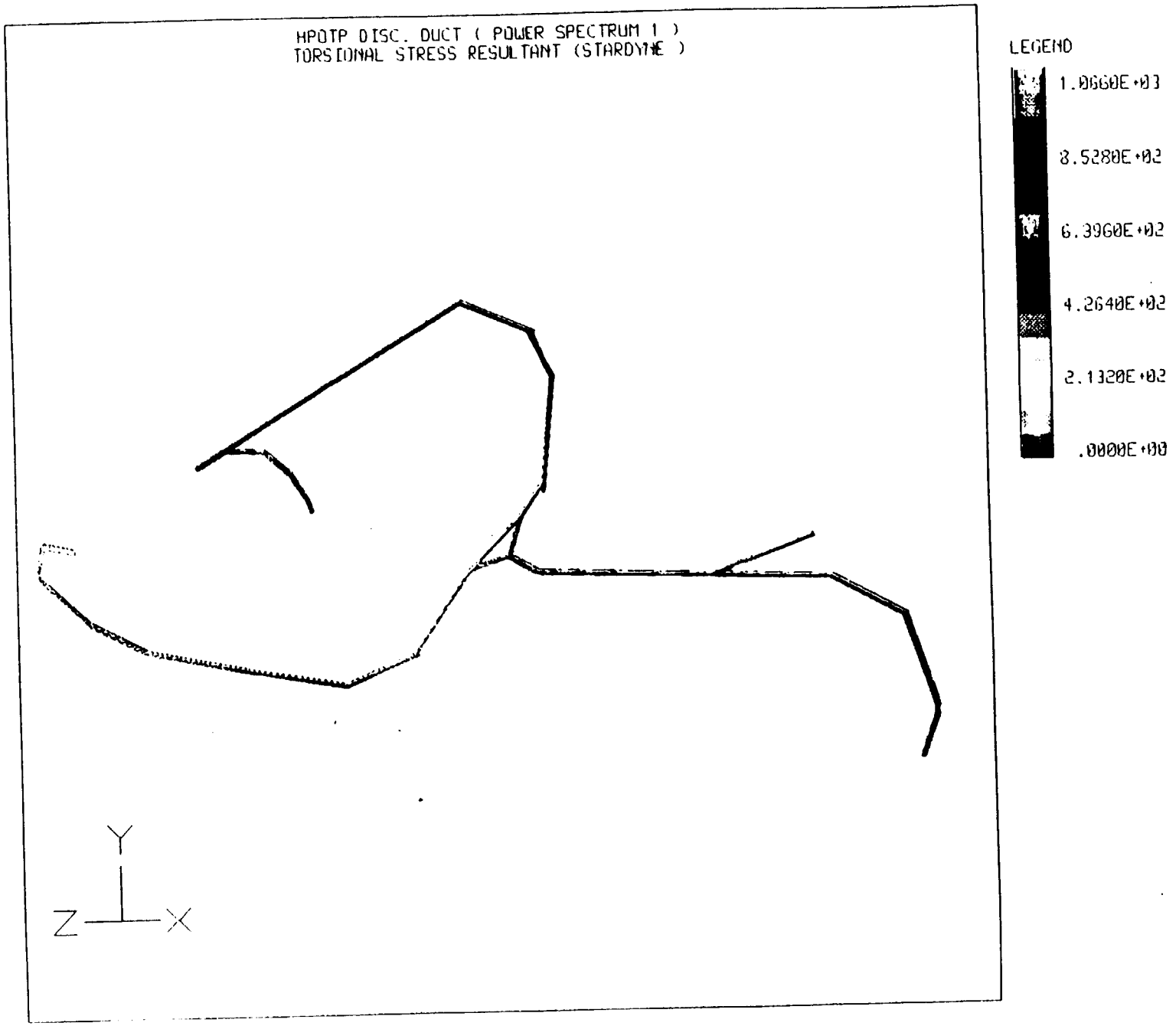

Figure 8.39 STARDYNE Torsional Stress Results Due to Power Spectrum 1

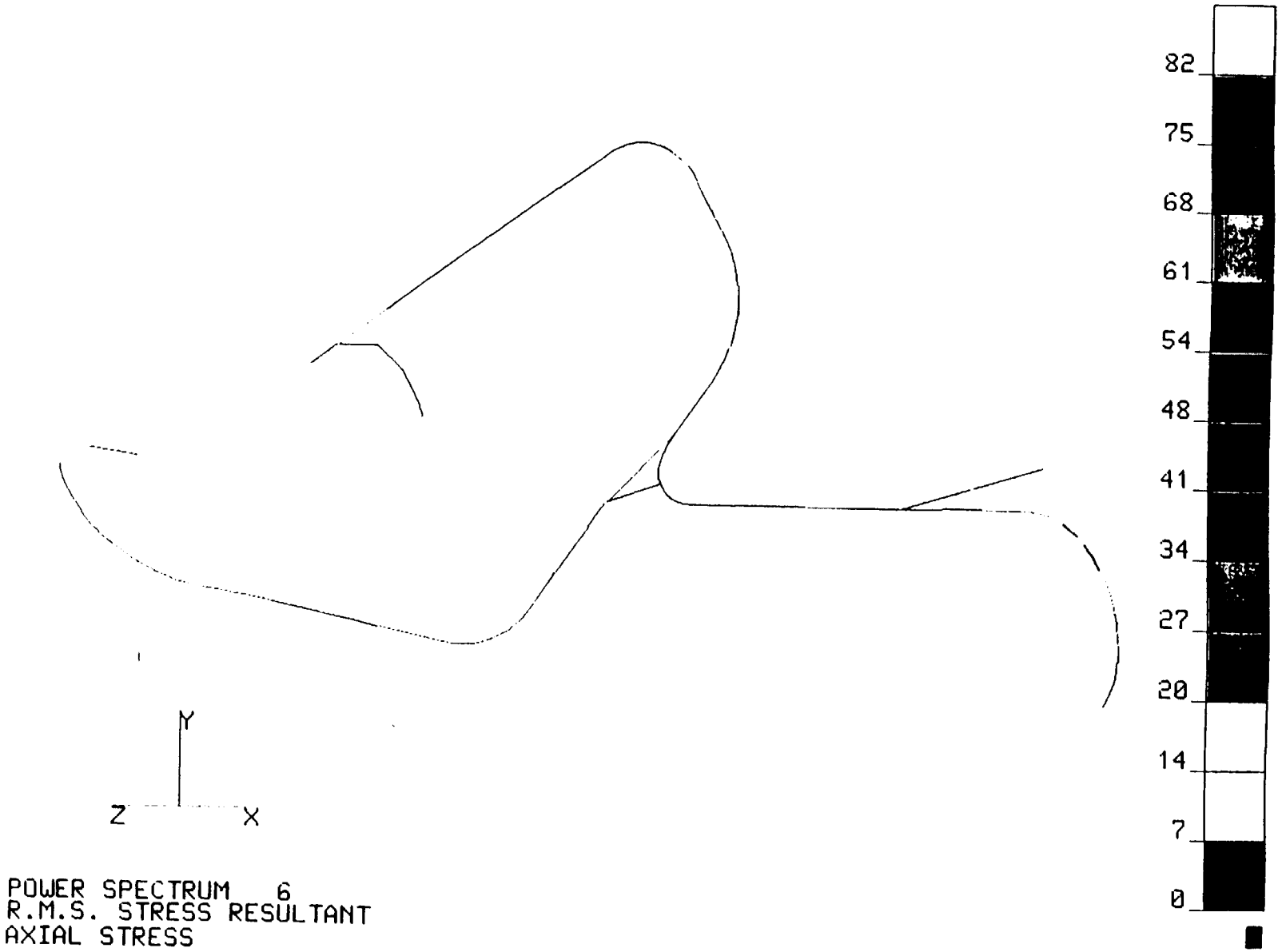

Figure 8.40 NESSUS Axial Stress Results Due to Power Spectrum 6

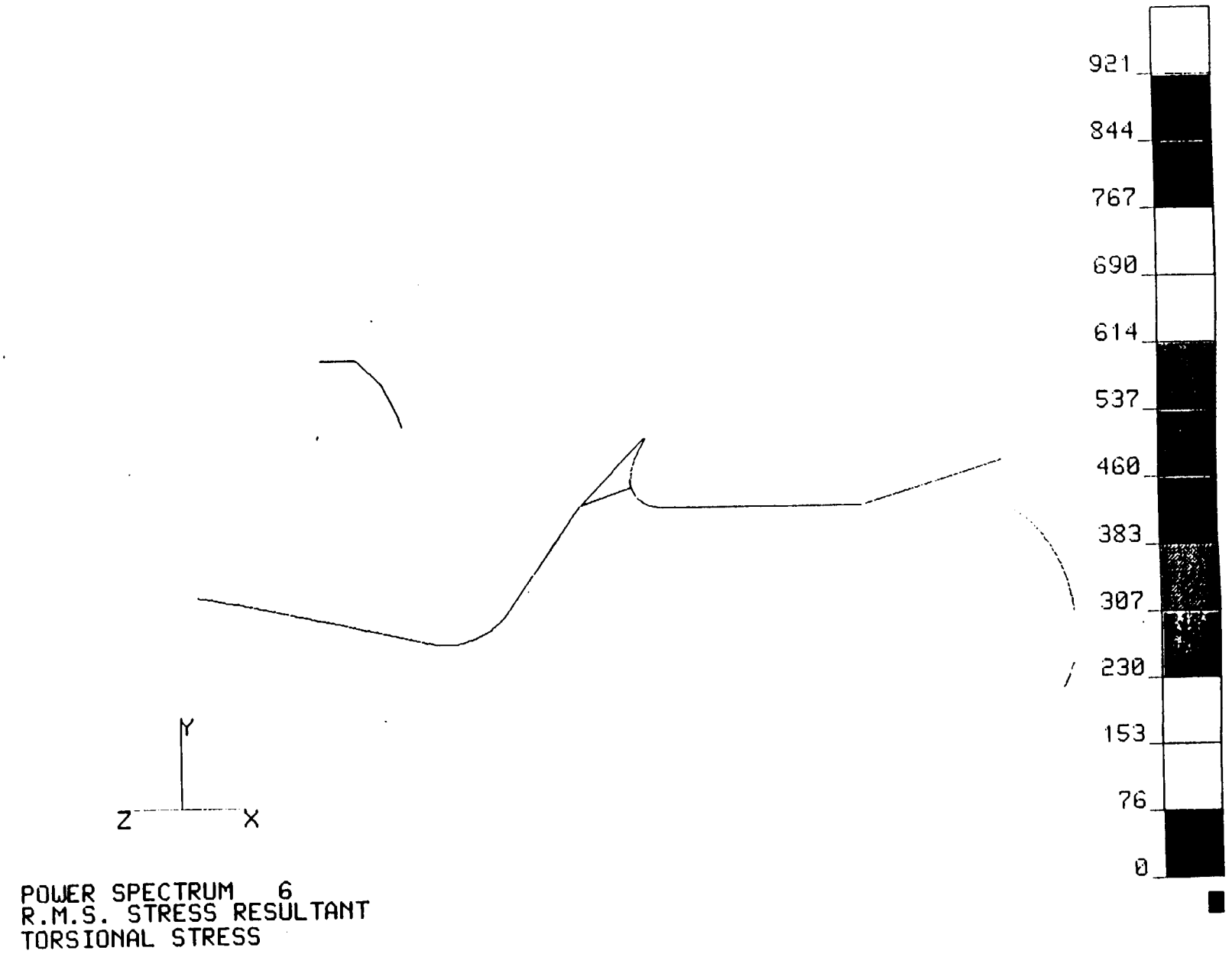

Figure 8.41 NESSUS Torsional Stress Results Due to Power Spectrum 6

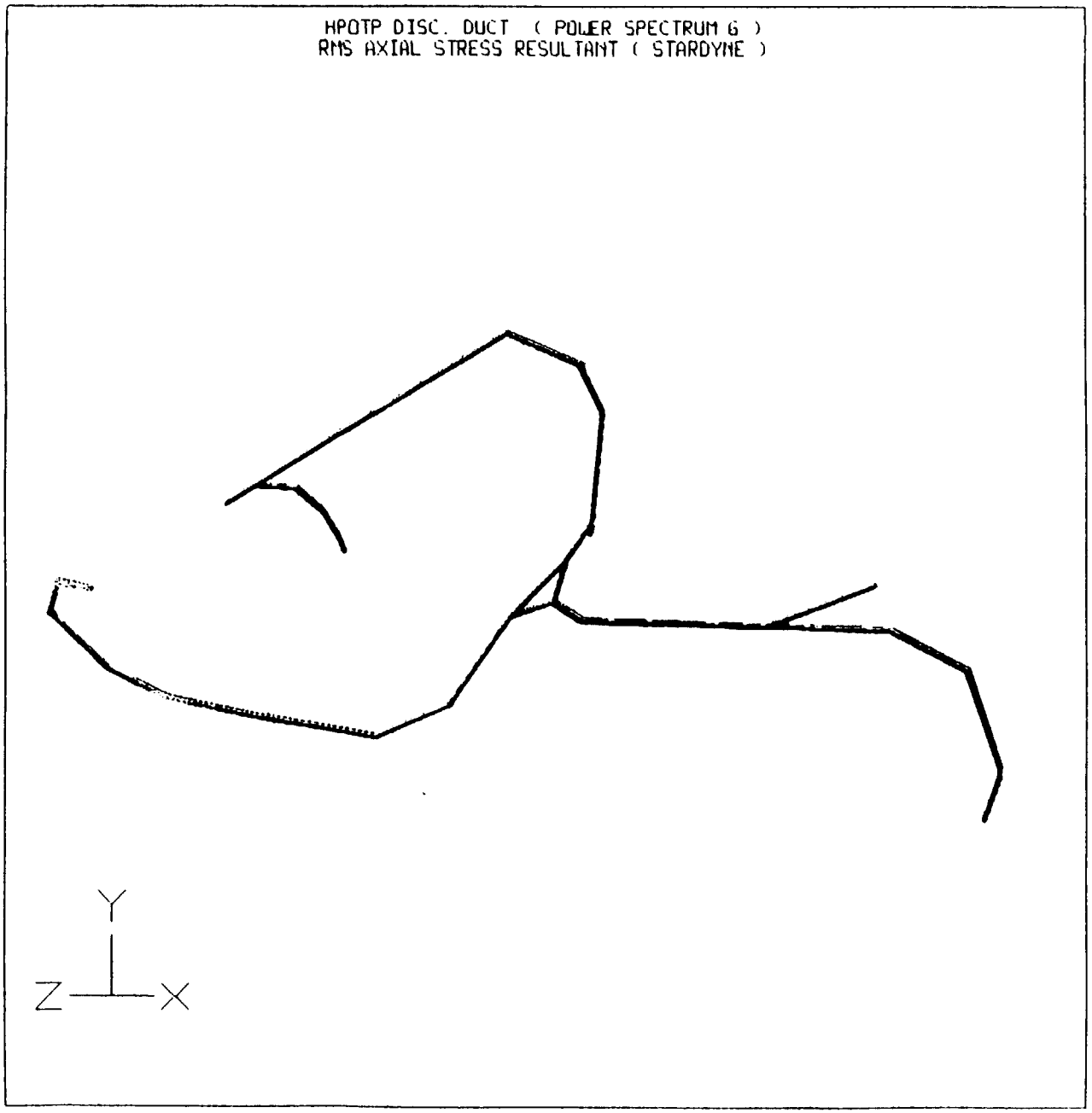
HPOTP DISC. DUCT (POWER SPECTRUM 6)
RMS AXIAL STRESS RESULTANT (STARDYNE)
LEGEND
7.1000E+01
5.6800E+01
4.2600E+01
2.8400E+01
1.4200E+01
.0000E+00
Y
Z
X

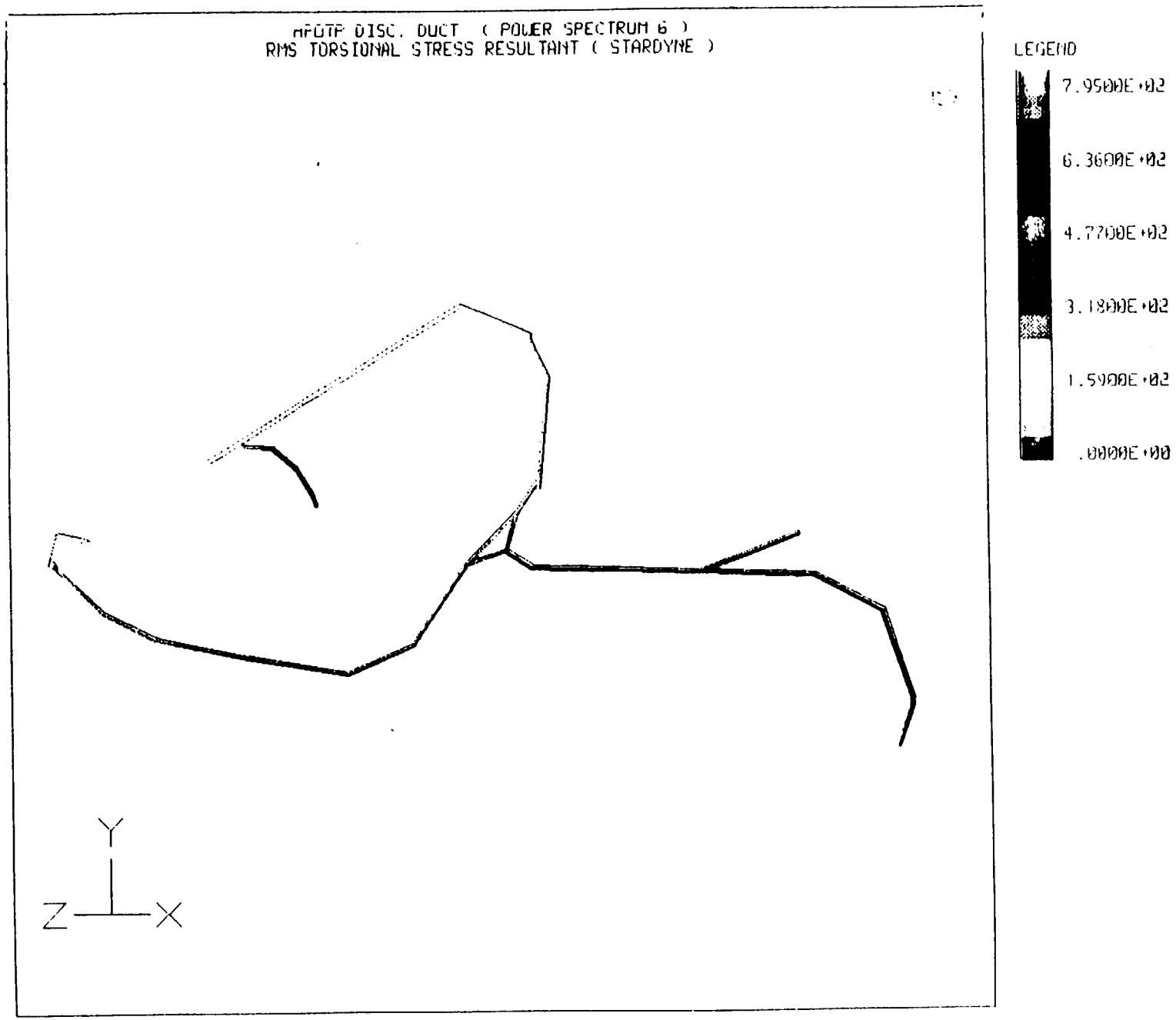

Figure 8.43 **STARDYNE Torsional Stress Results Due to Power Spectrum 6**

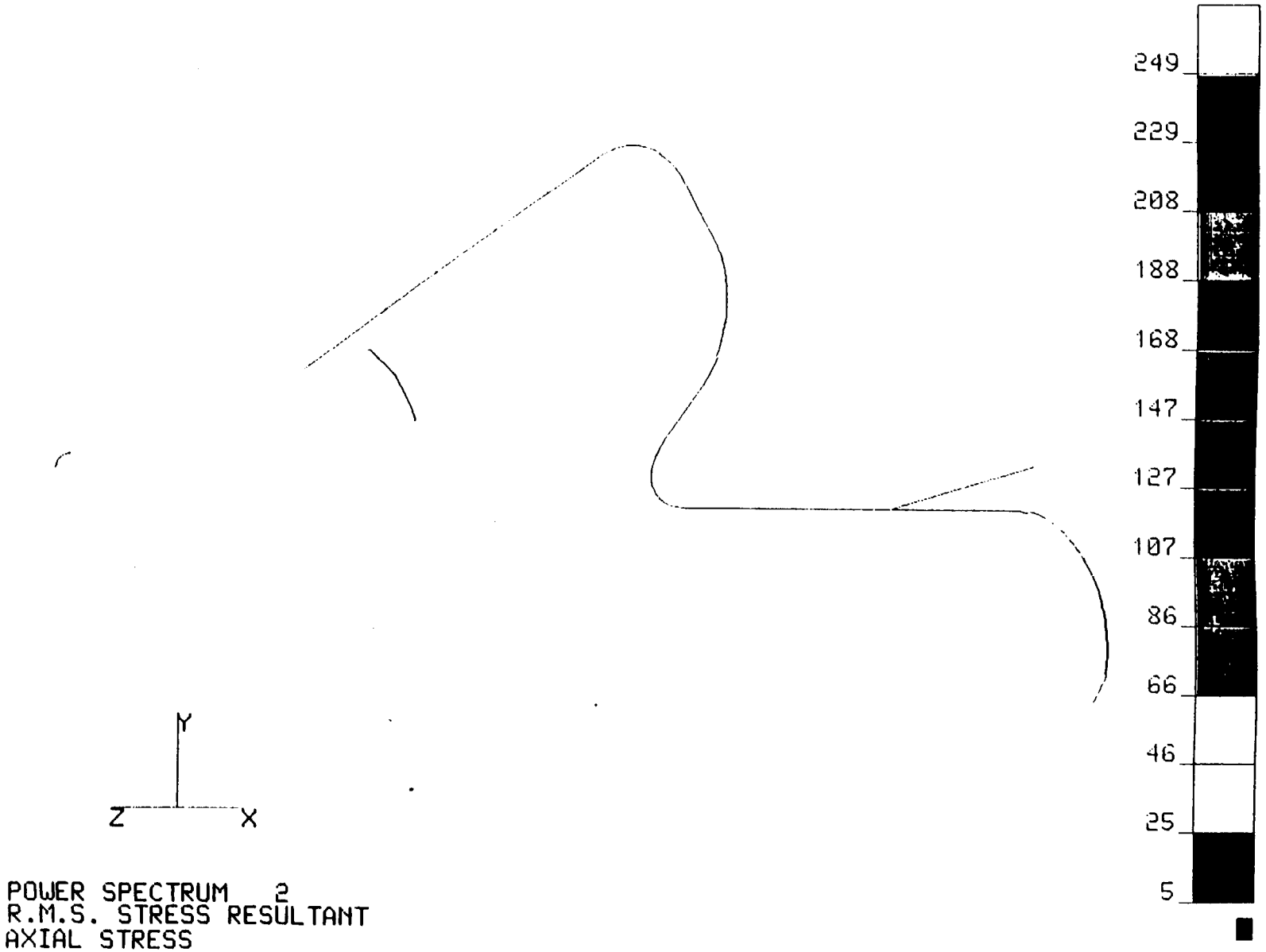

Figure 8.44 NESSUS Axial Stress Results Due to Power Spectrum 2

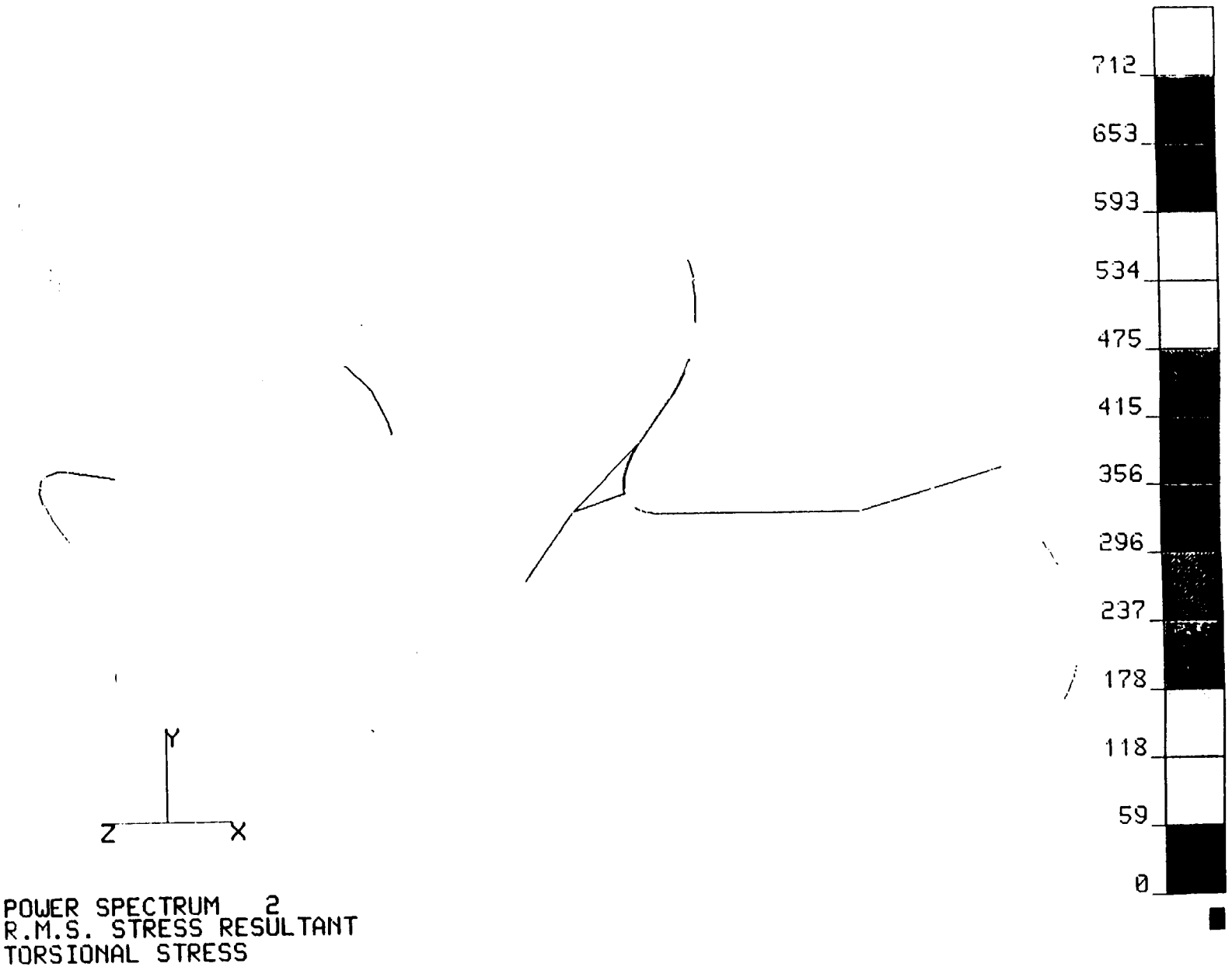

Figure 8.45 NESSUS Torsional Stress Results Due to Power Spectrum 2

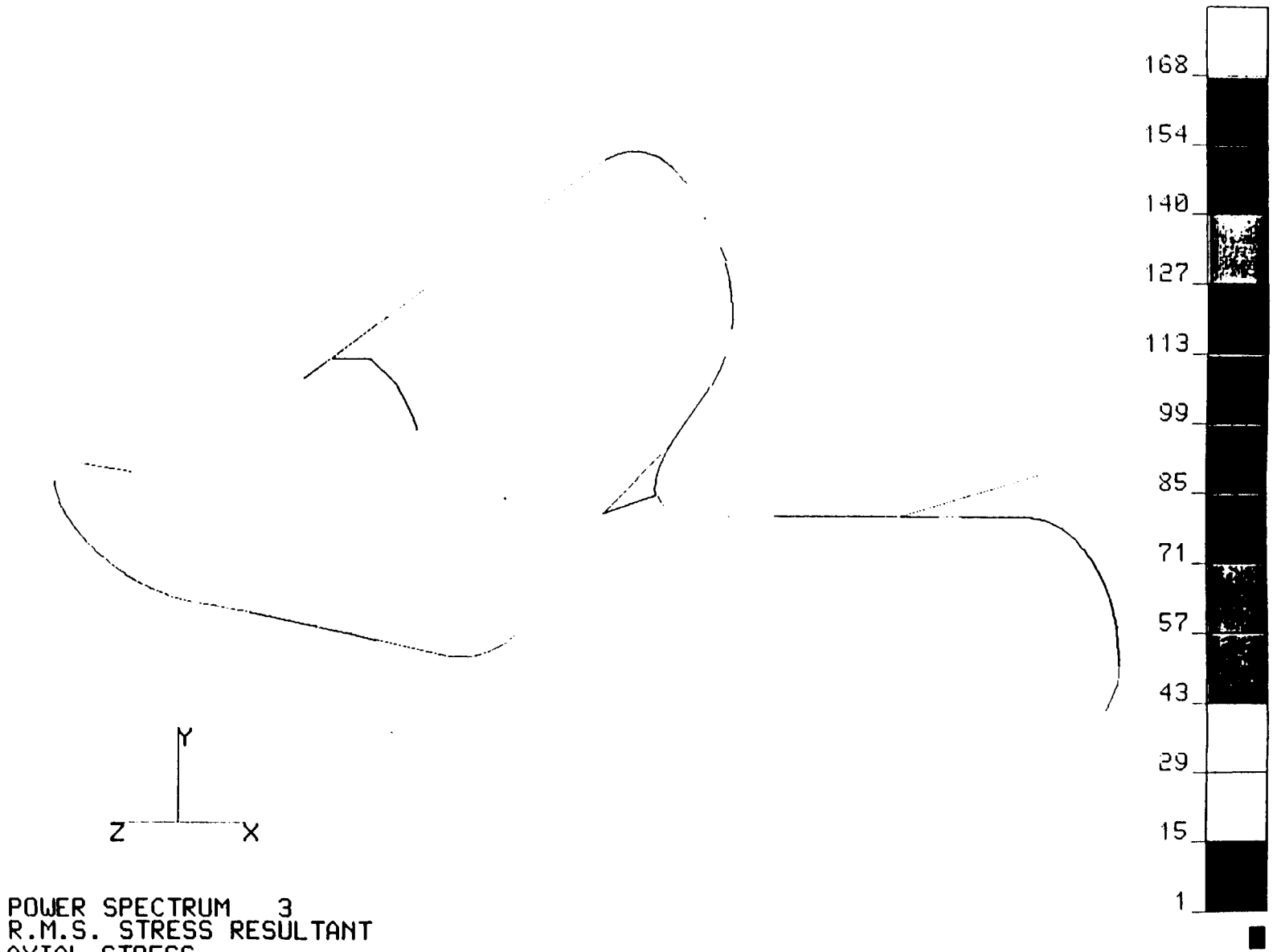

Figure 8.46 NESSUS Axial Stress Results Due to Power Spectrum 3

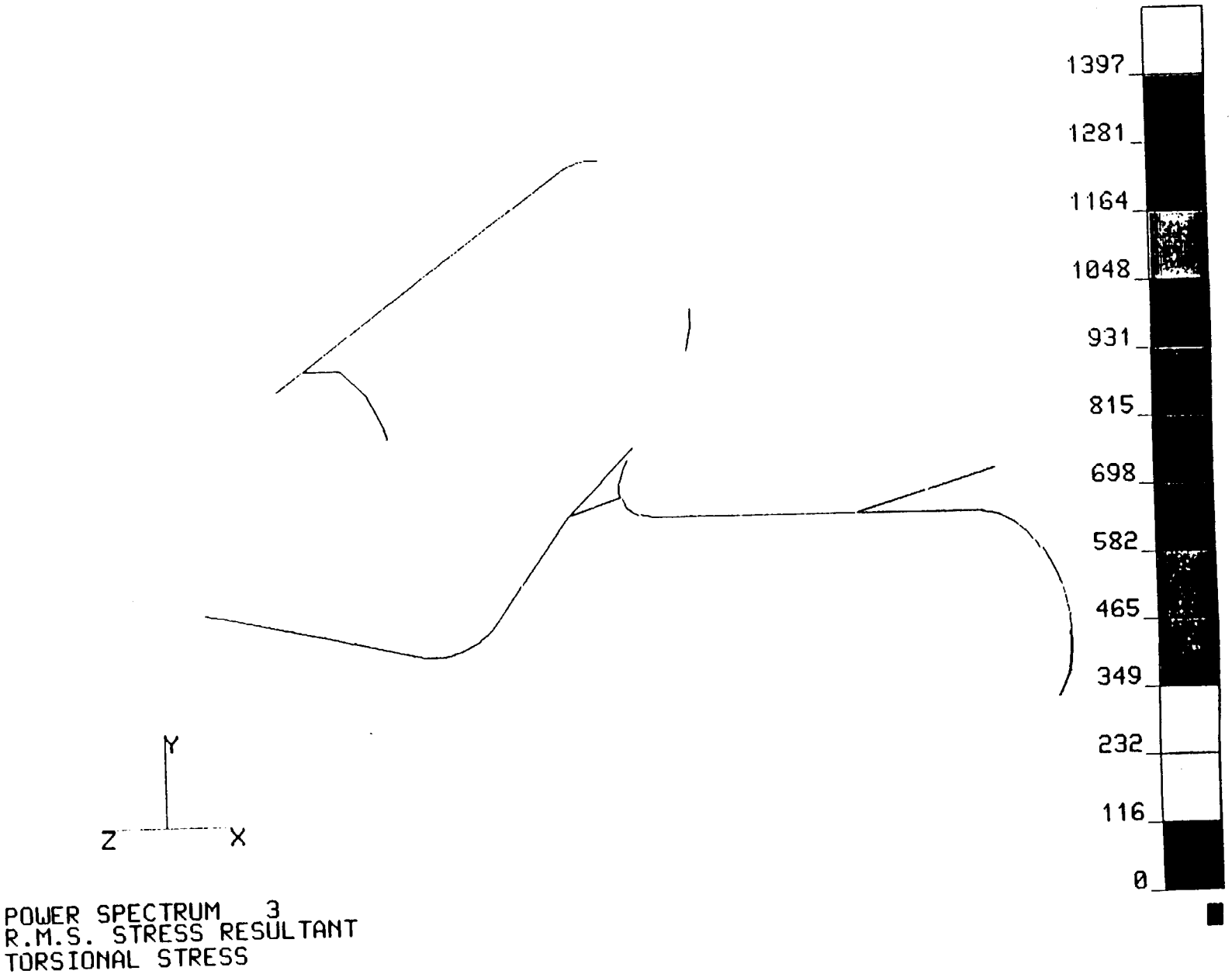

Figure 8.47 NESSUS Torsional Stress Results Due to Power Spectrum 3

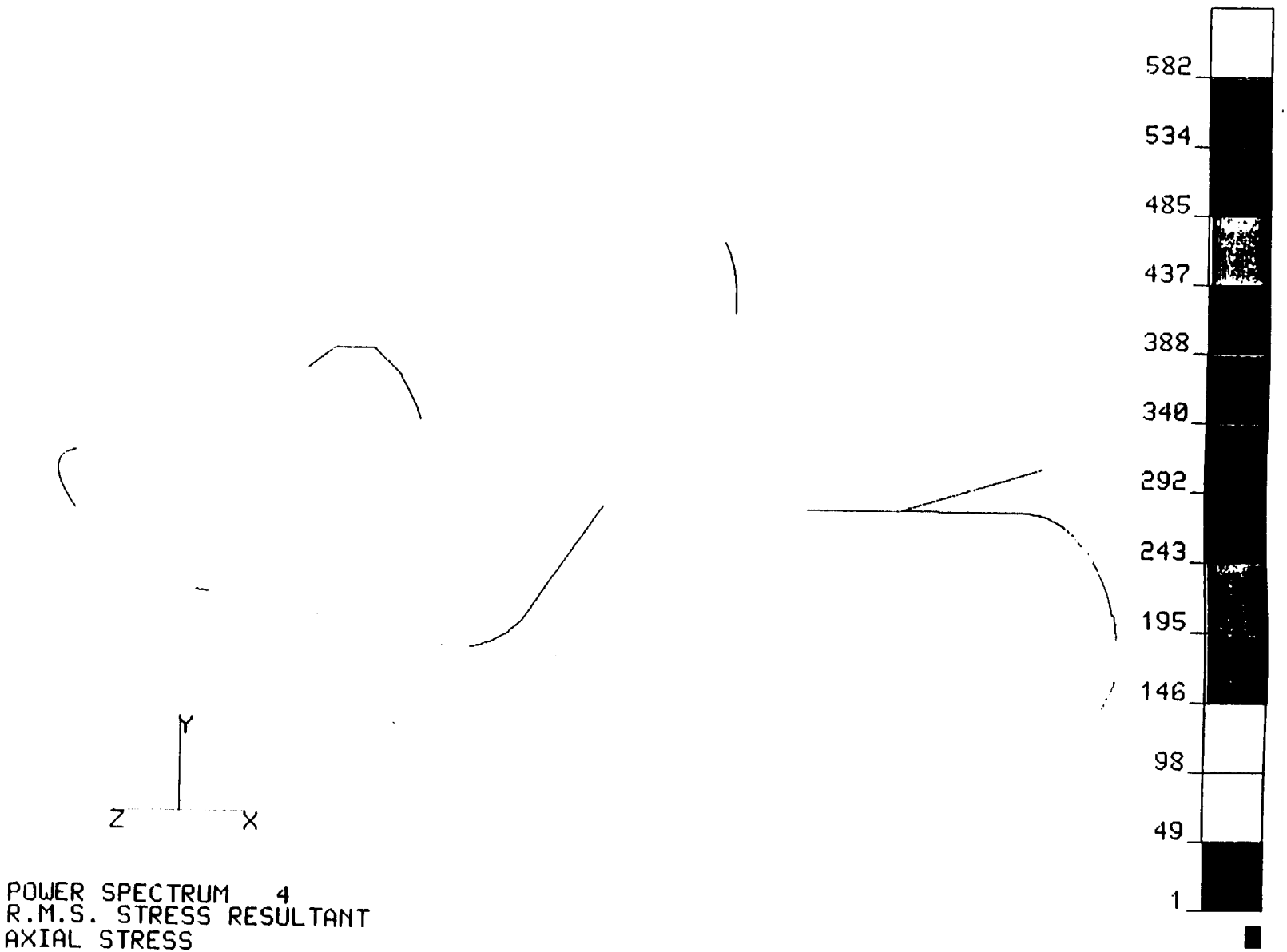

Figure 8.48 NESSUS Axial Stress Results Due to Power Spectrum 4

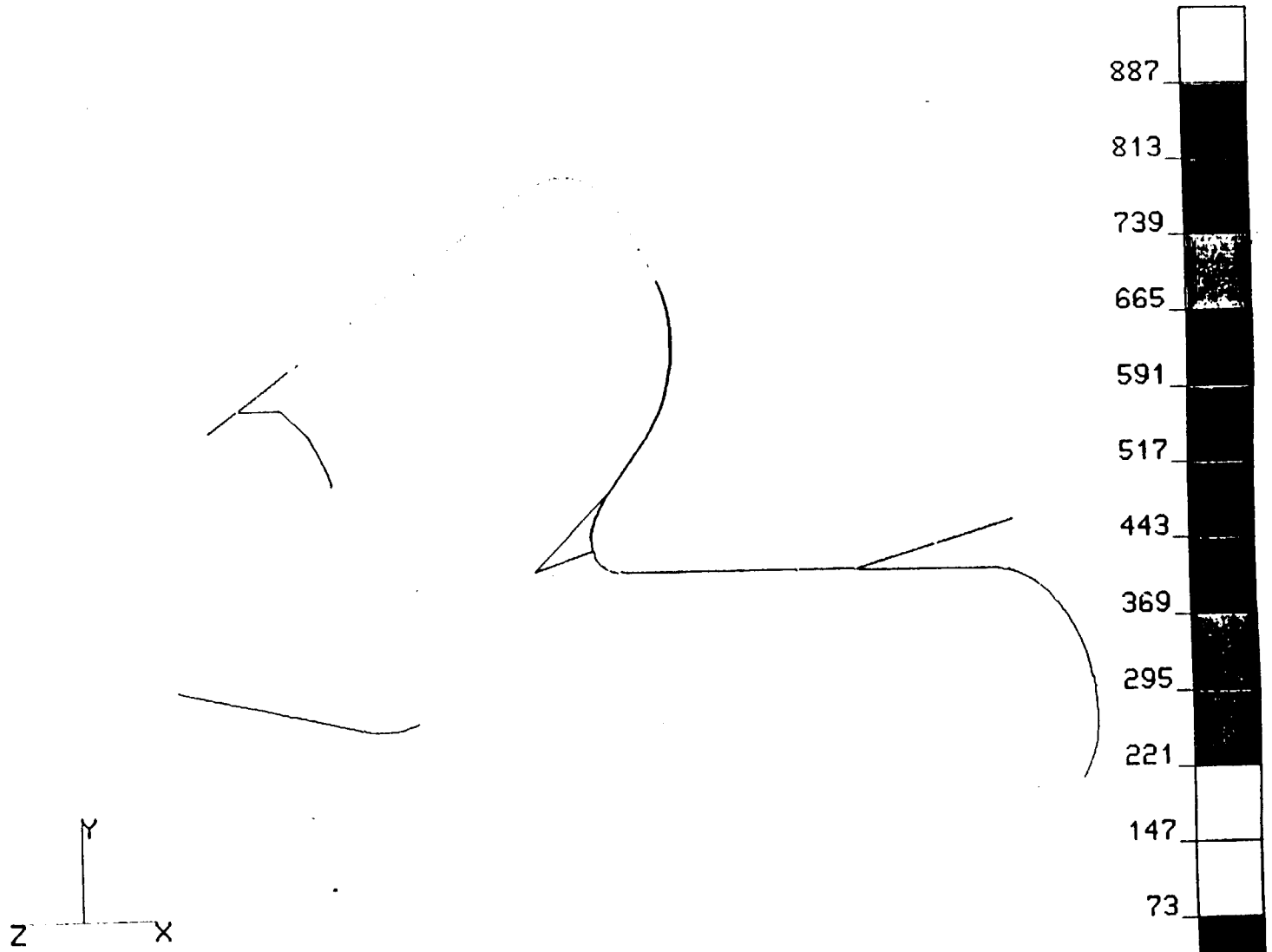

Figure 8.49 NESSUS Torsional Stress Results Due to Power Spectrum 4

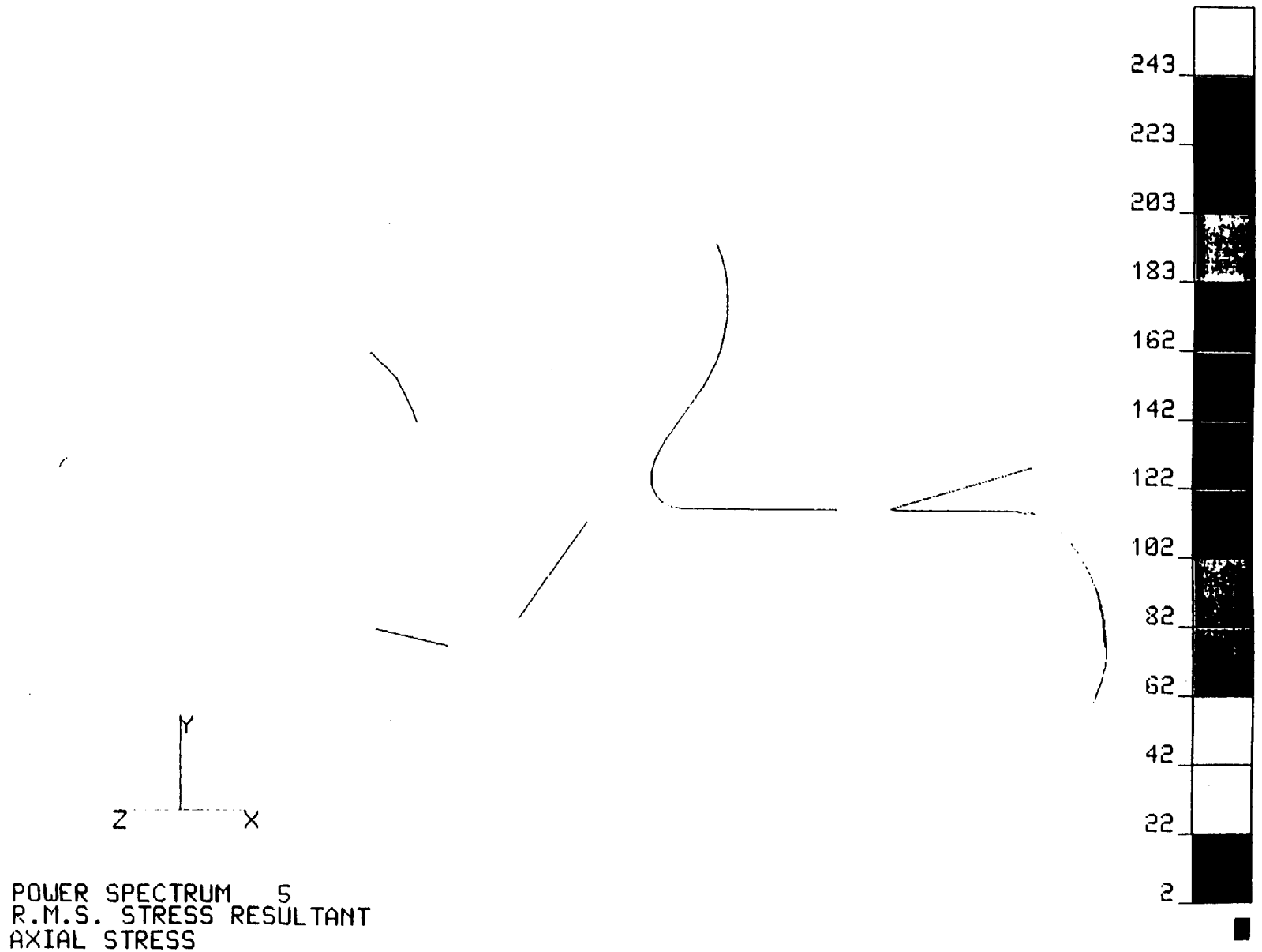

Figure 8.50 NESSUS Axial Stress Results Due to Power Spectrum 5

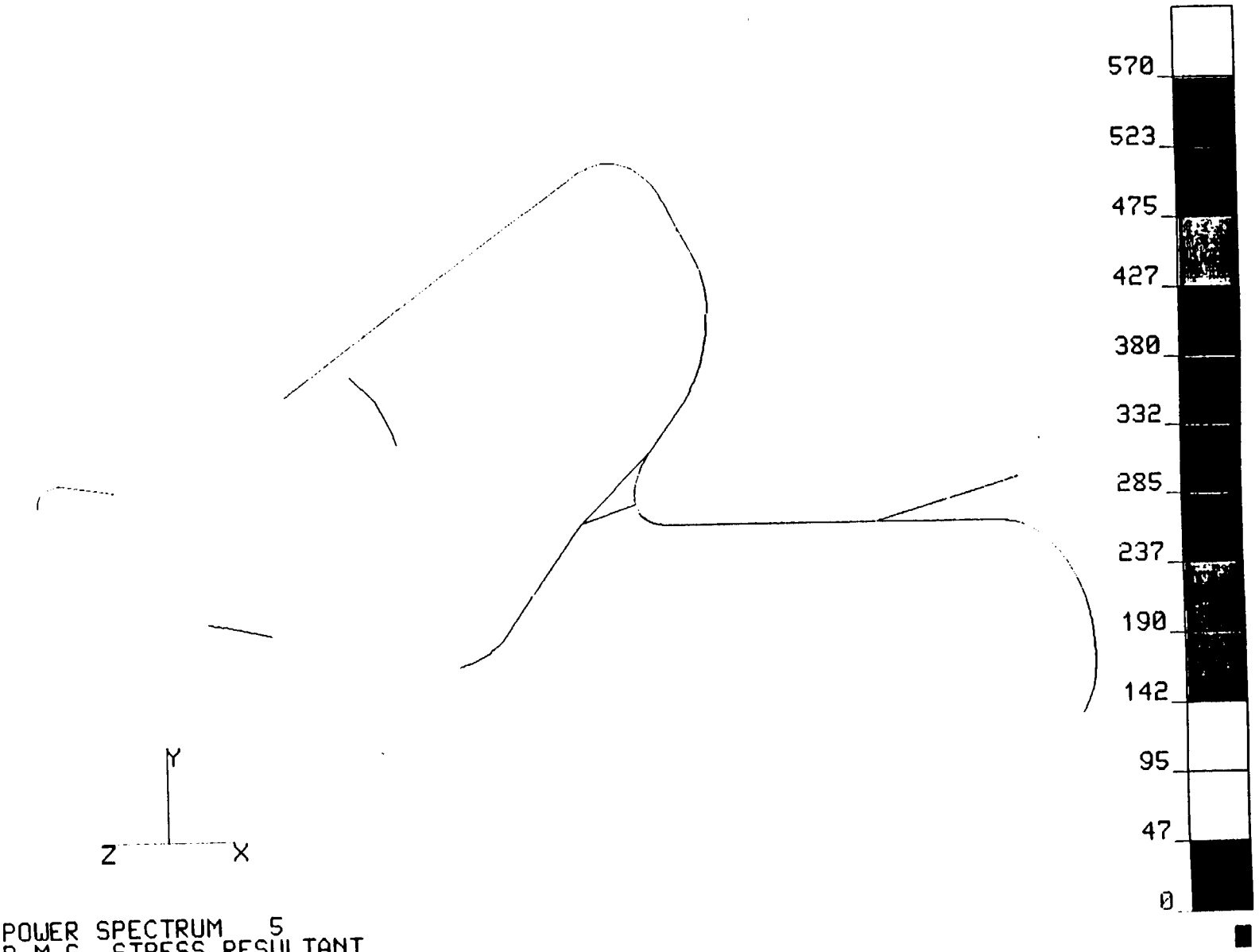

Figure 8.51 NESSUS Torsional Stress Results Due to Power Spectrum 5

8.9 Fiscal Year 1989 Effort

NESSUS verification efforts on high pressure oxidizer duct will continue. Random vibration analysis with probabilistic system parameters will be defined and a distribution of selected R.M.S. stress resultants and stress velocities at some critical locations will be reported. Then the total power contained in a PSD will be considered as additional random variables with realistic variations based on experimental data. Strategy for multiple random variables that affect the shape of the PSD will also be developed and verified. Verification efforts on LOX post and transfer ducts will be conducted. LOX post analysis will address probabilistic material nonlinear analysis. Transfer duct analysis will address probabilistic material and geometric nonlinear analysis.

9.0 PROBABILISTIC APPROXIMATE ANALYSIS METHODS (PAAM)

9.1 The Concept of an Approximate Method

9.1.1 Motivation

The most common structural analysis techniques in use today are finite element and boundary element methods, and these are both represented in the PSAM software. These techniques permit highly accurate three-dimensional modeling of structural geometry, thermal and mechanical load environment, and material properties. Both linear and nonlinear system response can often be estimated within a few percent of the actual experimental behavior. Unfortunately, these techniques can also be expensive and time-consuming. Particularly in the early stages of design, when geometries, loads, and materials are only tentative, it is not practical to assemble an exact, comprehensive three-dimensional model for every critical component. What is needed, typically, is some means of estimating the nature and rough magnitude of maximum stresses or displacements, natural frequencies, etc. Of further value is the identification of which design parameters exert the most influence on the total system performance, so that further design evolution is most efficient.

These needs are addressed in the PSAM software by the Probabilistic Approximate Analysis Methods (PAAM) module. The basic idea of PAAM is simple: make an approximate calculation of system response, including calculation of the associated probabilistic distributions, with minimal computation time and cost, based on a simplified representation of the geometry, loads, and material. The deterministic solution resulting should give a reasonable and realistic description of performance-limiting system responses, although some error will be inevitable. If the simple model has correctly captured the basic mechanics of the system, however, including the proper functional dependence of stress, frequency, etc. on design parameters, then the response sensitivities calculated may be of significantly higher accuracy. In other words, the calculated probabilistic distribution of the response variable may be in significant error only by some offset of the mean value.

9.1.2 Approach

Three factors make up the "approximate" analysis approach. The first is a simplified representation of the part geometry. Complex three-dimensional shapes are replaced wherever possible by equivalent structures which are simple plates, shells, beams, or pipes with relatively few descriptive parameters. The second factor is a similar simplification of the applied mechanical and thermal loads. Point loads, uniform fields, and linear or parabolic distributions are used to describe these quantities. Often a more complex load environment can be approximated through linear superposition of the simple descriptors.

The third factor in the PAAM methodology is the solution technique itself. Complex variational techniques with many degrees of freedom are replaced by simpler computational schemes. In some cases, it is possible to construct a simple mechanics-of-materials model, often in two dimensions. In other cases, more sophisticated closed form solutions can be derived or (preferably) adapted from previous research results in the literature. These may be based on elasticity or may employ approximate energy methods. Yet another analysis technique which meets the requirements for speed and efficiency is to assemble a crude finite element solution, based on the simplified geometry and utilizing few degrees of freedom. This type of FEM model would actually be transparent to the PAAM user in that the simple mesh and boundary conditions required would be generated automatically.

9.2 Fast Probability Integration Interface

The probabilistic analysis is performed by invoking one of the options in the FPI module. The FPI module has a full-distributional analysis capability in which the input random variables are defined using probability distributions. The computed probabilistic structural responses are represented by cumulative distribution functions (CDF's). The CDF for each response is computed at a number of user-selected response values or cumulative probabilities. For each response value or probability, it is assumed that a most probable point (or design point) exists in a joint, standardized, normal probability space. An iteration process involving linear response-surface (or limit state) approximations and normal-tail approximations is performed to determine the design point using the Rackwitz-Fiessler algorithm [1]. The CDF for each associated design point is then computed using an effective reliability analysis algorithm which takes into account the effect of non-linear response surface [2]. The closed form or simple numerical approximate solutions to particular structural analysis problems reside in independent user-written subroutines. FPI establishes linear or quadratic polynomial approximations to the limit state using a finite difference (central difference) scheme on the subroutines. Further information on the FPI algorithm has been published in previous PSAM Annual Reports.

The PAAM software package is essentially an integration of the standard off-the-shelf FPI program with the component-specific closed-form or simple numerical response functions. The standard FPI code was enhanced to perform reliability analysis on any user written response function. There is complete compatibility between FPI and PAAM. Additions to FPI are quickly integrated into the PAAM code. All of the FPI options such as selecting response levels or probability levels, Monte Carlo options, etc., are available in PAAM.

9.3 Formulations for Demonstration Components

The PSAM code is being demonstrated and validated by considering four representative critical components in the current Space Shuttle Main Engine (SSME). The same four components are considered in the PAAM code, which by its very nature is component-specific. It should be noted, however, that

the architecture of the PAAM software permits new closed-form expressions for these or other components to be quickly installed and evaluated, including all probabilistic considerations.

The four components permit a wide range of "approximate" solution strategies to be demonstrated. Two of the components, the LOX post and the transfer duct, are addressed with closed-form expressions based on mechanics-of-materials models or more complex analytical formulations adapted from the literature. The other two components, the turbine blade and the high pressure oxidizer duct, are treated with a simplified finite element-based solution.

9.3.1 Closed Form Solutions

The LOX post is part of the injector which introduces and meters the propellent flow to the combustion chamber after atomization and mixing. A diagram of the actual part is given in Figure 9.1, along with the PAAM simplified representation of the post. The post is modeled first as a beam with hollow circular cross-section. The end conditions are fully fixed at the inlet (top) end and elastically restrained at the outlet (bottom) end. The effective end stiffness there is represented by a rotational spring with some finite, non-zero stiffness. A thick-walled cylinder model is also used. Important loadings are internal and external pressures and temperatures, and transverse distributed loads due to fluid drag. The analysis must consider not only static stresses but also free and forced vibration due to transverse fluid flow and the possibility of buckling due to constrained axial thermal expansion. Complete details of the approximate solutions are given in Appendix D, Cases 2A.S (static solution, thick-walled cylinder model), 2B.S (static solution, beam model), and 2.V (vibration solution, beam model).

The vibration analysis of the LOX post provides good examples of solution strategies. The basic solution for free vibration of fixed-fixed and fixed-pinned uniform beams is available in handbooks [3]. Both natural frequencies and mode shapes are given in closed form in terms of geometry and material parameters and a frequency factor, λ, which to a first approximation is a simple function of the mode number and the bounding end condition. Solutions for intermediate end conditions (elastically restrained ends) are available in tabular form for a limited number of spring stiffnesses [4]. These results can be fitted with a simple empirical relationship to calculate λ for any mode number and any end condition. The possible effects of axial load or beam taper on natural frequencies can also be estimated from previously published expressions. The forced vibration solution follows with little additional difficulty. Assuming, for example, a harmonic transverse point load at some location along the beam, the response at any other point can be determined with knowledge of the receptance function [5]. This calculation results in a series which is dominated by the terms corresponding to the two nearest natural frequencies. Maximum outer fiber bending stresses are easily calculated by proper differentiation of the displacement expression. Additional terms can be added to include the effects of structural damping. Finally, it is no

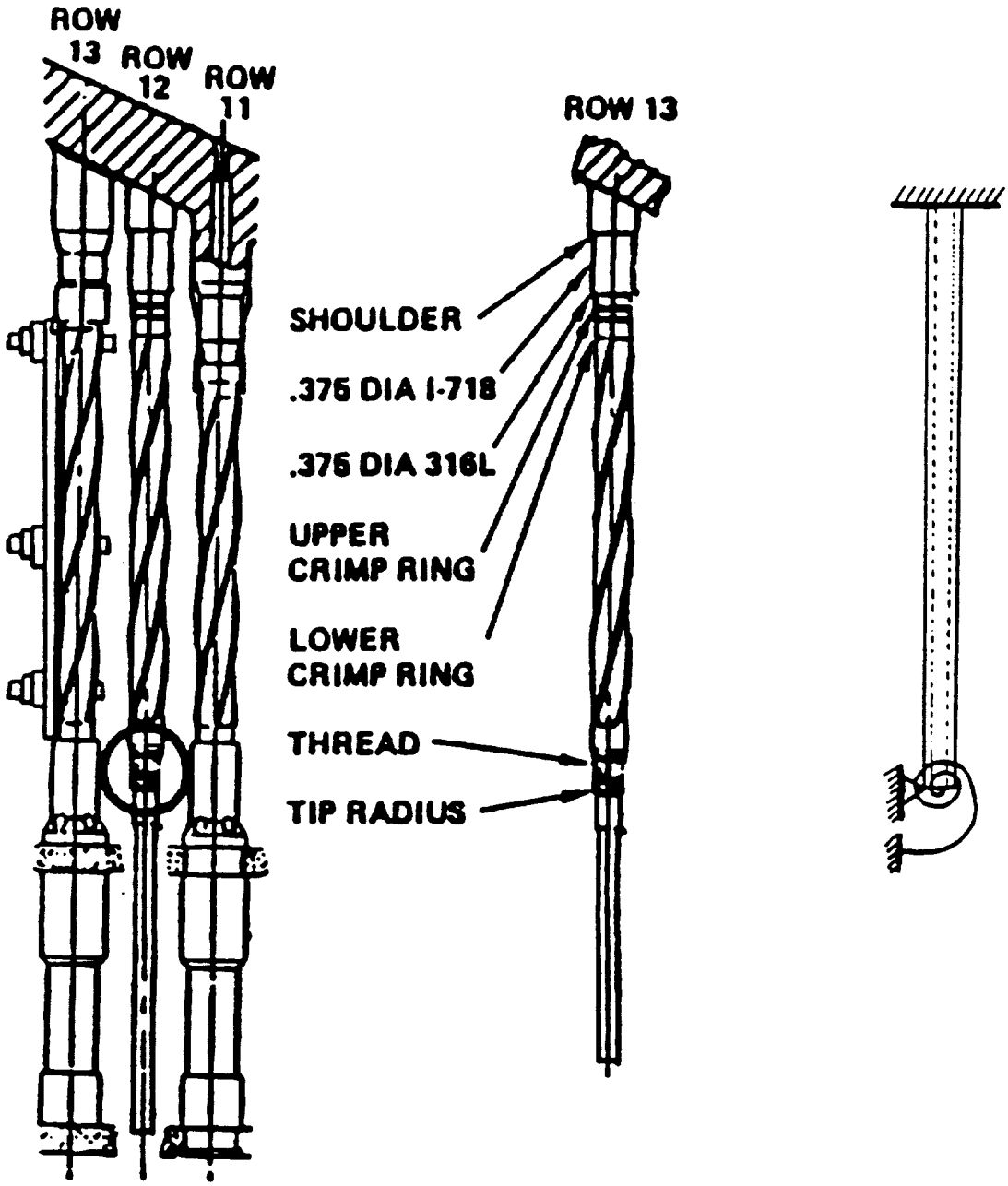

Figure 9.1 Diagram of SSME Liquid Oxygen Post (left) and PAAM Simplified Geometrical Representation (right)

more difficult to analyze random vibration from the same expressions written in terms of spectral densities and transfer functions. Multiple random loadings can be considered and require as additional input only the cross-spectral densities.

The transfer duct routes hot gases from the high pressure preburner turbines to the main injector torus manifold, where it is directed into the hot gas cavity of the main injector. A diagram of a typical duct is given in Figure 9.2, accompanied by a schematic of the PAAM simplified representation. The duct is modeled as a thin circular cylindrical shell with radius equal to the average radius of the actual conical shape. Stresses arise from a net external pressure and thermal gradients. Buckling is a failure mode of special concern. A general formulation is available for the calculation of natural frequencies, but only axisymmetric modes are considered for harmonic and random forced vibration caused by fluctuations in internal pressure. Full details of the models and equations are given in Appendix D, Cases 3.S (static) and 3.V (vibratory).

9.3.2 Simplified Finite Element Solutions

In some cases, development of a "simple" closed-form solution for a simplified load/geometry case is itself a complicated and tedious problem. An alternative approach is to develop a simplified finite element model. This is in no way comparable with the complex finite element models employed in the PFEM task. The PAAM FEM represents a highly simplified geometry with a limited number of elements. The model itself is actually transparent to the user. He only supplies dimensions of the part within specified geometrical constraints, and the code automatically generates the required simple mesh. Loads are similarly simple, and load inputs to the FEM are automatically generated from user description. Execution time is short.

Some preliminary work has been done to plan and assemble such models for two of the demonstration components, the turbine blade and the high pressure oxidizer duct (HPOD). The models will be constructed with the NESSUS/FEM software developed for the PSAM project.

The turbine blade will be modeled with two-dimensional plate elements allowing for limited variations in curvature, tilt, lean, twist, thickness, and width. Geometric parameters will typically be specified by the user for a limited number of points around the perimeter of the plate (e.g., the four corners), and the complete geometry will then be generated by linear or quadratic interpolation across the face. A similar scheme will be used for specification of the pressure loads and temperatures. The shroud will be modeled as a lumped mass and the platform as a variable stiffness. The effects of centrifugal loading will be considered.

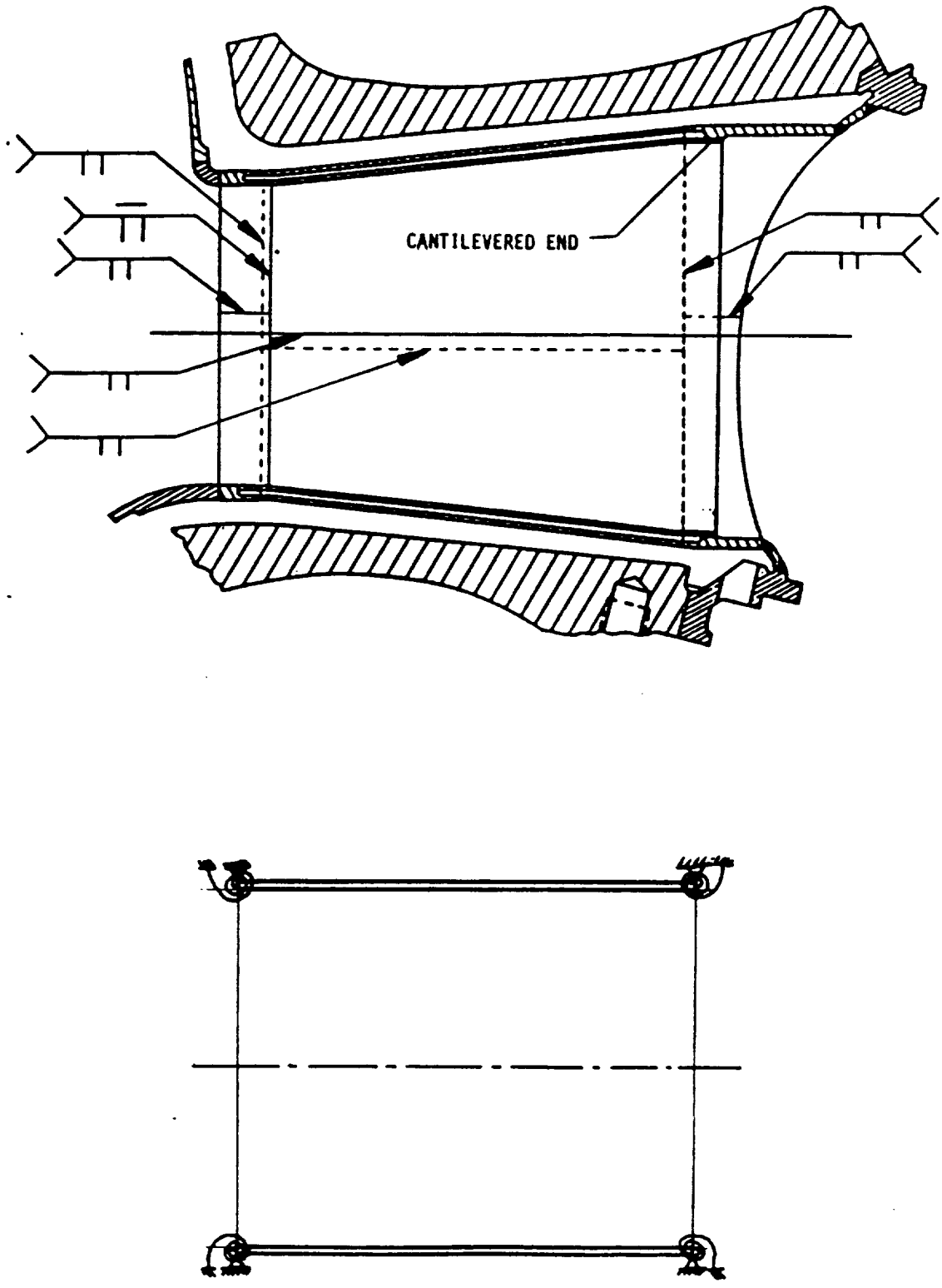

Figure 9.2 Diagram of SSME Transfer Duct (top) and PAAM Simplified Geometrical Representation (bottom)

The HPOD will be modeled with an assembly of a limited number of beam elements with hollow cross-section. All calculations will be based on thin-wall theory. Ovalization effects in the elbows will be incorporated with empirical adjustments to the calculated stresses based on ANSI/ASME flexibility factors. Static loads to be considered include internal pressures, flow momentum, vehicle acceleration, and temperatures. Dynamic loads include periodic and random base excitation and periodic and random pressure fluctuation.

9.4 Validation

A validation problem of the LOX Post thick cylinder model has been performed using realistic input data. An advanced first order and Monte Carlo analysis of the closed form solution were both performed.

The variable inputs for the LOX Post thick cylinder model are listed in Table 9.1.

Table 9.1

Definition of Random/Deterministic Variables

Variables	Distribution	Mean	COV
Inner Radius (R_i)	truncated Normal (±0.03)	0.94 in.	1.06%
Outer Radius (R_o)	truncated Normal (-0.002, +0.01)	1.10 in.	4.55%
Young's Modulus(E)	Normal	3.40E+7 psi	2%
Poisson's Ratio	Normal	.3594	2%
Coefficient of Thermal Expansion	Normal	5.65E-6 /R	5%
Internal Pressure(P_i)	Lognormal	3077 psi	4%
External Pressure(P_o)	Lognormal	3232 psi	4%
Internal Temperature(T_i)	Lognormal	194 R	1.55% (3 R)
External Temperature(T_o)	Lognormal	1444 R	1.55% (15 R)
Reference Temperature(T_{ref})	N/A	530 R	0%

Notes: All mean value data was obtained from the First Annual PSAM Report and Rocketdyne. The truncated normal limits for R_i and R_o along with the mean temperatures and COV of T_i and T_o were provided by Rocketdyne. Other statistical data such as distribution types and COV for the other random variables were determined from default values provided by Dr. Paul Wirsching and are not problem specific (see Table 9.3).

The input data for PAAM is identical to that for FPI with the exception that additional data is sometimes needed. This need is accommodated by adding the necessary response data after the model data. The keyword *RESPONSE indicates response data is being provided. In PAAM, the first data is the response function desired (i.e. LOX post thick cylinder, LOX post tapered beam, turbine blade, etc.). In the LOX Post thick cylinder example the response function is "2AS". The second data is a set of five integers. The third data is a set of five reals. This information can be used in any way desired by the user written subroutines. Additional information can be entered in any format as long as the user written routine reads the data properly. For the LOX Post thick cylinder example the first integer indicates the response type (i.e. hoop stress, radial stress or axial stress). The second integer indicates whether end constraints are imposed (11 - yes, 12 - no). The first real indicates the radial position of the desired response (0.0 = R_i, 1.0 = R_o).

The input file for an advanced mean value solution of the LOX Post thick cylinder model is listed in Table 9.2. The desired response is the hoop stress at the inner radius without end constraints.

Table 9.2

PAAM Input File for LOX Post Thick Cylinder Model

```
*FPI
THICK CYLINDER MODEL (2AS) - USER DEFINED HOOP STRESS
*RVNUM            10
*GFUNCTION         6
*DATASETNM         0
*METHOD            1
*PRINTOPT          0
*ANALTYP           0
*END
*DEFRANVR
RI
 0.9400000E+00 0.1000000E-01 0.1000000E+02
   0.91    0.97
RO
 0.1100000E+01 0.3300000E-02 0.1000000E+02
   1.098     1.11
E
 0.3403200E+08 0.6806400E+06 0.2000000E+01
XNU
 0.359375       0.00719        0.2000000E+01
ALPH
 0.5650000E-05 0.2830000E-06 0.2000000E+01
PI
 0.3077000E+04 0.1230000E+03 0.4000000E+01
PO
 0.3232000E+04 0.1292800E+03 0.4000000E+01
```

```
TI
 0.1940000E+03 0.3000000E+01 0.4000000E+01
TO
 0.1444000E+04 0.1500000E+02 0.4000000E+01
TREF
 0.5300000E+03 0.0000000E+00 0.2000000E+01
*END
*RESPONSE
C  LOX POST THICK CYLINDER MODEL
2AS
     1    11     0     0     0
   0.00000    0.00000    0.00000    0.00000    0.00000
*END
```

The results of the LOX post FPI and Monte Carlo analyses for hoop stress at the inner and outer radii are shown in Figures 9.3 and 9.4. The agreement between FPI and Monte Carlo is excellent for the closed form model. However, the hoop stress values clearly indicate that yielding will take place. A nonlinear model would be required to model this behavior correctly.

Figure 9.5 shows the sensitivity factors of the random variables for the hoop stress at R_i. The coefficient of thermal expansion clearly dominates. The internal and external radii are insignificant due to their tight tolerances. It should be pointed out that the COV used for the thermal coefficient (ALPHA), elastic modulus (E), Poisson's ratio (XNU), internal and external pressure (P_i and P_o) were chosen from default values given by Dr. Paul Wirsching (Table 9.3). This statistical data is suggested to be used when problem-specific data is not available. Use of improved statistical data may significantly alter the results. Special attention should be given in FY'89 to identification of more specific information about statistical distributions of input variables to the PAAM models.

Table 9.3

Default Distributions and COV for NESSUS Random Variables

VARIABLE	DISTRIBUTION	COV
E	Normal	0.02
n	Normal	0.02
G	Normal	0.02
r	Normal	0.02
a	Normal	0.05
Yield stress	Weibull	0.07
Coordinates	Normal	0.005
Thickness	Normal	0.005
Temperature	Lognormal	0.05
Pressure	Lognormal	0.04
Forces	Lognormal	0.02
Cross-sectional area	Normal	0.007
Inertia	Lognormal	0.02
Torsional constant	Lognormal	0.01
Springs	Lognormal	0.02
Blade angle - x,y,z	Normal	stdev = 0.1°
Material orientation	Normal	
Other	Lognormal	

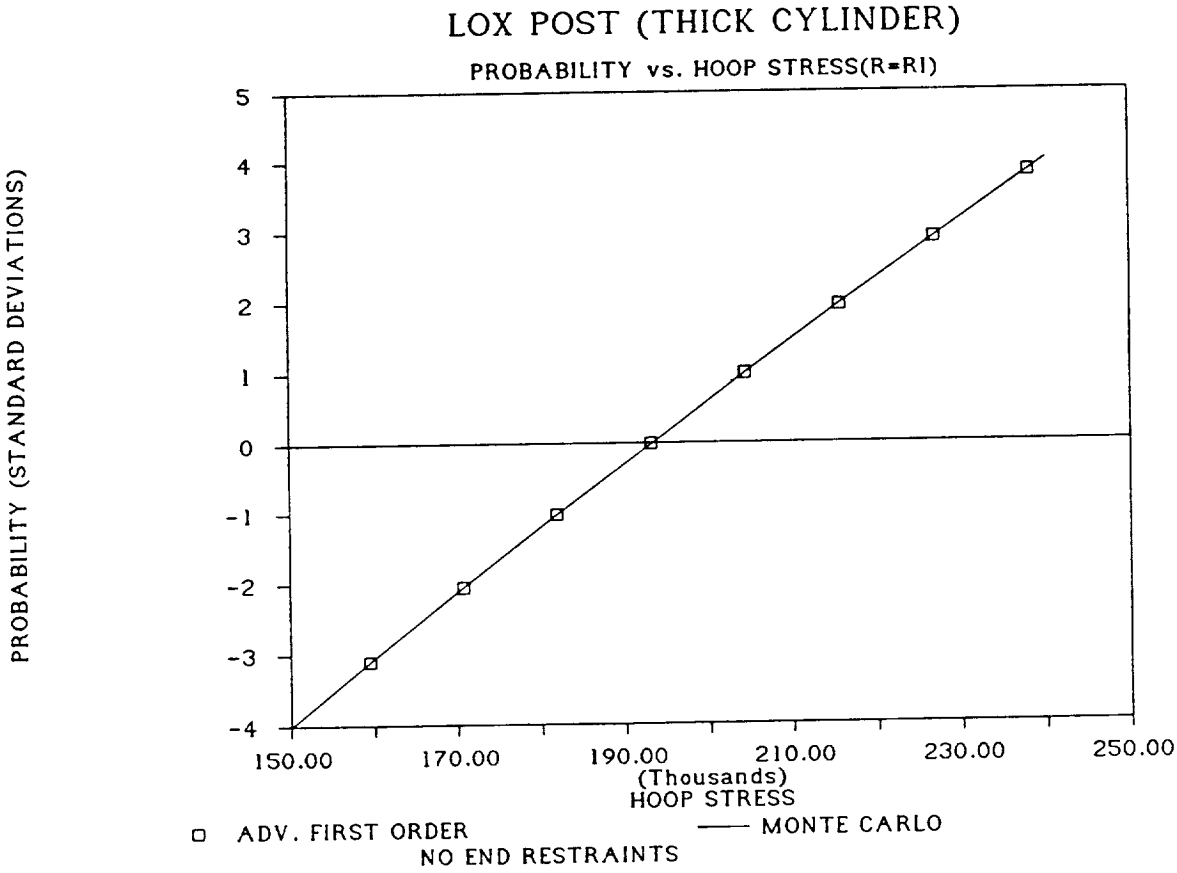

Figure 9.3 Cumulative Distribution Function of the LOX Post Hoop Stress at the Inner Radius

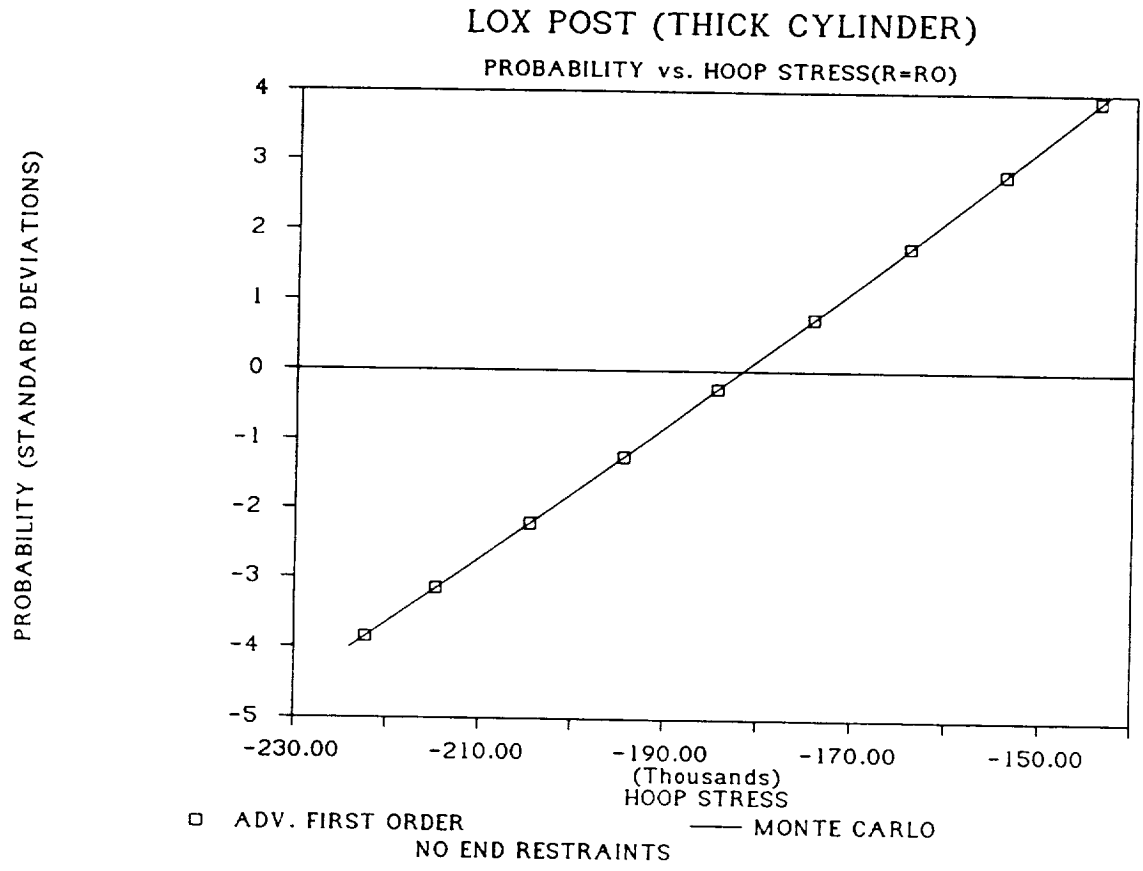

Figure 9.4 Cumulative Distribution Function of the LOX Post Hoop Stress at the Outer Radius

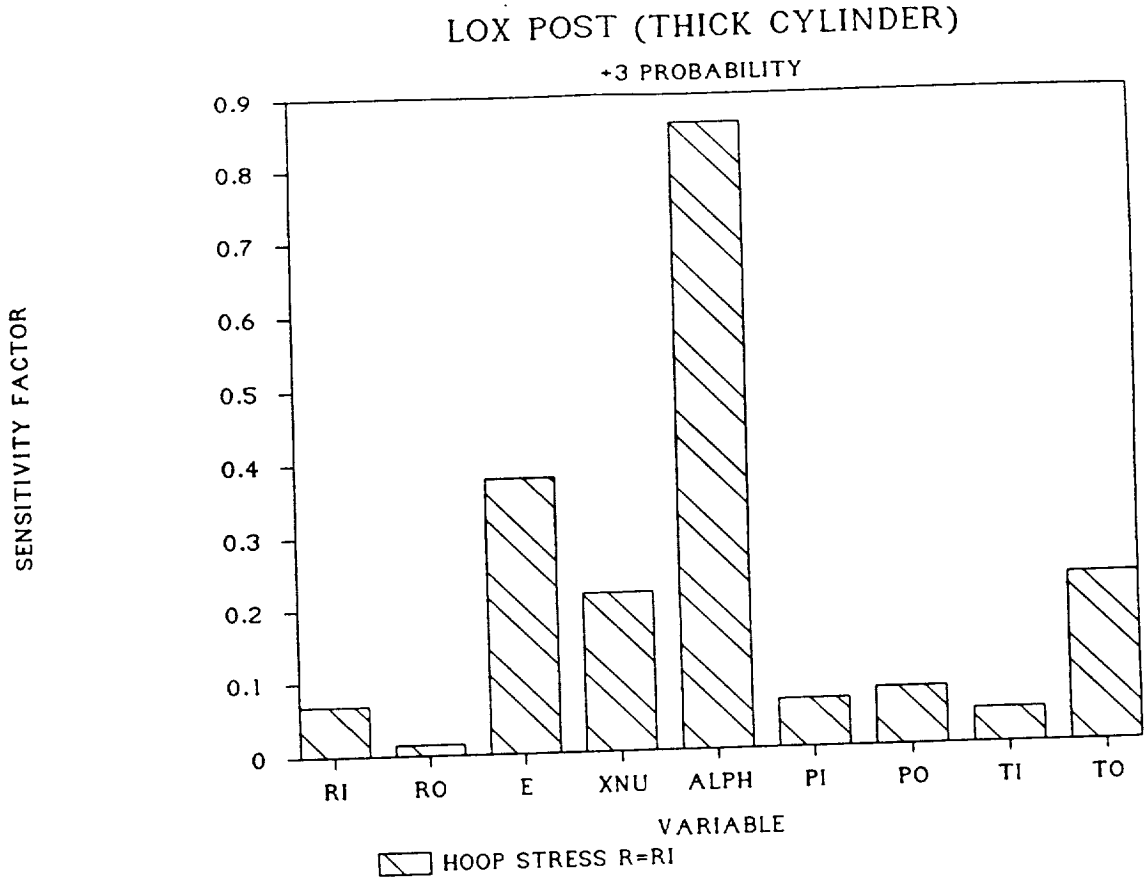

Figure 9.5 Sensitivity Factors for Random Variables in PAAM Analysis of LOX Post (Thick Cylinder Model, Calculation of Hoop Stress)

9.5 Future Work

Efforts in FY'89 will be focused on completing the development, coding, and validation of the simple linear models for all demonstration components. A majority of this work will involve the transparent FEM models for the turbine blade and HPOD.

Validation efforts will be extended by comparing PAAM results with NESSUS/FEM results for the PAAM models based on closed form expressions. A selected number of NESSUS finite element models corresponding to the simplified geometry and simplified loads of a PAAM model will be analyzed as validations of the PAAM analytical expressions and assumptions. Where possible, the PAAM results will also be compared to the NESSUS/FEM validation models which are based on more exact, complex representations of geometries and loads. This will provide some evaluation of the suitability of the geometry/load simplifications. This comparison will also permit some overall evaluation of the PAAM scheme relative to the conventional PSAM FEM scheme.

As funding permits, attention will be given to the development and validation of a select number of nonlinear models in order to demonstrate this general capability in the PAAM scheme.

9.6 References

[1] R. Rackwitz, and B. Fiessler, 1978, "Structural Reliability Under Combined Random Load Sequences," *Computers and Structures*, Vol. 9, pp. 489-494.

[2] Y.-T. Wu, and P.H. Wirsching, 1987, "New Algorithms for Structural Reliability Estimation," *J. Engineering Mechanics, ASCE*, Vol. 113, No., pp. 1319-1336.

[3] R.D. Blevins, 1979, *Formulas for Natural Frequency and Mode Shape*, Van Nostrand Reinhold, New York.

[4] R.C. Hibbeler, 1975, "Free Vibration of a Beam Support by Unsymmetrical Spring-Hinges," *J. Applied Mechanics, Trans, ASME*, Vol. 42, pp. 501-502.

[5] R.E.D. Bishop, and D.C. Johnson, 1979, *The Mechanics of Vibration*, Cambridge University Press.

10.0 STOCHASTIC THERMOVISCOPLASTICITY

10.1 Introduction

The constitutive theory of thermoviscoplasticity is extremely general in nature [1], and is capable of describing a very wide variety of material behaviors, ranging from linearly viscous fluids to rate independent elastoplastic solids. Most thermoviscoplastic (TVP) theories or material models, though, are phenomenological, with a feature of such models being their dependence on phenomenological parameters that serve to describe gross material characteristics such as hardening, softening, and hysteresis. These parameters usually are not directly related to the actual physical properties of the material that give rise to its gross behavioral characteristics. Thus, these models correlate a material's TVP behavior, but provide little or no insight into the active mechanisms that may be controlling the TVP behavior.

The purpose of the stochastic TVP material modeling effort within the PSAM project is to provide a sound basis for structural reliability modeling when stochastic TVP material behavior is to be included. The effort has been along two fronts. First, owing to the history (or path) dependent nature of TVP materials, and of phenomenological TVP material models that are typically used in calculations of structural response, a reasonable algorithm that preserves this path dependence has been proposed for calculating the evolution of the statistics of the TVP structure's response. An important aspect of this problem is that the structure's response statistics are directly related to the statistics of its material's initial state. Consequently, the second part consists of describing the initial material state in terms of physical, or "primitive", material properties that are readily observable (such as grain sizes and shapes, dislocation density, etc.) and whose statistical characteristics are more readily estimated. Calculations of probabilistic TVP material response using such "primitive", or mechanistic, constitutive models will yield insight into how the statistics of a phenomenological model's parameters are affected by the statistics of the readily observed "primitive" material variables.

10.2 Random Fields

The stochastic parameters of the probabilistic structural analysis problem may be split into two categories: the first being uncertainties in initial conditions; the second, uncertainties in external loading histories. The first category may contain uncertainties in initial material properties and uncertainties in the structure's initial geometry. In the most general case for random material behavior, the uncertainties in the initial material properties are described by random fields of these properties which initially span the structure. A random field is a function of three-dimensional space that possesses uncertainty of the parameters of the function, over the three-dimensional space [2].

The theory of random fields is fairly complex, but in practicality a finite element mesh is used to model the random field. Hence, the random fields can be reduced, as in the reference above, to sets of discrete, but correlated, random variables. To define the stochastic modeling problem, the uncertainties in the material properties need to be specified statistically. This is done by prescribing, as an initial condition, the joint probability density function (PDF) of these sets of (space-discrete) random material variables.

The second category of probabilistic variables may be introduced by prescribing uncertainties in the external loading history. In this case, the loading is a random function of time. Unlike the material modeling evolution, the stochastic nature of the loading can change at any time (e.g. random process). Similarly to before, the time axis can be discretized so that the loading history is prescribed through a set of discrete, correlated random variables with a specified joint PDF.

10.3 Probabilistic Evolution of TVP Behavior

It is taken as a basic tenant that, when a real TVP material is subject to a known loading history, its deformation mechanisms obey the laws of classical physics in a deterministic way, i.e., knowing its current history dependent microstructural state, and its current loading, the material "knows what to do," and it does not deform by means of a random process. If the constitutive model was to be a random process, then this behavior would be akin to having the material characteristics, at a material point, change without the influence of any thermodynamic force. This is equivalent to saying that the current behavior is not related to a physical set of initial conditions, and therefore, this violates an engineering sensibility for material behavior.

In short, for a real TVP material (of known geometry subject to a known loading history), the randomness of its initial state, or its microstructural primitive variables, is the sole source of its randomness at later times. Stochastic TVP material models should also exhibit this characteristic. So, a stochastic TVP material is one whose initial material state is random, but which for a known initial geometry and a known loading history, responds deterministically in an evolutionary or path dependent sense (given a realized set of initial material parameters).

The geometry of the structure is another probabilistic initial value problem. If one were to allow the structural geometry to change in an incrementally stochastic way during some known loading history, then once again, there seems to be no guarantee that a realizable initial structure exists that would evolve in a deterministic way, under any realizable loading history, to reach such a "non-deterministically changed" geometric state.

These concepts lead one to define a stochastic TVP structure as one whose initial material state and whose initial geometric configuration are random, but which under a known loading history, given a realized set of initial material and geometric parameters, responds deterministically in an evolutionary or path dependent sense.

10.3.1 Proposed Solution Algorithm

10.3.1.1- Overview

First, define $\mathbf{r}=\mathbf{r}(t)$ to be the response function of interest, where t is time. The function $\mathbf{r}$ is some subset of a complete realization, or analysis result. A realization is referred to herein as a physical occurrence out of many possible occurrences. For example: $\mathbf{r}$ could represent the realized deflection history at some critical location in the TVP structure; it could represent the realized history of a stress component at some critical location; or, in the extreme case, it could represent the entire solution to the structural analysis.

For the moment though, consider the case where $\mathbf{r}(t)$ is a scalar quantity. The probabilistic problem is then to find, given the statistical descriptions of the uncertain (or random) input parameters, the statistical description of $\mathbf{r}=\mathbf{r}(t)$. We choose, as this description, the response's cumulative probability distribution function (CDF), which will be denoted as $\mathbf{c}=\mathbf{c}(\mathbf{r};t)$. Note that the response's CDF also evolves with time. If $\mathbf{r}$ is not a scalar, for example if it is an n-vector $\mathbf{r}=(r_1,\ldots,r_n)$, then $\mathbf{c}$ is also an n-vector $\mathbf{c}=(c_1,\ldots,c_n)$, with c_i being the CDF of r_i $(i=1,\ldots,n)$.

Let $\mathbf{k}=(k_1,\ldots,k_N)$ represent the N discrete random parameters that describe the probabilistic TVP structure's random initial material and/or geometric state, and the random loading history to which it is subject, where the joint PDF of $\mathbf{k}$ is known. Also, denote the dependence of $\mathbf{r}$ on $\mathbf{k}$ as $\mathbf{r}=\mathbf{r}(\mathbf{k};t)$. The solution procedure presented below is based on the previously cited, fast probability integration (FPI) method of Wu. Given $\mathbf{r}=\mathbf{r}(\mathbf{k};t_0)$ and the joint PDF of $\mathbf{k}$ (t_0 is some fixed time), the FPI algorithm provides an efficient and accurate method for the calculation of $\mathbf{c}=\mathbf{c}(\mathbf{r};t_0)$. But, owing to the history dependence of the TVP structure, the function $\mathbf{r}=\mathbf{r}(\mathbf{k};t_0)$ is difficult (or at least potentially very time consuming) to calculate.

During the calculation of $\mathbf{c}=\mathbf{c}(\mathbf{r};t_0)$, the FPI code will need to evaluate $\mathbf{r}=\mathbf{r}(\mathbf{k};t_0)$ for many different values of $\mathbf{k}$. Conceptually then, for each evaluation of $\mathbf{r}$, a deterministic finite element analysis, for example, based on the particular needed realization of $\mathbf{k}$, needs to be performed in an incremental fashion integrating from time 0 to time t_0. Obviously, this is unacceptable if too many evaluations of $\mathbf{r}$ are needed.

A reasonable way to avoid the calculation of so many realizations is to construct an approximate analytical form for $\mathbf{r}=\mathbf{r}(\mathbf{k};t_0)$. The approach taken here is quite simple and, in fact, is the same that has been described by [3]. The idea is to pick several (say m) realizations of $\mathbf{k}$ (call them $\mathbf{k}_i$, $i=1,\ldots,m$), and calculate out to the latest time of interest the m deterministic TVP boundary value problems based on each of the $\mathbf{k}_i$'s in turn. Then, at t_0, a polynomial is fit to the m $(\mathbf{k}_i,\mathbf{r}_i=\mathbf{r}_i(\mathbf{k}_i;t_0))$ points, which provides an approximate analytical form for $\mathbf{r}=\mathbf{r}(\mathbf{k};t_0)$ that the FPI program can quickly evaluate when calculating

$\mathbf{c}=\mathbf{c}(\mathbf{r};t_0)$. Polynomial fits made at various other (fixed) times can then be used by the FPI program to calculate the evolution of $\mathbf{c}=\mathbf{c}(\mathbf{r};t)$ in time.

10.3.2 Example of Evolutionary Distributions

This example seeks to illustrate the nature of stochastic simulation of evolutionary relationships, such as occurs for TVP material response. The example will use pre-selected analytical response-time curves, which is done so that the exact expression for $\mathbf{c} = \mathbf{c}(\mathbf{r}; t)$ can be obtained and compared to the results of the FPI-based algorithm. The basic idea of the algorithm is to fit approximate response functions to evolved response-time curves at different time points, and to use the FPI algorithm to define the CDF results at user-selected time points. It will be seen that the algorithm is able to reproduce the exact results with excellent agreement. It will also be seen that the statistical nature of the answer is also evolving with time. In the next sub-section, this FPI-based algorithm will be applied to a simulated TVP material.

Let $\mathbf{r}$ be taken as a scalar (i.e., $\mathbf{r}=(r_1)$ and $\mathbf{c}=(c_1)$) and let N=1 (i.e., there is only one random variable, $\mathbf{k}=(k_1)$). For simplicity, denote (r_1) as r, (c_1) as c, and (k_1) as k. The PDF taken for k is

$$p(k) = -6k(k-1), \qquad 0<k<1. \tag{10.1}$$

Now choose, for example, five different k values (m=5) to span the range of interest, i.e., k=0.005, 0.250, 0.500, 0.750 and 0.995, and for each of these, say that a TVP boundary value problem was calculated out to a time of t=4 via incremental finite element analysis, which yielded the five traces of r vs t shown in the figure below.

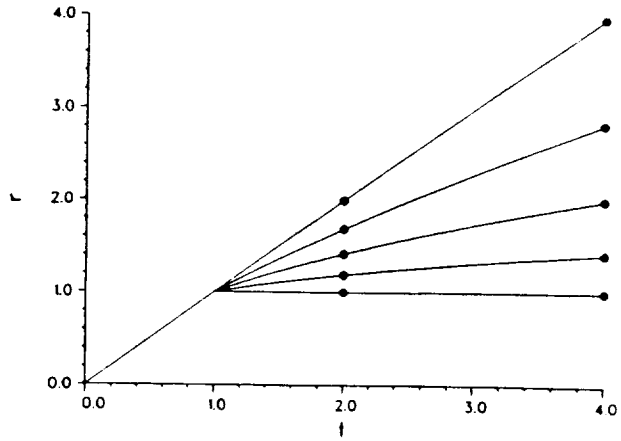

Figure 10.1(a). Realizations of Response vs. Time

The traces shown in the figure are actually plots of the response-time curve

$$r = t^k, \tag{10.2}$$

but, in general, the exact analytical form for these curves would not be known and is used here only for the sake of demonstration. Next, at some time of interest $t=t_0$, the five (k,r) points are used to define a fourth order polynomial, i.e.,

$$r = a_0 + a_1 k + a_2 k^2 + a_3 k^3 + a_4 k^4, \tag{10.3}$$

as the needed approximate analytical form for $r=r(k;t_0)$. For example, at $t_0=2$ one obtains,

$$a_0 = 1.0000008300 \qquad a_1 = 0.6929735040 \qquad a_2 = 0.2416176960 \tag{10.4}$$

$$a_3 = 0.0517377946 \qquad a_4 = 0.0136692352;$$

and at $t_0=4$,

$$a_0 = 1.000036140 \qquad a_1 = 1.378772670 \qquad a_2 = 1.020423210 \tag{10.5}$$

$$a_3 = 0.286825095 \qquad a_4 = 0.313897375.$$

The three equations above were used by the FPI program to obtain the CDF's $c(r;2)$ and $c(r;4)$ as indicated, respectively, by the +'s and squares in the figure below; the solid and dashed curves in the figure are the exact analytical solutions described above. As can be seen, this approach works quite well.

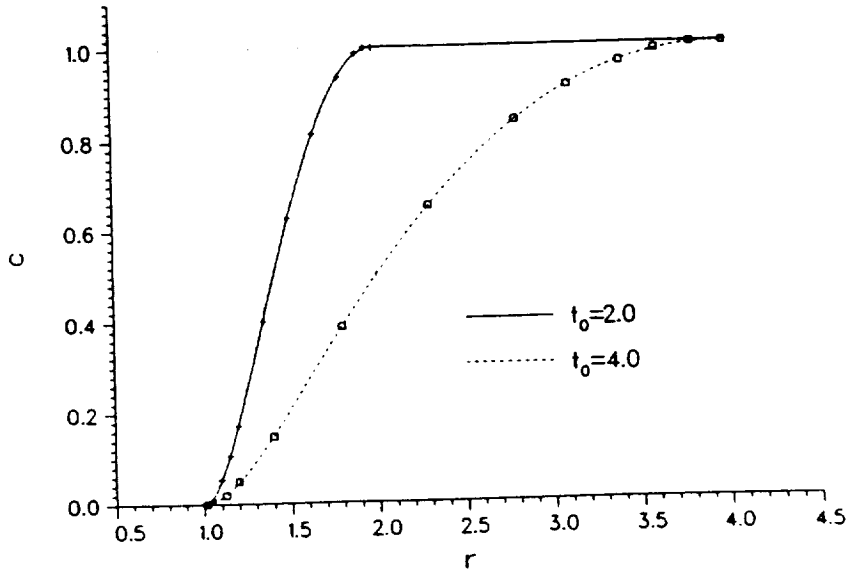

Figure 10.1(b). Calculated CDF at Two Time Levels

If $\mathbf{r}$ is a scalar and $\mathbf{k}=(k_1,k_2)$, then polynomial fits at various times could be made to, e.g.,

$$r = b_0 + b_1 k_1 + b_2 k_2 + b_3 k_1^2 + b_4 k_1 k_2 + b_5 k_2^2. \tag{10.6}$$

a procedure which would require that six realizations be obtained. Obviously, if there are many random variables, or if polynomial fits of high order are required, then the amount of computation can become excessive.

For TVP boundary value problems though, a solution procedure that would reduce the amount of computation is not readily evident, since, e.g., the perturbation technique of [4] does not appear to have an obvious extension to this case of history dependence. If one were to imagine the existence of a procedure that did allow for the calculation of only a few (or, ideally, one) realizations, then the FPI program would not have enough information to perform the evaluations of $\mathbf{r}=\mathbf{r}(\mathbf{k};t_0)$. Consequently, if the perturbation technique was applied to obtain this additionally required information by using, at t_0, one of the realizations as a base from which to perturb, then this would be equivalent to having the material deform by a random process. As was previously discussed, this is an unacceptable situation. Additional research is needed if a solution procedure more efficient than the one presented above is to be found.

Finally, it should be noted that perturbation techniques can be used for history insensitive nonlinear problems (such as the finite elasticity of a perfect rubber band), since it is irrelevant by what path one arrives at the current state. In such a case, a sensible algorithm would be to track a single realization $\mathbf{r}=\mathbf{r}(\mathbf{k};t)$, e.g., the one corresponding to the mean value of $\mathbf{k}$. Then, at some t_0 where $\mathbf{c}=\mathbf{c}(\mathbf{r};t_0)$ is desired, the $\mathbf{r}$-solution obtained from the mean value of $\mathbf{k}$ could be used as a base from which to iterate (e.g., using the equations of finite elasticity) toward and to any new $\mathbf{r}=\mathbf{r}(\mathbf{k};t_0)$ that the FPI program may require.

10.3.3 Probabilistic TVP Tension Test

As an example of probabilistic TVP material modeling, the above procedure is applied to a high-temperature (or creep) tension test. The creep model used is based on the mechanism of grain boundary sliding with grain boundary diffusional accommodation, and is similar in spirit to the model of [5].

The polycrystalline material is idealized as being a two-dimensional array of hexogonal grains, as depicted in Part (a) of the figure below, with the grain's current size and shape being defined by the lengths and d and l. As indicated in the figure, the assemblage is subjected to an overall tensile true stress σ_2, with the other overall in-plane stress components being zero. Under such a loading, the deformation is assumed to occur by grain boundary sliding in the mode shown by Part (b) of the figure, where the left and right grains are being "pulled in" by the

"void" on the grain boundary BE. In this state, the grain boundaries AB, BC, DE and EF have (local) compressive stresses acting normally across them, and the grain boundary BE has a tensile normal stress acting across it.

The local normal stresses lead to diffusional mass flux along the grain boundaries in the senses indicated by the arrows, and this removes mass from along the four oblique grain boundaries and deposits it in the "void" of grain boundary BE. In this way, the deformation is diffusionally accommodated.

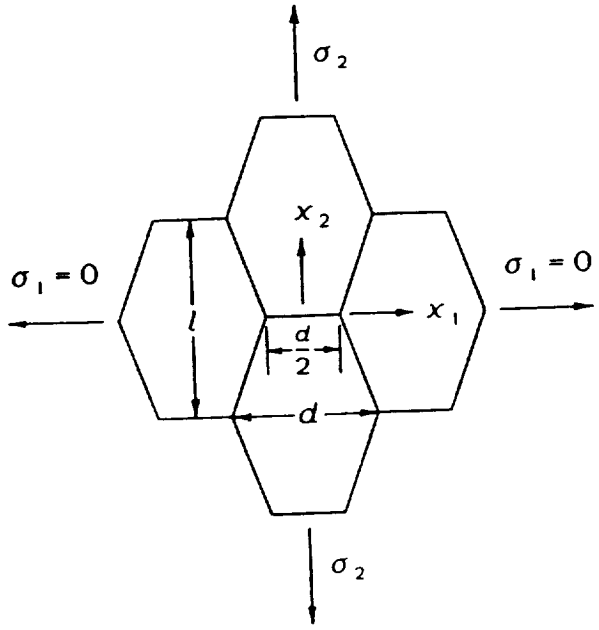

Figure 10.2(a). Idealized Two-Dimensional Microstructure

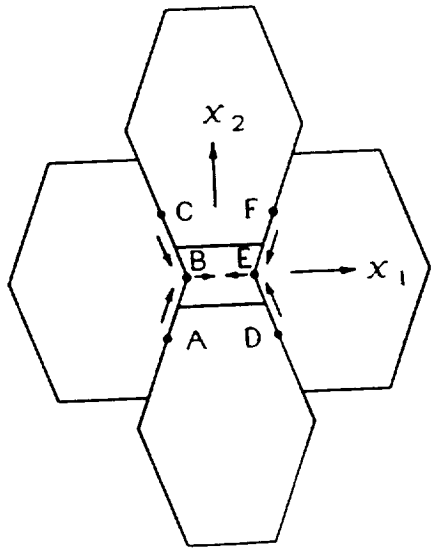

Figure 10.2(b). Grain Boundary Sliding Deformation Mode

In a method similar to that of [5], the grain boundary mass flux is taken proportional to $d\sigma_n/dS$ (where σ_n is the normal stress acting across the grain boundary, and S is the distance along the grain boundary). This, coupled with mass conservation allows one to find, for a given overall inelastic strain rate, $\dot{\epsilon}_2^I$, the corresponding distribution of σ_n along the grain boundaries. Force equilibrium applied to certain grain cross-sections, along with the assumption that the grain boundaries support no shear stress, then provides the corresponding value of σ_2.

The procedure [6] yields, for this orthotropic deformation mode, the simple flow rule

$$\dot{\epsilon}_2^I = \frac{24\sqrt{3}D}{d^3 f(A)}\sigma_2 \qquad \dot{\epsilon}_1^I = -\dot{\epsilon}_2^I \qquad \dot{\epsilon}_3^I = 0. \tag{10.7}$$

where $\dot{\epsilon}_i^I$ (i=1,2,3) are the three inelastic logarithmic strain rates along each of the coordinate axes (there are no shear strains), d is the current grain width as indicated in the above figure, and D is a diffusion coefficient (to be defined below). The function $f(A)$ is

$$f(A) = A^3\left(\frac{1}{4}+\frac{3}{4A^2}\right)\left\{\frac{1}{A^2}+\frac{\sqrt{3}}{8}\left(A-\frac{1}{A}\right)\sqrt{1+\frac{1}{3A^2}}\right\} \qquad A = \frac{2l}{\sqrt{3}d}. \tag{10.8}$$

where A is the current grain aspect ratio ($A = 1$ corresponds to the grains being regular hexagons). In the previous two equations, the current size and shape of the grains are determined from the simple evolution equations

$$\dot{l} = l\dot{\epsilon}_2 \qquad \dot{d} = d\dot{\epsilon}_1, \qquad \text{with} \qquad \dot{\epsilon}_i = \dot{\epsilon}_i^E + \dot{\epsilon}_i^I \tag{10.9}$$

where $\dot{\epsilon}_i$ and $\dot{\epsilon}_i^E$ (i=1,2,3) are, respectively, the total and elastic logarithmic strain rates. The diffusion coefficient D is given by

$$D = \frac{D_b\delta\Omega}{BT} \qquad D_b = D_b^0\exp\left(-\frac{Q_b}{RT}\right) \qquad R = N_{av}B, \tag{10.10}$$

where B is Boltzmann's constant, T is absolute temperature, and N_{av} is Avogadro's number. The grain boundary thickness δ is assumed to remain constant with time, as are the constants Ω (the molecular volume), D_b^0 (the limiting grain boundary diffusivity) and Q_b (the grain boundary diffusion activation energy).

The flow rule is implemented as follows. First the elasticity is taken as isotropic, i.e.,

$$C_{ij} = \begin{pmatrix} \lambda+2\mu & \lambda & \lambda \\ \lambda & \lambda+2\mu & \lambda \\ \lambda & \lambda & \lambda+2\mu \end{pmatrix} \qquad \dot{\sigma}_i = C_{ij}\dot{\epsilon}^E_j \tag{10.11}$$

where μ and λ are, respectively, the shear modulus and Lamé constant, $\dot{\sigma}_i$ (i=1,2,3) are the true normal stress rates along each of the coordinate directions (there are no shear stresses), and where the summation convention is used. Next, combining the last of the above two equations, the rate constitutive law is written as

$$\dot{\sigma}_i = C_{ij}\dot{\epsilon}_j - \dot{Y}_i, \qquad \text{with} \qquad \dot{Y}_i = C_{ij}\dot{\epsilon}^I_j. \tag{10.12}$$

Now, a uniaxial tension test with a prescribed tensile strain rate is modeled by prescribing the two-dimensional model's effective strain rate $\dot{\epsilon}_E$. Thus, the conditions

$$\dot{\sigma}_1 = 0 \qquad \dot{\epsilon}_3 = 0 \qquad \dot{\epsilon}_E = \sqrt{\frac{2}{3}(\dot{\epsilon}_1^2 + \dot{\epsilon}_2^2)} = \text{prescribed rate} \tag{10.13}$$

are used when eqn. (10.8) is integrated through time to obtain the two-dimensional model's stress-strain history. Finally, from this history, the effective (or uniaxial) strain ϵ_E vs effective (or uniaxial) stress

$$\sigma_E = \sqrt{\sigma_2^2 - \sigma_2\sigma_3 + \sigma_3^2} \tag{10.14}$$

curve is obtained.

The discrete points in the figure below show two experimental uniaxial stress-strain curves for B1900+Hf, a Ni-based superalloy, pulled at a constant strain rate of 8.3×10^{-5} sec^{-1} [7]. The continuous curves in the figure are the model results, also for $\dot{\epsilon}_E = 8.3 \times 10^{-5}$ sec^{-1}. The grain size of this material was quoted as 75 μm, and this was incorporated into the model by setting l = 75 μm and A = 1 as initial conditions. "Handbook" values for Ni [8] were used for δD^0_b (= 3.5×10^{-15} m^3/sec) and Ω (= 1.09×10^{-29} m^3), and Q_b = 72.5 kJ/mole was also used. Reference [8] quotes Q_b = 115 kJ/mole for Ni. At T = 1144K, the elasticity was specified as E = 165 GPa (Young's modulus) and $\nu = \lambda/(\lambda+\mu)/2 = 0.48$ (Poisson's ratio), and at T=1255K the specification was E=150 GPa and $\nu = 0.48$. As is seen, the model can be made to fit the experimental data reasonably well with reasonable values of the material constants, especially at the higher temperature.

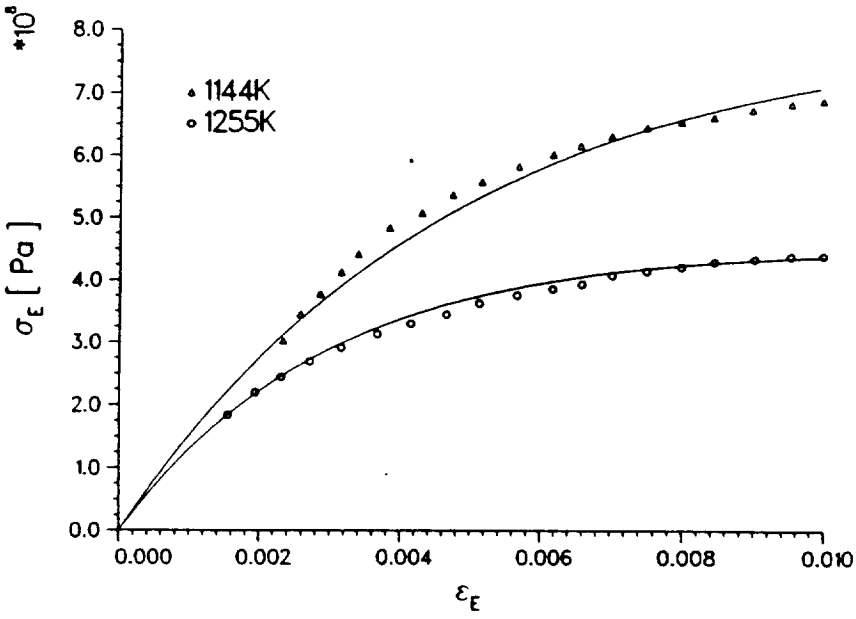

Figure 10.3. Comparison of Creep Model with Experimental Uniaxial Stress-Strain Data

In the current probabilistic problem, both the deformation and the material properties of the tensile bar are taken as being uniform with respect to space. The T=1255K case is considered, and all of the constants are as above, except that now E and Q_b are random, i.e.,

$$E = \frac{\mu(3\lambda + 2\mu)}{\lambda + \mu} = k_1 \qquad Q_b = k_2. \tag{10.15}$$

Also, the effective stress is taken as the response, i.e., $\sigma_E = r$. The variables E and Q_b are assumed to be statistically independent, and each has a truncated normal distribution as its PDF. The mean value of E, i.e., $\mu(E)$, is chosen as 150 GPa, and $\mu(Q_b)$ is chosen as 72.5 kJ/mole. The standard deviations for the problem are $\sigma(E)$ = 10 GPa and $\sigma(Q_b)$ = 0.5 kJ/mole. The cut-off values for both of these PDF's are taken to occur at plus and minus three standard deviations from the mean.

In order to construct accurate representations of $r = r(k; t_0)$, 25 separate realizations were calculated, each corresponding to one of the possible combinations of E = 120.5, 135.0, 150.0, 165.0 and 179.5 GPa, and Q_b = 71.05, 71.75, 72.50, 73.25 and 73.95 kJ/mole. The 25 resulting stress-strain curves are shown in the next figure, and at each of the three different time levels shown, i.e., t_0 = 10.0 sec (ϵ_E = 8.3 x

10^{-4}), 67.5 sec (ϵ_E = 5.6025 x 10^{-3}) and 300. sec (ϵ_E = 2.49 x 10^{-2}), the 25 (k, r) points were fit to a fourth order, two-dimensional Lagrangian polynomial, i.e., a polynomial whose individual terms are

(10.16)

$$
\begin{array}{ccccc}
1 & k_1 & k_1^2 & k_1^3 & k_1^4 \\
k_2 & k_1k_2 & k_1^2k_2 & k_1^3k_2 & k_1^4k_2 \\
k_2^2 & k_1k_2^2 & k_1^2k_2^2 & k_1^3k_2^2 & k_1^4k_2^2 \\
k_2^3 & k_1k_2^3 & k_1^2k_2^3 & k_1^3k_2^3 & k_1^4k_2^3 \\
k_2^4 & k_1k_2^4 & k_1^2k_2^4 & k_1^3k_2^4 & k_1^4k_2^4
\end{array}
$$

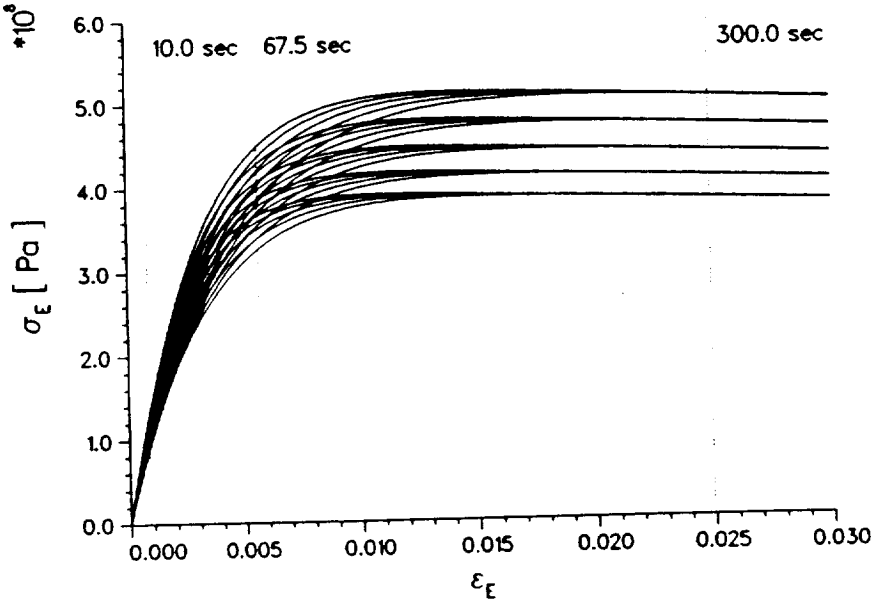

Figure 10.4. Stress-Strain Realizations for the Probabilistic Creep Problem

The three resulting polynomials were then used by the FPI program to obtain the CDF's $c(\sigma_E;\ 10.0\ \text{sec})$, $c(\sigma_E;\ 67.5\ \text{sec})$, and $c(\sigma_E;\ 300.0\ \text{sec})$, which are shown in the following figures. The probability levels of c are expressed in terms of the standard normal unit u, i.e.,

(10.17)

$$c = \frac{1}{2} + \frac{1}{2}\,\text{erf}\left(\frac{u}{\sqrt{2}}\right) \qquad \text{with} \qquad u = \frac{\sigma_E - \mu(\sigma_E)}{\sigma(\sigma_E)},$$

where "erf" is the error function (a normal distribution plots as a straight line on such a graph). As is seen, the character of the distribution changes in time: at t_0 = 10.0 and 300.0 sec, fairly high curvatures are exhibited in the distributions' tails, while at t_0 = 67.5

sec the curvature is less pronounced. This is due to the fact that, at t_0 = 10.0 sec, E is dominant (i.e., $\partial\sigma_\varepsilon/\partial Q_b \sim 0$) and at t_0 = 300.0 sec Q_b is dominant ($\partial\sigma_\varepsilon/\partial E \sim 0$), while at t_0 = 67.5 sec neither dominates.

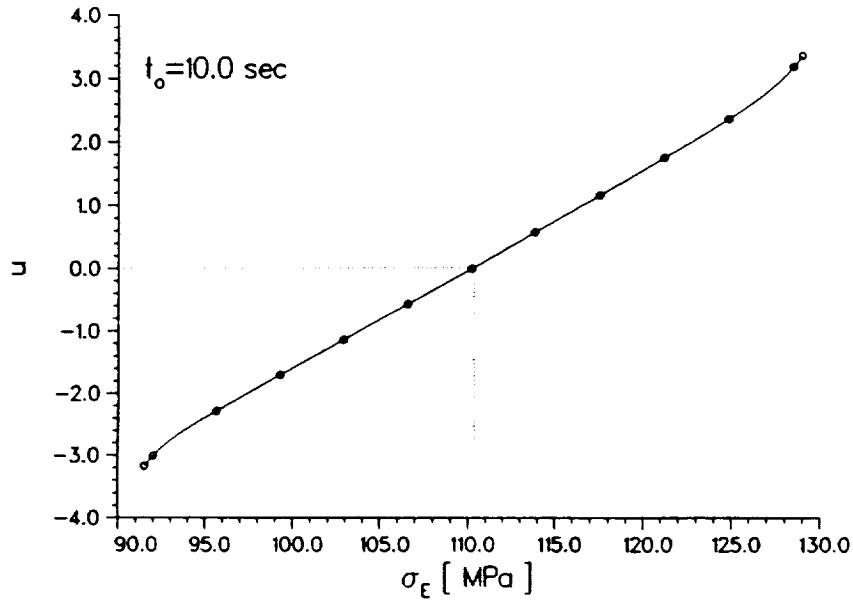

Figure 10.5(a). Calculated CDF for the Creep Problem at 10.0 sec

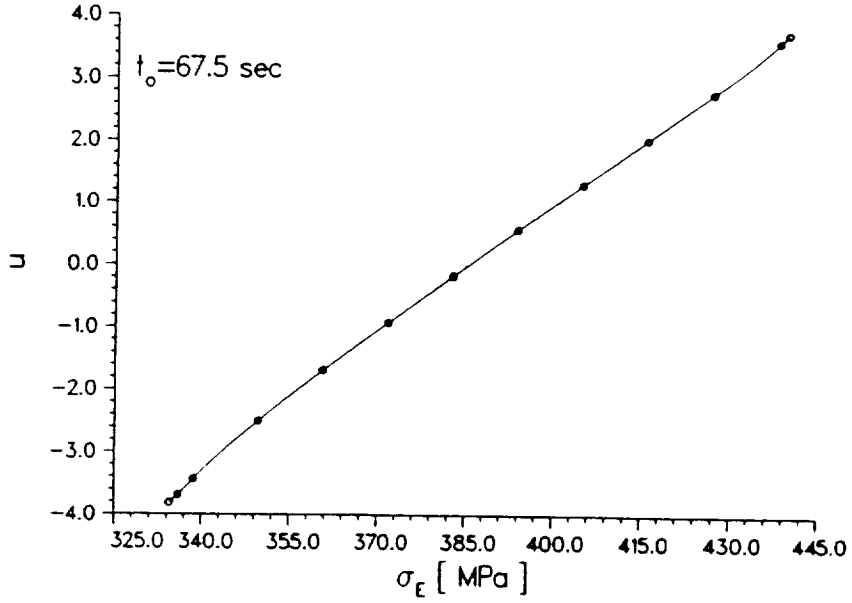

Figure 10.5(b). Calculated CDF for the Creep Problem at 67.5 sec

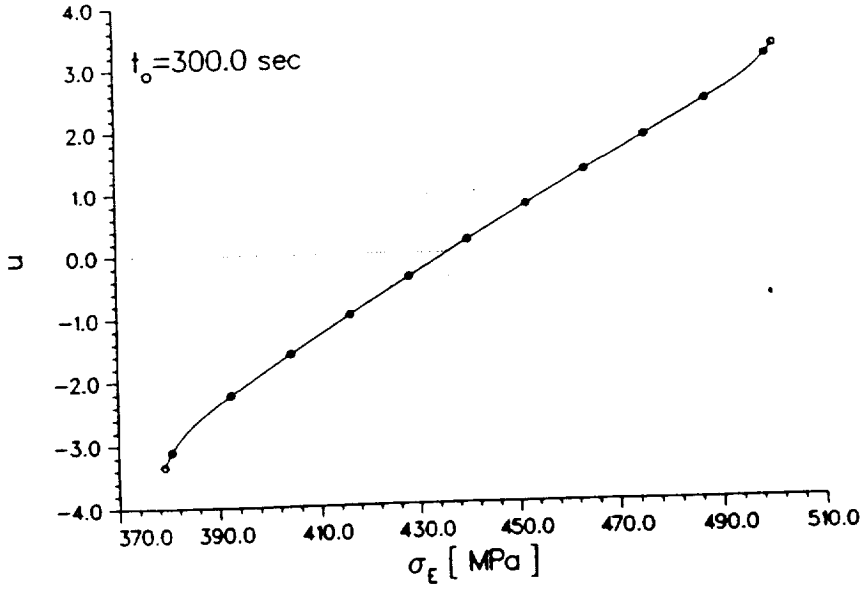

Figure 10.5(c). Calculated CDF for the Creep Problem at 300.0 sec

10.4 References

[1] K. P. Walker, K. P., 1981, "Research and Development Program for Nonlinear Structural Modeling with Advanced Time-Temperature Dependent Constitutive Relationships," NASA CR-165533.

[2] W.K. Liu, T. Belytschko, and A. Mani, 1986, "Random Field Finite Elements," *International Journal for Numerical Methods in Engineering*, 23, 1831-1845.

[3] Y.-T. Wu, and P.H. Wirsching, 1984, "Advanced Reliability Method for Fatigue Analysis," ASCE *Journal of Engineering Mechanics*, 110, 536-553.

[4] T.A. Cruse, O.H. Burnside, Y.-T. Wu, E.Z. Polch, and J.B. Dias, 1988, "Probabilistic Structural Analysis Methods for Select Space Propulsion System Structural Components," *Computers & Structures*, 29, 891-901.

[5] R. Raj, and M.F. Ashby, 1971, "On Grain Boundary Sliding and Diffusional Creep," *Metallurgical Transactions*, 2, 1113-1127.

[6] S.V. Harren, 1988, unpublished research.

[7] U.S. Lindholm, K.S. Chang, S.R. Bodner, R.M. Weber, R.T. Walker, and E.N. Cassenti, 1985, "Constitutive Modeling for Isotropic Materials (HOST): Second Annual Status Report," NASA CR-174980.

[8] A. Needleman, and J.R. Rice, 1980, "Plastic Creep Flow Effects in the Diffusive Cavitation of Grain Boundaries," *Acta Metallurgica*, 28, 1315-1332.

APPENDIX A

The Most Probable Point Locus Method for Constructing the Probability Distribution of a Response Variable

P. Wirsching
University of Arizona

THE MOST PROBABLE POINT LOCUS METHOD FOR CONSTRUCTING THE PROBABILITY DISTRIBUTION OF A RESPONSE VARIABLE

SUMMARY

The most probable point locus method (MPPL) is an iterative process to compute the CDF of a response variable (i.e., a function of several random variables). It was shown that the MPPL CDF converges to the exact after one iteration in five examples of non-linear response functions and non-normal variates. This is "good news" when the response function is implicit because the number of costly function evaluations required by MPPL is limited relative to other methods for constructing CDF's.

THE MOST PROBABLE POINT LOCUS (MPPL) ALGORITHM

Consider a response function

$$Z = Z(\underset{\sim}{X})$$

where $\underset{\sim}{X}$ is a vector of n random design factors. Z can be either explicit or implicit. Determine the CDF of Z, denoted as F_Z. If Z is an explicit function of $\underset{\sim}{X}$, then the construction of F_Z is straightforward using Monte Carlo or fast probability integration. All numerical reliability methods require many (100 to 10,000) function evaluations, a very fast operation with a digital computer if Z is an explicit function of $\underset{\sim}{X}$.

However, when Z is an implicit function (e.g., $Z(\underset{\sim}{X})$ defined only through a finite element code) a single function evaluation may be costly. So the fundamental question is how do we construct a high quality CDF of Z with a very minimum of function evaluations?

The most probable point locus method (MPPL) as proposed by Y. T. Wu may be close to the optimum in requiring a minimum number of function

evaluations relative to the accuracy of F_Z. There is no formal proof of this, but intuition suggests that it would be difficult to produce a reasonable estimate of F_Z with fewer function evaluations.

The basic MPPL scheme, an iterative process, is described in some detail in Table 1. A plot of the CDF as constructed by four MPPL iterations (moves) is shown in Fig. 1. But the key issue is the number of function evaluations required for each move. A summary of the function evaluations is shown in Table 2 for two different sets of points used to estimate the CDF. When nine points (four points on each side of the mean) are used to construct the CDF, it is expected that F_Z would be more accurate than the seven point approximation. However, experience has shown that high quality CDF's can be constructed with the seven point system.

EXAMPLES

Attached are five examples. In each case the response function is non-linear and/or some or all of the variates are non-normal. In all cases a nine point CDF scheme was employed and the CDF curves shown in the figures were fit by a cubic spline in the graphics program.

For each example there are four plots.

1. The CDF based on the linear approximation to the response function (Step 5 in Table 1).
2. The CDF after the 1st move. (Step 6 in Table 1).
3. The CDF after the 2nd move. (Step 9 in Table 1).
4. The CDF after the 3rd move. (Step 10 in Table 1).

The CDF of Z by the MPPL approximation is compared to the exact in all of the figures. Upon examination of the curves, the following general conclusions can be drawn.

1. $F_{\bar{Z}}$ estimated from a linear approximation to the response function is generally a poor approximation to the exact.
2. The first move produces, in all cases, a "good" approximation to the exact.
3. Little improvement is realized by the second and third moves.

These results are good news relative to the goal of limiting the number of function evaluations required. Assuming that a seven point scheme is used, the number of function evaluations is shown as a function of the number of variables in Fig. 2. Clearly, computer costs for the 1st move CDF will be small relative to the 2nd and 3rd iteration. A general (qualitative) conclusion is that the 1st move CDF will be the most "efficient."

Table 1

FLOW CHART FOR THE MOST PROBABLE POINT LOCUS PROBLEM

Input:

1. Response function, (explicit or implicit); $Z = Z(\underset{\sim}{X})$
2. Mean, std. dev. of each basic variable, X_i; i = 1,2, . . . N

Evaluate Z at mean values $\underset{\sim}{\mu}$ of $\underset{\sim}{X}$ and at perturbed values of $(\mu + 0.1\ \sigma_i)$ of each X_i, all other variables equal the means. There are a total of N + 1 function evaluations.

STEP 1

Using results of Step 1, estimate μ_Z and σ_Z using the approximate forms . . . . $\mu_Z \overset{\sim}{=} Z(\underset{\sim}{\mu})$

$$\sigma_Z \overset{\sim}{=} \sqrt{\Sigma\left(\frac{\partial Z}{\partial X}\right)^2 \sigma_i^2}$$

Derivatives evaluated from the perturbation results of Step 1.

STEP 2

Define the sample space for Z

$Z_j = \mu_Z + j\sigma_Z$

j = -4, -3, . . . , 0, 1, , , , 3, 4

Note: In this example, the CDF will be defined by 9 points, but the number is arbitrary

STEP 3

Using the results from Step 1, expand Z as linear functions about $\underset{\sim}{\mu}$

STEP 4

$Z = a_o + \Sigma a_i X_i$

Use Wu/FPI to compute:

1. β_j for each Z_j
2. Design point for each Z_j, denoted as X_j^*

THIS IS THE FIRST ESTIMATE OF THE CDF OF Z

STEP 5

STEP 6 (AMVFO)

1st MOVE: Improve the CDF of Z by an improved value of Z_j at each β_j, namely the value of Z_j at the design point $\underset{\sim}{X}_j^*$ from Step 5.

$$Z_j^* = Z(\underset{\sim}{X}_j^*)$$

$$j = -4, -3, -2, -1, 1, 2, 3$$

In this example, there are eight function evaluations. The choice is arbitrary. There could be fewer.

STEP 7

To further improve the CDF, obtain perturbed solutions for Z at all $\underset{\sim}{X}_j^*$, e.g., $Z(X_1^* + .1\sigma_{X_1}, X_2^*)$ for an example of two variables. Here there will be a total of N function evaluations.

STEP 8

Expand Z as a linear function at each $\underset{\sim}{X}_j^*$

STEP 9

2nd MOVE: Improve the estimate of the CDF of Z by an improved β at each Z_j of Step 6. For each Z of Step 8 use Wu/FPI to compute,

1. β_j for each Z_j
2. Design point for each Z_j denoted as $\underset{\sim}{X}_j^*$

STEP 10

3rd MOVE: Improve the CDF of Z by an improved value of Z_j at each β_j; namely the value of Z_i at the design point $\underset{\sim}{X}_j^*$ from step 9. Compute $Z_j^* = Z(\underset{\sim}{X}_j^*)$

$$j = -4, -3, -2, -1, 1, 2, 3 + 4$$

Here there are eight function evaluations.

At this point, the iteration process could be continued by repeating Steps 7 through 10. However, it is thought that there will be little improvement in the quality of the CDF.

Table 2. Number of Function Evaluations Required

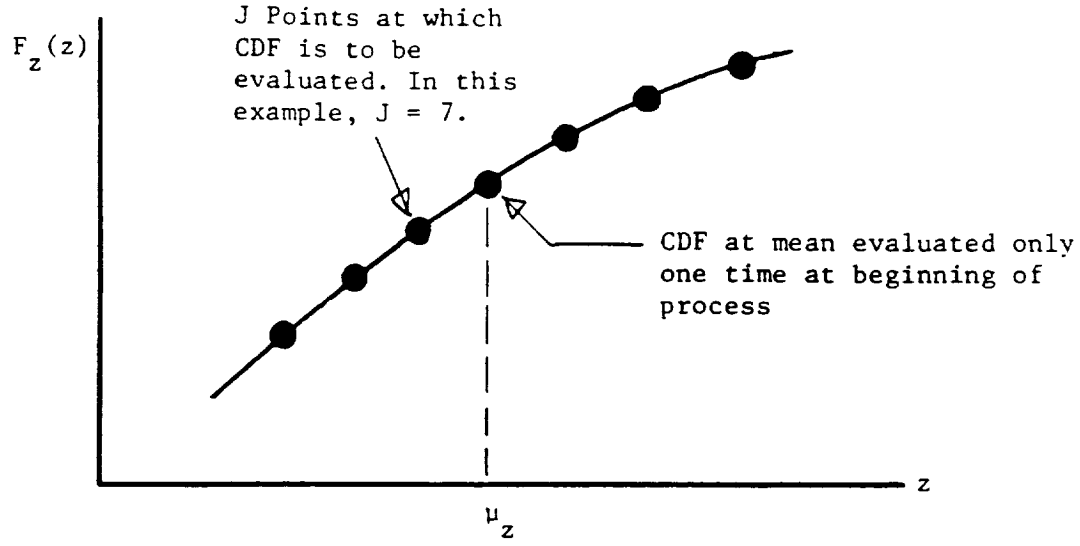

N = number of random variables

	Total Function Evaluations
First Estimation: Linear performance function	N + 1
1st Move. Function evaluation at each design point (except mean). J-1 evaluations	N + J
2nd Move. Construct linear function at each of the J-1 design points. At each point, need only the perturbed value for each of the N variables N(J-1 evaluations)	J(N + 1)
3rd Move. Function evaluation at each design point (except mean). J-1 evaluations	J(2 + N) - 1

Fig. 1 Construction of the CDF of Z by the Iterative MPPL

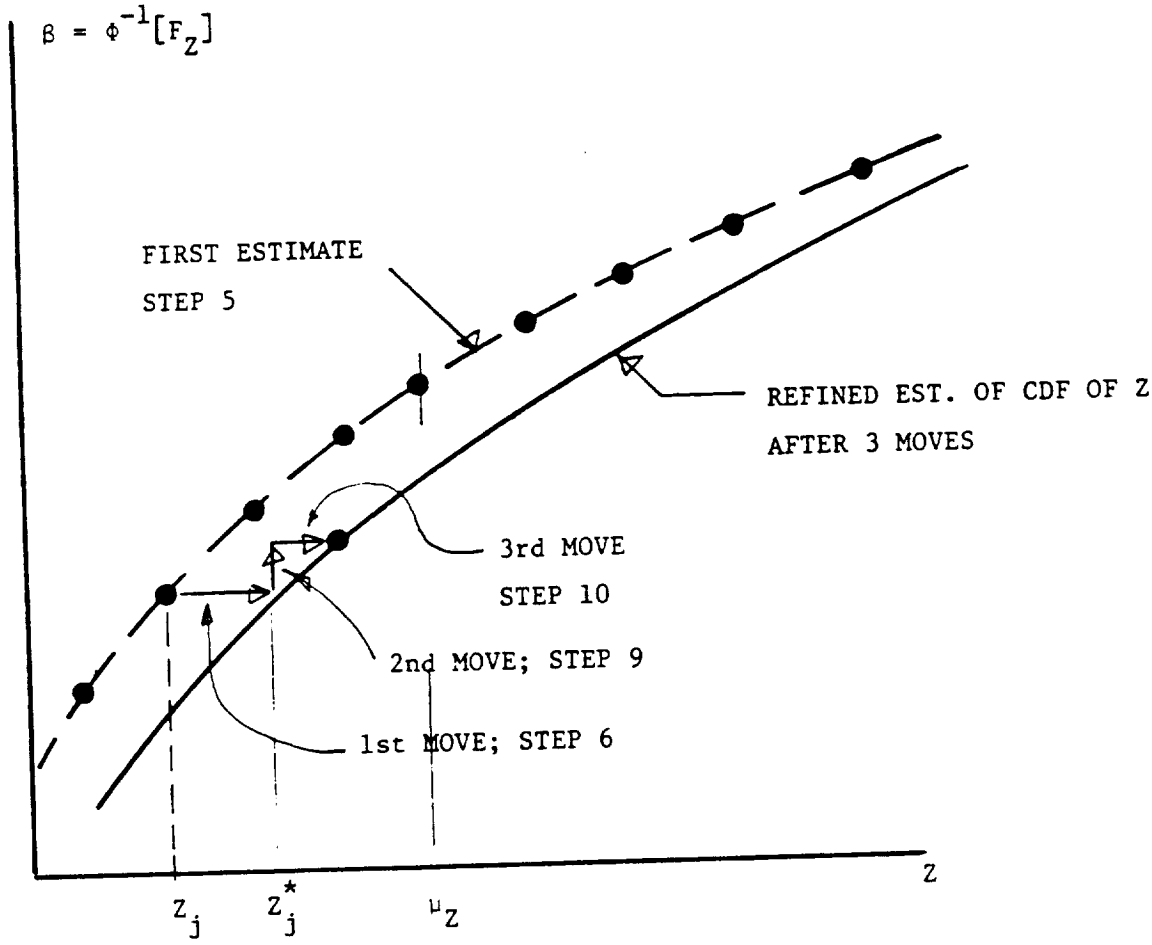

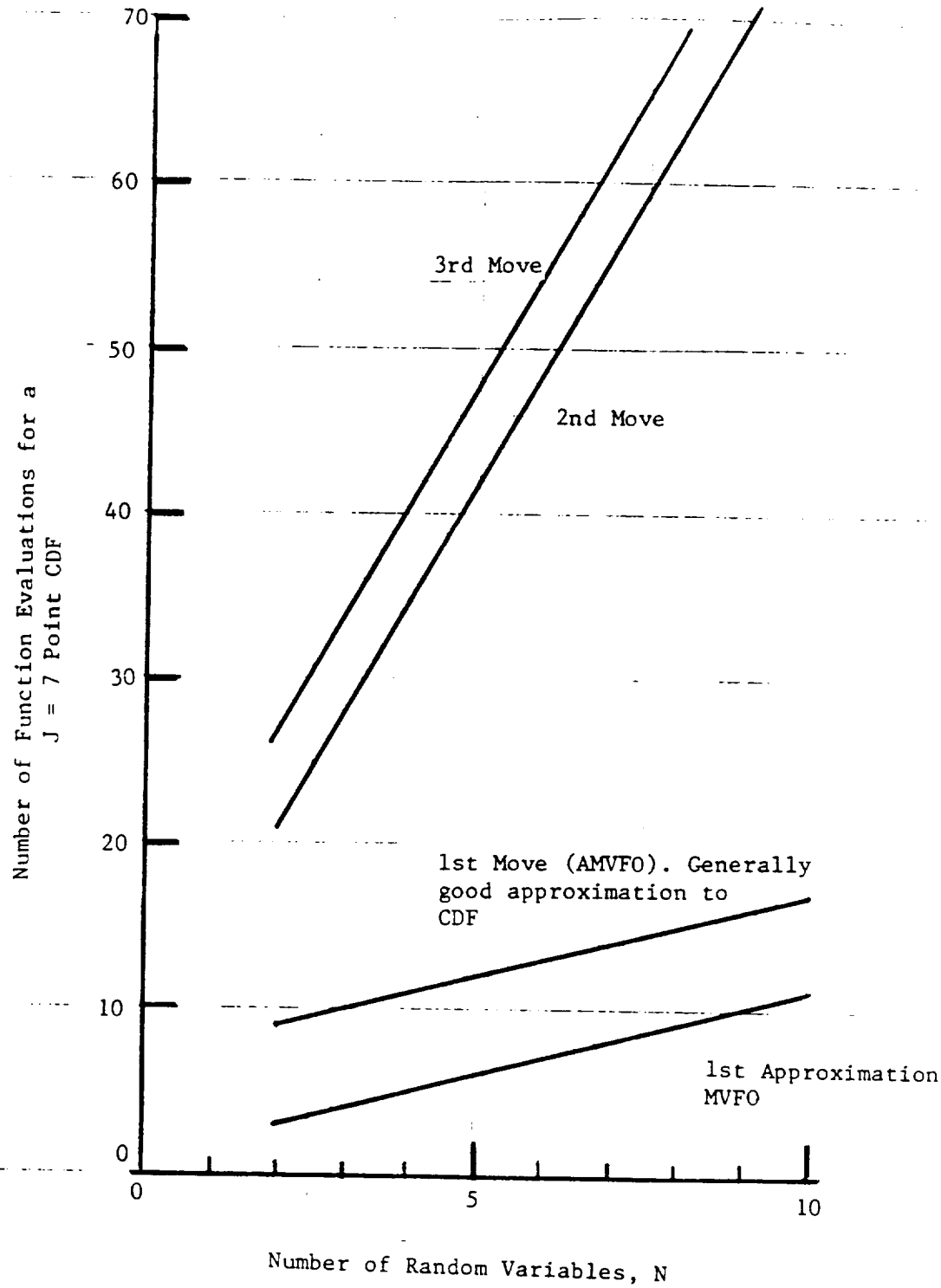

Fig. 2 Number of Function Evaluations vs. Number of Variables for a J = 7 Point CDF.

LINEAR PERFORMANCE FUNCTION

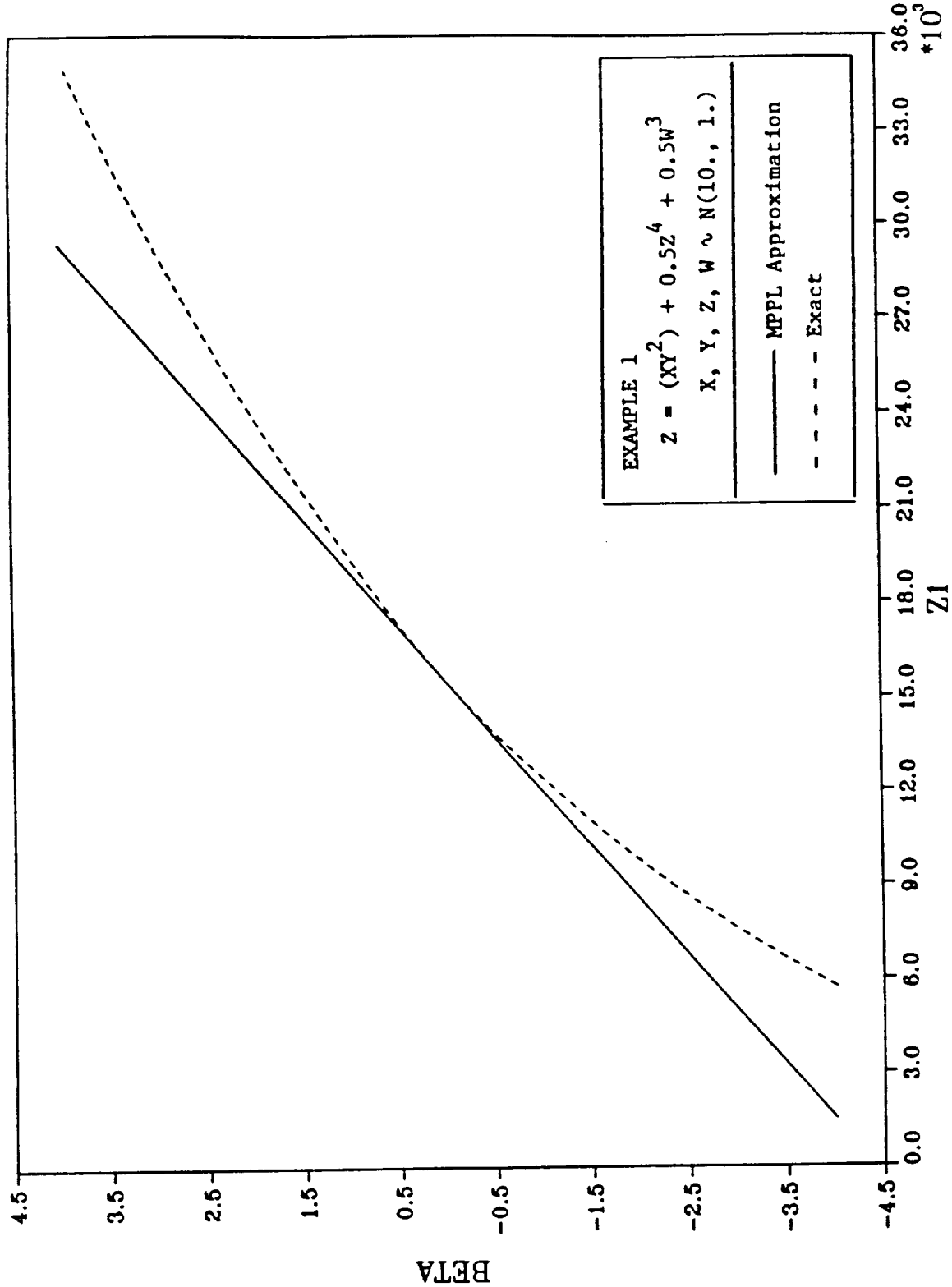

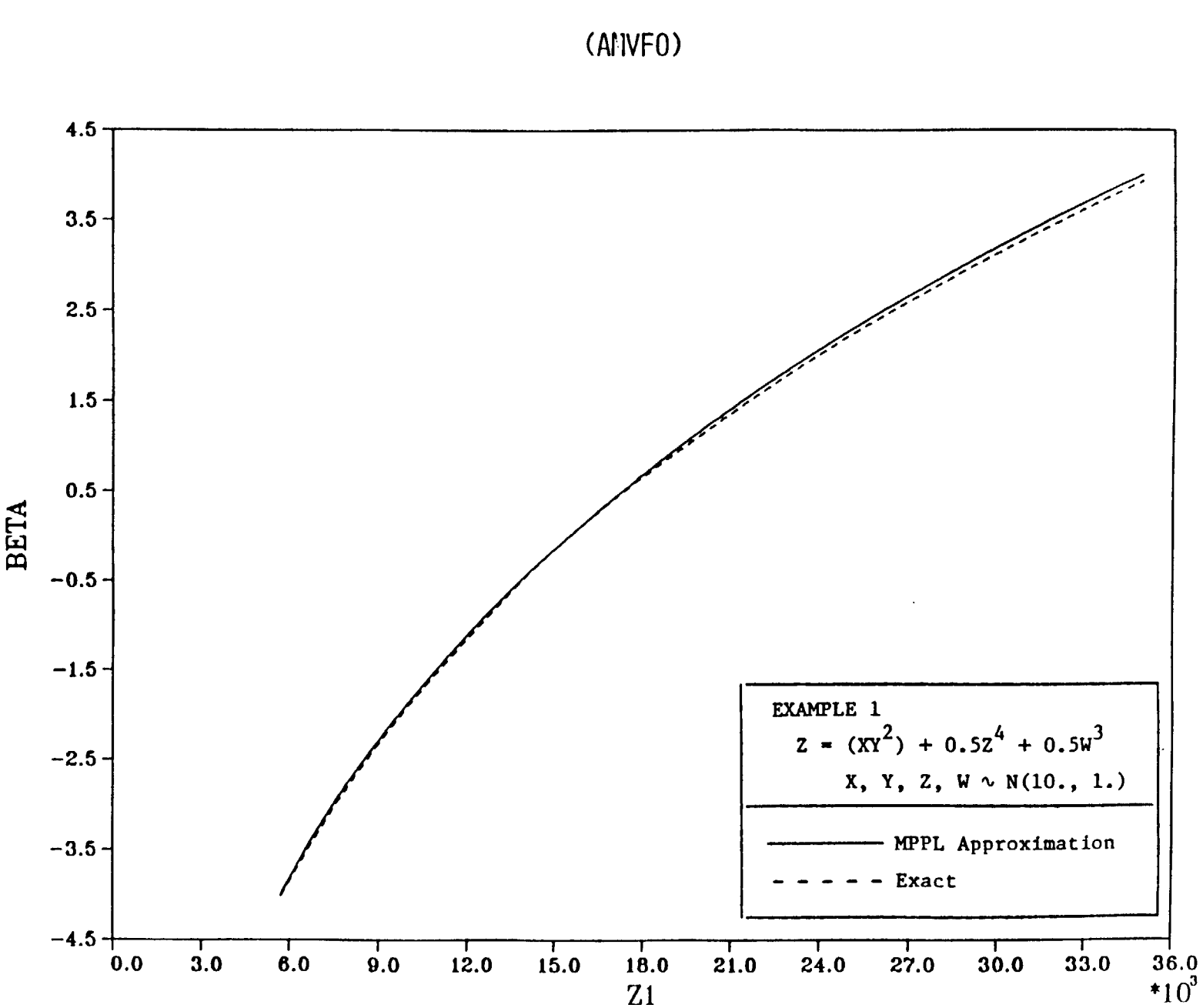
1ST MOVE
(ANVFO)
BETA
4.5
3.5
2.5
1.5
0.5
-0.5
-1.5
-2.5
-3.5
-4.5
0.0
3.0
6.0
9.0
12.0
15.0
18.0
21.0
24.0
27.0
30.0
33.0
36.0
Z1
*10^3
EXAMPLE 1
Z = (XY^2) + 0.5Z^4 + 0.5W^3
X, Y, Z, W ~ N(10., 1.)
MPPL Approximation
Exact

2ND MOVE

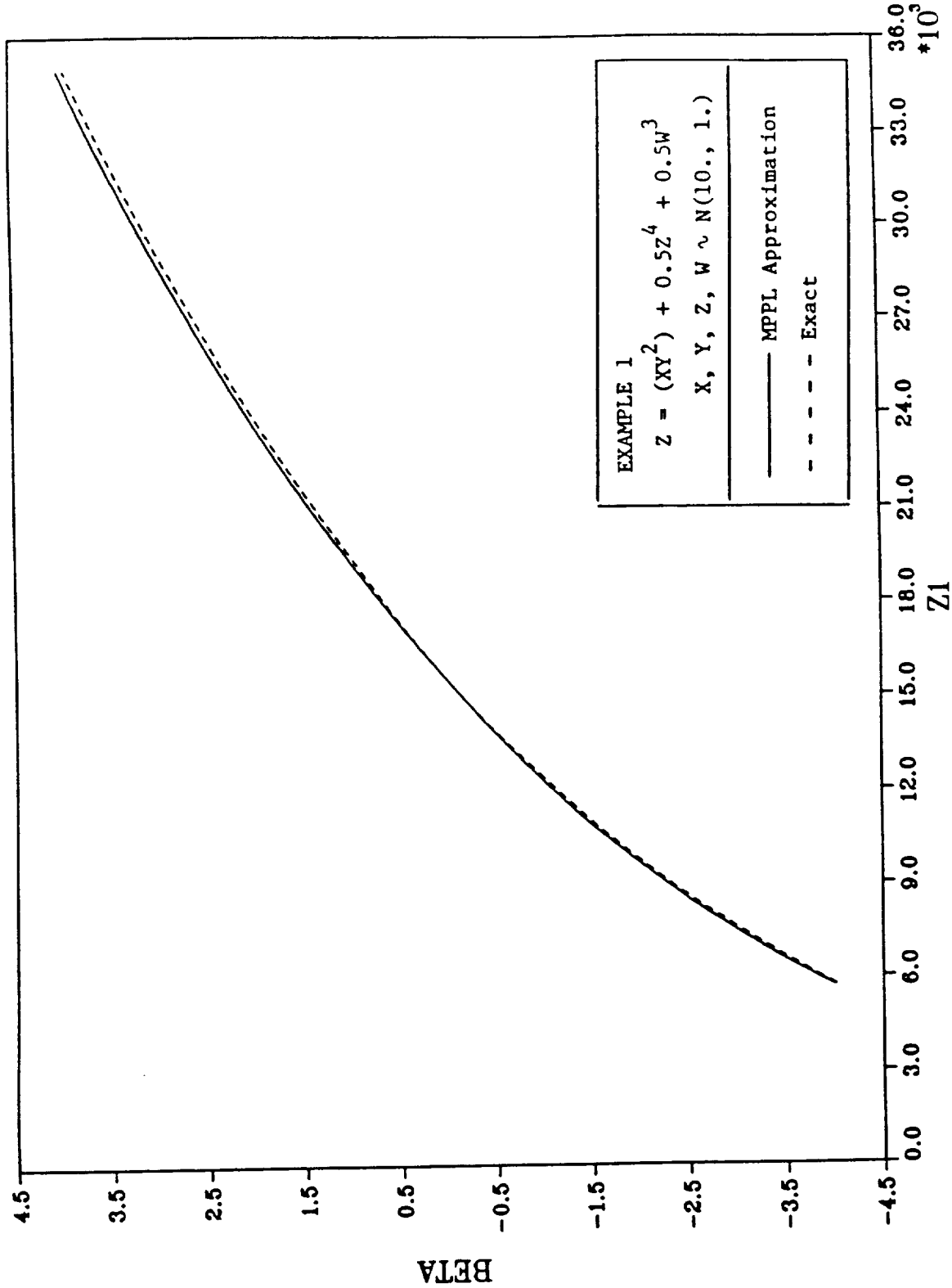
EXAMPLE 1
$Z = (XY^2) + 0.5Z^4 + 0.5W^3$
X, Y, Z, W ~ N(10., 1.)
MPPL Approximation
Exact
BETA
Z1
4.5
3.5
2.5
1.5
0.5
-0.5
-1.5
-2.5
-3.5
-4.5
0.0
3.0
6.0
9.0
12.0
15.0
18.0
21.0
24.0
27.0
30.0
33.0
36.0
*10^3

3RD MOVE

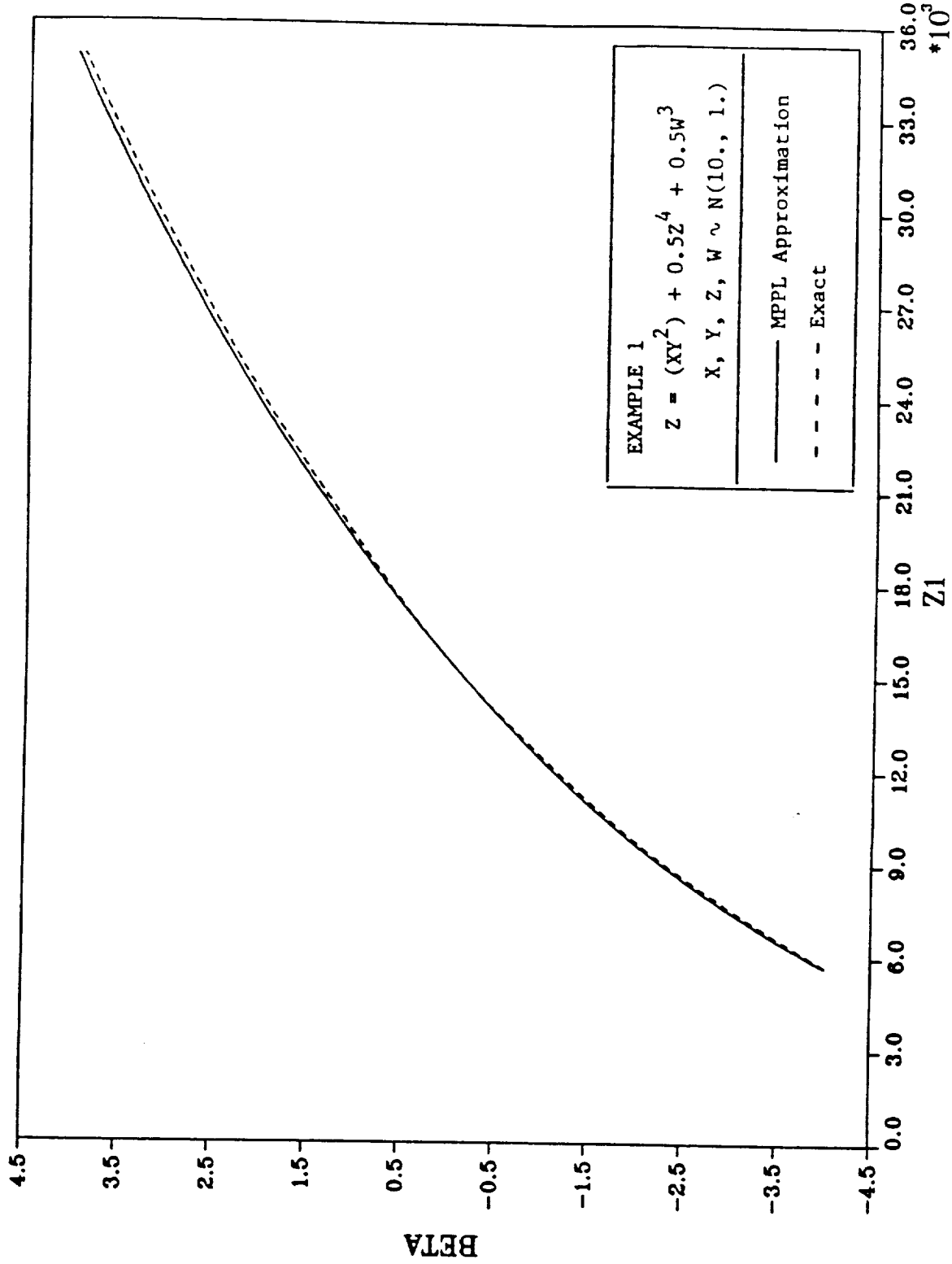
EXAMPLE 1
$Z = (XY^2) + 0.52^4 + 0.5W^3$
X, Y, Z, W ~ N(10., 1.)
MPPL Approximation
Exact
BETA
4.5
3.5
2.5
1.5
0.5
-0.5
-1.5
-2.5
-3.5
-4.5
0.0
3.0
6.0
9.0
12.0
15.0
18.0
21.0
24.0
27.0
30.0
33.0
36.0
*10^3
Z1

LINEAR PERFORMANCE FUNCTION

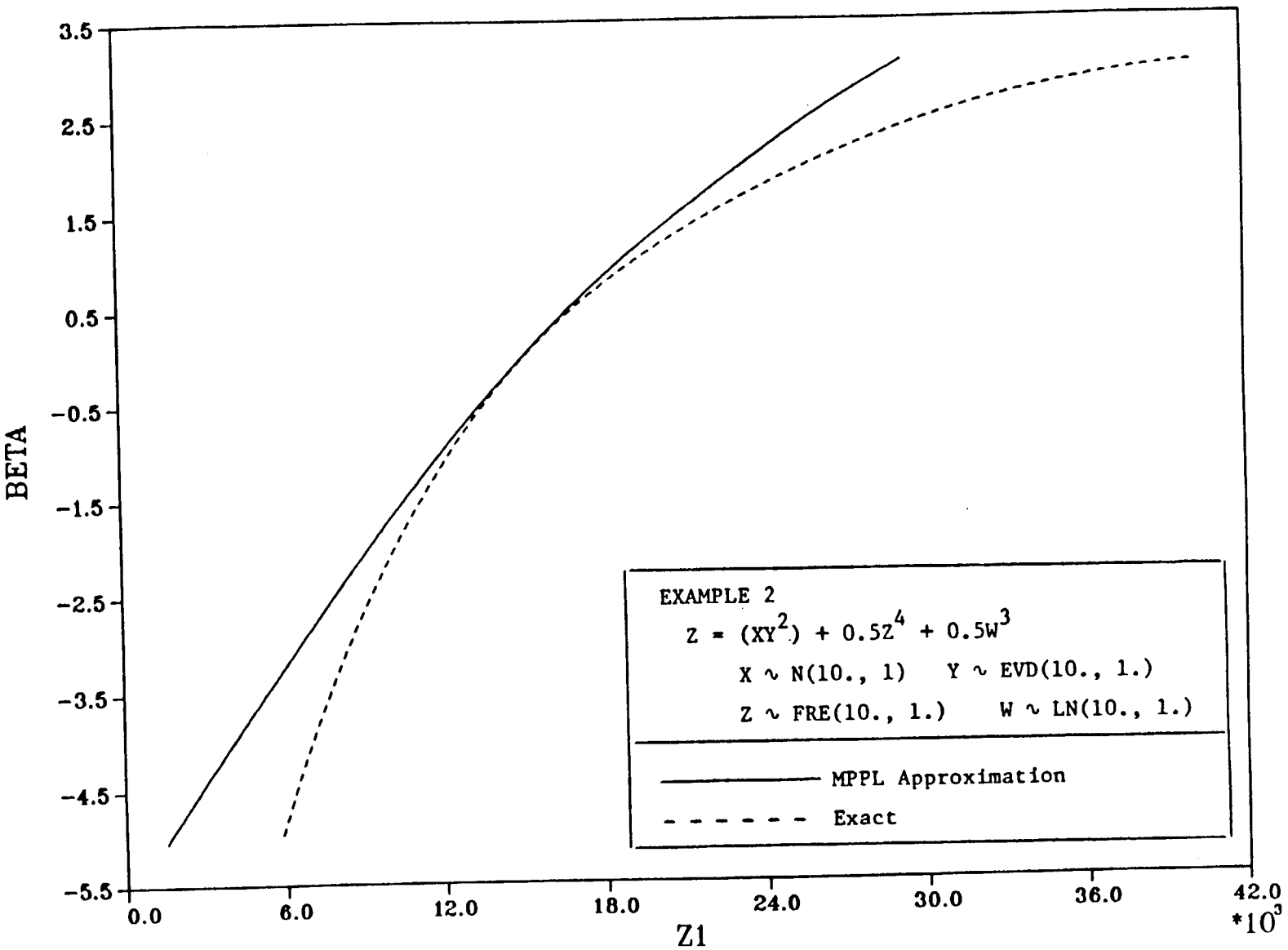

1ST MOVE

(AMVFO)

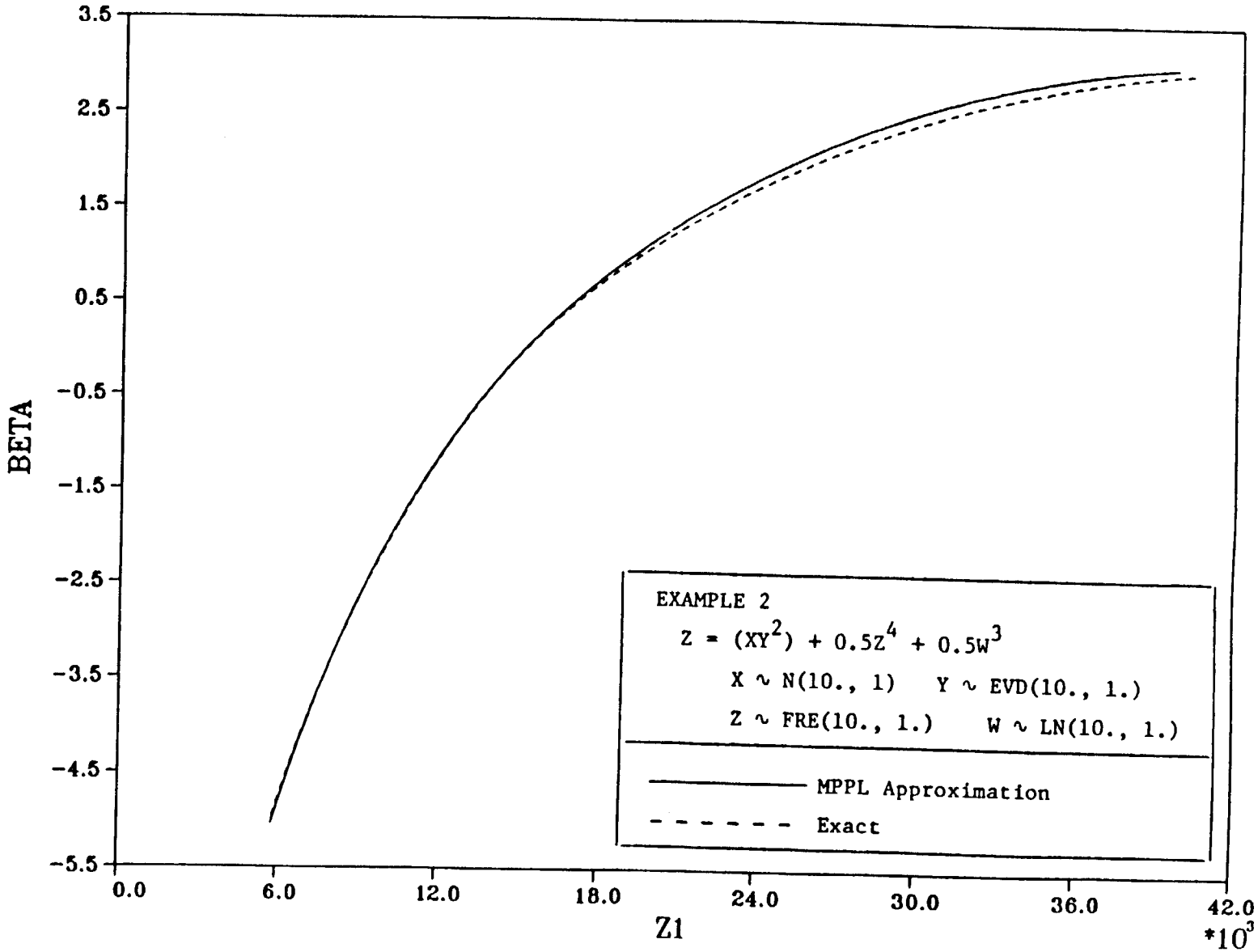

2ND MOVE

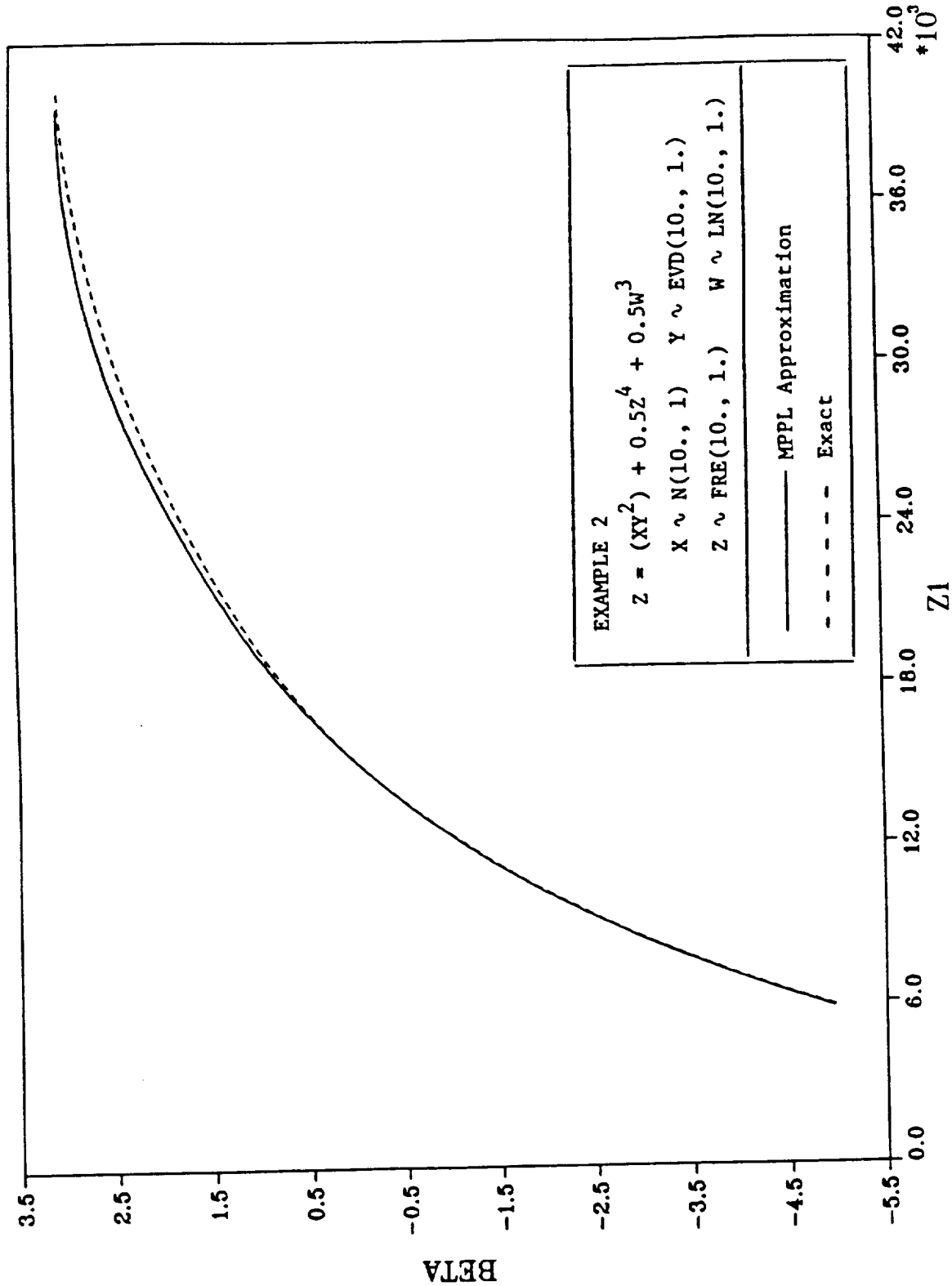
EXAMPLE 2
Z = (XY^2) + 0.52^4 + 0.5W^3
X ~ N(10., 1) Y ~ EVD(10., 1.)
Z ~ FRE(10., 1.) W ~ LN(10., 1.)
MPPL Approximation
Exact
BETA
Z1
3.5
2.5
1.5
0.5
-0.5
-1.5
-2.5
-3.5
-4.5
-5.5
0.0
6.0
12.0
18.0
24.0
30.0
36.0
42.0
*10^3

3RD MOVE

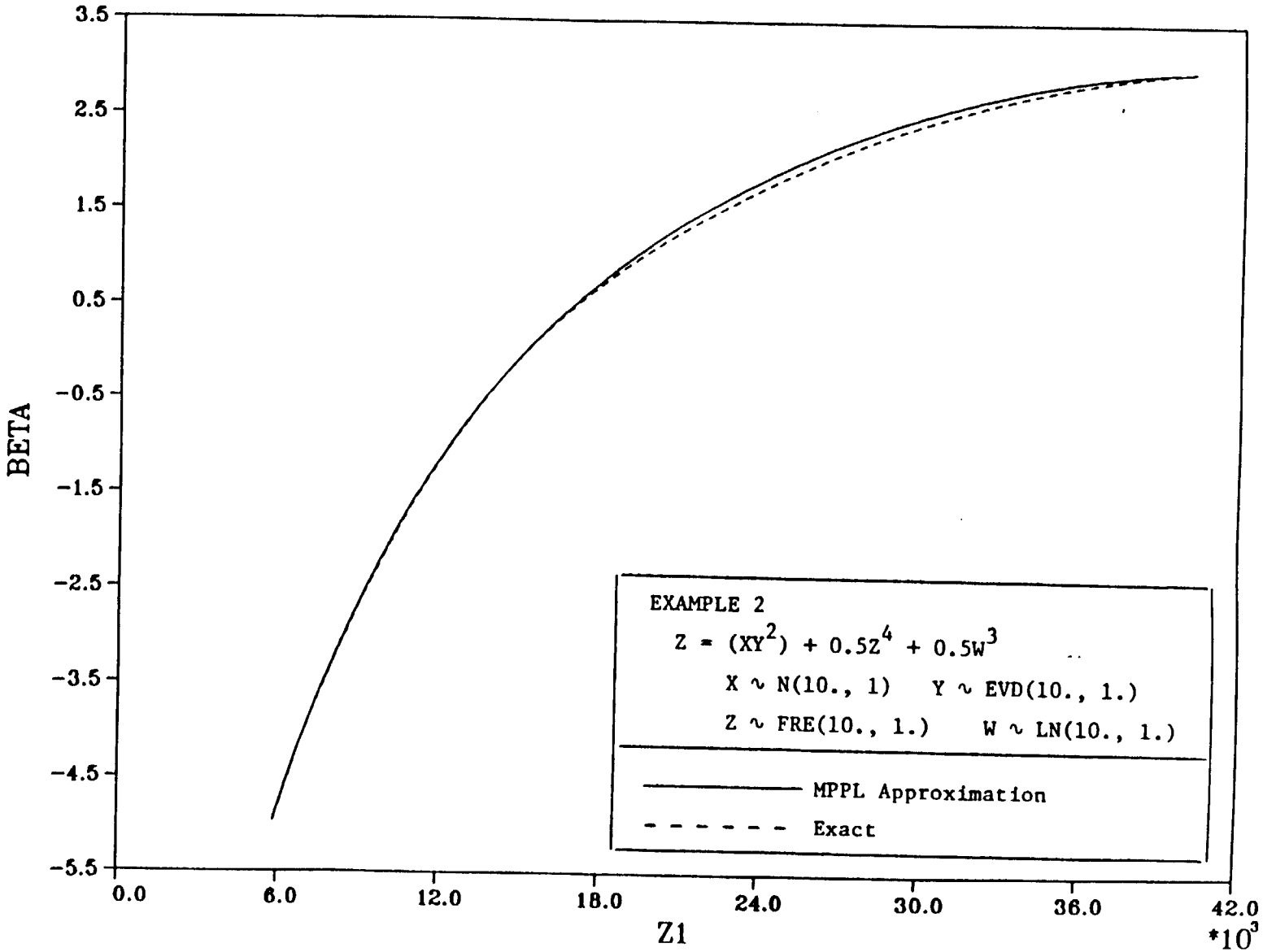
3.5
2.5
1.5
0.5
-0.5
-1.5
-2.5
-3.5
-4.5
-5.5
BETA
0.0
6.0
12.0
18.0
24.0
30.0
36.0
42.0
Z1
*10^3
EXAMPLE 2
Z = (XY^2) + 0.5Z^4 + 0.5W^3
X ∿ N(10., 1) Y ∿ EVD(10., 1.)
Z ∿ FRE(10., 1.) W ∿ LN(10., 1.)
MPPL Approximation
Exact

LINEAR PERFORMANCE FUNCTION

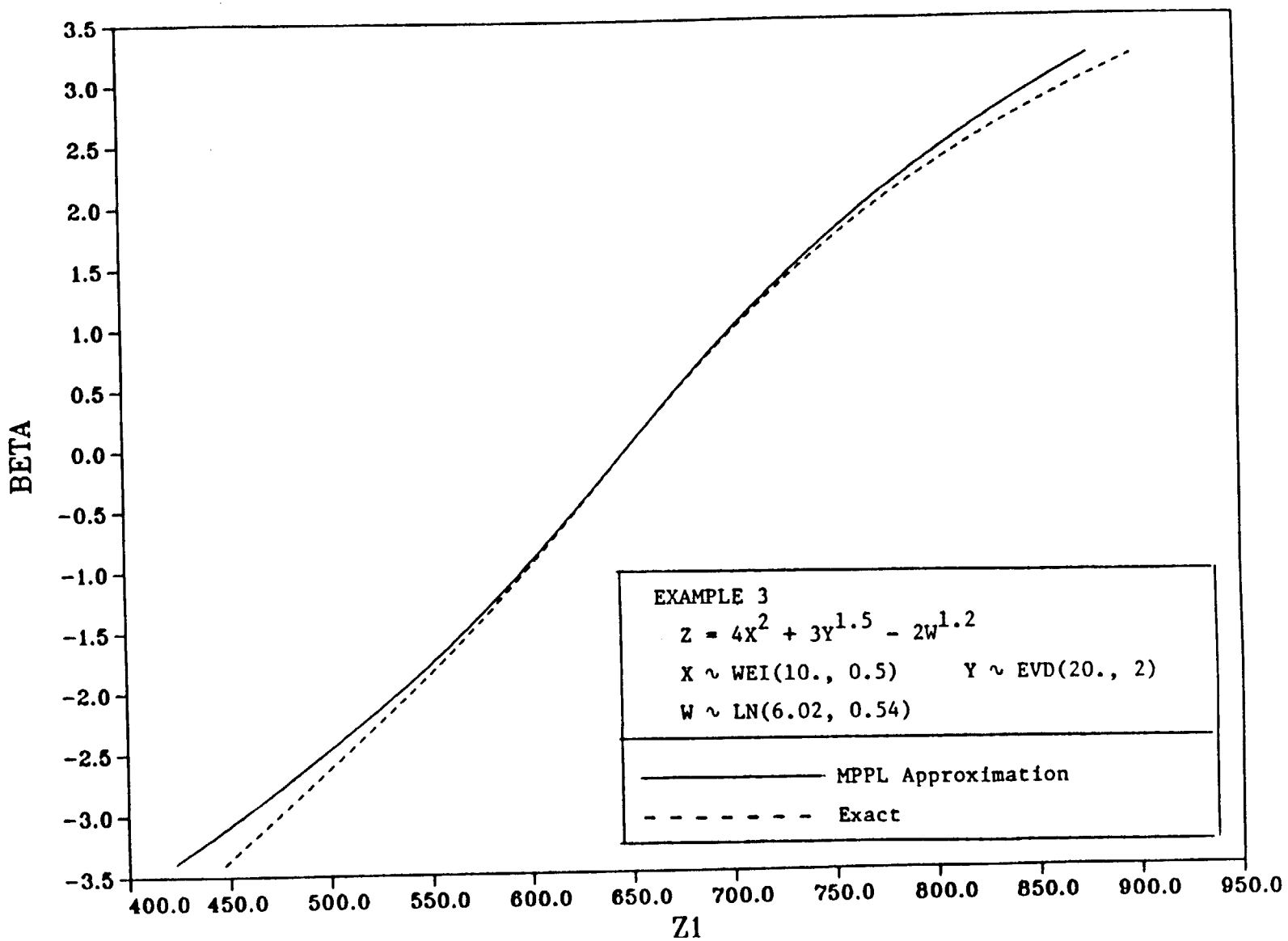

1ST MOVE

(AMVF0)

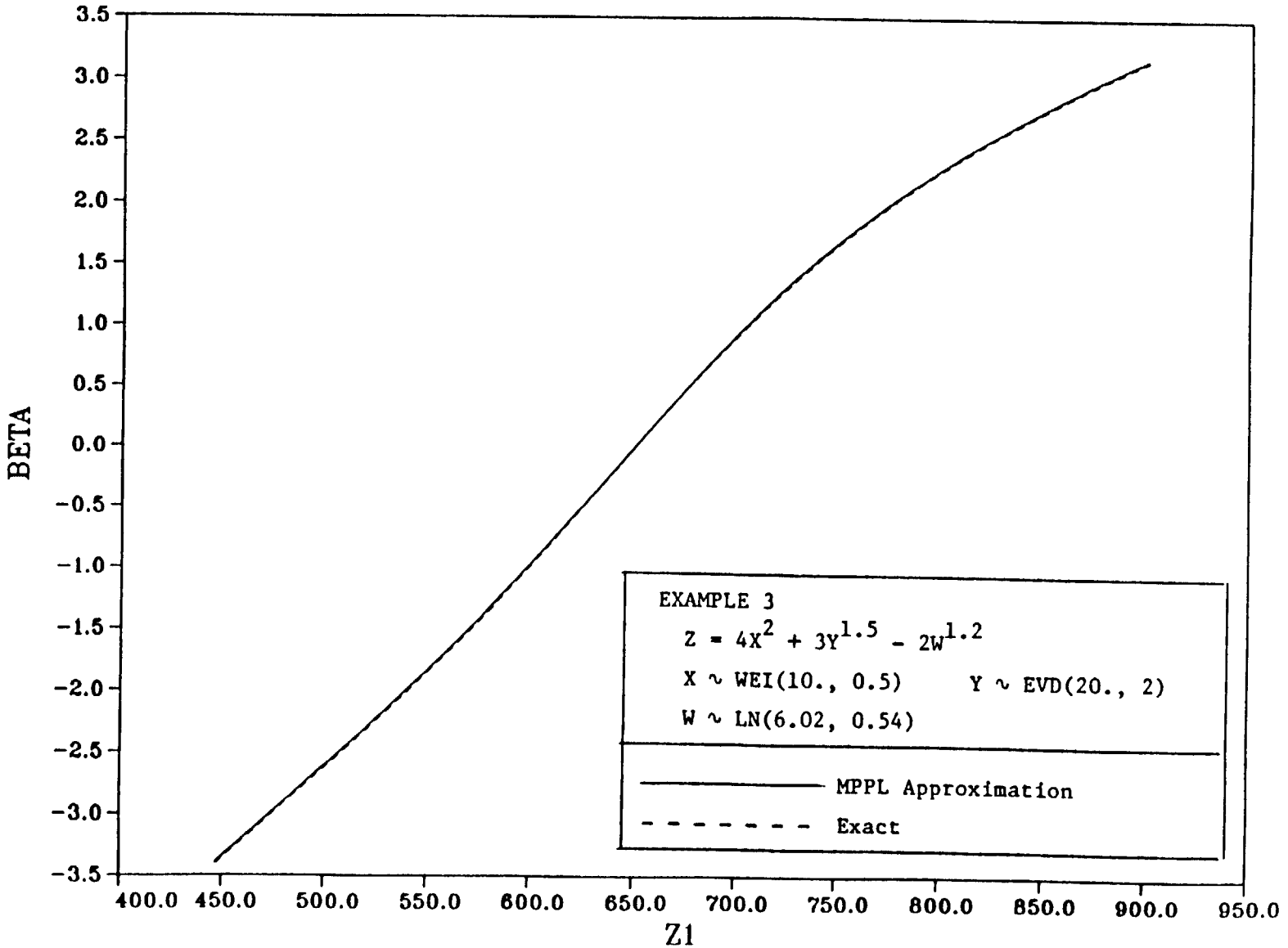

2ND MOVE

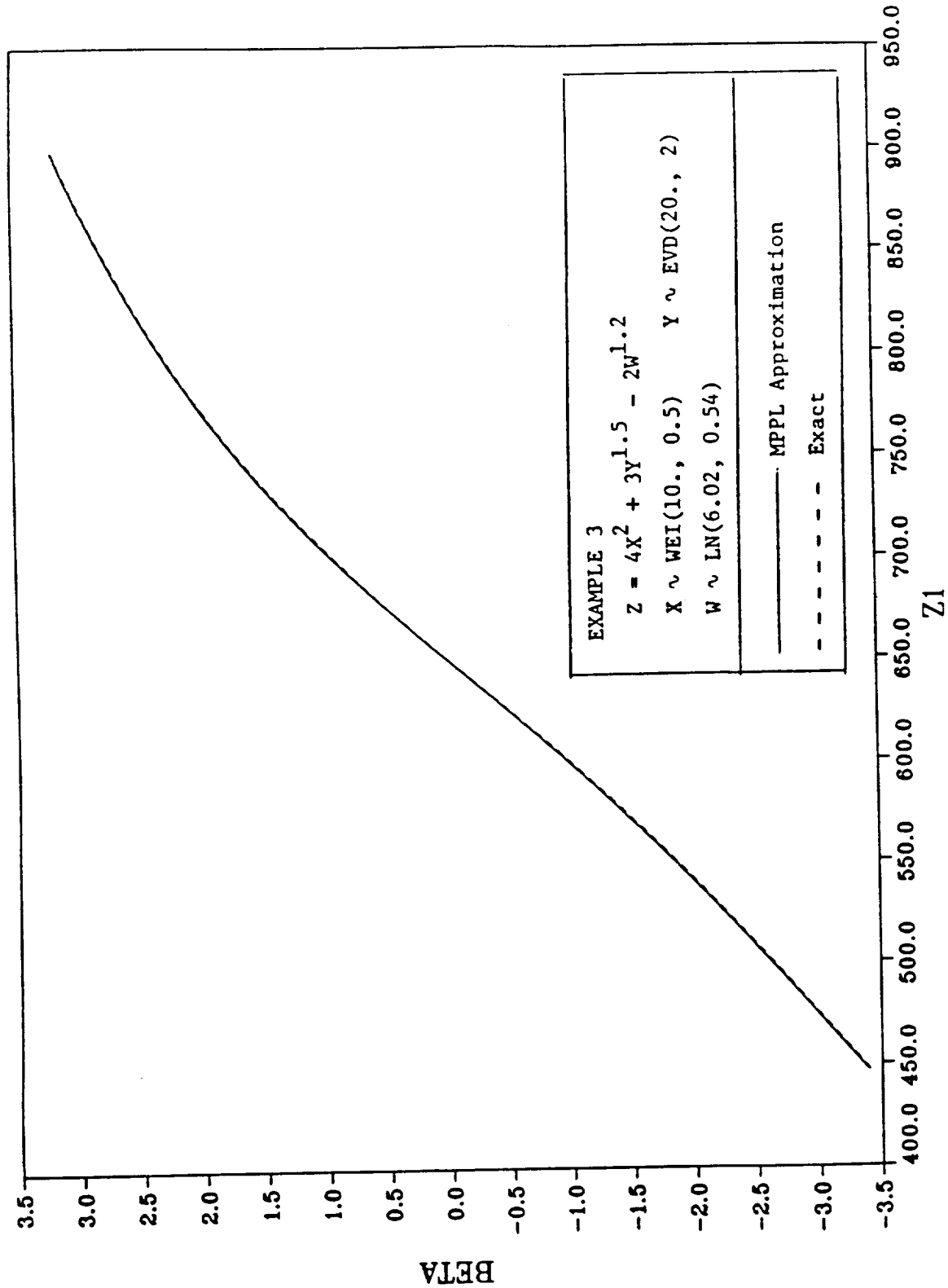
EXAMPLE 3
$Z = 4X^2 + 3Y^{1.5} - 2W^{1.2}$
X ~ WEI(10., 0.5)
Y ~ EVD(20., 2)
W ~ LN(6.02, 0.54)
MPPL Approximation
Exact
BETA
Z1
3.5
3.0
2.5
2.0
1.5
1.0
0.5
0.0
-0.5
-1.0
-1.5
-2.0
-2.5
-3.0
-3.5
400.0
450.0
500.0
550.0
600.0
650.0
700.0
750.0
800.0
850.0
900.0
950.0

3RD MOVE

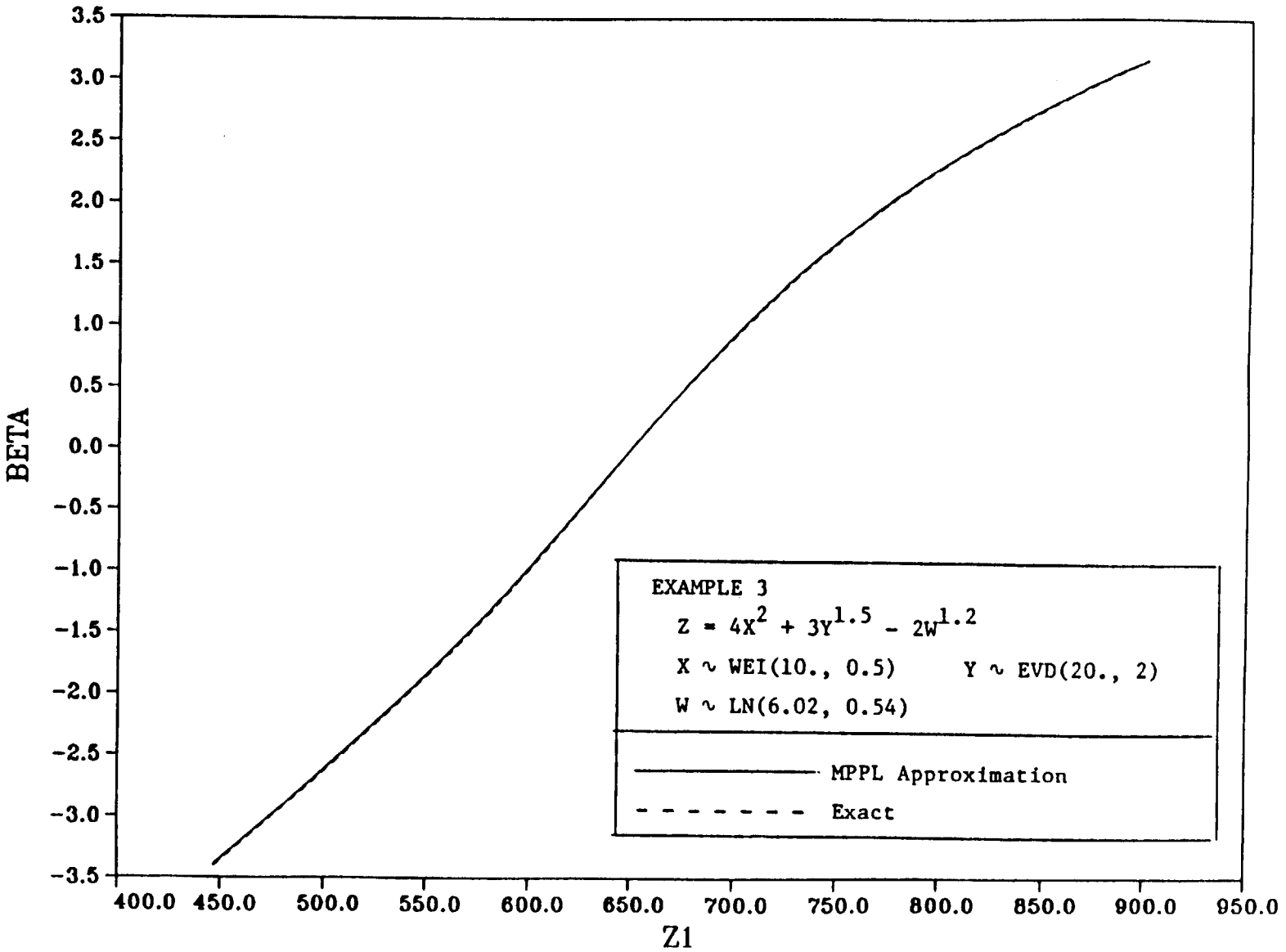
BETA
Z1
3.5
3.0
2.5
2.0
1.5
1.0
0.5
0.0
-0.5
-1.0
-1.5
-2.0
-2.5
-3.0
-3.5
400.0
450.0
500.0
550.0
600.0
650.0
700.0
750.0
800.0
850.0
900.0
950.0
EXAMPLE 3
Z = 4X^2 + 3Y^1.5 - 2W^1.2
X ~ WEI(10., 0.5)
Y ~ EVD(20., 2)
W ~ LN(6.02, 0.54)
MPPL Approximation
Exact

LINEAR PERFORMANCE FUNCTION

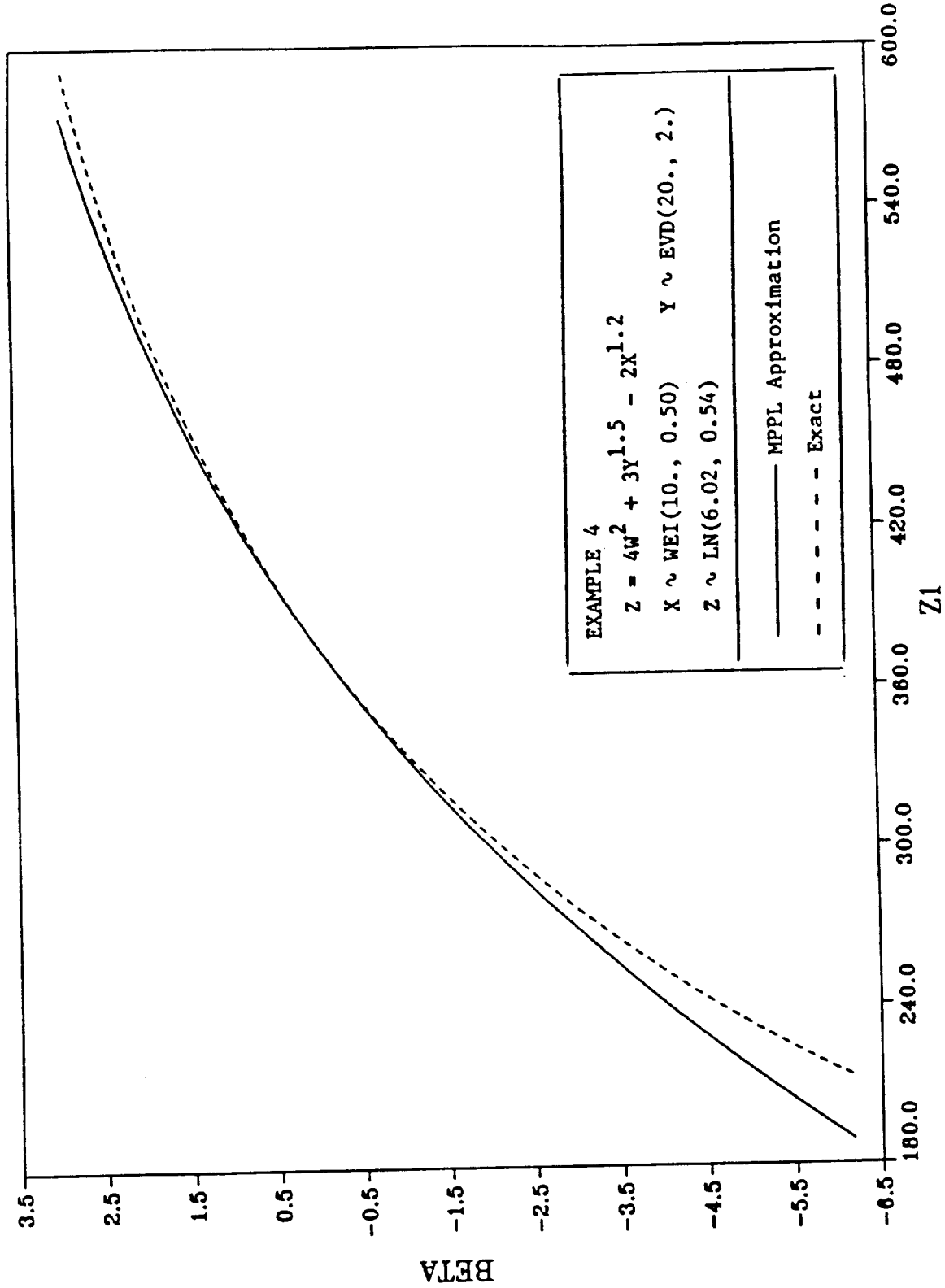

4

1ST MOVE

(AMVFO)

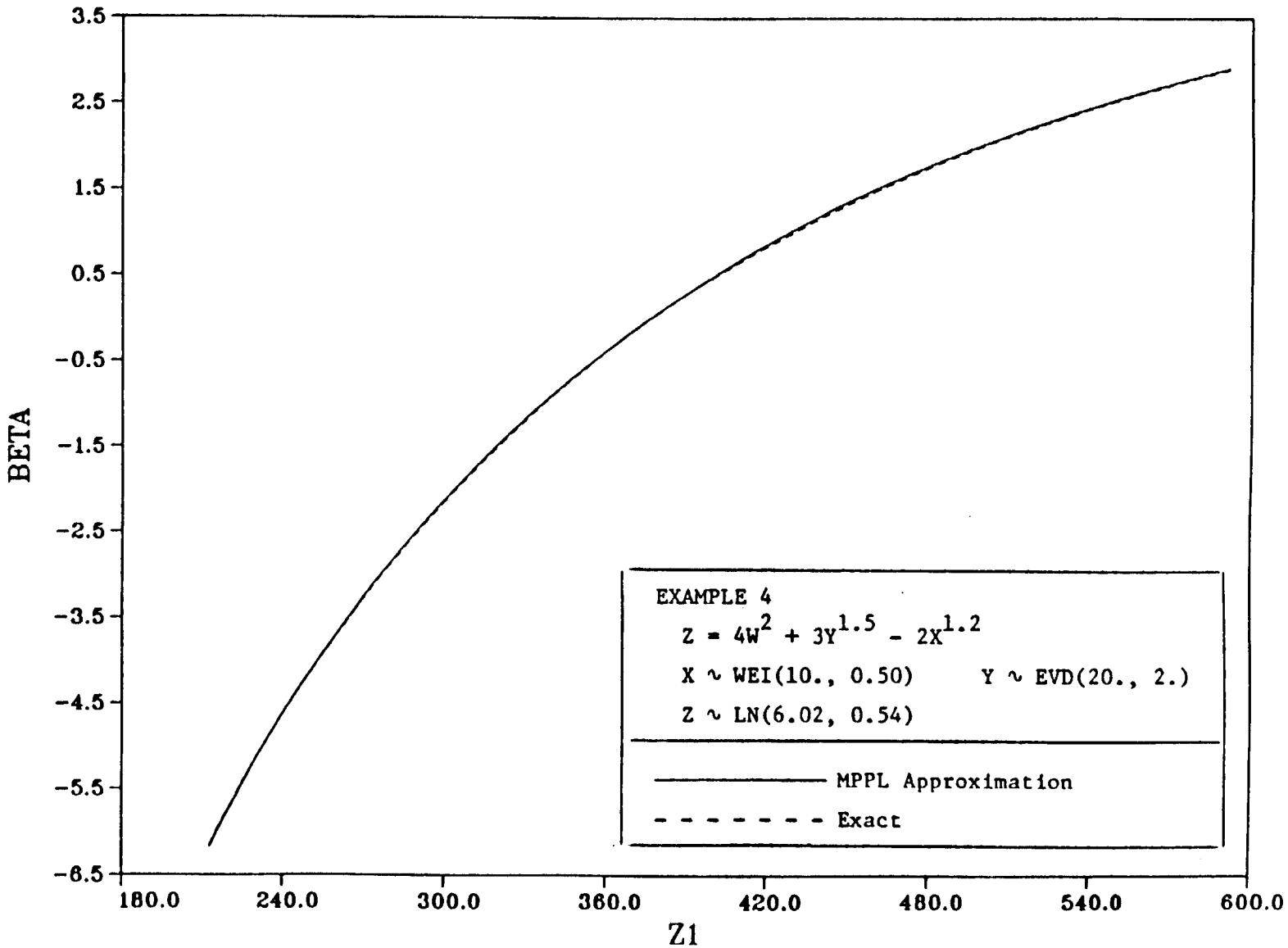

2ND MOVE

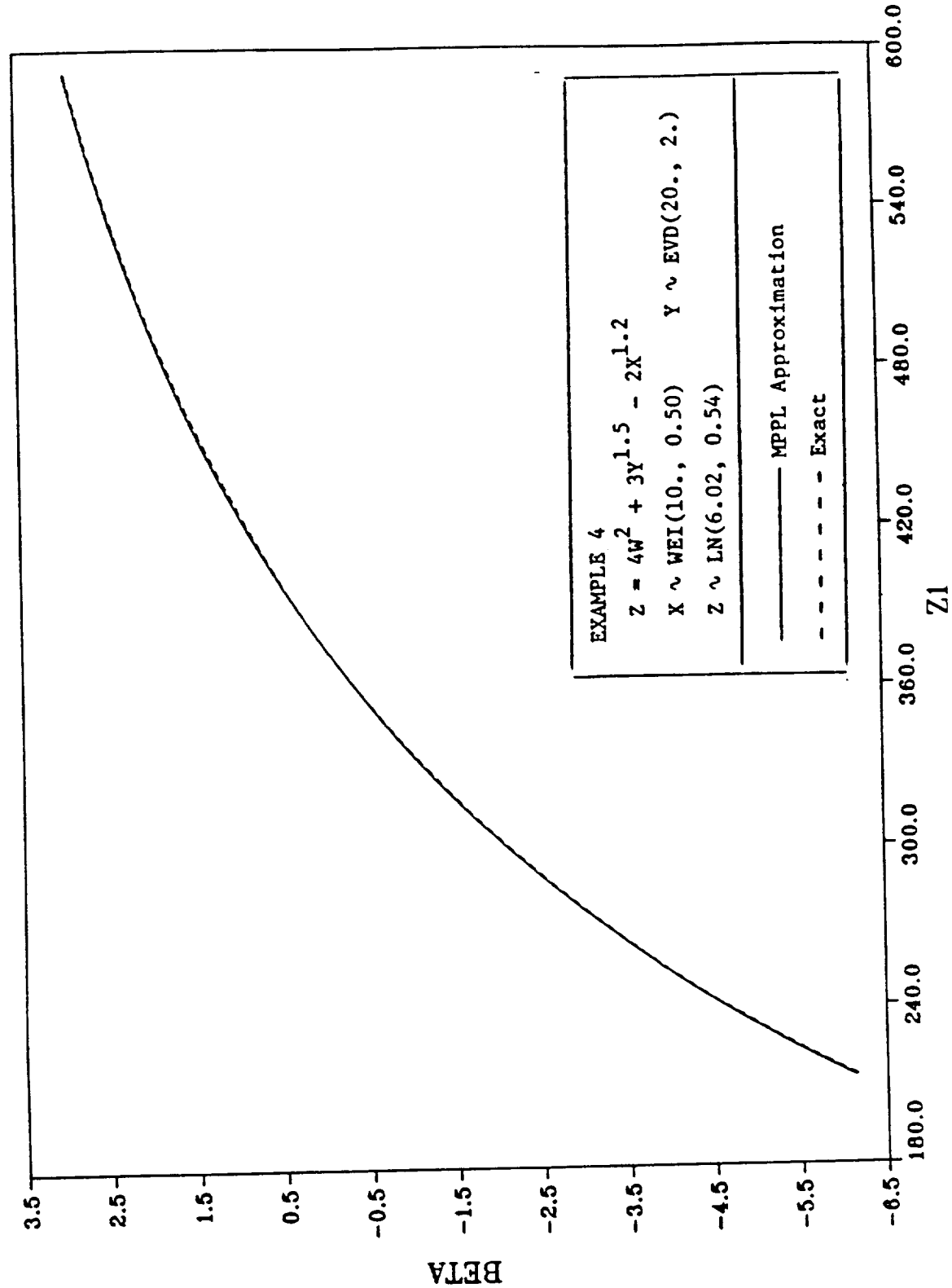
EXAMPLE 4
$Z = 4W^2 + 3Y^{1.5} - 2X^{1.2}$
X ~ WEI(10., 0.50)
Y ~ EVD(20., 2.)
Z ~ LN(6.02, 0.54)
MPPL Approximation
Exact
BETA
Z1
3.5
2.5
1.5
0.5
-0.5
-1.5
-2.5
-3.5
-4.5
-5.5
-6.5
180.0
240.0
300.0
360.0
420.0
480.0
540.0
600.0

3RD MOVE

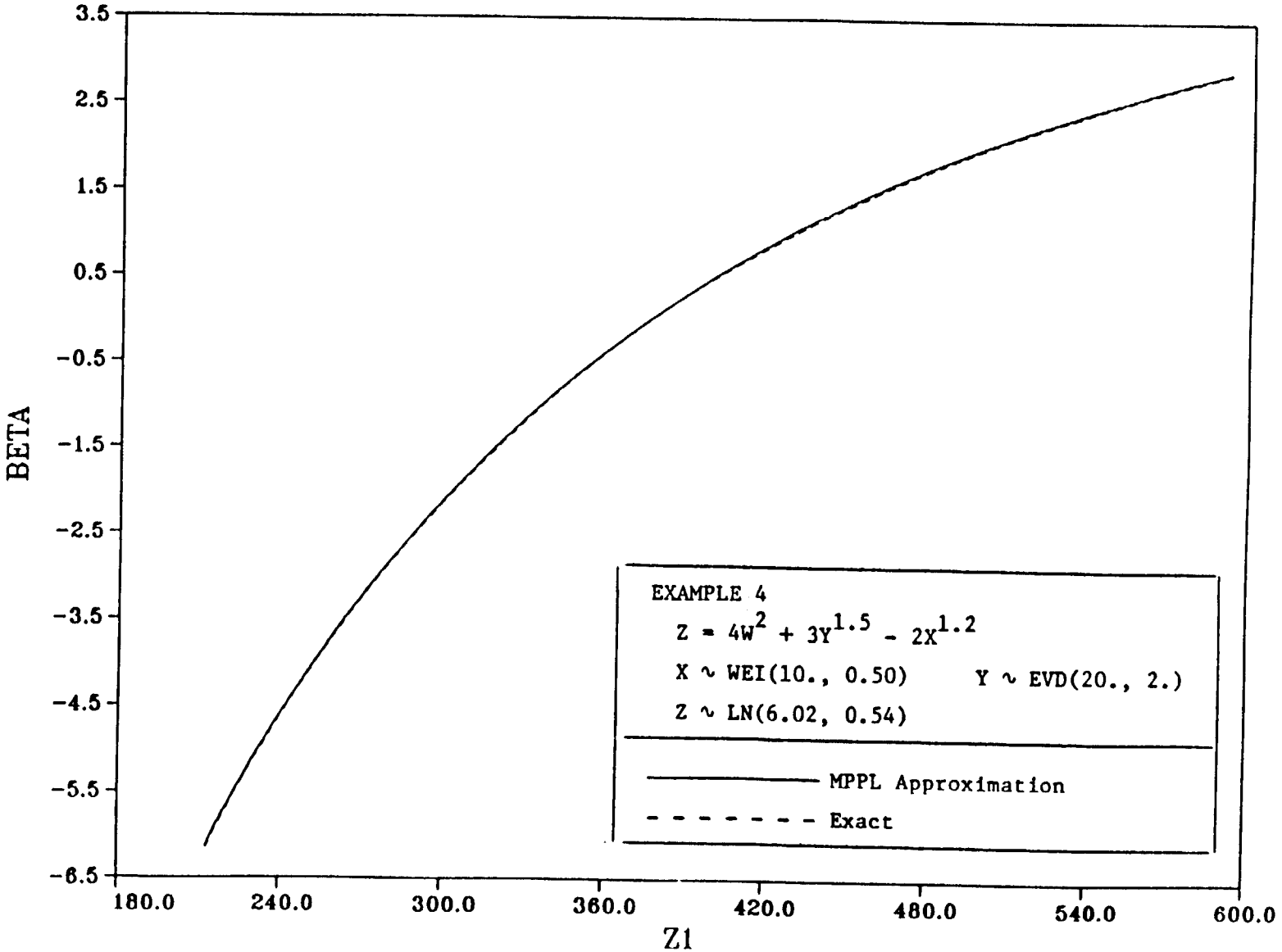
3.5
2.5
1.5
0.5
-0.5
-1.5
-2.5
-3.5
-4.5
-5.5
-6.5
BETA
180.0
240.0
300.0
360.0
420.0
480.0
540.0
600.0
Z1
EXAMPLE 4
Z = 4W^2 + 3Y^1.5 - 2X^1.2
X ~ WEI(10., 0.50)
Y ~ EVD(20., 2.)
Z ~ LN(6.02, 0.54)
MPPL Approximation
Exact

EXAMPLE 5

EXAMPLE: ESTABLISH CDF OF Δ_1

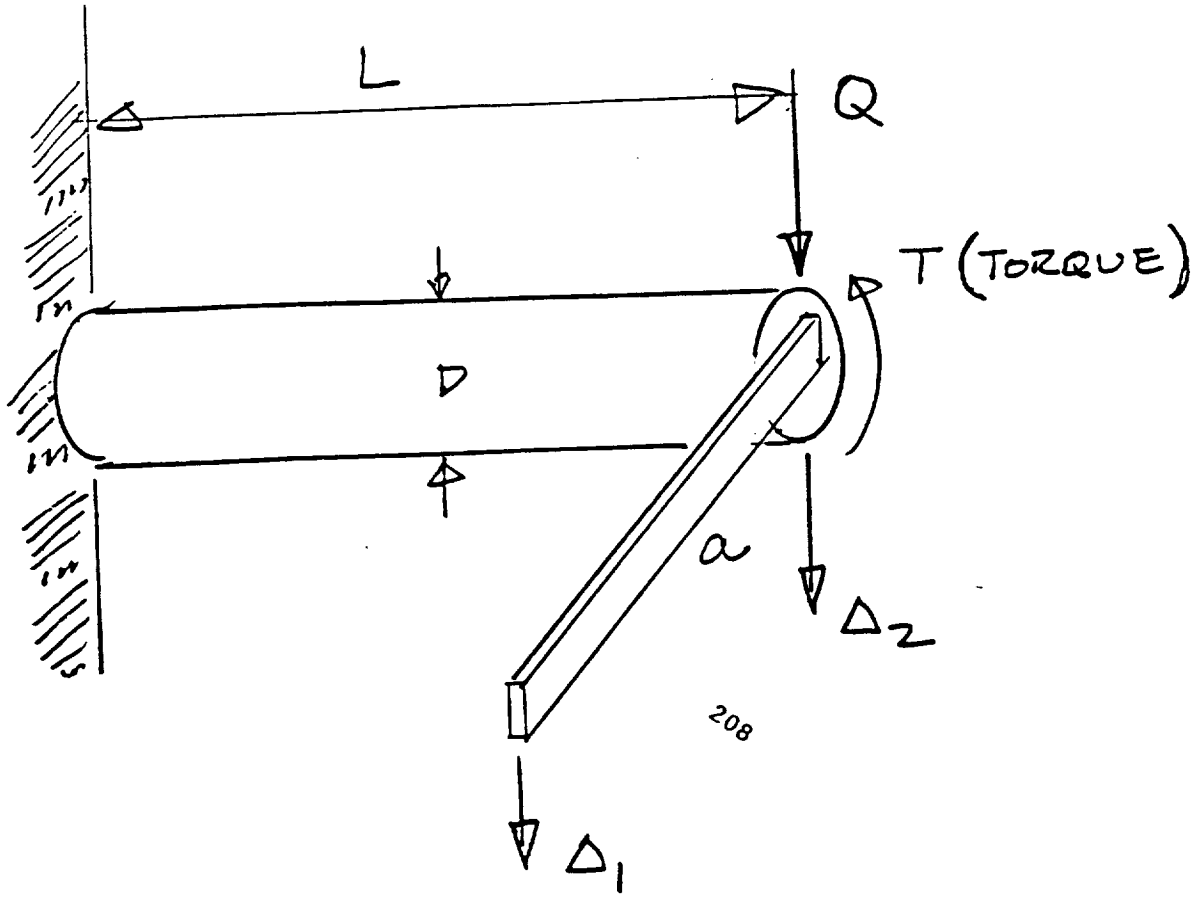

$$\Delta_1 = \frac{QL^3}{3E\left(\frac{\pi D^4}{64}\right)} + \frac{aTL}{G\left(\frac{\pi D^4}{32}\right)}$$

2ND MOVE

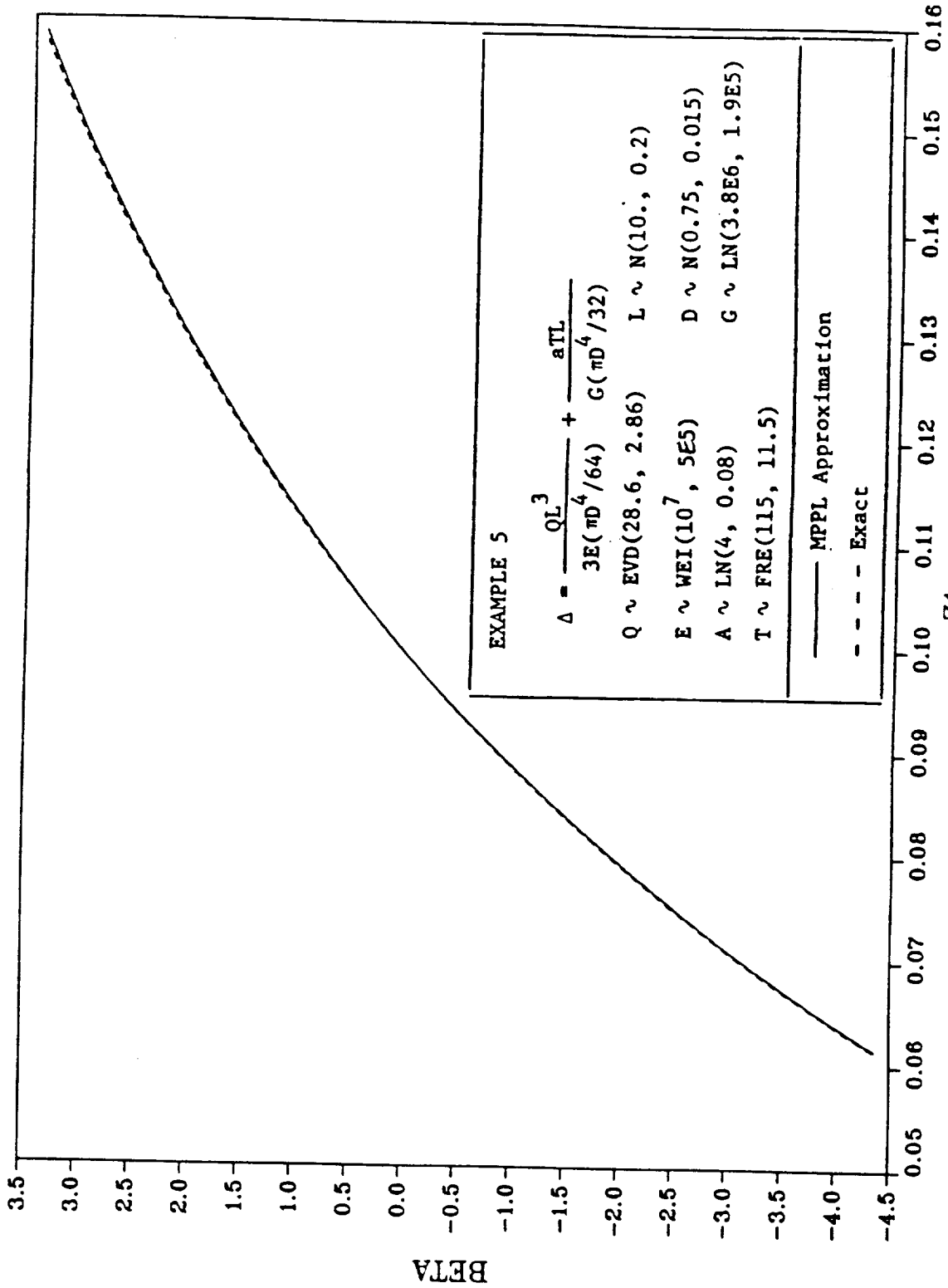
EXAMPLE 5
$\Delta = \frac{QL^3}{3E(\pi D^4/64)} + \frac{aTL}{G(\pi D^4/32)}$
Q ~ EVD(28.6, 2.86)
L ~ N(10., 0.2)
E ~ WEI(10^7, 5E5)
D ~ N(0.75, 0.015)
A ~ LN(4, 0.08)
G ~ LN(3.8E6, 1.9E5)
T ~ FRE(115, 11.5)
MPPL Approximation
Exact
BETA
Z1
3.5
3.0
2.5
2.0
1.5
1.0
0.5
0.0
-0.5
-1.0
-1.5
-2.0
-2.5
-3.0
-3.5
-4.0
-4.5
0.05
0.06
0.07
0.08
0.09
0.10
0.11
0.12
0.13
0.14
0.15
0.16

LINEAR APPROX.

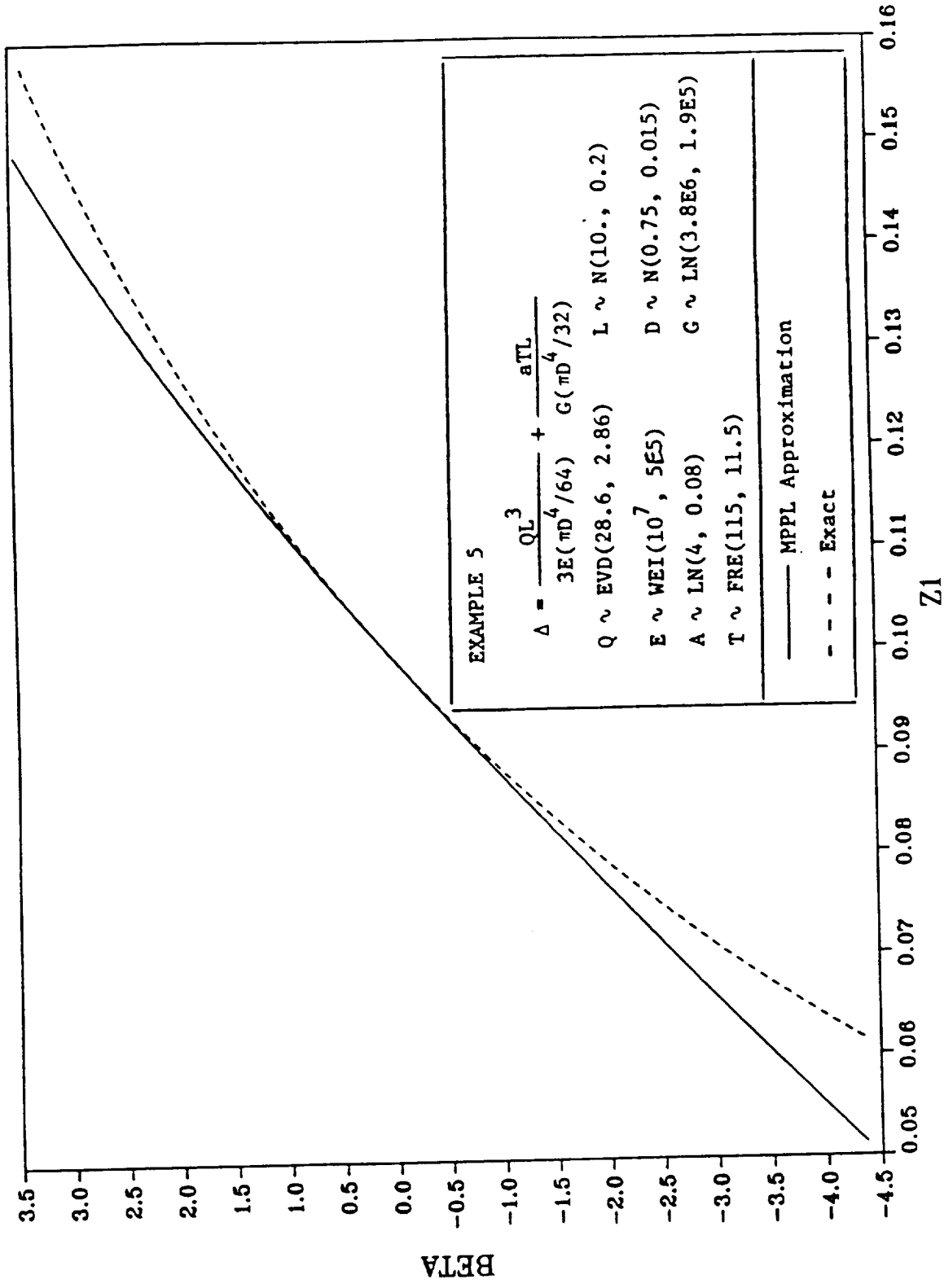

1ST MOVE

(AMVFO)

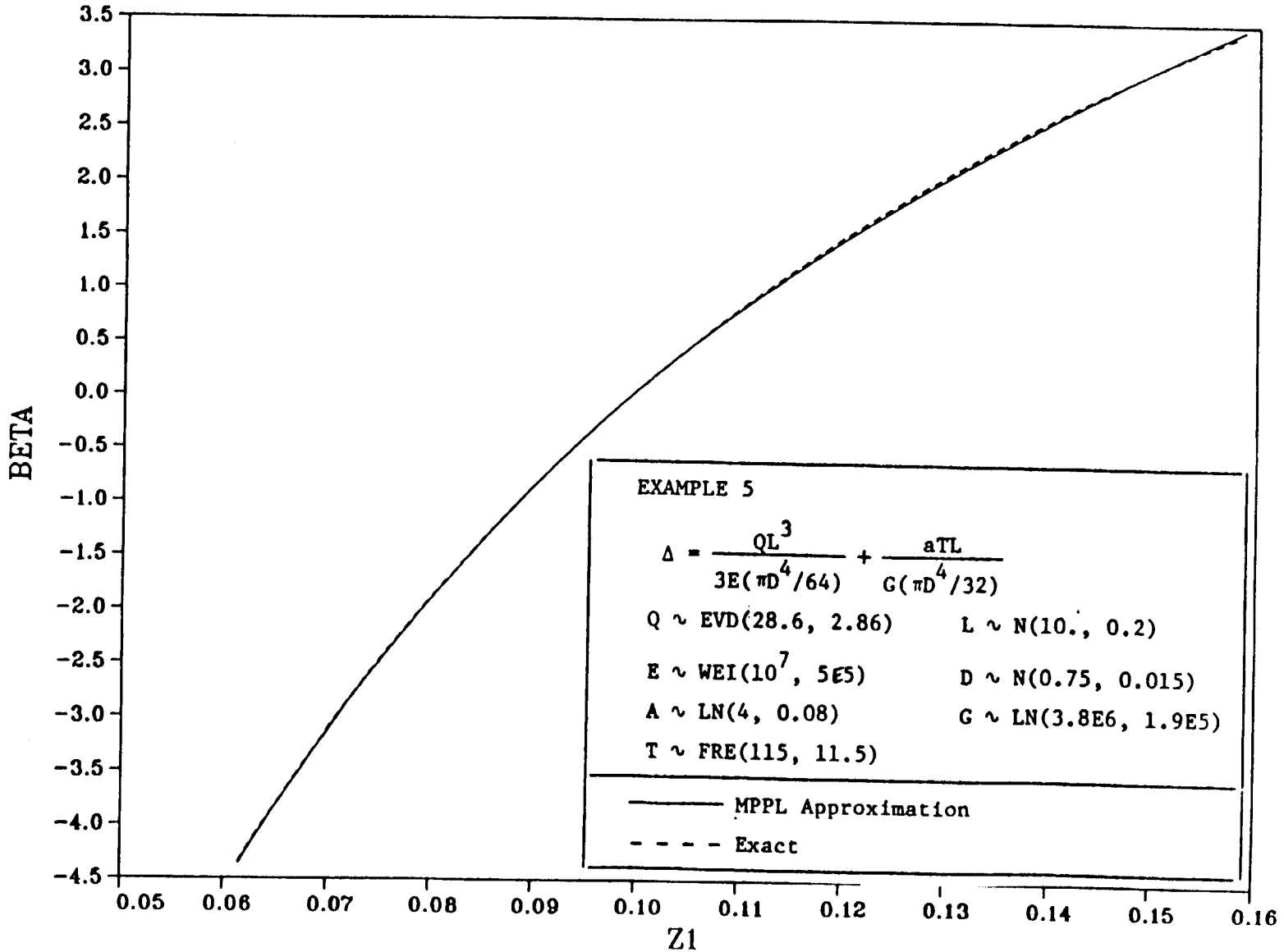

3RD MOVE

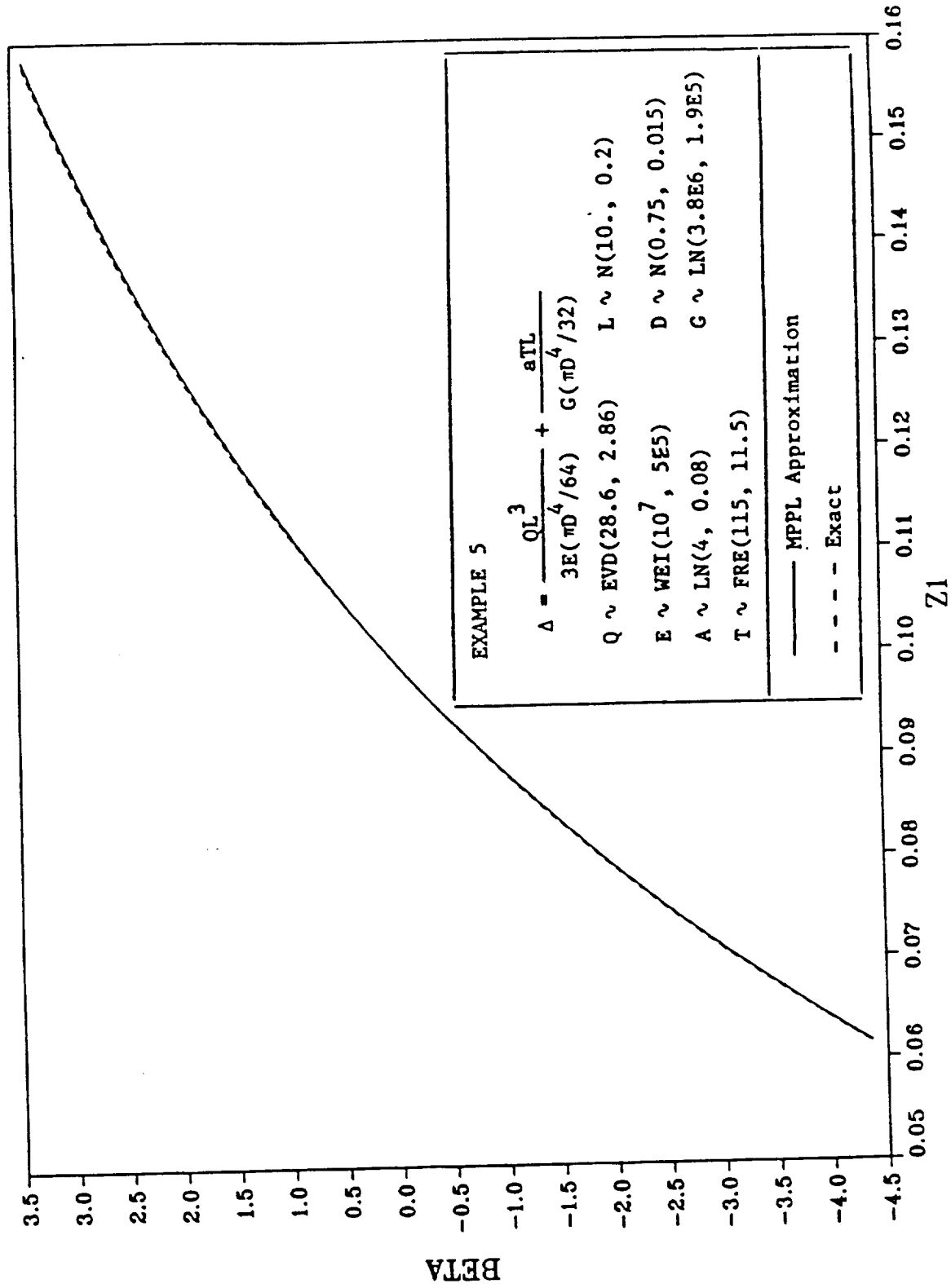
EXAMPLE 5
$\Delta = \frac{QL^3}{3E(\pi D^4/64)} + \frac{aTL}{G(\pi D^4/32)}$
Q ~ EVD(28.6, 2.86)
L ~ N(10., 0.2)
E ~ WEI(10^7, 5E5)
D ~ N(0.75, 0.015)
A ~ LN(4, 0.08)
G ~ LN(3.8E6, 1.9E5)
T ~ FRE(115, 11.5)
MPPL Approximation
Exact
BETA
Z1
3.5
3.0
2.5
2.0
1.5
1.0
0.5
0.0
-0.5
-1.0
-1.5
-2.0
-2.5
-3.0
-3.5
-4.0
-4.5
0.05
0.06
0.07
0.08
0.09
0.10
0.11
0.12
0.13
0.14
0.15
0.16

APPENDIX B

A Study on the Performance of AMVFO

P. Wirsching
University of Arizona

A STUDY ON THE PERFORMANCE OF AMVFO

PRELIMINARY REMARKS

Growing experience by all participants in PSAM is suggesting that accurate estimates of the CDF of a response variable can be made by MPPL with one move (AMVFO). This result is particularly useful for NESSUS because a "high quality" CDF can be constructed with a minimum of function evaluations.

The rapid convergence of MPPL was first observed by Y. T. Wu, the author of MPPL. But now there has been extensive experience with this algorithm. This report documents results obtained at UA.

A SUMMARY OF AMVFO EXPERIENCES AT UA

Attached are reference to 30 examples for which AMVFO solutions have been obtained. Unique to each example are:

1) The functional form, $Z = Z(\underset{\sim}{X})$ where X is the vector of independent random variables.
2) The distribution family for each X_i.
3) Statistical parameters for each X_i.

For the first 18 examples, there are direct comparisons between the AMVFO generated CDF and the exact. The exact solution is obtained by Wu/FPI. Percent errors on $\beta = \phi^{-1}(F_Z)$ are presented.

For Examples 19 through 30, no specific comparisons are reported because there was very close agreement between the two solutions.

A CLOSER LOOK AT THOSE CASES WHERE ERRORS ARE THE LARGEST

Some additional studies were made of those cases where the apparent errors in AMVFO were the largest, i.e., Examples 10, 15, 16, 17, and 18. Plots of the CDF are included for each of these examples. Note that the "exact" solution is obtained by Wu/FPI. Experience has indicated that Wu/FPI, used for the exact solution, may have as much as a 5% error (and sometimes a little higher). Errors in Wu/FPI could explain at least part of the observed differences. In fact, for Examples 9 and 10, the results of Wu/FPI differ depending on which variable is chosen as the dependent variable in the performance function as specified in the program.

As an independent check, a Monte Carlo program (using the Harbitz algorithm) was employed to compute point probabilities at selected Z-values. The results are presented for each of the five examples mentioned above. Generally these results seem to confirm that Wu/FPI is close to the exact solution, and that errors are introduced principally by the AMVFO process.

To pursue this issue, MPPL is executed for three moves for each of the five examples. Percent deviations with the Monte Carlo solution are listed. Upon review of the results, it is not clear, in general, that the 3-move MPPL solution will always converge to the exact.

CONCLUSIONS

It is difficult to draw general conclusions from this limited study of 30 examples. However, on the basis of this experience, AMVFO seems to be robust. The largest errors in $\beta = \Phi^{-1}(F_Z)$ were about 10%.

It comes as no surprise that deviations between the AMVFO and exact CDF's are largest in the tails. Unfortunately, there does not seem that there is anything that can be done a priori to predict the magnitude of the error.

It also appears that generally additional moves (the 2nd and 3rd) in MPPL do not consistently and substantially improve the estimate of the CDF. With the exception of special cases in the extreme tails of the distribution there does not seem to be much value gained by continuing beyond the AMVFO solution.

This study should continue to examine functional forms which may cause problems.

EXAMPLE 1 :

LIMIT STATE FUNCTION : Z = 3X + 2Y + W

VARIABLE DIST. (MEAN/MED,STD/COV) : (MED AND COV FOR LN DIST. ONLY)

X-WEI(10.,1.), Y-FRE(10.,1.), W-EVD(10.,1.)

	AMVFO SOLUTION		EXACT SOLUTION		
Z VALUE	BETA	Pf	BETA	Pf	% ERROR (BETA)
45.0330	-3.400100	.336858E-03	-3.4030	.333303E-03	.0853
48.7750	-2.665400	.384488E-02	-2.6660	.383803E-02	.0225
52.5170	-1.897600	.288743E-01	-1.8980	.288480E-01	.0211
56.2580	-1.029500	.151622E+00	-1.0310	.151270E+00	.1457
63.7420	1.075000	.858813E+00	1.0760	.859036E+00	.0930
67.7420	2.036900	.979170E+00	2.0370	.979175E+00	.0049
71.2250	2.758100	.997093E+00	2.7590	.997101E+00	.0326
74.9670	3.273400	.999469E+00	3.2740	.999470E+00	.0183

EXAMPLE 2 :

LIMIT STATE FUNCTION : Z = X Y

VARIABLE DIST. (MEAN/MED,STD/COV) : (MED AND COV FOR LN DIST. ONLY)

X-WEI(10.,2.), Y-FRE(8.,1.)

	AMVFO SOLUTION		EXACT SOLUTION		
Z VALUE	BETA	Pf	BETA	Pf	% ERROR (BETA)
13.4880	-4.233100	.115321E-04	-4.0478	.258636E-04	4.3774
28.3960	-2.957100	.155281E-02	-2.8816	.197837E-02	2.5532
44.8540	-1.955300	.252738E-01	-1.9195	.274605E-01	1.8309
62.0110	-1.007700	.156799E+00	-.9821	.163025E+00	2.5404
99.4330	1.050400	.853233E+00	1.0854	.861128E+00	3.3321
122.0900	2.003000	.977411E+00	2.0587	.980239E+00	2.7808
145.6800	2.712200	.996658E+00	2.7559	.997073E+00	1.6112
168.0000	3.214200	.999346E+00	3.2352	.999392E+00	.6534

EXAMPLE 3 :

LIMIT STATE FUNCTION : Z = X**2 + 0.5*Y**2

VARIABLE DIST. (MEAN/MED,STD/COV) : (MED AND COV FOR LN DIST. ONLY)

X-N(10.,1.), Y-N(10.,1.)

	AMVFO SOLUTION		EXACT SOLUTION		
Z VALUE	BETA	Pf	BETA	Pf	% ERROR (BETA)
74.9590	-4.000000	.316860E-04	-4.0180	.293612E-04	.4500
91.0170	-3.000000	.134997E-02	-3.0250	.124323E-02	.8333
108.8800	-2.000000	.227501E-01	-2.0260	.213823E-01	1.3000
128.5400	-1.000000	.158655E+00	-1.0230	.153154E+00	2.3000
173.2600	1.000000	.841345E+00	.9780	.835963E+00	2.2000
198.3200	2.000000	.977250E+00	1.9760	.975923E+00	1.2000
225.1800	3.000000	.998650E+00	2.9750	.998535E+00	.8333
253.8500	4.000000	.999968E+00	3.9720	.999964E+00	.7000

EXAMPLE 4 :

LIMIT STATE FUNCTION : Z = X*Y**2 + X**3

VARIABLE DIST. (MEAN/MED,STD/COV) : (MED AND COV FOR LN DIST. ONLY)

X-WEI(1.,0.1), Y-EVD(1.,0.1)

	AMVFO SOLUTION		EXACT SOLUTION		
Z VALUE	BETA	Pf	BETA	Pf	% ERROR (BETA)
.7113	-3.205850	.673385E-03	-3.2030	.680084E-03	.0889
.9482	-2.534135	.563629E-02	-2.5350	.562239E-02	.0341
1.2371	-1.824495	.340386E-01	-1.8210	.343034E-01	.1916
1.5857	-1.021351	.153544E+00	-1.0190	.154101E+00	.2302
2.4829	1.054400	.854150E+00	1.0710	.857915E+00	1.5744
3.0353	2.193113	.985850E+00	2.1960	.985954E+00	.1316
3.6866	3.137531	.999148E+00	3.1380	.999149E+00	.0149
4.4524	3.899628	.999952E+00	3.8960	.999951E+00	.0930

EXAMPLE 5 :

LIMIT STATE FUNCTION : Z = (X*Y)**2 + 0.5*W**3

VARIABLE DIST. (MEAN/MED,STD/COV) : (MED AND COV FOR LN DIST. ONLY)

X-N(10.,1.), Y-N(10.,1.), W-N(10.,1.)

	AMVFO SOLUTION		EXACT SOLUTION		
Z VALUE	BETA	Pf	BETA	Pf	% ERROR (BETA)
3119.8560	-3.998916	.318315E-04	-3.9370	.412708E-04	1.5483
4335.4460	-2.999298	.135308E-02	-2.9550	.156341E-02	1.4769
5923.2870	-1.999437	.227805E-01	-1.9630	.248230E-01	1.8224
7952.9570	-.998969	.158905E+00	-.9620	.168025E+00	3.7007
13645.9300	.998969	.841095E+00	1.0290	.848260E+00	3.0063
17478.2100	1.999437	.977220E+00	2.0280	.978720E+00	1.4286
22090.2900	2.999298	.998647E+00	3.0250	.998757E+00	.8569
27581.5900	3.998916	.999968E+00	4.0230	.999971E+00	.6023

EXAMPLE 6 :

LIMIT STATE FUNCTION : Z = X*Y**2 + 0.5*W**4 + 0.5*U**3

VARIABLE DIST. (MEAN/MED,STD/COV) : (MED AND COV FOR LN DIST. ONLY)

X-N(10.,1.), Y-N(10.,1.), W-N(10.,1.), U-N(10.,1.)

	AMVFO SOLUTION		EXACT SOLUTION		
Z VALUE	BETA	Pf	BETA	Pf	% ERROR (BETA)
2025.2320	-3.998916	.318315E-04	-3.8050	.709262E-04	4.8492
2614.3090	-2.999298	.135308E-02	-2.9390	.164643E-02	2.0104
3495.9250	-1.999437	.227805E-01	-1.9840	.236278E-01	.7721
4757.9910	-.998969	.158905E+00	-.9980	.159140E+00	.0970
8833.0310	.998969	.841095E+00	.9980	.840860E+00	.0970
11879.7500	1.999437	.977220E+00	2.0050	.977519E+00	.2782
15774.3900	2.999298	.998647E+00	2.9990	.998646E+00	.0099
20662.8000	3.998916	.999968E+00	3.9920	.999967E+00	.1729

24/5, 24/6

MISSING

EXAMPLE 7 :

LIMIT STATE FUNCTION : Z = X*Y**2 + 0.5*W**4 + 0.5*U**3

VARIABLE DIST. (MEAN/MED,STD/COV) : (MED AND COV FOR LN DIST. ONLY)

X-N(10.,1.), Y-EVD(10.,1.), W-FRE(10.,1.)
U-LN(9.95037,.1)

	AMVFO SOLUTION		EXACT SOLUTION		
Z VALUE	BETA	Pf	BETA	Pf	% ERROR (BETA)
2269.4400	-8.555800	.585269E-17	-8.4590	.134840E-16	1.1314
3086.2300	-4.757521	.981134E-06	-4.7200	.118062E-05	.7887
4029.0300	-2.312219	.103828E-01	-2.3080	.104995E-01	.1825
5139.9380	-.775700	.218963E+00	-.7750	.219170E+00	.0902
8194.8680	.932774	.824532E+00	.9330	.824590E+00	.0242
10287.7100	1.448784	.926301E+00	1.4490	.926331E+00	.0149
12837.5400	1.856761	.968327E+00	1.8560	.968273E+00	.0410
15906.5400	2.192935	.985844E+00	2.1920	.985810E+00	.0426

EXAMPLE 8 :

LIMIT STATE FUNCTION : Z = X**5 + X*Y**4

VARIABLE DIST. (MEAN/MED,STD/COV) : (MED AND COV FOR LN DIST. ONLY)

X-N(1.,0.1), Y-N(1.,0.1)

	AMVFO SOLUTION		EXACT SOLUTION		
Z VALUE	BETA	Pf	BETA	Pf	% ERROR (BETA)
.3769	-3.998920	.318309E-04	-3.9950	.323621E-04	.0980
.6003	-2.999300	.135307E-02	-3.0110	.130201E-02	.3901
.9233	-1.999400	.227825E-01	-2.0180	.217956E-01	.9303
1.3774	-.998970	.158905E+00	-1.0210	.153627E+00	2.2053
2.8356	.998970	.841095E+00	.9770	.835715E+00	2.1993
3.9358	1.999400	.977218E+00	1.9730	.975752E+00	1.3204
5.3604	2.999300	.998647E+00	2.9630	.998477E+00	1.2103
7.1774	3.998920	.999968E+00	3.9430	.999960E+00	1.3984

EXAMPLE 9 ; CASE I

LIMIT STATE FUNCTION : Z = (X*Y)**2 + 0.5*W**4 + 0.5*U**3

VARIABLE DIST. (MEAN/MED,STD/COV) : (MED AND COV FOR LN DIST. ONLY)

X-N(10.,1.), Y-N(10.,1.), W-N(10.,1.), U-N(10.,1.)
(EXACT SOLUTION FROM FPI; USE X AS X(1))

	AMVFO SOLUTION		EXACT SOLUTION		
Z VALUE	BETA	Pf	BETA	Pf	% ERROR (BETA)
7495.8040	-2.999298	.135308E-02	-3.0460	.115961E-02	1.5571
9087.6890	-2.249443	.122421E-01	-2.2930	.109240E-01	1.9363
10934.8100	-1.499299	.668981E-01	-1.5300	.630084E-01	2.0477
13063.1600	-.748760	.227001E+00	-.7790	.217990E+00	4.0387
18273.8400	.748760	.772999E+00	.7030	.758972E+00	6.1114
21414.4600	1.499299	.933102E+00	1.4500	.926471E+00	3.2881
24952.9000	2.249443	.987758E+00	2.1890	.985702E+00	2.6870
28921.4600	2.999298	.998647E+00	2.9330	.998321E+00	2.2105

EXAMPLE 9 ; CASE II

LIMIT STATE FUNCTION : Z = (X*Y)**2 + 0.5*W**4 + 0.5*U**3

VARIABLE DIST. (MEAN/MED,STD/COV) : (MED AND COV FOR LN DIST. ONLY)

X-N(10.,1.), Y-N(10.,1.), W-N(10.,1.), U-N(10.,1.)
(EXACT SOLUTION FROM FPI; USE Z AS X(1))

	AMVFO SOLUTION		EXACT SOLUTION		
Z VALUE	BETA	Pf	BETA	Pf	% ERROR (BETA)
7495.8040	-2.999298	.135308E-02	-3.0290	.122689E-02	.9903
9087.6890	-2.249443	.122421E-01	-2.2760	.114230E-01	1.1806
10934.8100	-1.499299	.668981E-01	-1.5200	.642555E-01	1.3807
13063.1600	-.748760	.227001E+00	-.7670	.221541E+00	2.4360
18273.8400	.748760	.772999E+00	.7310	.767610E+00	2.3719
21414.4600	1.499299	.933102E+00	1.4790	.930430E+00	1.3539
24952.9000	2.249443	.987758E+00	2.2290	.987093E+00	.9088
28921.4600	2.999298	.998647E+00	2.9800	.998559E+00	.6434

EXAMPLE 10 ; CASE I

LIMIT STATE FUNCTION : Z = (X*Y)**2 + 0.5*W**4 + 0.5*U**3

VARIABLE DIST. (MEAN/MED,STD/COV) : (MED AND COV FOR LN DIST. ONLY)

X-N(10.,1.), Y-EVD(10.,1.), W-FRE(10.,1.), U-LN(9.95037,.1)
(EXACT SOLUTION FROM FPI; USE X AS X(1))

	AMVFO SOLUTION		EXACT SOLUTION		
Z VALUE	BETA	Pf	BETA	Pf	% ERROR (BETA)
7532.7660	-3.627000	.143402E-03	-3.6240	.145076E-03	.0827
9099.4890	-2.606500	.457368E-02	-2.6210	.438365E-02	.5563
10934.6500	-1.635000	.510245E-01	-1.6540	.490637E-01	1.1621
13062.7800	-.725965	.233930E+00	-.7390	.229953E+00	1.7955
18284.3500	.805360	.789694E+00	.7780	.781716E+00	3.3972
21421.7400	1.429682	.923596E+00	1.3630	.913559E+00	4.6641
24944.5600	1.957630	.974863E+00	1.8460	.967554E+00	5.7023
29364.4100	2.482820	.993483E+00	2.2000	.986097E+00	11.3911

EXAMPLE 10 ; CASE II

LIMIT STATE FUNCTION : Z = (X*Y)**2 + 0.5*W**4 + 0.5*U**3

VARIABLE DIST. (MEAN/MED,STD/COV) : (MED AND COV FOR LN DIST. ONLY)

X-N(10.,1.), Y-EVD(10.,1.), W-FRE(10.,1.), U-LN(9.95037,.1)
(EXACT SOLUTION FROM FPI; USE Z AS X(1))

	AMVFO SOLUTION		EXACT SOLUTION		
Z VALUE	BETA	Pf	BETA	Pf	% ERROR (BETA)
7532.7660	-3.627000	.143402E-03	-3.6210	.146769E-03	.1654
9099.4890	-2.606500	.457368E-02	-2.6170	.443535E-02	.4028
10934.6500	-1.635000	.510245E-01	-1.6540	.490637E-01	1.1621
13062.7800	-.725965	.233930E+00	-.7340	.231474E+00	1.1068
18284.3500	.805360	.789694E+00	.8080	.790455E+00	.3278
21421.7400	1.429682	.923596E+00	1.4020	.919542E+00	1.9362
24944.5600	1.957630	.974863E+00	2.0470	.979671E+00	4.5652
29364.4100	2.482820	.993483E+00	2.4670	.993187E+00	.6372

EXAMPLE TEN : Z = (X*Y)**2 + 0.5*W**4 + 0.5*U**3
X–N(10.,1.), Y–EVD(10.,1.), W–FRE(10.,1.), U–LN(10.,1.)

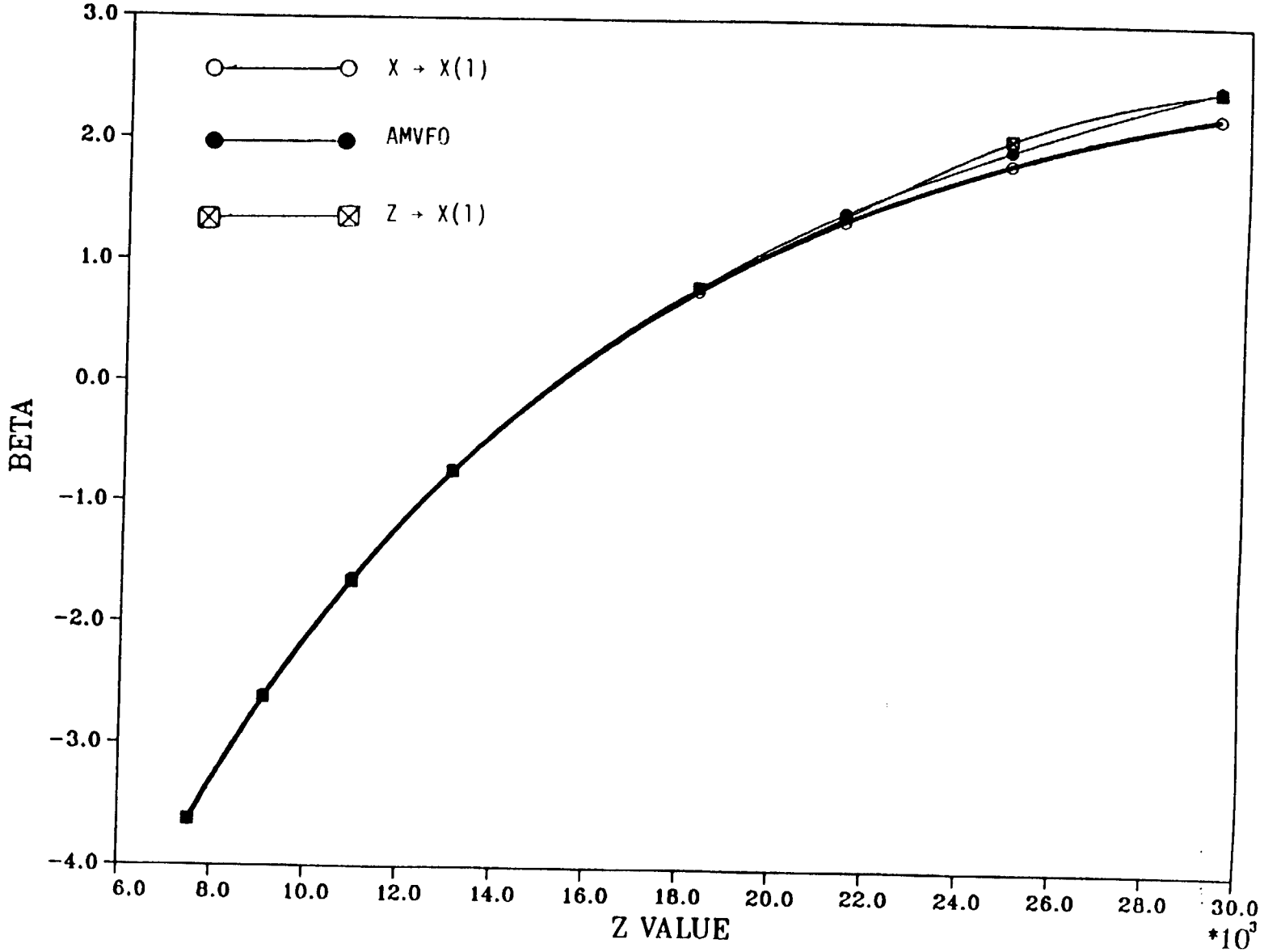

Monte Carlo Solution for Selected Points in Example 10

Z value	29364.4	24944.6
β, AMVFO	2.483	1.958
β, Wu/FPI	2.200	1.846
β, Monte Carlo (Harbitz)	2.350	1.890
95% Confidence Intervals for Monte Carlo	(2.321, 2.384)	(1.858, 1.924)
% Error in AMVFO relative to Monte Carlo	5.6	3.6
MPPL Solution after 3rd move	2.500	1.967
% Error in MPPL (3 moves) relative to Monte Carlo	6.3	4.1

EXAMPLE 11 :

LIMIT STATE FUNCTION : Z = (L/D**4)*(6.79*Q*L**2/E+10.186*A*T/G)

VARIABLE DIST. (MEAN/MED,STD/COV) : (MED AND COV FOR LN DIST. ONLY)

Q-N(28.56,2.856), L-N(10.,.2), E-N(1.E7,5.E5),D-N(.75,.015)
A-N(4.0,0.08), G-N(3.8E6,1.9E5), T-N(115.,11.5)

	AMVFO SOLUTION		EXACT SOLUTION		
Z VALUE	BETA	Pf	BETA	Pf	% ERROR (BETA)
.0609	-4.000000	.316860E-04	-3.9660	.365606E-04	.8500
.0691	-3.000000	.134997E-02	-2.9850	.141796E-02	.5000
.0783	-2.000000	.227501E-01	-1.9950	.230214E-01	.2500
.0887	-1.000000	.158655E+00	-1.0000	.158655E+00	.0000
.1133	1.000000	.841345E+00	.9980	.840860E+00	.2000
.1279	2.000000	.977250E+00	1.9940	.976924E+00	.3000
.1443	3.000000	.998650E+00	2.9870	.998591E+00	.4333
.1627	4.000000	.999968E+00	3.9750	.999965E+00	.6250

EXAMPLE 12 :

LIMIT STATE FUNCTION : Z = (L/D**4)*(6.79*Q*L**2/E+10.186*A*T/G)

VARIABLE DIST. (MEAN/MED,STD/COV) : (MED AND COV FOR LN DIST. ONLY)

Q-EVD(28.56,2.856), L-N(10.,.2), E-WEI(1.E7,5.E5), D-N(.75,.015)
A-LN(4.0,0.02), G-LN(3.8E6,0.05), T-FRE(115.,11.5)

	AMVFO SOLUTION		EXACT SOLUTION		
Z VALUE	BETA	Pf	BETA	Pf	% ERROR (BETA)
.0615	-4.361100	.647553E-05	-4.3660	.633206E-05	.1124
.0694	-3.211800	.659594E-03	-3.2200	.641016E-03	.2553
.0784	-2.091200	.182550E-01	-2.0940	.181299E-01	.1339
.0886	-.991910	.160621E+00	-.9990	.158897E+00	.7148
.1133	1.040600	.850969E+00	1.0580	.854972E+00	1.6721
.1278	1.928200	.973085E+00	1.9520	.974531E+00	1.2343
.1432	2.737600	.996905E+00	2.7480	.997002E+00	.3799
.1586	3.455000	.999725E+00	3.4180	.999685E+00	1.0709

EXAMPLE 13 :

LIMIT STATE FUNCTION : Z = (X Y)**2

VARIABLE DIST. (MEAN/MED,STD/COV) : (MED AND COV FOR LN DIST. ONLY)

X-WEI(10.,2.), Y-FRE(8.,1.)

	AMVFO SOLUTION		EXACT SOLUTION		
Z VALUE	BETA	Pf	BETA	Pf	% ERROR (BETA)
807.3593	-2.955106	.156288E-02	-2.8814	.197963E-02	2.4942
1654.0090	-2.193385	.141398E-01	-2.1523	.156868E-01	1.8731
2846.9300	-1.484133	.688869E-01	-1.4550	.728347E-01	1.9630
4408.6280	-.764057	.222417E+00	-.7395	.229802E+00	3.2141
8896.7500	.791370	.785636E+00	.8202	.793949E+00	3.6431
12162.9900	1.551912	.939658E+00	1.5951	.944655E+00	2.7829
16417.0000	2.205871	.986304E+00	2.2626	.988170E+00	2.5717
21247.7700	2.714446	.996681E+00	2.7580	.997092E+00	1.6045

EXAMPLE 14 :

LIMIT STATE FUNCTION : Z = (X Y)**3

VARIABLE DIST. (MEAN/MED,STD/COV) : (MED AND COV FOR LN DIST. ONLY)

X-WEI(10.,2.), Y-FRE(8.,1.)

	AMVFO SOLUTION		EXACT SOLUTION		
Z VALUE	BETA	Pf	BETA	Pf	% ERROR (BETA)
90357.2400	-1.953609	.253737E-01	-1.9184	.275301E-01	1.8023
151943.600	-1.483706	.689435E-01	-1.4547	.728762E-01	1.9550
238449.100	-1.007343	.156885E+00	-.9817	.163124E+00	2.5456
355325.400	-.516413	.302783E+00	-.4919	.311395E+00	4.7468
714129.700	.529881	.701903E+00	.5525	.709697E+00	4.2687
982362.300	1.049881	.853114E+00	1.0841	.860840E+00	3.2593
1341195.00	1.552116	.939683E+00	1.5948	.944622E+00	2.7501
1822217.00	2.004785	.977507E+00	2.0606	.980329E+00	2.7841

EXAMPLE 15 :

LIMIT STATE FUNCTION : Z = X Y W

VARIABLE DIST. (MEAN/MED,STD/COV) : (MED AND COV FOR LN DIST. ONLY)

X-N(10.,2.), Y-N(8.,1.), W-N(6.,0.8)

	AMVFO SOLUTION		EXACT SOLUTION		
Z VALUE	BETA	Pf	BETA	Pf	% ERROR (BETA)
111.5100	-3.998916	.318315E-04	-3.6840	.114833E-03	7.8750
177.6034	-2.999198	.135353E-02	-2.8440	.222762E-02	5.1747
259.9768	-1.999437	.227805E-01	-1.8960	.289800E-01	5.1733
360.2393	-.998969	.158905E+00	-.9200	.178786E+00	7.9050
620.8680	.998969	.841095E+00	1.0660	.856788E+00	6.7101
784.4523	1.999437	.977220E+00	2.0590	.980253E+00	2.9790
972.3621	2.999298	.998647E+00	3.0490	.998852E+00	1.6571
1186.2070	3.998916	.999968E+00	4.0320	.999972E+00	.8273

EXAMPLE FIFTEEN : Z = X Y W
X–N(10.,2.), Y–N(8.,1.), W–N(6.,.8)

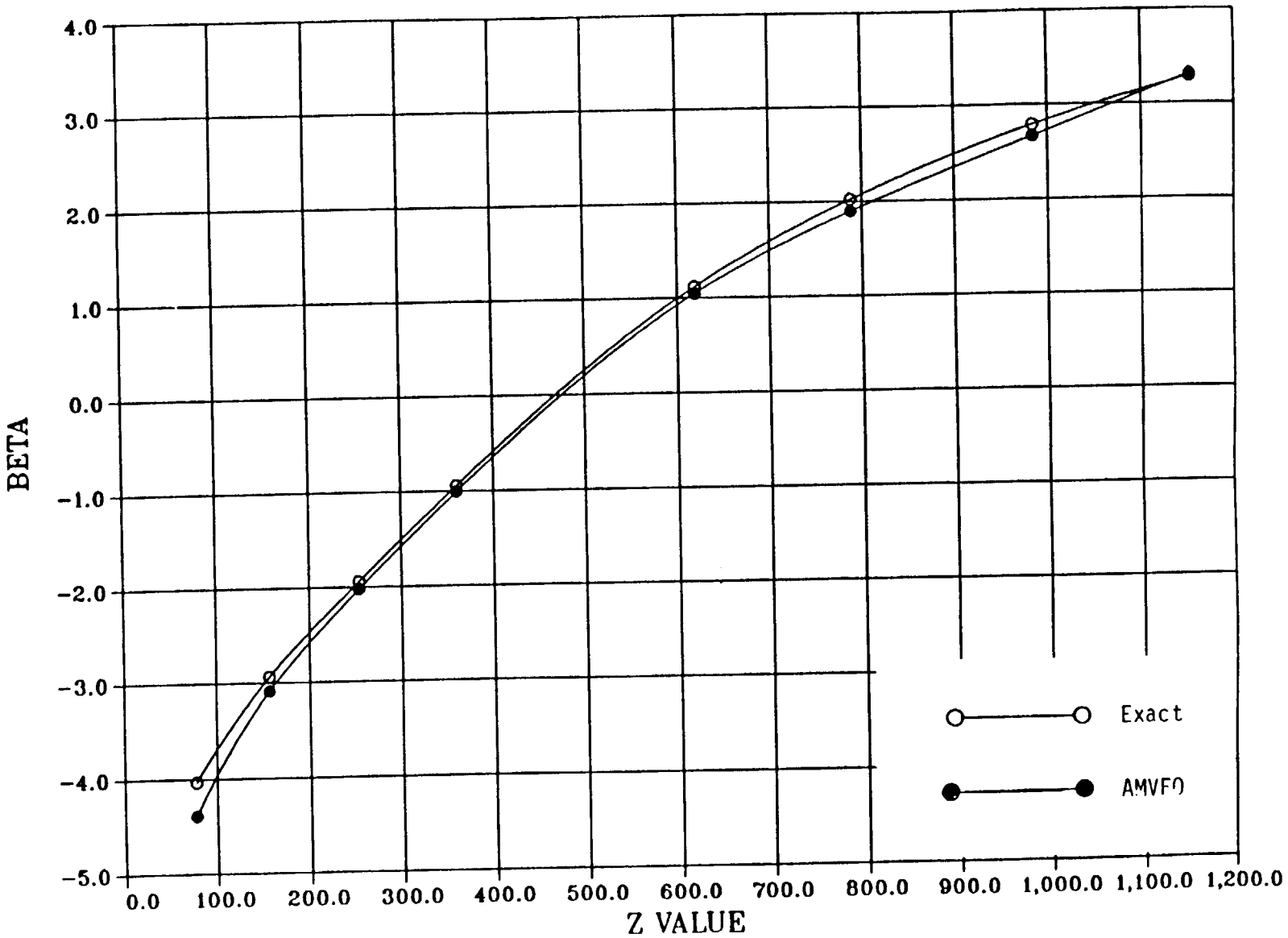

Monte Carlo Solution for Selected Points in Example 19

Z value	111.51	177.60	259.98
β, AMVFO	-3.998	-2.999	-1.999
β, Wu/FPI	-3.684	-2.844	-1.896
β, Monte Carlo (Harbitz)	-3.669	-2.813	-1.886
95% Confidence Intervals for Monte Carlo	(-3.649; -3.698)	(-2.792, -2.839)	(-1.863,
% Error in AMVFO relative to Monte Carlo	9.0	6.6	6.0
MPPL Solution after 3rd move	-3.778	-2.940	-1.980
% Error in MPPL (3 moves) relative to Monte Carlo	3.0	4.5	5.0

EXAMPLE 16 :

LIMIT STATE FUNCTION : Z = X Y W

VARIABLE DIST. (MEAN/MED,STD/COV) : (MED AND COV FOR LN DIST. ONLY)

X-WEI(10.,2.), Y-FRE(8.,1.), W-EVD(6.,0.6)

	AMVFO SOLUTION		EXACT SOLUTION		
Z VALUE	BETA	Pf	BETA	Pf	% ERROR (BETA)
77.3040	-4.388275	.571725E-05	-4.0360	.271985E-04	8.0276
156.9944	-3.088883	.100462E-02	-2.9370	.165709E-02	4.9171
253.7254	-2.019468	.217192E-01	-1.9400	.261898E-01	3.9351
360.4638	-1.006387	.157115E+00	-.9430	.172840E+00	6.2985
619.1482	1.043337	.851604E+00	1.1170	.868003E+00	7.0603
787.8300	1.897304	.971106E+00	2.0220	.978412E+00	6.5723
984.0049	2.665438	.996156E+00	2.7850	.997324E+00	4.4856
1151.5420	3.310339	.999534E+00	3.2820	.999485E+00	.8561

EXAMPLE SIXTEEN : Z = X Y W
X–WEI(10.,2.), Y–FRE(8.,1.), W–EVD(6.,.8)

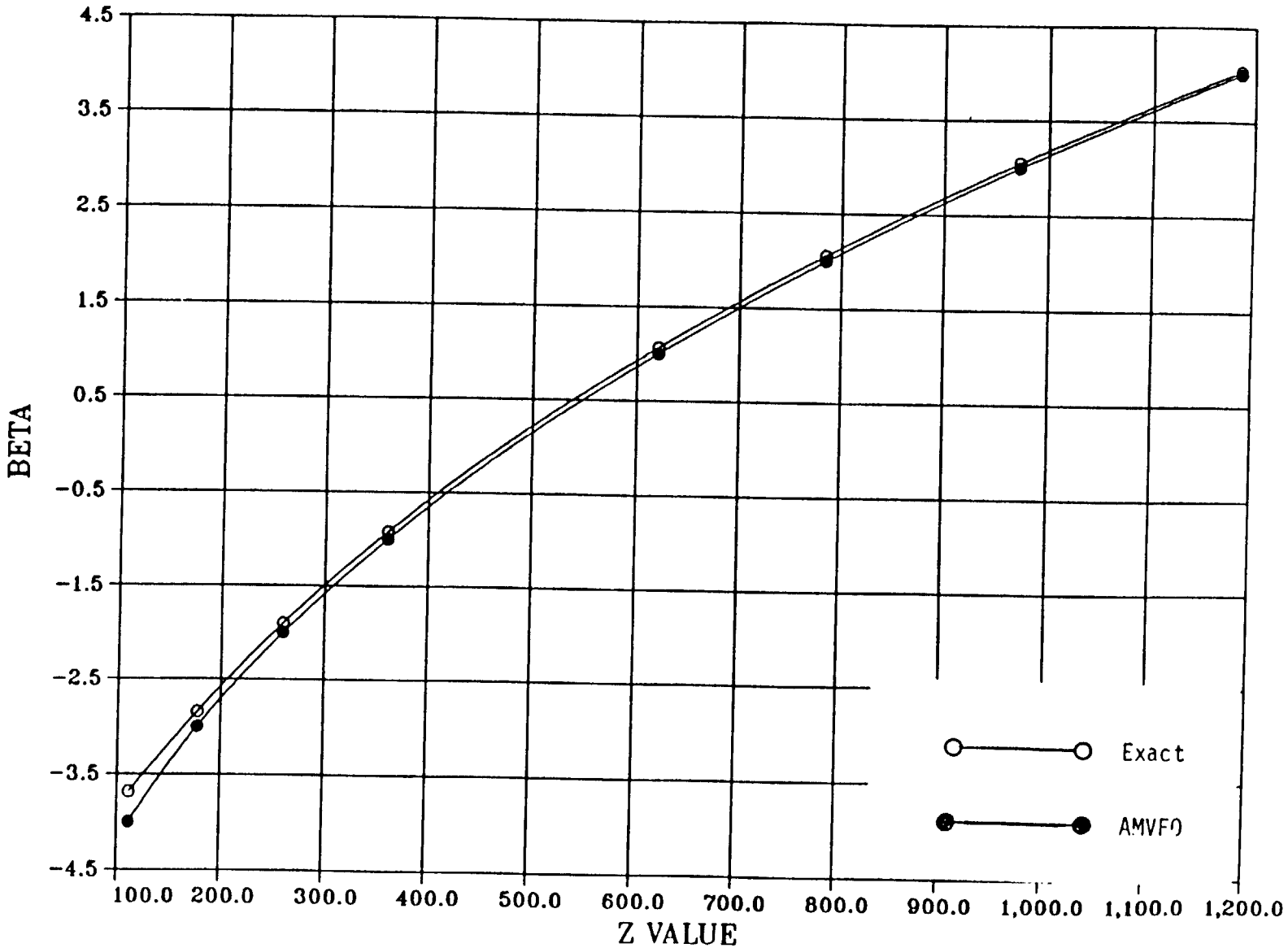

Monte Carlo Solution for Selected Points in Example 16

Z value	77.3	156.99	619.15
β, AMVFO	-4.388	-3.088	1.0433
β, Wu/FPI	-4.036	-2.937	1.117
β, Monte Carlo (Harbitz)	-4.023	-2.919	1.102
95% Confidence Intervals for Monte Carlo	(-3.999, -4.055)	(-2.895, 2.951)	(1.075, 1.126
% Error in AMVFO relative to Monte Carlo	9.1	5.8	5.3
MPPL Solution after 3rd move	-4.080	-2.980	1.030
% Error in MPPL (3 moves) relative to Monte Carlo	1.4	2.1	6.5

EXAMPLE 17 :

LIMIT STATE FUNCTION : Z = X*Y**2*W

VARIABLE DIST. (MEAN/MED,STD/COV) : (MED AND COV FOR LN DIST. ONLY)

X-WEI(10.,2.), Y-FRE(8.,1.), W-EVD(6.,0.6)

	AMVFO SOLUTION		EXACT SOLUTION		
Z VALUE	BETA	Pf	BETA	Pf	% ERROR (BETA)
363.3479	-5.232059	.839807E-07	-4.6020	.209444E-05	12.0423
926.2241	-3.541243	.199165E-03	-3.3140	.459915E-03	6.4170
1717.4930	-2.243117	.124446E-01	-2.1410	.161370E-01	4.5525
2668.5220	-1.048516	.147200E+00	-.9800	.163543E+00	6.5346
5342.5160	1.070247	.857746E+00	1.1490	.874722E+00	7.3584
7219.3570	1.857397	.968373E+00	1.9070	.971740E+00	2.6706
9337.5020	2.425469	.992356E+00	2.4540	.992936E+00	1.1763
11673.7000	2.858362	.997871E+00	2.8670	.997928E+00	.3022

EXAMPLE SEVENTEEN : Z = X*Y**2*W
X–WEI(10.,2.), Y–FRE(8.,1.), W–EVD(6.,.8)

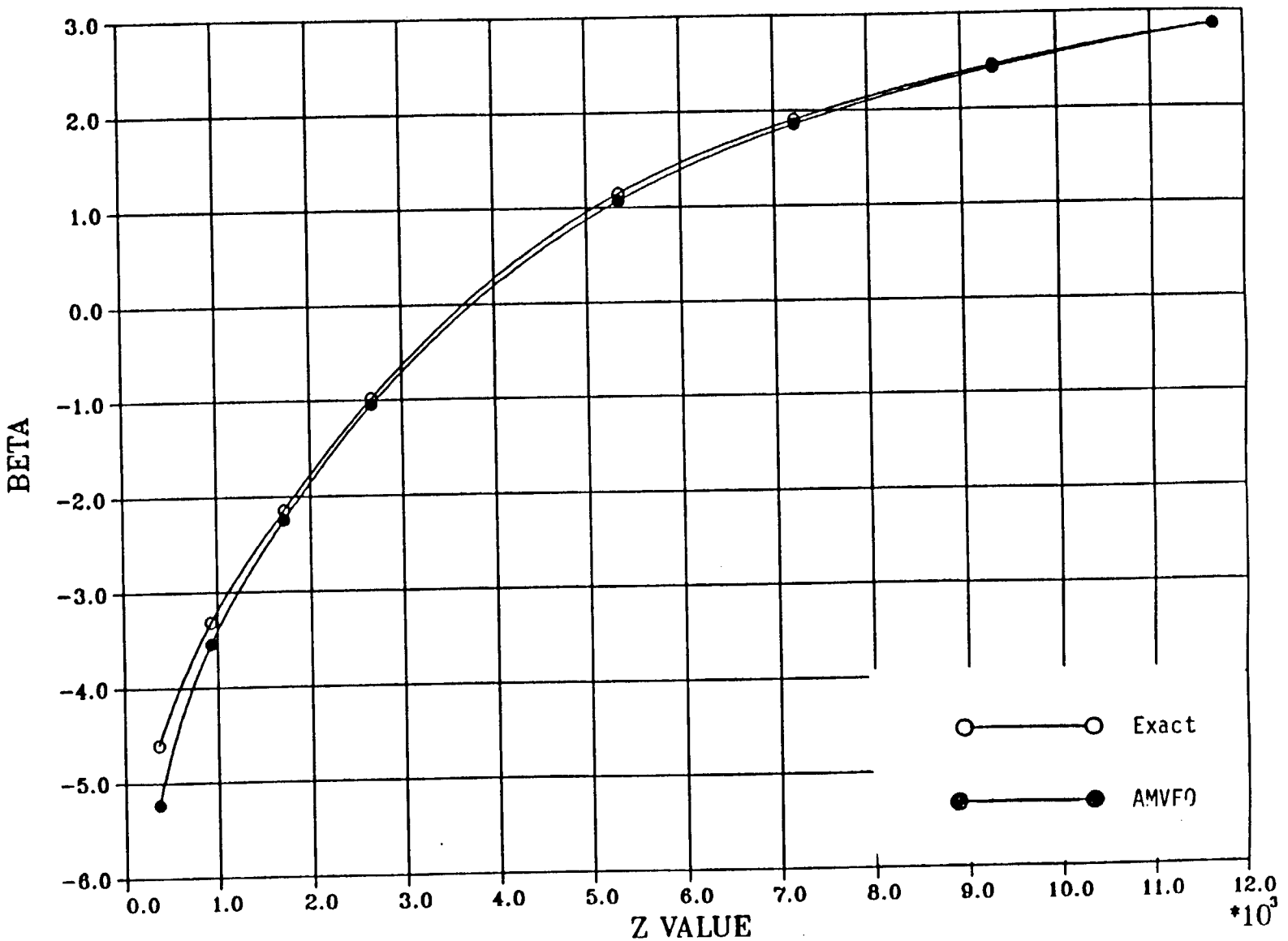

Monte Carlo-Solution for Selected Points in Example 17

Z value	363.35	926.22
β, AMVFO	-5.232	-3.541
β, Wu/FPI	-4.602	-3.314
β, Monte Carlo (Harbitz)	-4.613*	-3.331
95% Confidence Intervals for Monte Carlo		(-3.307, -3.363)
% Error in AMVFO relative to Monte Carlo	13.4	6.3
MPPL Solution after 3rd move	-4.700	-3.37
% Error in MPPL (3 moves) relative to Monte Carlo	1.9	1.2

EXAMPLE 18 :

LIMIT STATE FUNCTION : Z = X*Y**2*W - 0.5*Y*W**2

VARIABLE DIST. (MEAN/MED,STD/COV) : (MED AND COV FOR LN DIST. ONLY)

X-WEI(10.,2.), Y-FRE(8.,1.), W-EVD(6.,0.6)

	AMVFO SOLUTION		EXACT SOLUTION		
Z VALUE	BETA	Pf	BETA	Pf	% ERROR (BETA)
290.0668	-5.190314	.105168E-06	-4.4700	.391445E-05	13.8780
838.3711	-3.515534	.219478E-03	-3.2690	.539702E-03	7.0127
1616.3430	-2.231815	.128136E-01	-2.1280	.166685E-01	4.6516
2549.8740	-1.048558	.147191E+00	-.9810	.163296E+00	6.4429
5167.1910	1.078238	.859536E+00	1.1470	.874309E+00	6.3773
7011.5710	1.854104	.968138E+00	1.9090	.971869E+00	2.9608
9087.6650	2.429086	.992432E+00	2.4540	.992936E+00	1.0257
11399.7100	2.854161	.997842E+00	2.8680	.997935E+00	.4849

EXAMPLE EIGHTEEN : Z = X*Y**2*W − 0.5*Y*W**2
X−WEI(10.,2.), Y−FRE(8.,1.), W−EVD(6.,0.8)

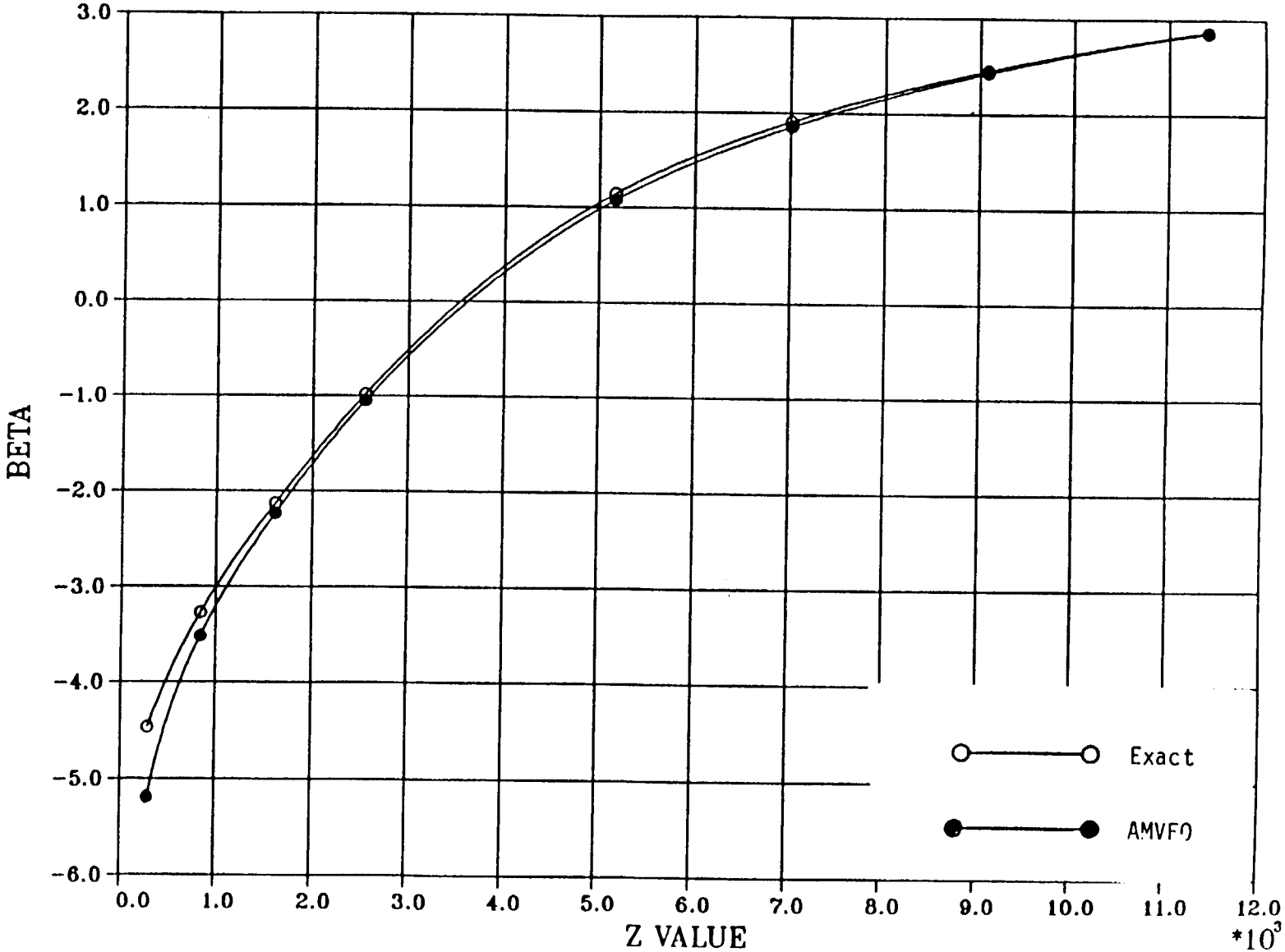

Monte Carlo Solution for Selected Points in Example 18

Z value	290.07	838.37
β, AMVFO	-5.190	-3.515
β, Wu/FPI	-4.470	-3.269
β, Monte Carlo (Harbitz)	-4.472*	-3.280
95% Confidence Intervals for Monte Carlo		(-3.256, -3.312)
% Error in AMVFO relative to Monte Carlo	16.1	7.2
MPPL Solution after 3rd move	-4.540	-3.325
% Error in MPPL (3 moves) relative to Monte Carlo	1.5	1.4

*Monte Carlo by mean value method with stratified sampling.

During our studies, we have also worked the following examples. In all cases the agreement between AMVFO and the exact solutions for at least one point in the tail has been "excellent".

EXAMPLE 19 :

LIMIT STATE FUNCTION : Z = 2 X - Y + 2 W

VARIABLE DIST. (MEAN/MED,STD/COV) : (MED AND COV FOR LN DIST. ONLY)

X-WEI(10.,1.0), Y-FRE(10.,1.0), W-EVD(10.,1.)

EXAMPLE 20 :

LIMIT STATE FUNCTION : Z = X**1.2 + 0.05*Y**1.2

VARIABLE DIST. (MEAN/MED,STD/COV) : (MED AND COV FOR LN DIST. ONLY)

X-N(10.,1.), Y-N(10.,1.)

EXAMPLE 21 :

LIMIT STATE FUNCTION : Z = X**1.5 + 0.05*Y**1.5

VARIABLE DIST. (MEAN/MED,STD/COV) : (MED AND COV FOR LN DIST. ONLY)

X-N(10.,1.), Y-N(10.,1.)

EXAMPLE 22 :

LIMIT STATE FUNCTION : Z = X**1.5 + 0.05*Y**1.5

VARIABLE DIST. (MEAN/MED,STD/COV) : (MED AND COV FOR LN DIST. ONLY)

X-WEI(10.,1.), Y-EVD(10.,1.)

EXAMPLE 23 :

LIMIT STATE FUNCTION : Z = 4*X**2 + 3*Y**1.5 - 2*W**1.2

VARIABLE DIST. (MEAN/MED,STD/COV) : (MED AND COV FOR LN DIST. ONLY)

X-WEI(10.,0.5), Y-EVD(20.,2.), W-LN(6.0,0.09)

EXAMPLE 24 :

LIMIT STATE FUNCTION : Z = 4*X**2 + 3*Y**1.5 - 2*W**1.2

VARIABLE DIST. (MEAN/MED,STD/COV) : (MED AND COV FOR LN DIST. ONLY)

X-LN(10.,0.05), Y-LN(20.,0.1), W-LN(6.0,0.09)

EXAMPLE 25 :

LIMIT STATE FUNCTION : Z = -2*X**2 + 3*Y**1.5 + 4*W**1.2

VARIABLE DIST. (MEAN/MED,STD/COV) : (MED AND COV FOR LN DIST. ONLY)

X-WEI(10.,0.5), Y-EVD(20.,2.), W-LN(6.0,0.09)

EXAMPLE 26 :

LIMIT STATE FUNCTION : Z = X Y

VARIABLE DIST. (MEAN/MED,STD/COV) : (MED AND COV FOR LN DIST. ONLY)

X-N(10.,2.), Y-N(8.,1.)

EXAMPLE 27 :

LIMIT STATE FUNCTION : Z = (X Y)**2

VARIABLE DIST. (MEAN/MED,STD/COV) : (MED AND COV FOR LN DIST. ONLY)

X-N(10.,1.), Y-N(10.,1.)

EXAMPLE 28 :

LIMIT STATE FUNCTION : Z = (X Y)**3

VARIABLE DIST. (MEAN/MED,STD/COV) : (MED AND COV FOR LN DIST. ONLY)

X-N(10.,1.), Y-N(10.,1.)

EXAMPLE 29 :

LIMIT STATE FUNCTION : Z = (X Y)**4

VARIABLE DIST. (MEAN/MED,STD/COV) : (MED AND COV FOR LN DIST. ONLY)

X-N(10.,1.), Y-N(10.,1.)

EXAMPLE 30 :

LIMIT STATE FUNCTION : Z = (X Y)**5

VARIABLE DIST. (MEAN/MED,STD/COV) : (MED AND COV FOR LN DIST. ONLY)

X-N(10.,1.), Y-N(10.,1.)

APPENDIX C

Flow Chart for Analysis to Compute CDF's
of Correlated Response Variables

P. Wirsching
University of Arizona

FLOW CHART FOR ANALYSIS TO COMPUTE CDF'S OF CORRELATED RESPONSE VARIABLES

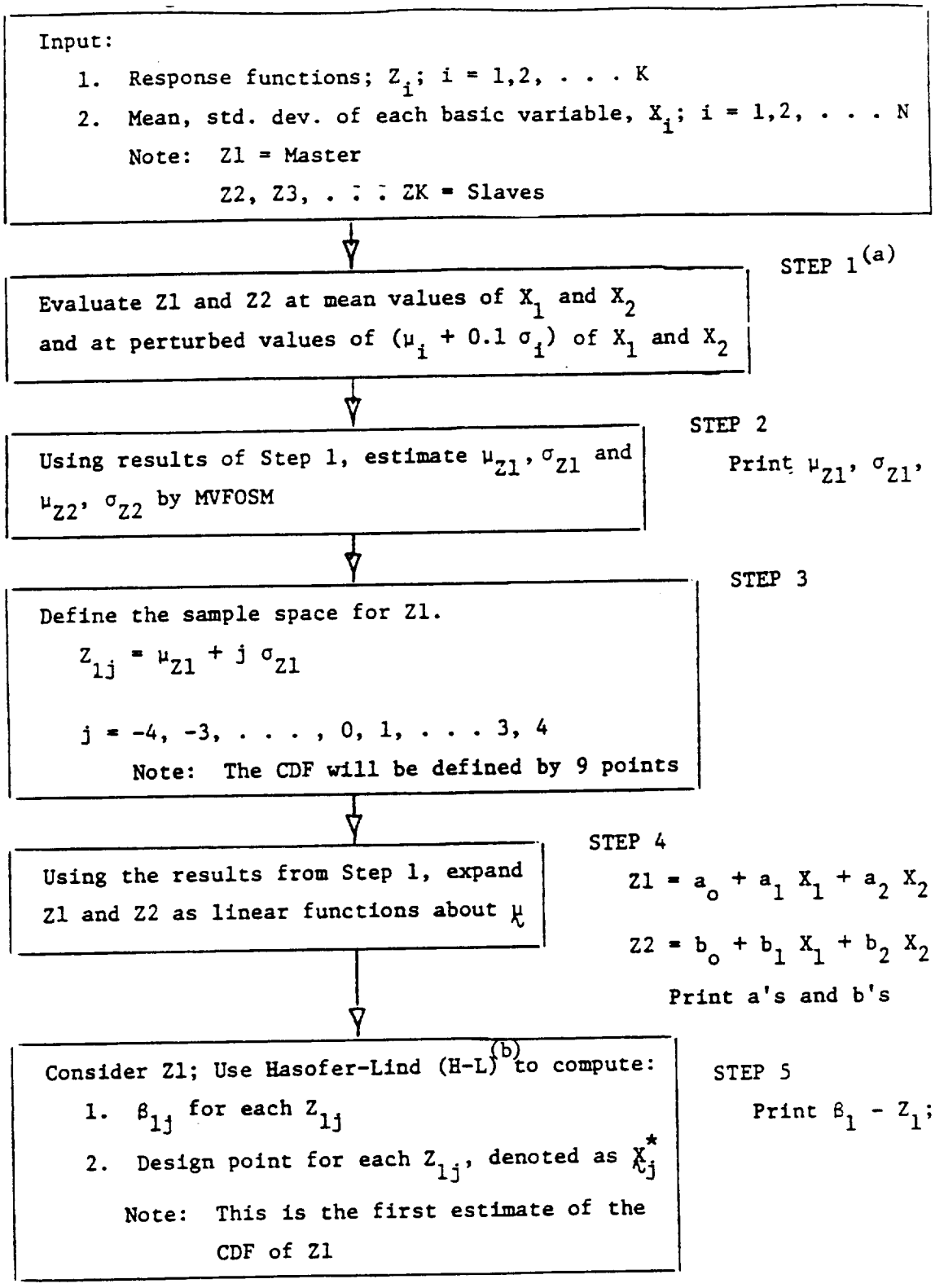

Notes:

(a) Hereafter in this chart, N = K = 2 for simplicity.

(b) H-L is used in MPPL3. Wu/FPI is used in MPPL9 in place of H-L.

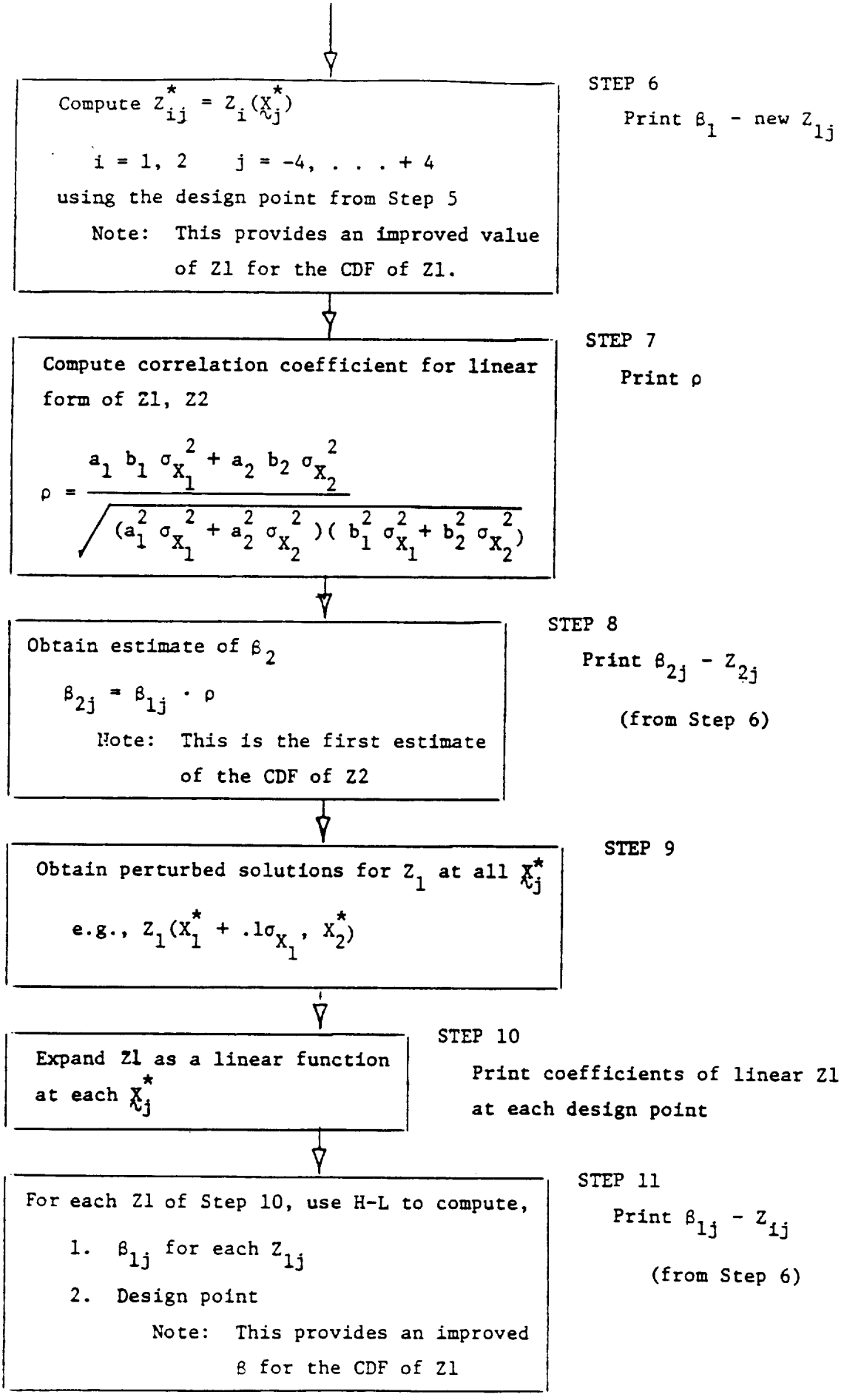
Compute $Z_{ij}^* = Z_i(\underset{\sim}{X}_j^*)$
i = 1, 2 j = -4, . . . + 4
using the design point from Step 5
Note: This provides an improved value of Z1 for the CDF of Z1.
STEP 6
Print β_1 - new Z_{1j}
Compute correlation coefficient for linear form of Z1, Z2
$\rho = \frac{a_1 b_1 \sigma_{X_1}^2 + a_2 b_2 \sigma_{X_2}^2}{\sqrt{(a_1^2 \sigma_{X_1}^2 + a_2^2 \sigma_{X_2}^2)(b_1^2 \sigma_{X_1}^2 + b_2^2 \sigma_{X_2}^2)}}$
STEP 7
Print ρ
Obtain estimate of β_2
$\beta_{2j} = \beta_{1j} \cdot \rho$
Note: This is the first estimate of the CDF of Z2
STEP 8
Print β_{2j} - Z_{2j}
(from Step 6)
Obtain perturbed solutions for Z_1 at all $\underset{\sim}{X}_j^*$
e.g., $Z_1(X_1^* + .1\sigma_{X_1}, X_2^*)$
STEP 9
Expand Z1 as a linear function at each $\underset{\sim}{X}_j^*$
STEP 10
Print coefficients of linear Z1 at each design point
For each Z1 of Step 10, use H-L to compute,
1. β_{1j} for each Z_{1j}
2. Design point
Note: This provides an improved β for the CDF of Z1
STEP 11
Print β_{1j} - Z_{ij}
(from Step 6)

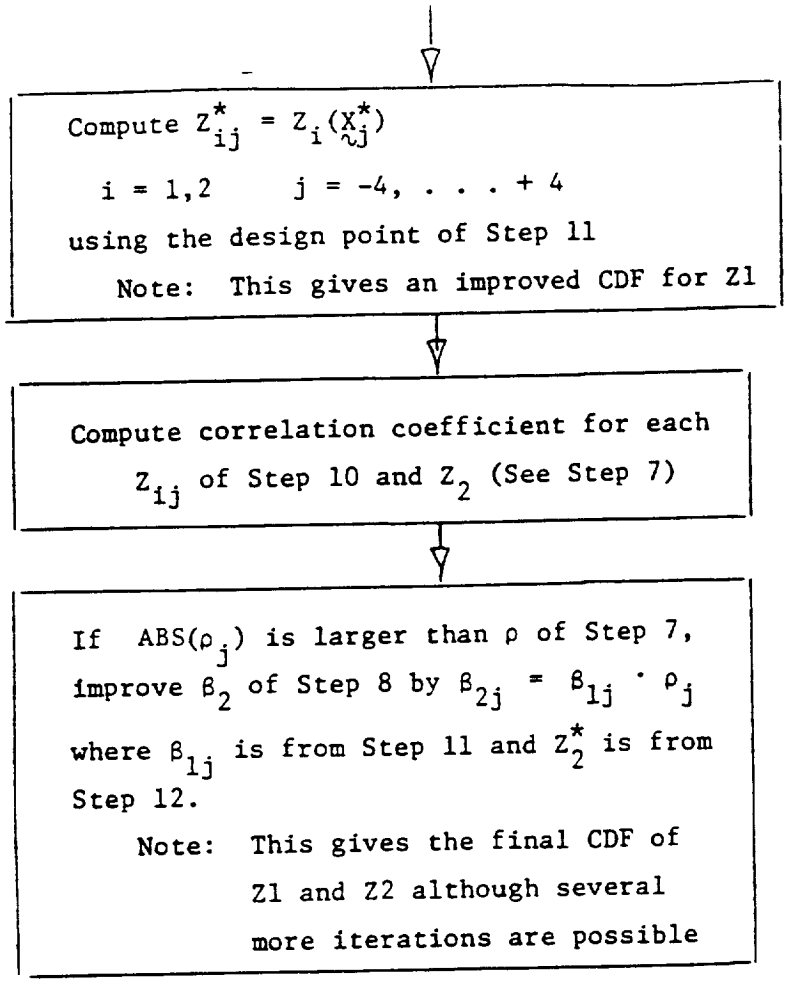

STEP 12

Print $\beta_{1j} - Z^*_{1j}$ (Step 12)

STEP 13

Print ρ_j

STEP 14

$\beta_{1j} - Z_{1j}$ (Step 12)

Print $\beta_{2j} - Z_{2j}$ (Step 8 or Step 14 pairs)

APPENDIX D

Details of Approximate Structural Models for PAAM

R.C. McClung
Southwest Research Institute

APPROXIMATE ANALYSIS CASE 2A.S

COMPONENT:	LOX post
MODEL:	Thick-walled cylinder
ANALYSIS TYPE:	Static analysis of independent pressure and temperature loadings
RESPONSE TYPES:	Stresses in hoop, radial, and axial directions

ANALYTICAL MODELS:

The LOX post is here modeled as a thick-walled cylinder subjected to different internal and external pressures and temperatures.

Pressure Loading

The stresses in a thick-walled cylinder due to internal and external pressure are available from the classical Lame' solution as

$$\sigma_r = \frac{(r_o/r)^2(p_o - p_i)}{k^2 - 1} + \frac{p_i - p_o k^2}{k^2 - 1}$$

$$\sigma_\theta = -\frac{(r_o/r)^2(p_o - p_i)}{k^2 - 1} + \frac{p_i - p_o k^2}{k^2 - 1}$$

where

$$k = \frac{r_o}{r_i}$$

and

p_i, p_o = inner, outer pressure
r = radial position
r_i, r_o = inner, outer radii
σ_r, σ_θ = radial stress, hoop stress

See Timoshenko and Goodier, Theory of Elasticity, 3rd edition, 1970, pp. 69-71.

If the ends are restrained against axial motion, so that an axial stress is induced by the attempted axial expansion or contraction, that axial stress is given by

$$\sigma_a = \frac{2\nu(p_i - p_o k^2)}{k^2 - 1}$$

Thermal Loading

Assume a steady-state temperature distribution with internal temperature T_i and external temperature T_o. An appropriate solution which satisfies $\nabla^2 T = 0$ is

$$T = T_o + (T_i - T_o)\frac{\ln(r_o/r)}{\ln(k)}$$

The solutions are then given by

$$\sigma_r = \beta\frac{(r_o/r)^2 - 1}{k^2 - 1} - \beta\frac{\ln(r_o/r)}{\ln(k)}$$

$$\sigma_\theta = -\beta\frac{(r_o/r)^2 + 1}{k^2 - 1} + \beta\frac{1 - \ln(r_o/r)}{\ln(k)}$$

$$\sigma_a = -\frac{2\beta}{k^2 - 1} + \beta\frac{1 - 2\ln(r_o/r)}{\ln(k)}$$

where

$$\beta = \frac{\alpha E(T_i - T_o)}{2(1 - \nu)}$$

and

E = Young's modulus
ν = Poisson's ratio
α = coefficient of thermal expansion

These equations are based on the assumption of no end restraint. If the ends are restrained to prevent axial motion, then the axial stress is given by

$$\sigma_a = \frac{2(1 - \nu - k^2)}{k^2 - 1}\theta_i + \frac{2\nu k^2}{k^2 - 1}\theta_o + \beta\frac{\nu - 2\ln(r_o/r)}{\ln(k)}$$

where

$$\theta = \frac{\alpha E T}{2(1 - \nu)}$$

In this expression, T should be interpreted as the difference between the actual temperature at some location and the reference temperature at which there are no thermally induced stresses or strains. Note that if the entire cylinder experiences a uniform temperature rise, this equation gives the axial stress as $-\alpha E T$.

See Timoshenko and Goodier, pp. 448-451, J. Chakrabarty, Theory of Plasticity, 1987, pp. 334-337, and M. G. Derrington, "The Onset of Yield in a Thick Cylinder Subjected to Uniform Internal or External Pressure and Steady Heat Flow," Int. J. Mechanical Sci., Vol. 4, 1962, pp. 83-103.

INPUT VARIABLES:

Geometry

r_i, r_o - inner and outer radius

Material

E - Young's modulus
ν - Poisson's ratio
α - coefficient of thermal expansion

Loads

p_i, p_o - internal and external pressures
T_i, T_o - average wall temperatures at inside and outside surfaces of cylinder
T_{ref} - reference temperature

RESPONSE VARIABLES:

σ_{max} - maximum stress in shell, with corresponding orientation and location

$\sigma_\phi(r), \sigma_r(r), \sigma_a(r)$ - hoop, radial, or axial stress at user-defined location

APPROXIMATE ANALYSIS CASE 2B.S

COMPONENT:	LOX post
MODEL:	Hollow cylindrical beam with elastic end restraint
ANALYSIS TYPE:	Static analysis of axial loads due to pressure and temperature, transverse loads due to fluid drag, and buckling due to axial loads.
RESPONSE TYPES:	axial stresses, onset of elastic instability

ANALYTICAL MODELS:

The LOX post is modeled as a simple beam with a constant cross-section corresponding to a hollow circle. One end is assumed to be rigidly fixed and the other end is elastically restrained. This restraint is characterized by two spring constants: k_a is the resistance to axial motion in an equation of the form $F = k_a u$, and k_b is the resistance to rotation in an equation of the form $M = k_b \theta$. In both cases, a rigid end condition may be selected by choosing $k \to \infty$.

Axial stress due to differential pressure across face plate

$$\sigma_a = \frac{F_a}{\pi(r_o^2 - r_i^2)}$$

where

σ_a = axial stress
F_a = axial load due to pressure differential
r_i = inner radius
r_o = outer radius

Axial temperature gradient

Assuming a linear distribution of temperature from the inlet end to the outlet end,

$$F_T = \frac{\alpha L(T_{out} - T_0) + \frac{1}{2}(T_{in} - T_{out})}{\left(\frac{1}{k_a} - \frac{L}{AE}\right)}$$

$$\sigma_a = \frac{F_T}{A}$$

where

F_T = induced axial load (positive value denotes compression)
T_{out}, T_{in} = temperatures at outlet end and inlet end
T_0 = reference temperature at which no thermally induced stresses or strains are present
L = length of beam
α = coefficient of thermal expansion
E = Young's modulus
A = cross-sectional area of beam = $\pi(r_o^2 - r_i^2)$

Transverse Load due to Fluid Drag

The maximum bending moment in the beam when subjected to a uniformly distributed transverse load occurs at the fixed end and is given by the expression

$$M_{max} = \frac{wL^2}{8}\left\{1 - \left(\frac{1}{12\beta}\right)\right\}$$

where

$$\beta = \frac{1}{4} + \frac{EI}{k_0 L}$$

$$I = \frac{\pi(r_o^2 - r_i^2)}{4}$$

and

w = magnitude of the distributed load
M = bending moment

The maximum bending moment in the beam when subjected to a transverse point load P at a distance x from the fixed end occurs at one of the two ends, depending on the value of x/L. At the fixed end, the moment is

$$M = Px\left(1 - \frac{x}{L}\right)\left\{\left(1 - \frac{x}{2L}\right) - \frac{x}{8L\beta}\right\}$$

and at the elastically restrained end, the moment is

$$M = \frac{Px^2}{4L\beta}\left(1 - \frac{x}{L}\right)$$

The axial stress associated with these bending moments is given by the well-known form

$$\sigma_a = \frac{Mr}{I}$$

Onset of Elastic Instability

Estimates of the critical load for buckling are based on more general expressions developed by Timoshenko and Gere, Theory of Elastic Stability, 2nd edition, 1961, pp. 59ff. Those expressions result in transcendental equations for the critical load. The equations given here are empirical fits to the exact solution. The exact solution and empirical expression are compared graphically in Fig. 2B.S.1. The possible effects of simultaneous transverse loading are not considered.

$$\frac{F_{cr}}{F_{ref}} = 2 + 2\left\{\frac{2}{\pi}\sec^{-1}\left(.296\frac{k_0 L}{EI} + 1\right)\right\}^{2.1}$$

where

$$F_{ref} = \frac{\pi^2 EI}{L^2}$$

and

F_{cr} = critical axial buckling load

INPUT VARIABLES:

Geometry

L - length of beam

r_i, r_o - inner and outer radius

k_a, k_b - axial and bending stiffness

Material

E - Young's modulus

α - coefficient of thermal expansion

Loads

T_0 - reference temperature at which no thermally induced stresses or strains are present

T_{out}, T_{in} - average wall temperatures at outlet end and inlet end

p - pressure differential across face plate

w - distributed transverse load due to fluid drag

$P(x)$ - transverse point load due to fluid drag acting at a distance x from the fixed end

RESPONSE VARIABLES:

σ_a - axial stress (maximum value, value at user-defined location)

F/F_{cr} - ratio of axial load to critical buckling load

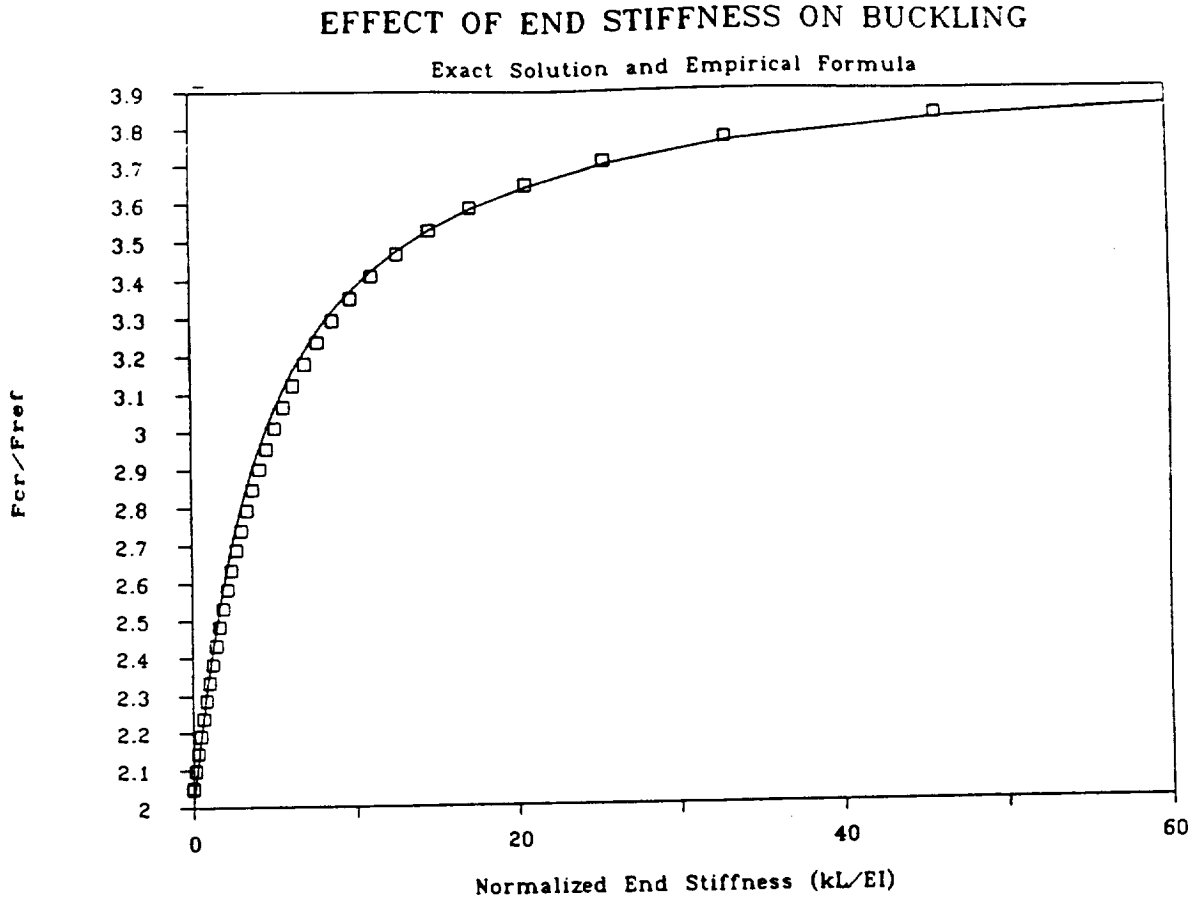

Figure 2B.S.1. Comparison of Exact Solution and Empirical Formula for Effect of End Stiffness on Critical Buckling Load

APPROXIMATE ANALYSIS CASE 2.V

COMPONENT:	LOX post
MODEL:	Hollow cylindrical beam with elastic end restraint
ANALYSIS TYPE:	Vibration
RESPONSE TYPES:	Natural frequencies and mode shapes Transverse displacement and bending stress response to harmonic and random excitation

ANALYTICAL MODEL:

Free Vibration

The natural frequencies are given by the expression

$$f_i = \frac{\lambda_i^2}{2\pi L^2}\sqrt{\frac{EI}{\rho A}}$$

where

$$I = \frac{\pi(r_o^4 - r_i^4)}{4}$$

$$A = \pi(r_o^2 - r_i^2)$$

f = frequency (hertz)
i = mode number
λ = frequency factor
L = length of beam
E = Young's modulus
ρ = mass density
A = cross-sectional area of beam
r_i, r_o = inner, outer radius

An equation of this type is given in R. D. Blevins, Formulas for Natural Frequency and Mode Shape, New York: Van Nostrand Reinhold, 1979.

Values for λ_i are given approximately by the following expressions, depending on the boundary conditions at the two ends of the beam:

fixed-pinned: $\lambda_i^{(p)} = i\pi + \pi/4$

fixed-fixed: $\lambda_i^{(f)} = i\pi + \pi/2$

For the lowest fundamental modes, it is necessary to use more exact values for the frequency factors. These are as follows:

Mode Number	Fixed-Fixed	Fixed-Pinned
1	4.730040744863	3.92660231
2	7.853204624096	7.06858275
3	10.99560783800	10.21017612
4	14.13716549126	13.35176878
5	17.27875965740	16.49336143
6	20.42035224563	
7	23.56194490204	
8	26.70353755551	
9	29.84513020910	

More precise values for λ_i at the higher mode numbers were taken from T.-C. Chang and R. R. Craig, Jr., "Normal Modes of Uniform Beams," *J. Engineering Mechanics Div., ASCE*, Vol. 95, August 1969, pp. 1027-1031.

Elastic end restraint is accommodated. The nondimensional quantity $k_\theta L/EI$ is evaluated to determine the appropriate end condition. Here k_θ is a rotational spring stiffness with units of [force*length] satisfying the relationship $M = k_\theta \theta$. Note that if $k_\theta L/EI < .01$, the variable end condition is approximately pinned, while if $k_\theta L/EI > 1000$, the end condition is effectively fixed. A first approximation to the LOX post geometry is to assume that the inlet end is fixed and the outlet end has some finite elastic stiffness. A smooth, continuous empirical relationship which estimates the frequency factor with acceptable accuracy for all $k_\theta L/EI$ is given by

$$\lambda_i = i\pi + C_i \psi_i$$

where

$$C_i = \lambda_i^{(p)} - i\pi$$

Note that C_i reduces to $\pi/4$ for $i > 5$. The ψ_i term is equal to

$$\psi_i = \left[\left(\frac{\lambda_i^{(f)} - i\pi}{\lambda_i^{(p)} - i\pi}\right) - 1\right]\left[1 - \exp\left\{-\left(\frac{1}{30}\frac{k_\theta L}{EI}\right)^{0.7}\right\}\right] + 1$$

This empirical relationship is compared directly with tabulated results from an exact analysis (R. C. Hibbeler, "Free Vibration of a Beam Supported by Unsymmetrical Spring-Hinges," J. Applied Mechanics, Trans. ASME, Vol. 42, 1975, pp. 501-502) in Fig. 2.V.1. Note that ψ_i ranges between 1 (pinned) and approximately 2 (fixed). The empirical relationship is less exact for truly intermediate stiffnesses (e.g., $k_\theta L/EI = 10$), where no single equation can easily correlate the frequency factors for all mode numbers. The function is smooth and gives the proper sense of the analytical results over the full range of $k_\theta L/EI$ values and is quite accurate nearer the limiting conditions, which are likely more relevant to the actual design. Note also that at higher modes, the end conditions are less and less significant. For the fifth mode, fixed-fixed and pinned-pinned frequencies differ by only 10%.

Mode shapes are given approximately by the expression

$$\phi_i = \cosh(\beta_i) - \cos(\beta_i) - \sigma_i\{\sinh(\beta_i) - \sin(\beta_i)\}$$

where

$$\beta_i = \frac{\lambda_i x}{L}$$

$$\sigma_i = \frac{\cosh(\lambda_i) - \cos(\lambda_i)}{\sinh(\lambda_i) - \sin(\lambda_i)}$$

Note that x=0 corresponds to the fixed end.

An axial load may have some effect on the natural frequency. An approximate formula for this effect is

$$f_i|_{P=0} = f_i|_{P=0}\sqrt{1 + \frac{F}{F_{cr}}\frac{\lambda_1^2}{\lambda_i^2}}$$

where F_{cr} is the critical buckling load (see Approximate Analysis Case 2B.S). Note that compressive loads (F negative) decrease the natural frequency and tensile loads increase the natural frequency. The changes in mode shape resulting from axial load are very small and may be neglected.

If it is desirable to include a slight taper in the beam, this can be accommodated approximately by making appropriate adjustments in the moment of inertia and cross-sectional area. Effective values for these two quantities are given by making the substitution

$$r_{eff} = \sqrt{ab}$$

where a and b are the appropriate radial dimensions at the two ends of the beam. This adjustment does not account for changes in the mode shape caused by the taper, but gives a first-order correction for the natural frequencies. For further information, see R. P. Goel, "Transverse Vibrations of Tapered Beams," J. Sound and Vibration, Vol. 47, 1976, pp. 1-7, and H. D. Conway and J. F. Dubil, "Vibration Frequencies of Truncated-Cone and Wedge Beams," J. Applied Mechanics, Trans. ASME, Vol. 32, 1965, pp. 932-934.

Forced Vibration

A simple particular solution for the forced vibration problem is based on the principle of receptances and considers only those response terms having the same frequency as the excitation. For a harmonic transverse point loading at the point $x = x_1$ of the form

$$f(x_1, t) = P_0 e^{i\omega t}$$

the response at the point $x = x_2$ is given by

$$y(x_2, t) = \alpha_{12} P_0 e^{i\omega t}$$

where

$$\alpha_{12} = \sum_{j=1}^{\infty} \frac{\phi_j(x_1)\phi_j(x_2)}{A\rho L(\omega_j^2 - \omega^2)}$$

is the receptance. The form of $\phi_j(x)$ is given above in the discussion of mode shapes for free vibration. The series form of the receptance is usually dominated by the terms corresponding to the two nearest natural frequencies.

The maximum outer fiber bending stresses at $x = x_2$ due to a harmonic point load at $x = x_1$ are given by the form

$$\sigma(x_2, t) = \gamma_{12} P_0 e^{i\omega t}$$

where

$$\gamma_{12} = \sum_{j=1}^{\infty} \frac{r_0 E \phi_j(x_1)\phi_j''(x_2)}{A\rho L(\omega_j^2 - \omega^2)}$$

and

$$\phi_i''(x) = \left(\frac{\lambda_i}{L}\right)^2 \{\cosh(\beta_i) + \cos(\beta_i) - \sigma_i[\sinh(\beta_i) + \sin(\beta_i)]\}$$

If the point load P_0 is replaced by a uniformly distributed load W per unit length, then similar equations hold true. P_0 is replaced by W, and $\phi_i(x_1)$ in the expressions for α_{12} and γ_{12} is replaced by the term

$$\left(\frac{L}{\lambda_i}\right)\{\sinh(\lambda_i)-\sin(\lambda_i)-\sigma_i[\cosh(\lambda_i)+\cos(\lambda_i)]+2\sigma_i\}$$

More general equations can be written to include the effects of hysteretic or structural damping. The original differential equation of motion

$$m\ddot{\xi}(t)+m\omega^2\xi(t)=F(t)$$

is modified in the stiffness term to the form

$$m\ddot{\xi}(t)+m\omega^2(1+i\eta_i)\xi(t)=F(t)$$

where η_i is the structural damping factor corresponding to the ith mode. Then we can write for the receptance the expression

$$\alpha_{12}=\sum_{j=1}^{\infty}\frac{\phi_j(x_1)\phi_j(x_2)}{A\rho L}(X_j-iY_j)$$

where

$$X_j=\frac{\omega_j^2-\omega^2}{(\omega_j^2-\omega^2)^2+\eta_j^2\omega_j^4}$$

$$Y_j=\frac{\eta_j\omega_j^2}{(\omega_j^2-\omega^2)^2+\eta_j^2\omega_j^4}$$

Note that the complex conjugate of the receptance is given by

$$\alpha_{12}^{*}=\sum_{j=1}^{\infty}\frac{\phi_j(x_1)\phi_j(x_2)}{A\rho L}(X_j+iY_j)$$

Random Vibration

The spectral density $S_{y_1}(\omega)$ of the motion of x_1 is related to the spectral density $S_{P_2}(\omega)$ of the load $P(t)$ at point x_2 by the relationship

$$S_{y_1}(\omega)=|\alpha_{12}|^2 S_{P_2}(\omega)$$

If multiple point loads are involved, the PSD of the response at a point x_1 is given by

$$S_{y_1}(\omega)=\sum_{r=1}^{n}\sum_{s=1}^{n}\alpha_{1P_r}^{*}\alpha_{1P_s}S_{P_rP_s}(\omega)$$

where $S_{P_rP_s}(\omega)$ is the cross spectral density of the loads P_r and P_s. When $r=s$, the term denotes the simple spectral density of the appropriate load P.

Similar expressions can be written for the spectral density of the response stresses by appropriate substitution of γ for α.

Mean square values for the response variables are obtained by numerically integrating the spectral density of the desired response variable over a specified range of excitation frequencies. The selection of specific frequency bands for the integration scheme must consider the locations of the natural frequencies.

INPUT VARIABLES:

Geometry

L - length of beam

r_i, r_o - inner and outer radius of beam

Material

E - Young's modulus

ρ - mass density

k_b - rotational spring stiffness at the elastically restrained end of the beam

Loads

$P_n(x_n)$ - magnitude of nth harmonic point load, located at position x_n

W - magnitude of harmonic uniform distributed load

ω - circular frequency of harmonic exciting force

η - structural damping factor

power spectral density and cross-spectral density of multiple random excitations

RESPONSE VARIABLES:

f_i - natural frequencies

$y_i(x)$ - normalized mode shapes for free vibration

$y(x)$ - amplitude of displacement response to harmonic forced vibration

$\sigma(x)$ - amplitude of stress response to harmonic forced vibration

power spectral density of transverse displacements and bending stresses at various positions along the beam

mean square values of the displacements and stresses

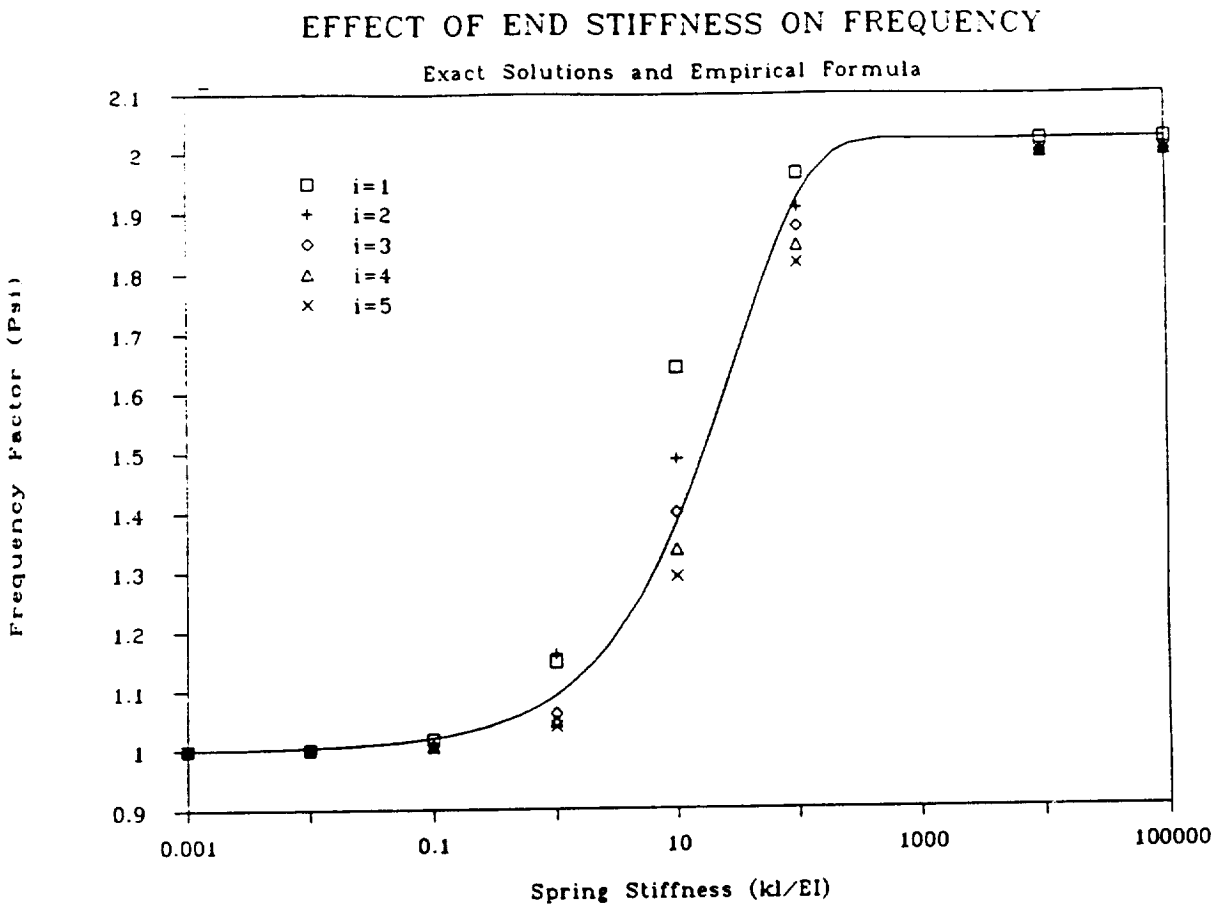
EFFECT OF END STIFFNESS ON FREQUENCY
Exact Solutions and Empirical Formula
Frequency Factor (Psi)
2.1
2
1.9
1.8
1.7
1.6
1.5
1.4
1.3
1.2
1.1
1
0.9
i=1
i=2
i=3
i=4
i=5
0.001
0.1
10
1000
100000
Spring Stiffness (kl/EI)

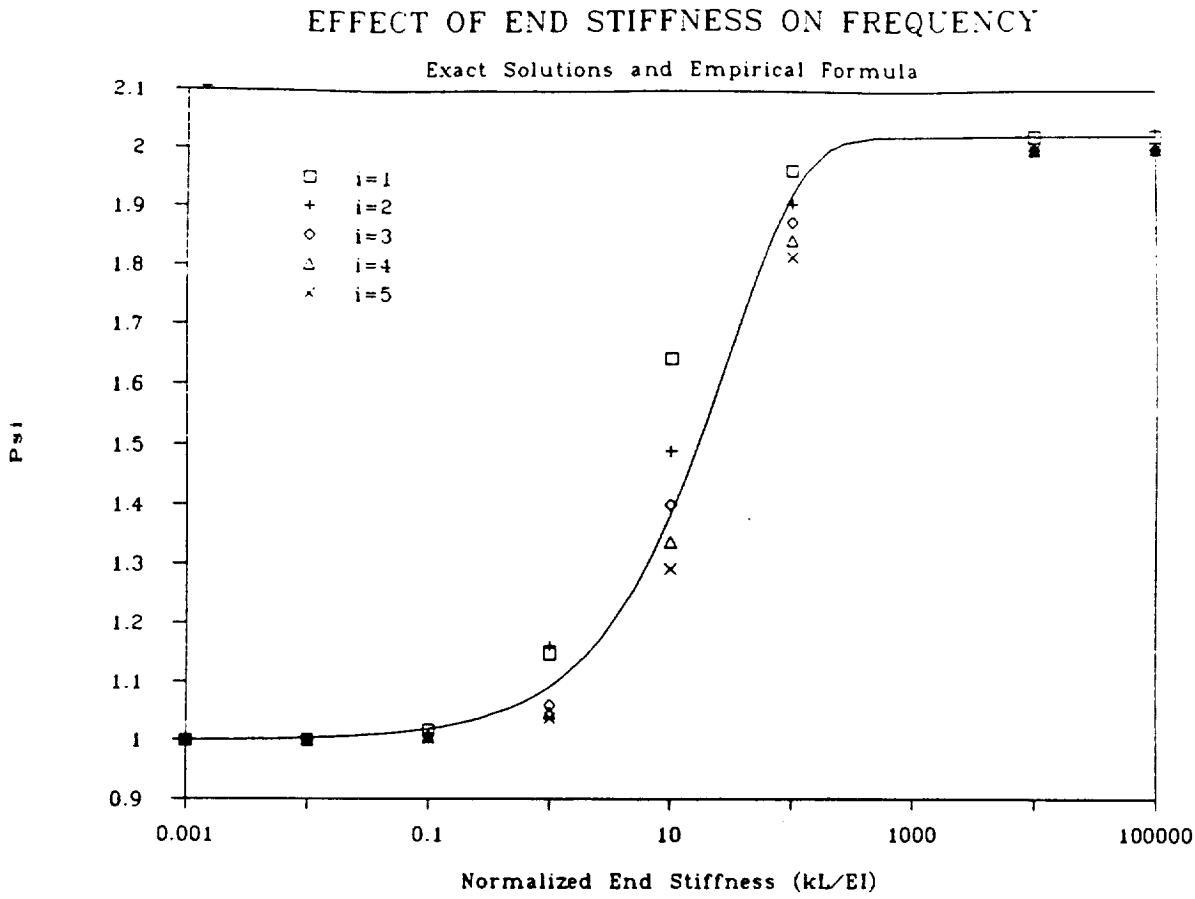

Figure 2.V.1. Comparison of Exact Solutions and Empirical Formula for Effect of End Stiffness on Natural Frequencies

APPROXIMATE ANALYSIS CASE 3.S

COMPONENT:	Transfer duct
MODEL:	Circular cylindrical shell
ANALYSIS TYPE:	Static analysis of independent pressure and temperature loadings, including buckling
RESPONSE TYPES:	Stresses and displacements Onset of elastic instability

ANALYTICAL MODELS:

The transfer duct is typically conical in shape with a circular or elliptic cross-section. The semi-vertex angle of the cone is typically small, however, and for that geometry it is sufficiently accurate to approximate the shape as an equivalent cylinder. This is a cylinder with radius equal to the average radius of the cone and length equal to the meridional length of the cone. As a further simplification appropriate to an approximate method, cross-sections are assumed to be circular.

Static Stresses

Static stresses arise from both the external pressure and the thermal gradients. Here we will calculate stresses at two locations: the midsection of the cylinder, equidistant between the two ends and assumed to be free of end effects; and at the ends, where we assume the cylinder to be rigidly clamped. We must be careful to maintain a consistent sign convention, such that compressive stresses are negative and tensile stresses positive.

External pressure causes membrane stresses in the shell. These can be estimated from common thin-shell theory as

$$\sigma_h = -\frac{pa}{h}$$

where σ_h indicates the hoop stress, p the external pressure (greater than the internal pressure), a the mean radius of the cylinder, and h the thickness of the cylinder wall. Note that a positive external pressure leads to a negative (compressive) hoop stress. If the cylinder is constrained against axial expansion or contraction, there will be an induced axial stress equal to

$$\sigma_a = \nu\sigma_h$$

These expressions are all applicable away from the ends. Near the ends there is assumed to be total constraint, which induces certain bending stresses. An axial stress at the ends can be calculated as

$$\sigma_a = \frac{6p}{2h^2\beta^2}$$

where

$$\beta^4 = \frac{3(1-\nu^2)}{a^2h^2}$$

This is an outer fiber stress which will have different sign on the inner and outer surfaces of the cylinder wall. For a positive external pressure, the axial stress will be compressive on the outside and tensile on the inside. A corresponding hoop stress will be generated according to $\sigma_h = \nu\sigma_a$. These results are developed from the work of Timoshenko and Woinowsky-Krieger, Theory of Plates and Shells, 2nd edition, 1959, pp. 466-501.

There are two possible sources of thermal stresses to be considered here. The first is that the entire cylinder experiences an increase in average temperature from the stress-free reference temperature. The second is that there is a thermal gradient through the thickness of the cylinder wall.

We consider first the thermally induced stresses at some distance from the ends. A uniformly distributed change in temperature causes no thermal stresses in the absence of restraint. If the ends are restrained against axial motion, there will be an induced axial stress equal to

$$\sigma_a = -E\alpha\Delta T_{avg}$$

where ΔT_{avg} is the average temperature change in the entire shell, E is Young's modulus, and α is the coefficient of thermal expansion. The negative sign indicates that a positive temperature change causes a compressive stress.

The radial displacement due to a uniform thermal expansion is given by

$$w = \alpha a \Delta T_{avg}$$

A uniform thermal gradient through the thickness characterized by ΔT_h (where the temperature on the inside is higher) results in stresses

$$\sigma_h = \sigma_a = \pm\frac{E\alpha\Delta T_h}{2(1-\nu)}$$

In this case, the stresses are tensile on the outer surface and compressive on the inner surface.

Stresses near the ends are more complex and, of course, depend more directly on the end conditions. Here we will consider the limiting condition of fixed end conditions. A uniform thermal expansion of the entire cylinder results in an additional axial stress at the end of

$$\sigma_a = \mp\frac{\sqrt{3}}{\sqrt{1-\nu^2}}E\alpha\Delta T_{avg}$$

(where the minus sign denotes compression on the outer surface) and an additional hoop stress at the end of

$$\sigma_h = -E\alpha\Delta T_{avg}$$

The radial displacement is zero at the ends under these conditions, of course, but it increases to 1.067 of its midsection value at the location $\beta x = 2.4$ before dropping back to the steady level.

See again Timoshenko and Woinowsky-Krieger, pp. 497-501, and also H. D. Tabakman and Y. J. Lin, "Quick Way to Calculate Thermal Stresses in Cylindrical Shells," Machine Design, September 21, 1978, pp. 138-143.

Buckling

Buckling can be caused by the combined action of a uniform external pressure and the restrained thermal expansion of the shell, which induces a compressive axial stress. The recommended practice for the calculation of critical buckling loads due to these conditions is given by the linear rule

$$R_c + R_p = \left(\frac{\sigma}{\sigma_{cr}}\right) + \left(\frac{p}{p_{cr}}\right) = 1$$

where R_c and R_p are the ratios of allowable to critical load for each load type considered independently.

The critical compressive buckling stress is given by the form

$$\sigma_{cr} = \frac{\gamma_1 E}{\sqrt{3(1-\nu^2)}}\left(\frac{h}{a}\right)$$

where γ_1 is an empirical factor used to correct the disparity between theory and experiment. A suggested expression for γ_1 is

$$\gamma_1 = 1 - 0.901(1 - e^{-\phi})$$

where

$$\phi = \frac{1}{16}\sqrt{\frac{a}{h}}$$

The critical external pressure is calculated as

$$p_{cr} = \frac{0.855}{(1-\nu^2)^{\frac{3}{4}}}\frac{E\sqrt{\gamma_2}}{\left(\frac{a}{h}\right)^{\frac{3}{2}}\left(\frac{L}{a}\right)}$$

Here $\sqrt{\gamma_2}$ is conservatively estimated as 0.75.

These equations are based on the recommendations of NASA SP-8007, Buckling of Thin-walled Circular Cylinders, August 1968 (rev.), one of a series of NASA space vehicle design criteria monographs.

The end conditions can have a complex influence on the critical buckling load, depending on the nature of the end restraint. One factor is the restraint against rotation of the ends, analogous to the influence of fixed or pinned ends on the behavior of a slender column. This effect is considerably less significant for cylindrical shells, since the buckled shape usually corresponds to larger numbers of axial and circumferential nodes. The equations given above are for simply supported ends, which is a slightly conservative estimate. Another, more complicated factor, arises due to constraint against radial displacement at the ends. When the shell heats up and expands, there will be not only an axial expansion but also a circumferential and radial expansion. Far from the ends, this expansion will be unrestrained, but at the ends there may be some restraint which prevents or limits the displacements. This will cause some bowing of the cylinder wall, and this initial prebuckling deformation will further reduce the critical axial load. This is a complex nonlinear effect, and its analysis is further complicated by uncertainties regarding the exact nature of the end conditions in the actual component. As a first approximation for the current linear PAAM code, we will neglect all end effects.

INPUT VARIABLES:

Geometry

L - equivalent length of cylinder
a - equivalent mean radius of cylinder
h - thickness of cylinder wall

Material

E - Young's modulus
ν - Poisson's ratio
α - coefficient of thermal expansion

Loads

p - external pressure
T_i, T_o - temperatures at inner and outer surface of wall
T_{ref} - reference temperature at which no thermally-induced stresses or strains are present

RESPONSE VARIABLES:

σ_x, σ_θ - axial and hoop stresses at the ends and at the mid-section of the shell
critical buckling ratio

APPROXIMATE ANALYSIS CASE 3.V

COMPONENT:	Transfer duct
MODEL:	Circular cylindrical shell
ANALYSIS TYPE:	Vibration
RESPONSE TYPES:	Natural frequencies and mode shapes Response to harmonic and random excitation

ANALYTICAL MODELS:

Free Vibration

Typical transfer ducts are generally conical in shape with circular or elliptical cross-sections. These cones are here analyzed as "equivalent cylinders," cylinders having their radius equal to the average radius of the cone and their length equal to the meridional length of the cone. For small semivertex angles, this approximation is quite good, as confirmed by R. F. Hartung and W. A. Loden, "Axisymmetric Vibration of Conical Shells," Journal of Spacecraft and Rockets, Vol. 7, No. 10, October 1970, pp. 1153-1159, and also by G. Herrmann and I. Mirsky, "On Vibration of Conical Shells," Journal of the Aerospace Sciences, Vol. 25, 1958, pp. 451-458. Other nondimensional parameters, including the ratio of length to radius, were considered when assessing the adequacy of the approximation.

Another issue to be resolved is the matter of boundary conditions. Several different end conditions are possible, including restraint of radial displacement, axial displacement, and rotation at the ends. Many combinations are possible. K. Forsberg ("Influence of Boundary Conditions on the Modal Characteristics of Thin Cylindrical Shells," AIAA Journal, Vol. 2, No. 12, December 1964, pp. 2150-2157) has suggested that the most significant influence on natural frequencies is due to the condition placed on the axial displacement. These effects are most pronounced for the lowest natural frequencies. As the number of axial half-waves increases, the model characteristics for all boundary conditions converge to similar values. The present analysis will assume the ends to be clamped with full restraint against axial motion, the conditions analyzed by Arnold and Warburton in the reference given above. Forsberg's results suggest that no significant errors will be introduced by this assumption for the geometries typical of the transfer duct.

Internal pressure can have a significant effect on the natural frequency response of the cylindrical shell, as shown by Y. C. Fung, E. E. Sechler, and A. Kaplan, "On the Vibration of Thin Cylindrical Shells Under Internal Pressure," Journal of the Aeronautical Sciences, Vol. 24, 1957, pp. 650-651. This effect seems to be pronounced only for larger number of circumferential waves and thinner shells, however, and so it is neglected in the present analysis.

General Formulation

R. N. Arnold and G. B. Warburton ("The Flexural Vibrations of Thin Cylinders," Proc. Inst. Mech. Engrs., London, Vol. 167, Ser. A, 1953, pp. 62-74) have presented an approximate solution technique for the free vibration of circular cylinders which gives results for numbers of circumferential waves greater than or equal

to two and any number of axial waves greater than or equal to one. The determination of natural frequencies by their method depends on the solution of the cubic equation

$$\Delta^3 - R_2\Delta^2 + R_1\Delta - R_0 = 0$$

where

$$f = \frac{1}{2\pi a}\sqrt{\frac{Eg\Delta}{\rho(1-\nu^2)}}$$

and

Δ = frequency factor
f = frequency
a = mean radius of cylinder
E = Young's modulus
g = gravitational constant
ρ = density
ν = Poisson's ratio

The coefficients R_0, R_1, R_2 are given by lengthy expressions involving the numbers of axial and circumferential waves, the radius, length, and wall thickness of the cylinder, and other variables related to an axial wavelength factor. Full equations are given in Appendix I of the original paper. Solution of the cubic equation above results in three positive real roots, but only the lowest value is of significance to the problem at hand.

Solution of this series of equations for different wave numbers permits identification of the mode shape corresponding to the lowest natural frequency, which can change dramatically with cylinder geometry.

The displacements corresponding to these natural frequencies are given by the following equations:

$$u = A\left\{-\sin\left(\frac{\mu x}{a}\right) + k\sinh\left(\frac{\mu x}{a}\right)\right\}\cos(n\phi)$$

$$v = B\left\{\cos\left(\frac{\mu x}{a}\right) + k\cosh\left(\frac{\mu x}{a}\right)\right\}\sin(n\phi)$$

$$w = C\left\{\cos\left(\frac{\mu x}{a}\right) + k\cosh\left(\frac{\mu x}{a}\right)\right\}\cos(n\phi)$$

for even numbers of axial nodes and

$$u = A\left\{\cos\left(\frac{\mu x}{a}\right) - k\cosh\left(\frac{\mu x}{a}\right)\right\}\cos(n\phi)$$

$$v = B\left\{\sin\left(\frac{\mu x}{a}\right) - k\sinh\left(\frac{\mu x}{a}\right)\right\}\sin(n\phi)$$

$$w = C\left\{\sin\left(\frac{\mu x}{a}\right) - k\sinh\left(\frac{\mu x}{a}\right)\right\}\cos(n\phi)$$

for odd numbers of axial nodes where u, v, and w are the displacements in the axial, circumferential, and radial directions, ϕ is the angular coordinate, and n is the number of circumferential waves. The axial wavelength factor μ is given by

$$\frac{\mu_m L}{a} = \left(\frac{2m-1}{2}\right)\pi$$

Here m is the number of axial half-waves ($m+1$ is the number of axial nodes) and L is the length of the cylinder. The coefficient k is equal to

$$k = \frac{\sin\left(\frac{\mu L}{2a}\right)}{\sinh\left(\frac{\mu L}{2a}\right)}$$

The constants A, B, and C can be determined by solving three simultaneous equations given in Appendix I of Arnold and Warburton. In general, the radial displacement will be the largest.

Axisymmetric Vibration

Simpler expressions are possible for axisymmetric vibratory modes, where displacements are only radial and $n=0$. Here we take advantage of the similarity between the governing differential equation for the vibration of a circular cylinder and the transverse vibration of a beam on an elastic foundation. The equations are identical if EI for the beam is replaced by the flexural rigidity D of the cylinder, the foundation stiffness E_f is replaced by the quantity Eh/a^2, where h is the cylinder wall thickness, and the mass per unit length ρA of the beam is replaced by the mass per unit area ρh of the cylinder. Here D is calculated as

$$D = \frac{Eh^3}{12(1-\nu^2)}$$

A further simplification is possible because the natural frequencies of a beam on an elastic foundation, f_i, are related to the natural frequencies of the corresponding beam without the elastic foundation, f_{i0} by the relationship

$$f_i = \sqrt{f_{i0}^2 + \frac{E_f}{4\rho A \pi^2}}$$

See J. W. Stafford, "Natural Frequencies of Beams and Plates on an Elastic Foundation with a Constant Modulus," J. of the Franklin Institute, Vol. 284, 1967, pp. 262-264. The mode shapes of the beam are not affected by the addition of the foundation. Therefore, we may take advantage of expressions developed earlier for the transverse vibration of the LOX post in order to describe the natural frequencies and mode shapes of the circular cylinder.

Carrying out the necessary calculations and simplifications, we have for the circular cylinder

$$f_i = \sqrt{\frac{\lambda_i^4 D}{4\pi^2 L^4 \rho h} + \frac{E}{4\pi^2 a^2 \rho}}$$

where λ_i is determined from the information and equations presented in Approximate Analysis Case 2.V, vibration of the LOX post. The model requires that one end of the cylinder be rigidly clamped, but allows the cylinder walls at the other end to be elastically restrained against rotation. In order to consider elastic end restraint in the cylinder based on the equations developed for the beam, two modifications are required. The first is the substitution of the flexural rigidity D for the term EI when calculating ψ_i. The second is a change in the units of k_θ to [force*length/length], since the moment in the expression $M = k_\theta \theta$ is a meridional bending moment with units [force*length/length]. The final form of ψ_{i_1} then, is

$$\psi_i = \left[\left(\frac{\lambda_i^{(f)} - i\pi}{\lambda_i^{(p)} - i\pi}\right) - 1\right]\left[1 - \exp\left\{-\left(\frac{1}{30}\frac{k_b L}{D}\right)^{0.7}\right\}\right] + 1$$

The radial displacement w is given in normalized form by the expression

$$w_i = \cosh(\beta_i) + \cos(\beta_i) - \sigma_i\{\sinh(\beta_i) + \sin(\beta_i)\}$$

where

$$\beta_i = \frac{\lambda_i x}{L}$$

$$\sigma_i = \frac{\cosh(\lambda_i) - \cos(\lambda_i)}{\sinh(\lambda_i) - \sin(\lambda_i)}$$

Note that $x = 0$ corresponds to the fixed end.

Harmonic Forced Vibration

The governing differential equation for the general, non-axisymmetric vibration of the cylinder is sufficiently complex to prevent any simple solutions for harmonic forced vibration, and therefore this problem lies beyond the scope of an approximate method. Some solutions are possible, however, for axisymmetric vibration ($n=0$) based on the analogy with a beam on an elastic foundation.

For an axisymmetric, harmonic line loading P_o per unit length at the axial position $x = x_1$ of the form

$$f(x_1, t) = P_0 e^{i\omega t}$$

the axisymmetric displacement response at the axial position $x = x_2$ is given by

$$w(x_2, t) = \alpha_{12} P_0 e^{i\omega t}$$

where

$$\alpha_{12} = \sum_{j=1}^{\infty} \frac{w_j(x_1) w_j(x_2)}{h\rho L(\omega_j^2 - \omega^2)}$$

The outer fiber bending stresses (in the axial direction) are given by

$$\sigma(x_2, t) = \gamma_{12} P_0 e^{i\omega t}$$

where

$$\gamma_{12} = \sum_{j=1}^{\infty} \frac{6D w_j(x_1) w_j''(x_2)}{h^3 \rho L(\omega_j^2 - \omega^2)}$$

and

$$w_i''(x) = \left(\frac{\lambda_i}{L}\right)^2 \{\cosh(\beta_i) + \cos(\beta_i) - \sigma_i[\sinh(\beta_i) + \sin(\beta_i)]\}$$

Similar expressions are possible for uniform pressure loadings and systems with structural damping, by analogy to the expressions given in Approximate Analysis Case 2.V, vibration analysis of the LOX post.

Random Vibration

The response of the cylinder to random axisymmetric excitation is based on the expressions developed previously for harmonic excitation, following the form of equations derived for the LOX post (q.v.).

INPUT VARIABLES:

Geometry

L - length of shell

a - mean radius of shell

h - thickness of shell wall

Material

E - Young's modulus

ν - Poisson's ratio

ρ - density

k_b - rotational spring stiffness at the elastically restrained end of the cylinder

RESPONSE VARIABLES:

f_{min} - minimum natural frequency and corresponding wave numbers

$f(m,n)$ - natural frequencies corresponding to various combinations of the wave numbers

$w(x)$ - amplitude of radial displacement response to axisymmetric harmonic excitation

$\sigma(x)$ - amplitude of outer fiber bending stress response to axisymmetric harmonic excitation

power spectral density of radial displacements and bending stresses at various positions along the cylinder for axisymmetric random excitation

mean square values of the displacements and stresses

APPENDIX E

Validation of LOX Post Thick Cylinder Model

H.R. Millwater
Southwest Research Institute

Validation of the PAAM code

A validation problem of the Lox Post thick cylinder model was performed using realistic input data obtained from the first annual PSAM report, the Rocketdyne division and best engineering estimates. An advanced first order and Monte Carlo analysis of the closed form solution were performed. In addition, a Nessus finite element model of a thick cylinder was performed to check against the closed form model.

The variable inputs for the Lox Post thick cylinder model are listed in Table 1.

Table 1. Definition of random/deterministic variables

Variables	Distribution	Mean	COV
Inner Radius (Ri)	truncated Normal (±0.03)	0.94	1.06%
Outer Radius (Ro)	truncated Normal (-0.002, +0.01)	0.94	4.55%
Young's Modulus(E)	Normal	3.4032E+07	2%
Poisson's Ratio	Normal	.359375	2%
Thermal coefficient	Normal	5.65E-6	5%
Internal Pressure(Pi)	Lognormal	3077	4%
External Pressure(Po)	Lognormal	3232	4%
Internal Temperature(Ti)	Lognormal	194 R	1.55% (3 R)
External Temperature(To)	Lognormal	1444 R	1.55% (15 R)
Reference Temperature(Tref)	N/A	530 R	0%

Notes: All mean value data was obtained from the 1st annual PSAM report and Rocketdyne. The truncated normal limits for Ri and Ro along with the mean temperatures and COV of Ti and To were provided by Rocketdyne. Other statistical data such as distribution types and COV for the other random variables were determined from default values provided by Dr. Paul Wirsching and are not problem specific, see Table 2.

The input data for PAAM is identical to FPI with the exception that additional data is sometimes needed. This need is accommodated by adding the necessary response data after the model data. The keyword *RESPONSE indicates response data is being provided. In PAAM, the first data is the response function desired (i.e. Lox post thick cylinder, Lox post tapered beam, Turbine blade, etc.). In the Lox Post thick cylinder example the response function is "2AS". The second data is a set of five integers. The third data is a set of five reals. This information can be used anyway desired by the user written subroutines. Additional information can be entered in any format as long as the user

written routine reads the data properly. For the Lox Post thick cylinder example the first integer indicates the response type (i.e. hoop stress, radial stress or axial stress); the second integer indicates whether end constraints are imposed (11 - yes, 12 - no). The first real indicates the radial position of the desired response; between 0.0 = RI to 1.0 = RO.

The input file for an Advanced Mean Value solution of the Lox Post thick cylinder model is listed. The desired response is the hoop stress at the inner radius without end constraints.

```
*FPI
THICK CYLINDER MODEL (2AS) - USER DEFINED HOOP STRESS
*RVNUM            10
*GFUNCTION         6
*DATASETNM         0
*METHOD            1
*PRINTOPT          0
*ANALTYP           0
*END
*DEFRANVR
RI
 0.9400000E+00 0.1000000E-01 0.1000000E+02
   0.91    0.97
RO
 0.1100000E+01 0.3300000E-02 0.1000000E+02
   1.098     1.11
E
 0.3403200E+08 0.6806400E+06 0.2000000E+01
XNU
 0.359375       0.00719        0.2000000E+01
ALPH
 0.5650000E-05 0.2830000E-06 0.2000000E+01
PI
 0.3077000E+04 0.1230000E+03 0.4000000E+01
PO
 0.3232000E+04 0.1292800E+03 0.4000000E+01
TI
 0.1940000E+03 0.3000000E+01 0.4000000E+01
TO
 0.1444000E+04 0.1500000E+02 0.4000000E+01
TREF
 0.5300000E+03 0.0000000E+00 0.2000000E+01
*END
*RESPONSE
C  LOX POST THICK CYLINDER MODEL
2AS
     1    11      0      0      0
    0.00000     0.00000     0.00000     0.00000     0.00000
*END
```

The results of the Lox post FPI and Monte Carlo analyses for hoop stress at the inner and outer radii are shown in figures 1. and 2. The agreement between FPI and Monte Carlo is excellent for the closed form model. However, the hoop stress values clearly indicate that yielding will take place and a nonlinear model should be developed.

Figure 3. shows the sensitivity at +3 standard deviations of the random variables for the hoop stress at Ri. The coefficient of thermal expansion clearly dominates. The internal and external radii are insignificant do to their tight tolerances. It should be pointed out that the COV used for the thermal coefficient (ALPHA), elastic modulus (E), Poisson's ratio (XNU), internal and external pressure (Pi and Po) were chosen from default values given by Dr. Paul Wirsching. This statistical data is suggestions to be used when problem specific data is not available. Use of improved statistical data may significantly alter the results.

Table 2. Default distributions and COV for NESSUS random variables:

VARIABLE	DISTRIBUTION	COV
E	Normal	.02
n	Normal	.02
G	Normal	.02
r	Normal	.02
a	Normal	.05
Yield stress	Wiebull	.07
Coords	Normal	.005
Thickness	Normal	.005
Temp	Lognormal	.05
Press	Lognormal	.04
Forces	Lognormal	.02
x-sect area	N	.007
Inertia	L	.02
Torsional constant	L	.01
springs	L	.02
blade angle - x,y,z	N	stdev = 0.1°
Material Orientation	N	
Other	Lognormal	

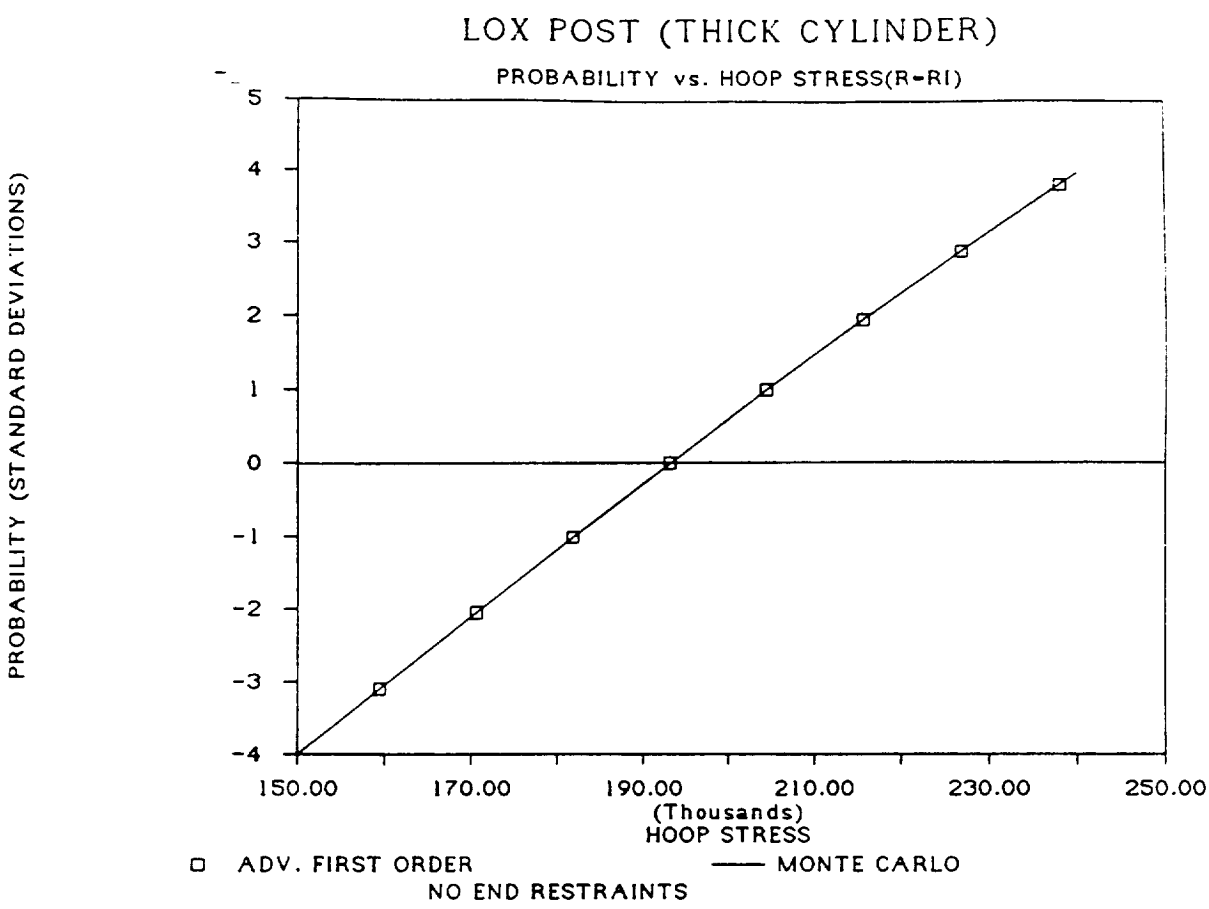
LOX POST (THICK CYLINDER)
PROBABILITY vs. HOOP STRESS(R-RI)
PROBABILITY (STANDARD DEVIATIONS)
5
4
3
2
1
0
-1
-2
-3
-4
150.00
170.00
190.00
210.00
230.00
250.00
(Thousands)
HOOP STRESS
ADV. FIRST ORDER
MONTE CARLO
NO END RESTRAINTS

Figure 1.

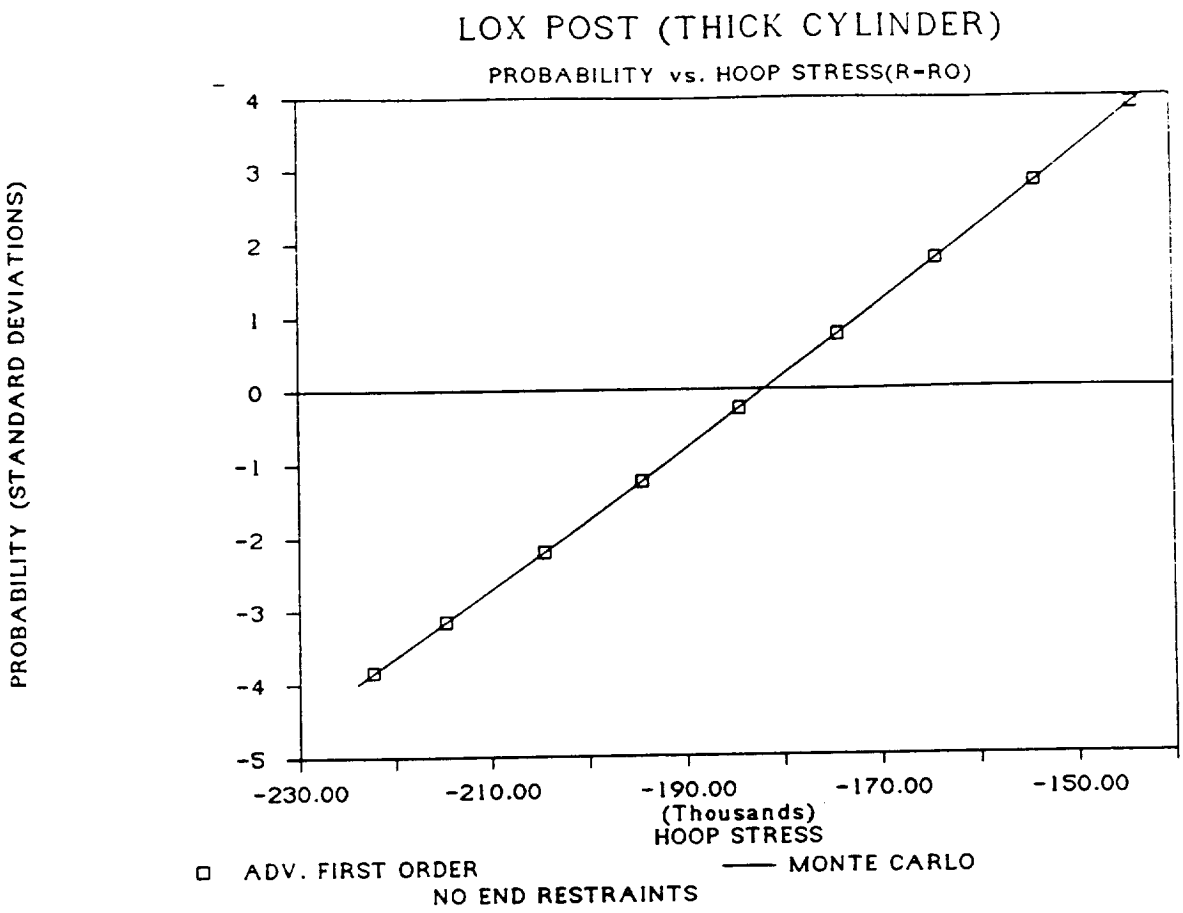
LOX POST (THICK CYLINDER)
PROBABILITY vs. HOOP STRESS(R-RO)
PROBABILITY (STANDARD DEVIATIONS)
4
3
2
1
0
-1
-2
-3
-4
-5
-230.00
-210.00
-190.00
-170.00
-150.00
(Thousands)
HOOP STRESS
ADV. FIRST ORDER
MONTE CARLO
NO END RESTRAINTS

Figure 2.

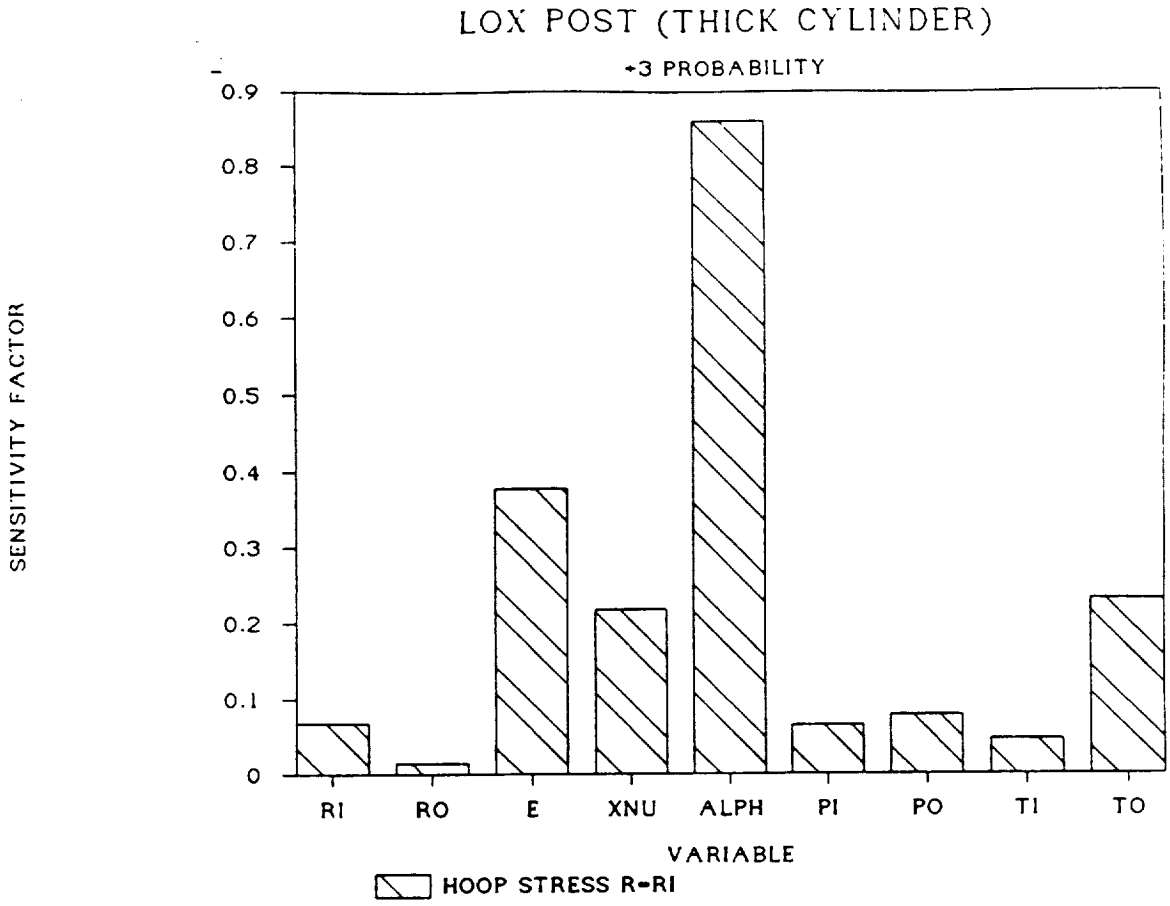
LOX POST (THICK CYLINDER)
+3 PROBABILITY
SENSITIVITY FACTOR
0.9
0.8
0.7
0.6
0.5
0.4
0.3
0.2
0.1
0
RI
RO
E
XNU
ALPH
PI
PO
TI
TO
VARIABLE
HOOP STRESS R-RI

Figure 3.

APPENDIX F

Validation Cases

Y.-T. Wu
O.H. Burnside
Southwest Research Institute

VALIDATION CASE 4

TITLE: Rotating Beam (Timoshenko beam elements)

PROBLEM: Determine the probabilistic distributions of the first bending natural frequency and the tip displacement of a rotating beam

TYPE: Centrifugal loading and stress stiffening effects

RESPONSES: First bending frequency and tip displacement

FEM MODEL: NESSUS element type 98 - Timoshenko beam element
Number of elements = 10
Number of nodes = 11 (6 degrees-of-freedom per node)
Boundary condition: cantilevered

Figure V4-1. Sketch and FEM model

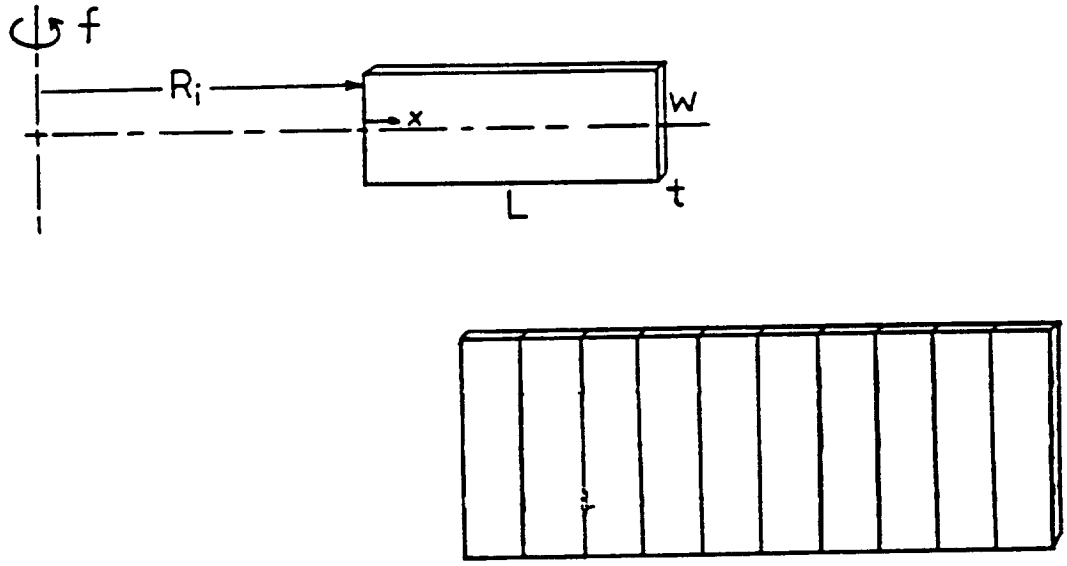

ANALYTICAL SOLUTION:

Assumed first bending mode shape: (x**4 -4*L*x**3 + 6*L**2*x**2)/L**4

Frequency = SQRT { 1.0384 * E * t**2 / (r*L**4) + (1.173+6.6/L) * f**2

Tip displacement = r * (f**2) * (l**3) * (1 + Ri/L) / (3.*E)

where
E = modulus
r = mass density
w = width
t = thickness
L = length
f = rotating frequency = 400 rad/sec
Ri= inside radius = 4.237 in.

DEFINITION OF RANDOM/DETERMINISTIC VARIABLES

Number of Random Variables = 5

Variables	Distribution	Median	Coef. of Variati
Young's Modulus	Lognormal	29E+06 psi	10%
Length	Lognormal	3.844 in	5%
Thickness	Lognormal	0.0416 in	5%
Width	Lognormal	1.424 in	5%
Density	Lognormal	9E-4 lb-sec^2/in^4	5%
Rotating Frequency	Fixed	400 rad/sec	
Radius Ri*	Fixed	4.237	

*Note: see Figure V4-1

NESSUS CONVERGENCE/PERTURBATION SETTINGS (NESSUS 2.7)

1. Modal extraction:
   *MODAL 1 0 1
2. Parameter Data:
   *PERT 5 5 0(Eigenvalue re-solution)
3. Convergence criteria:
   Increment 0:
   *ITER 0 5
   20 1.E-04
   Increment 1:
   *ITER 0 5
   20
4. Perturbation Settings:
   +0.001 standard deviation for length.
   +0.1 standard deviations for the remaining random variables.

SOLUTION COMPARISON:

1. Deterministic solutions using the mean values of random variables:

Table V4-1 Comparisons of the deterministic solutions

	Theory	NESSUS	NESSUS/Theory
Frequency	853.0	855.6	1.003
Tip displacement	2.4945E-4	2.4829E-4	0.99534

2. Probabilistic solutions for the frequency and the displacement at selected probabilistic levels:
   Simulation: Monte Carlo (sample size = 500,000)
   NESSUS: Mean-Value-First-Order (MVFO) solution
   Advanced MVFO solution
   (See Figures V4-2 and V4-3)

REMARKS: Date: 2/26/88 NESSUS 2.7 PFEM

1. The perturbation range for the length was selected to be very small (0.001 std.) to avoid convergence instability.

2. The 'adjusted' exact curves in Figures V4-2 and V4-3 are defined using the ratios of the NESSUS mean solutions to the theoretical mean solutions. (see Table V4-1)

Figure V4-2 First Bending Frequency

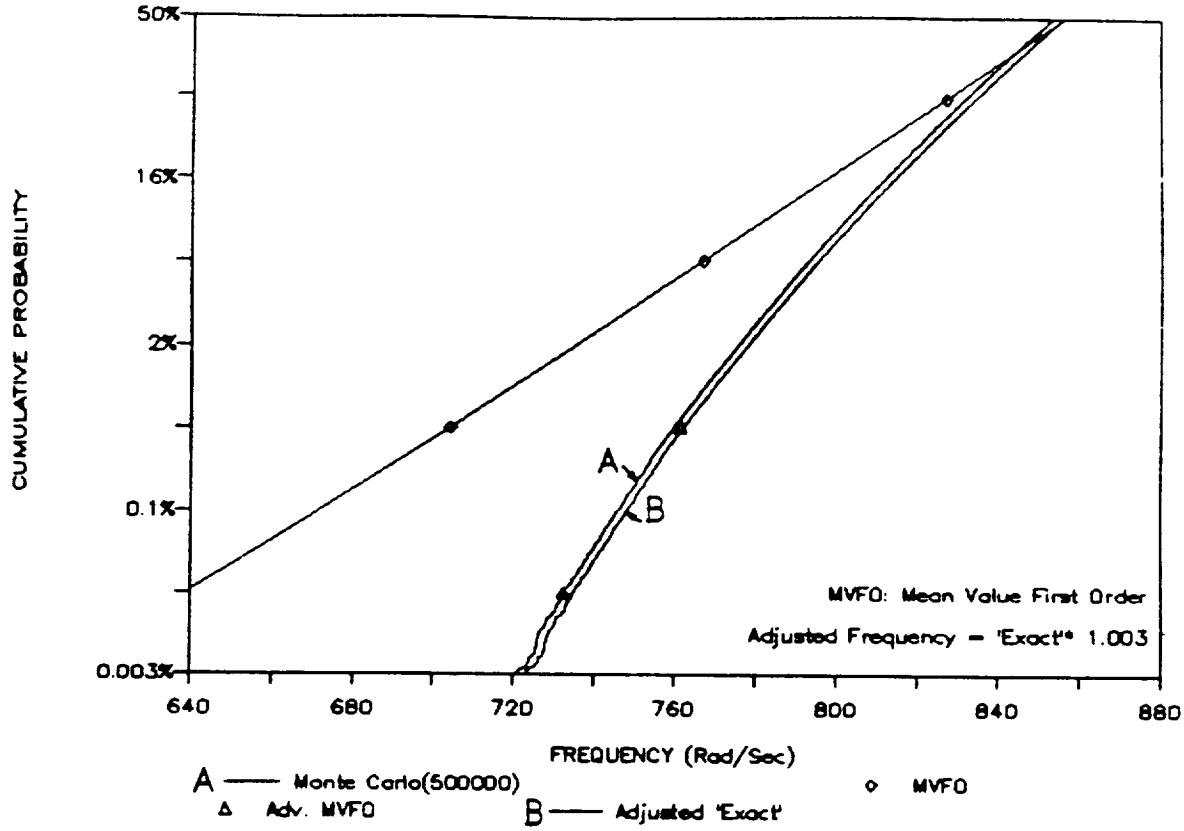

Figure V4-3 Tip Displacement

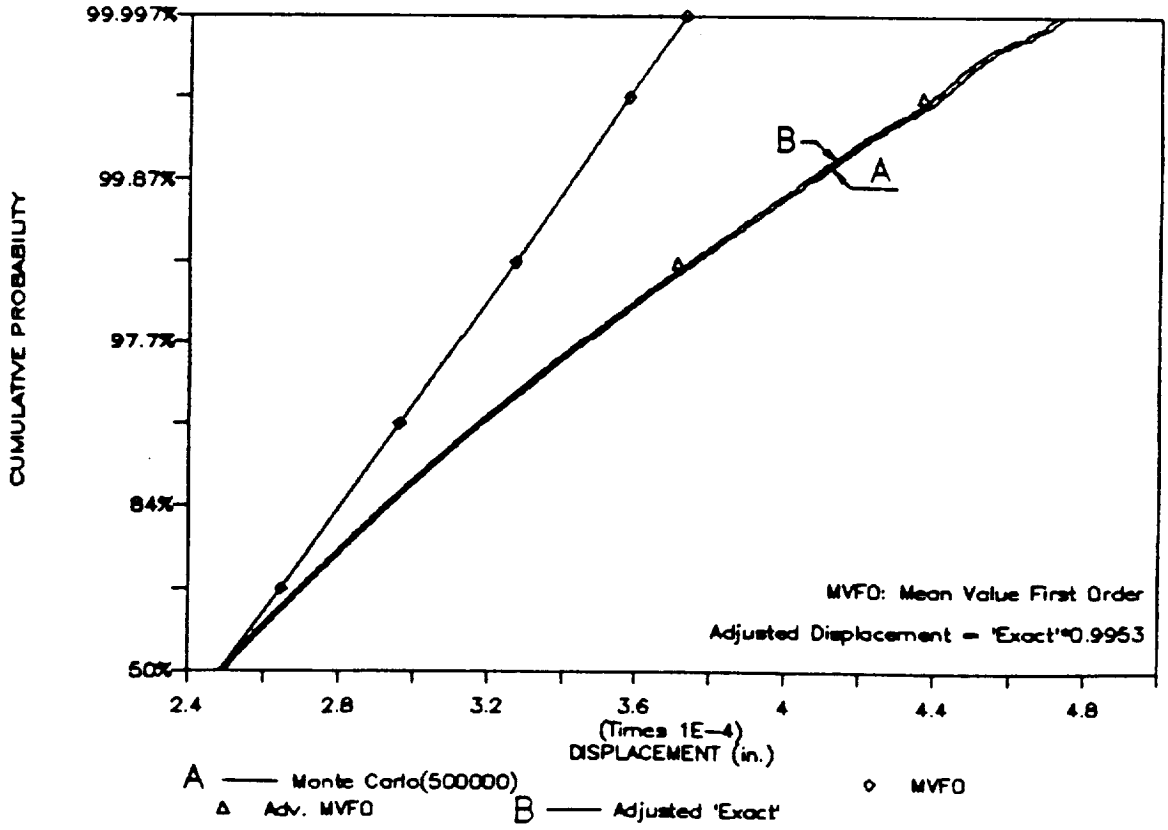

VALIDATION CASE 8

TITLE: Static Analysis of Spherical Shell

PROBLEM: A spherical shell is subjected to uniform internal pressure loads. Determine the probabilistic distribution of the maximum stress.

TYPE: Static, fully correlated pressure loading

RESPONSES: Stress

FEM MODEL: NESSUS element type 75 Four-node assumed strain axisymmetric
Number of elements = 200
Number of nodes = 211 (6 degrees-of-freedom per node)
(Nodes 181 to 211 constitute 20 collapsed, 3-node elements)
Boundary condition : fixed at base (node 1 to node 21)

Figure V8 - 1 Sketch and FEM Model

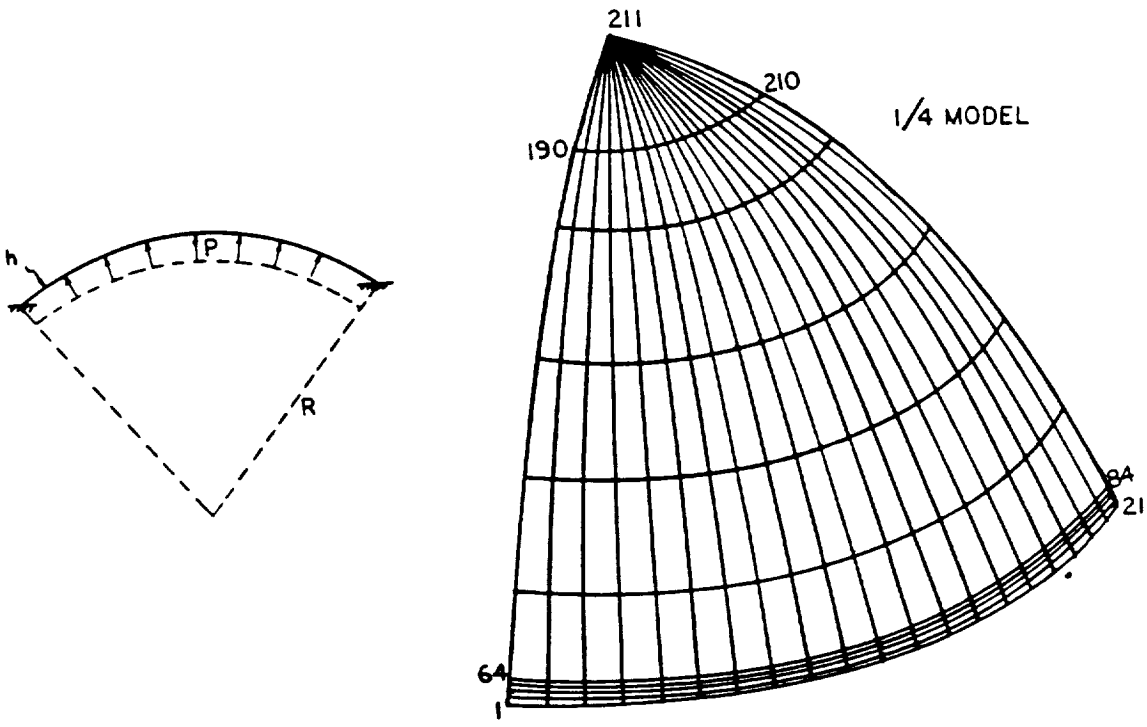

ANALYTICAL MODEL:
Analytical Solution: $S_{max} = 1.2 * (R * P)/h$

where R = radius
P = internal pressure
h = thickness

Reference: Timoshenko and Woinowsky-Krieger, Theory of Plates and Shells 2nd ed., p544

DEFINITION OF RANDOM/DETERMINISTIC VARIABLES

Number of Random Variables = 2

Variables	Distribution	Mean	Coef. of Variat:
Pressure P	Lognormal	284 psi	10%
Thickness h	Lognormal	2.36 in	5%

NESSUS CONVERGENCE/PERTURBATION SETTINGS

1. Convergence Limit:
   Max. number of iterations allowed: 30
   Max. allowable rel. error in the residuals: 0.0003
2. Perturbation Range:
   +0.1 standard deviations for both random variables.

SOLUTION COMPARISON:

1. Deterministic solution using mean values of random variables:

	Stress
Theory	8130.1 psi
NESSUS	7883.5 psi
Ratio	1.03

2. Probabilistic solutions at selected probabilistic levels:
   Theory: Exact (Stress is also a lognormal variable)
   NESSUS: Mean Value First Order (MVFO) solution
   Advanced Mean Value First Order solution (AMVFO)
   First iteration solution
   (See Figure V8-2)

REMARKS:

1. The perturbation convergence limit must be small enough to insure at least one iteration will be performed in NESSUS perturbation.

2. For the probabilistic solution (see Figure V8-2), an adjusted 'exa solution was defined by dividing the theoretical solution by a factor of 1.028. This factor is selected to match the two solutions at the 5 probability level.

Figure V8-2 Probabilistic Analysis Results - Comparisons of the NESSUS and the Theoretical Solutions

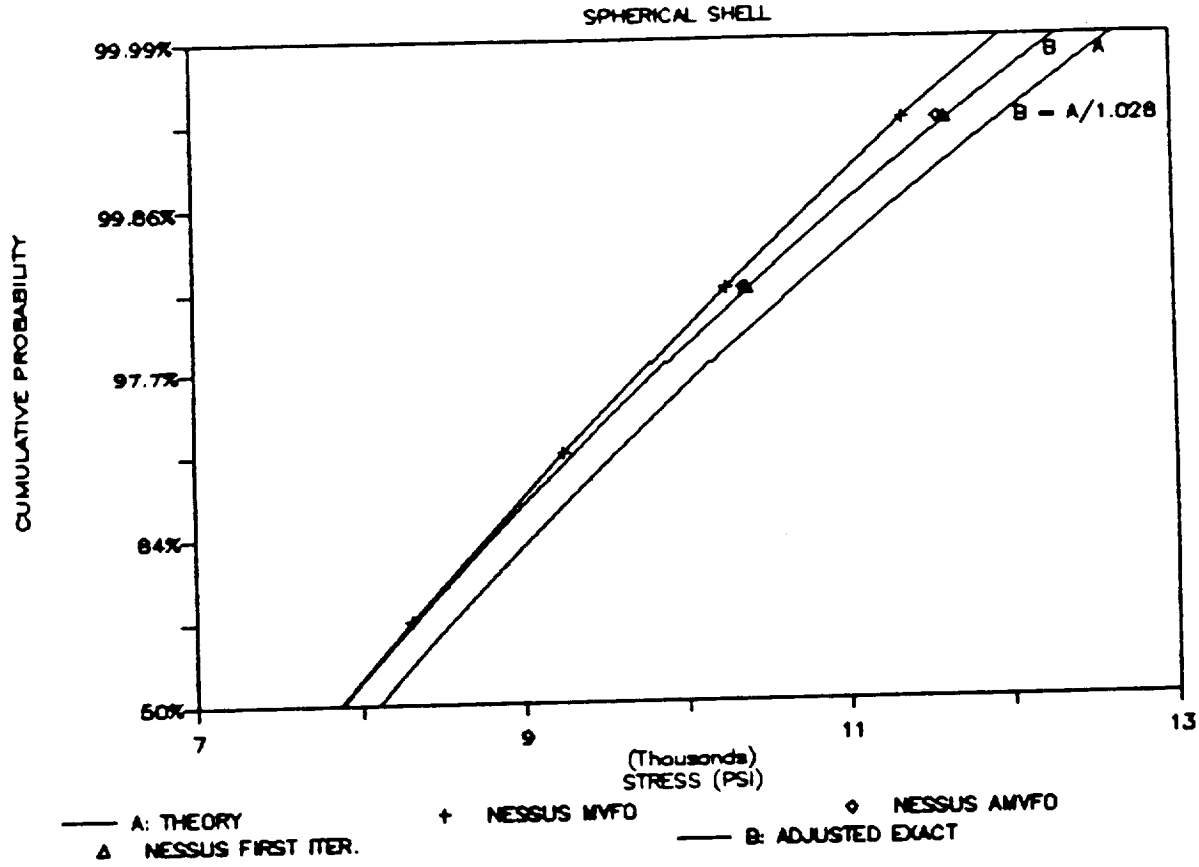

VALIDATION CASE 11

TITLE: [illegible]

PROBLEM: [illegible]

TYPE: [illegible]

RESPONSES: Critical Pressure

FEM MODEL: NESSUS element type 75 - four-node shell element
Number of elements = 24
Number of nodes = 50 (6 degrees-of-freedom per node)
Boundary conditions: Node 1,2,49 and 50 fixed
Node 1 to 48 fixed in Z Dir. and X & Y rotation

Figure 1. Sketch and FEM model

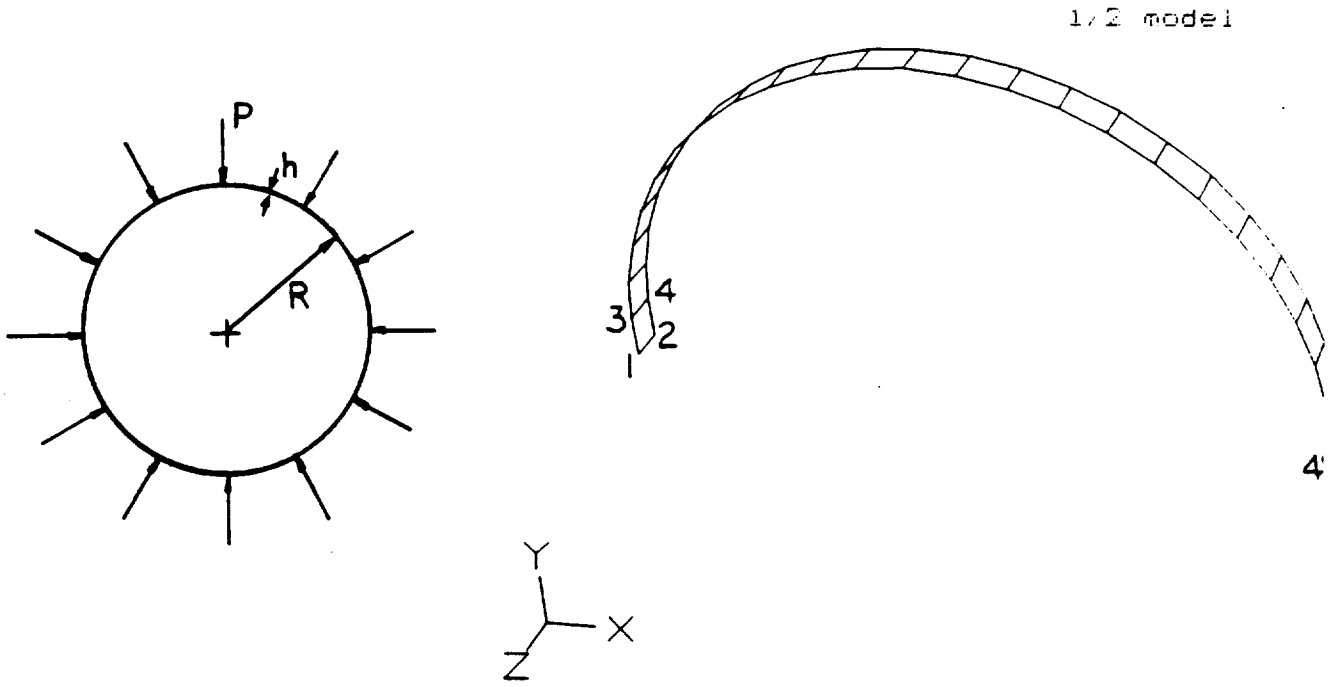

ANALYTICAL SOLUTION:

$$P = \{E/4(1-\nu^2)\}*\{h/R\}^3$$

where P = critical pressure
E = modulus
h = thickness
R = radius
ν = Poisson's ratio

Reference: R. J. Roark and W. C. Young, Formulas for Stress and Strain, Fifth edition, p. 556, McGraw Hill Book Co.

DEFINITION OF RANDOM/DETERMINISTIC VARIABLES

Number of Random Variables = 2

Variables	Distribution	Median	Coef. of Variation
Young's Modulus	Lognormal	10E+06 psi	5%
Thickness	Lognormal	0.1 in	5%
Radius	Deterministic	10 in.	-
Poisson's ratio	Deterministic	0.3	-

NESSUS CONVERGENCE/PERTURBATION SETTINGS (NESSUS 2.7 Version)

1. In PARAMETER DATA *PERT 2 2
   In MODEL DATA *ITER 0 2
   10 0.0001

2. Perturbation Range:
   +0.1 standard deviations for both random variables.

SOLUTION COMPARISON:

1. Deterministic solution using mean values of random variables:

Theory	NESSUS	Ratio
2.743	3.04408	1.1097

2. Probabilistic solutions at selected probabilistic levels:
   Theory: Exact CDF based on analytical solution
   NESSUS: (Using PFEM module)
   Mean-Value-First-Order (MVFO) solution
   Advanced MVFO solution
   (See Figure 2 for comparison)

REMARKS:

1. In Fig. 2, an adjusted 'exact' probabilistic solution was derived by multiplying the exact solution by a factor of 1.1097. This factor is the ratio of the FEM solution to the exact solution, computed at the median values.

Figure 2

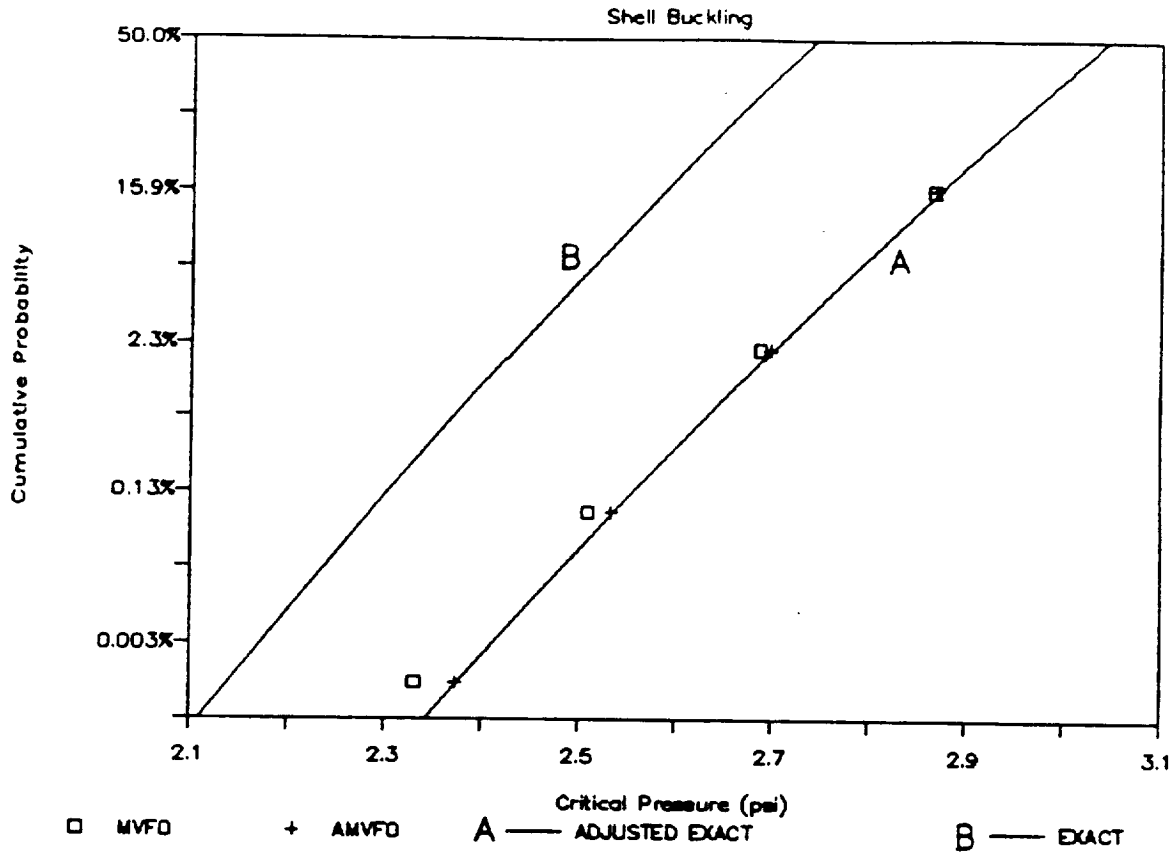

VALIDATION CASE 12

TITLE: Random Vibration Analysis of Cantilever Beam

PROBLEM: Determine the probabilistic distribution of the root-mean-square of the tip displacement

TYPE: Base-excited random vibration

RESPONSES: Tip displacement root-mean-square

FEM MODEL: NESSUS element type 98 - Two-node Timoshenko beam element
Number of elements = 20
Number of nodes = 21 (6 degrees-of-freedom per node)
Boundary conditions: Base-excited cantilever

Figure V12 - 1 FEM model

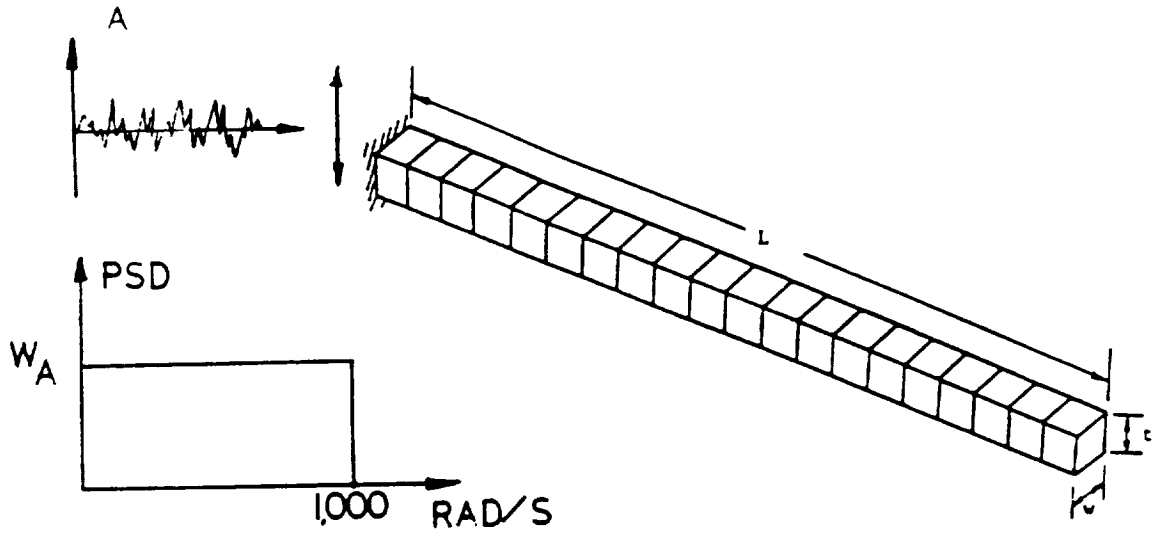

ANALYTICAL SOLUTION (single-degree-of-freedom approximation):

Mean-square displacement

$$= 1.7075 * (L^6 * W_A * r^{1.5}) / (E^{1.5} * t^3 * Xi)$$

where L = length
W_A = acceleration (power) spectral density
r = mass density (per unit volume)
E = modulus of elasticity
t = thickness
Xi = damping factor

Reference: Clough, R. W., and Penzien, J., Dynamics of Structures, McGraw-Hill, New York (1975)

DEFINITION OF RANDOM/DETERMINISTIC VARIABLES

Number of Random Variables = 8

Variables	Distribution	Median	Coef. of Varia
Young's Modulus	Lognormal	10^6 psi	3%
Length	Normal	20 in	1%
Thickness	Normal	0.98 in	1%
Width*	Normal	1.0 in	1%
Density	Lognormal	2.5-^4 lb-sec^2/in^4	2%
Damping	Lognormal	0.05	10%
Acceleration PSD	Lognormal	1.0 in^2/sec^3-rad	10%
PSD Cut off freq.*	Normal	1000 Rad/sec	10%

*Note: These two variables have no random effect on tip displaceme

NESSUS CONVERGENCE/PERTURBATION SETTINGS

1. *ITER 0
   20 0.001
2. Perturbation settings:
   +0.1 standard deviations for all random variables.

SOLUTION COMPARISON: (NESSUS 3.1)

1. Deterministic solution using mean values of random variables:

	Root-Mean-Square Displacement
Theory	5.384E-04 in
NESSUS	5.593E-04 in
NESSUS/Theory	1.0388

2. Probabilistic solutions at selected probabilistic levels:

   Simulation: Monte Carlo (sample size = 100,000)
   NESSUS: Mean-Value-First-Order (MVFO)
   Advanced MVFO (AMVFO)
   First iteration
   (See Figure V12 - 2)

REMARKS: (NESSUS 3.1, September 1988)

1. The mean first- and second-mode frequencies are 498 rad/sec and 3
   rad/sec, respectively. The cutoff frequency (1000 rad/sec) was
   chosen to excite, approximately, only the first mode.
2. The perturbation solutions are based on re-calculations.

Figure V12 - 2

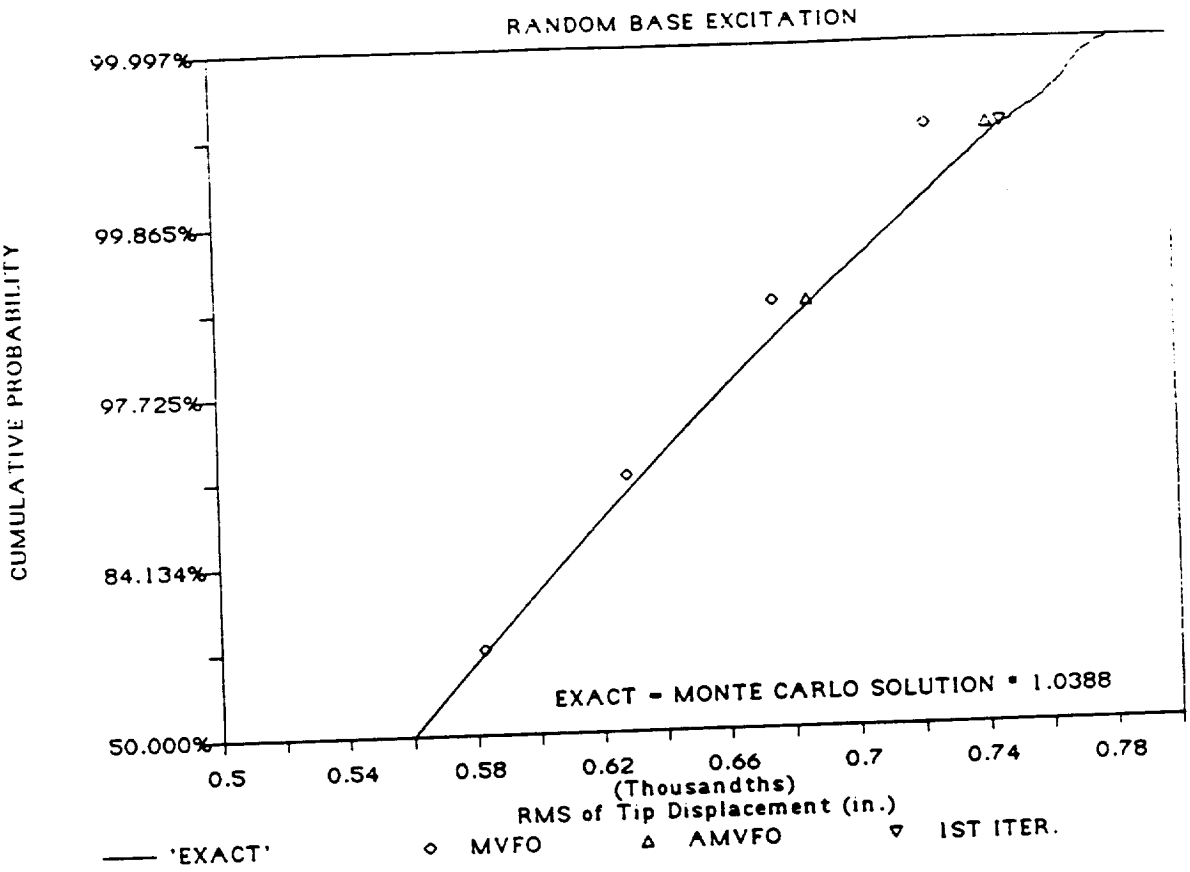
RANDOM BASE EXCITATION
99.997%
99.865%
97.725%
84.134%
50.000%
CUMULATIVE PROBABILITY
0.5
0.54
0.58
0.62
0.66
0.7
0.74
0.78
(Thousandths)
RMS of Tip Displacement (in.)
EXACT - MONTE CARLO SOLUTION * 1.0388
'EXACT'
MVFO
AMVFO
IST ITER.

APPENDIX G

PBEM Example Problem

H.R. Millwater
Southwest Research Institute

PBEM EXAMPLE PROBLEM

The PBEM example problem is to determine the probabilistic response of a cantilever beam of dimensions 10 x 0.99 x 1.0 with a constant axial end load. The model consists of 6 elements with 20 nodes and is shown in figure ?. The response variable is the end axial displacement. The sensitivity of the response variable to the random variables was determined with PBEM. The relavent data was extracted from the perturbation data base by PREFPI and probabilistic analysis was performed with FPI. The random variable input data is listed in table ?.

Table ? Definition of random/deterministic variables

Variables	Distribution	Mean	COV
end load	normal	100.0 psi	10%
Elastic modulus	normal	10.E+6	10%
length	normal	10.0 in.	10%

Response variable - end axial displacement

Results

Figure ? shows the mean value first order (MVFO) solution for PBEM along with the analytical solution. In addition, the advanced mean value first order solution (AMVFO) at the +3.0 standard deviation level was computed by resolving the problem used the most probable design points as input. The results agree well with the analytical solution. This technique is identically equivalent to the FEM procedure. Thus, the same analysis technique can be used for both FEM and BEM.

APPENDIX 2

PBEM input file

(comments are listed on the right in parenthises)

```
**ECHO
**CASE CONTROL
  TITLE   PBEM TEST OF CANTILEVERED BEAM - L=10,T=.99,W=1.0
  TIMES                1.0000
**MATERIAL PROPERTY
  ID MAT1
  ISOTROPIC
    TEMPERATURE      70.0000
    EMODULUS         1.00000E+07
    POISSON          .000000
**GMR
  ID REG1
  MAT MAT1
  TREFERENCE       70.0000
  POINTS
         1      0.00000          0.4950000          0.5000
         2     10.00000          0.4950000          0.5000
         3     10.00000         -0.4950000          0.5000
         4      0.00000         -0.4950000          0.5000
         5      5.00000          0.495              0.5
         6     10.0              0.0                0.5
         7      5.0             -0.495              0.5
         8      0.0              0.0                0.5
         9      0.00000          0.4950000         -0.5000
        10     10.00000          0.4950000         -0.5000
        11     10.00000         -0.4950000         -0.5000
        12      0.00000         -0.4950000         -0.5000
        13      5.00000          0.495             -0.5
        14     10.0              0.0               -0.5
        15      5.0             -0.495             -0.5
        16      0.0              0.0               -0.5
        17      0.0              0.495              0.0
        18     10.0              0.495              0.0
        19     10.0             -0.495              0.0
        20      0.0             -0.495              0.0
 SURFACE SURF11
```

```
    TYPE QUAD
    ELEMENTS
            1      2 5 1 8 4 7 3 6
            2      1 5 2 18 10 13 9 17
            3      2 6 3 19 11 14 10 18
            4      3 7 4 20 12 15 11 19
            5      11 15 12 16 9 13 10 14
            6      4 8 1 17 9 16 12 20
  NORMAL       1 +
**BCSET
  ID TRACTION
   VALUE
  GMR  REG1
  SURFACE SURF11
    ELEMENTS      3
  TIMES                1.0000
  TRACTION   1
    SPLIST ALL
    T  1        1.00000E+02
**BCSET
  ID RIGBODX
   VALUE
  GMR  REG1
  SURFACE SURF11
    ELEMENTS      6
  TIMES                1.0000
  RIGID   1
**BCSET
  ID RIGBODY
   VALUE
  GMR  REG1
  SURFACE SURF11
    ELEMENTS      6
  TIMES                1.0000
  RIGID   2
**BCSET
  ID RIGBODZ
   VALUE
  GMR  REG1
```

```
  SURFACE SURF11
    ELEMENTS      6
  TIMES                1.0000
  RIGID   3
**PROB                                  (START OF PROBABILISTIC DATA)
**DEFINE 1                              (R.V. 1 = end load)
  100.0    10.0                        (mean, standard deviation)
  BCSET                                (format identical to
  ID TRACTION                            (deterministic)
   VALUE
  GMR  REG1
  SURFACE SURF11
    ELEMENTS      3
  TIMES                1.0000
  TRACTION   1
    SPLIST ALL
    T  1        1.00000E+00
**DEFINE 2                              (R.V. 2 = elastic mod)
10000000.   1000000.
  MATERIAL PROPERTY
  ID MAT1
  ISOTROPIC
    TEMPERATURE      70.0000
    EMODULUS         1.00000            (perturb only Elastic Mod)
    POISSON          .000000            (factor for Poisson = 0)
**DEFINE 3                              (R.V. 3 = beam length)
  10.0   1.0
  GMR
  ID REG1
  MAT MAT1
  TREFERENCE       70.0000
  POINTS                                (perturb only length)
         1      0.00000          0.00000          0.0000
         2      1.00000          0.00000          0.0000
         3      1.00000          0.00000          0.0000
         4      0.00000          0.00000          0.0000
         5      0.50000          0.0              0.0
         6      1.0              0.0              0.0
         7      0.5              0.0              0.0
         8      0.0              0.0              0.0
```

```
        9       0.00000          0.00000          0.0000
       10       1.00000          0.00000          0.0000
       11       1.00000          0.00000          0.0000
       12       0.00000          0.00000          0.0000
       13       0.50000          0.0              0.0
       14       1.0              0.0              0.0
       15       0.5              0.0              0.0
       16       0.0              0.0              0.0
       17       0.0              0.0              0.0
       18       1.0              0.0              0.0
       19       1.0              0.0              0.0
       20       0.0              0.0              0.0
  SURFACE SURF11
    TYPE QUAD
    ELEMENTS
            1      2 5 1 8 4 7 3 6
            2      1 5 2 18 10 13 9 17
            3      2 6 3 19 11 14 10 18
            4      3 7 4 20 12 15 11 19
            5      11 15 12 16 9 13 10 14
            6      4 8 1 17 9 16 12 20
  NORMAL        1 +
**PERT     1
    1          0.1      1                  (define random variable
**PERT     2                                number, perturbation factor
    2          0.1      1                  and solution type for each
**PERT     3                                perturbation - solution type
    3          0.1      1                  1 = resolution)
**END
```

APPENDIX H

Verification Studies of the Advanced Boundary Element Code BEST3D

S.T. Raveendra
T.A. Cruse
Southwest Research Institute

1.0 SUMMARY

This report describes the verification studies of BEST3D [1] code for efficiency and accuracy. The boundary element code was run on CRAY X-MP at NASA LeRC and the results were mostly compared to the finite element results obtained using a MARC program [2]. Unlike the FEM code, the boundary element code was not optimized to run on CRAY, thus, the run time comparison does not give a good indication of the efficiency of the BEM code. Nevertheless, the results give a good guide as to the improvements necessary to make a general purpose computer program such as BEST3D to be competitive to FEM codes.

2.0 VERIFICATION RESULTS

2.1 Analysis of T-Joint Beam

TITLE: TJOINT

PROBLEM: Elastic Stress Analysis of T-Joint Model with a semi-elliptic crack at the weld

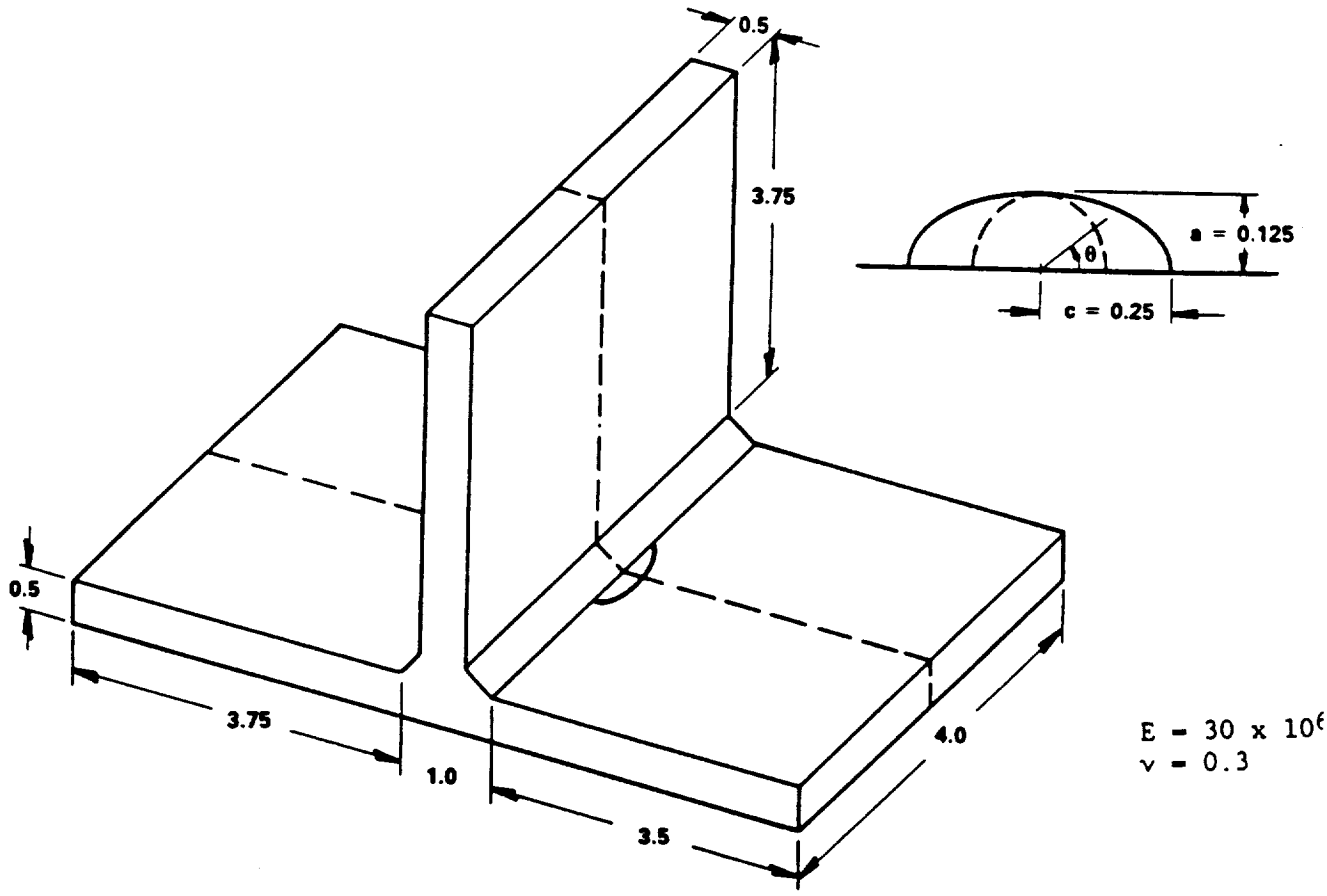

Figure 1. T-Joint Beam with Elliptic Flaw

BEM MODEL:

Number of Regions	- 4
Number of Symmetry	- 0
Element Type	- Quadratic
Number of Elements	- 212
Number of Nodes	- 560

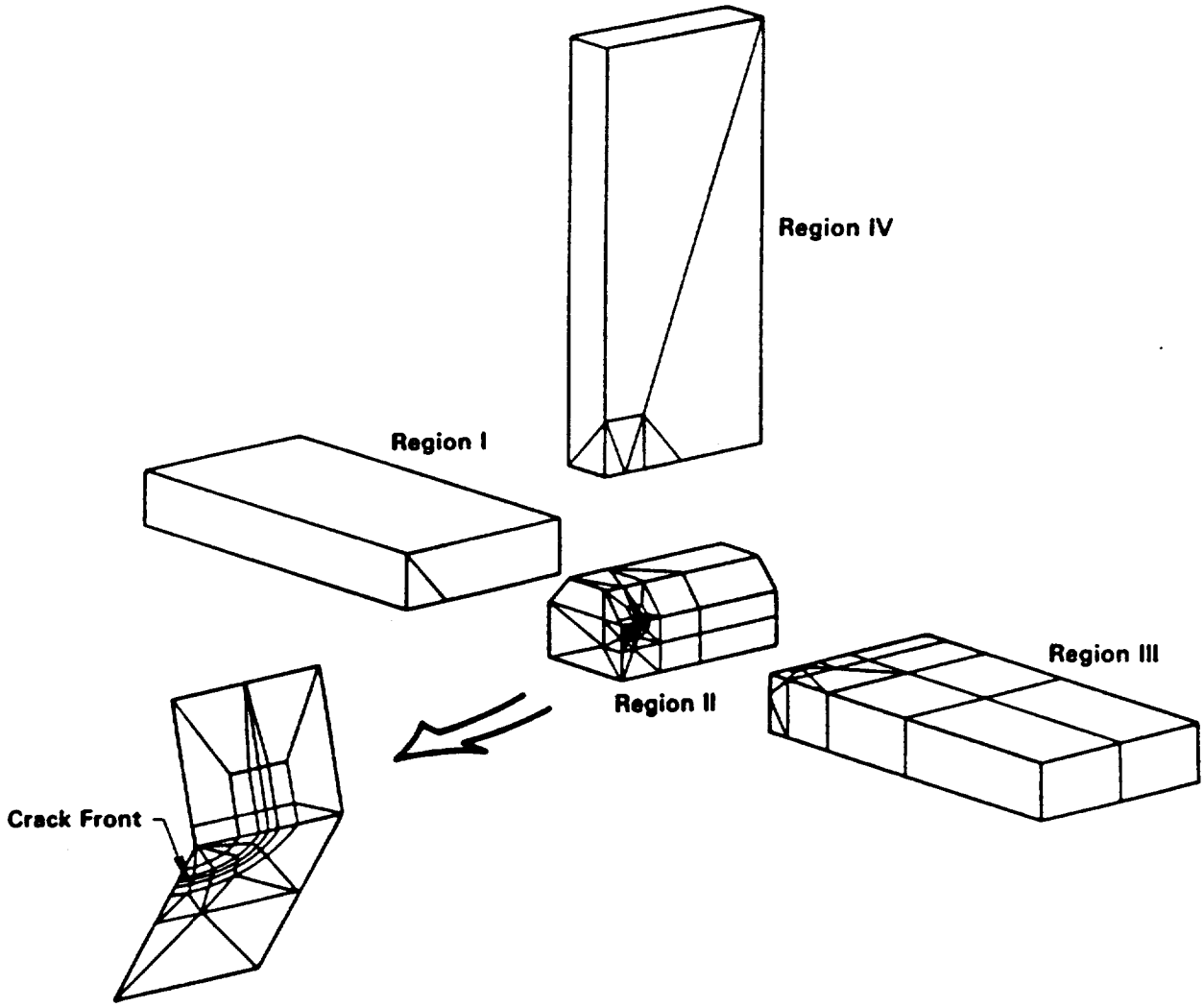

Figure 2. Multi-region BEM Map for T-Joint Beam

COMPARISON MODEL: Two-Dimensional Plane Strain Model Using BIECRX code [3]

Element Type - Linear
Number of Elements - 143
Number of Nodes - 144

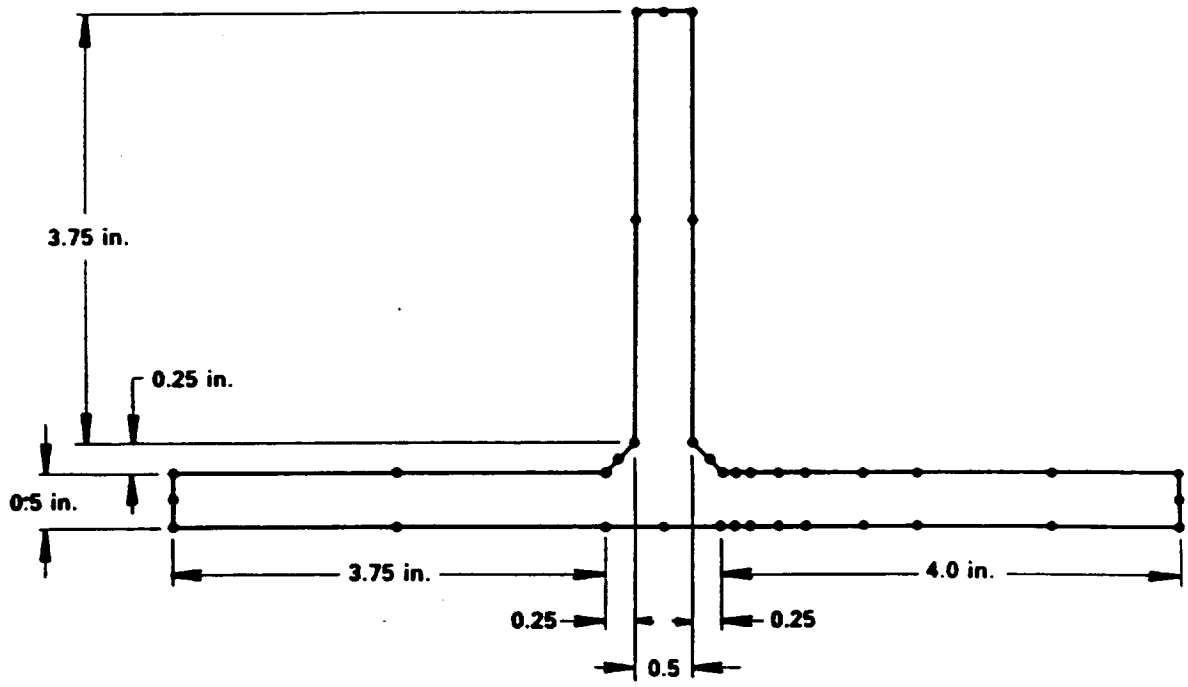

Figure 3. Plane Strain BEM Map

SOLUTION COMPARISON:

Solution Time = 571 sec

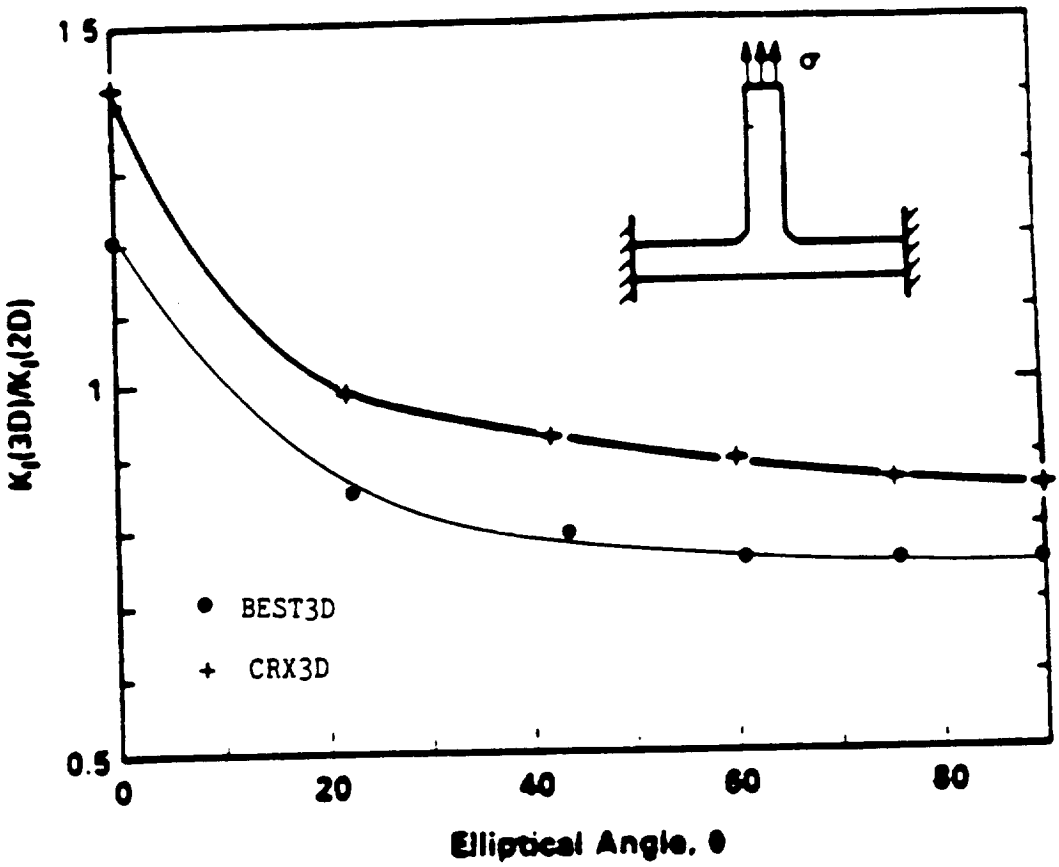

Figure 4. Mode I Stress Intensity Factor Comparison

REMARKS:

Figure 4 shows the mode I stress intensity factor along the crack front normalized with respect to two-dimensional plane strain solution. The results indicate that the mode I response is similar to the plane strain response at the interior of the body, but the stress intensity factor at the surface is higher, as expected. The BEST3D results shown are by using standard quadratic elements, whereas, the CRX3D [3] results are due to the same three-dimensional model with special crack-tip elements. Attempt to use quarter point element at the crack front by moving the mid-side node to quarter point was not successful since the BEST3D program failed in subroutine ERCTRL. This was due to the fact that some of the source points were *too close* to some of the field elements. The sub-segmentation scheme employed estimated the size of the subdivided element dimension as zero. The manual does to give any indication as to the size of the element that could be used with the code. Also no error message was given to enable the user to find the area of difficulty in the mesh.

An error in subroutine GEOMAT of the code was detected while verifying this model. The part of the code that searches for the largest dimension was as follows:

```
   40 XLEN = 0
      DO 20 I = 1, NNODET
        DO 10 J=1,NDEGF
          IF (ABS(ARRA(J,I)).LE.XLEN) GOTO 10
          XLEN = ARRA(J,I)
   10   CONTINUE
   20 CONTINUE
```

The corrected statements are as follows:

```
   40 XLEN = 0
      DO 20 I = 1, NNODET
        DO 10 J=1,NDEGF
          IF (ABS(ARRA(J,I)).LE.XLEN) GOTO 10
          XLEN = ABS(ARRA(J,I))
   10   CONTINUE
   20 CONTINUE
```

Without this modification, it is possible for XLEN to have a final value of zero.

Further, a modification to the tolerance value in subroutine COMCYC was necessary to run this model. This subroutine matches the nodes of interfaces by checking the difference between the distance between nodes at the interfaces to an absolute value of 0.01. When the distance between the nodes was smaller than this tolerance, the wrong nodes were matched at the

interface. For the purpose of running this model, we used a tolerance value of 0.001. A relative, rather than absolute value may be used to eliminate this problem.

2.2 Analysis of Double Notch Specimen

TITLE: DOUBLE NOTCH

PROBLEM:
(1) Double Notch Model Subjected to Traction Loading
  (a) Linear Boundary Elements [2.1]
  (b) Quadratic Boundary Elements [2.2]
(2) Double Notch Model Subjected to Displacement Loading
  (a) Linear Boundary Elements [2.3]
  (b) Quadratic Boundary Elements [2.4]
(3) Double Notch Rotated About the Z-Axis [2.5]

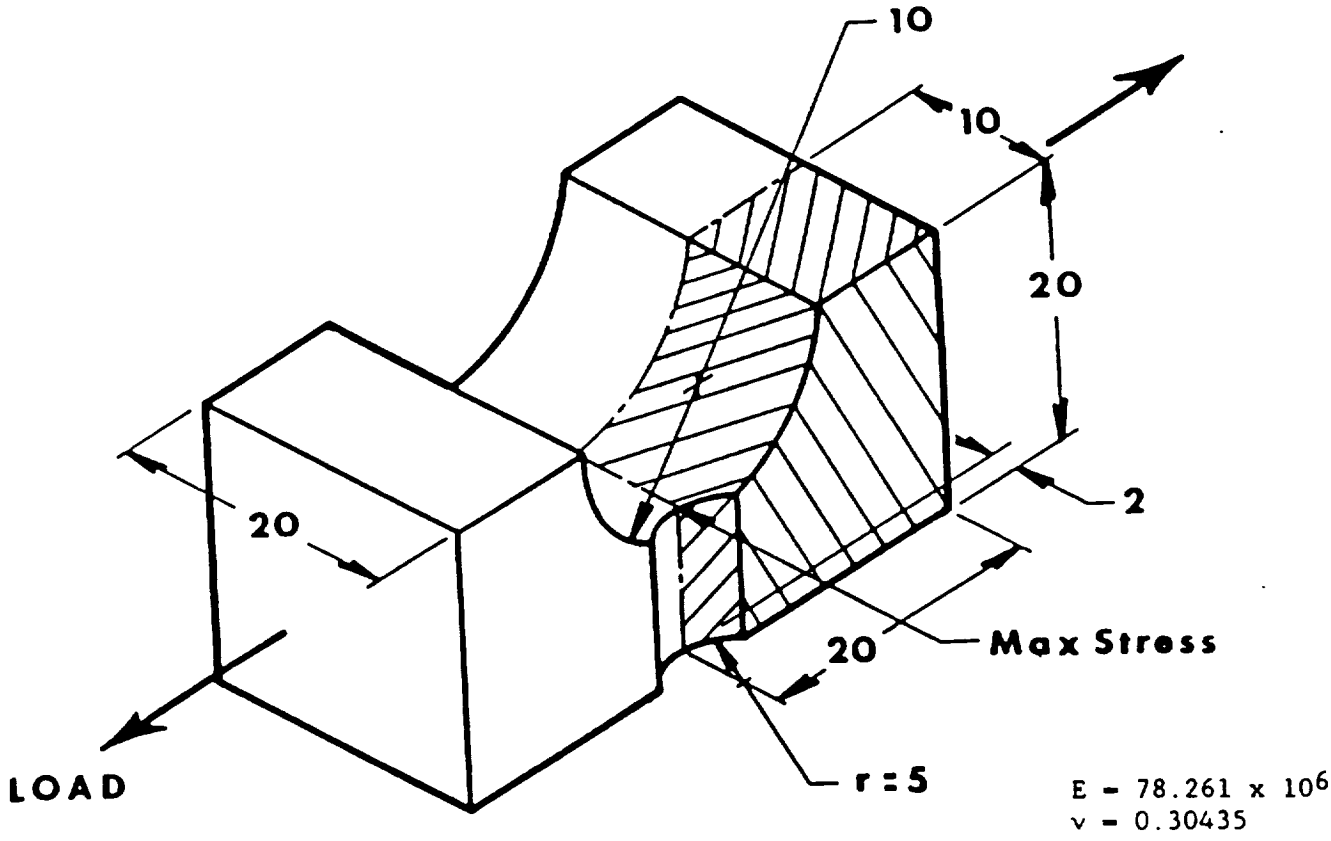

Figure 5. Double Notch Specimen

BEM MODEL: Number of Regions - 1
Number of Symmetries - 2

Table 1

	2.1	2.2	2.3	2.4	2.5
Elements	24	24	24	24	24
Nodes	23	69	23	69	69

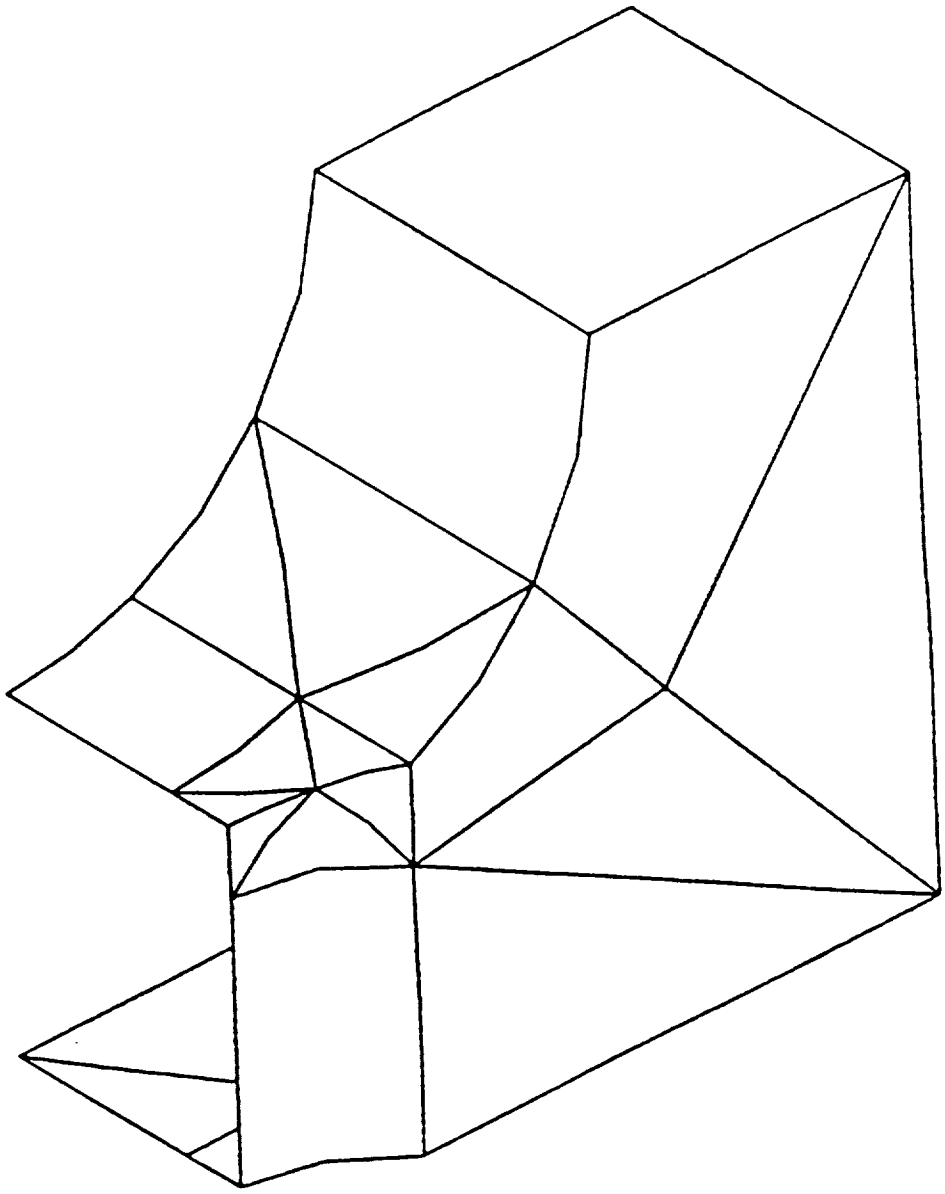

Figure 6. BEM Map for Double Notch

COMPARISON MODEL: MARC Finite Element Program
Element Type - 20-noded elements
Number of Elements - 150
Number of Nodes - 188

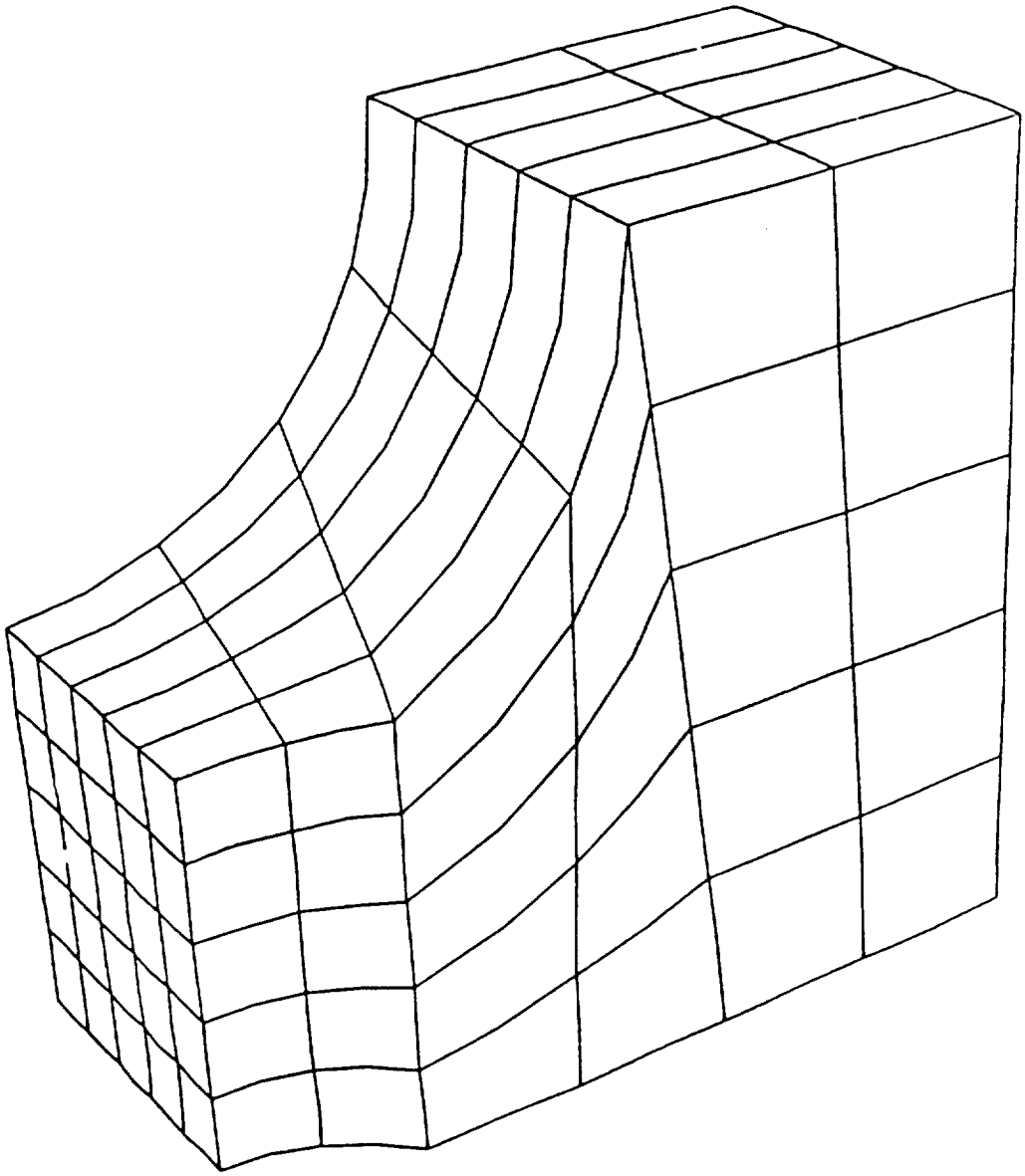

Figure 7. FEM Map for Double Notch

SOLUTION COMPARISON:

Table 2 : Stress Concentration Factors - Traction Loading

	K_T	CPU (sec)
BEM (2.1)	14.53	11
BEM (2.2)	17.64	36
FEM	15.33*	49

Table 3 : Stress Concentration Factors - Displacement Loading

	K_T	CPU (sec)
BEM (2.3)	6.72	11
BEM (2.4)	7.66	36
FEM	6.45*	49

Table 4 : Centrifugal Loading

	$\sigma_{max}/\sigma_{app}$	CPU (sec)
BEM (2.5)	15.96	36
FEM	13.82*	45+

* at Gauss points

+ smaller output selected

REMARKS:

The stress concentration factors indicate that quadratic modeling increases the accuracy of the problem; however, the use of higher interpolation results in longer run time. The lower values of FEM stress concentration factors were partly due to the evaluation of the quantities at the nearest integration point compared to BEM values evaluated at the surface nodal point. The BEM run time for this model compares favorably with the FEM times. A primary advantage of BEM over FEM for this problems is the ease of generating and verifying the BEM surface model.

There was an incompatibility between the program and input manual in Geometry Definition Section (Section 5.5). For linear elements, the keyword according to program manual was LINE, whereas, the program recognized LINI as the keyword for linear elements. When ran with the wrong keyword, the program executed without any error message using the default option. It is useful if the program warns the user when non-recognizable keywords are encountered.

The record length of the direct access file FT32 was too small and had to be increased from 18,000 characters to 108,672 characters in subroutine BCASSM.

2.3 Analysis of Turbine Blade Model

TITLE: _ TURBINE BLADE

PROBLEM: Free Vibration and Quasi-static Analysis of Turbine Blade Model with Body Force Loading

(1) Turbine Blade Model Subjected to Pressure Loading
  (a) Linear Boundary Elements [3.1]
  (b) Quadratic Boundary Elements [3.2]

(2) Turbine Blade Model Subjected to Centrifugal Loading
  (a) Fixed Boundary Condition [3.3]
  (b) Spring Boundary Condition [3.4]

(3) Free Vibration Analysis of Turbine Blade Model [3.4]

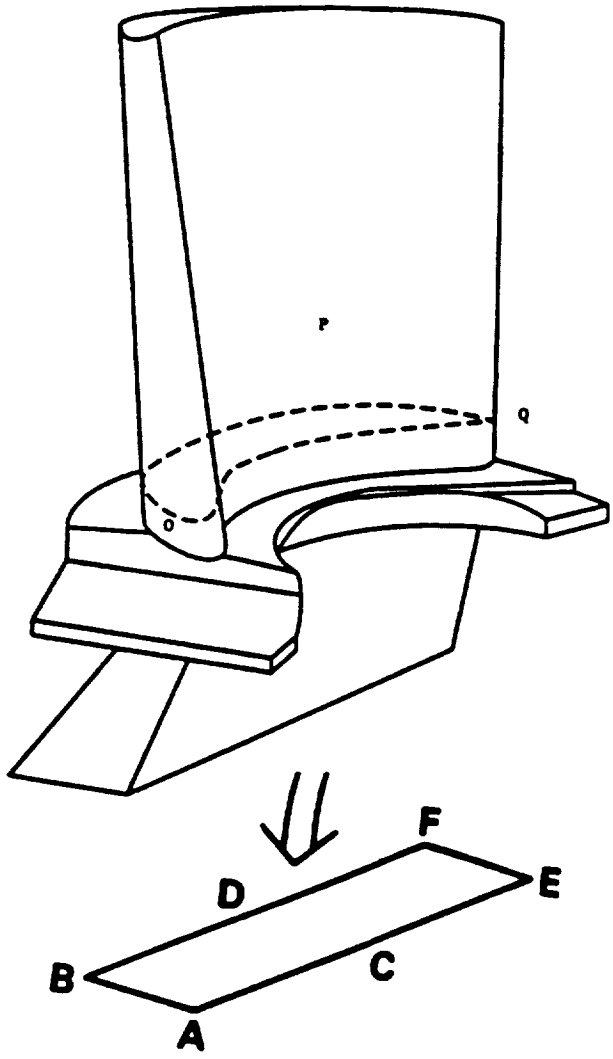

$E = 18.4 \times 10^6$
$\nu = 0.386$
$\rho = 0.000805$
$\Omega = 3936.1$

Figure 8. Turbine Blade Model

BEM MODEL: Number of Regions - 3
Number of Symmetry - 0

Table 5

	3.1	3.2	3.3	3.4	3.5
Elements	333	333	359	359	359
Nodes	339	999	1080	1080	1080

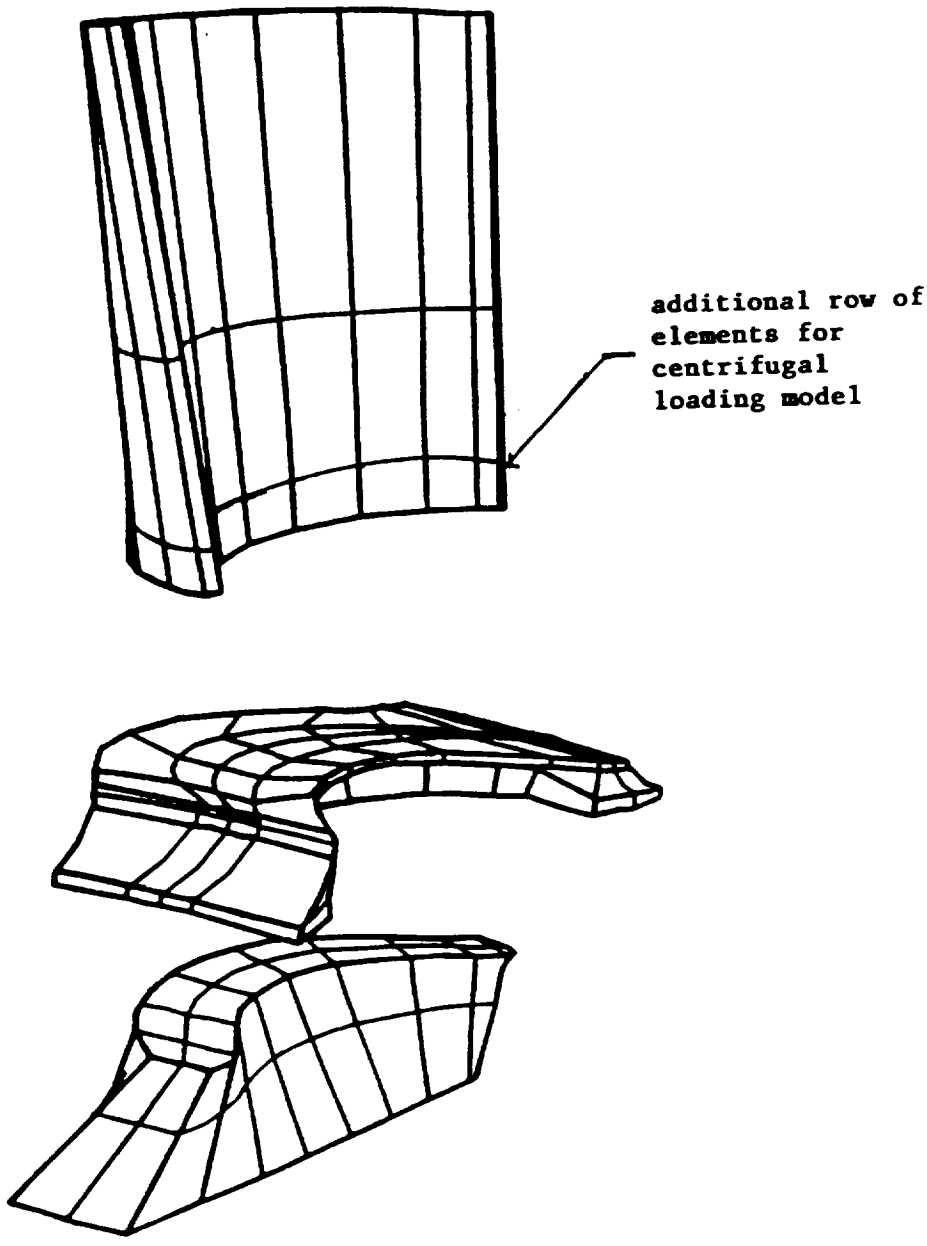

Figure 9. Multi-Region BEM Simulation of Turbine Blade Model

COMPARISON MODEL: MARC Finite Element Program
Element Type - MARC Element #7 (8 & 6 noded elements)
Number of Elements - 1456
Number of Nodes - 2454

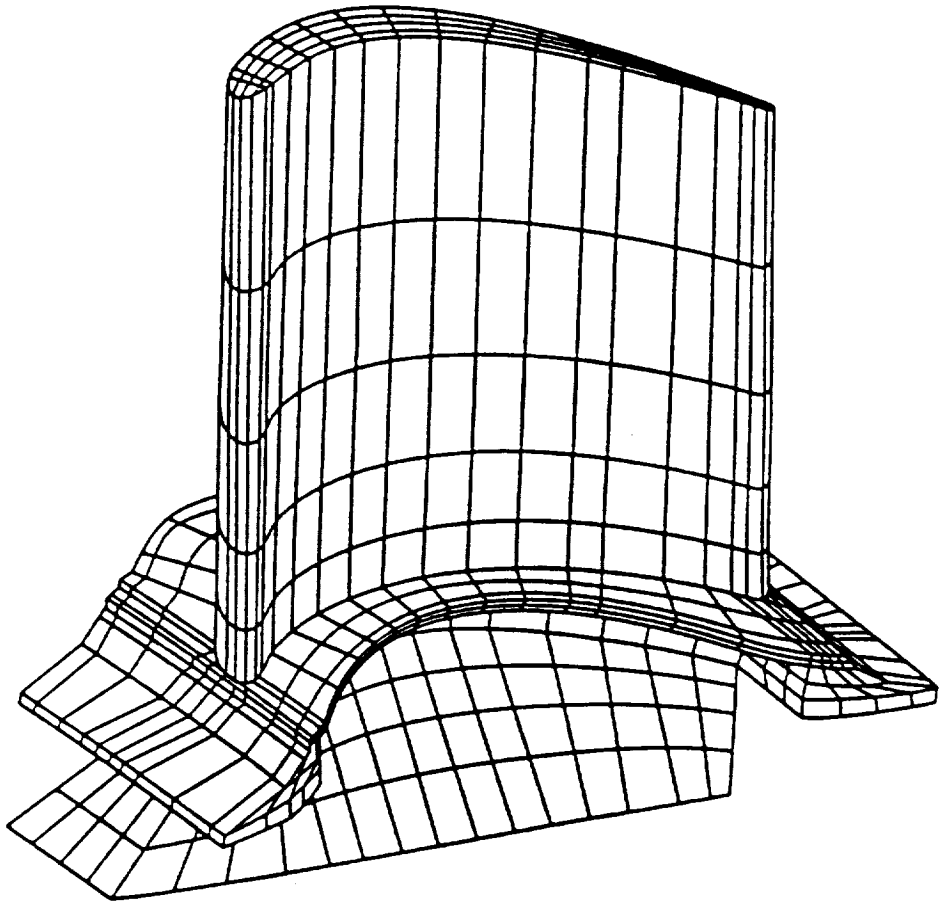

Figure 10. FEM Mesh for Turbine Blade Model

SOLUTION COMPARISON:

Table 6 : Pressure Loading

	σ_{xx}/σ_{app}						CPU (sec)
	A	B	C	D	E	F	
BEM (3.1)	67	-6	43	-89	41	-20	355
BEM (3.2)	81	12	33	-177	79	-21	1839
FEM	85	15	40	-134	118	-19	78

Table 7 : Centrifugal Loading - Fixed Base

	σ_{xx}/σ_{app}			CPU (sec)
	O	P	Q	
BEM (3.3)	-0.048	0.701	0.137	1994
FEM	0.094	0.605	0.204	83

Table 8 : Centrifugal Loading - Spring Base

	σ_{xx}/σ_{app}			CPU (sec)
	O	P	Q	
BEM (3.4)	-0.115	0.692	0.101	1999
FEM	0.080	0.600	0.214	82

Table 9 : Free-Vibration

	Mode 1	Mode 2	Mode 3	CPU (sec)
BEM (3.5)	job aborted			
FEM	27382	46296	55236	426

REMARKS:

Table 6 compares the vertical stress at the fixed base (see Figure 8) due to pressure loading normal to the surface at the airfoil. The results are again improved by using quadratic boundary elements; the results due to quadratic elements compare well with the FEM results. Unlike the BEM results, the FEM values were evaluated at integration points nearest to the corresponding surface points.

The stresses at the airfoil near the interface due to the rotation of the turbine blade about the horizontal axis are compared in Table 7 and 8. The results in Table 7 were obtained assuming fixed boundary conditions at the base, while the results in Table 8 were due to spring boundary conditions.

The BEM run times for the turbine blade model are considerably larger than the corresponding times using FEM. These were mainly due to the need to use much finer boundary element mesh than necessary for boundary data interpolation necessitated by the complexity of the geometry. A detailed investigation of the run time efficiency is given in Section 3.

For the purpose of comparison with finite element method, an additional row of elements at the airfoil near the interface was created. While this did not cause any problem for the centrifugal loading case, it was not so for the pressure cases (3.1 and 3.2). The application of pressure normal to the airfoil surface was simplified by the use of local boundary conditions which permitted the imposition of load with respect to local coordinates. While the user's manual specified the maximum number of points with local coordinates system definition as 500, the code was not compatible with this number. In the code, it appears that the local coordinate system definition nodes are stored by element, thus the limit appears to be dependent on the number of elements with local coordinates system. The pressure loading example was thus run without one row of elements at the interface.

A variety of problems were encountered in running the turbine blade model for natural frequency analysis. Initially, it was noted that the number of points allowed per sub-region for free-vibration analysis, in subroutine BMASS, was smaller than the value specified in the user's manual. This was increased to the required size to permit testing of turbine blade model. The job using modified code aborted with the following error message:

```
READ ON UNIT FT19 I0020 - RECORD LENGTH EXCEEDED
                        - BEGINNING OF TRACEBACK
                        - $TRBK  WAS CALLED BY IOERP% AT 3104125d
                        - IOERP% WAS CALLED BY %$RUV% AT 3112247d
                        - %$RUV% WAS CALLED BY BMASS  AT 3054736a(LINE
                                                        NUMBER    191)
                        - BMASS  WAS CALLED BY BCASSM AT 3072322d(LINE
```

NUMBER 103)

- BCASSM WAS CALLED BY BEST3D AT 3070700c(LINE

NUMBER 88)

An attempt to correct this error was unsuccessful. The failure occurred after 7000 seconds of execution time.

2.4 Analysis of Hollow Sphere

TITLE: - HOLLOW SPHERE

PROBLEM: Elastoplastic Analysis of Hollow Sphere due to Internal Pressure

(1) Iterative Solution Procedure

(a) Internal/External radius ratio = 0.5 [4.1]

(b) Internal/External radius ratio = 0.8 [4.2]

(c) Internal/External radius ratio = 0.9 [4.3]

(2) Non-Iterative Solution Procedure

(a) Internal/External radius ratio = 0.9 [4.4]

(3) Particular Integral Approach

(a) Internal/External radius ratio = 0.9 [4.5]

BEM MODEL: Number of Regions - 1

Number of Symmetry - 0

Number of Nodes - 68

Number of Elements - 22 (8-noded, quadratic)

Number of Cells - 5 (20-noded, quadratic)

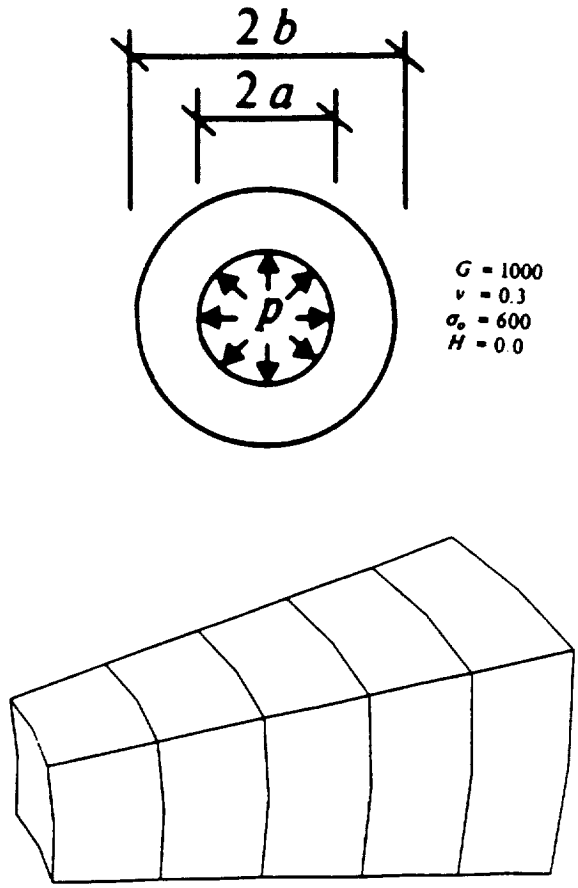

Figure 11. BEM Model for Hollow Sphere

COMPARISON MODEL: Analytical Results [5]

SOLUTION COMPARISON:

Table 10 : Solution Times

	4.1	4.2	4.3	4.4	4.5
CPU (sec)	214	137	132	134	67

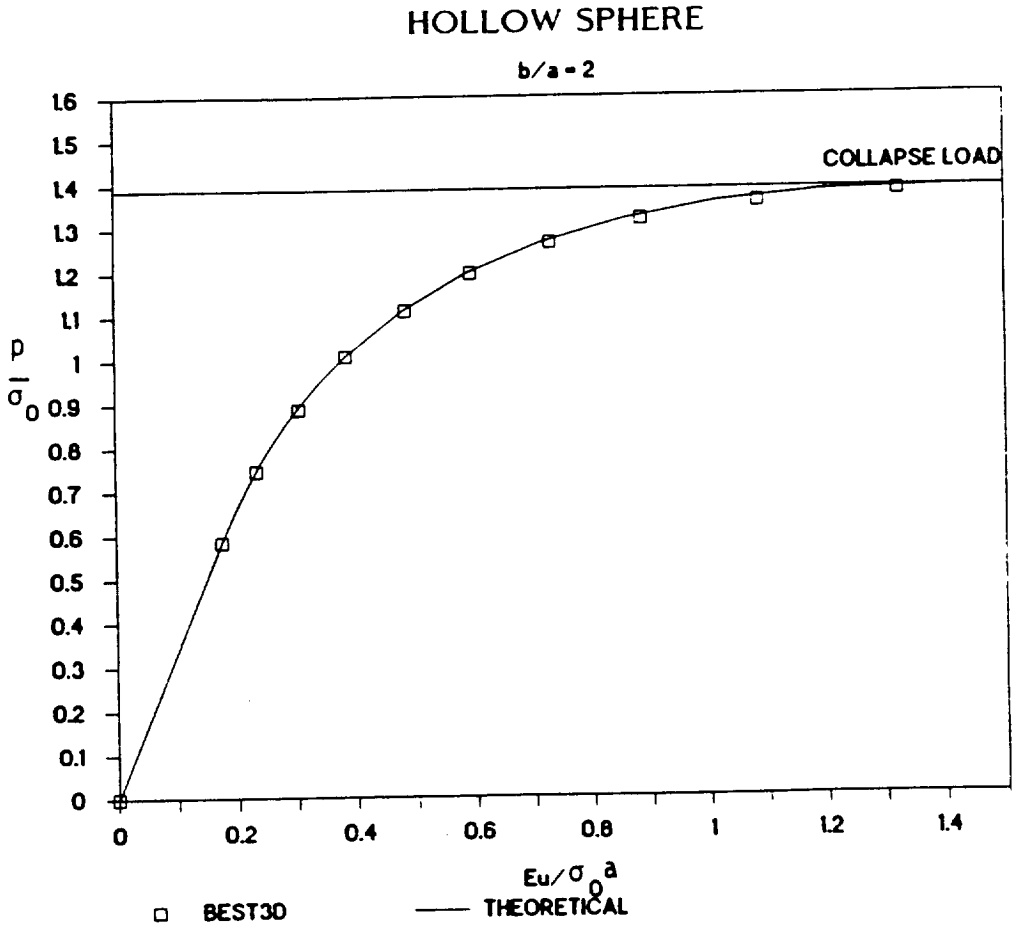

Figure 12. Load-Deformation Response for Hollow Sphere (b/a = 2)

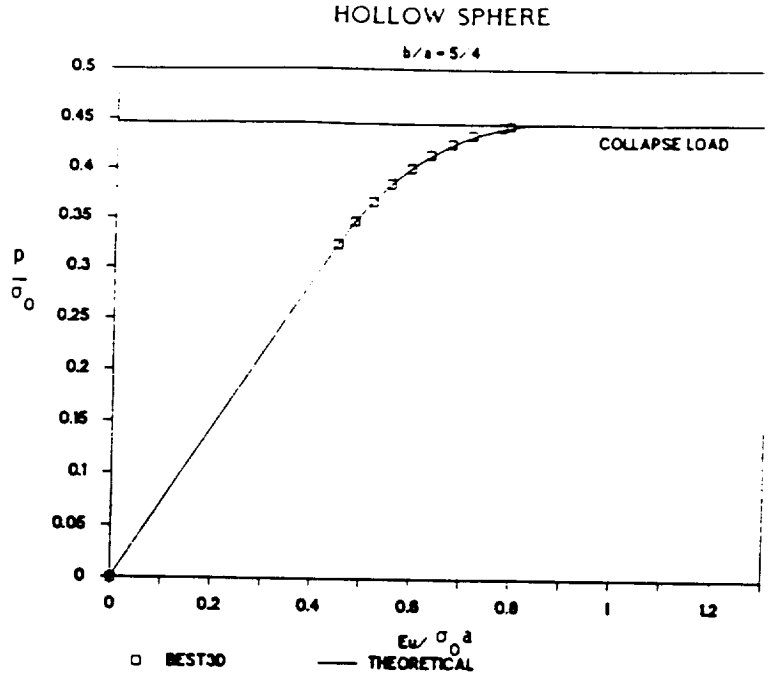

Figure 13. Load-Deformation Response for Hollow Sphere (b/a = 5/4)

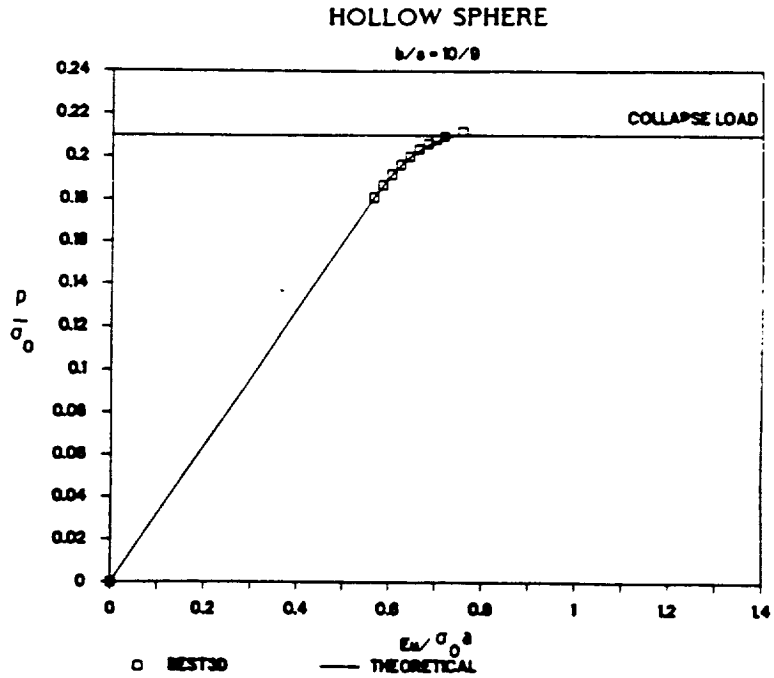

Figure 14. Load-Deformation Response for Hollow Sphere (b/a = 10/9)

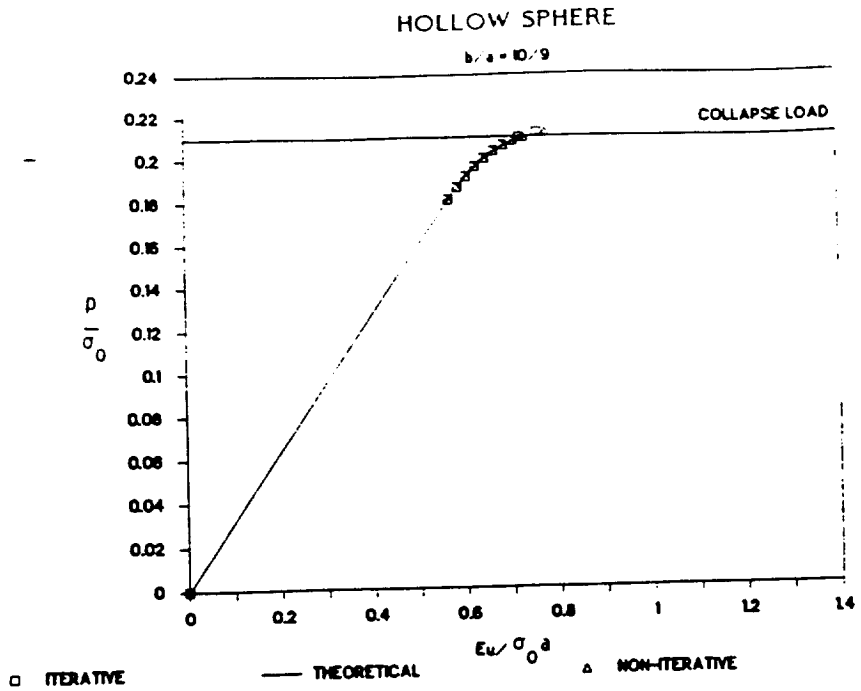

Figure 15. Plastic Collapse Response of Thin Hollow Sphere Using the Variable Stiffness Procedure

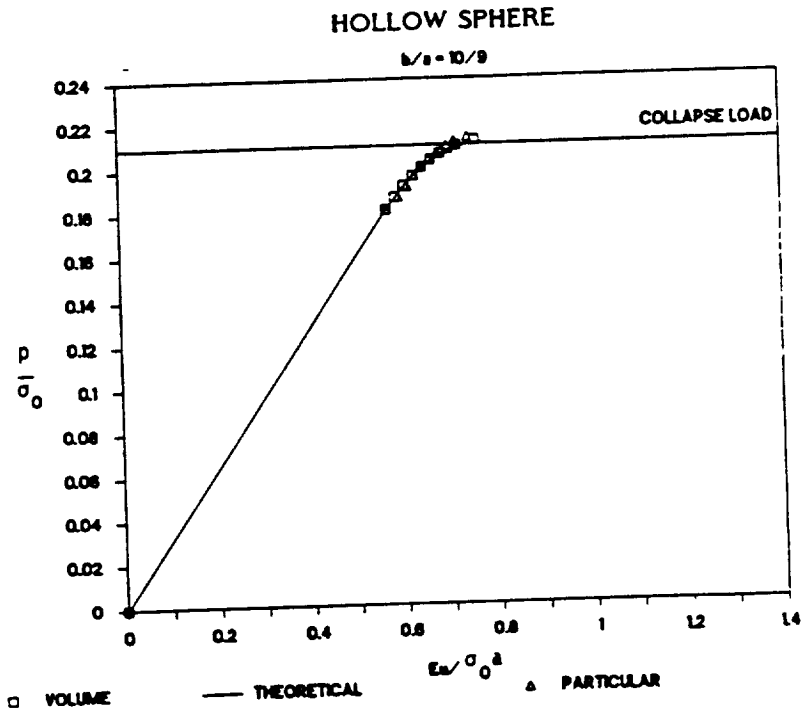

Figure 16. Plastic Collapse Response of Thin Hollow Sphere Using Particular Integral Procedure

REMARKS:

Three different boundary element models were selected to represent thick and thin hollow spheres. In all three cases, the outer radius was kept at 20 and the inner radius was changed such that the ratio of outer radius to inner radius varied from 2 to 10/9. The BEM map shown in Figure 11 corresponds to a b/a radius of 2. For the thinner models, the distance along the thickness was scaled accordingly.

Figures 12 - 16 show the load displacement response due to internal pressure. The displacements were monitored at the outer radius of the spheres. The comparison of BEST3D results to analytical values indicate excellent accuracy of the BEM procedure. A comparison of time for cases 4.3 and 4.4 indicate that computing time for the iterative and non-itertaive solution procedures, are essentially the same for this example, however, the results based on particular integral techniques is the most efficient computationally. The difference in accuracies between various solution procedures were too small to be noticeable.

The requirements for volume modeling are not explained clearly in the user's manual. The manual does not specify whether the volume cell and surface element nodes need to be matched. The code includes two types of volume cells; quadratic cells and constant plastic strain cells. However, the user's manual wrongly implies the constant strain cell as linear cell.

A solid sphere or cylindrical model could not be modeled using a segment of the body as was done for hollow sphere. The local boundary conditions at zero radius is not permissible in the current code and gives erroneous results. This limitation is not pointed out in the user's manual.

Convergence of solution is not identified by the code for a non-iterative solution procedure. Due to this, a collapse load in Figure 15 was assumed, based on displacement solutions. Inclusion of an automated scheme to check collapse is essential for general usage of the non-iterative procedure.

2.5 Analysis of Cantilever Beam

TITLE: - CANTILEVER BEAM

PROBLEM: Transient Analysis of Cantilever Beam
(1) Free Vibration Analysis [5.1]
(2) Forced Vibration Analysis [5.2]

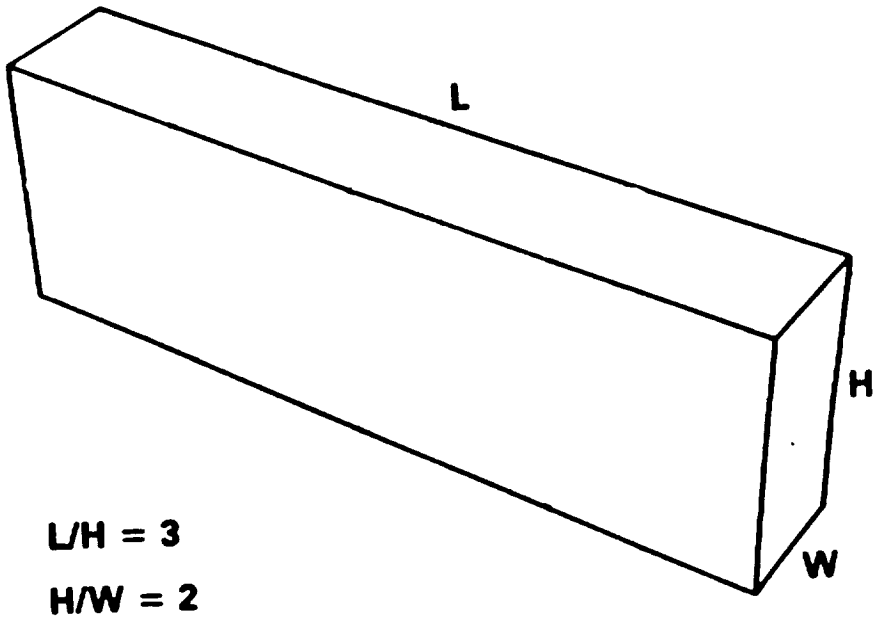

$E = 30 \times 10^6$
$\nu = 0.3$
$\rho = 0.0007339$

Figure 17. Cantilever Beam Model

BEM MODEL: Number of Regions - 1
Number of Symmetry - 0

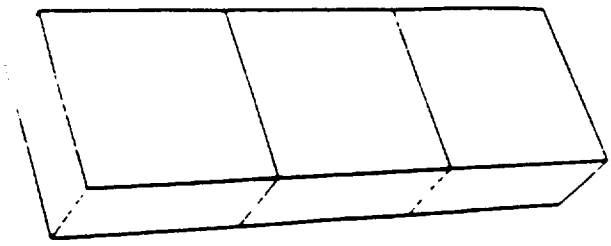

a) BEM Map 1

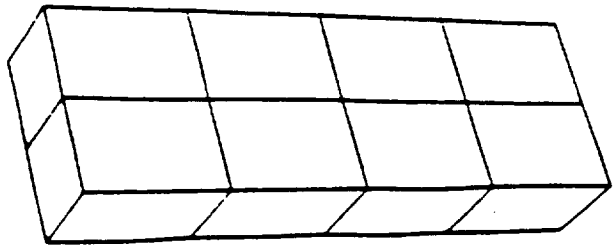

b) BEM Map 2

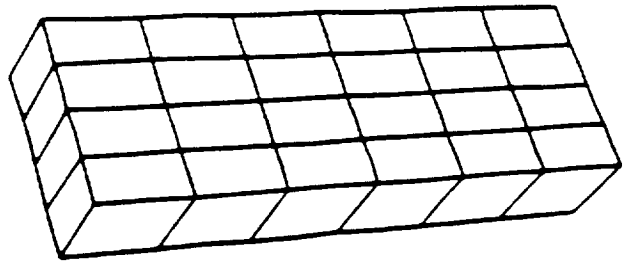

c) BEM Map 3

Figure 18. BEM Maps for Cantilever Beam Model

COMPARISON MODEL: MARC Finite Element Program
Element Type : 8 noded Linear Elements

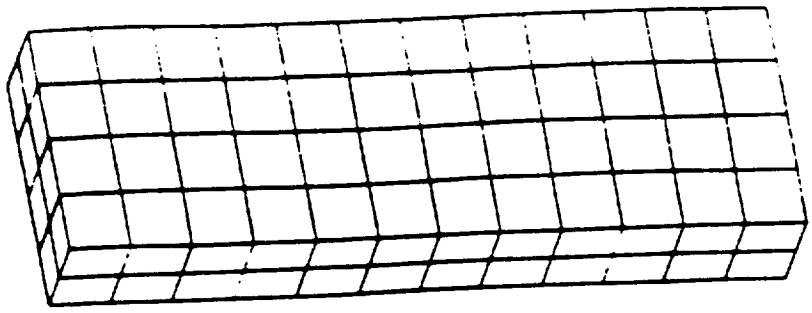

a) FEM Map 1

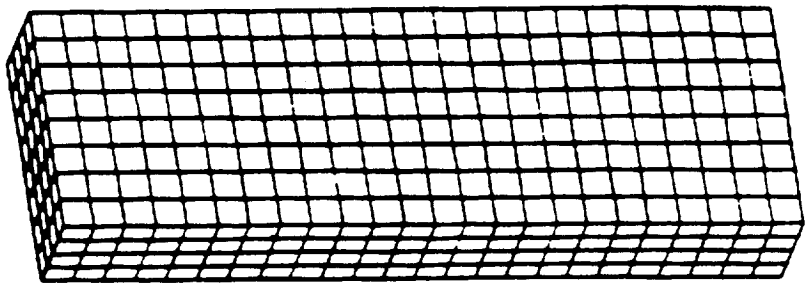

b) FEM Map 2

Figure 19. FEM Meshes for Cantilever Beam Model

SOLUTION COMPARISON:

- Table 11 : Natural Frequencies from BEST3D

	Natural Frequencies					CPU(sec) CRAY X-MP	Nodes/ Elements
	Mode 1	Mode 2	Mode 3	Mode 4	Mode 5		
BEM-1	2683	5412	13473	16749	24918	14	44/14
BEM-2	2807	5310	12728	16210	24262	48	86/28
BEM-3	2836	5288	12591	15889	24061	365	206/68

Table 12 : Comparison of Natural Frequencies

	Natural Frequencies					CPU(sec) VAX 8700	Nodes/ Elements
	Mode 1	Mode 2	Mode 3	Mode 4	Mode 5		
BEM-1	2683	5412	13473	16749	24918	336	44/14
FEM-1	3033	5449	13191	17227	25141	158	195/96
FEM-2	2885	5354	12778	16224	24522	801	1125/768

REMARKS:

Three BEM and two FEM models were generated as shown in Figures 18 and 19, respectively. Table 11 compares the first five normal modes of natural frequency obtained from BEST3D runs. The results indicate that considerably accurate results can be obtained by using a crude model as the first BEM map in Figure 18. An attempt to run the FEM models using MARC on CRAY was unsuccessful as the results did not converge. However, the results from the same FEM models converged on VAX 8700 using the VAX version of the MARC program. To compare the results, we ran BEM model 1 on VAX 8700 as well. These results indicate that the BEM approach is a viable alternative to FEM procedure for free-vibration analysis. It should be noted that in the current FEM modeling, the cantilever beam was modeled as a continuum. The FEM approach using beam elements for this problem will be considerably cheaper, nevertheless, for general three-dimensional bodies where continuum modeling is required, the BEM method is competitive.

The forced vibration analysis of cantilever beam model using the boundary element method procedure was not completed due to unrealistic constraint in the BEST3D code input structure for time-domain forced vibration analysis. The problem we selected for the analysis corresponds to the application of the load to a maximum value in a very short time followed by gradual relaxation of load. In BEST3D code, the load needs to be applied such that the time interval that can be used during the analysis should be less or equal to the loading time. Since there is no facility to change this time step at later times, we were required to use the same time step throughout. This requires the use of an unrealistic number of time steps, thus, the forced vibration analysis for the cantilever beam model was not completed.

3.0 INVESTIGATION OF NUMERICAL INTEGRATION OF SURFACE INTEGRALS

3.1 Alternative Integration Schemes

Consider the run time divided broadly according to various tasks during the solution of a double notch specimen analyzed in Section 2.1. The run times for various tasks on VAX 8700 for a model of 69 nodes and 24 quadratic boundary elements is as follows:

(a) Surface integration time = 336 sec
(b) Initial matrix assembly time = 11 sec
(c) Solution time = 33 sec

This example illustrates that about 88 percent of the total computer time was spent on evaluating the discretized boundary integrals. An efficient and accurate procedure for the evaluation of surface integrals is, therefore, essential for the BEM to be competitive to FEM. The BEST3D code uses a sub-segmentation scheme for the evaluation of non-singular integrals and transformation based on polar coordinates for singular integrals. The sub-segmentation scheme is essentially based on finding the element dimension to satisfy a specified error tolerance derived from approximate Gaussian error rules. The sub-element evaluation also considers the distance between the source point and the element over which the integration is performed.

An alternative procedure proposed recently in the context of surface integral evaluation of boundary integral equations is the variable transformation procedure. In this procedure, the integral points are weighted towards the *singular node* by a transformation procedure, thus, no element subdivision is used. In the current investigation a third-degree polynomial transformation is used [6].

The variable transformation procedure weights integration points according to the distance between the source point and the element of interest; the weighting becomes less pronounced for elements that are far away from the source point. The transformation procedure requires additional operation than the operations from regular application of integration rules. To avoid unnecessary calculations for elements that are beyond a certain distance from the source point regular integration procedures can be used. Thus, a regular and variable transformation procedures can be combined such that regular integration is performed for *far* elements and variable transformation procedure is used for near elements.

Initially, we considered a hollow sphere with an external radius to internal radius ratio of 2 subjected to internal pressure. The BEM map used is shown in Figure 11. The model was run using subdivision (SD), variable transformation (VT) and variable transformation combined with regular integration (VR) procedures. Figure 20 shows the normalized hoop stress along

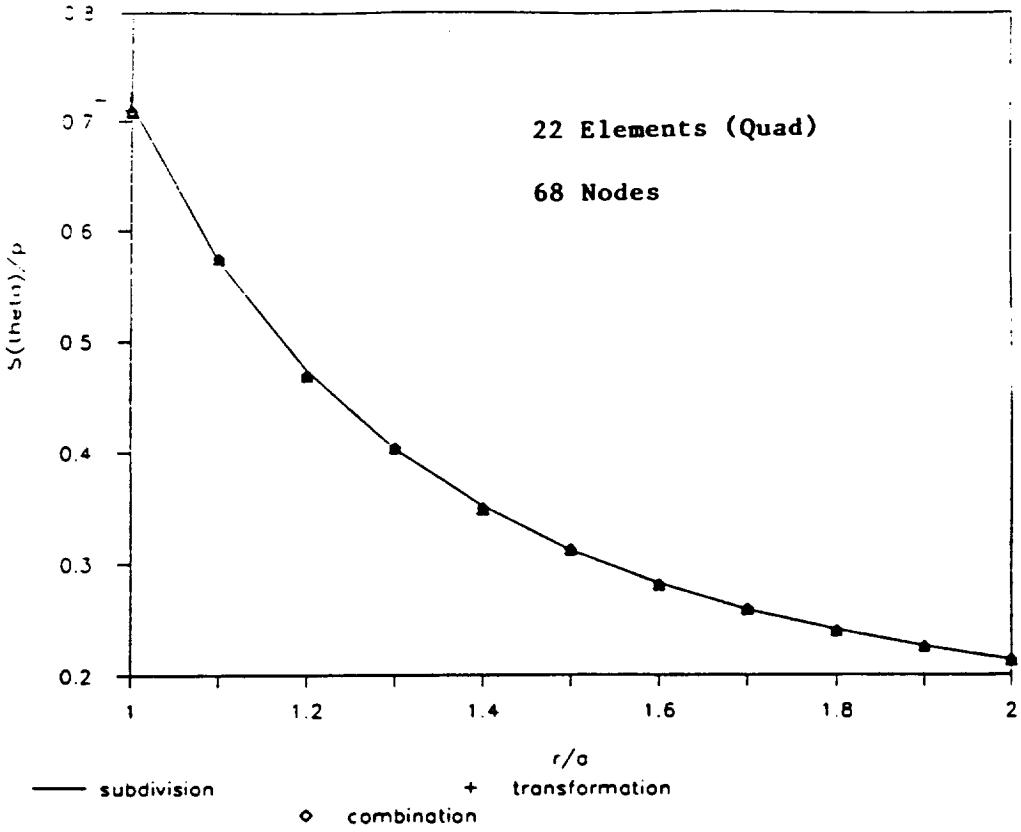

Figure 20. Hoop Stress of Hollow Sphere for Different Integration Schemes

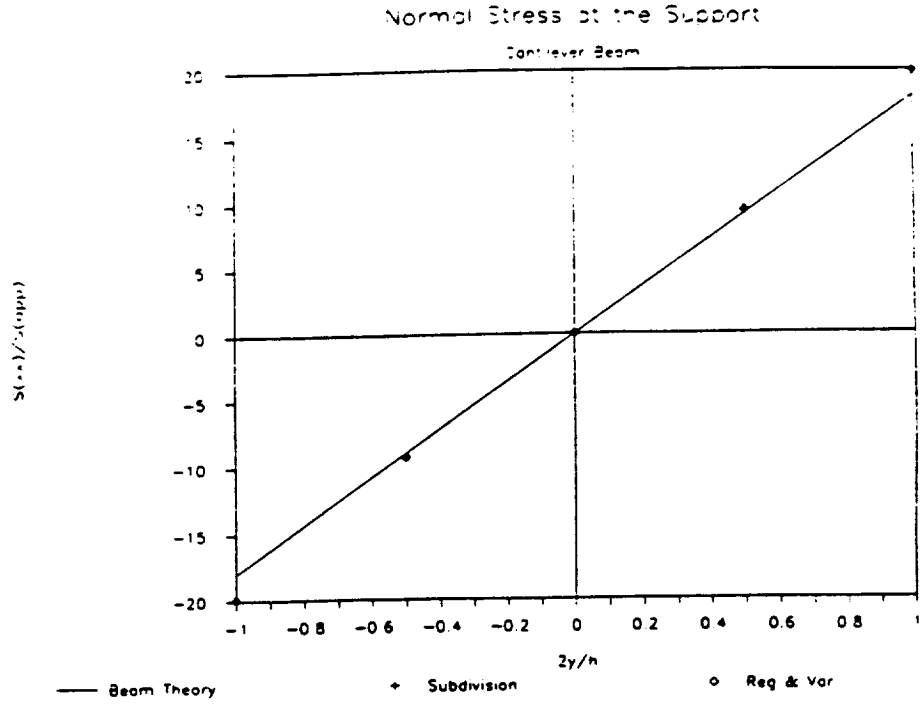

Figure 21. Normal Stress at the Support of Cantilever Beam for Different Integration Schemes

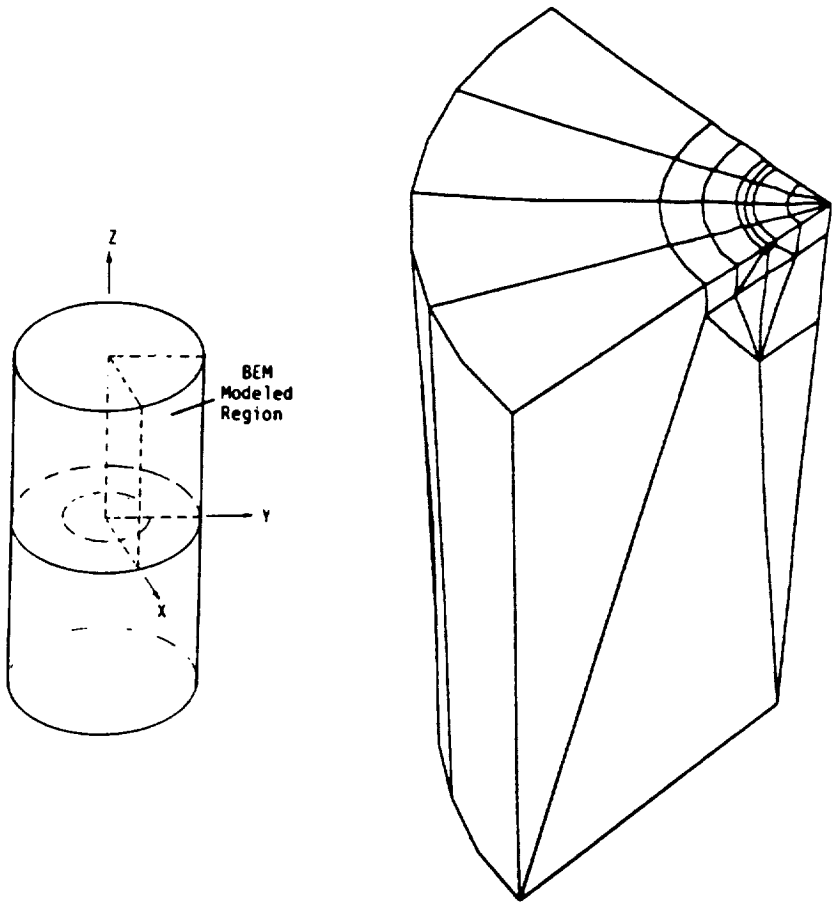

Figure 22. BEM Map for Circular Crack Model

the radius of the sphere using various procedures; the results are essentially identical. The integration times due to various procedures are summarized in Table 13 indicating a slight reduction in computing time using the VR procedure.

Table 13 : Comparison of Integration Procedure for Hollow Sphere

	Integration time CPU (sec)
SD	129
VT	126
VR	116

The cantilever beam model shown in Figure 18 (BEM map 2) fixed at one end and subjected to a shear loading on the other end was run using various integration procedures. The results for normal stress the support short in Figure 21 are essentially identical for different integration procedures. The computing time shown in Table 14 also indicates a small advantage of the VR procedure.

Table 14 : Comparison of Integration Procedure for Cantilever Beam

	Integration time CPU (sec)
SD	185
VR	175

The results using variable transformation procedure for the hollow sphere and cantilever problems does show any substantial saving in computer times since the boundary discretization used in the above models were *regular*, thus, the sub-division requirement is negligible. To see the effect of integration procedures on a graded mesh we analyzed a circular crack model shown in Figure 22. The computing time shown in Table 15 indicates a saving of more than 25 percent using the VR procedure. However, the stress intensity factors shown in Table 15 indicates considerable error using the VR procedure. However, the results using VR procedure also was angularly dependent, thus, they do not meet acceptable accuracy requirements.

Table 15 : Circular Crack Results and Computing Times

	K_I/σ	Integration time CPU (sec)
SD	1.02	959
VR	1.17-1.34	702

Currently, we do not have a way to estimate the error in variable transformation procedures. The variable transformation results, thus, does not seem to be as reliable as the subdivision method as implemented currently.

3.2 Error Tolerance on Efficiency and Accuracy

While the subdivision algorithm implemented in BEST3D indicates high accuracy, the computing time in relation to overall solution time is too high. One factor that dictates the degree of subdivision is integration error tolerance. Here, we investigate the effect of error tolerance on computing time and accuracy. The default value of error tolerance used in BEST3D code is 0.001.

Initially we examined a double notch specimen by changing the error tolerance from 0.001 to 10^6. The results for stress concentration factor and integration time in Table 16 indicates that while the change in stress concentration factor was negligible the computed time was reduced almost by a factor of 2.

Table 16 : Effect of Error Tolerance - Double Notch Model*

	K_T	Integration time CPU (sec)
0.001	7.06	273
0.01	7.06	221
0.1	7.06	185
1	7.06	171
100	7.07	152
10^6	7.08	144

* symmetric faces were modeled

Finally, we analyzed the circular crack model shown in Figure 22. The results in Table 17 again indicate that the value of error tolerance hardly affect the accuracy of the solution but improves the computing time substantially.

Table 17 : Effect of Error Tolerance - Circular Crack

	K_I/σ	Integration time CPU (sec)
0.001	1.02	959
1	1.02	689
1000	1.02	645

4.0 CONCLUDING REMARKS

The boundary element results using BEST3D computer program for the cases tested indicated high accuracy of the code. Some areas of concern detected while running the code are presented with result in Section 2. While the code is efficient for the analysis of bulk structures such as double notch specimen, the efficieny for thin structures such as the turbine blade mode is not very encouraging. It appears that a major area for improvement is the numerical evaluation of discretized integrals. A limited study reported in Section 3 shows that while the subdivision algorithm used in BEST3D code is reliable, it is not very efficient, especially when the default error tolerance is used. A reliable and efficient numerical integration procedure for general three-dimensional boundary integrals is still lacking. Further effort in devising alternative schemes such as a combination of analytical and numerical procedures is desirable.

While the evaluation of discretized integrals is one problem area, it is not the only one. For example, consider the turbine blade model problem examined in Section 2.3. The run time for the model can be divided broadly into three parts (e.g., Case 3.4):

(a) Surface integration time - 718 sec
(b) Initial matrix assembly time - 534 sec
(c) Solution time - 743 sec

In analyzing a thing structure such as turbine blade model, the task of evaluating numerous near singular integrals imposes a heavy burden. In all these analyses, we used the default value for the error tolerance, however, the results reported in Section 3 indicate that the accuracy of the results is

not diminished considerably by the use of higher error tolerance. Thus, the surface integration time may be reduced by using a higher error tolerance than the default value used in Section 2 analyses.

It is also evident that the computing time for matrix assembly and solution is also substantial for a large scale problem such as the turbine blade model. The matrix manipulation involved in these two tasks may be made substantially efficient by rearranging some matrix operation and optimizing the code.

Finally, the BEST3D code used was essentially developed for mini-frame computer, thus, does not take advantage of the architecture of the super computer used for the current run time comparison. Assembly and solution of BEM system can be improved considerably by optimizing the code for CRAY computers. Therefore, an efficient, reliable, and accurate numerical integration procedure as well as optimization of the code are necessary to make a reasonable comparison of general purpose BEM code such as BEST3D to corresponding FEM codes that are specifically tailored for CRAY.

5.0 REFERENCE

[1] Wilson, R. B. and Banerjee, P. K. BEST3D User's Manual, Version 2.0, Prepared for NASA under Contract NAS3-23697 (1987)

[2] MARC Research Corporation. MARC General Purpose Finite Element Program User Manual (1985)

[3] Cruse, T. A. and Cardinal, J. W. User's Manual for BIECRX : A 2-D Fracture Mechanics Deck, SwRI (1983)

[4] Raveendra, S. T. and Cruse, T. A. User's Manual for CRX3D : A 3-D Fracture Mehcanics Program, SwRI (1987)

[5] Mendelson, A. Plasticity, Theory and Application, MacMillan, New York (1968)

[6] Telles, J. C. F. A Self-Adaptive Co-ordinate Transformation for efficient numerical Evaluation of General Boundary Element Integrals, International Journal for Numerical Methods in Engineering, Vol. 24 (1987)

REPORT DOCUMENTATION PAGE

Form Approved
OMB No. 0704-0188

1. AGENCY USE ONLY (*Leave blank*)	2. REPORT DATE	3. REPORT TYPE AND DATES COVERED
	October 1991	Final Contractor Report 4th Annual Report

4. TITLE AND SUBTITLE
Probabilistic Structural Analysis Methods (PSAM) for Select Space Propulsion System Components
(4th Annual Report)

5. FUNDING NUMBERS
WU-553-13-00

6. AUTHOR(S)

7. PERFORMING ORGANIZATION NAME(S) AND ADDRESS(ES)
Southwest Research Institute
6220 Culebra Road
San Antonio, Texas 78284

8. PERFORMING ORGANIZATION REPORT NUMBER
None

9. SPONSORING/MONITORING AGENCY NAMES(S) AND ADDRESS(ES)
National Aeronautics and Space Administration
Lewis Research Center
Cleveland, Ohio 44135-3191

10. SPONSORING/MONITORING AGENCY REPORT NUMBER
NASA CR-187198
SWRI-06-8339

11. SUPPLEMENTARY NOTES
Project Manager, C.C. Chamis, Structures Division, NASA Lewis Research Center, (216) 433-3252.

12a. DISTRIBUTION/AVAILABILITY STATEMENT
Unclassified - Unlimited
Subject Category 39

12b. DISTRIBUTION CODE

13. ABSTRACT (*Maximum 200 words*)

This annual report summarizes the fourth year of technical developments on the NESSUS system for Probabilistic Structural Analysis Methods. The effort focused on the continued expansion of the Probabilistic FEM code, the implementation of the Probabilistic Boundary Element Method (PBEM), and the implementation of the Probabilistic Approximate Methods (PAppM) code. The principal focus for the PFEM code is the addition of a multilevel structural dynamics capability. The strategy includes probabilistic loads, treatment of material, geometry uncertainty, and full probabilistic variables. Enhancements are included for the Fast Probability Integration (FPI) algorithms and the addition of Monte Carlo simulation as an alternate. Work on the expert system and boundary element developments continues. The enhanced capability in the computer codes is validated by applications to turbine blade and to oxidizer duct.

14. SUBJECT TERMS
Computer code; Buckling analysis; Structural dynamics; Time domain; Frequency domain; Probabilistic algorithms; Finite elements; Validation cases; Verification; Approximate analysis; Thermoviscoplasticity

15. NUMBER OF PAGES
382

16. PRICE CODE
A17

17. SECURITY CLASSIFICATION OF REPORT	18. SECURITY CLASSIFICATION OF THIS PAGE	19. SECURITY CLASSIFICATION OF ABSTRACT	20. LIMITATION OF ABSTR
Unclassified	Unclassified	Unclassified	

NASA